



6-2020

Experimental and Numerical Investigation of Free Water Surface Evaporation in Case of Natural Convection

Hassan Fagehi

Western Michigan University, hmmf-987@hotmail.com

Follow this and additional works at: <https://scholarworks.wmich.edu/dissertations>



Part of the Mechanical Engineering Commons

Recommended Citation

Fagehi, Hassan, "Experimental and Numerical Investigation of Free Water Surface Evaporation in Case of Natural Convection" (2020). *Dissertations*. 3581.

<https://scholarworks.wmich.edu/dissertations/3581>

This Dissertation-Open Access is brought to you for free and open access by the Graduate College at ScholarWorks at WMU. It has been accepted for inclusion in Dissertations by an authorized administrator of ScholarWorks at WMU. For more information, please contact wmu-scholarworks@wmich.edu.



EXPERIMENTAL AND NUMERICAL INVESTIGATION OF FREE WATER SURFACE
EVAPORATION IN CASE OF NATURAL CONVECTION

by

Hassan Fagehi

A dissertation submitted to the Graduate College
in partial fulfillment of the requirements
for the degree of Doctor of Philosophy
Mechanical and Aerospace Engineering
Western Michigan University
June 2020

Doctoral Committee:

Parviz Merati, Ph.D., Chair
Tianshu Liu, Ph.D.
Christopher Cho, Ph.D.
Dewei Qi, Ph.D.

Copyright by
Hassan Fagehi
2020

EXPERIMENTAL AND NUMERICAL INVESTIGATION OF FREE WATER SURFACE EVAPORATION IN CASE OF NATURAL CONVECTION

Hassan Fagehi, Ph.D.

Western Michigan University, 2020

Evaporation of water can be considered an essential part of the hydrological cycle. It is important for many technological applications such as industrial cooling towers, air conditioning, solid material drying, distillation, and liquid film cooling. Moreover, the interfacial convection caused by the density gradient belongs to Rayleigh convection, which plays an important role in the evaporation process by means of intensifying heat and mass transfer, as in an isopropanol–water system. In addition, natural convection, which can be defined as a buoyancy-driven flow, is important in astrophysics, geophysics, and numerous engineering applications such as solar energy systems, cooling of electrical equipment, ventilation, and passive cooling in nuclear power plants.

In the current work, an experimental study along with a numerical simulation investigation of free water surface evaporation in case of natural convection is carried out. First, an experiment is conducted to predict Sherwood–Rayleigh correlation for free water surface evaporation in case of natural convection in the range of $1.4 \times 10^9 < Ra < 1.1 \times 10^{11}$, which is based on measuring the room air temperature, the bulk water temperature, the surface temperature, the room relative humidity, and the mass loss due to evaporation. A second experiment is performed utilizing particle image velocimetry (PIV), to investigate the flow pattern in the case of a free surface undergoing evaporation. This investigation of flow pattern is conducted for the side and top of a water tank. In addition, numerical two-dimensional (2-D) and three-dimensional (3-D) simulations are carried

out in order to study the flow pattern along with rise in temperature. As a part of the numerical simulation, a user-defined function (UDF) code is developed and compiled to investigate the surface evaporation. A comparison follows of the numerical simulation and experimental work. Finally, an experiment is implemented using stereo particle image velocimetry (SPIV) to calculate the third velocity component. Subsequently, the effect of the third component on the flow pattern and velocity magnitude is addressed and discussed.

ACKNOWLEDGEMENTS

First and foremost, I would like to especially thank my advisor Prof. Parviz Merati for his guidance, support, and encouragement throughout my work, without which this work would not have been possible. I am very lucky and thankful to have him as my advisor; he is always trying to improve his student's knowledge.

I would also like to extend my thanks to my committee members, Prof. Tianshu Liu, Prof. Chris Cho, and Prof. Dewei Qi, for reviewing my work and for their guidance and suggestions to improve the quality of this work.

I would also like to thank my family, especially my mother, my wife, my daughter, and my son for their support and patience. Their support is a big part of my accomplishment. Also, I thank all my friends and classmates especially Hassan Ghazwani, Mofareh Ghazwani and David Moussa for their support and helpful comments.

Hassan Fagehi

TABLE OF CONTENTS

ACKNOWLEDGEMENTS	ii
LIST OF TABLES	vi
LIST OF FIGURES	vii
NOMENCLATURE	xvi
CHAPTER	
1. INTRODUCTION	1
1.1 Evaporation	1
1.2 Natural Convection.....	3
1.3 Dimensionless Numbers.....	8
1.3.1 Sherwood Number	8
1.3.2 Rayleigh Number	8
1.4 Particle Image Velocimetry (PIV).....	9
1.5 Statistical Calculations	12
1.5.1 Velocity Magnitude	12
1.5.2 Vorticity	13
1.5.3 Turbulent Kinetic Energy	13
1.6 Chapter Conclusion	14
2. LITERATURE SURVEY AND OBJECTIVES OF THE CURRENT STUDY	15
2.1 Literature Survey	15
2.2 Motivation	18
2.3 Objectives of Current Study	20
2.4 Chapter Conclusion	21
3. NUMERICAL SIMULATION.....	22
3.1 Introduction	22
3.2 Governing Equations.....	24
3.3 User-Defined Function (UDF)	28
3.4 Two-Dimensional (2-D) Analysis	29
3.4.1 Geometry and Meshing.....	29

Table of Contents—continued

3.4.2	Results and Discussion	33
3.5	Three-Dimensional (3-D) Analysis	73
3.5.1	Geometry and Meshing.....	73
3.5.2	Results and Discussion	77
3.6	Chapter Conclusion	128
4.	EXPERIMENTAL WORK	129
4.1	Prediction of Sherwood–Rayleigh Correlation	129
4.1.1	Experimental Setup.....	129
4.1.2	Experimental Procedure.....	131
4.1.3	Results and Discussion	134
4.2	Particle Image Velocimetry (PIV) for Water from the Side	144
4.2.1	Experimental Setup.....	144
4.2.2	Experimental Procedure.....	147
4.2.3	Results and Discussion	149
4.3	Particle Image Velocimetry (PIV) for Water from the Top	198
4.3.1	Experimental Setup.....	198
4.3.2	Experimental Procedure.....	199
4.3.3	Results and Discussion	200
4.4	Stereo Particle Image Velocimetry (SPIV)	241
4.4.1	Experimental Setup.....	241
4.4.2	Experimental Procedure.....	242
4.4.3	Results and Discussion	243
4.5	Uncertainty Analysis	262
4.6	Chapter Conclusion	263
5.	COMPARISON OF NUMERICAL SIMULATION AND EXPERIMENTAL WORK....	264
5.1	Temperature Comparison	264
5.2	Velocity Comparison	265
5.3	Chapter Conclusion	267
6.	CONCLUSION	268
	REFERENCES	269

Table of Contents—continued

APPENDICES	273
Appendix A (UDF Code)	274
Appendix B (LabVIEW Window)	276

LIST OF TABLES

1.1	Seeding materials for liquid flows	11
2.1	Summary of previous efforts at investigating the Sh–Ra relation upon undergoing natural convection evaporation.	17
3.1	The 2-D meshing details.	31
3.2	The boundary conditions details.	32
3.3	Fluids' properties.	33
3.4	The 3-D meshing details.	76
4.1	Physical properties of the working fluid (water) at the mean temperature (36.25°C).	134
4.2	The range and accuracy of the measuring devices.	262

LIST OF FIGURES

1.1	Factors affecting evaporation.....	1
1.2	Schematic of the transport processes.	2
1.3	Experimental setup for Rayleigh–Bénard convection.	4
1.4	Experimental setup for particle image velocimetry [30].	11
1.5	Double cavity Nd:YAG PIV-laser [31].	12
2.1	The previous work for Sherwood–Rayleigh correlation.....	20
3.1	CFD overview.....	23
3.2	Regimes of multiphase flow.	24
3.3	2-D CFD geometry.	29
3.4	2-D CFD grid meshing.	30
3.5	Contours of volume fraction of (a) air, (b) water, and (c) vapor.	34
3.6	The three different locations for X–Y plot	36
3.7	Temperature at 2 s (a) Contour, (b) XY plot.	37
3.8	Velocity at 2 s (a) Contour, (b) XY plot.....	38
3.9	Temperature at 1205 s (a) Contour, (b) XY plot.	40
3.10	Velocity at 1205 s (a) Contour, (b) XY plot, (c) Velocity vector in the air domain, (d) Velocity contour in the water domain.....	41
3.11	Vorticity at 1205 s (a) Contour, (b) Vorticity vector in the water domain, (c) XY plot.....	43
3.12	Turbulence kinetic energy at 1205 s (a) Contour, (b) XY plot.....	46
3.13	Surface evaporation at 1205 s (a) Contour, (b) XY plot.....	47
3.14	Temperature at 2350 s (a) Contour, (b) XY plot.	49
3.15	Velocity at 2350 s (a) Contour, (b) Velocity vector in the water domain, (c) XY plot.	50

List of Figures—continued

3.16	Vorticity at 2350 s (a) Contour, (b) Vorticity vector in the water domain, (c) XY plot.	52
3.17	Turbulence kinetic energy at 2350 s (a) Contour, (b) XY plot.....	54
3.18	Surface evaporation at 2350 s (a) Contour, (b) XY plot.....	56
3.19	Temperature at 7200 s (a) Contour, (b) XY plot.	57
3.20	Velocity at 7200 s (a) Contour, (b) Velocity vector in the water domain, (c) XY plot.	59
3.21	Vorticity at 7200 s (a) Contour, (b) Vorticity vector in the water domain, (c) XY plot.	61
3.22	Turbulence kinetic energy at 7200 s (a) Contour, (b) XY plot.....	63
3.23	Surface evaporation at 7200 s (a) Contour, (b) XY plot.....	65
3.24	Temperature at 12925 s (a) Contour, (b) XY plot.	66
3.25	Velocity at 12925 s (a) Contour, (b) Velocity vector in the water domain, (c) XY plot.	67
3.26	Vorticity at 12925 s (a) Contour, (b) Vorticity vector in the water domain, (c) XY plot.	70
3.27	Turbulence kinetic energy at 12925 s (a) Contour, (b) XY plot.....	72
3.28	Surface evaporation at 12925 s (a) Contour, (b) XY plot.....	74
3.29	3-D CFD geometry.	75
3.30	3-D CFD grid meshing.	76
3.31	Contours of volume fraction of (a) air and (b) water.....	78
3.32	The three different locations for contour (a) top view and (b) side view.	79
3.33	The three different locations for X-Y plot.	80
3.34	Temperature at 235 s (a) Contour of the geometry, (b) Contour of the top view sections, (c) Contour of the side view sections, (d) XY plot.	81

List of Figures—continued

3.35	Velocity at 235 s (a) Contour of the geometry, (b) Top view for the tank, (c) Contour of the top view sections, (d) Contour of the side view sections, (e) Contour in the water domain, (f) XY plot.	84
3.36	Turbulence kinetic energy at 235 s (a) Contour of the geometry, (b) Contour of the top view sections, (c) Contour of the side view sections, (d) XY plot.	88
3.37	Vorticity at 235 s (a) Contour of the geometry, (b) Contour of the top view sections, (c) Contour of the side view sections, (d) XY plot.	90
3.38	Temperature at 1180 s (a) Contour of the geometry, (b) Contour of the top view sections, (c) Contour of the side view sections, (d) XY plot.	93
3.39	Velocity at 1180 s (a) Contour of the geometry, (b) Top view for the tank, (c) Contour of the top view sections, (d) Contour of the side view sections, (e) Contour in the water domain, (f) XY plot.	96
3.40	Turbulence kinetic energy at 1180 s (a) Contour of the geometry, (b) Contour of the top view sections, (c) Contour of the side view sections, (d) XY plot.	100
3.41	Vorticity at 1180 s (a) Contour of the geometry, (b) Contour of the top view sections, (c) Contour of the side view sections, (d) XY plot.	102
3.42	Temperature at 3050 s (a) Contour of the geometry, (b) Contour of the top view sections, (c) Contour of the side view sections, (d) XY plot.	105
3.43	Velocity at 3050 s (a) Contour of the geometry, (b) Top view for the tank, (c) Contour of the top view sections, (d) Contour of the side view sections, (e) Contour in the water domain, (f) XY plot.	108
3.44	Turbulence kinetic energy at 3050 s (a) Contour of the geometry, (b) Contour of the top view sections, (c) Contour of the side view sections, (d) XY plot.	112
3.45	Vorticity at 3050 s (a) Contour of the geometry, (b) Contour of the top view sections, (c) Contour of the side view sections, (d) XY plot.	114
3.46	Temperature at 4680 s (a) Contour of the geometry, (b) Contour of the top view sections, (c) Contour of the side view sections, (d) XY plot.	117
3.47	Velocity at 4680 s (a) Contour of the geometry, (b) Top view for the tank, (c) Contour of the top view sections, (d) Contour of the side view sections, (e) Contour in the water domain, (f) XY plot.	120
3.48	Turbulence kinetic energy at 4680 s (a) Contour of the geometry, (b) Contour of the top view sections, (c) Contour of the side view sections, (d) XY plot.	123

List of Figures—continued

3.49	Vorticity at 4680 s (a) Contour of the geometry, (b) Contour of the top view sections, (c) Contour of the side view sections, (d) XY plot.	126
4.1	Schematic of experimental setup.	131
4.2	(a) Photograph of water tank before insulation, (b) Photograph of experimental setup after insulation.	132
4.3	The range of Rayleigh number in the current work versus temperature difference ($^{\circ}\text{C}$) ..	133
4.4	The time traces of the water bulk temperature, ambient temperature, and the water surface temperature for $D = 0.17$ m.	135
4.5	The time traces of the relative humidity for $D = 0.17$ m.	136
4.6	Evaporation mass and evaporation rate versus time for $D = 0.17$ m.	136
4.7	The mass flux versus time for $D = 0.17$ m.	137
4.8	The mass transfer coefficient versus time for $D = 0.17$ m.	138
4.9	The vapor pressure deficit (VPD) versus temperature difference for $D = 0.17$ m.	138
4.10	The time traces of the water bulk temperature, ambient temperature, and the water surface temperature for $D = 0.24$ m.	139
4.11	The time traces of the relative humidity for $D = 0.24$ m.	140
4.12	Evaporation mass and evaporation rate versus time for $D = 0.24$ m.	140
4.13	The mass flux versus time for $D = 0.24$ m.	141
4.14	The mass transfer coefficient versus time for $D = 0.24$ m.	141
4.15	The vapor pressure deficit (VPD) versus temperature difference for $D = 0.24$ m.	142
4.16	The temperature comparison between $D = 0.24$ m and $D = 0.17$ m versus time.	143
4.17	The evaporation rate comparison between $D = 0.24$ m and $D = 0.17$ m versus time.	143
4.18	The comparison of correlation in the current work with the previous work.	145
4.19	Schematic of experimental setup.	146
4.20	Photograph of experimental setup.	147

List of Figures—continued

4.21 Two frames of the row of images at t_i and $t_{i+\Delta t}$ before processing. 149

4.22 (a) Velocity magnitude, (b) XY plot for vertical velocity, (c) XY plot for horizontal velocity at $D = 0.17$ m and $T_b = 28^\circ\text{C}$ 150

4.23 (a) Vorticity magnitude, (b) XY plot for vertical vorticity, (c) XY plot for horizontal vorticity at $D = 0.17$ m and $T_b = 28^\circ\text{C}$ 152

4.24 (a) Turbulent kinetic energy magnitude, (b) XY plot for vertical turbulent kinetic energy, (c) XY plot for horizontal turbulent kinetic energy at $D = 0.17$ m and $T_b = 28^\circ\text{C}$ 154

4.25 (a) Velocity magnitude, (b) XY plot for vertical velocity, (c) XY plot for horizontal velocity at $D = 0.17$ m and $T_b = 38^\circ\text{C}$ 155

4.26 (a) Vorticity magnitude, (b) XY plot for vertical vorticity, (c) XY plot for horizontal vorticity at $D = 0.17$ m and $T_b = 38^\circ\text{C}$ 157

4.27 (a) Turbulent kinetic energy magnitude, (b) XY plot for vertical turbulent kinetic energy, (c) XY plot for horizontal turbulent kinetic energy at $D = 0.17$ m and $T_b = 38^\circ\text{C}$ 160

4.28 (a) Velocity magnitude, (b) XY plot for vertical velocity, (c) XY plot for horizontal velocity at $D = 0.17$ m and $T_b = 46^\circ\text{C}$ 161

4.29 (a) Vorticity magnitude, (b) XY plot for vertical vorticity, (c) XY plot for horizontal vorticity at $D = 0.17$ m and $T_b = 46^\circ\text{C}$ 163

4.30 (a) Turbulent kinetic energy magnitude, (b) XY plot for vertical turbulent kinetic energy, (c) XY plot for horizontal turbulent kinetic energy at $D = 0.17$ m and $T_b = 46^\circ\text{C}$ 165

4.31 (a) Velocity magnitude, (b) XY plot for vertical velocity, (c) XY plot for horizontal velocity at $D = 0.17$ m and $T_b = 50^\circ\text{C}$ 166

4.32 (a) Vorticity magnitude, (b) XY plot for vertical vorticity, (c) XY plot for horizontal vorticity at $D = 0.17$ m and $T_b = 50^\circ\text{C}$ 168

4.33 (a) Turbulent kinetic energy magnitude, (b) XY plot for vertical turbulent kinetic energy, (c) XY plot for horizontal turbulent kinetic energy at $D = 0.17$ m and $T_b = 50^\circ\text{C}$ 170

4.34 (a) Velocity magnitude, (b) XY plot for vertical velocity, (c) XY plot for horizontal velocity at $D = 0.24$ m and $T_b = 28^\circ\text{C}$ 172

List of Figures—continued

4.35	(a) Vorticity magnitude, (b) XY plot for vertical vorticity, (c) XY plot for horizontal vorticity at $D = 0.24$ m and $T_b = 28^\circ\text{C}$.	174
4.36	(a) Turbulent kinetic energy magnitude, (b) XY plot for vertical turbulent kinetic energy, (c) XY plot for horizontal turbulent kinetic energy at $D = 0.24$ m and $T_b = 28^\circ\text{C}$.	176
4.37	(a) Velocity magnitude, (b) XY plot for vertical velocity, (c) XY plot for horizontal velocity at $D = 0.24$ m and $T_b = 38^\circ\text{C}$.	178
4.38	(a) Vorticity magnitude, (b) XY plot for vertical vorticity, (c) XY plot for horizontal vorticity at $D = 0.24$ m and $T_b = 38^\circ\text{C}$.	180
4.39	(a) Turbulent kinetic energy magnitude, (b) XY plot for vertical turbulent kinetic energy, (c) XY plot for horizontal turbulent kinetic energy at $D = 0.24$ m and $T_b = 38^\circ\text{C}$.	182
4.40	(a) Velocity magnitude, (b) XY plot for vertical velocity, (c) XY plot for horizontal velocity at $D = 0.24$ m and $T_b = 46^\circ\text{C}$.	184
4.41	(a) Vorticity magnitude, (b) XY plot for vertical vorticity, (c) XY plot for horizontal vorticity at $D = 0.24$ m and $T_b = 46^\circ\text{C}$.	186
4.42	(a) Turbulent kinetic energy magnitude, (b) XY plot for vertical turbulent kinetic energy, (c) XY plot for horizontal turbulent kinetic energy at $D = 0.24$ m and $T_b = 46^\circ\text{C}$.	188
4.43	(a) Velocity magnitude, (b) XY plot for vertical velocity, (c) XY plot for horizontal velocity at $D = 0.24$ m and $T_b = 50^\circ\text{C}$.	189
4.44	(a) Vorticity magnitude, (b) XY plot for vertical vorticity, (c) XY plot for horizontal vorticity at $D = 0.24$ m and $T_b = 50^\circ\text{C}$.	191
4.45	(a) Turbulent kinetic energy magnitude, (b) XY plot for vertical turbulent kinetic energy, (c) XY plot for horizontal turbulent kinetic energy at $D = 0.24$ m and $T_b = 50^\circ\text{C}$.	194
4.46	Comparison of horizontal velocity near the water–air interface for $T_b = 50^\circ\text{C}$ at $D = 0.17$ m and $D = 0.24$ m.	195
4.47	Comparison of horizontal velocity near the water–air interface for different temperature at $D = 0.17$ m.	196
4.48	Comparison of horizontal velocity near the water–air interface for different temperature at $D = 0.24$ m.	196

List of Figures—continued

4.49	Streamlines for different temperatures at $D = 0.17$ m	197
4.50	Streamlines for different temperatures at $D = 0.24$ m	197
4.51	Schematic of experimental setup.	198
4.52	Photograph of experimental setup.	199
4.53	Two frames of the row of images before processing at t_i and $t(i+\Delta t)$	200
4.54	(a) Velocity magnitude, (b) Surface velocity magnitude, (c) XY plot for velocity at $T_b = 28^\circ\text{C}$	201
4.55	(a) Vorticity magnitude, (b) Surface vorticity magnitude, (c) XY plot for vorticity at $T_b = 28^\circ\text{C}$	203
4.56	(a) TKE magnitude, (b) Surface TKE magnitude, (c) XY plot for TKE at $T_b = 28^\circ\text{C}$	205
4.57	(a) Velocity magnitude, (b) Surface velocity magnitude, (c) XY plot for velocity at $T_b = 38^\circ\text{C}$	207
4.58	(a) Vorticity magnitude, (b) Surface vorticity magnitude, (c) XY plot for vorticity at $T_b = 38^\circ\text{C}$	209
4.59	(a) TKE magnitude, (b) Surface TKE magnitude, (c) XY plot for TKE at $T_b = 38^\circ\text{C}$	211
4.60	(a) Velocity magnitude, (b) Surface velocity magnitude, (c) XY plot for velocity at $T_b = 48^\circ\text{C}$	213
4.61	(a) Vorticity magnitude, (b) Surface vorticity magnitude, (c) XY plot for vorticity at $T_b = 48^\circ\text{C}$	215
4.62	(a) TKE magnitude, (b) Surface TKE magnitude, (c) XY plot for TKE at $T_b = 48^\circ\text{C}$	216
4.63	(a) Velocity magnitude, (b) Surface velocity magnitude, (c) XY plot for velocity at $T_b = 50^\circ\text{C}$	218
4.64	(a) Vorticity magnitude, (b) Surface vorticity magnitude, (c) XY plot for vorticity at $T_b = 50^\circ\text{C}$	220
4.65	(a) TKE magnitude, (b) Surface TKE magnitude, (c) XY plot for TKE at $T_b = 50^\circ\text{C}$	222

List of Figures—continued

4.66	(a) Velocity magnitude, (b) Surface velocity magnitude, (c) XY plot for velocity at $D = 0.07$ m	224
4.67	(a) Vorticity magnitude, (b) Surface vorticity magnitude, (c) XY plot for vorticity at $D = 0.07$ m	226
4.68	(a) TKE magnitude, (b) Surface TKE magnitude, (c) XY plot for TKE at $D = 0.07$ m	228
4.69	(a) Velocity magnitude, (b) Surface velocity magnitude, (c) XY plot for velocity at $D = 0.14$ m	230
4.70	(a) Vorticity magnitude, (b) Surface vorticity magnitude, (c) XY plot for vorticity at $D = 0.14$ m	232
4.71	(a) TKE magnitude, (b) Surface TKE magnitude, (c) XY plot for TKE at $D = 0.14$ m	234
4.72	(a) Velocity magnitude, (b) Surface velocity magnitude, (c) XY plot for velocity at $D = 0.21$ m	236
4.73	(a) Vorticity magnitude, (b) Surface vorticity magnitude, (c) XY plot for vorticity at $D = 0.21$ m	238
4.74	(a) TKE magnitude, (b) Surface TKE magnitude, (c) XY plot for TKE at $D = 0.21$ m	239
4.75	Schematic of the experimental setup	241
4.76	Photograph of the experimental setup	242
4.77	Schematic of the SPIV self-calibration [47].....	244
4.78	Two frames of the row images for each camera before processing at t_i and $t(i+\Delta t)$	244
4.79	(a) Velocity magnitude for all three components, (b) Velocity V_x , (c) Velocity V_y , (d) Velocity V_z at $T_b = 28^\circ\text{C}$	246
4.80	(a) XY plot for vertical velocity magnitude for all three components, (b) XY plot for horizontal velocity magnitude for all three components at $T_b = 28$	248
4.81	(a) Comparison of vertical velocity magnitude for three components and two components, (b) Comparison of horizontal velocity magnitude for three components and two components at $T_b = 28$	249
4.82	3-D plot for velocity magnitude and direction.....	250

List of Figures—continued

4.83	(a) Velocity magnitude for all three components, (b) Velocity V_x , (c) Velocity V_y , (d) Velocity V_z at $T_b = 38^\circ\text{C}$	252
4.84	(a) XY plot for vertical velocity magnitude for all three components, (b) XY plot for horizontal velocity magnitude for all three components, at $T_b = 38$	254
4.85	(a) Comparison of vertical velocity magnitude for three components and two components, (b) Comparison of horizontal velocity magnitude for three components and two components, at $T_b = 38$	255
4.86	3-D plot for velocity magnitude and direction.....	256
4.87	(a) Velocity magnitude for all three components, (b) Velocity V_x , (c) Velocity V_y , (d) Velocity V_z at $T_b = 50^\circ\text{C}$	258
4.88	(a) XY plot for vertical velocity magnitude for all three components, (b) XY plot for horizontal velocity magnitude for all three components at $T_b = 50$	260
4.89	(a) Comparison of vertical velocity magnitude for three components and two components, (b) Comparison of horizontal velocity magnitude for three components and two components at $T_b = 50$	261
4.90	3-D plot for velocity magnitude and direction.....	262
5.1	The comparison of temperature development in the water tank for numerical simulation and experimental work versus time	265
5.2	The comparison of the horizontal velocity near the water–air surface for numerical simulation and experimental work.....	266
5.3	The comparison of velocities from both numerical simulation and experimental work	266

NOMENCLATURE

T_b	Water bulk temperature
T_s	Surface temperature
T_∞	Ambient temperature
ΔT	Temperature difference
\dot{m}''	Evaporation rate
\bar{u}	Average wind speed
p_s	Vapor pressure at the water surface
p_∞	Pressure at the air side
$f(\bar{u})$	Wind speed function
q_1	Convective heat flux
h_t	Heat transfer coefficient
Sh	Sherwood number
Sc	Schmidt number
Ra	Rayleigh number
\mathcal{D}	Diffusion coefficient
ν	Kinematic viscosity
μ	Viscosity
Nu	Nusselt number
h_m	Mass transfer coefficient
W	Characteristic length

Nomenclature—continued

$\Delta\rho$	Density differences
\emptyset	Humidity
$\bar{\rho}$	Average moist air density
Pr	Prandtl number
D	Depth of water
β	Volumetric expansivity
α	Thermal diffusivity
g	Gravity
A	Area
V	Velocity
$\vec{\omega}$	Vorticity
k	Turbulent kinetic energy

Subscripts

b	bulk
s	surface
∞	ambient
w	water
v	vapor
x	x-direction
y	y-direction
z	z-direction

1. INTRODUCTION

1.1 Evaporation

Evaporation of water can be considered to be an essential part of the hydrological cycle. Evaporation is the process that occurs on the surface, where the liquid changes to gaseous state after reaching a specific temperature. Moreover, evaporation can occur by the transfer of heat energy even below the boiling point. Evaporation is a critical process for many engineering applications such as distillation, industrial cooling towers, and air conditioning. Water temperature, wind pressure, and humidity are some factors that affect evaporation, as can be seen in Figure 1.1.

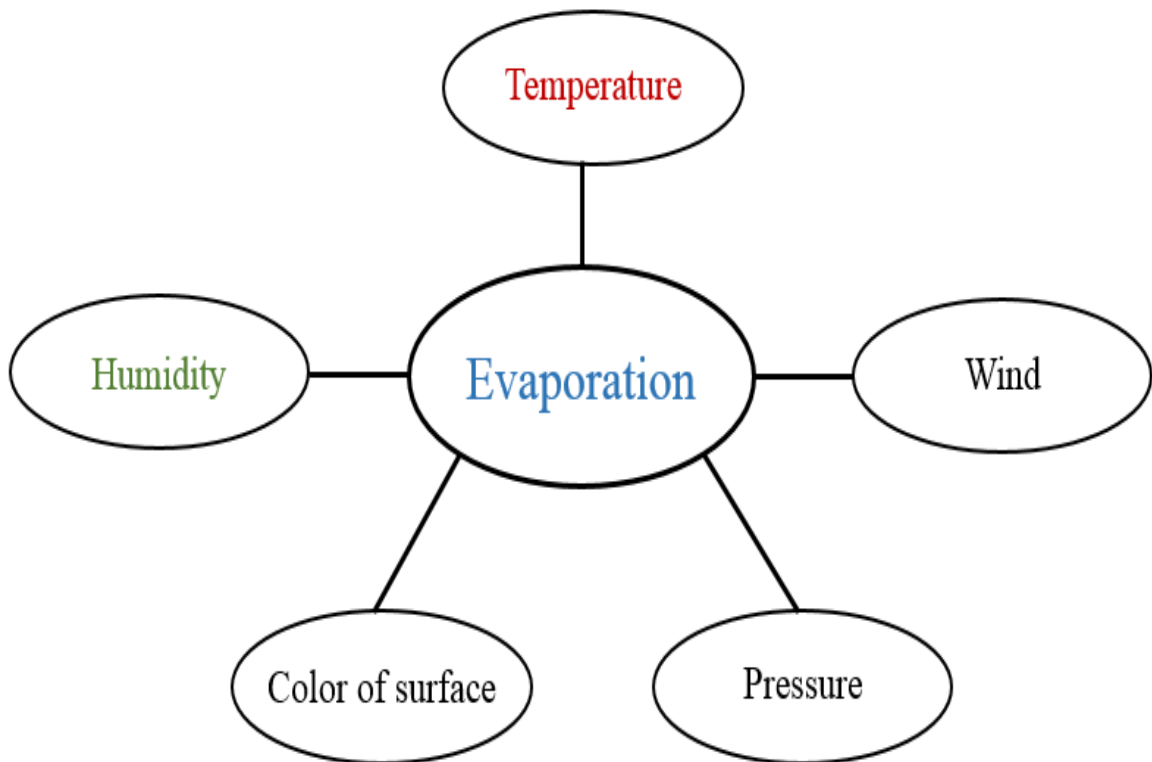


Figure 1.1: Factors affecting evaporation.

According to the kinetic theory of evaporation, molecules of water are in a constant state of random motion, colliding with one another, and rebounding in the liquid state. The molecules

can be held in balance by cohesive force. The gaseous molecules can be created when some of these molecules gain sufficient kinetic energy to overcome this cohesive force and break down from the water surface [1]. In case of a heated body, the bulk water temperature becomes higher than the air temperature. Hence, the evaporation into the surrounding air by natural convection will start at the surface. Due to the evaporation cooling of the air and water interface, the surface temperature will be less than the bulk water temperature. As a result of the temperature difference, the buoyancy process occurs in the water, where it is indicated as evaporative convection [2]. This can be seen schematically in Figure 1.2.

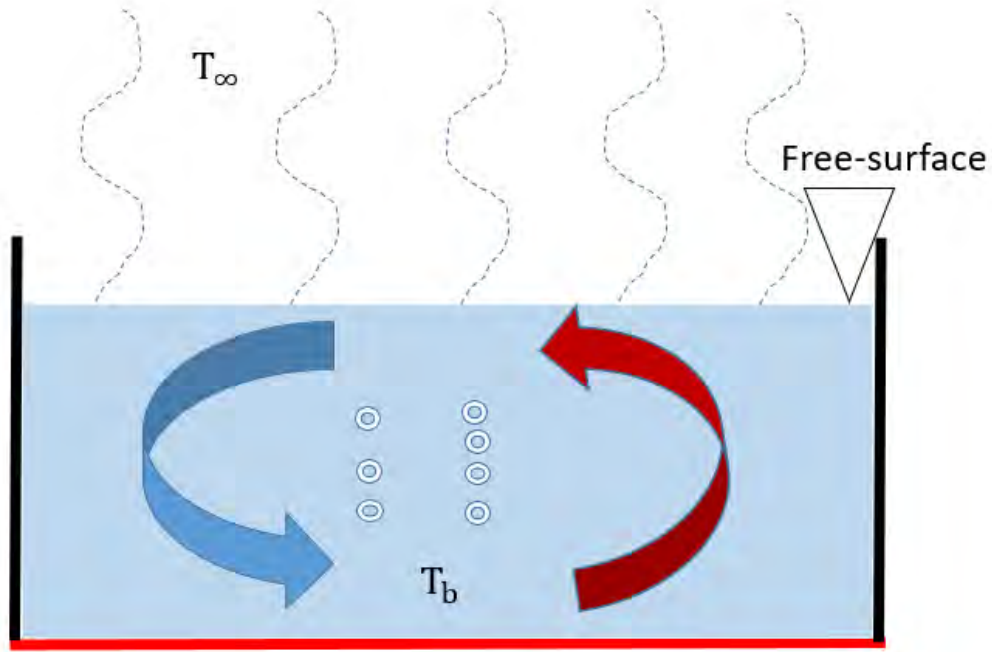


Figure 1.2: Schematic of the transport processes.

In other words, once the water surface cools, it becomes denser and descends through the bulk layer towards the bottom where the warmer fluid rises through the bulk towards the surface. Moreover, a buoyant plume structure forms at the interface with the air due to two factors: (i) the surface temperature is higher than the bulk temperature, and (ii) the relatively high concentration of water vapor at the surface makes the air/vapor mixture there less dense than the surrounding air.

Many studies have been conducted to estimate the evaporation rate. Sartori [3] explained that empirical relationships from some of the studies produce a scattering of evaporation estimates about $40\text{mg}/\text{m}^2\text{s} < \dot{m}'' < 300\text{mg}/\text{m}^2\text{s}$, which relates to the inability of these equations to predict the relevant physical processes that drive evaporation. Some of these studies [4] [5] [6] [3] [7] describe evaporation as a function of the vapor pressure at the water surface, the pressure at the air, and the average wind speed, as

$$\dot{m}'' = f(\bar{u})(p_s - p_\infty) \quad (1.1)$$

where \dot{m}'' is the evaporation rate, \bar{u} is the average wind speed, p_s is the vapor pressure at the water surface, and p_∞ is the pressure at the air.

As recommended by [6], the wind speed function $f(\bar{u})$ can be given as

$$f(\bar{u}) = a + b\bar{u} \quad (1.2)$$

where a and b are fitting constants that can be obtained from data. Note that the above equation cannot precisely predict the evaporation rate for low speed wind or absence of wind, which is a natural convection process [8] [9].

1.2 Natural Convection

Convection can be classified into three categories based on the mechanism of heat transfer, such as natural, mixed, or forced convection. Regardless of these three categories, the convection process can be given by

$$q_1 = \frac{h_t}{\Delta T} \quad (1.3)$$

where q_1 is the convective heat flux, ΔT is the temperature difference, and h_t is the heat transfer coefficient.

The investigation of natural convection started with the work of Rayleigh [10] and Bénard [11]. Rayleigh–Bénard convection can be represented by two isothermal plates maintained at different temperatures, as shown in Figure 1.3. The fluid layer is cooled from above and heated from below in order to produce a fixed temperature difference. This results in buoyant instability due to the density gradient in the fluid layer.

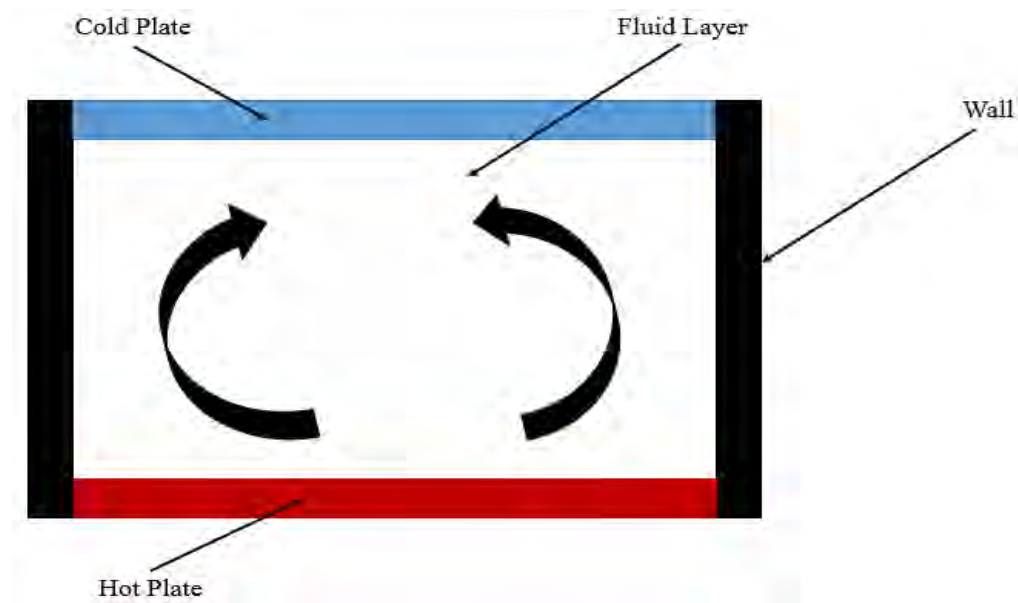


Figure 1.3: Experimental setup for Rayleigh–Bénard convection.

One dimensionless coefficient of mass transfer is the Sherwood number, which is related to natural convection in the air, along with the Rayleigh number. By using the power law,

$$Sh = C \cdot Sc^x Ra_a^n \quad (1.4)$$

where Sh is Sherwood number, C the coefficient, Sc the Schmidt number, x and n are the power law exponents, and Ra_a is the Rayleigh number.

The Schmidt number can be defined as

$$Sc = \frac{\nu}{\mathcal{D}} = \frac{\mu}{\mathcal{D}\rho} \quad (1.5)$$

where ν and \mathcal{D} are the kinematic viscosity and diffusion coefficient respectively, and μ is the viscosity of the fluid. The Sherwood number or the dimensionless mass transfer coefficient can be given as

$$Sh = \frac{h_m W}{\mathcal{D}} \quad (1.6)$$

where Sh is the Sherwood number, h_m the mass transfer coefficient, W the characteristic length, and \mathcal{D} the diffusion coefficient for water vapor in air.

The mass transfer coefficient can be defined as

$$h_m = \frac{\dot{m}''}{\Delta\rho_{wv}} \quad (1.7)$$

where $\Delta\rho_{wv}$ is the difference of water vapor density between the immediate surface region and the ambient air, which can be given as

$$\Delta\rho_{wv} = \rho_{wv}^{sat}(T_s) - \phi\rho_{wv}^{sat}(T_\infty) \quad (1.8)$$

where $\rho_{wv}^{sat}(T_s)$ is the saturation density of water vapor at the surface temperature, $\rho_{wv}^{sat}(T_\infty)$ is the saturation density of water vapor at the ambient temperature, and ϕ is the ambient relative humidity.

Now, the Rayleigh number can be defined as

$$Ra_a = \frac{g\Delta\rho W^3}{\bar{\rho}\nu\alpha} = \frac{g\Delta\rho W^3}{\bar{\rho}\nu^2} Pr \quad (1.9)$$

where g is the gravitational acceleration, $\Delta\rho$ is the density difference, $\bar{\rho}$ is the average moist air density, ν is the kinematic viscosity, and α is the thermal diffusivity of air.

The density difference and the average moist air density are defined respectively as

$$\Delta\rho = \rho_\infty - \rho_s \quad (1.10)$$

$$\bar{\rho} = \frac{\rho_\infty + \rho_s}{2} \quad (1.11)$$

where ρ_{∞} is the density of vapor mixture in the ambient air and ρ_s is the density of vapor mixture at the surface. Note that $\Delta\rho$ and $\Delta\rho_{wv}$ are different, where $\Delta\rho$ is the air/water vapor mixture density difference and $\Delta\rho_{wv}$ is the water vapor density difference.

Moreover, the Rayleigh number was defined by Goldstein et al. [12], Lloyd et al. [13], and Sparrow et al. [14] as follows

$$Ra_L = \frac{g\Delta\rho L^3}{\bar{\rho}vD} = \frac{g\Delta\rho L^3}{\bar{\rho}v^2} Sc \quad (1.12)$$

where L is the characteristic length. Note that the above equation cannot be used in case the buoyancy is dissipated by thermal and viscous diffusion. Therefore, Equation (1.9) will be used in this situation.

In addition, in the case of the intensity of the buoyancy-driven flow and the resulting heat transfer, the dimensionless relation can be defined in terms of the Nusselt number and Rayleigh number as

$$Nu = B \cdot Pr^y \cdot Ra_w^n \quad (1.13)$$

where Nu is the Nusselt number, B a coefficient, y and n are the power law exponents, and Pr is the Prandtl number.

The Prandtl number can be given by

$$Pr = \frac{\nu}{\alpha} \quad (1.14)$$

where ν and α are the kinematic viscosity and thermal diffusivity respectively of the fluid.

The Nusselt number can be defined as

$$Nu = \frac{hD}{k} \quad (1.15)$$

where h is the heat transfer coefficient, D is the depth of the fluid layer, and k is the thermal conductivity of the fluid. The heat transfer coefficient is given by

$$h = \frac{q''}{\Delta T} \quad (1.16)$$

where q'' is the convective heat flux, and ΔT is the temperature difference which can be given as

$$\Delta T = T_b - \bar{T}_s \quad (1.17)$$

where T_b and \bar{T}_s are the water bulk temperature and the average surface temperature, respectively.

In order to measure the thermal instability causing a buoyant flow within the fluid, the Rayleigh number is defined as

$$Ra_w = \frac{\beta g \Delta T D^3}{\nu \alpha} \quad (1.18)$$

where β is the volumetric expansivity of the fluid.

It is important to note that the Schmidt number defined in Eq. (1.5) and the power law in Eq. (1.4) can be used to calculate the diffusive properties of the evaporating fluid. This can be considered when comparing the evaporative behavior of different fluids. In the current study, water is the only fluid where the power law in Eq. (1.4) is not considered. Hence, the power law in Eq. (1.4) can be rewritten as

$$Sh = B Sc^{1/3} Ra_a^n \quad (1.19)$$

where B is the Sherwood–Rayleigh power law prefactor. In the current work, the Schmidt number will be considered as practically constant throughout the experiments, based on previous research work. Moreover, the result can be compared with other fluids where the dependence of Schmidt number is considered.

1.3 Dimensionless Numbers

1.3.1 Sherwood Number

The Sherwood number (also called the mass transfer Nusselt number) is a ratio of convective to diffusive mass transport and can be determined from the measured data using Eq. (1.6). The Sherwood number is an analogue of Nusselt number in heat transfer, which is Nusselt number for mass transfer. As the Sherwood number is an analogue of Nusselt number, it is important to know the basics of it. The Nusselt number (Nu) is the ratio of convective to conductive heat transfer across the boundary, where convection includes both advection and diffusion. By considering Fourier's law

$$q = -kA\nabla T \quad (1.20)$$

where k is thermal conductivity, T the temperature of the fluid, and A the area. It is known that

$$\nabla' = L\nabla \quad (1.21)$$

and

$$T' = \frac{T - T_h}{T_h - T_c} \quad (1.22)$$

From the above three equations, the following equation can be derived

$$-\nabla' T' = \frac{L}{kA(T_h - T_c)} q = \frac{hL}{k} \quad (1.23)$$

Hence, the Nusselt number can be defined as

$$Nu = \frac{hL}{k} \quad (1.24)$$

1.3.2 Rayleigh Number

The Rayleigh number is associated with buoyancy-driven flow, also known as free convection or natural convection. Once the Rayleigh number is below a critical value for the fluid, heat transfer is primarily in the form of conduction. On the other hand, when it exceeds the critical value, heat

transfer is primarily in the form of convection. The Rayleigh number is a product of two dimensionless numbers, the Grashof number and the Prandtl number. The Grashof number and the Prandtl number describe the relationship between buoyancy and viscosity within a fluid and the relationship between momentum diffusivity and thermal diffusivity, respectively. Temperature and concentration differences occur between the surface of the water and the air. The evaporation process causes the vapor concentration to be highest and the temperature to be lowest at the water surface. As a result, the density difference between the air-water vapor mixture at the surface of the water and in the air stream results in natural convection, which can be quantified by the Rayleigh number as given by Eq. (1.9). Moreover, the Rayleigh number can be used to show the presence and strength of convection in a fluid body, as defined in Eq. (1.18).

1.4 Particle Image Velocimetry (PIV)

The first definition of particle image velocimetry (PIV) can be traced back more than 100 years to Ludwig Prandtl who developed and used flow measurement techniques in a water channel with a suspension of mica particles [15]. In 1977, feasibility of laser speckle velocimetry (LSV) in laminar tube flow was demonstrated [16] [17]. However, the name particle image velocimetry (PIV) was introduced in 1984 [18], in a scientific paper which claimed that the LSV mode of low seeding density should be classified more properly as PIV [19]. The technique became popular because it offered a new and quite promising way of studying the fluid flow structure. Moreover, some researchers have developed PIV to improve the efficiency of optical and digital methods in the assessment of PIV recordings [20] [21]. However, the major improvement in PIV was the use of a cross-correlation CCD camera in synchronization with a double oscillator Nd:YAG laser source [22].

Fluid flow velocity can be measured by using different methods, either direct or indirect. The direct methods contain probes that are placed directly in the fluid flow and measure the

velocity at a single point, such as the Pitot tube and the hot-wire probe. On the other hand, the indirect methods such as laser Doppler anemometry (LDA) and particle image velocimetry (PIV) do not disturb the fluid flow. However, the first concept of particle image velocimetry (PIV) goes back over a hundred years to Ludwig Prandtl who designed and used flow measurement techniques with a suspension of mica particles in a water channel [23] [24]. Particle image velocimetry (PIV) includes flow measuring techniques that record the displacement of small particles in a particular region of a fluid [25] [26].

The experimental setup of a particle image velocimetry system typically includes five subsystems, which are the flow test rig, seeding particles, pulsed laser system with light sheet optics, CCD digital camera system, and data acquisition and processing software [27]. To elaborate, the seeding particles must be illuminated along with the flow at least twice within a short period of time. Moreover, the light scattered by the particles must be recorded either on a single frame or on a double frame. Post-processing is needed in order to handle the large volume of data which can be collected. Setup for PIV is shown in Figure 1.4, where the small tracer particles are added to the flow assuming that the tracer particles move with the flow velocity between the two illuminations. The light sheet along with the flow is illuminated twice by using a laser, where the time delay between pulses depends on the mean flow velocity and the magnification at imaging [28]. Some of the different particles which can be used for PIV flow measurement within liquid are listed in Table 1.1 [29].

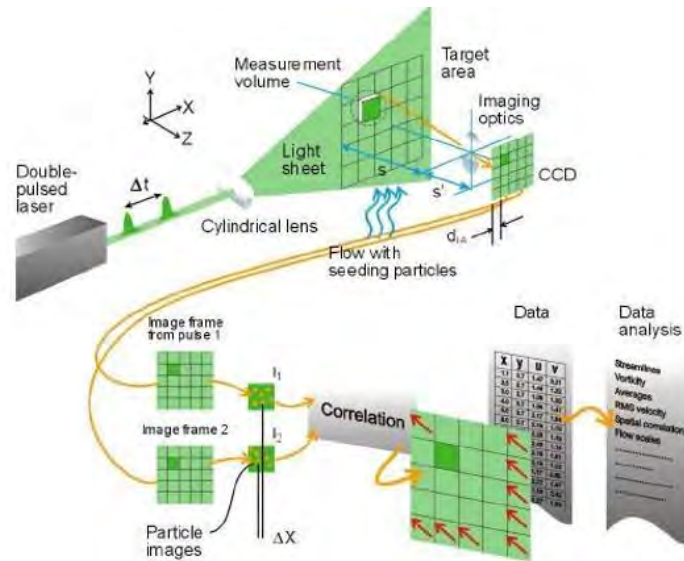


Figure 1.4: Experimental setup for particle image velocimetry [30].

Table 1.1: Seeding materials for liquid flows.

Type	Material	Mean diameter in μm
Solid	Polystyrene	10 – 100
	Aluminum flakes	2 – 7
	Hollow glass sphere	10 – 100
	Granules for synthetic coating	10 – 500
Liquid	Different oil	50 – 500
Gaseous	Oxygen bubbles	50 – 1000

Lasers are widely used in PIV technique due to their ability to emit monochromatic light with high energy density, which can easily be bundled into thin light sheets to illuminate and record the tracer particles. PIV can be used along with either continuous wave lasers or pulsed lasers. The pulsed lasers are frequency-doubled Nd: YAG (neodymium: yttrium aluminum garnet) lasers

producing 0.1 to 0.3 joules/pulse, at a repetition rate of tens of Hz, as can be seen in Figure 1.5. The advantage of pulsed lasers is that the laser pulse has a short duration. A delay box that produces trigger signals must be used to ensure that the lasers, camera, and computer are synchronized. However, once two lasers are used, extreme care must be exercised to ensure that the two laser sheets overlap exactly inside the test-section, because the lack of this overlap can lead to poor correlation and unsatisfactory results.

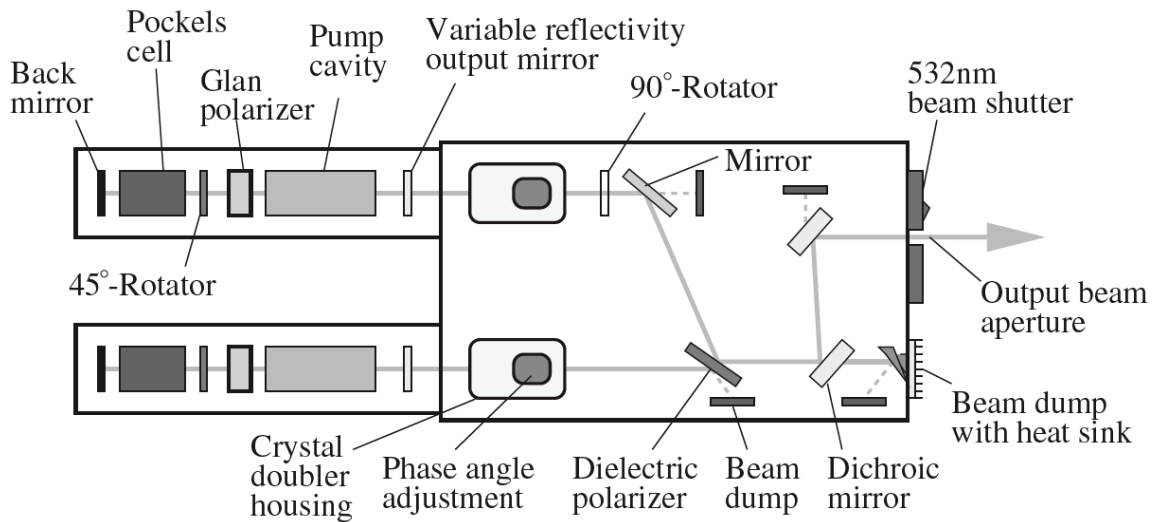


Figure 1.5: Double cavity Nd:YAG PIV-laser [31].

1.5 Statistical Calculations

1.5.1 Velocity Magnitude

In order to calculate the velocity magnitude of the two component and three component velocity field, V , Eq. (1.25) and Eq. (1.26) are used

$$V = (V_x^2 + V_y^2 + V_z^2)^{0.5} \quad (1.25)$$

$$V = (V_x^2 + V_y^2)^{0.5} \quad (1.26)$$

where V is the velocity magnitude, V_x represents x component of the velocity, V_y the y component of the velocity, and V_z the z component of the velocity.

1.5.2 Vorticity

Vorticity is the local rotation of a fluid element about an axis, and is defined as the curl of the velocity field as it flows

$$\vec{\omega} = \nabla \times \vec{u} \quad (1.27)$$

Which can be expanded for

$$\vec{\omega} = \left(\frac{\partial w}{\partial x} - \frac{\partial v}{\partial z} \right) i + \left(\frac{\partial u}{\partial z} - \frac{\partial w}{\partial x} \right) j + \left(\frac{\partial v}{\partial x} - \frac{\partial u}{\partial y} \right) k \quad (1.28)$$

which can be reduced into the following for the two-dimensional plane

$$\omega = \left(\frac{\partial v}{\partial x} - \frac{\partial u}{\partial y} \right) \quad (1.29)$$

where ω is the vorticity.

1.5.3 Turbulent Kinetic Energy

The turbulent kinetic energy, k , is the kinetic energy per unit mass of the turbulent fluctuations in a turbulent flow as given by

$$k = \frac{1}{2} (\overline{uu} + \overline{vv}) \quad (1.30)$$

where u and v represent the velocity fluctuations in the x and y direction, respectively, which are calculated using Reynolds decomposition as defined in Eq. (1.31) and Eq. (1.32) below, where the tilde represents the instantaneous components (\tilde{u} , \tilde{v}) and the capital letter represents the time-average components (U , V).

$$u = \tilde{u} - U \quad (1.31)$$

$$v = \tilde{v} - V \quad (1.32)$$

1.6 Chapter Conclusion

The concepts of evaporation and natural convection have been discussed in this chapter, which will be helpful to understand the fundamentals of this topic. Some measurement techniques used in the experimental work are also explained. Moreover, some of the important factors are defined, and can be used in the current study. In the following chapter, the background of free water surface evaporation in case of natural convection and the related previous work are studied and investigated in order to define the objectives and direction of the current study.

2. LITERATURE SURVEY AND OBJECTIVES OF THE CURRENT STUDY

2.1 Literature Survey

Research investigating free water surface evaporation in the case of natural convection either experimentally or numerically is limited. In 1938, Sharpley et al. [30] studied evaporation from water in a heated circular pan into quiet air. The temperature limit was in the range of 63 to 93° F. The diameter of the pan was one foot and it was 6 inches deep. Relative humidity was 50 to 54%. An electrical heating element was placed below the evaporation pan to supply thermal energy to the water. It was concluded that the Sherwood–Rayleigh relation can be given by

$$Sh = 1.254Sc^{1/3}Ra^{0.213} \quad (2.1)$$

Later on, the same group [31] used the same experimental facility to study the evaporation of heated water using a one-foot pan. As a result, the Sherwood–Rayleigh relation was defined as

$$Sh = 4.687Sc^{1/3}Ra^{0.121} \quad (2.2)$$

In 1973, Goldstein et al. [12] experimentally investigated the sublimation of naphthalene due to natural convection. Circular, square, and rectangular planforms were used in these tests. By using characteristic lengths equal to the ratio of the surface area to the perimeter, a common correlation for all three planforms was predicted. The characteristic lengths were defined as

$$L^* = \frac{A}{P} \quad (2.3)$$

where A is the surface area for planform and P is the perimeter. Although the experiment was not for water, it still studies mass transfer due to natural convection, which can be related to this work. As a result, the Sherwood–Rayleigh relation determined was

$$Sh = 0.435Sc^{1/3}Ra^{0.250} \quad (2.4)$$

One year later, Lloyd and Moran [13] studied the mass transfer of copper ions into a liquid solution due to natural convection, using electrochemical techniques. Moreover, the characteristic lengths were used here as well. The equation obtained for the Sherwood–Rayleigh relation was

$$Sh = 0.038Sc^{1/3}Ra^{0.255} \quad (2.5)$$

In 1983, Sparrow et al. [14] investigated evaporation by using a series of water-filled pans in a cork-lined room. In this experiment, the temperature of the air was higher than the temperature of the water, so the buoyancy driven was downward flow. Circular pans ranging in diameter from 8.9 to 30.7 cm were used in the experiment. As a result, the authors came up with an equation for Sherwood–Rayleigh relation as

$$Sh = 0.764Sc^{1/3}Ra^{0.205} \quad (2.6)$$

In 2009, Bower et al. [32] experimentally studied evaporation due to natural convection by using a heated water tank. Evaporation rates, the relevant temperatures, and the relative humidity were measured. The experiment was conducted using insulated glass tanks which were different in depth or width. Water was heated to a particular temperature and then allowed to cool down, which can cause an unstable temperature gradient along with convection. The air-side Sherwood and Rayleigh numbers were obtained and compared to previous work. In addition, they also briefly discussed the possible effect of water-side natural convection on evaporation. The Sherwood–Rayleigh relation found was as follows

$$Sh = 0.230Sc^{1/3}Ra^{0.321} \quad (2.7)$$

In 2015, Kumar et al. [33] investigated the evaporation caused by natural convection for a heated water tank. The water tank was insulated, with the water temperature being higher than the ambient temperature. Actually, three different temperature profiles were used: water heated from below, water left to cool after being heated, water heated from above by using an IR heater, and

water heated from above in a very shallow tank. Evaporation rates were measured using a high precision balance. The water and ambient temperatures were measured along with the water surface temperature. A thermal camera was used to monitor the water surface temperature. An immersion heater was used to heat a glass tank that had dimensions of 18x18x10 cm. The authors concluded that the Sherwood number along with the same Rayleigh number showed a difference of 2–10 % in the case of heating from above and below. The Sherwood–Rayleigh relation found was as follows

$$Sh = 0.313Sc^{1/3}Ra^{0.292} \quad (2.8)$$

Note that the characteristic length as defined in Eq. (1.22) was used in references 6 to 8 as shown in Table 2.1.

Table 2.1: Summary of previous efforts at investigating the Sh–Ra relation upon undergoing natural convection evaporation.

$Sh = BSc^{1/3}Ra^n$				
Reference	Sc	B	n	Ra
1.Sharpley et al. [30]	0.6	1.057	0.213	$10^6 < Ra < 4.5 \times 10^7$
2.Sharpley et al. [31]	0.6	0.645	0.241	$9.3 \times 10^6 < Ra < 4.5 \times 10^7$
3.Sparrow et al. [14]	0.6	0.764	0.205	$-6 \times 10^5 < Ra < -2 \times 10^4$
4.Bower et al. [32]	0.6	0.230	0.321	$9.6 \times 10^5 < Ra < 5.7 \times 10^8$
5.Kumar et al. [33]	0.6	0.313	0.292	$10^4 < Ra < 1.5 \times 10^7$
6.Goldstein et al. [12]	2.5	0.435	0.250	$2 \times 10^2 < Ra_{L^*} < 5 \times 10^3$
7.Lloyd and Moran [13]	2200	0.038	0.255	$2 \times 10^4 < Ra_{L^*} < 8 \times 10^6$
8.Bower et al. [32]	0.6	0.196	0.322	$2 \times 10^4 < Ra_{L^*} < 9 \times 10^6$

Some of the research in the literature focuses on studying Rayleigh convection, where the particle image velocimetry technique is involved. However, none of these studies reflect a comprehensive study of the flow pattern in case of a free water surface undergoing evaporation. In 2014, Chen et al. [34] conducted an experiment to investigate the velocity distribution in Rayleigh convection that was caused by acetone volatilization in acetone-ethyl acetate binary system. As a result of particle image velocimetry (PIV), the enhancement factor of mass transfer increases with the Ra number and Re_G number. In addition, the mass transfer coefficient can be increased up to four-fold by Rayleigh convection. Moreover, by fitting the experimental data, a new correlation for the estimation of the mass transfer coefficient was proposed.

In 2008, Buffone et al. [35] experimentally studied evaporation driven convection underneath a meniscus (liquid–vapor interface) formed in a vertically oriented capillary tube. The convective structure was detected by using a μ -PIV technique. Moreover, an IR camera was used to measure temperature gradients that were generated by the heater along the capillary wall and along the liquid–vapor interface. The study concluded that the meniscus interfacial temperature profile is key for the onset of thermocapillary convection which is observed experimentally. In 2007, Corvaro et al. [36] conducted a numerical and experimental analysis that was performed to study the natural convection heat transfer in a square cavity heated from below and cooled by the sidewalls. Particle image velocimetry (PIV) was used to measure the velocity fields at the same Rayleigh numbers (air was used as the working fluid).

2.2 Motivation

Free water surface evaporation in case of natural convection has been the subject of investigation for many years. Study of this topic is important from the practical and industrial points of view; the interest is justified by its many applications. The storage of fresh water for

human use and consumption, agricultural irrigation, and large-scale power generation are also dependent on this transport process. Moreover, evaporation is critical for many engineering applications such as industrial cooling towers, air conditioning, solid material drying, distillation, and liquid film cooling. However, it is clear that the number of studies of Sherwood–Rayleigh correlation for natural convection undergoing evaporation in the case of a free water surface is limited. Moreover, a review of the previous work shows a lot of variation, as indicated in the last section, which can affect the prediction for water evaporation in the case of natural convection, especially at a high Rayleigh number. This variation at a high Rayleigh number can be clarified by plotting the previous correlations as shown in Figure 2.1. However, as can be seen in Table 2.1, Rayleigh number for all the work that has been done is less than 10^8 . In the current work, therefore, the Rayleigh number is higher than the previous work ($1.4 \times 10^9 < Ra < 1.1 \times 10^{11}$), so as to cover this range of Rayleigh number. In addition, none of the studies conducted in the past reported a correlation at a Rayleigh number in the range of ($1.4 \times 10^9 < Ra < 1.1 \times 10^{11}$) along with numerical and experimental investigation for evaporation effects on the water flow pattern. Also, the effect of water tank depth on the natural convection evaporation is investigated here, which can be considered as one of the motivations for the current work. Moreover, none of the studies have addressed the effect of the third component of the flow pattern, as done in the current case, which is considered here by involving stereo particle image velocimetry (SPIV). Hence, the current work conducts numerical and experimental investigation along with predicting a new correlation at higher Rayleigh number.

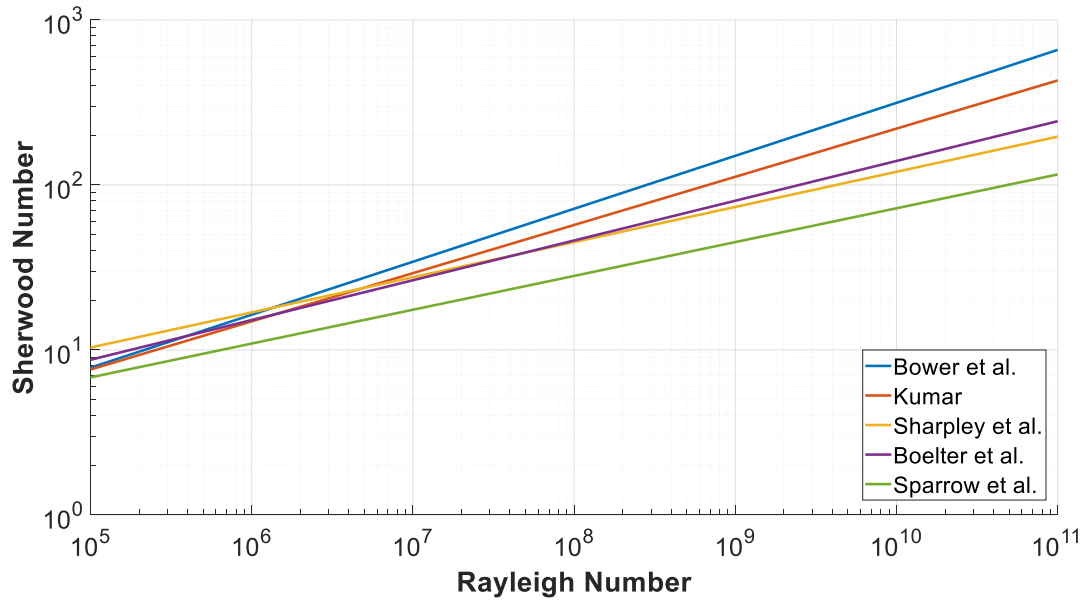


Figure 2.1: The previous work for Sherwood–Rayleigh correlation.

2.3 Objectives of Current Study

From the previous literature reviewed, it can be noticed that these studies showed some variation in the results, especially at a higher Rayleigh number, as plotted in Figure 2.1 above. Also, apart from the limitation of study numbers, some of which are listed in Table 2.1, none of these studies reported a correlation at a higher Rayleigh number, which is considered in the current work in order to increase the accuracy of evaporation prediction. Moreover, none of the studies conducted in the past reported numerical along with experimental investigation of evaporation effects on the water flow pattern, as considered and compared in the current work. The flow pattern at the free water surface undergoing evaporation is also investigated here for the side and top of the water tank using the particle image velocimetry (PIV) technique. In addition, two-dimensional (2-D) and three-dimensional (3-D) numerical simulations are carried out along with a developed user defined function (UDF), to investigate flow pattern and surface evaporation inside the water tank. Therefore, a comparison between numerical simulation and experimental work is discussed.

Finally, stereo particle image velocimetry (SPIV) is utilized to calculate the third velocity component and investigate its effect on the flow pattern and velocity magnitude. Hence, the overall goal for the current work was to carry out a comprehensive experimental and numerical study of free water surface evaporation in case of natural convection, along with its flow pattern from side and top.

2.4 Chapter Conclusion

The background of research on free water surface evaporation in case of natural convection and previous work were addressed in depth and investigated in this chapter, to arrive at and define the objectives and direction of the current study, towards covering the gaps in this area. In the following chapter, the developed numerical simulation work (2-D and 3-D) using ANSYS FLUENT 2019 R2 is presented and discussed in detail.

3. NUMERICAL SIMULATION

The overall objective of this chapter is to discuss the results of the numerical simulation that was developed using ANSYS FLUENT 2019 R2, which is extensively used in academia and industry. The governing equations that were used are addressed here, along with the geometry, mesh and solution method. In addition, the user-defined function (UDF) code for simulating the surface evaporation, which was written in Microsoft Visual Studio and compiled with ANSYS FLUENT, is also discussed.

3.1 Introduction

The use of computational fluid dynamics (CFD) for modeling transport phenomena and heat transfer within a given geometry has become a common approach for designing and providing detailed solutions to complex operational problems. Fluid dynamics is defined as the science of fluid motion. Fluid flow is commonly studied in one of three ways: experimental fluid dynamics, theoretical fluid dynamics, and numerically by CFD. CFD is used for predicting fluid flow, heat transfer, mass transfer, and related phenomena by solving the mathematical equations which govern these processes, using numerical methods and algorithms. Therefore, the CFD codes consist of three main elements, which are a pre-processor, a solver, and a post-processor [37], as shown in Figure 3.1. Pre-processing is that whereby a mesh geometry is created and then can be passed to FLUENT. Moreover, boundary conditions are applied to the geometry to characterize inlet and outlet regions, the presence of walls, fluid and solid regions, and so on. Next, the solver (FLUENT) imports the mesh and uses a discretized solution algorithm to solve the governing equations through an iterative process in order to obtain convergence. Finally, the post-processor is used to generate results such as contour and vector plots and scaled graphs, to achieve the desired results.

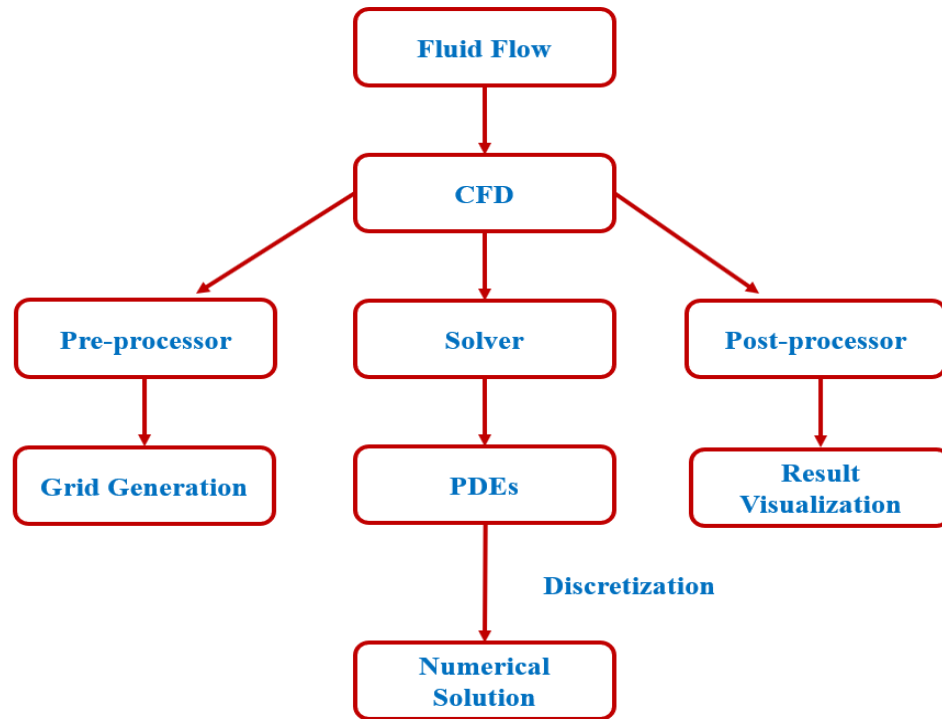


Figure 3.1: CFD overview.

Multiphase flow is defined as the simultaneous flow of several phases. A phase is basically one of the states of matter and it can be solid, liquid, or gas. From a practical engineering point of view, one of the most significant design difficulties is in working with the multiphase flow, such as the mass, momentum, and energy transfer rates. Some of these processes can be quite sensitive to the geometric distribution or topology of the components within the flow [38]. Hence, it is crucial to define the multiphase flow regime, which is the description of the morphological arrangement of the components or the flow pattern [39]. Multiphase flow regimes can be divided into four categories: gas–liquid or liquid–liquid flows; gas–solid flows; liquid–solid flows; and three-phase flows, as can be seen in Figure 3.2. Vapor is a substance that is a mixture of two phases at room temperature, which is called the gas–liquid phase. Free surface flow is one type of gas–liquid flow, which is considered in this work.

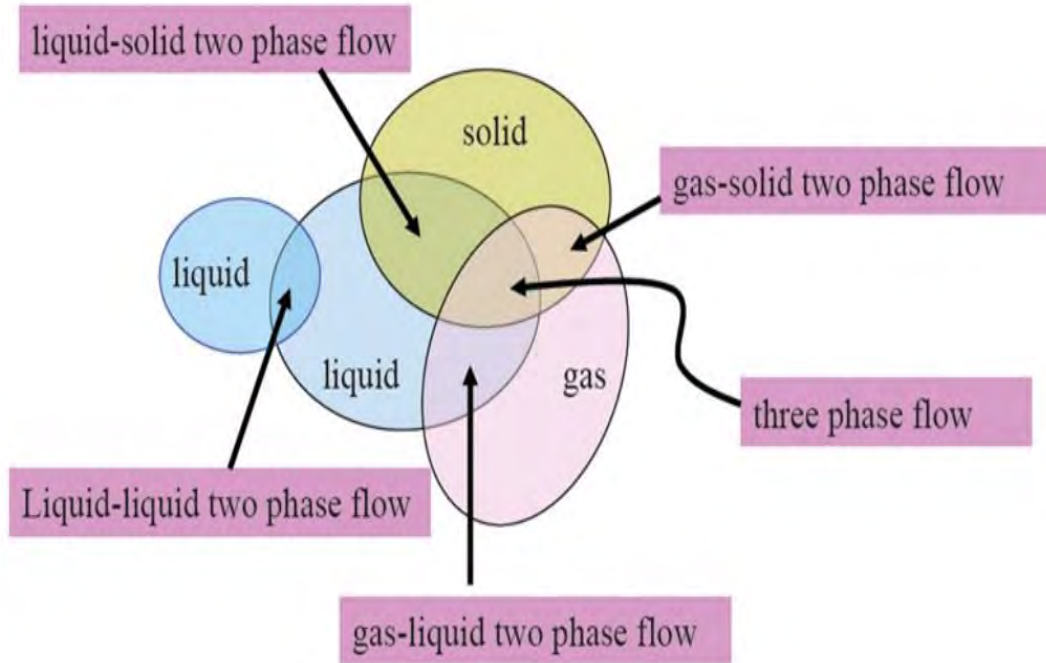


Figure 3.2: Regimes of multiphase flow.

3.2 Governing Equations

In CFD, the volume of fluid (VOF) method is one of the best-known methods for volume tracking and locating the free surface, which is the case in this work. VOF can be used to simulate two or more immiscible fluids and for tracking of the interfaces between the phases. The solution is accomplished by solving a continuity equation for the volume fraction of these phases. The equation of the volume fraction q^{th} phase has the following form:

$$\frac{1}{\rho_q} \left[\frac{\partial}{\partial t} (\alpha_q \rho_q) + \nabla \cdot (\alpha_q \rho_q \vec{v}_q) \right] = S_{\alpha q} + \sum_{p=1}^n (\dot{m}_{pq} - \dot{m}_{qp}) \quad (3.1)$$

where \dot{m}_{pq} is the mass transfer from phase q to phase p and \dot{m}_{qp} is the mass transfer from phase p to phase q .

The volume fraction equation can be solved either through implicit or explicit time discretization, with explicit time discretization being used in this work. The explicit time discretization is given in the following form:

$$\frac{\alpha_q^{n+1} \rho_q^{n+1} - \alpha_q^n \rho_q^n}{\Delta t} V + \sum_f (\rho_q U_f^n \alpha_{q,f}^n) = \sum_{p=1}^n (\dot{m}_{pq} - \dot{m}_{qp}) + S_{aq} V \quad (3.2)$$

where $n + 1$ is the index for new (current) time step, n is the index for previous time step, $\alpha_{q,f}^n$ is the face value of the q^{th} volume fraction, computed from the first or second-order upwind, QUICK, modified HRIC, or CICSAM scheme, V is the volume of the cell, and U_f^n is volume flux through the face, based on normal velocity.

The energy equation which is shared as well among the phases is given below

$$\frac{\partial}{\partial t} (\rho E) + \nabla \cdot (\vec{v} (\rho E + p)) = \nabla \cdot (k_{eff} \nabla T) + S_h \quad (3.3)$$

The VOF model treats energy E and temperature T as mass-averaged variables:

$$E = \frac{\sum_{q=1}^n \alpha_q \rho_q E_q}{\sum_{q=1}^n \alpha_q \rho_q} \quad (3.4)$$

where total energy E_q , enthalpy h for ideal gases (air phase), and enthalpy h for incompressible flows (water phase) are defined as follows, respectively

$$E_q = h - \frac{p}{\rho} + \frac{v^2}{2} \quad (3.5)$$

$$h = \sum_s M_s h_s \quad (3.6)$$

$$h = \sum_s M_s h_s + \frac{p}{\rho} \quad (3.7)$$

Moreover, the single momentum equation is given in the following form:

$$\frac{\partial}{\partial t} (\rho \vec{v}) + \nabla \cdot (\rho \vec{v} \vec{v}) = -\nabla p + \nabla \cdot [\mu (\nabla \vec{v} + \nabla \vec{v}^T)] + \rho \vec{g} + \vec{F} \quad (3.8)$$

The turbulence has to be included in this type of simulation for multiphase flow. Hence, the shear-stress transport (SST) $k - \omega$ model was used in this work. The (SST) $k - \omega$ model equations are given as:

$$\frac{\partial}{\partial t}(\rho k) + \frac{\partial}{\partial x_i}(\rho k u_i) = \frac{\partial}{\partial x_j} \left(\Gamma_k \frac{\partial k}{\partial x_j} \right) + \tilde{G}_k - Y_k + S_k \quad (3.9)$$

and

$$\frac{\partial}{\partial t}(\rho \omega) + \frac{\partial}{\partial x_i}(\rho \omega u_i) = \frac{\partial}{\partial x_j} \left(\Gamma_\omega \frac{\partial \omega}{\partial x_j} \right) + G_\omega - Y_\omega + D_\omega + S_\omega \quad (3.10)$$

where \tilde{G}_k is the generation of turbulence kinetic energy due to mean velocity gradients, G_ω is the generation of ω , Γ_k and Γ_ω are the effective diffusivities of k and ω respectively, Y_k and Y_ω are the dissipation of k and ω due to turbulence, S_k and S_ω are user-defined source terms, and D_ω is the cross-diffusion term.

In addition, the effective diffusivities for the SST $k - \omega$ model are defined as

$$\Gamma_k = \mu + \frac{\mu_t}{\sigma_k} \quad (3.11)$$

$$\Gamma_\omega = \mu + \frac{\mu_t}{\sigma_\omega} \quad (3.12)$$

where σ_k and σ_ω are the turbulent Prandtl numbers for k and ω , and μ_t is the turbulent viscosity. σ_k , σ_ω , and μ_t can be given respectively as

$$\sigma_k = \frac{1}{F_1/\sigma_{k,1} + (1-F_1)/\sigma_{k,2}} \quad (3.13)$$

$$\sigma_\omega = \frac{1}{F_1/\sigma_{\omega,1} + (1-F_1)/\sigma_{\omega,2}} \quad (3.14)$$

$$\mu_t = \frac{\rho k}{\omega} \frac{1}{\max\left[\frac{1}{\alpha^*}, \frac{S F_2}{a_1 \omega}\right]} \quad (3.15)$$

where S is the strain rate magnitude. The blending functions F_1 and F_2 are defined as follows

$$F_1 = \tanh(\Phi_1^4) \quad (3.16)$$

$$\Phi_1 = \min \left[\max \left(\frac{\sqrt{k}}{0.09\omega y}, \frac{500\mu}{\rho y^2 \omega} \right), \frac{4\rho k}{\sigma_{\omega,2} D_{\omega}^+ y^2} \right] \quad (3.17)$$

$$D_{\omega}^+ = \max \left[2\rho \frac{1}{\sigma_{\omega,2}} \frac{1}{\omega} \frac{\partial k}{\partial x_j} \frac{\partial \omega}{\partial x_j}, 10^{-10} \right] \quad (3.18)$$

$$F_2 = \tanh(\Phi_2^2) \quad (3.19)$$

$$\Phi_2 = \max \left[2 \frac{\sqrt{k}}{0.09\omega y}, \frac{500\mu}{\rho y^2 \omega} \right] \quad (3.20)$$

where y and D_{ω}^+ are the distance to the next surface and the positive portion of the cross-diffusion term, respectively.

The production of turbulence kinetic energy \widetilde{G}_k is defined as

$$\widetilde{G}_k = \min(G_k, 10\rho\beta^*k\omega) \quad (3.21)$$

Therefore, the production of ω is given as

$$G_{\omega} = \frac{\alpha}{v_t} \widetilde{G}_k \quad (3.22)$$

Moreover, the description of multiphase flow is related to the concept of phasic volume fractions α_q . The volume fractions describe the space occupied by every phase, and the laws of conservation of mass and momentum are satisfied by every phase independently. Likewise, derivation of the conservation equations can be executed by ensemble averaging the instantaneous local balance for each of the phases [40], or by using the mixture theory approach [41]. The volume of the phase V_q is given as

$$V_q = \int_V \alpha_q dV \quad (3.23)$$

where

$$\sum_{q=1}^n \alpha_q = 1 \quad (3.24)$$

The effective density of phase $\hat{\rho}_q$ is defined as

$$\hat{\rho}_q = \alpha_q \rho_q \quad (3.25)$$

Where ρ_q is the physical density of phase q . The volume fraction equation can be solved either by implicit or explicit time discretization as given in Eq. (2).

3.3 User-Defined Function (UDF)

A user-defined function (UDF) is a function that you program which can be loaded with the ANSYS FLUENT solver to increase the standard features of the code [42]. UDF can be used for defining your own boundary conditions, material properties, and source terms for the flow regime, as well as to specify customized model parameters such as DPM, multiphase models, initialize a solution, or enhance postprocessing. UDF can be written in any C programming language using any text editor, and the code file is saved as a .c extension, where one source file can contain a single UDF or multiple UDFs. All UDF code must contain the udf.h file inclusion directive (`#include "udf.h"`) at the beginning of the code file. This udf.h file allows definitions of defined macros and other ANSYS FLUENT-provided macros and functions to be included during the compilation process. Furthermore, it is necessary to note that the UDF values that are uploaded to a solver or returned by the solver are stated in SI units. In addition, code files that contain UDFs can be either interpreted or compiled in ANSYS FLUENT. First, source files are interpreted and loaded directly at runtime in a single-step process for interpreted UDFs. Second, for compiled UDF, the process has two different steps, which are building the code and then loading it into ANSYS FLUENT. After the code is either interpreted or compiled to ANSYS FLUENT, UDFs will become available and selectable in dialog boxes. Hence, it can be hooked to a solver by choosing the function name in the appropriate dialog box. In this work, the UDF code was developed and written in Microsoft Visual Studio in order to simulate the surface evaporation at the water–air interface. The source file code for UDF was compiled and hooked to the solver by choosing the function name. A source file code was developed and written in this work in order to

simulate the surface evaporation. Basically, the properties of fluids (water and air) were defined along with the variables. In addition, the saturation pressure for water vapor was computed by using the polynomial fit. The molar fraction from mass fraction and the interfacial area density were computed and calculated as well. Hence, the mass transfer rate can be calculated. The source file code (UDF) can be seen in Appendix A.

3.4 Two-Dimensional (2-D) Analysis

3.4.1 Geometry and Meshing

The geometry used for the testing was of a water tank with dimensions of $35 \times 35 \times 40 \text{ cm}^3$. The tank was filled with water up to 24 cm and open to the ambient air. The bottom of the tank is an aluminum plate that is fixed at a temperature of 50°C where the other four sides are insulated. Two-Dimensional was considered for the purpose of simplification, as can be seen in Figure 3.3. The tank only allows evaporation and heat transfer from the free interface surface, not the sides. This makes the study more accurate and provides one dimension of diffusion for the falling rate model.

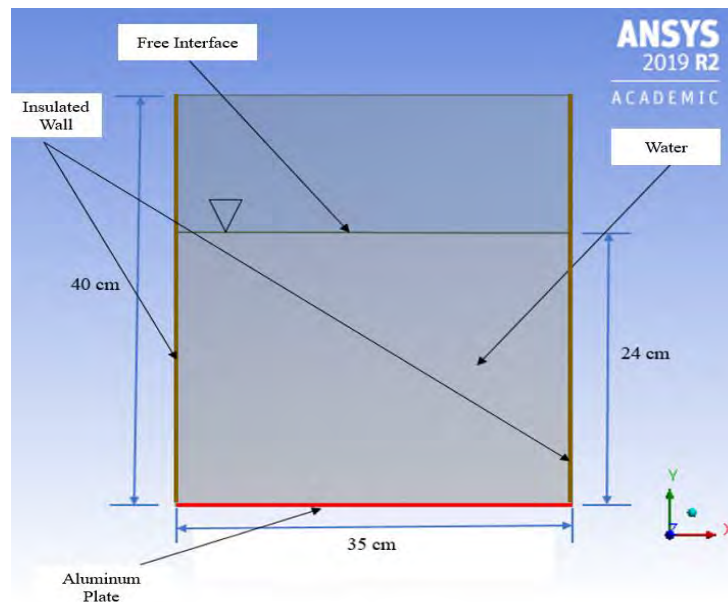
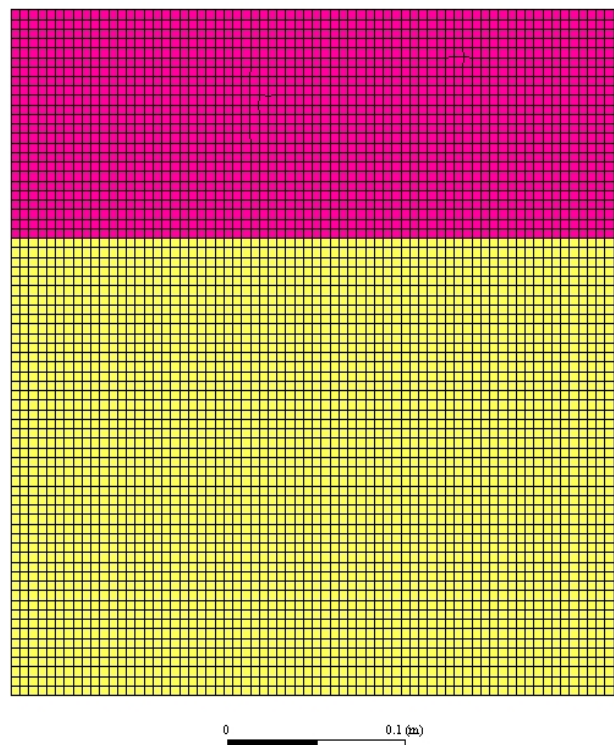


Figure 3.3: 2-D CFD geometry.

A mesh is that where the geometry is broken up into a control volume or cells. Every cell is defined by a set of nodes, a cell center, and the faces that bound the cell. ANSYS FLUENT uses internal data structures in order to define the domain(s) of the mesh. Therefore, this is used to assign an order to cells, cell faces, and nodes in a mesh, and to establish connectivity between adjacent cells. Cells and cell faces are gathered into zones that mostly define the physical components of the model such as inlets, outlets, walls, and fluid regions. In this work, the mesh was generated by ANSYS FLUENT as shown in Figure 3.4. The mesh details are listed in Table 3.1, where the number of nodes and elements are 498211 and 496800, respectively.



ANSYS
2019 R2
ACADEMIC

Figure 3.4: 2-D CFD grid meshing.

Table 3.1: The 2-D meshing details.

Description	Explanation
Number of nodes	498211
Number of elements	496800
Element order	Linear
Element size	0.0005
Export format	standard
Smoothing	Medium
Average surface area	0.0621 m^2

One of the most important parameters is the boundary conditions where all the simulation regions can be defined. The tank was filled with water up to 24 cm as we discussed earlier. The rest of the tank is open to the ambient pressure and temperature, which is the case of natural convection. Heat is generated from the bottom by the aluminum plate, where all the side walls are insulated. The top part is defined as a pressure outlet in the setup section. Table 3.2 shows the details about the boundary conditions, whereas the properties of the fluid that were used in this simulation are listed in Table 3.3.

Table 3.2: The boundary conditions details.

Domain	Boundaries	
Air zone	Air zone symmetry 1	
	Type	Symmetry
	Air zone symmetry 2	
	Type	Symmetry
	Ceiling	
	Type	Pressure outlet
	Interior air zone water zone air zone	
	Type	Interface
	Wall air zone	
	Type	Wall
water zone	Wall water zone	
	Type	Wall
	Heat wall	
	Type	Wall
	Interior air zone water zone air zone	
	Type	Interface
	water zone symmetry 1	
	Type	Symmetry
	water zone symmetry 2	
	Type	Symmetry

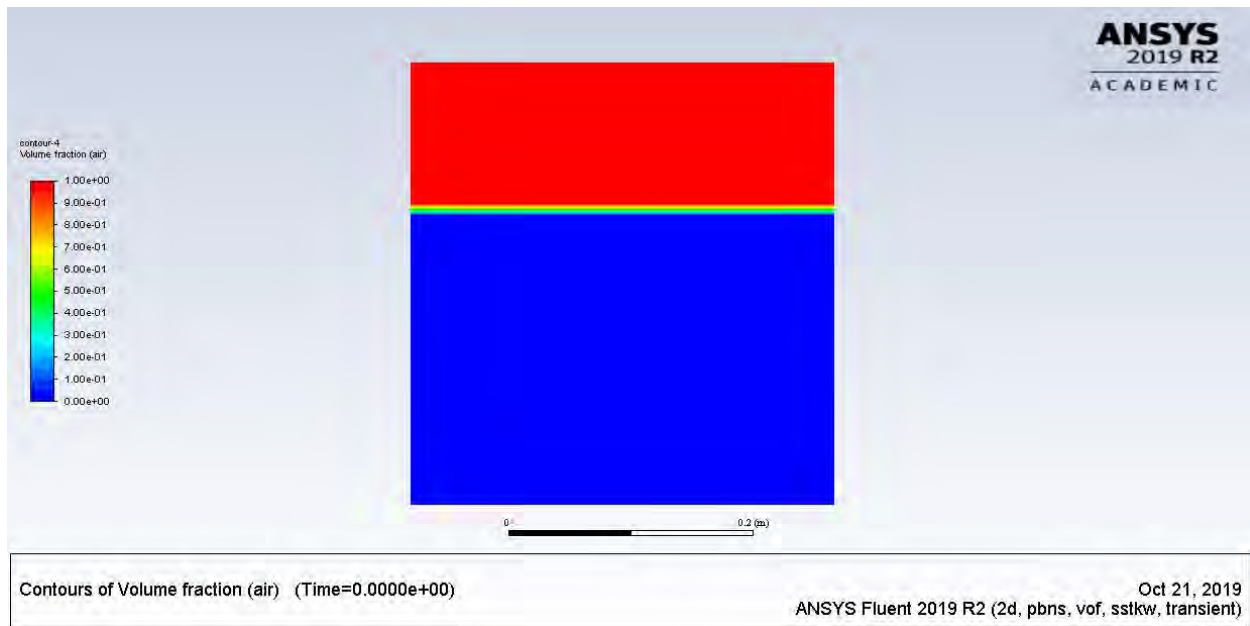
Table 3.3: Fluids' properties.

Fluid	Properties	Value	Properties	Value
Air	Density	1.225	Viscosity	$1.7894 * 10^{-5}$
	Specific heat	1006.43	Molecular weight	28.966
	Thermal conductivity	0.0242	Reference temperature	298.15
Water	Density	998.2	Viscosity	0.001003
	Specific heat	4182	Molecular weight	18.0152
	Thermal conductivity	0.6	Reference temperature	298
Vapor	Density	0.5542	Viscosity	$1.34 * 10^{-5}$
	Specific heat	<i>Piecewise – Polynomial</i>	Molecular weight	18.01534
	Thermal conductivity	0.0261	Reference temperature	298.15

3.4.2 Results and Discussion

Now, the results obtained by using the CFD for 2-D model are presented and discussed. The numerical investigation was used to carry out simulation of heat and mass transfer in the water tank along with surface evaporation in case of natural convection. ANSYS FLUENT built-in post-processor was used to calculate mass-averaged conditions and produce graphs and contour plots for the entire solution. As known, the air and water temperatures control the evaporation rate and the heat transfer across the water–air interface. Moreover, they also affect the air and water velocity fields. Hence, in this work, the calculation was run as time-dependent (transient), where the aluminum plate was fixed at 50°C and the other fluids at the room temperature. The temperature distribution of water rises with time, in order to reach the desired temperature which is 50°C. At the same time, the surface evaporation (volume fraction of vapor) was monitored as well by compiling the developed UDF code. Moreover, the velocity inside the water and above the free water surface were

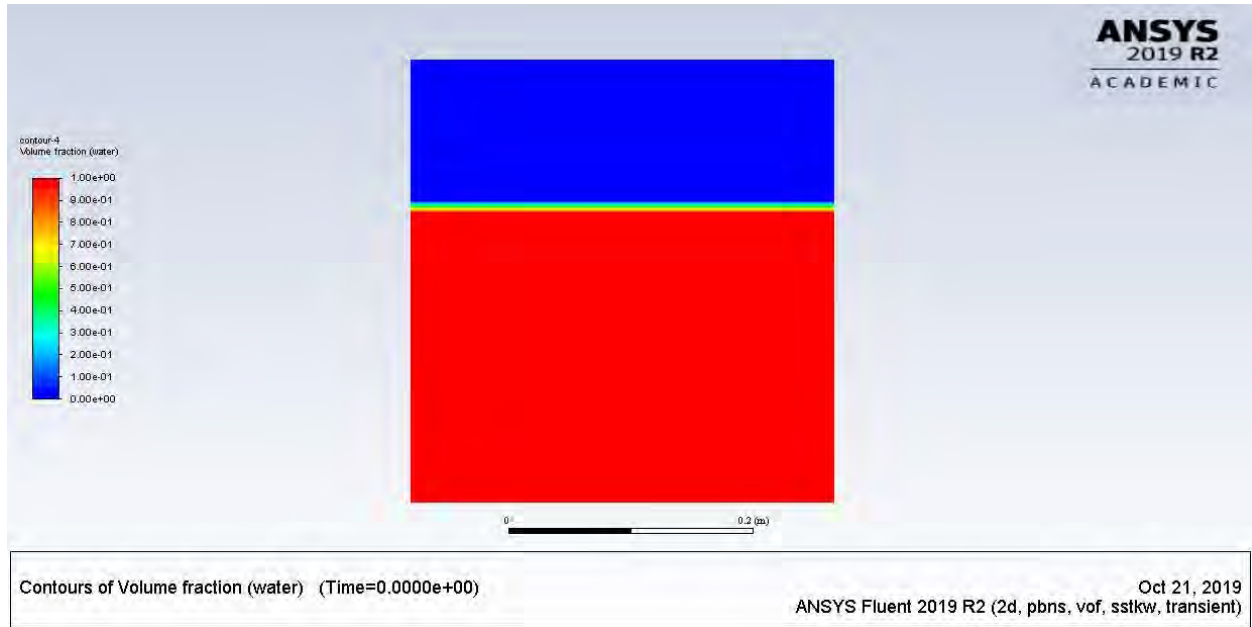
investigated as well. The results were recorded at different timesteps in order to pursue the developing flow behavior, heat and mass transfer, along with the surface evaporation. However, Figure 3.5 shows the volume fraction of air, water, and vapor after patching them and before running the calculation (at $t = \text{zero seconds}$). It is clear that in Figure 3.5 (a), the air domain has a volume fraction of 100 %, where the water domain is 0 %. In contrast, in Figure 3.5 (b) the water domain has a volume fraction of 100 %, where the air domain is 0 %. Accordingly, the vapor has a volume fraction of 100 %, where the air domain is 0 % at all the domains. Note that all the results hereafter are shown as contour and x-y plot. The X–Y plot presents the result at three different locations of tank width, i.e., at $x = 0$, $x = 15 \text{ cm}$, and $x = -15 \text{ cm}$, as shown clearly in Figure 3.6.



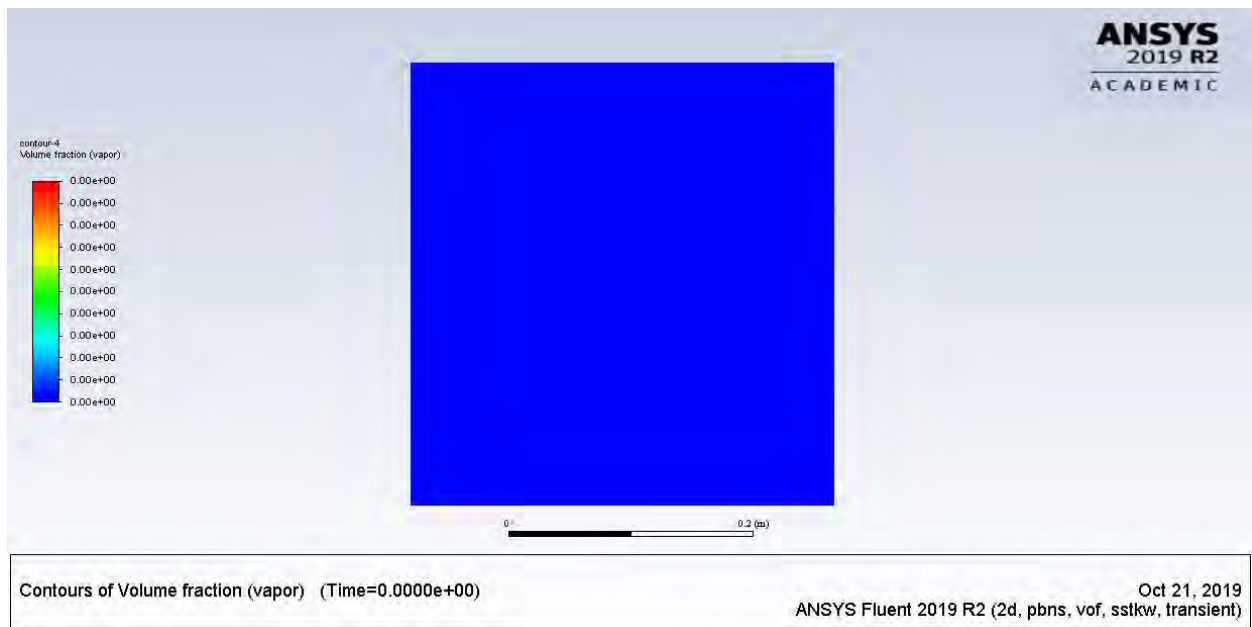
(a)

Figure 3.5: Contours of volume fraction of (a) air, (b) water, and (c) vapor.

Figure 3.5—continued



(b)



(c)

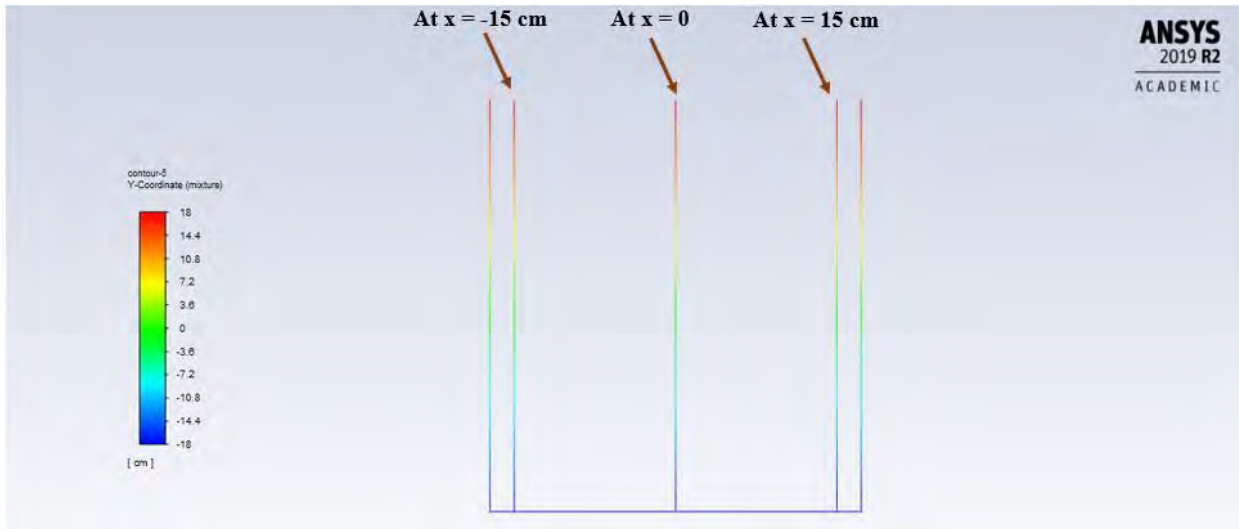


Figure 3.6: The three different locations for X–Y plot.

1) At t = 2 Seconds

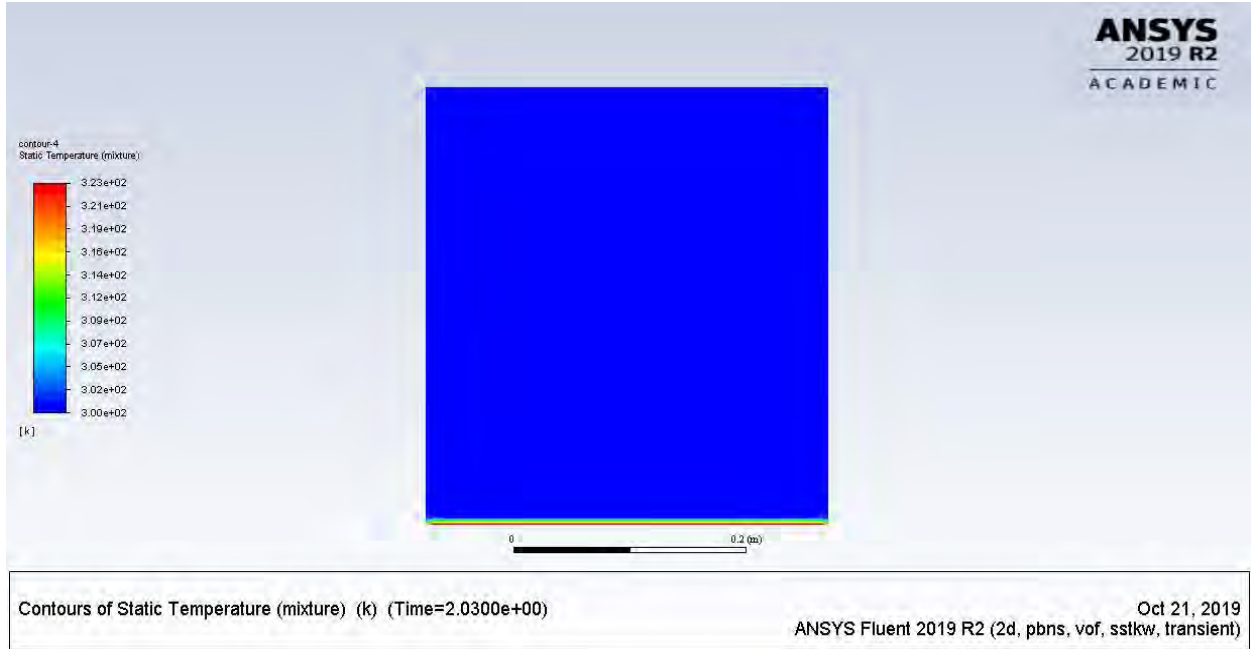
(a) Temperature

As was mentioned earlier, the results were reported at different timesteps, where in Figure 3.7 the contour and plot of the temperature are shown at 2 seconds. It is clear that the water is still at room temperature. In addition, as is visible the water starts to heat up at the bottom of the tank. In Figure 3.7 (b), the plot of the temperature is presented at three different locations of tank width, at $x = 0$, $x = 15$ cm, and $x = -15$ cm. The x-axis represents the height of the tank, and the y-axis the temperature distribution. The temperature is identical at all three different locations of tank width.

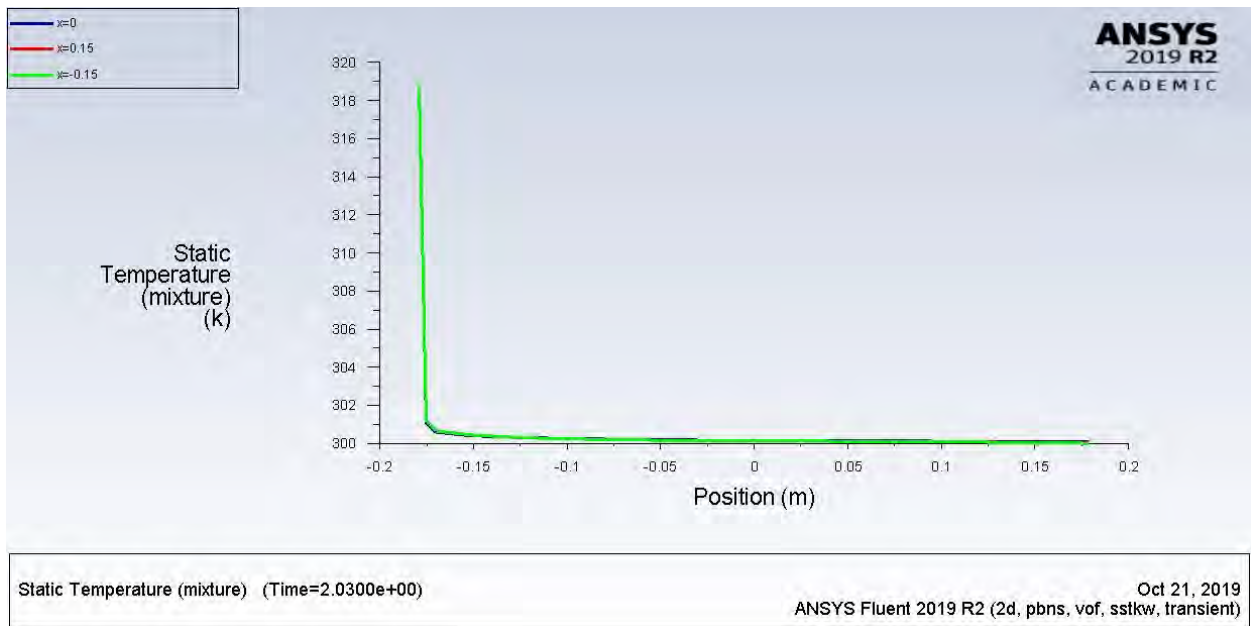
(b) Velocity

The velocity magnitude for both contour and plot are shown in Figure 3.8. It can be seen in Figure 3.8 (a) that the velocity of air above the water surface has started to develop. The air is flowing from the upper side of the tank, which is open to the ambient air. Meanwhile, the velocity of the water which is related to the buoyancy forces is very negligible due to the small temperature at this time. This is visible in Figure 3.8 (b), where the velocity is very small before the interface and

increases gradually after that. Finally, it is essential to note that the velocity above the free water surface is less than 0.15 m/s, which is in the range of natural convection based on the literature.

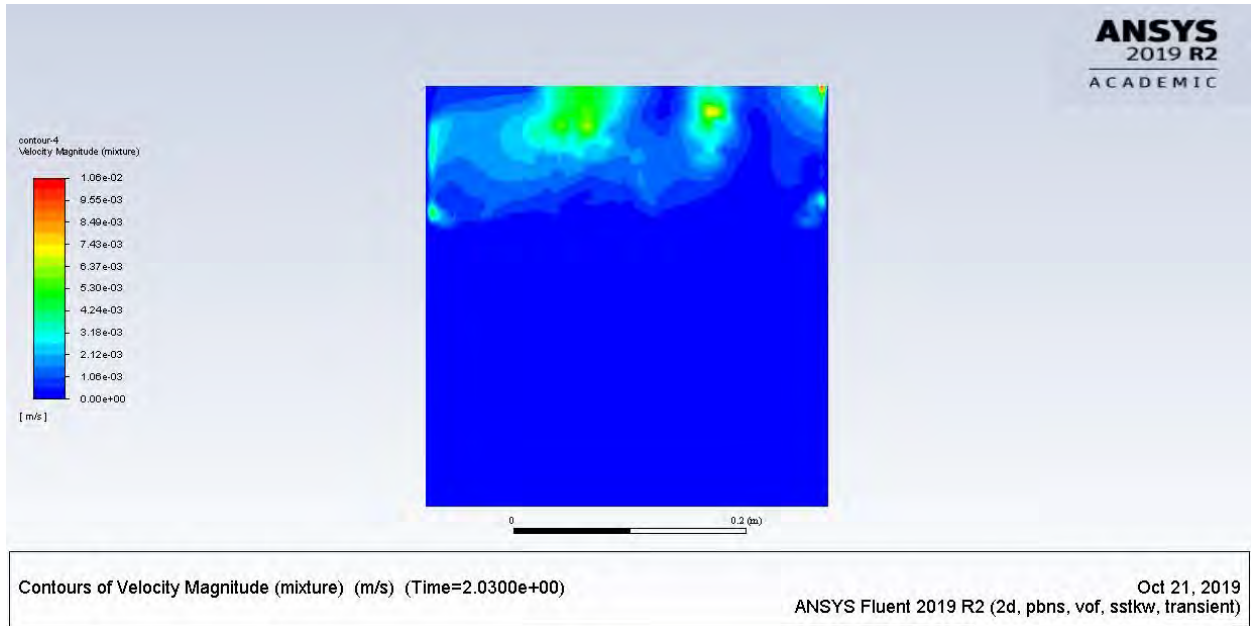


(a)

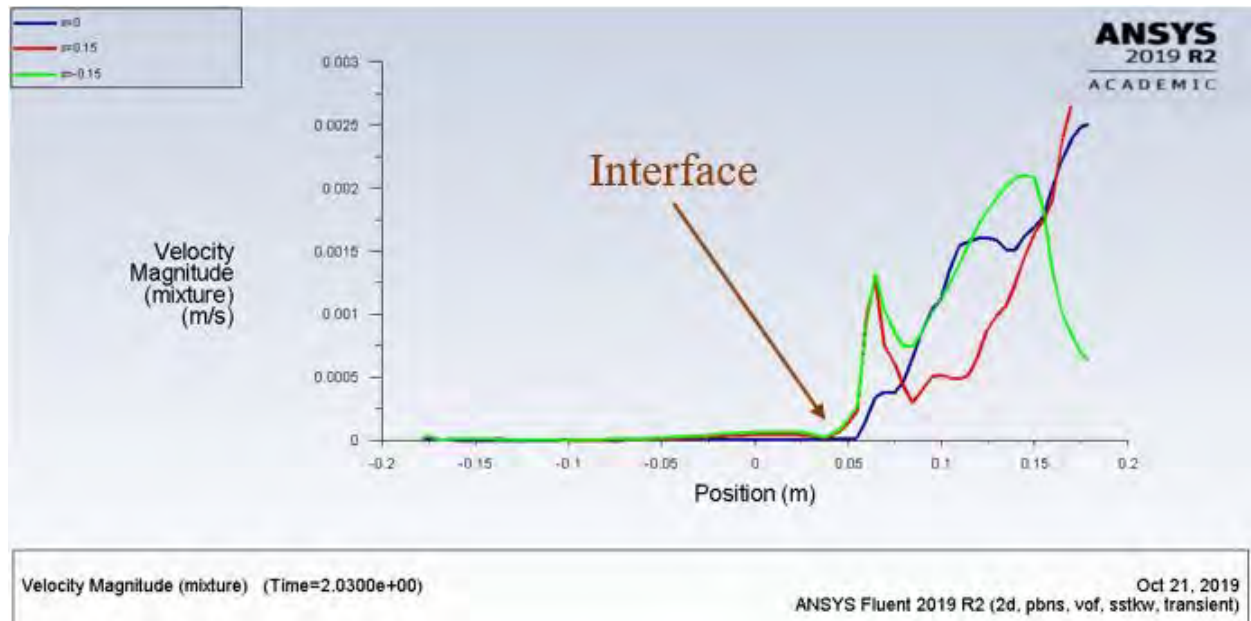


(b)

Figure 3.7: Temperature at 2 s (a) Contour, (b) XY plot.



(a)



(b)

Figure 3.8: Velocity at 2 s (a) Contour, (b) XY plot.

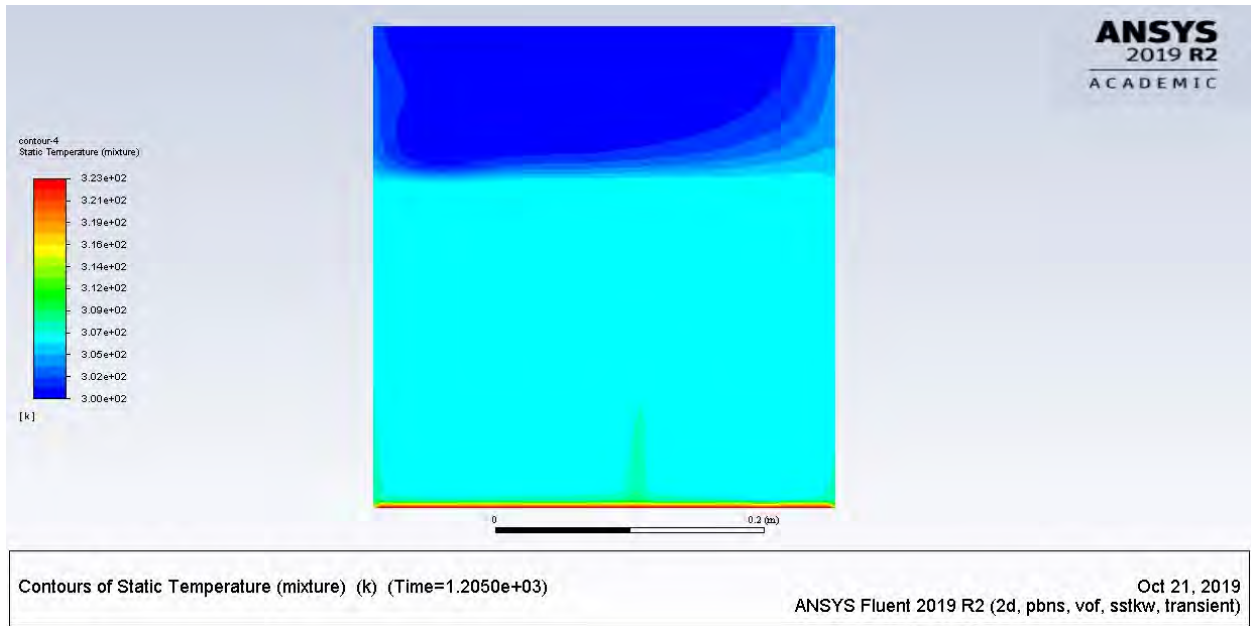
2) $t = 1205$ Seconds

(a) Temperature

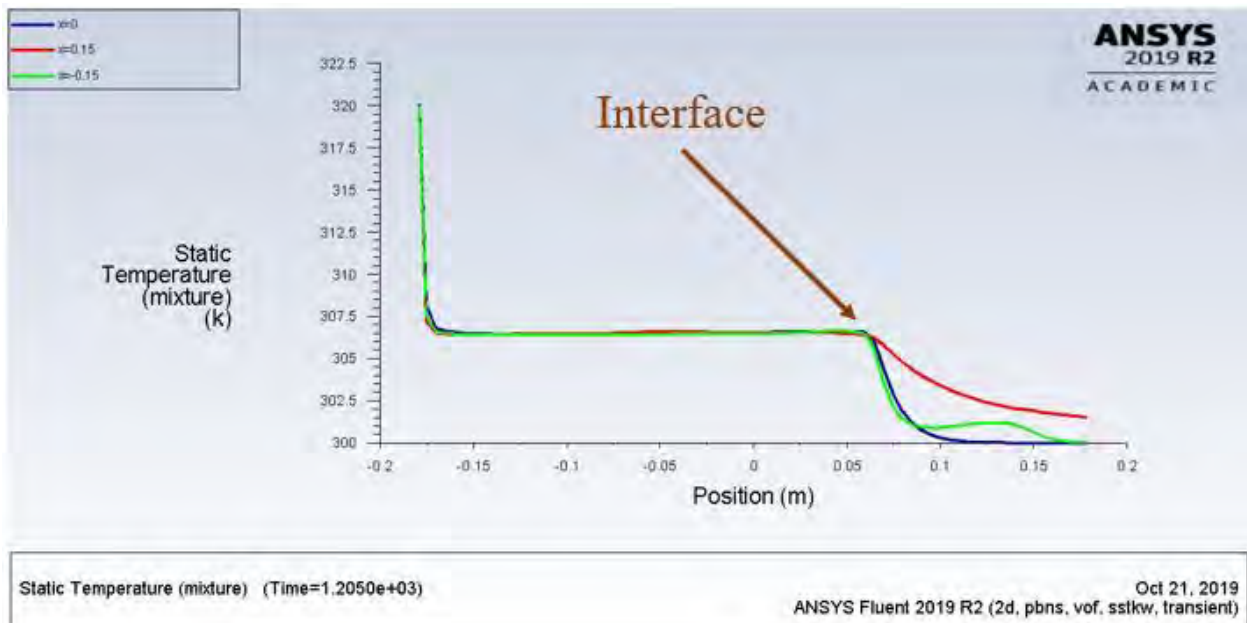
As can be seen in Figure 3.9, the temperature of water keeps rising along with time. In Figure 3.9 (a), the temperature of the water reaches about 34°C at $t = 1205\text{s}$. Therefore, the temperature of the air rises up near the sidewalls due to increase in the water temperature. This is clear in Figure 3.9 (b), where the temperature at the two sides is higher than at the center where the temperature in the water domain is identical.

(b) Velocity

In Figure 3.10, the velocity magnitude for contour, plot, and vector for the air domain are shown. It is evident from Figure 3.10 (a) that the velocity of air above the water surface is higher than the water domain, where the air flows above the water surface and circulates back to the ambient air. Meanwhile, the velocity of the water which is related to the buoyancy forces is visible due to the higher temperature at this time. This can be seen clearly in Figure 3.10 (b), where the velocity of water alone is shown on a smaller scale. Therefore, the rotation of these two cells inside the water demonstrates the development of Bénard–Rayleigh convection due to temperature and density differences. Figure 3.10 (c) shows the velocity difference before and after the interface. In Figure 3.10 (d) the direction of flow can be seen, where the air comes down, and once it reaches the water surface it then flows up due to temperature difference between the air and the water surface.

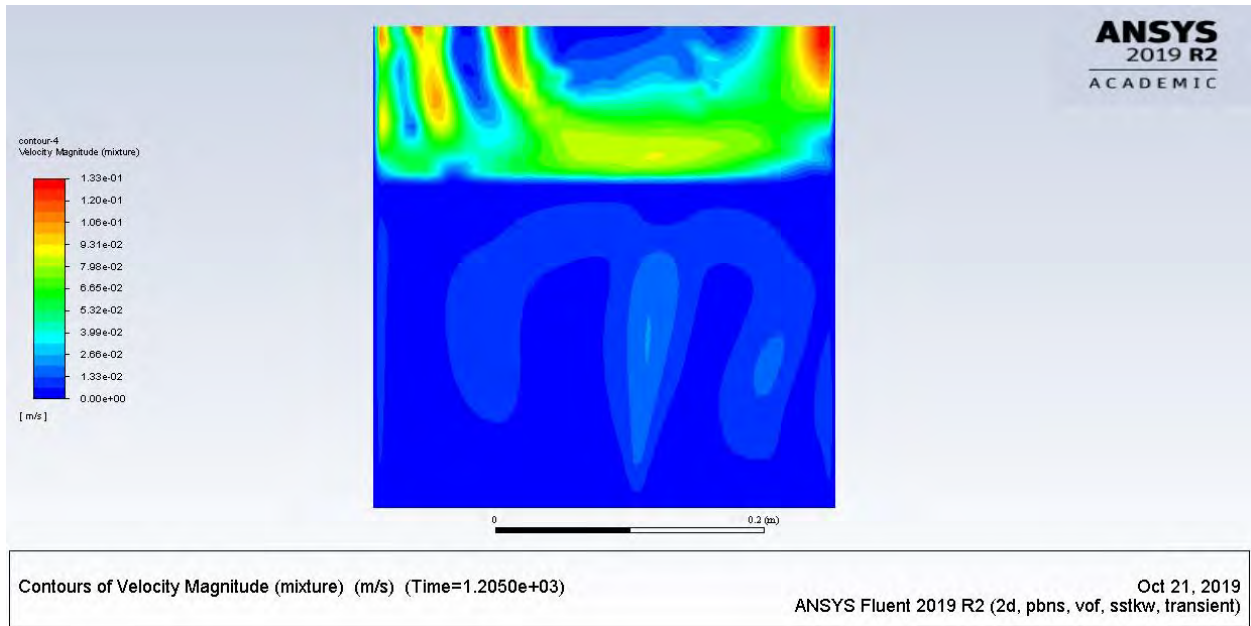


(a)

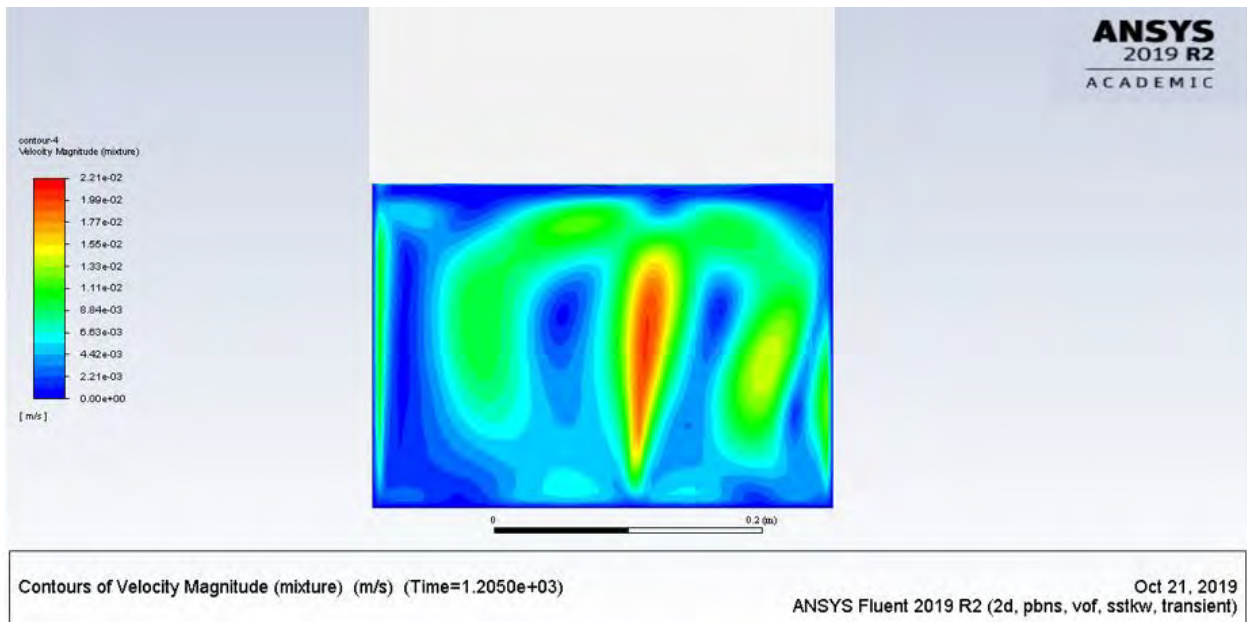


(b)

Figure 3.9: Temperature at 1205 s (a) Contour, (b) XY plot.



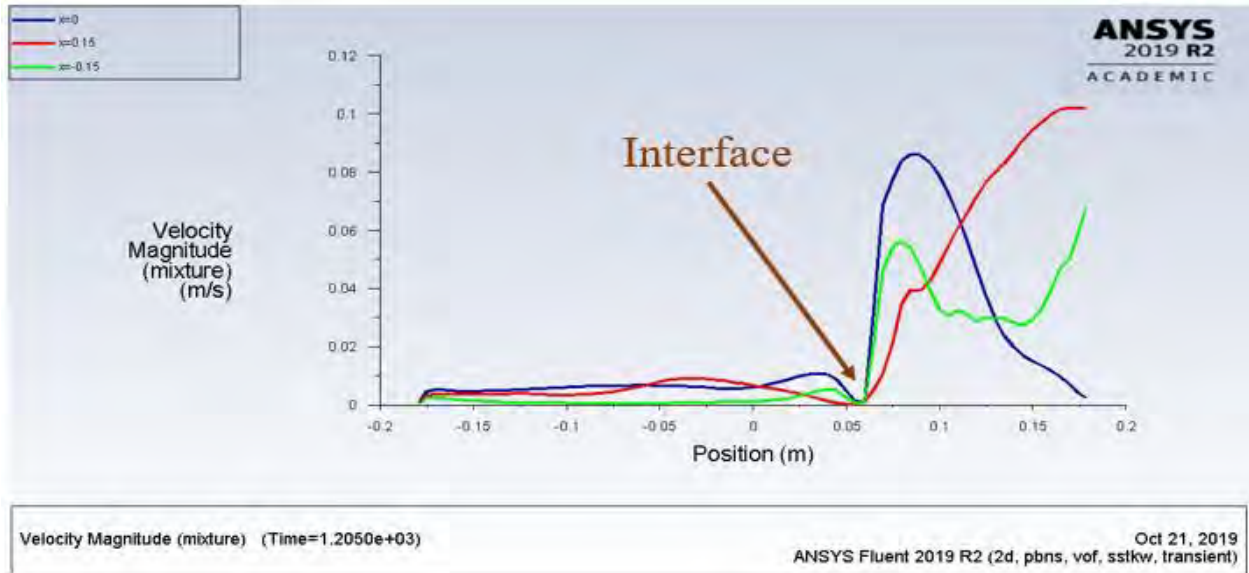
(a)



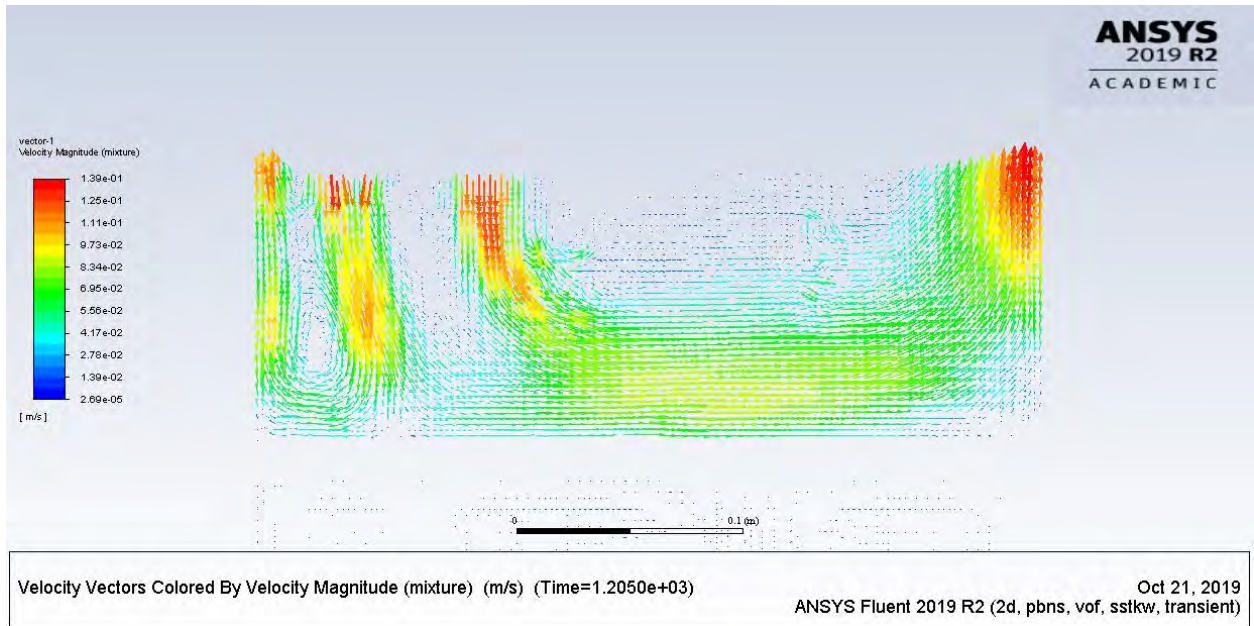
(b)

Figure 3.10: Velocity at 1205 s (a) Contour, (b) XY plot, (c) Velocity vector in the air domain, (d) Velocity contour in the water domain.

Figure 3.10—continued



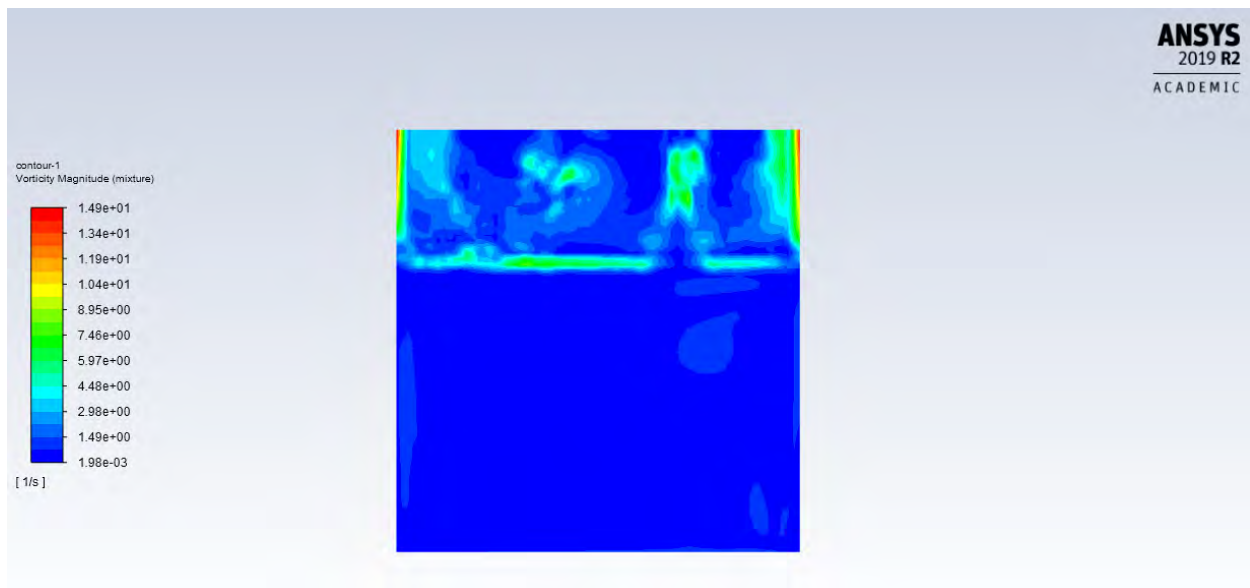
(c)



(d)

(c) Vorticity

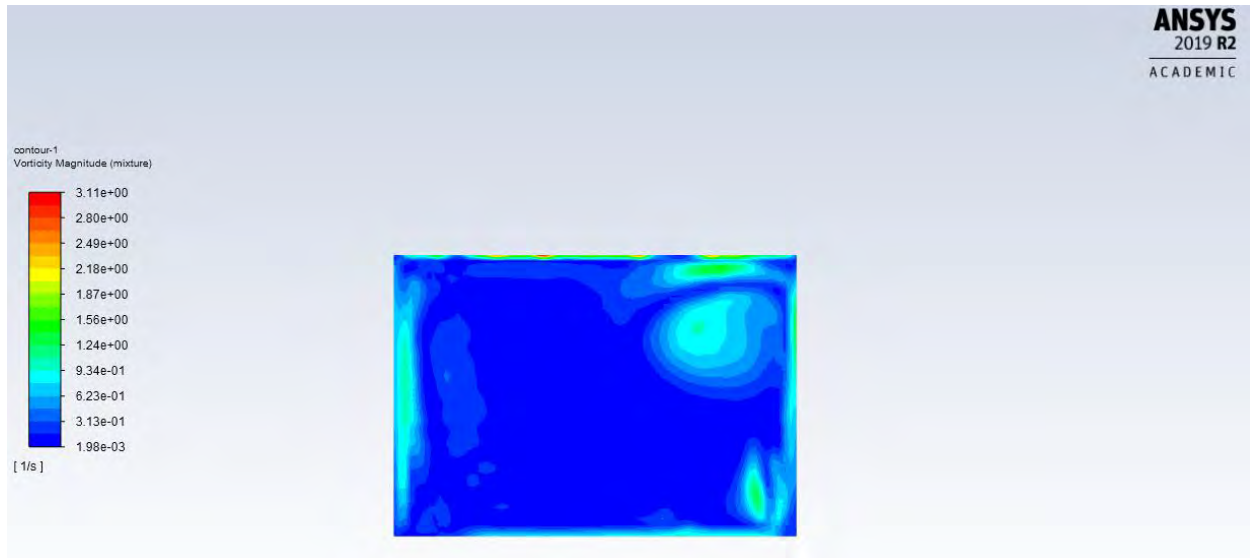
Vorticity contour is shown in Figure 3.11 (a) for air and water domain, where the vorticity is higher at the air side. It is clear that vorticity at the sides of the tank is higher, which can be related to the circulation at this region. It can also be seen that the vorticity is higher at the water–air interface, which is mainly related to the higher movement at this area. In Figure 3.11 (b) vorticity at the water domain is shown, where it is higher at the wall sides, bottom, and top due to higher velocity at these locations compared to the rest. Moreover, in the water domain the vorticity is still very small compared to the air domain [refer to Figure 3.11 (c)]. It is evident that after the interface vorticity begins to gradually increase [refer to Figure 3.11 (c)].



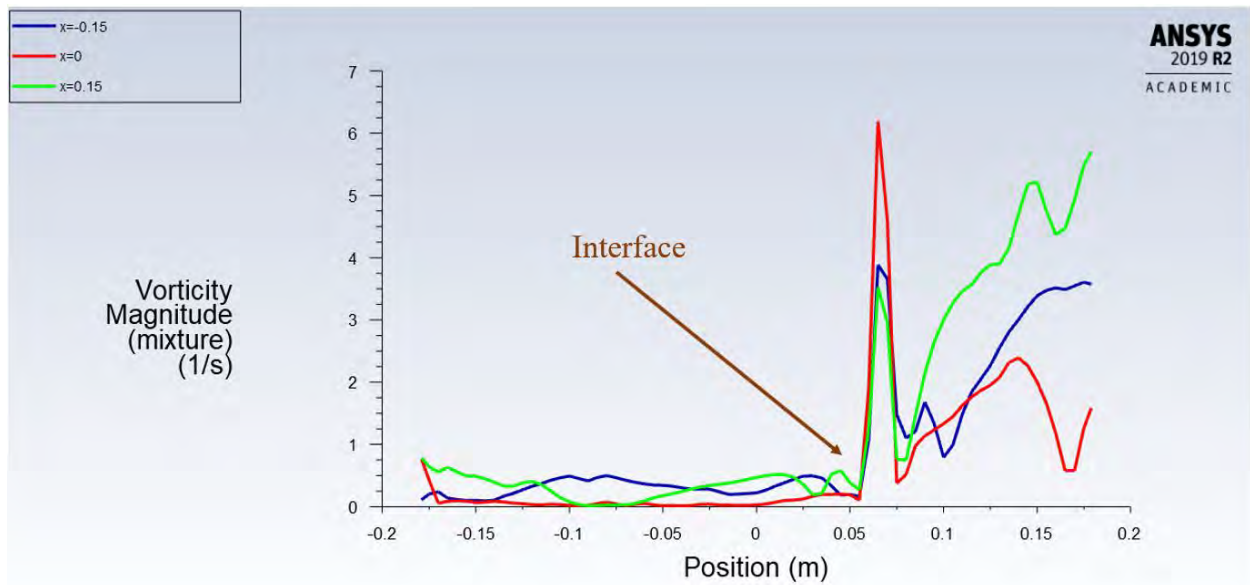
(a)

Figure 3.11: Vorticity at 1205 s (a) Contour, (b) Vorticity vector in the water domain, (c) XY plot.

Figure 3.11—continued



(b)



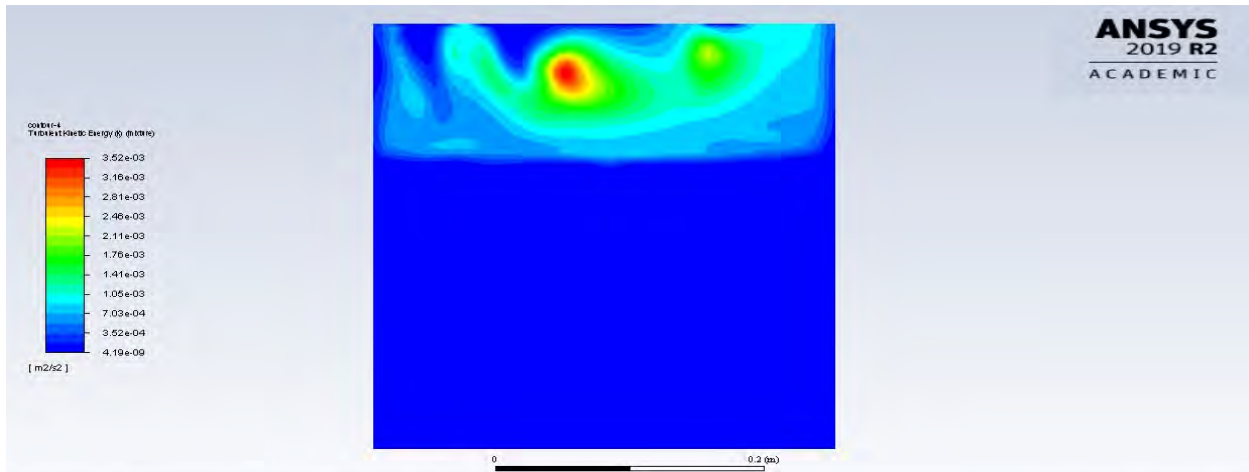
(c)

(d) Turbulence Kinetic Energy

Turbulence kinetic energy (TKE) can be formed by fluid shear, friction, buoyancy, or external forces at low-frequency eddy scales. TKE contour is shown in Figure 3.12 (a), where the TKE is higher at the air domain due to the higher velocity. Moreover, in the water domain the TKE is very small, as seen in Figure 3.12 (b). It is clear that after the interface, TKE begins to gradually increase [refer to Figure 3.12 (b)].

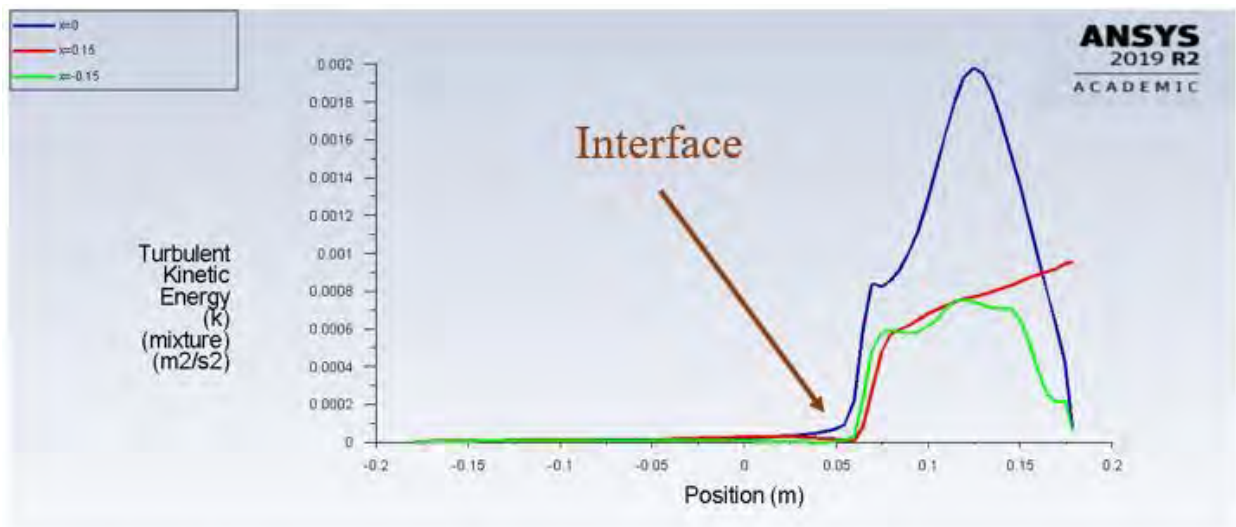
(e) Surface Evaporation

As discussed earlier, the surface evaporation was simulated along with rise in temperature by using the developed UDF code. The code was written and compiled with ANSYS FLUENT in order to simulate the surface evaporation at the water–air interface. Due to the cohesive force, the molecules can be held in balance, where the gaseous molecules can be created when some of these molecules gain sufficient kinetic energy. Hence, the cohesive force will break down at the water surface and the evaporation will start by natural convection. This can be seen clearly in Figure 3.13 (a), where the surface evaporation begins to develop at the water–air interface. At this time, where $t = 1205$ s, the volume fraction of vapor is 3.5 %. This is shown in Figure 3.13 (b) at three different locations on the x-axis along with the y-axis.



Contours of Turbulent Kinetic Energy (k) (mixture) (m2/s2) (Time=1.2050e+03) Oct 21, 2019
ANSYS Fluent 2019 R2 (2d, pbns, vof, sstk, transient)

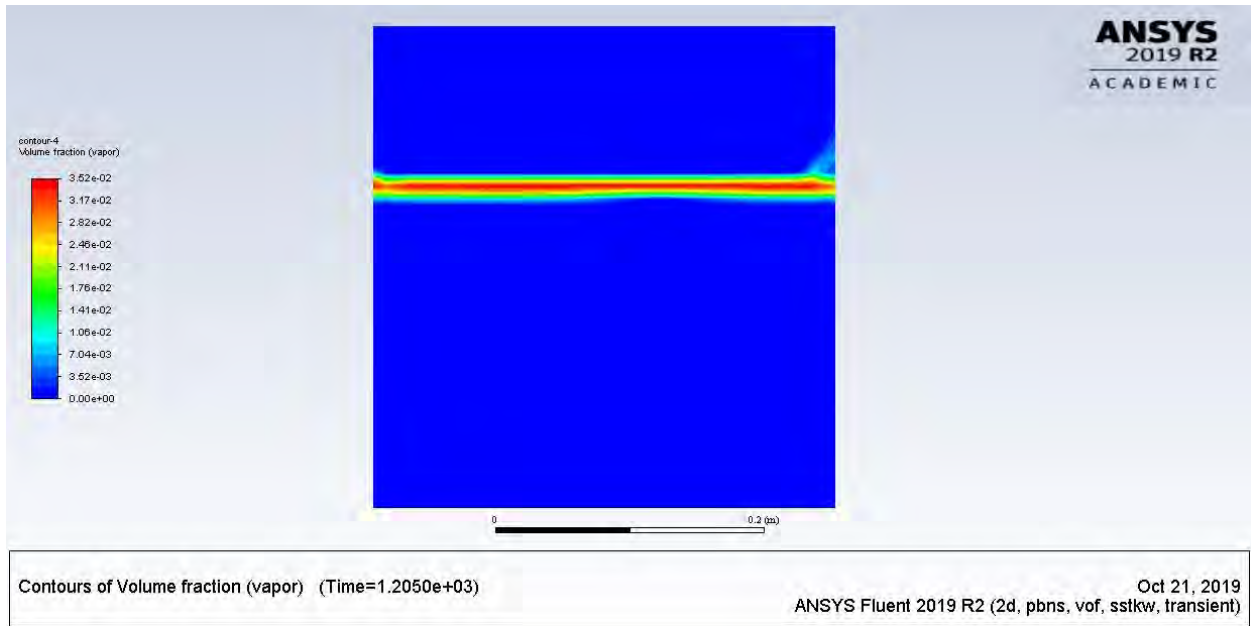
(a)



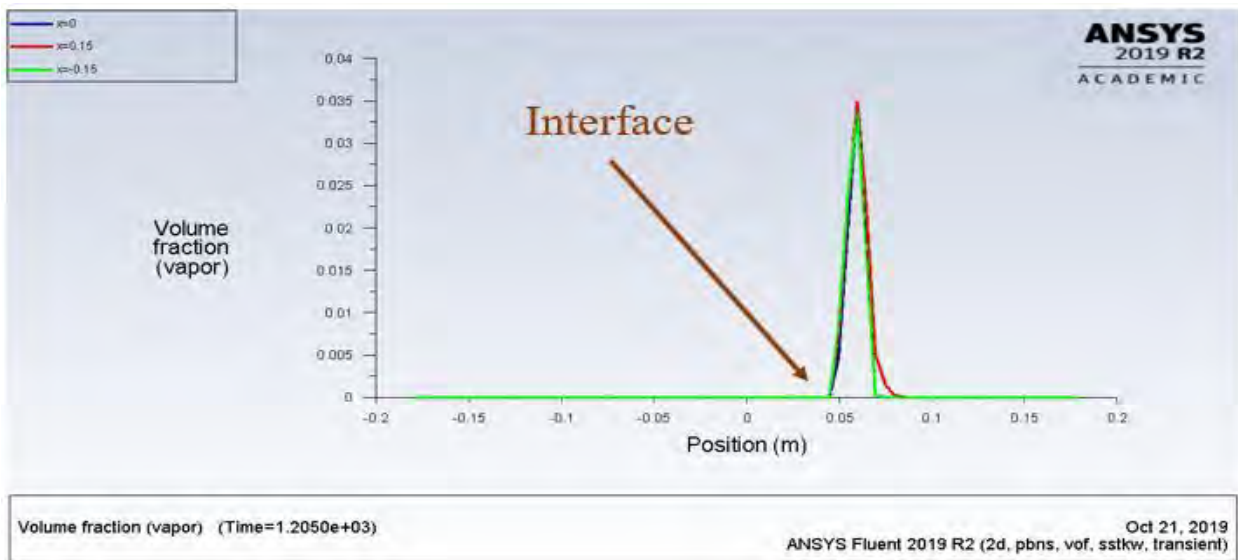
Turbulent Kinetic Energy (k) (mixture) (m2/s2) (Time=1.2050e+03) Oct 21, 2019
ANSYS Fluent 2019 R2 (2d, pbns, vof, sstk, transient)

(b)

Figure 3.12: Turbulence kinetic energy at 1205 s (a) Contour, (b) XY plot.



(a)



(b)

Figure 3.13: Surface evaporation at 1205 s (a) Contour, (b) XY plot.

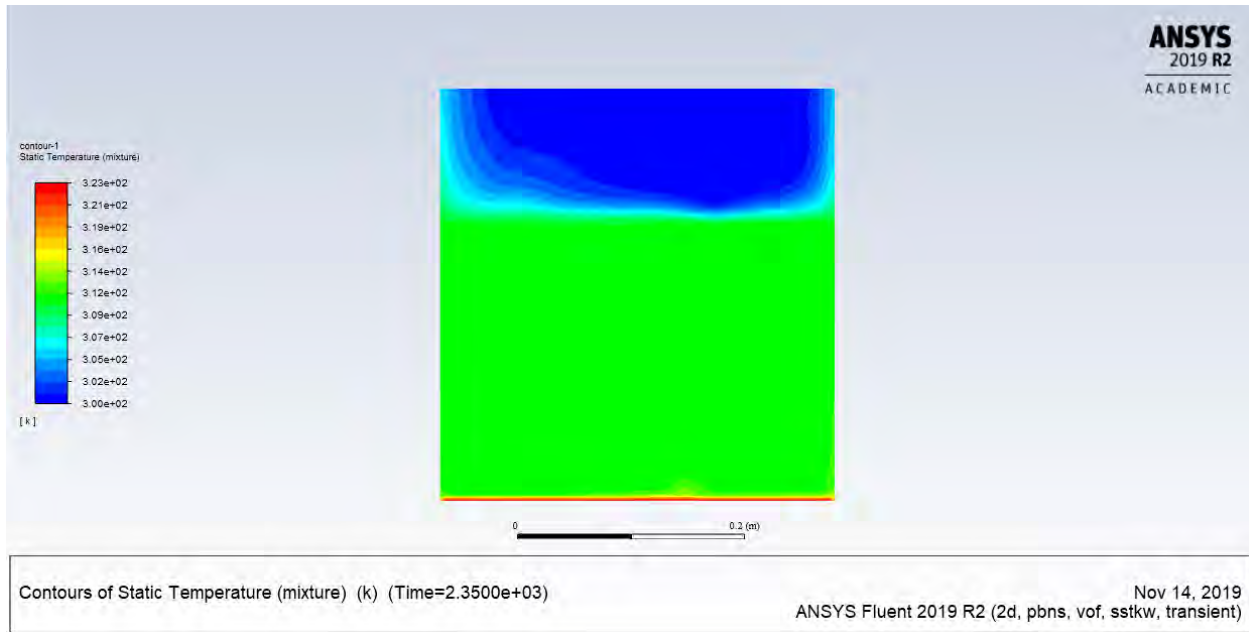
3) At $t = 2350$ Seconds

a) Temperature

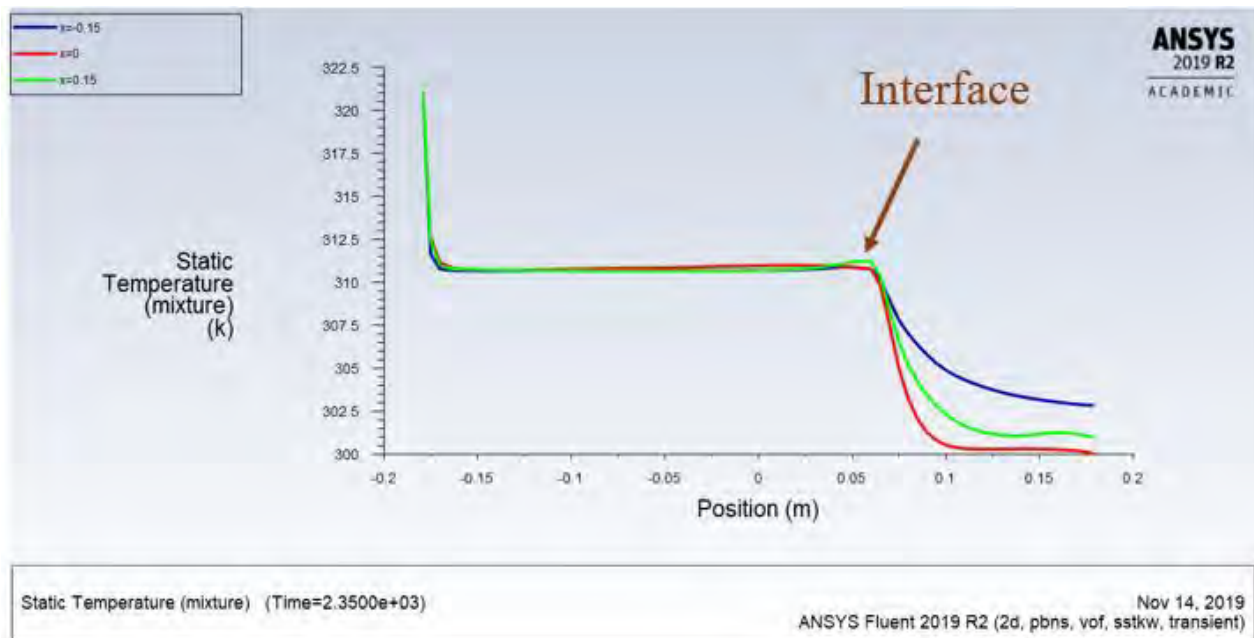
The temperature of the water keeps rising along with time, as can be seen in Figure 3.14. Figure 3.14 (a) shows the contour temperature, where it is clear that the temperature of the water has reached about 38°C . It is evident that the temperature of the air domain remains at the room temperature. However, the temperature at the two sides of the tank is higher than at the center in the air domain, which is related to the circulation of air in this region. In Figure 3.14 (b), the plot shows the temperature before and after the water–air interface at three different locations.

b) Velocity

Figure 3.15 shows the velocity magnitude for contour, vector for the water domain, and plot. It can be seen in Figure 3.15 (a) that the velocity of air above the water surface is higher at this time compared to the velocity at $t = 1205$ s. This can be related to the evaporation from the free water surface, which increases the circulation in the air domain and hence the velocity. Moreover, it is clear that the direction of velocity vectors in the air domain where two vortices are observed. These two vortices started from the top of the tank, coming down to the water surface and then circulating up to the ambient air [refer to Figure 3.15 (a)]. Meanwhile, the velocity of the water domain which relates to the buoyancy forces is shown in Figure 3.15 (b). Therefore, the rotation of two vortices inside the water due to the development of Bénard–Rayleigh convection can be seen. It is clear that these two vortices started from the bottom of the tank, going up to the water surface and then circulating down to the water. Figure 3.15 (c) shows the velocity difference before and after the interface.

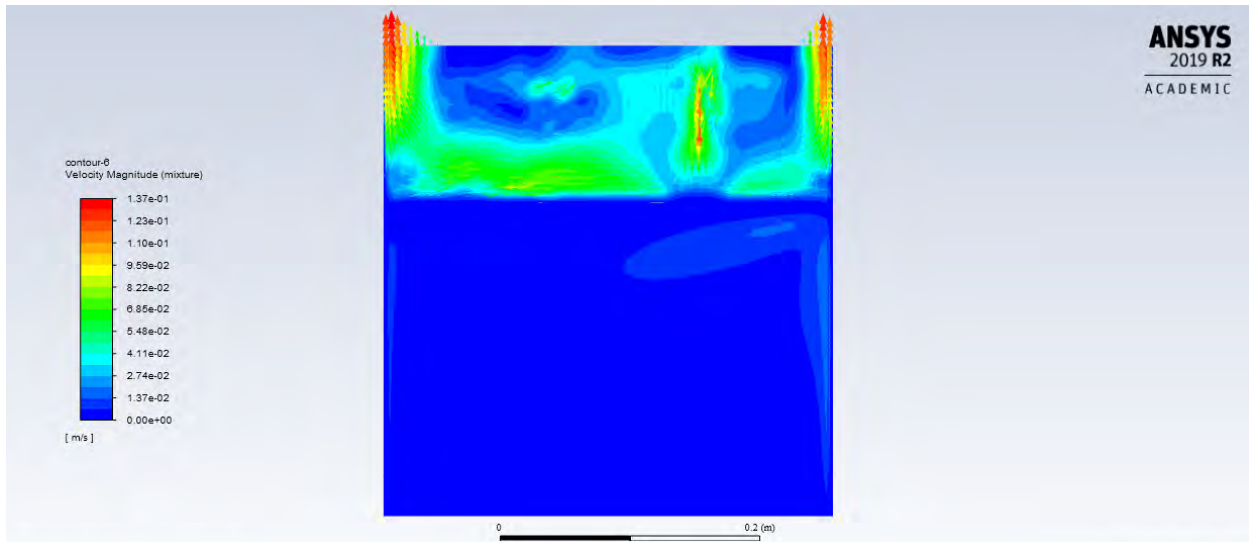


(a)



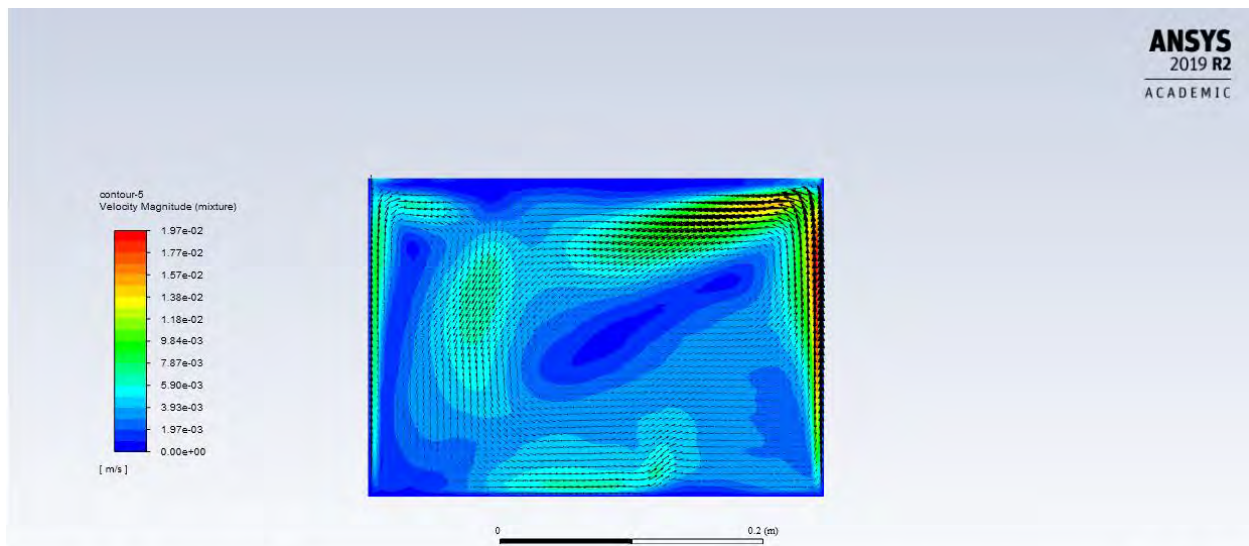
(b)

Figure 3.14: Temperature at 2350 s (a) Contour, (b) XY plot.



scene-1 (Time=2.3500e+03) Nov 14, 2019
ANSYS Fluent 2019 R2 (2d, pbns, vof, sstkw, transient)

(a)

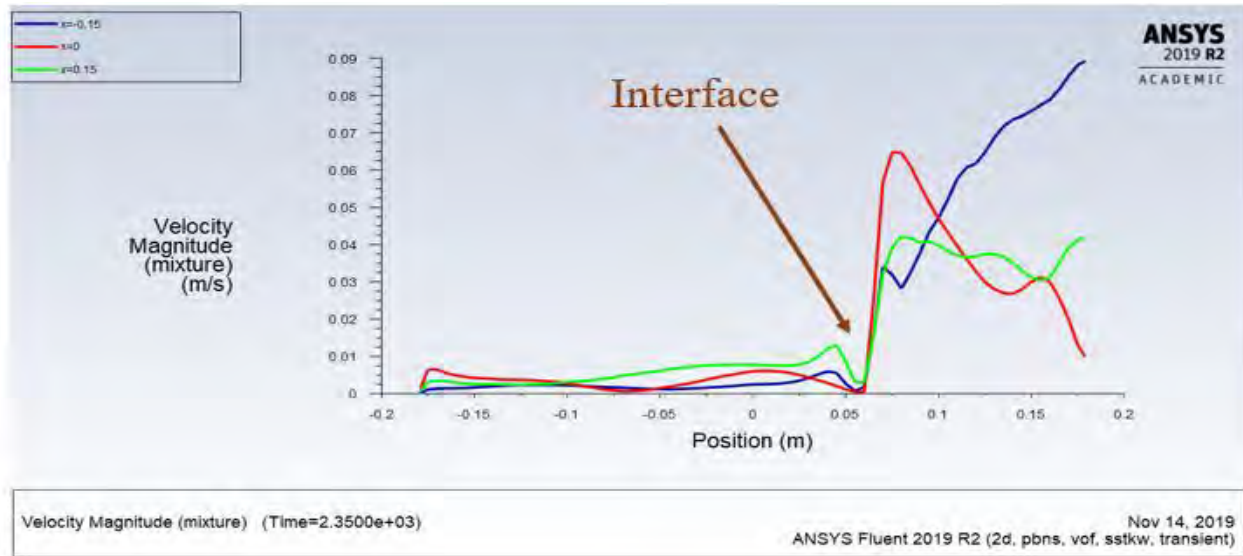


water-velocity (Time=2.3500e+03) Nov 14, 2019
ANSYS Fluent 2019 R2 (2d, pbns, vof, sstkw, transient)

(b)

Figure 3.15: Velocity at 2350 s (a) Contour, (b) Velocity vector in the water domain, (c) XY plot.

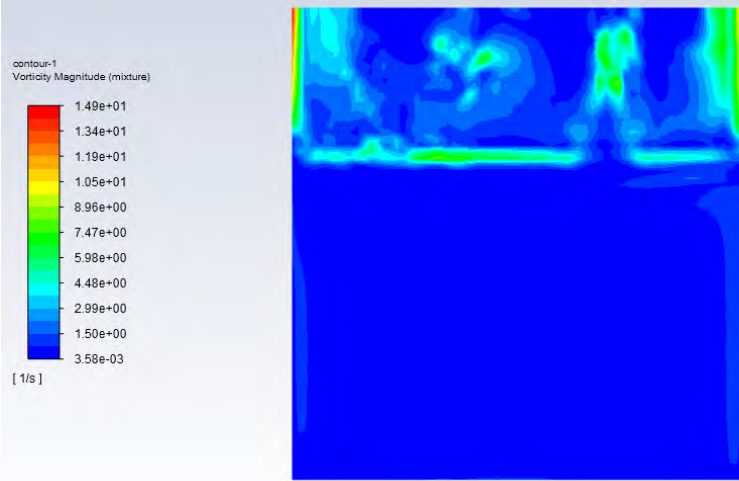
Figure 3.15—continued



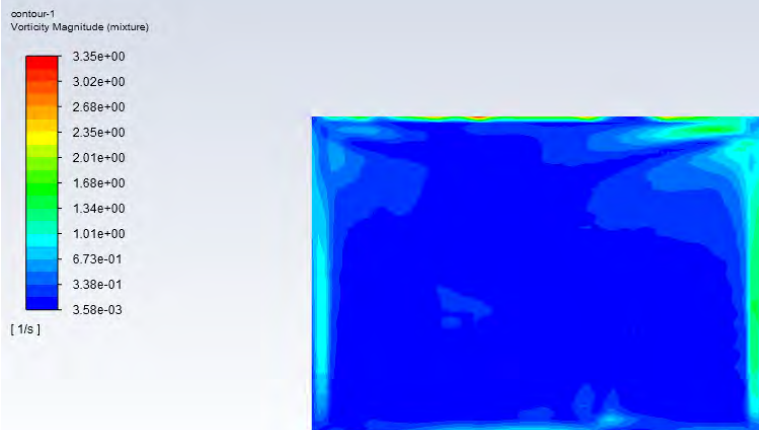
(c)

c) Vorticity

Vorticity contour is shown in Figure 3.16 (a) for air and water domain, where the vorticity is higher at the air side. It is clear that there is higher vorticity at the sides of the tank, which can be related to the circulation at this region. Moreover, it can be seen that the vorticity is higher at the water–air interface, which is mainly related to the higher movement and evaporation rate at this area. In Figure 3.16 (b) vorticity at the water domain is shown, where it is higher at the wall sides, bottom, and top due to higher velocity at these locations compared to the rest. Moreover, the vorticity in the water domain is still very small compared to that in the air domain [refer to Figure 3.16 (c)]. However, it is higher than the vorticity at $t = 1205$ s, due to higher velocity at this time. It is clear that vorticity begins to gradually increase after the interface [refer to Figure 3.16 (c)].



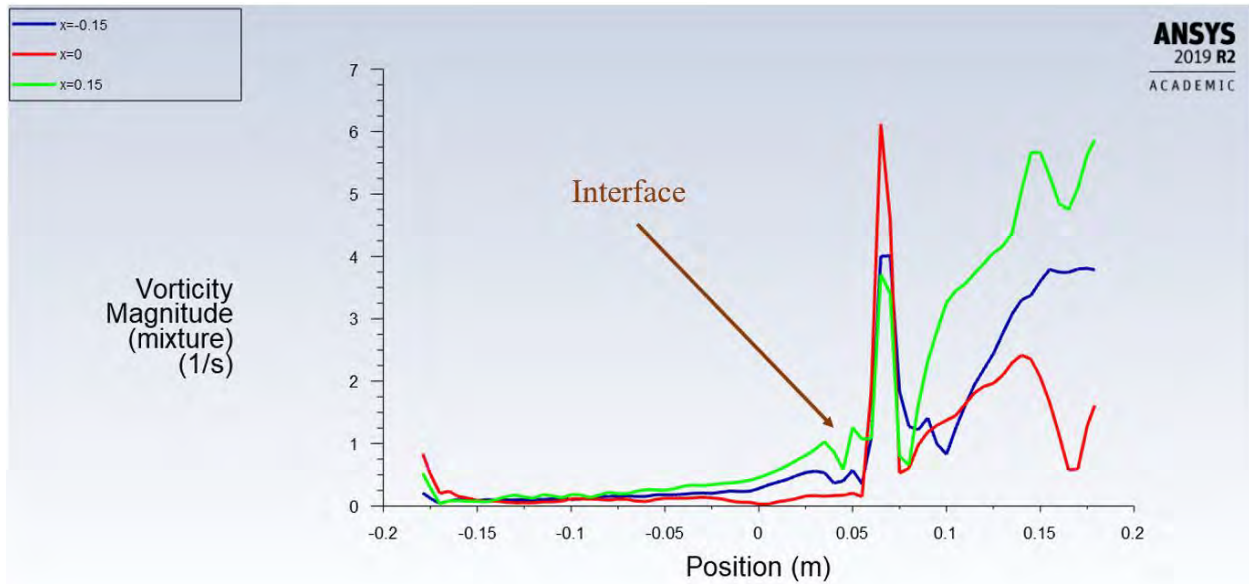
(a)



(b)

Figure 3.16: Vorticity at 2350 s (a) Contour, (b) Vorticity vector in the water domain, (c) XY plot.

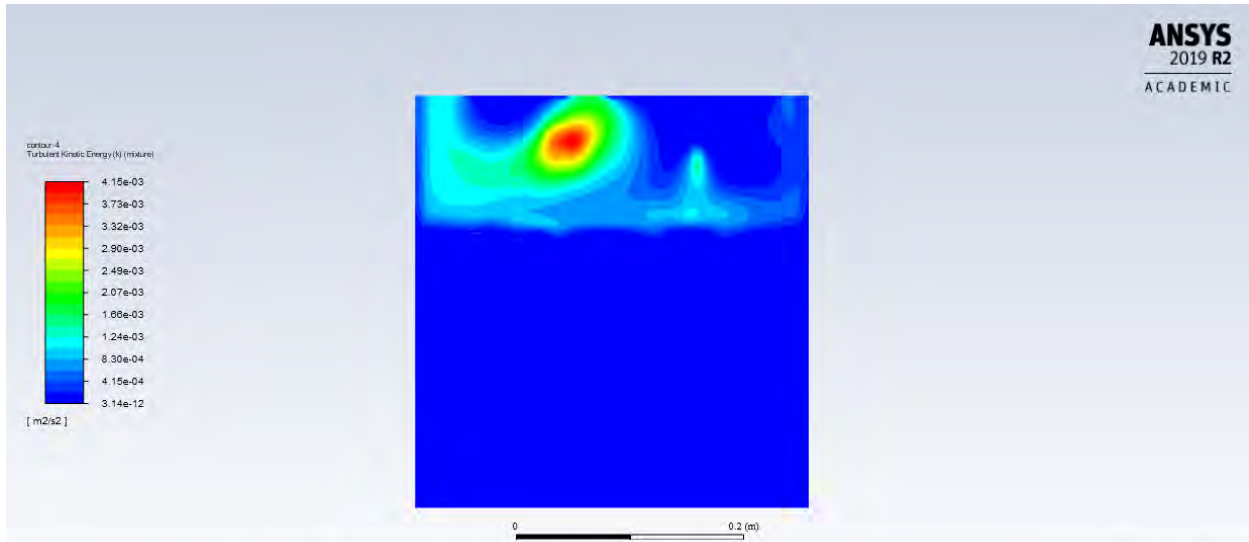
Figure 3.16—continued



(c)

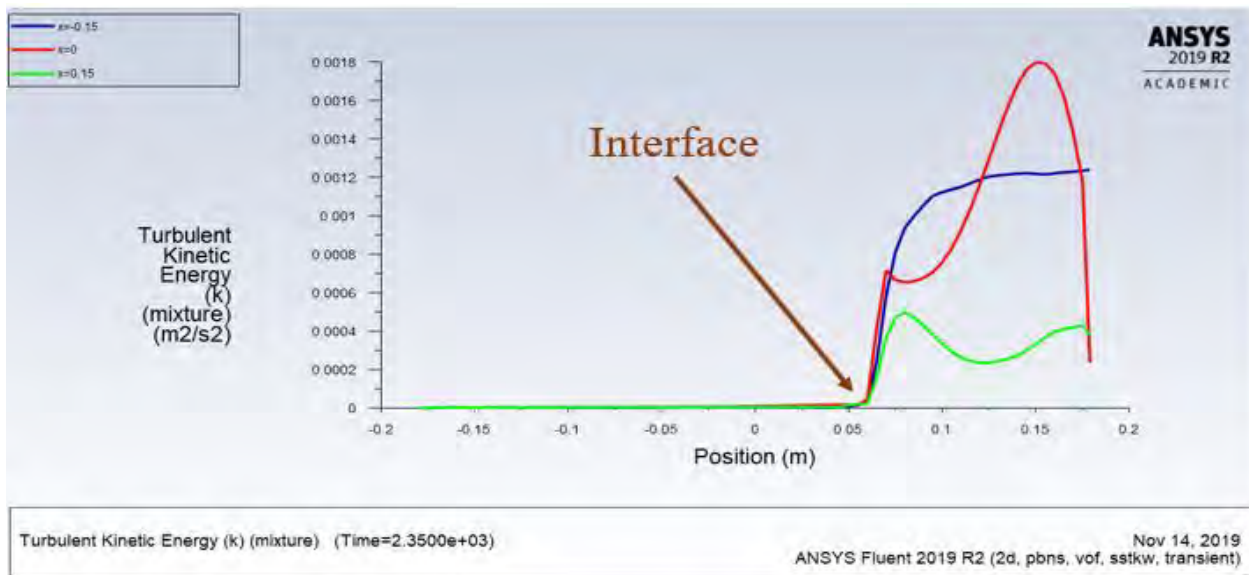
d) Turbulence Kinetic Energy

Turbulence kinetic energy (TKE) contour is shown in Figure 3.17 (a), where the TKE is higher at the air domain due to the higher velocity. In addition, TKE at this time is higher than the TKE at 1205 s, which is related to the higher velocity. Moreover, in the water domain the TKE is still very small compared to that in the air domain, as evident in Figure 3.17 (b). It is clear that TKE begins to gradually increase after the interface [refer to Figure 3.17 (b)].



Contours of Turbulent Kinetic Energy (k) (mixture) (m2/s2) (Time=2.3500e+03) Nov 14, 2019
ANSYS Fluent 2019 R2 (2d, pbns, vof, sstkw, transient)

(a)



(b)

Figure 3.17: Turbulence kinetic energy at 2350 s (a) Contour, (b) XY plot.

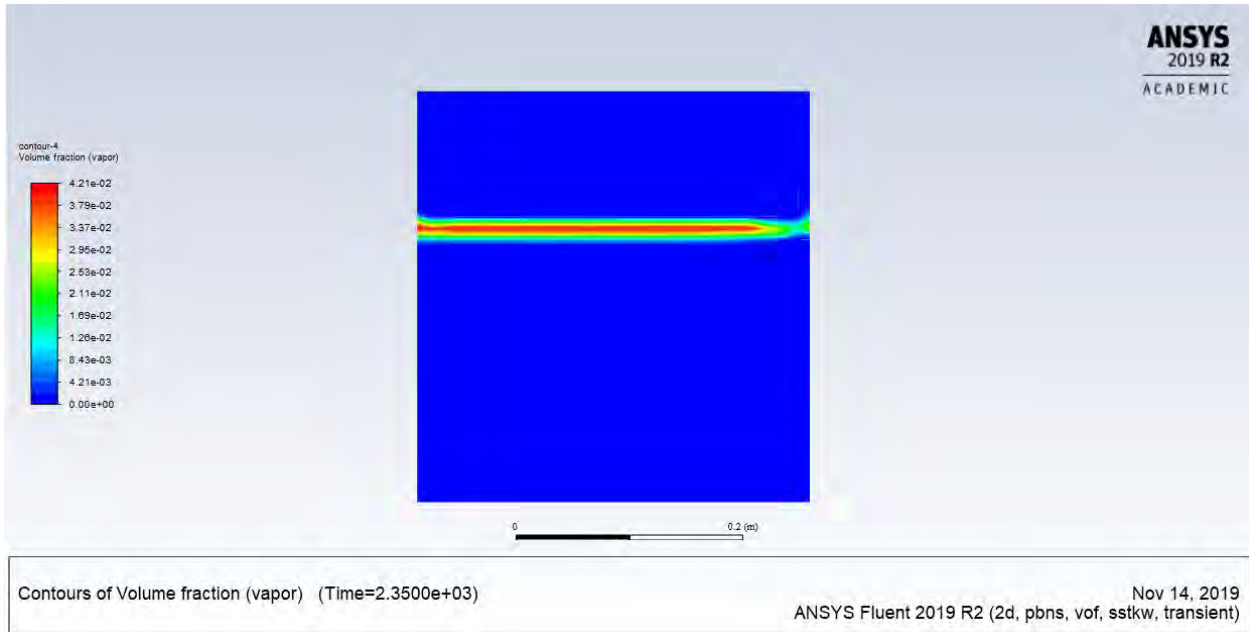
e) Surface Evaporation

The surface evaporation at this time is shown in Figure 3.18. This can be seen clearly in Figure 3.18 (a), where the surface evaporation started to increase at the water–air interface. At this time, where $t = 2350$ s, the volume fraction of vapor is 4.21 %, which is higher compared to the fraction of vapor at $t = 1205$ s. This increase is mainly related to the rising temperature of the water. This is shown in Figure 3.18 (b) at three different locations on the x-axis along with the y-axis.

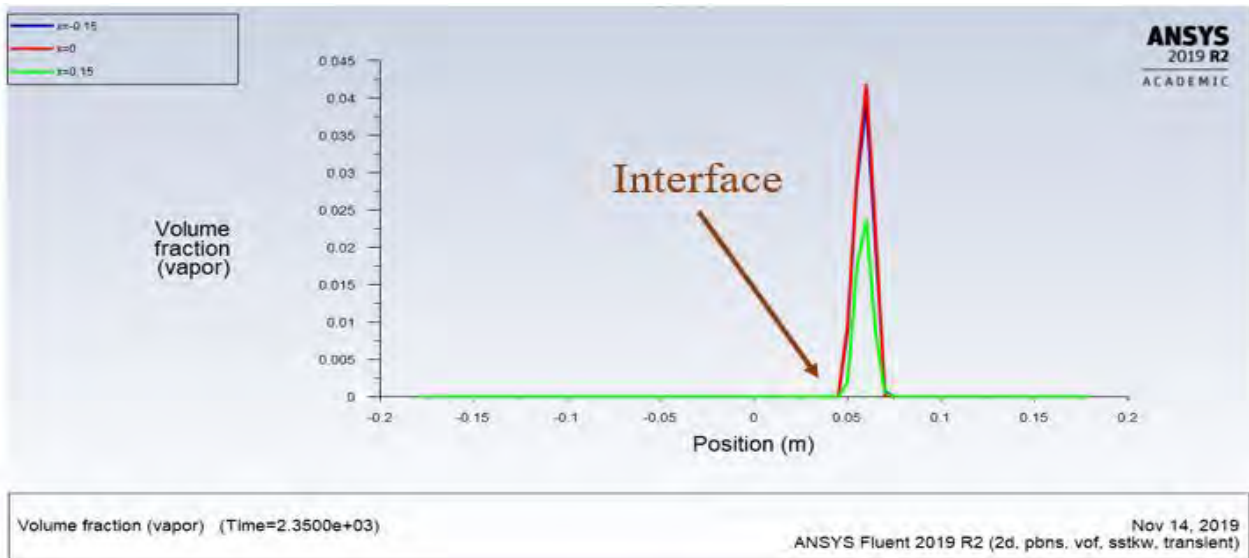
4) At $t = 7200$ Seconds

a) Temperature

The temperature of the water keeps rising with time, as seen in Figure 3.19. Figure 3.19 (a) shows the contour temperature, where it is clear that the temperature of the water has reached about 46°C. It is evident that the temperature of the air domain remains at the room temperature. However, the temperature at the two sides of the tank is higher than at the center in the air domain, which is related to the circulation of air in this region. In Figure 3.19 (b), the plot shows the temperature before and after the water–air interface at three different locations. It is clear that the water domain is close to reaching the desired temperature at this time. It can also be seen that the temperature at the water–air interface decreases gradually to room temperature at the top of the tank [refer to Figure 3.19 (b)].

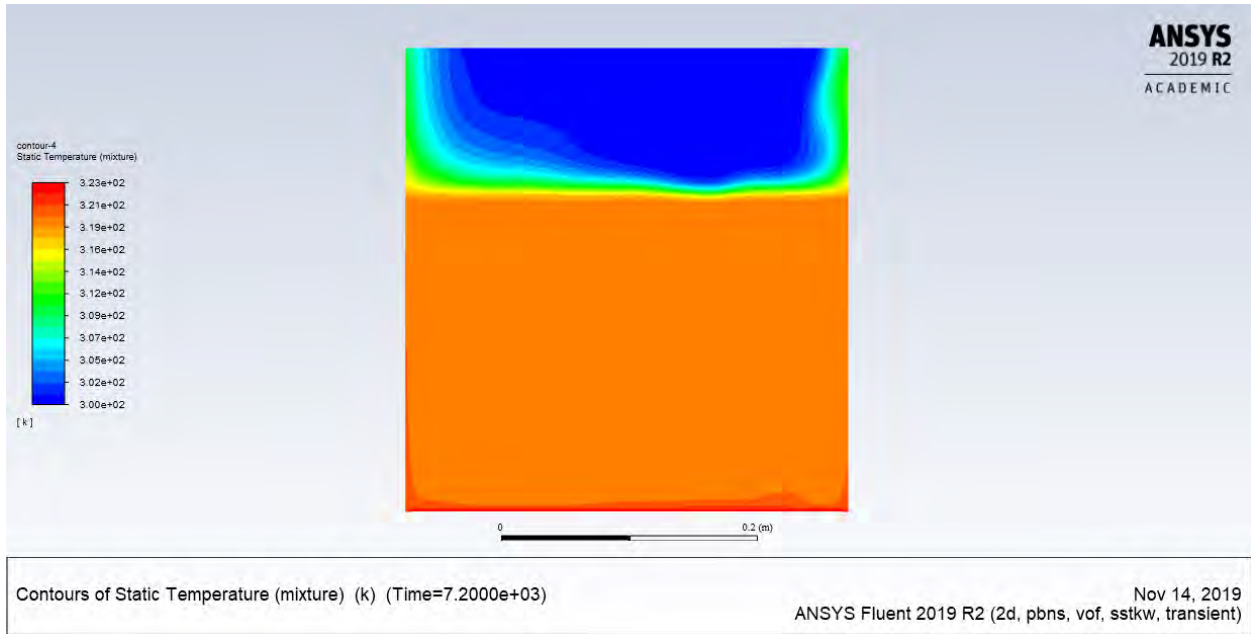


(a)

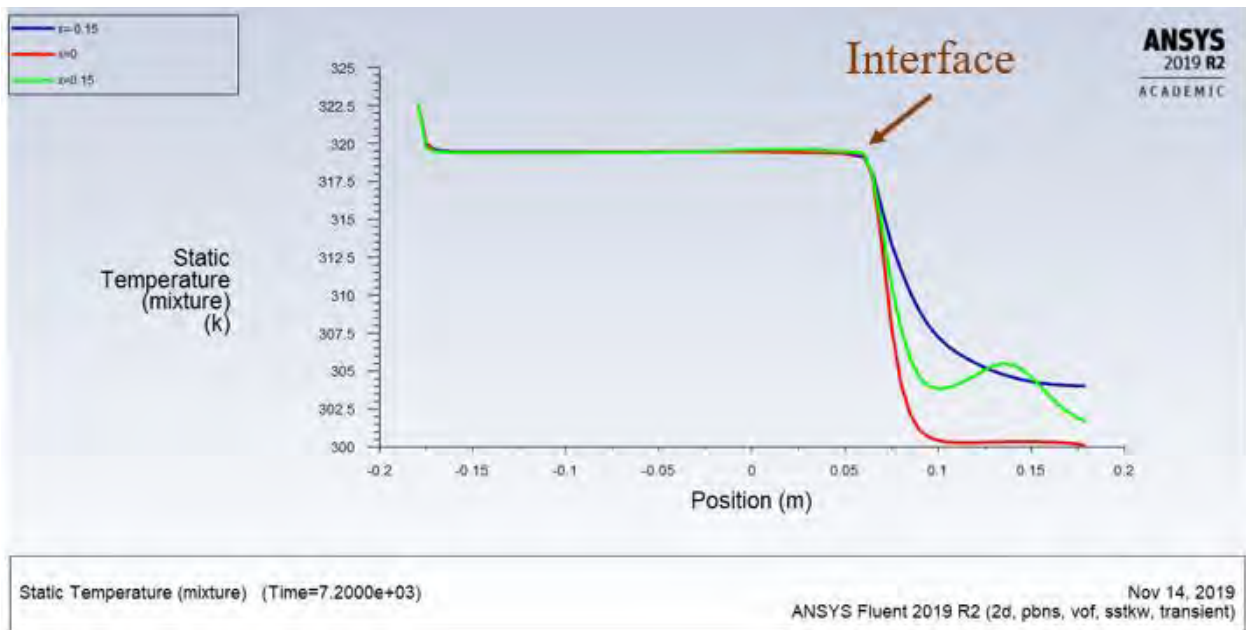


(b)

Figure 3.18: Surface evaporation at 2350 s (a) Contour, (b) XY plot.



(a)

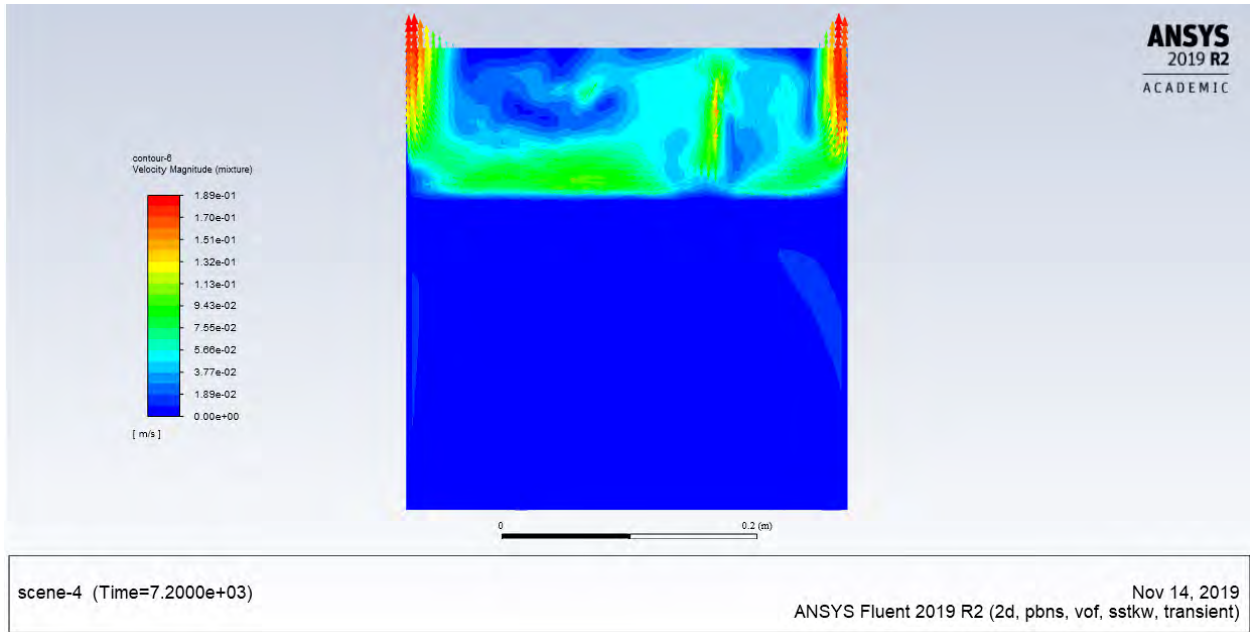


(b)

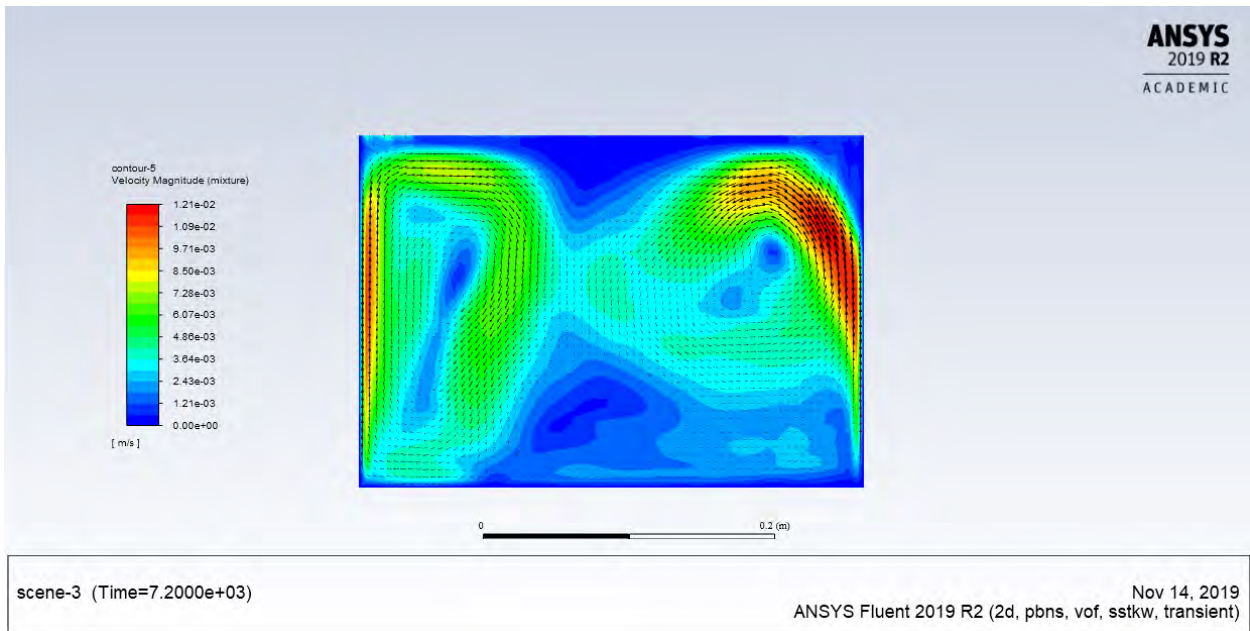
Figure 3.19: Temperature at 7200 s (a) Contour, (b) XY plot.

b) Velocity

In Figure 3.20, the velocity magnitude for contour, vector for the water domain, and plot are shown. It can be seen in Figure 3.20 (a) that the velocity of air above the water surface is higher at this time compared to the velocity at $t = 2350$ s. This can be related to the evaporation coming from the free water surface, which increases the circulation in the air domain and hence the velocity. Moreover, the direction of velocity vectors in the air domain is clear, where two vortices are observed. These two vortices started from the top of the tank coming down to the water surface and then circulating up to the ambient [refer to Figure 3.20 (a)]. Meanwhile, the velocity of the water domain which is related to the buoyancy forces is shown in Figure 3.20 (b). Therefore, the rotation of two vortices inside the water due to the development of Bénard–Rayleigh convection can be seen. It is clear that these two vortices started from the bottom of the tank, going up to the water surface and then circulating down to the water. Figure 3.20 (c) shows the velocity difference before and after the interface.



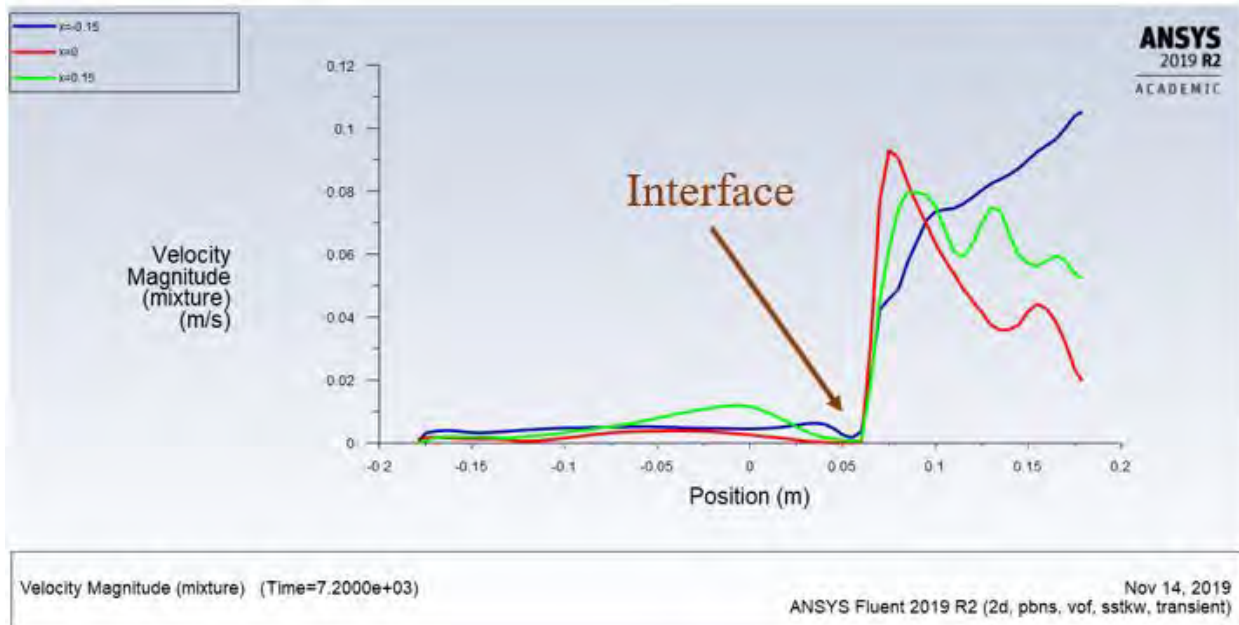
(a)



(b)

Figure 3.20: Velocity at 7200 s (a) Contour, (b) Velocity vector in the water domain, (c) XY plot.

Figure 3.20—continued

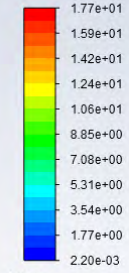


(c)

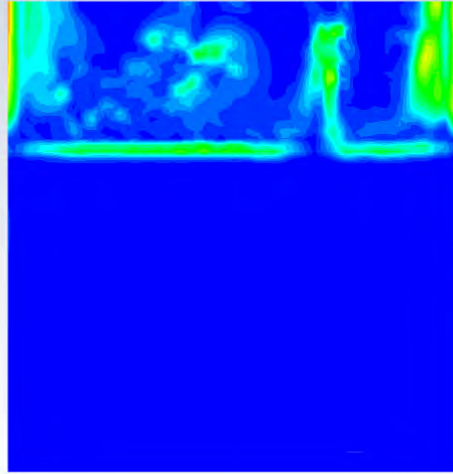
c) Vorticity

Vorticity contour is shown in Figure 3.21 (a) for air and water domain, where the vorticity is higher at the air side. It is clear that vorticity is higher at the sides of the tank, which can be related to the circulation at this region and this time compared to $t = 2350$ s. In addition, it can be seen that the vorticity is higher at the water–air interface, which is mainly related to the higher movement and the evaporation rate in this area. Figure 3.21 (b) shows vorticity in the water domain, where it is higher at the wall sides, bottom, and top due to higher velocity at these locations compared to the rest. Moreover, the vorticity in the water domain is still very small compared to the air domain [refer to Figure 3.21 (c)]. However, the vorticity has increased at this time compared to $t = 2350$ s, due to higher velocity at this time. It is clear that vorticity begins to gradually increase after the interface [refer to Figure 3.21 (c)].

contour-1
Vorticity Magnitude (mixture)

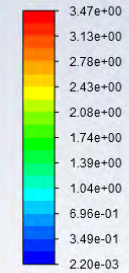


[1/s]

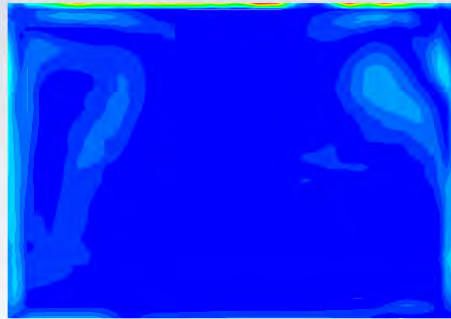


(a)

contour-1
Vorticity Magnitude (mixture)



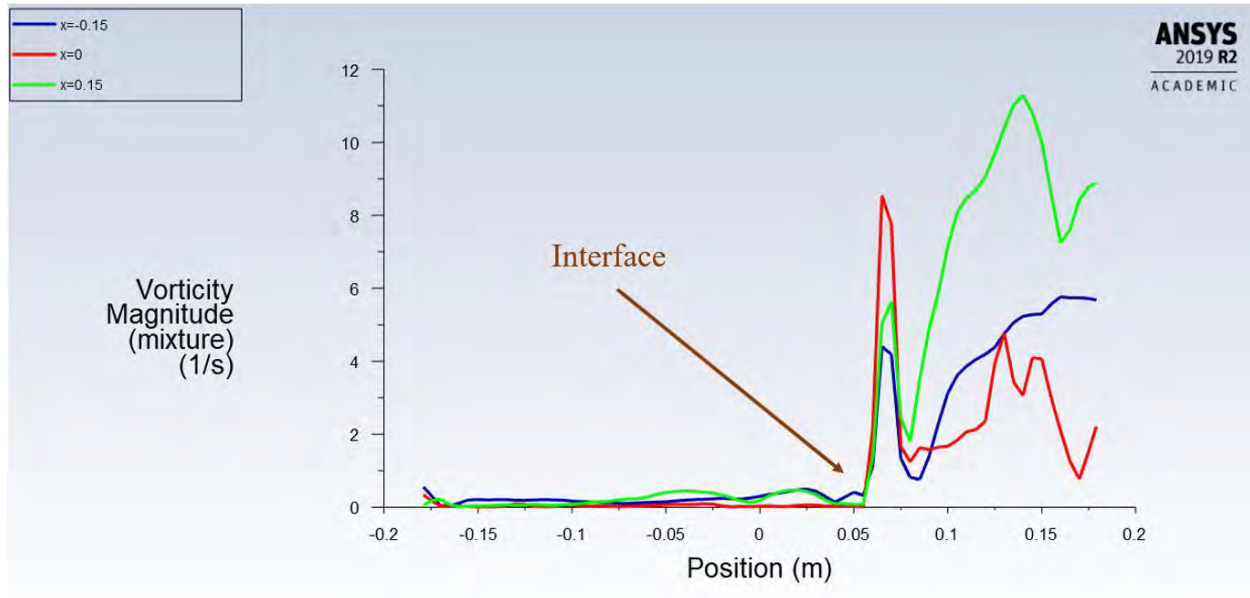
[1/s]



(b)

Figure 3.21: Vorticity at 7200 s (a) Contour, (b) Vorticity vector in the water domain, (c) XY plot.

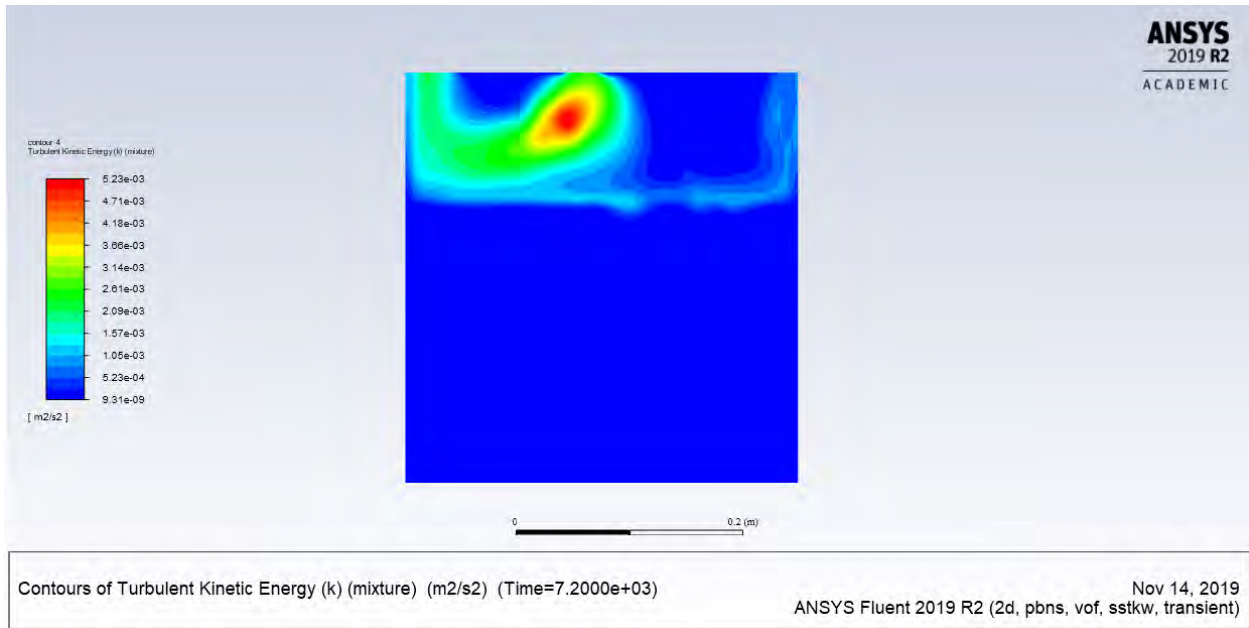
Figure 3.21—continued



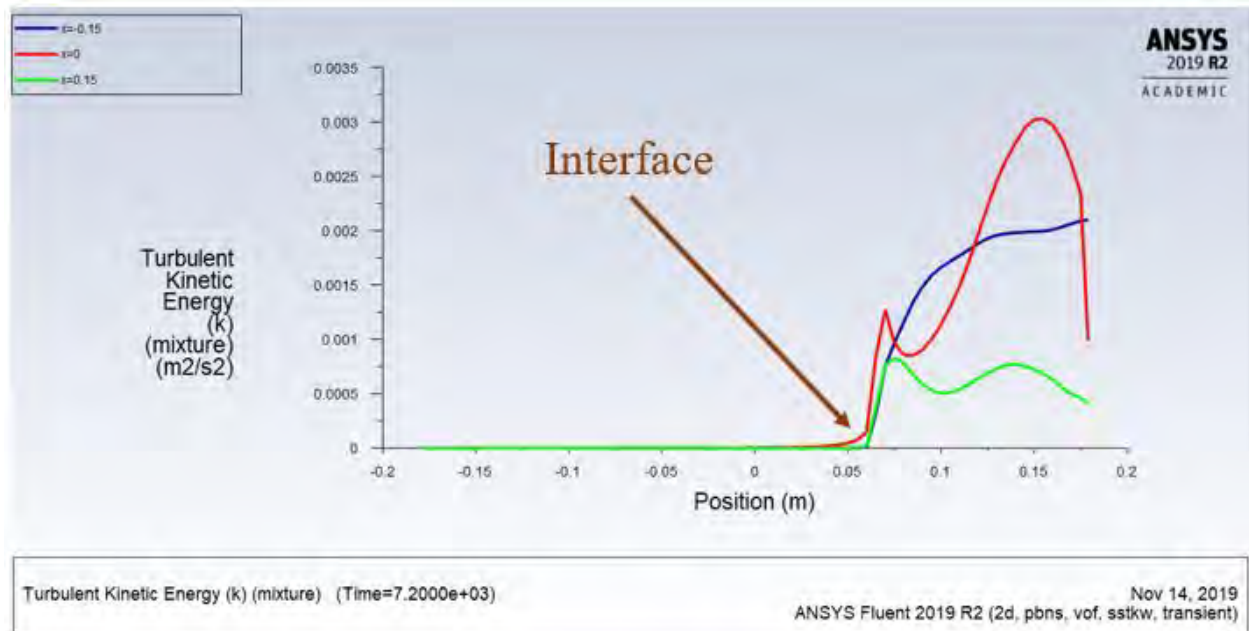
(c)

d) Turbulence Kinetic Energy

Turbulence kinetic energy (TKE) contour is shown in Figure 3.22 (a), where the TKE is higher at the air domain due to the higher velocity. In addition, TKE at this time is higher than the TKE at 2350 s, which is related to the higher velocity. Moreover, in the water domain the TKE is still very small compared to the air domain, as can be seen in Figure 3.22 (b). It is clear that TKE begins to gradually increase after the interface [refer to Figure 3.22 (b)].



(a)



(b)

Figure 3.22: Turbulence kinetic energy at 7200 s (a) Contour, (b) XY plot.

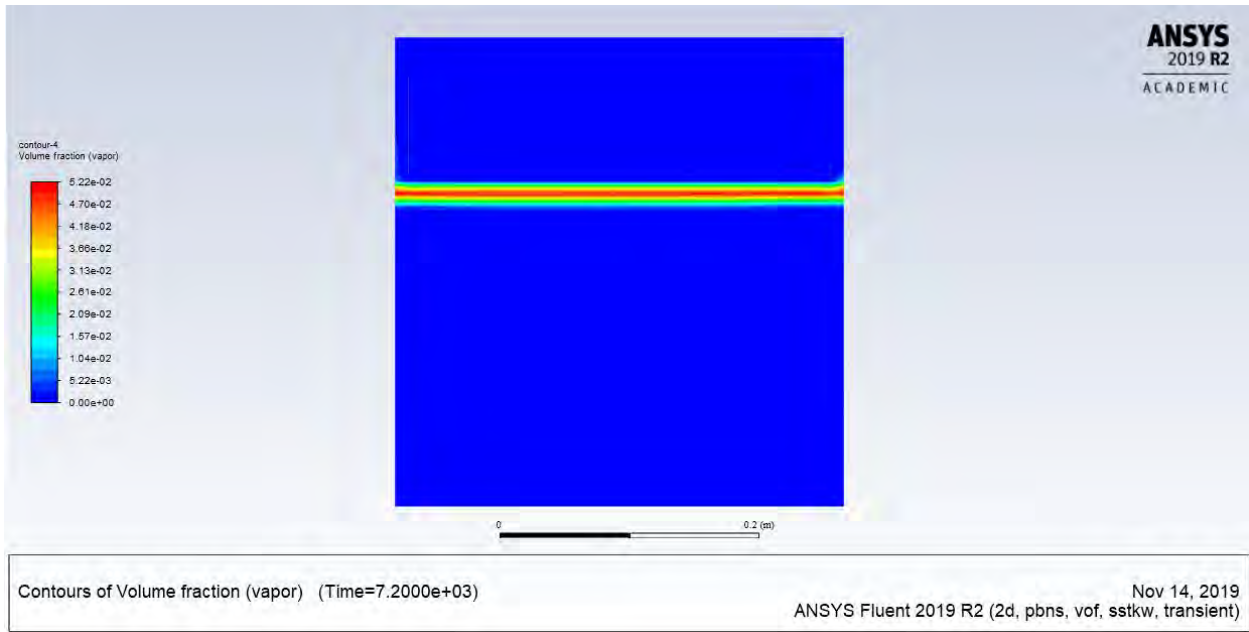
e) Surface Evaporation

The surface evaporation at this time is shown in Figure 3.23. This can be seen clearly in Figure 3.23 (a), where the surface evaporation started to increase at the water–air interface. At this time, where $t = 7200$ s, the volume fraction of vapor is 5.22 %, which is higher compared to the fraction of vapor at $t = 2350$ s. This increase is mainly related to the rising temperature of the water. This is shown in Figure 3.23 (b) at three different locations on the x-axis along with the y-axis.

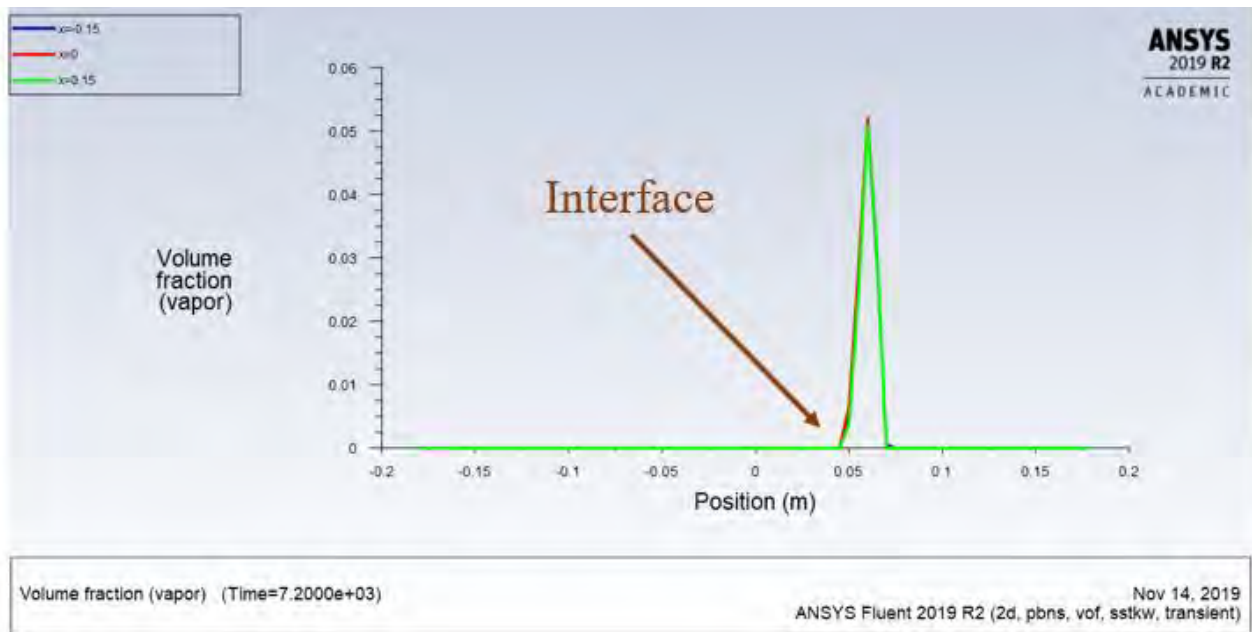
5) At $t = 12925$ Seconds

a) Temperature

The temperature of the water keeps rising with time until it reaches the desired temperature of 50°C , as can be seen in Figure 3.24. Figure 3.24 (a) shows the contour temperature, where it is clear that the temperature of the water has reached the highest temperature. It is evident that the temperature of the air domain remains at the room temperature. However, the temperature at the two sides of the tank and in the middle is higher than at the other locations in the air domain, which is related to the circulation of air in this region to remove the heat. In Figure 3.24 (b), the plot shows the temperature before and after the water–air interface at three different locations. It is clear that the water domain has reached the desired temperature at this time. Moreover, it can be seen that the temperature at the water–air interface decreases gradually to room temperature at the top of the tank [refer to Figure 3.24 (b)].

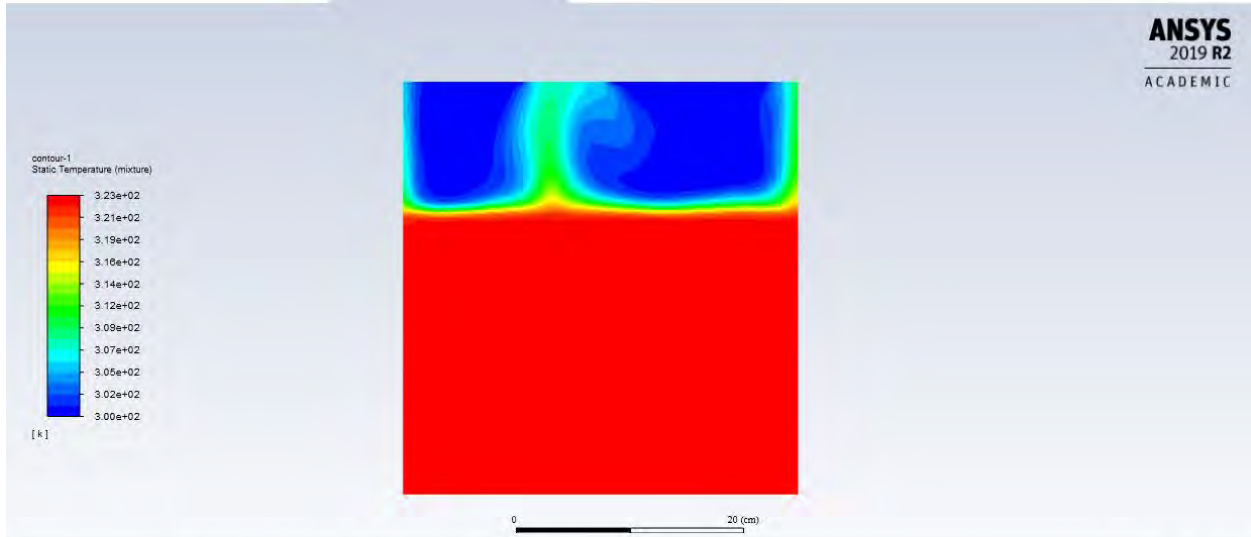


(a)



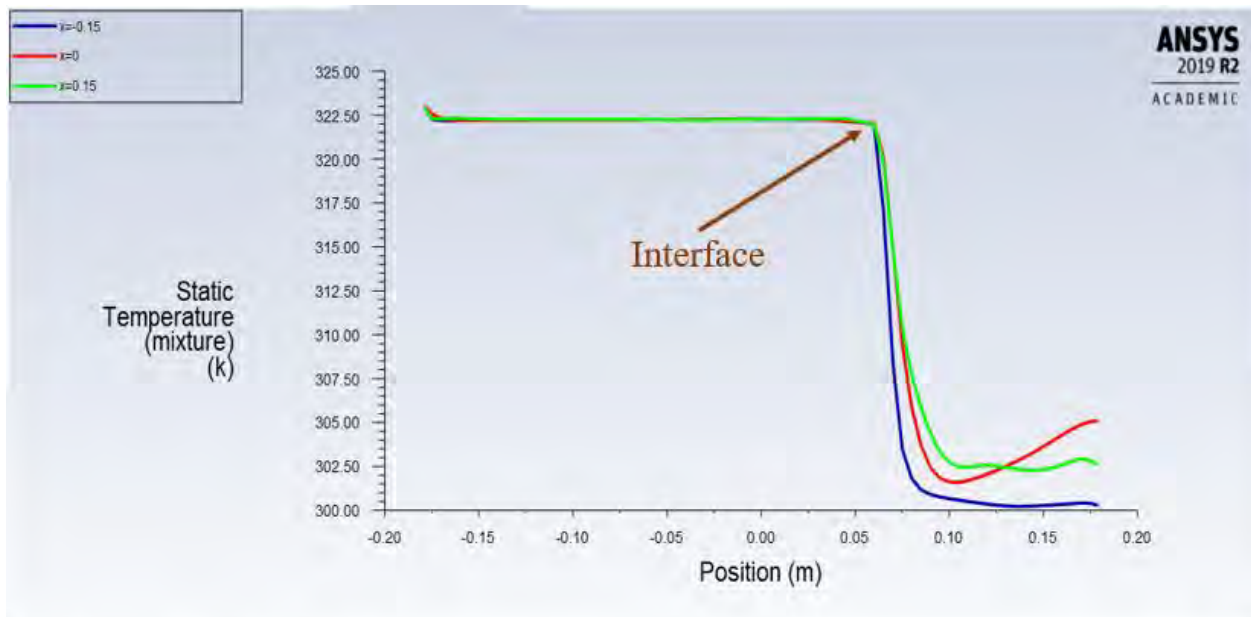
(b)

Figure 3.23: Surface evaporation at 7200 s (a) Contour, (b) XY plot.



Contours of Static Temperature (mixture) (k) (Time=1.2925e+04) Dec 04, 2019
ANSYS Fluent 2019 R2 (2d, pbns, vof, sstk, transient)

(a)



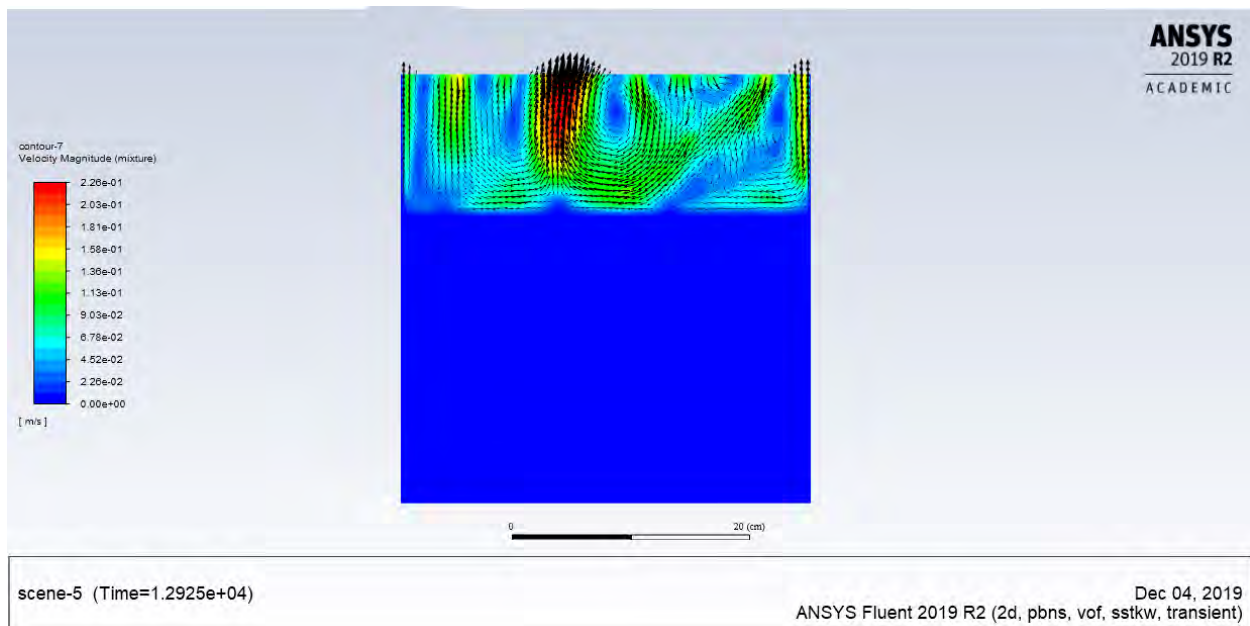
Static Temperature (mixture) (Time=1.2925e+04) Dec 04, 2019
ANSYS Fluent 2019 R2 (2d, pbns, vof, sstk, transient)

(b)

Figure 3.24: Temperature at 12925 s (a) Contour, (b) XY plot.

b) Velocity

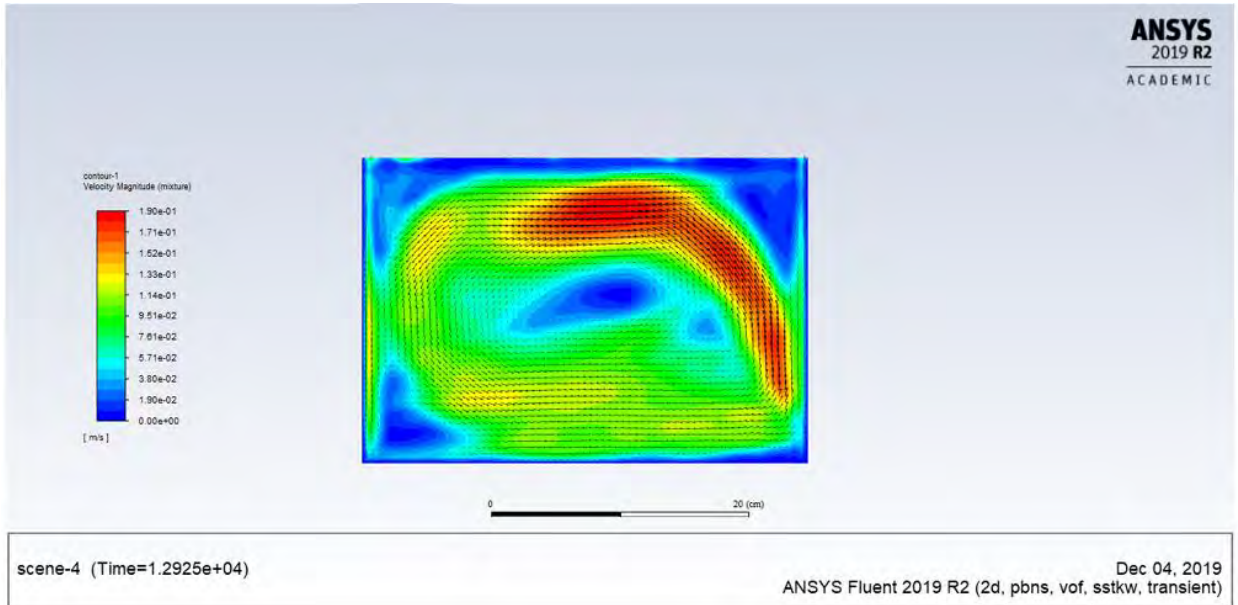
Figure 3.25 shows the velocity magnitude for contour, vector for the water domain, and plot. It can be seen in Figure 3.25 (a) that the velocity of air above the water surface is higher at this time compared to the velocity at $t = 7200$ s. This can be related to the evaporation from the free water surface along with temperature rise, which increases the circulation in the air domain and hence the velocity. Moreover, the direction of velocity vectors in the air domain is clear, where two vortices are observed coming down and then exiting to the ambient air at the center. These two vortices started from the top of the tank, coming down to the water surface and then circulating up to the ambient air [refer to Figure 3.25 (a)]. Meanwhile, the velocity of the water domain which is related to the buoyancy forces is shown in Figure 3.25 (b). Here, the rotation of one vortex instead of two compared to earlier is noticeable, which is due to the steady state of temperature and its reaching the highest value. This movement is related to the development of Bénard–Rayleigh convection. It is



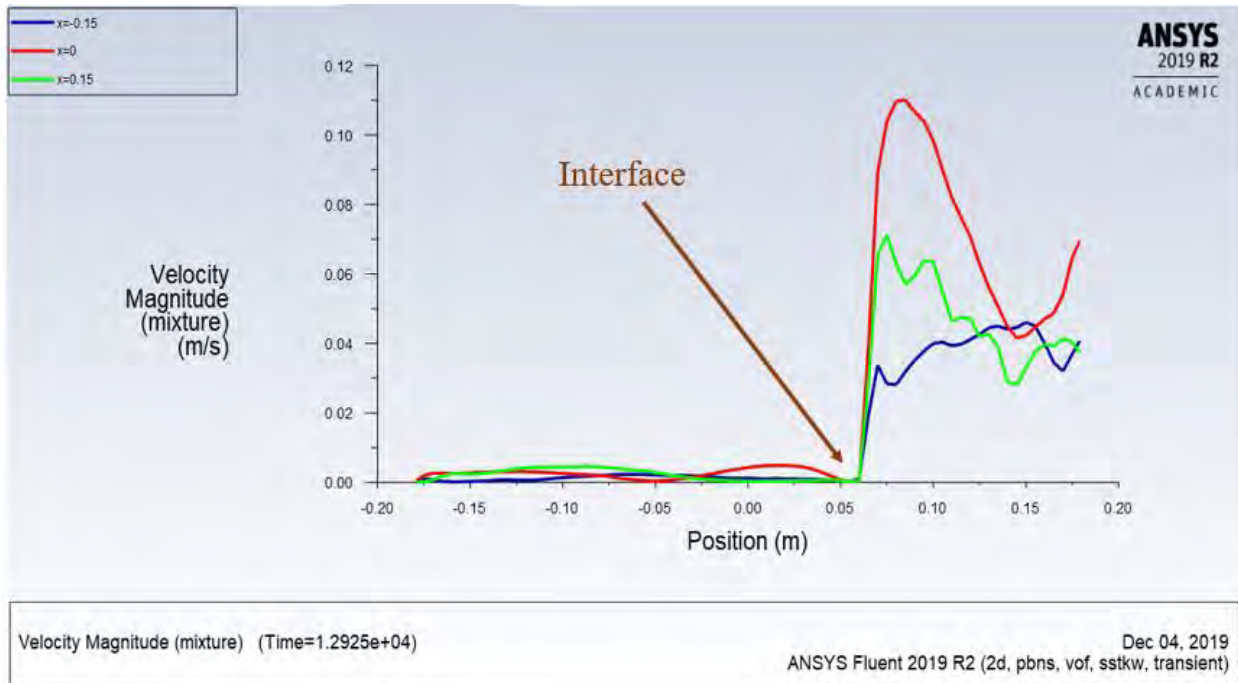
(a)

Figure 3.25: Velocity at 12925 s (a) Contour, (b) Velocity vector in the water domain, (c) XY plot.

Figure 3.25—continued



(b)

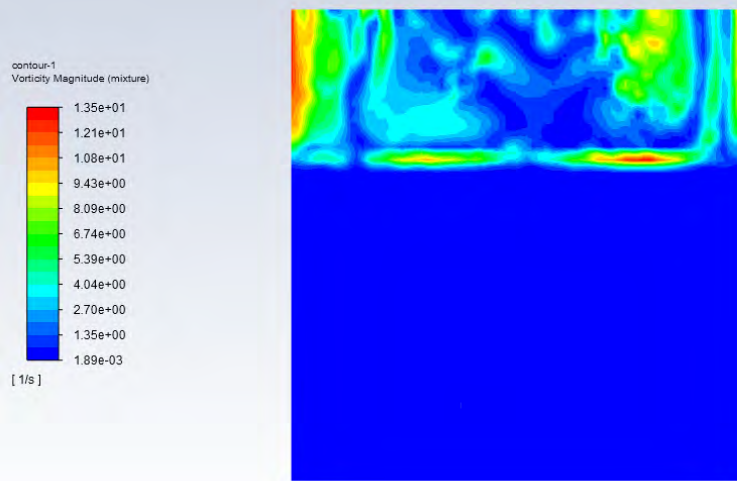


(c)

clear that this vortex started from the bottom of the tank, going up to the water surface and then circulating down to the water, where the highest value is near the water surface. This is due to the temperature difference between the bulk water and its surface. Figure 3.25 (c) shows the velocity difference before and after the interface.

c) Vorticity

Vorticity contour is shown in Figure 3.26 (a) for air and water domain, where the vorticity is higher at the air side. It is clear that vorticity is higher at the sides of the tank, which can be related to the circulation at this region and this time compared to $t = 7200$ s. In addition, it can be seen that the vorticity is higher at the water–air interface, which is mainly related to the higher movement and evaporation rate in this area. In Figure 3.26 (b), vorticity at the water domain is shown, where it is higher at the wall sides, bottom, and top due to higher velocity at these locations compared to the rest. Moreover, the vorticity in the water domain is still very small compared to that in the air domain [refer to Figure 3.26 (c)]. However, the vorticity has increased at this time compared to $t = 7200$ s due to higher velocity at this time, especially near the free water surface. It is clear that vorticity begins to gradually increase after the interface [refer to Figure 3.26 (c)].



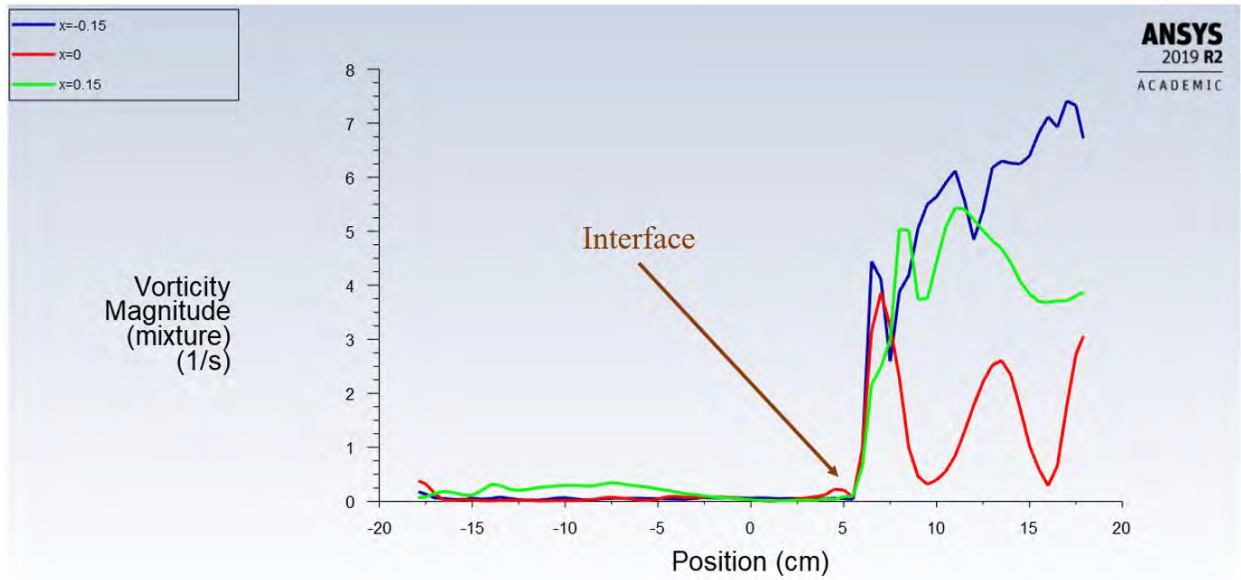
(a)



(b)

Figure 3.26: Vorticity at 12925 s (a) Contour, (b) Vorticity vector in the water domain, (c) XY plot.

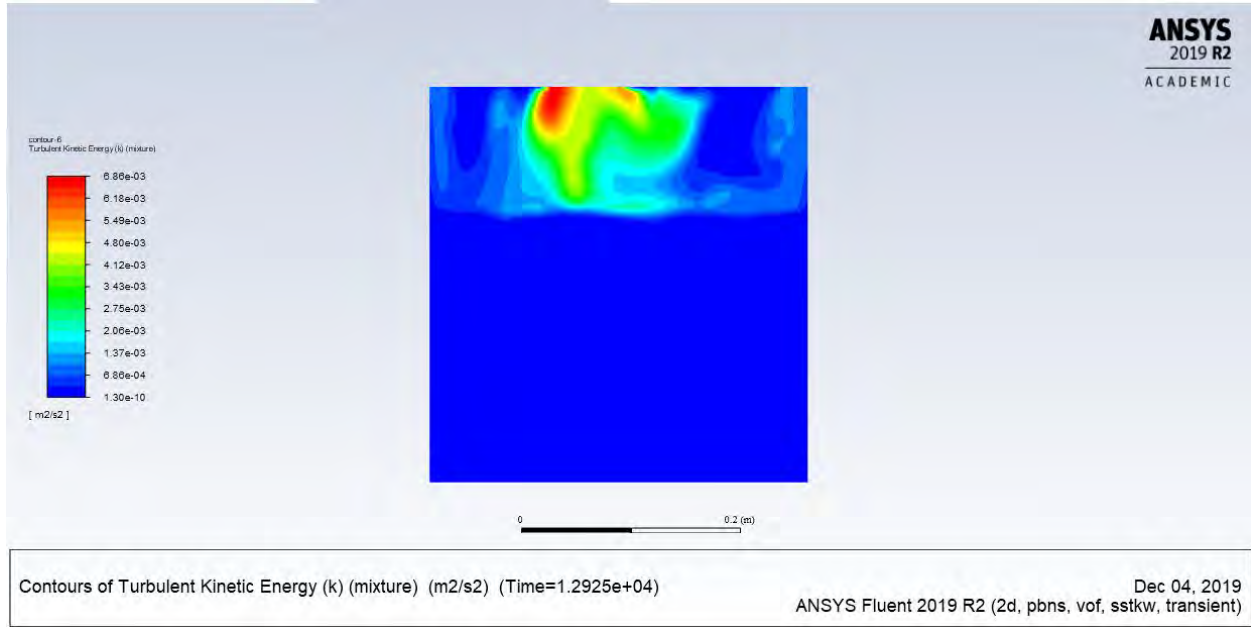
Figure 3.26—continued



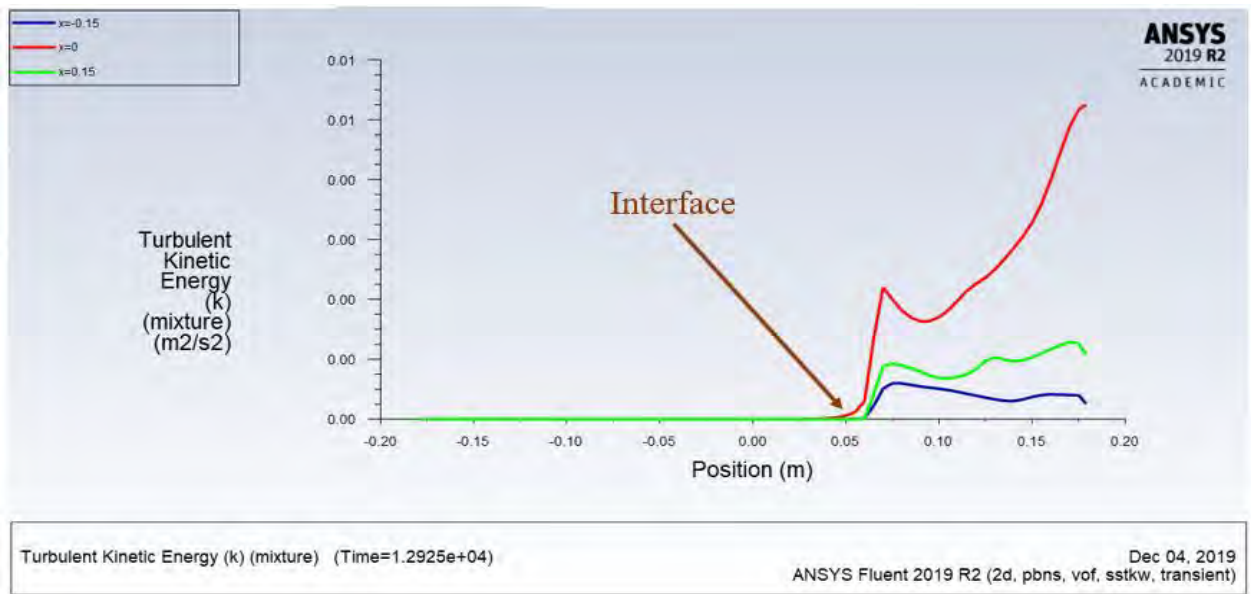
(c)

d) Turbulence Kinetic Energy

Turbulence kinetic energy (TKE) contour is shown in Figure 3.27 (a), where the TKE is higher in the air domain due to the higher velocity. In addition, TKE at this time is higher than the TKE at 7200 s, which is related to the higher velocity. Moreover, in the water domain the TKE is still very small compared to the air domain, as can be seen in Figure 3.27 (b). It is clear that TKE begins to gradually increase after the interface [refer to Figure 3.27 (b)].



(a)



(b)

Figure 3.27: Turbulence kinetic energy at 12925 s (a) Contour, (b) XY plot.

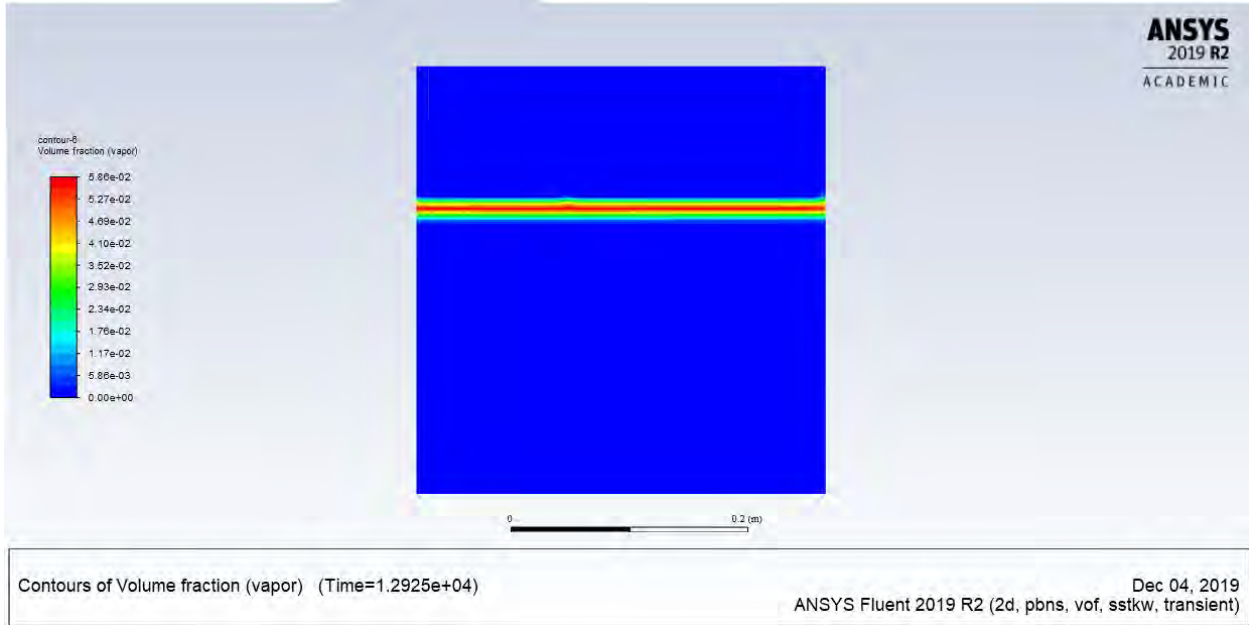
e) Surface evaporation

The surface evaporation at this time is shown in Figure 3.28. This can be seen clearly in Figure 3.28 (a), where the surface evaporation has started to increase at the water–air interface. At this time, when the desirable temperature has been reached, the volume fraction of vapor is 5.86 %, which is higher compared to the fraction of vapor at $t = 7200$ s. This increase is mainly related to the rising temperature of the water. This can be seen in Figure 3.28 (b) at three different locations on the x-axis along with the y-axis.

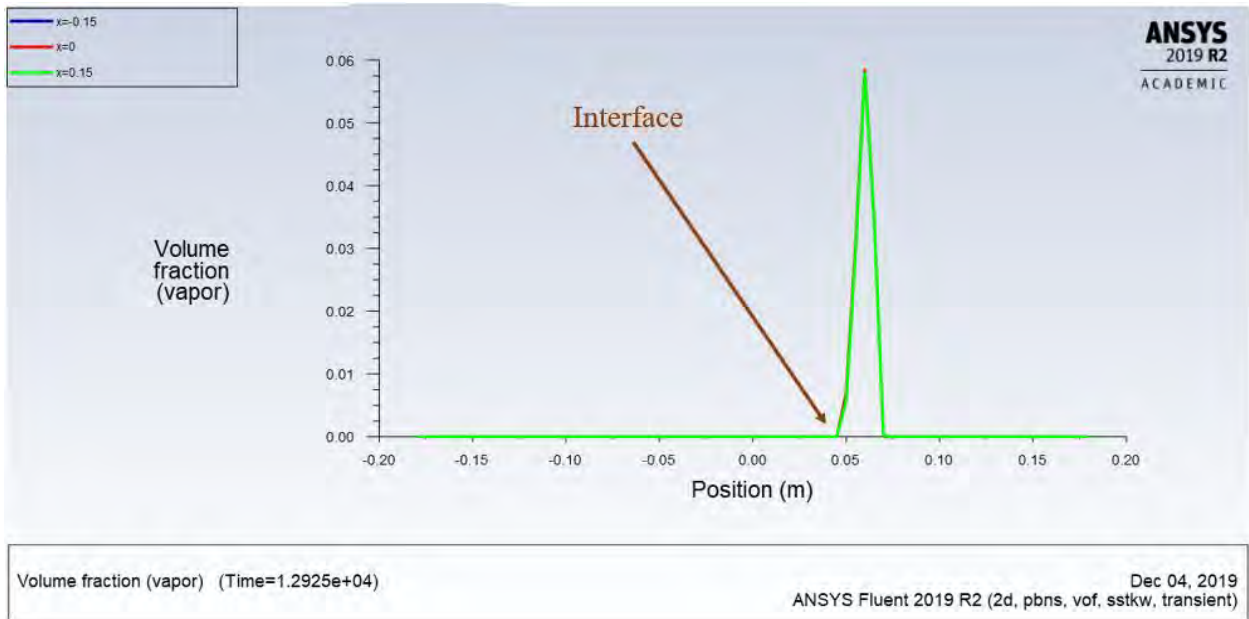
3.5 Three-Dimensional (3-D) Analysis

3.5.1 Geometry and Meshing

Three-dimensional (3-D) analysis was carried out as well in this work. For 3-D simulation, a quarter of the water tank was considered, for purposes of simplification. The geometry used for the testing was a water tank with dimensions of $8.75 \times 8.75 \times 40 \text{ cm}^3$, as can be seen in Figure 3.29. The tank was filled with water up to 24 cm and was open to ambient air. The bottom of the tank was an aluminum plate that is fixed at a temperature of 50°C , where the other four sides were insulated. The tank only allowed evaporation and heat transfer from the free interface surface, not the sides. This made the study more accurate and provided one dimension of diffusion for the falling rate model.



(a)



(b)

Figure 3.28: Surface evaporation at 12925 s (a) Contour, (b) XY plot.

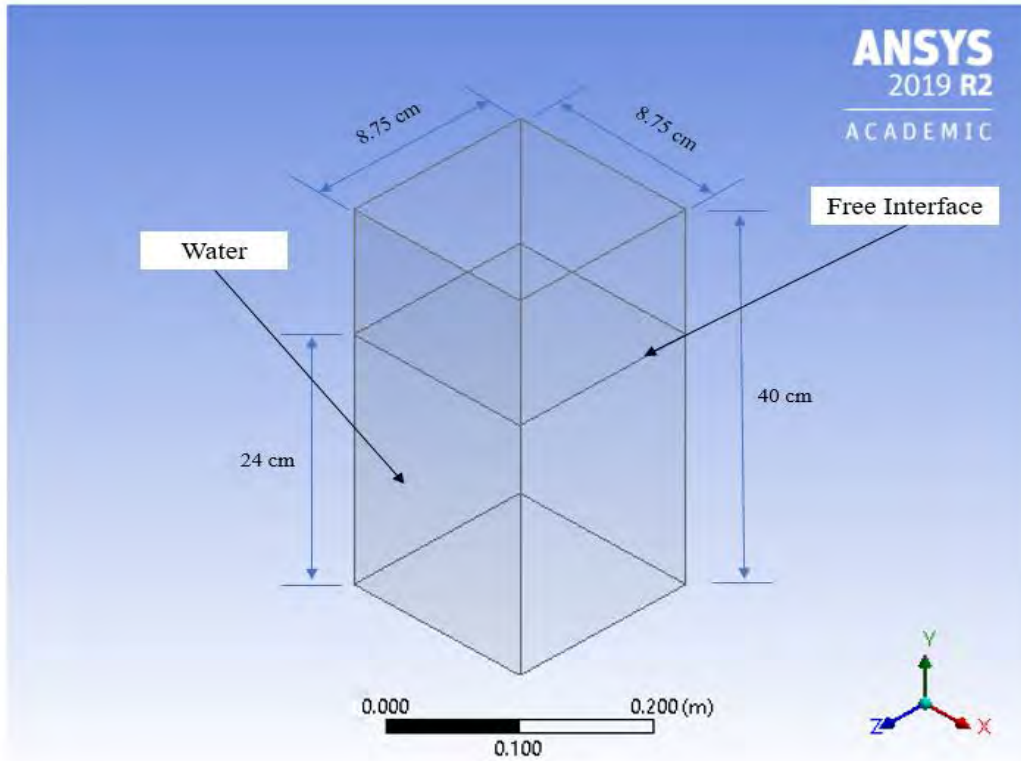


Figure 3.29: 3-D CFD geometry.

A mesh can be defined as a geometry that is broken up into a control volume or cells. Every cell is defined by a set of nodes, a cell center, and the faces that bound the cell. ANSYS FLUENT employs internal data structures in order to define the domain(s) of the mesh. Therefore, this is used to assign an order to cells, cell faces, and nodes in a mesh, and to establish connectivity between adjacent cells. Cells and cell faces are gathered into zones that mostly define the physical components of the model such as inlets, outlets, walls, and fluid regions. In this work, the mesh was generated by ANSYS FLUENT, as shown in Figure 3.30. The mesh details are listed in Table 3.4, where the number of nodes and elements are 509141 and 490000, respectively.

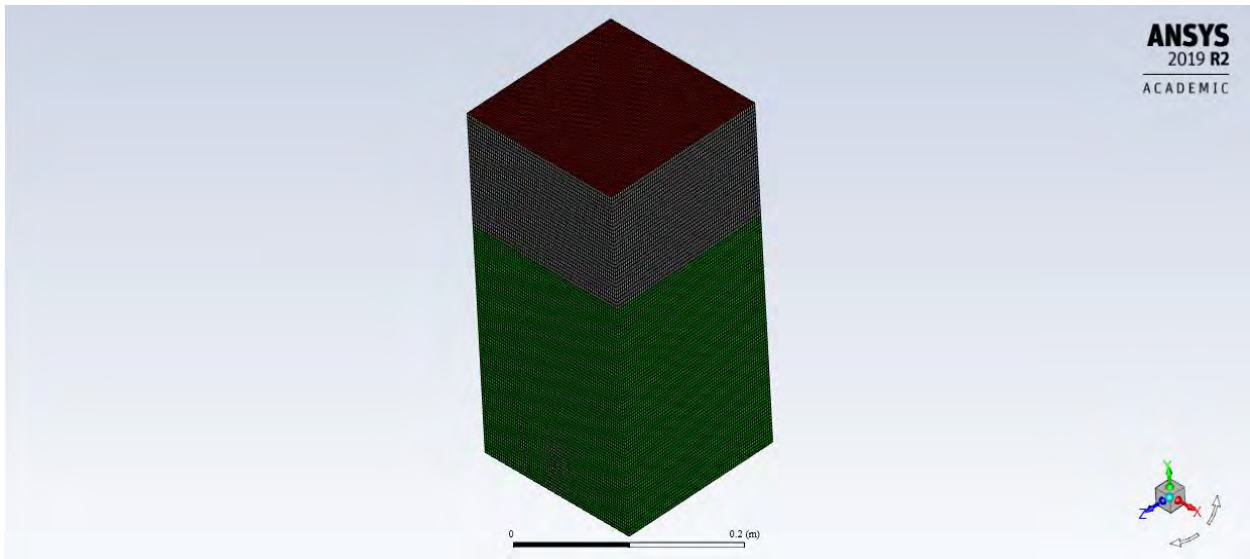


Figure 3.30: 3-D CFD grid meshing.

Table 3.4: The 3-D meshing details.

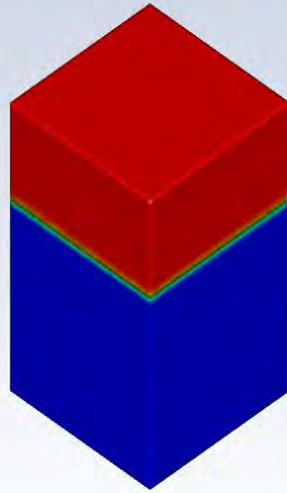
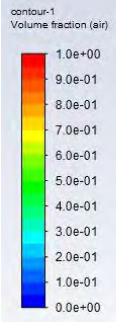
Description	Explanation
Number of nodes	509141
Number of elements	490000
Element order	Linear
Element size	0.0005
Export format	standard
Smoothing	Medium
Average surface area	0.0312 m^2

Among the most important parameters are the boundary conditions, where all the simulation regions can be defined. The tank was filled with water up to 24 cm as mentioned before. The rest of the tank is open to the ambient pressure and temperature, which is the case of natural convection. Heat is generated from the bottom by the aluminum plate where all the sides walls are insulated. The top part is defined as a pressure outlet in the setup section. The details about the boundary

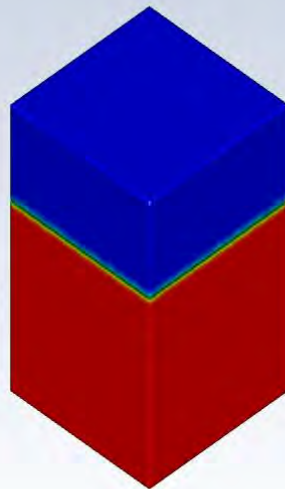
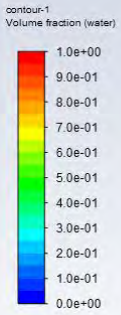
conditions and the properties of the fluid, which were used in this simulation, are the same as for 2-D (refer to Table 3.2 and Table 3.3, respectively).

3.5.2 Results and Discussion

The results obtained by using the CFD for 3-D model are presented and discussed here. The numerical investigation was used to carry out the simulation of heat and mass transfer in the water tank in case of natural convection flows. ANSYS FLUENT built-in post-processor was used to calculate mass-averaged conditions and produce graphs and contour plots for the entire solution. Therefore, in this work, the calculation was run as time-dependent (transient), where the aluminum plate was fixed at 50°C and the other fluids at the room temperature. The temperature distribution of water rises with time until it reaches the desired temperature of 50°C. At the same time, the velocity inside the water and above the free water surface was investigated as well. The turbulent kinetic energy and the vorticity also were investigated in this model. The results were recorded at different timesteps in order to pursue the developing flow behavior and heat and mass transfer inside the water tank. However, Figure 3.31 shows the volume fraction of air and water after patching them and before running the calculation (at $t = \text{zero seconds}$). It is clear that in Figure 3.31 (a) the air domain has a volume fraction of 100 %, where the water domain is 0 %. In contrast, in Figure 3.31 (b) the water domain has a volume fraction of 100 %, with the air domain at 0 %. Note that all the results hereafter are shown as contour and x-y plot. The contour figures are presented from top and side views at four different locations, as can be seen in Figure 3.32 (a) and Figure 3.32 (b), respectively. The X-Y plot presents the result at three different locations of tank width, at $z = 0$, $z = 7.5 \text{ cm}$ and $z = -7.5 \text{ cm}$, which is clearly shown in Figure 3.33.



(a)

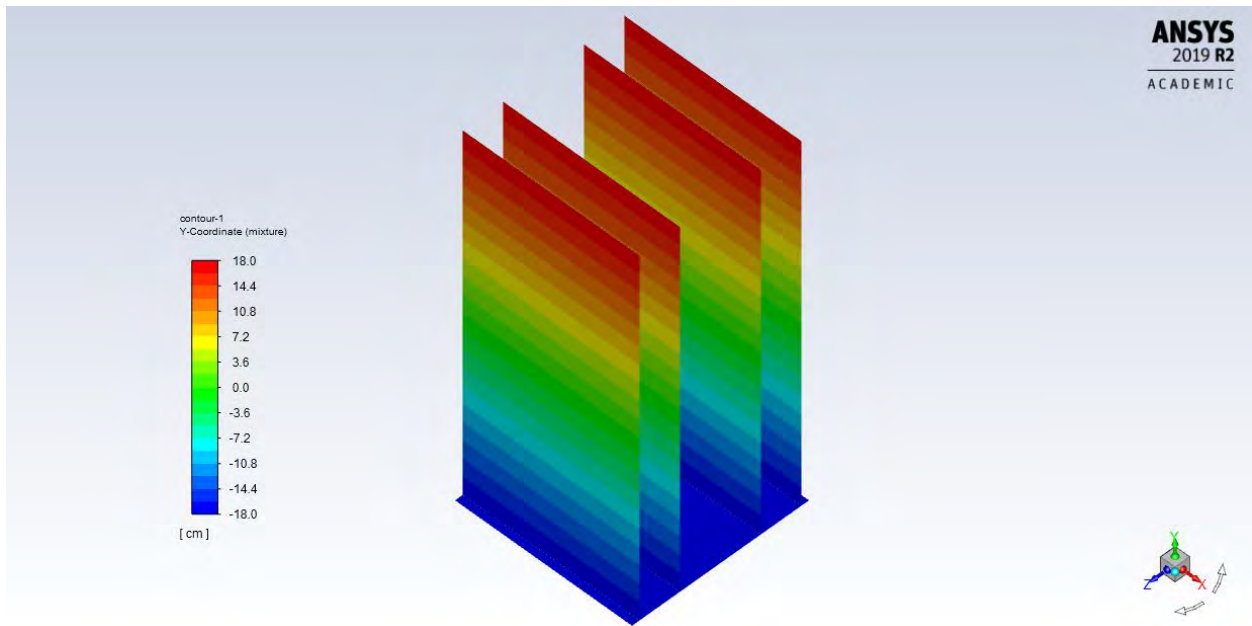


(b)

Figure 3.31: Contours of volume fraction of (a) air and (b) water.



(a)



(b)

Figure 3.32: The three different locations for contour (a) top view and (b) side view.

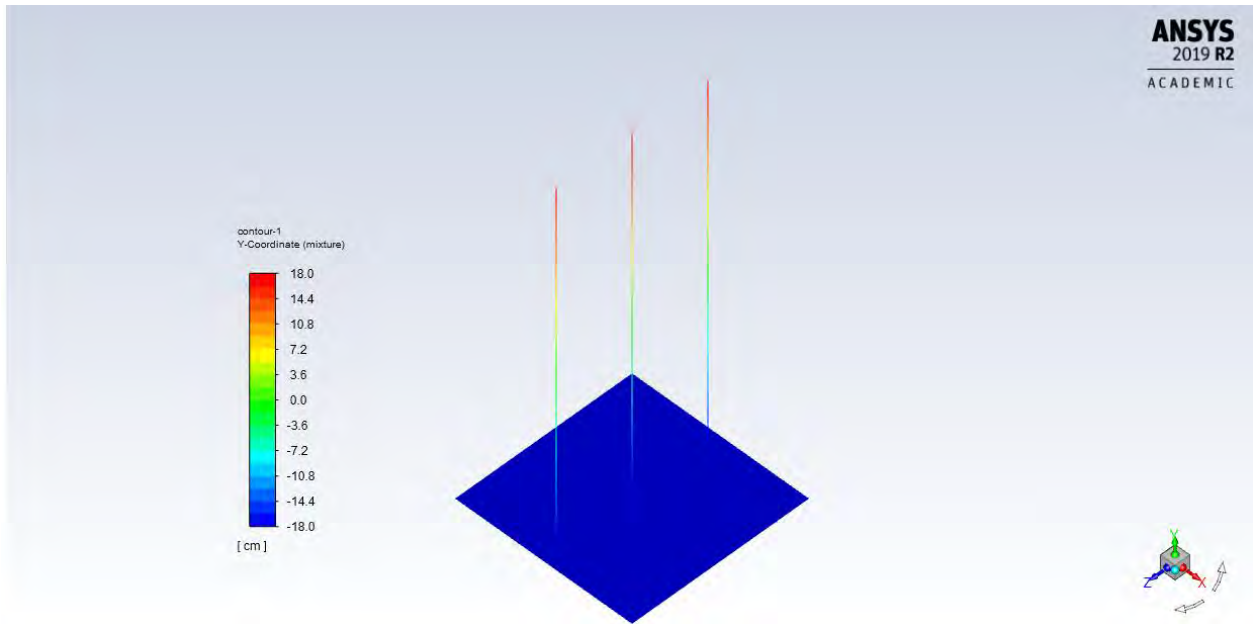
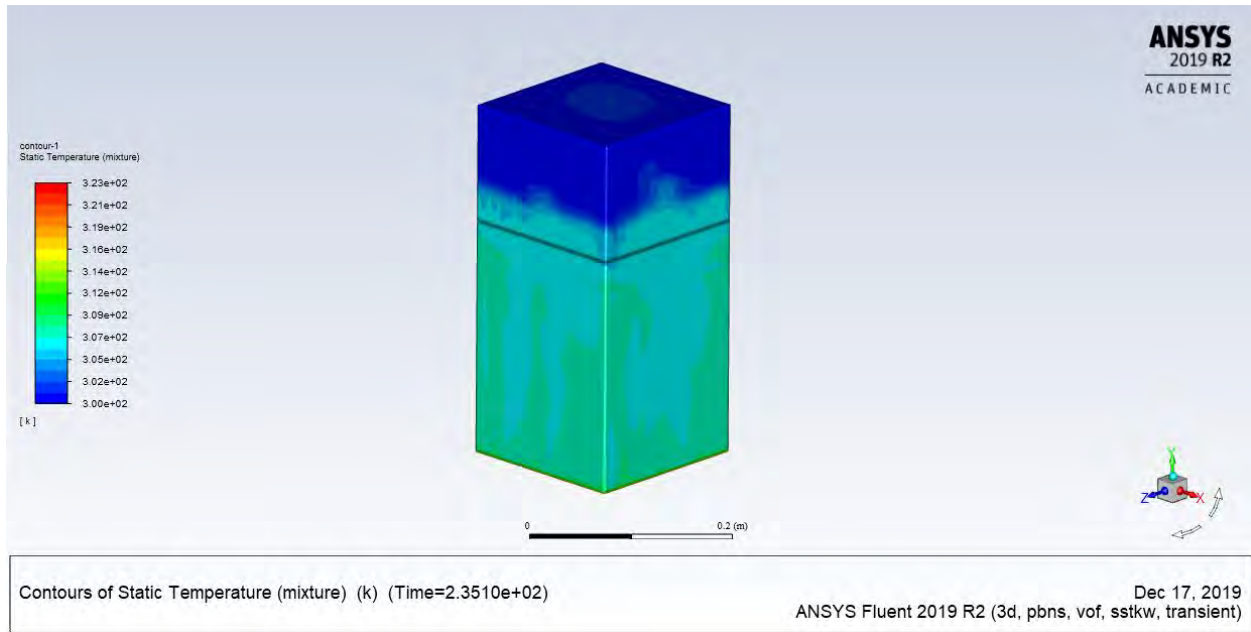


Figure 3.33: The three different locations for X-Y plot.

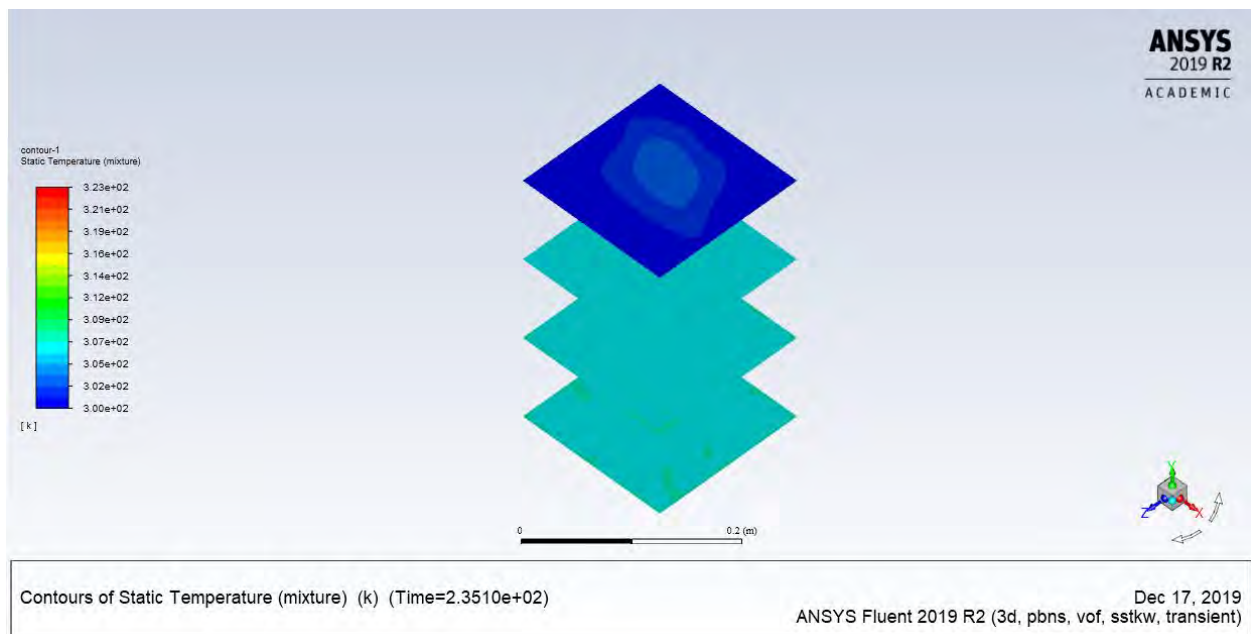
1) At $t = 235$ Seconds

(a) Temperature

The temperature of the water starts rising with time, as can be seen in Figure 3.34. Figure 3.34 (a) shows the contour temperature of the 3-D geometry, where it is clear that the temperature of the water has reached about 34°C . It is evident that the temperature of the air domain remains at the room temperature due to the circulation of air to the ambient air. Looking at the top view sections, it is clear that the temperature at the center of the tank is higher than at the sides in air domain, which is related to the circulation of air in this region [refer to Figure 3.34 (b)]. However, it can be seen that the temperature starts to rise at the first section from the bottom of the tank. In Figure 3.34 (c), the side view sections are shown, where it is clear that the temperatures are equivalent at all locations. The plot in Figure 3.34 (d) represents the temperature before and after the water–air interface at three different locations.



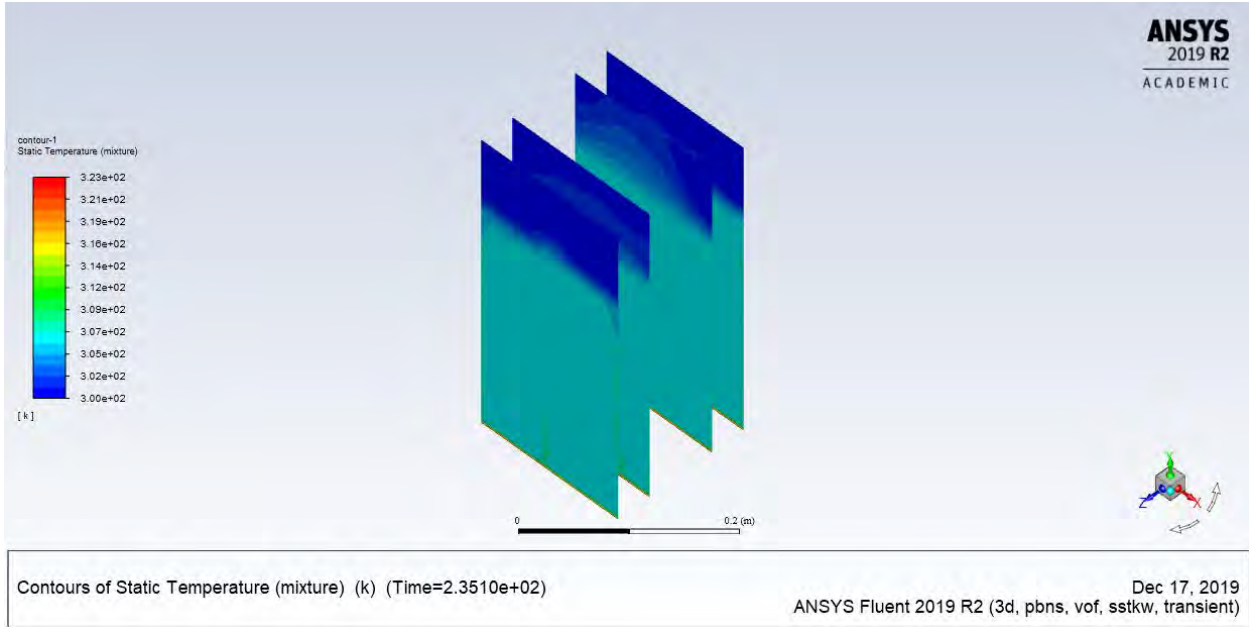
(a)



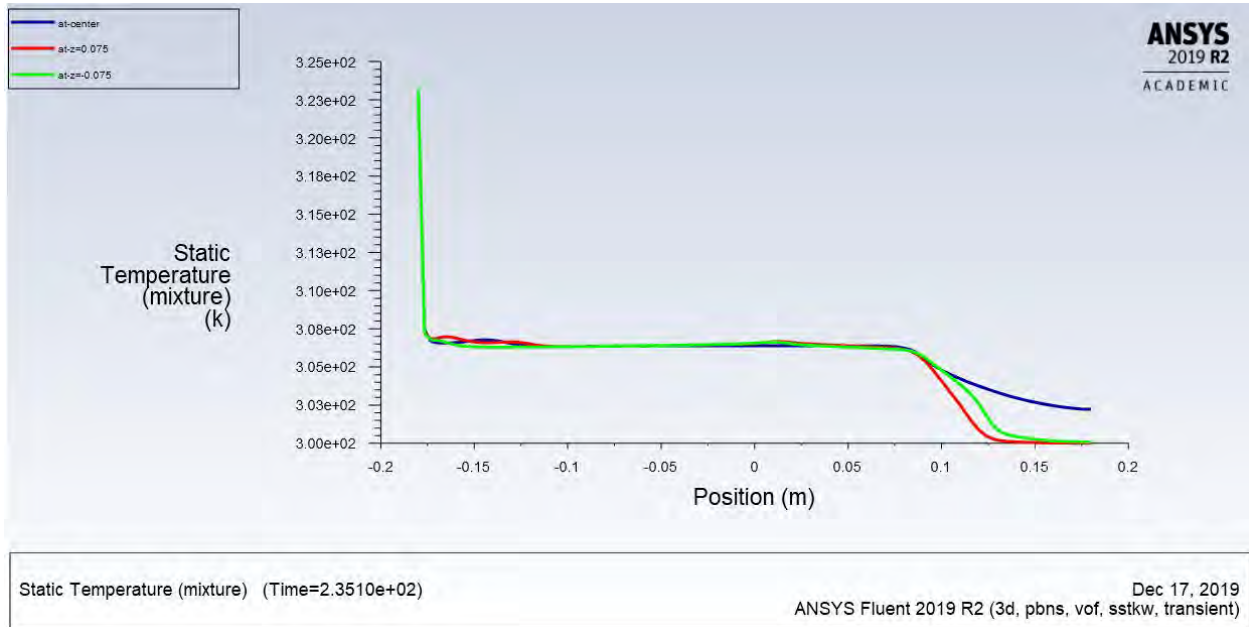
(b)

Figure 3.34: Temperature at 235 s (a) Contour of the geometry, (b) Contour of the top view sections, (c) Contour of the side view sections, (d) XY plot.

Figure 3.34—continued



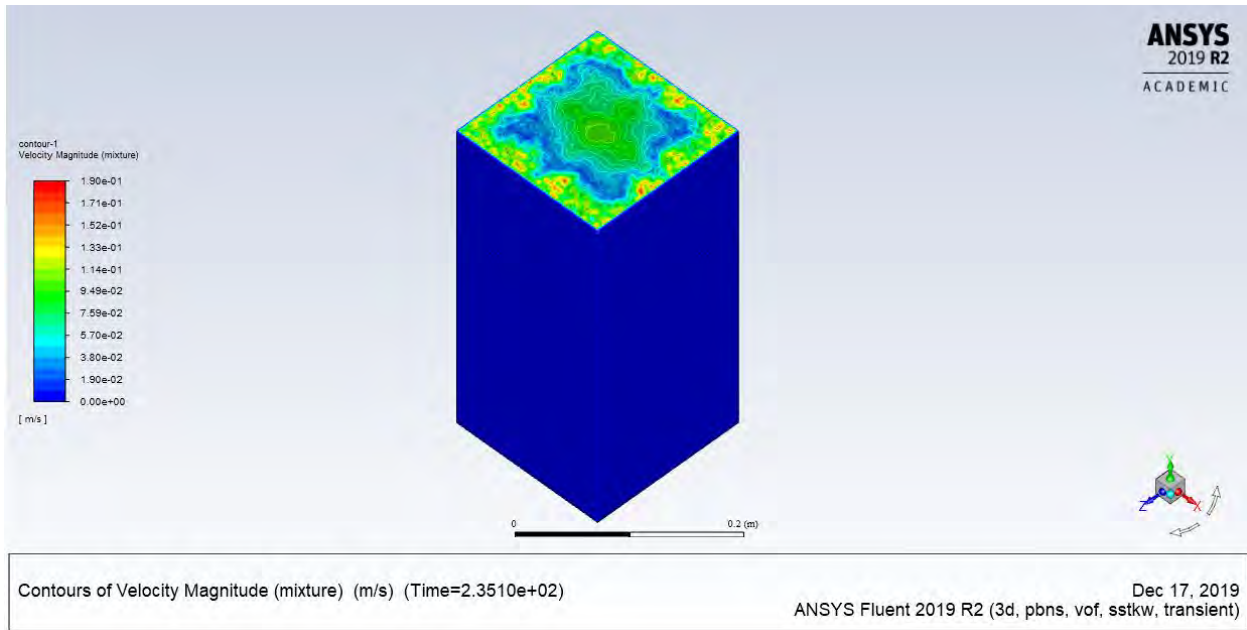
(c)



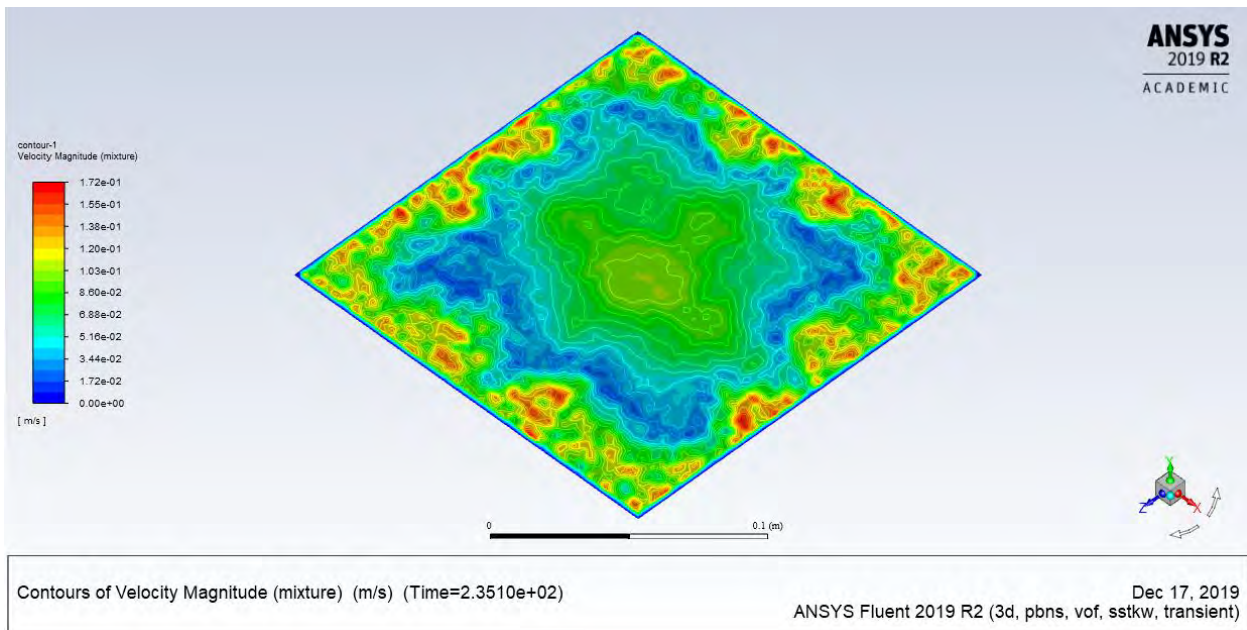
(d)

(b) Velocity

The velocity magnitude for contour and plot is shown in Figure 3.35. It can be seen in Figure 3.35 (a) that a higher velocity is demonstrated in the top view/at the top compared to the rest of the tank. It is interesting here to see the Bénard–Rayleigh convection cell that developed at the surface. These cell patterns are developed as a result of rising temperature and gravity effect at this time, as can be clearly seen in Figure 3.35 (b). In Figure 3.35 (c), the top view sections at four different locations are shown, where the higher velocity is seen to be at the top. In addition, the cell patterns are clearly visible but with lesser velocity. Moreover, the side views at four different locations are presented in Figure 3.35 (d), where the velocity is higher at the air domain. However, the velocity in the water domain is lesser compared with that in the air domain, which can still be seen and is shown with a small scale in Figure 3.35 (e). One reason for a higher velocity developing above the water surface can be related to the evaporation coming from the free water surface along with rising temperature, which increases the circulation in the air domain and hence the velocity. It is clear that this vortex in air domain started from the bottom of the tank, going up to the water surface and then circulating down to the water, where the highest value is near the water surface. This is due to the temperature difference between the bulk water and its surface. It is clear from Figure 3.35 (e) that it was at the bottom of tank where the Bénard–Rayleigh convection started to develop. Figure 3.35 (f) shows the plot of the velocity difference before and after the interface at three different locations where the velocity increased rapidly above the interface.



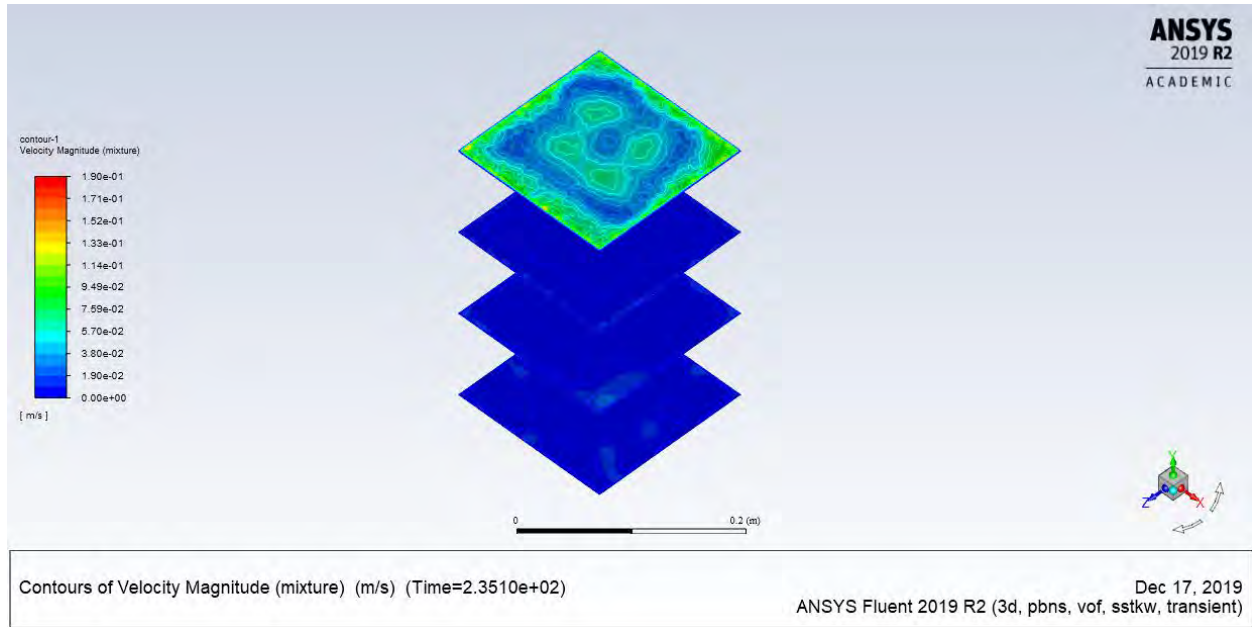
(a)



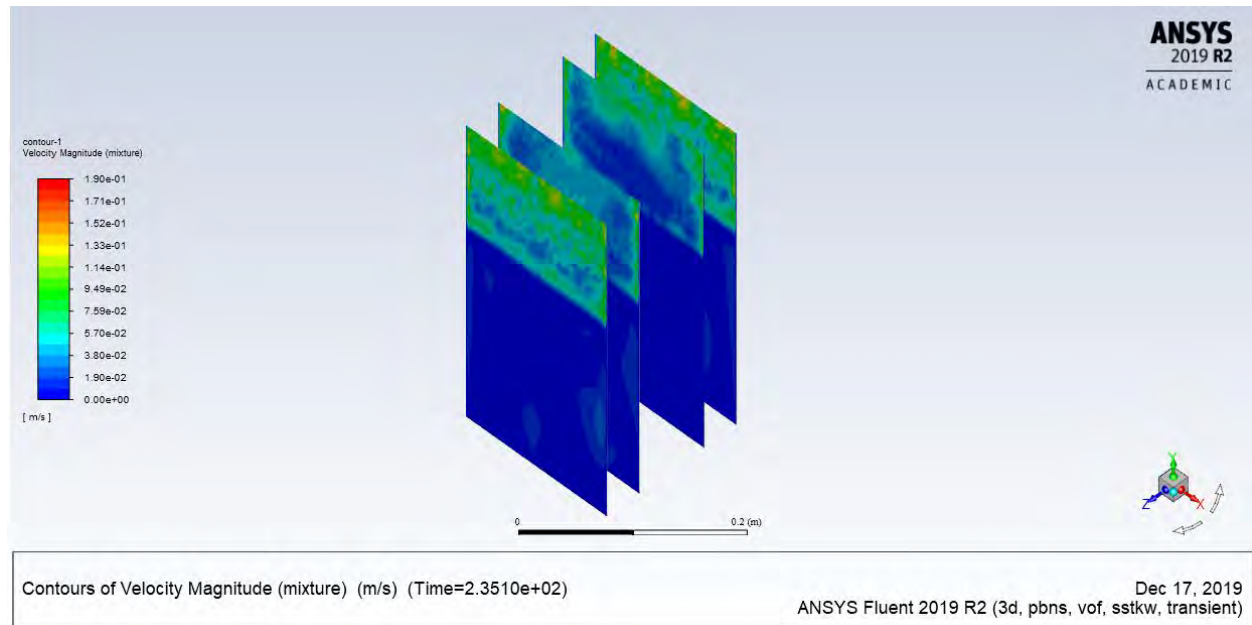
(b)

Figure 3.35: Velocity at 235 s (a) Contour of the geometry, (b) Top view for the tank, (c) Contour of the top view sections, (d) Contour of the side view sections, (e) Contour in the water domain, (f) XY plot.

Figure 3.35—continued

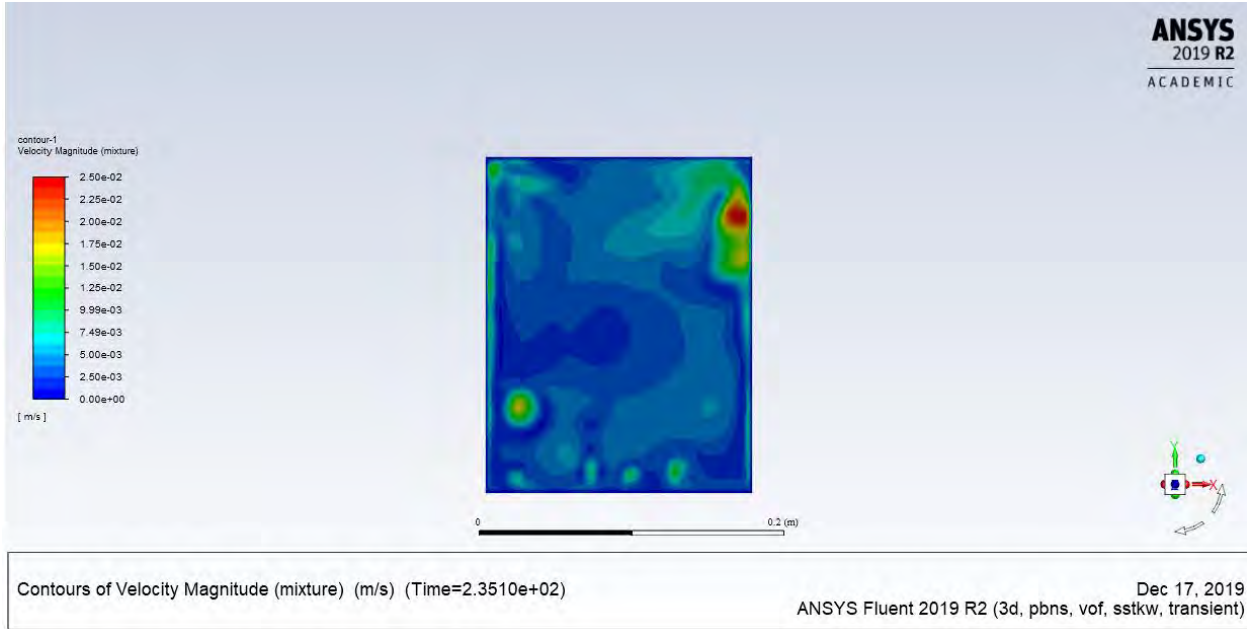


(c)

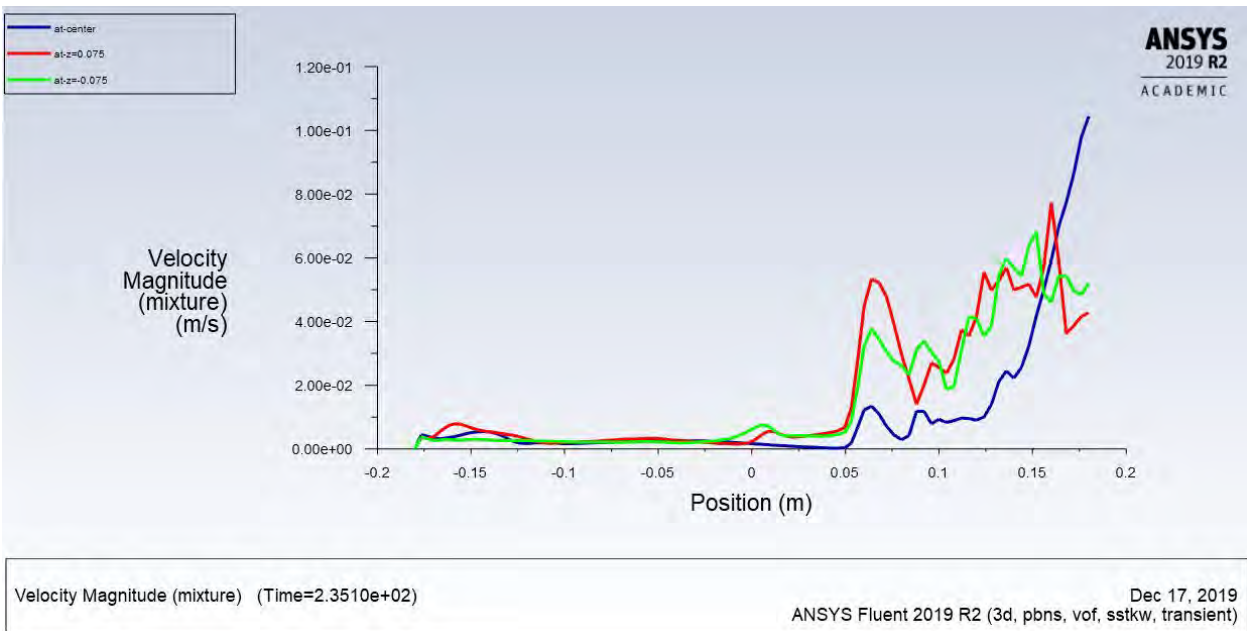


(d)

Figure 3.35—continued



(e)



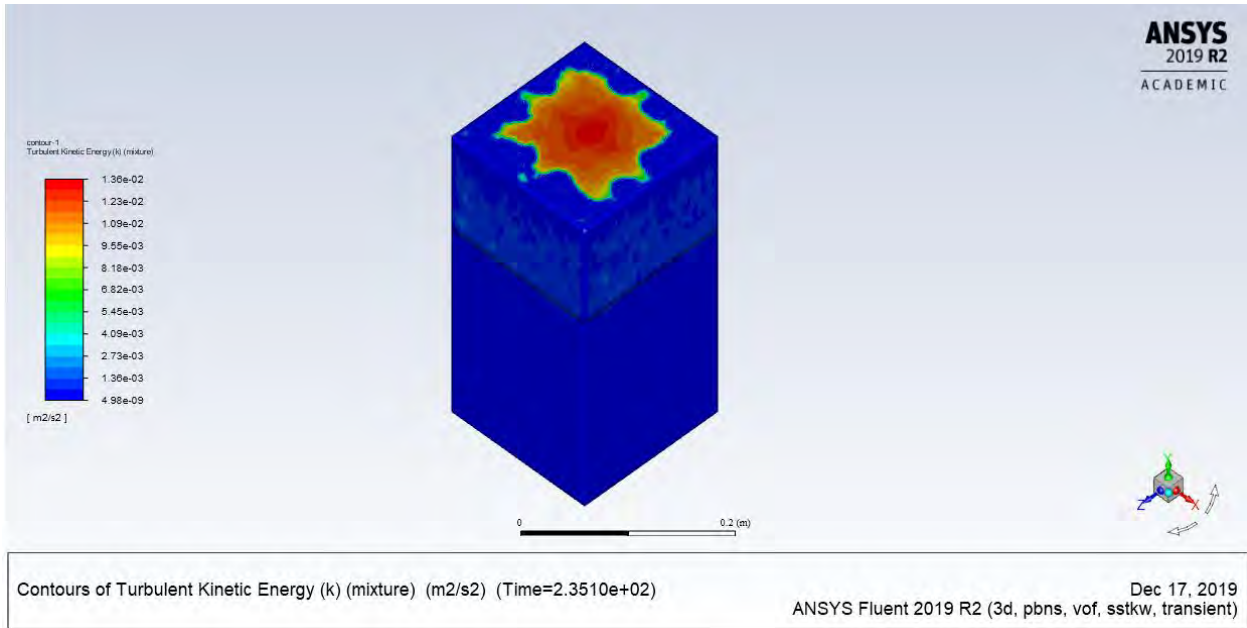
(f)

(c) Turbulence Kinetic Energy

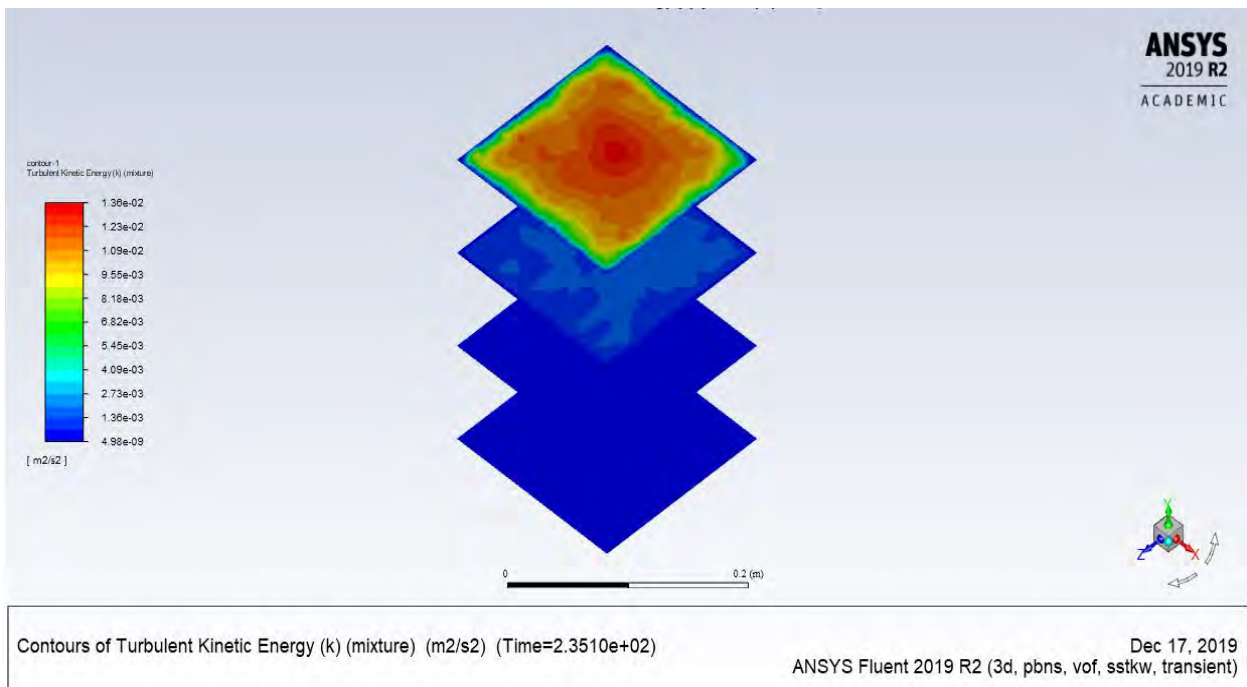
Turbulence kinetic energy (TKE) contour is shown in Figure 3.36 (a), where the TKE is higher at the air domain due to the higher velocity. It is clear that there is a higher spot of TKE at the top of the tank, which is obviously related to the heat and evaporation coming from the water surface to the ambient air. In Figure 3.36 (b), TKE at top view sections at four different locations is shown, where it is higher at the top compared to the rest. TKE at side view sections for four different location is presented in Figure 3.36 (c), wherein the value is clearly higher at the air domain due to the air circulation. By comparing these four sections, it can be seen that TKE at the two sections in the middle of the tank is higher than at the side due to the evaporation at the center of the tank. Moreover, in the water domain the TKE is still very small compared to the air domain [refer to Figure 3.36 (c)]. It is clear that TKE begins to gradually increase after the interface [refer to Figure 3.36 (d)].

(d) Vorticity

Vorticity contour is shown in Figure 3.37 (a), where the vorticity is higher at the air domain. It is clear that vorticity is higher at the sides of the tank, which can be related to the circulation at this region. In Figure 3.37 (b), vorticity at top view sections at four different locations is shown, where it is higher at the top compared to the rest. Vorticity at side view sections for four different locations is presented in Figure 3.37 (c), wherein the value is clearly higher at the air domain due to the air circulation. By comparing these four sections, it can be seen that vorticity at the two sections in the middle of the tank is lesser than at the sides due to the circulation at the sides of the tank. Moreover, in the water domain the vorticity is still very small compared to the air domain [refer to Figure 3.37 (c)]. It is clear that vorticity begins to gradually increase after the interface [refer to Figure 3.37 (d)].



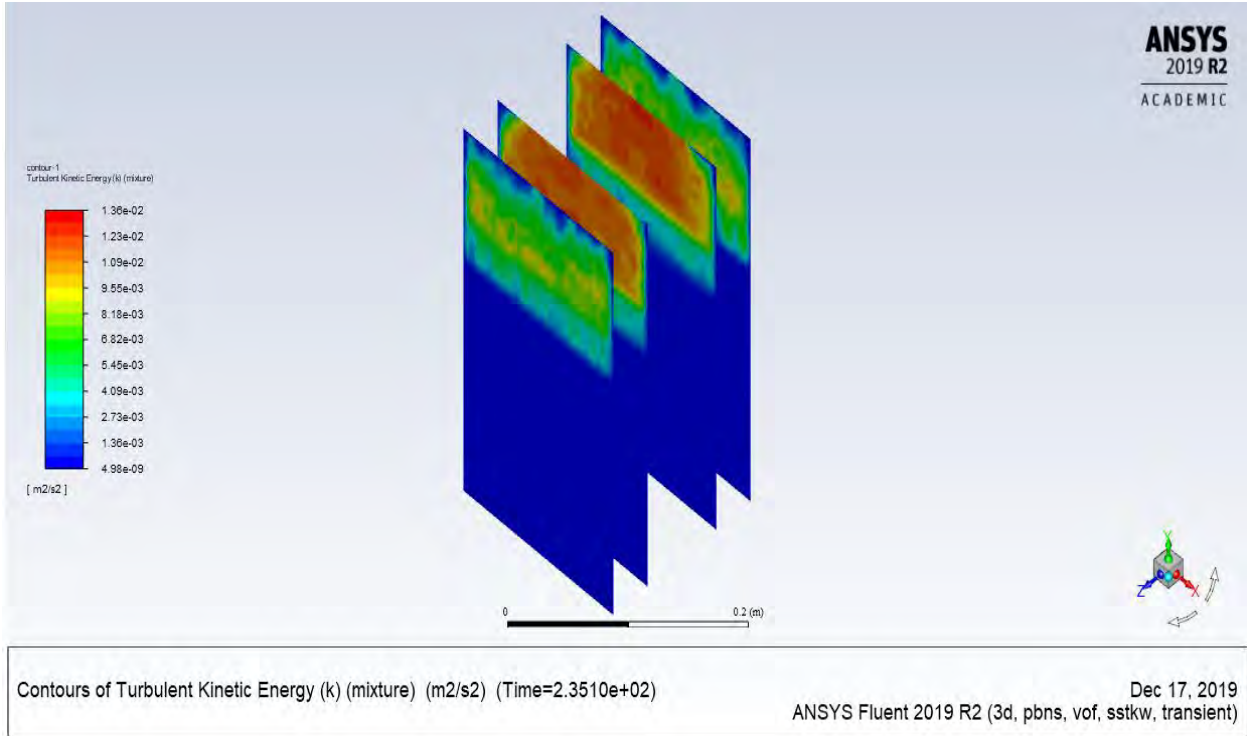
(a)



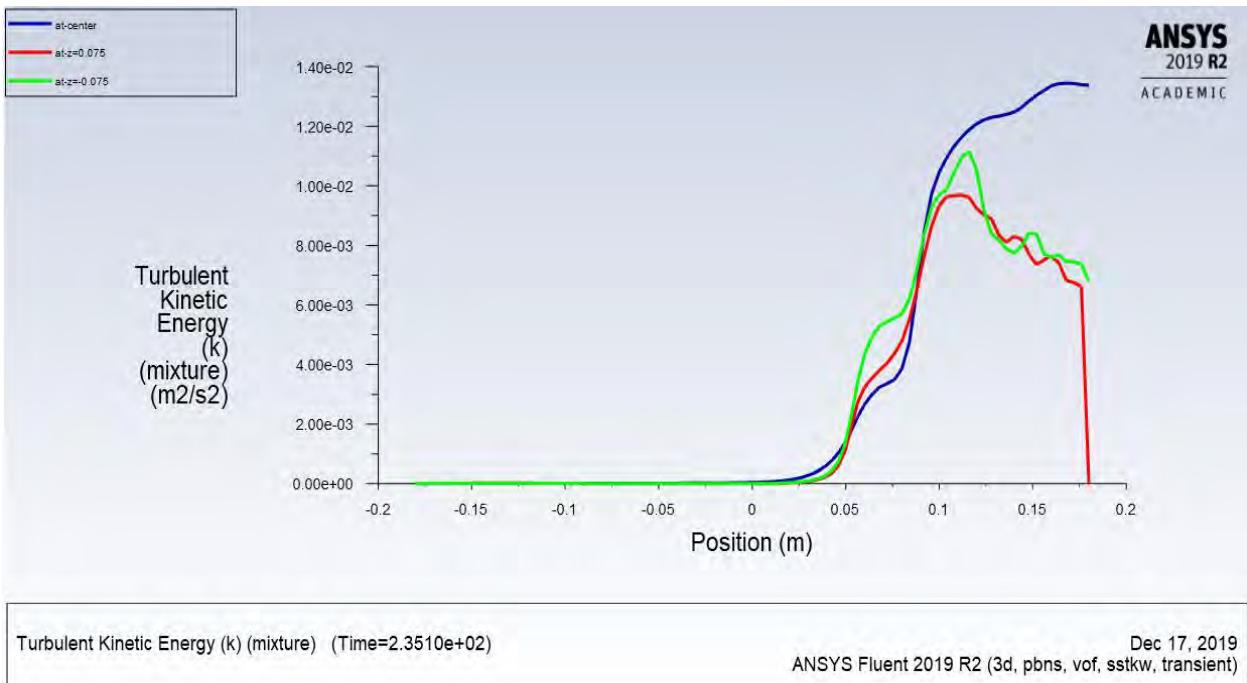
(b)

Figure 3.36: Turbulence kinetic energy at 235 s (a) Contour of the geometry, (b) Contour of the top view sections, (c) Contour of the side view sections, (d) XY plot.

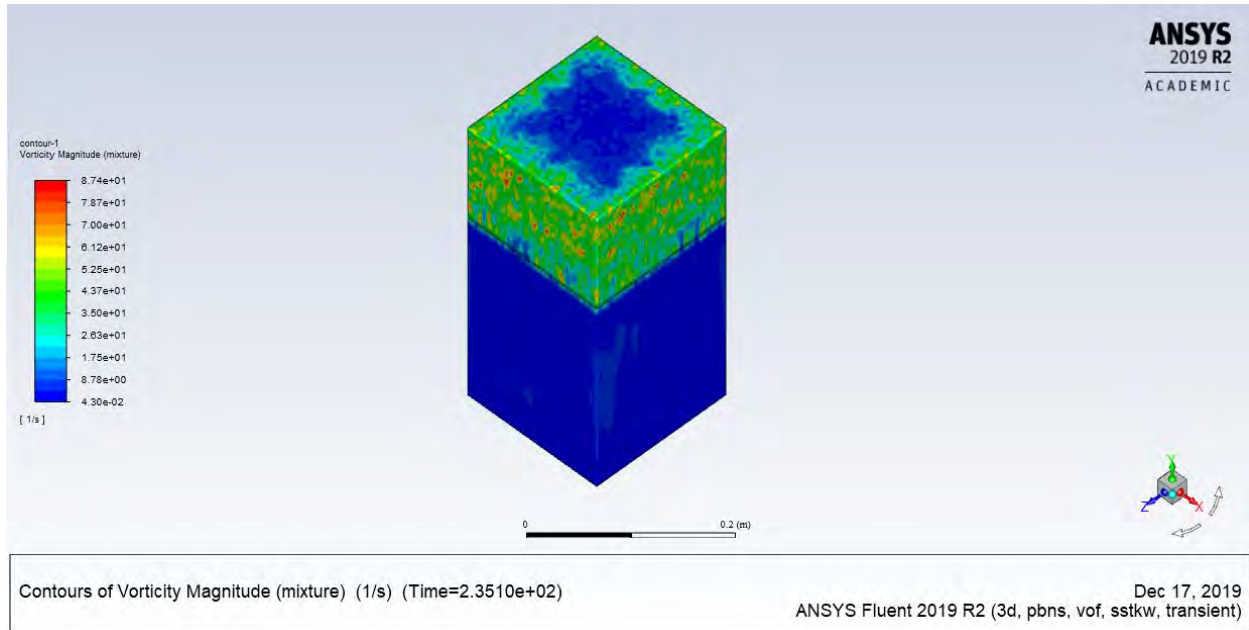
Figure 3.36—continued



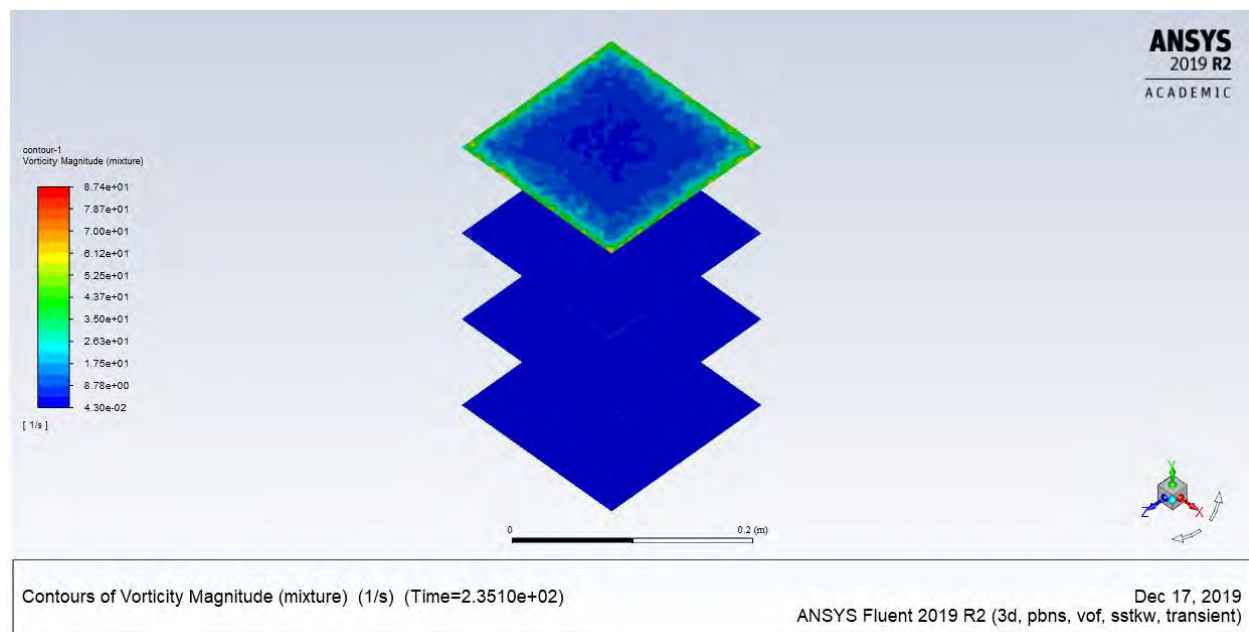
(c)



(d)



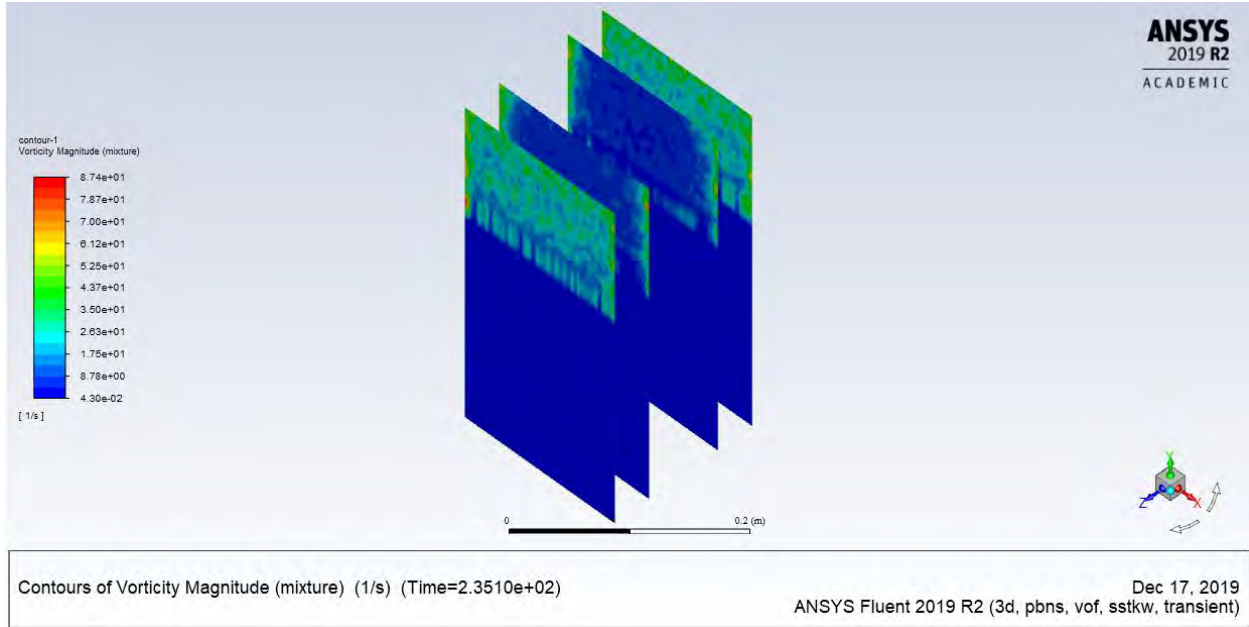
(a)



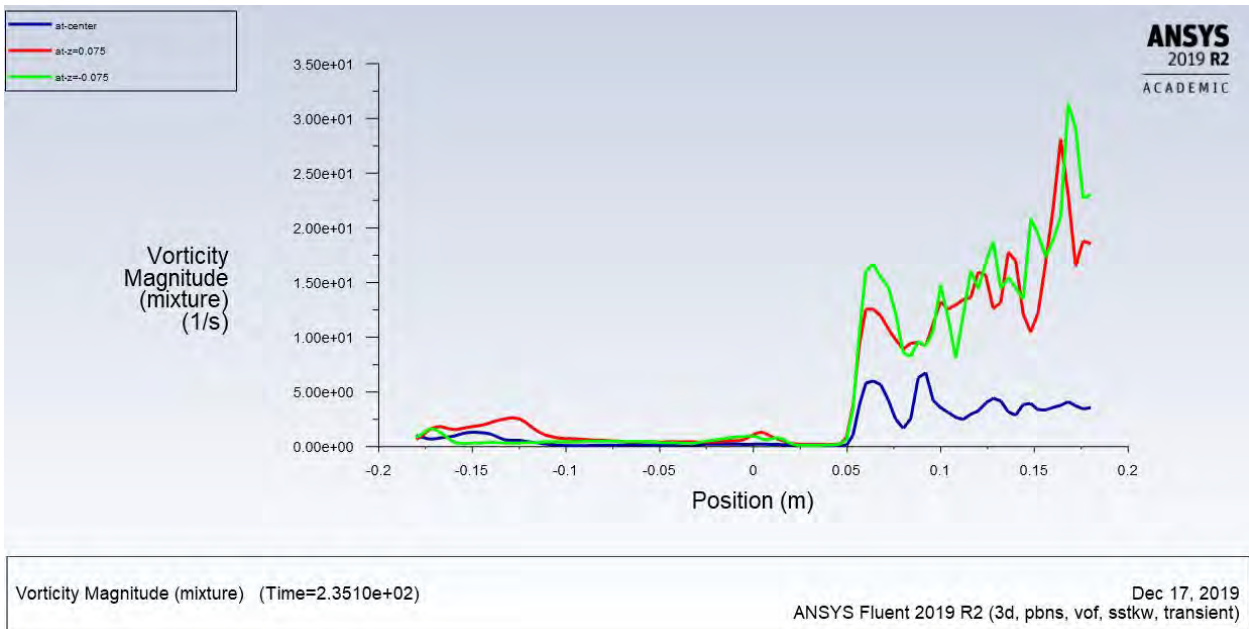
(b)

Figure 3.37: Vorticity at 235 s (a) Contour of the geometry, (b) Contour of the top view sections, (c) Contour of the side view sections, (d) XY plot.

Figure 3.37—continued



(c)

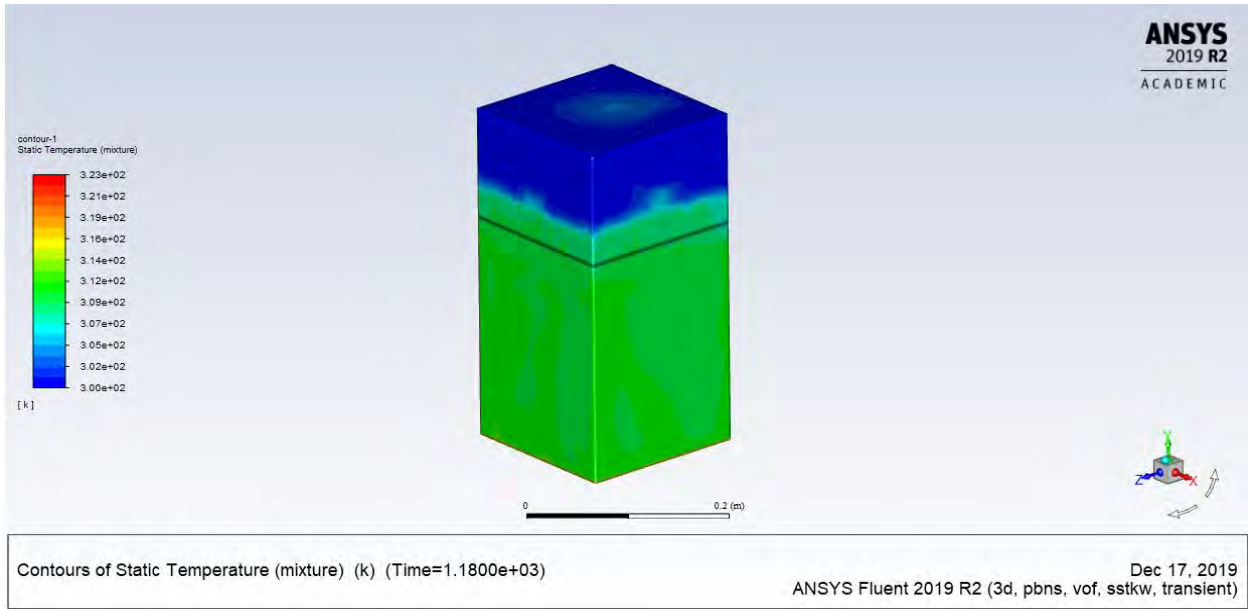


(d)

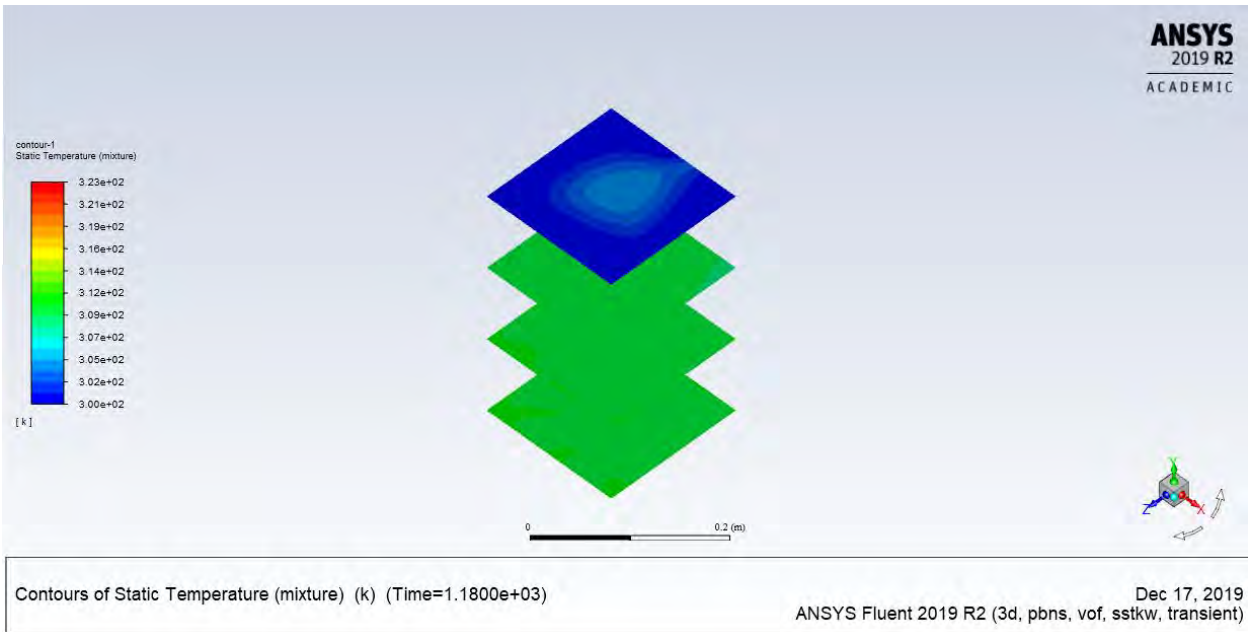
2) At $t = 1180$ Seconds

(a) Temperature

The temperature of the water keeps rising with time, as can be seen in Figure 3.38. Figure 3.38 (a) shows the contour temperature of the 3-D geometry, where it is clear that the temperature of the water has reached about 37°C . It is evident that the temperature of the air domain remains at room temperature due to circulation to the ambient air. However, in the air domain, the temperature starts to increase from the sides at this time. By looking at the top view sections, it is clear that the temperature at the center of the tank is higher than at the sides in air domain, which is related to the circulation of air in this region [refer to Figure 3.38 (b)]. In addition, it can be seen that the temperature starts to rise at the first section from the bottom of the tank. The side views of the sections are shown in Figure 3.38 (c), from which it is clear that the temperature is equivalent at all locations. The plot in Figure 3.38 (d) shows the temperature before and after the water–air interface at three different locations, wherefrom it is clear that the temperature is higher at the center of the tank in the air domain.



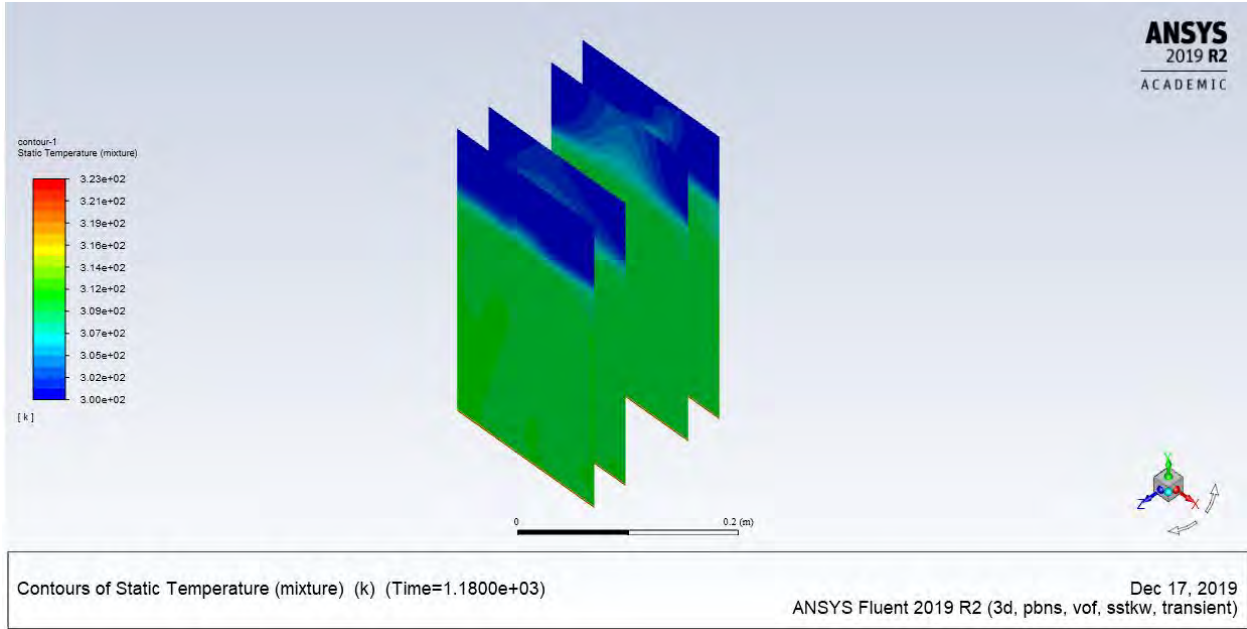
(a)



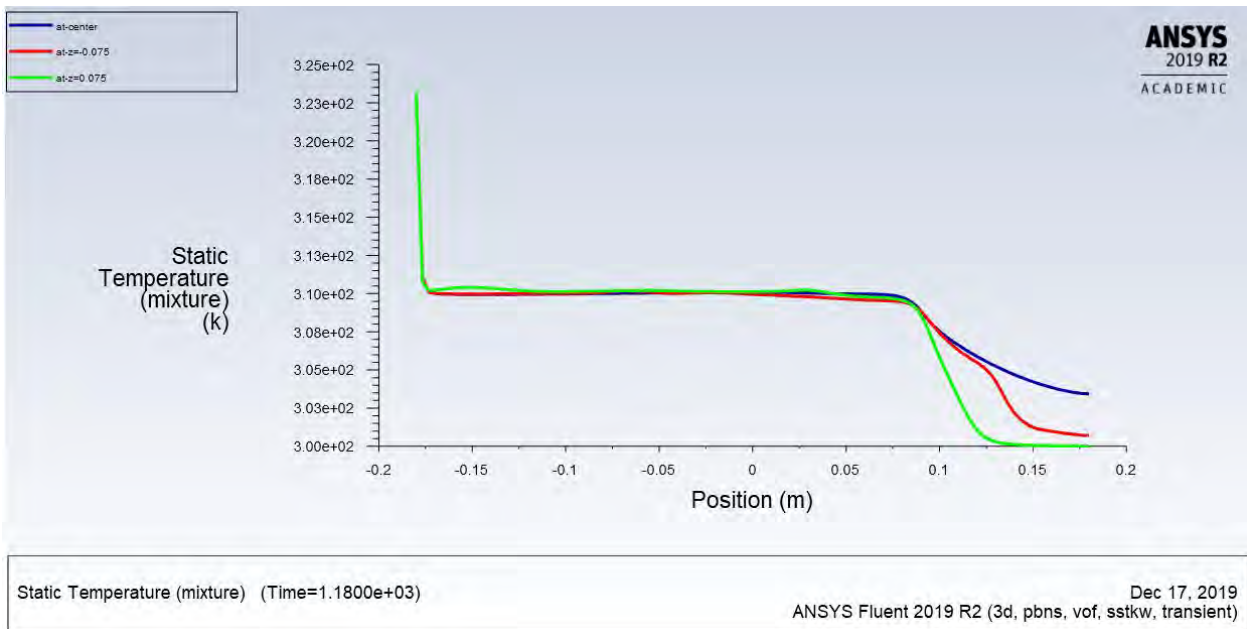
(b)

Figure 3.38: Temperature at 1180 s (a) Contour of the geometry, (b) Contour of the top view sections, (c) Contour of the side view sections, (d) XY plot.

Figure 3.38—continued



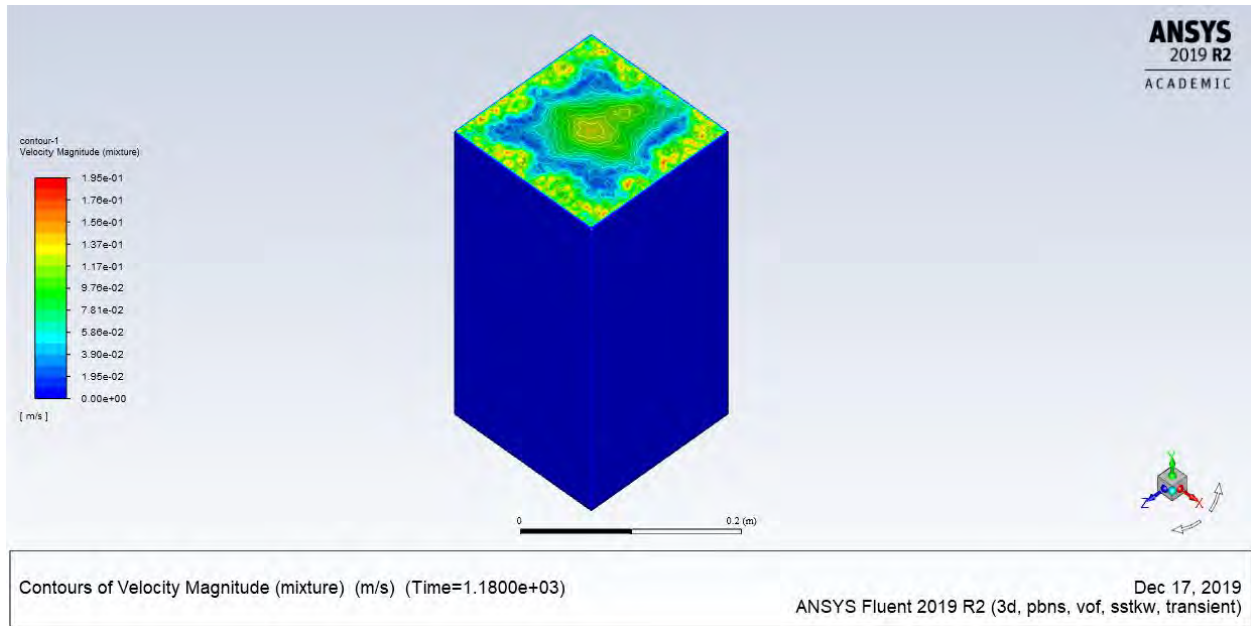
(c)



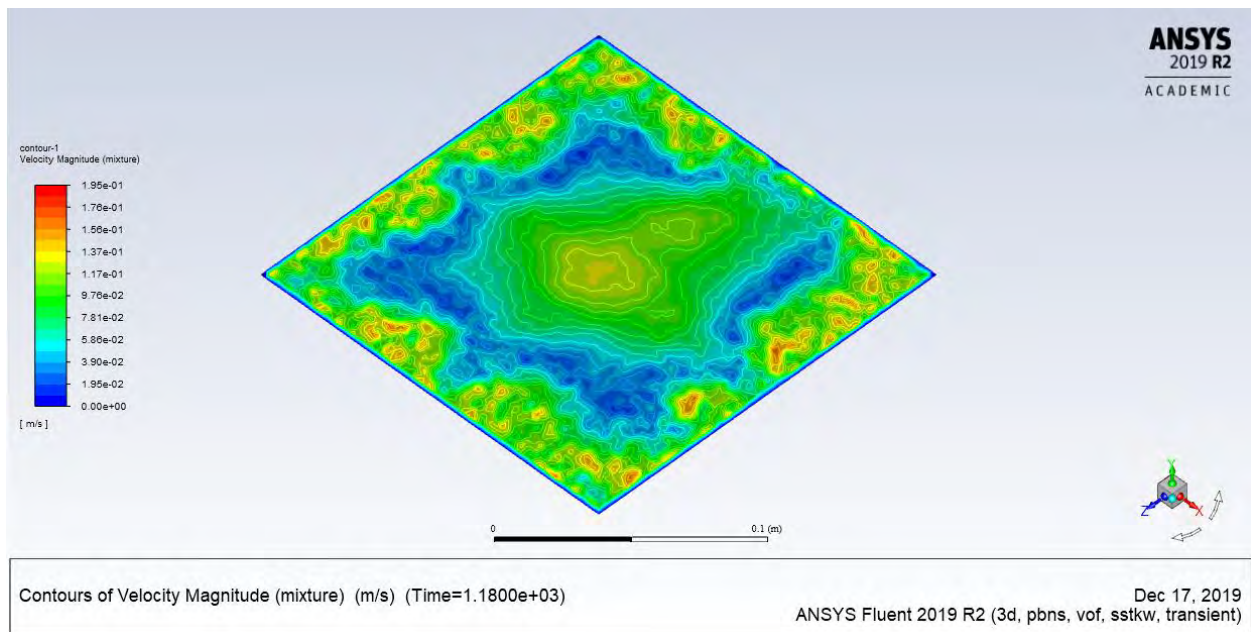
(d)

(b) Velocity

The velocity magnitude for contour and plot is shown in Figure 3.39. It can be seen in Figure 3.39 (a) that the velocity of the top view is higher compared to the velocity at $t = 235$ s, which is due to the temperature rising and the water evaporation at this time. Moreover, it is interesting here to see the Bénard–Rayleigh convection cell that has developed at the surface. These cell patterns are developed as a result of rising temperature and gravity effect at this time, as can be clearly seen in Figure 3.39 (b). In Figure 3.39 (c), the top view sections at four different locations are shown, where the higher velocity is found to be at the top. In addition, the cell patterns are clearly visible, although with lesser velocity. Moreover, the side views at four different locations are presented in Figure 3.39 (d), where the velocity is higher at the air domain. However, the velocity in the water domain is lesser compared to that in the air domain, where it can still be noticed and is shown with small scale in Figure 3.39 (e). One reason for a higher velocity developing above the water surface can be related to the evaporation coming from the free water surface along with rising temperature, which increases the circulation in the air domain and hence the velocity. It is clear that this vortex in air domain started from the bottom of the tank, going up to the water surface and then circulating down to the water, where the highest value is near the water surface. This is due to the temperature difference between the bulk water and its surface. It is clear from Figure 3.39 (e) that it is at the bottom of tank where the Bénard–Rayleigh convection started to develop. Figure 3.39 (f) shows the plot of the velocity difference before and after the interface at three different locations where the velocity has increased rapidly above the interface, especially at the center of the tank, due to the air circulation.



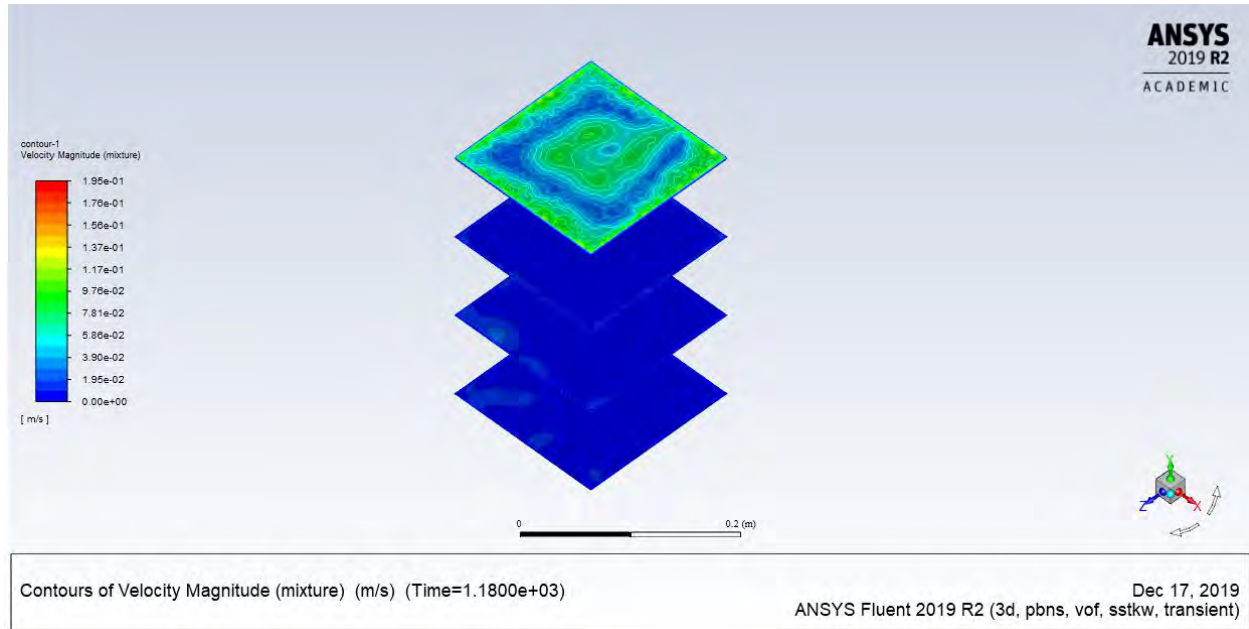
(a)



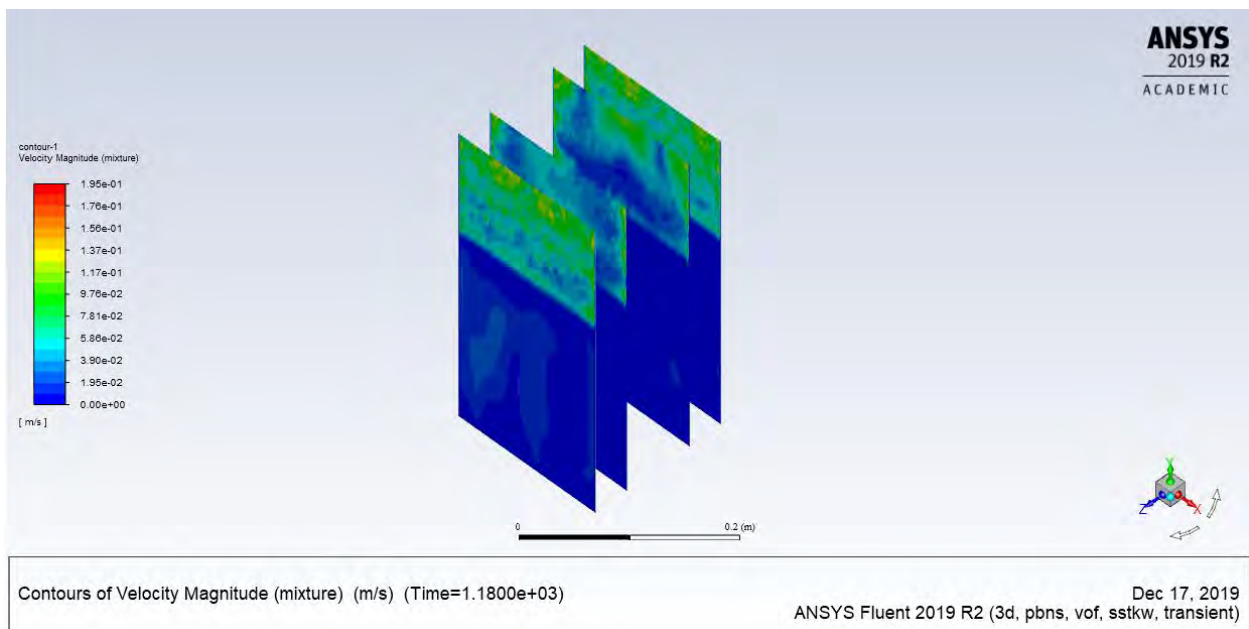
(b)

Figure 3.39: Velocity at 1180 s (a) Contour of the geometry, (b) Top view for the tank, (c) Contour of the top view sections, (d) Contour of the side view sections, (e) Contour in the water domain, (f) XY plot.

Figure 3.39—continued

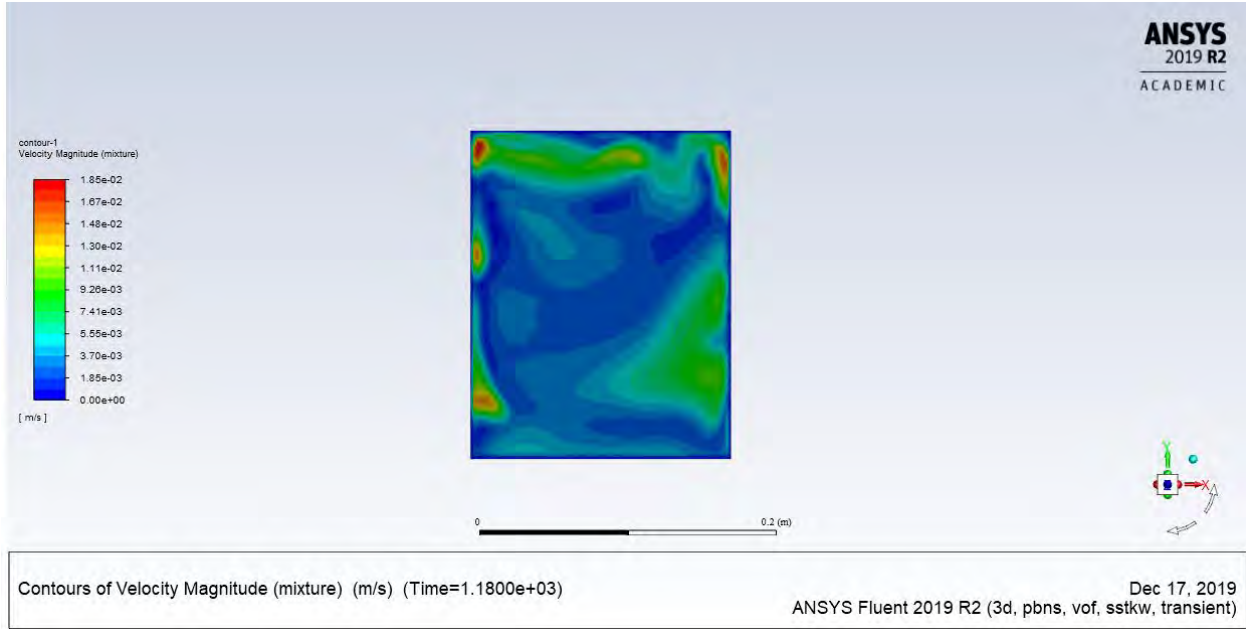


(c)

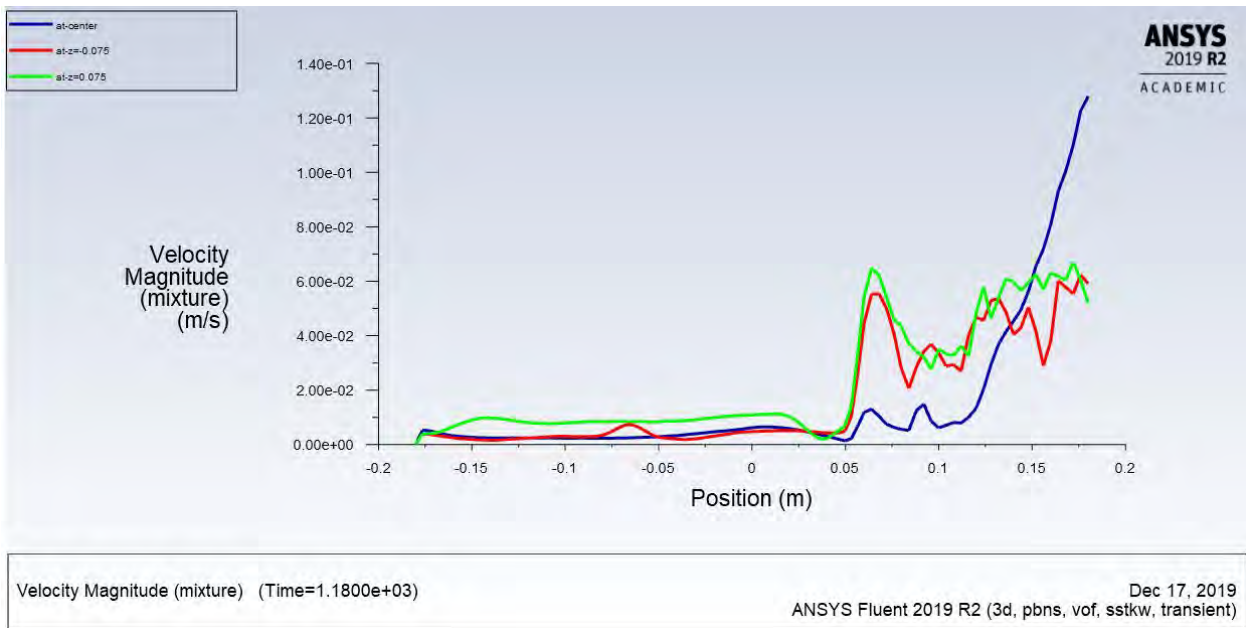


(d)

Figure 3.39—continued



(e)



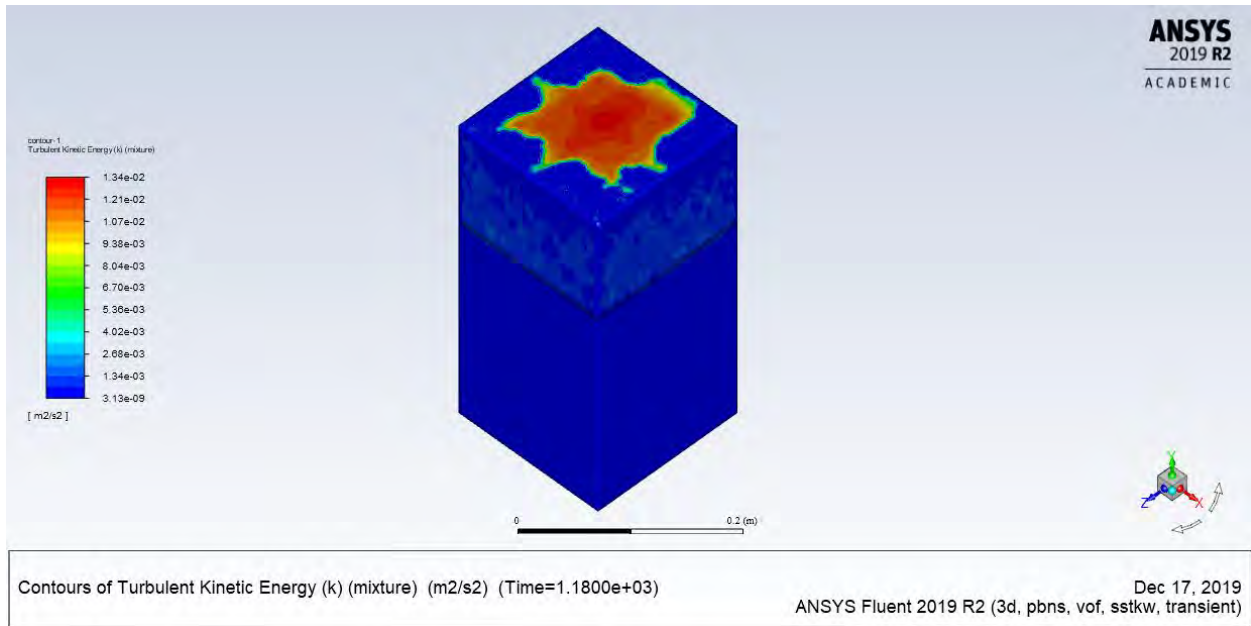
(f)

(c) Turbulence Kinetic Energy

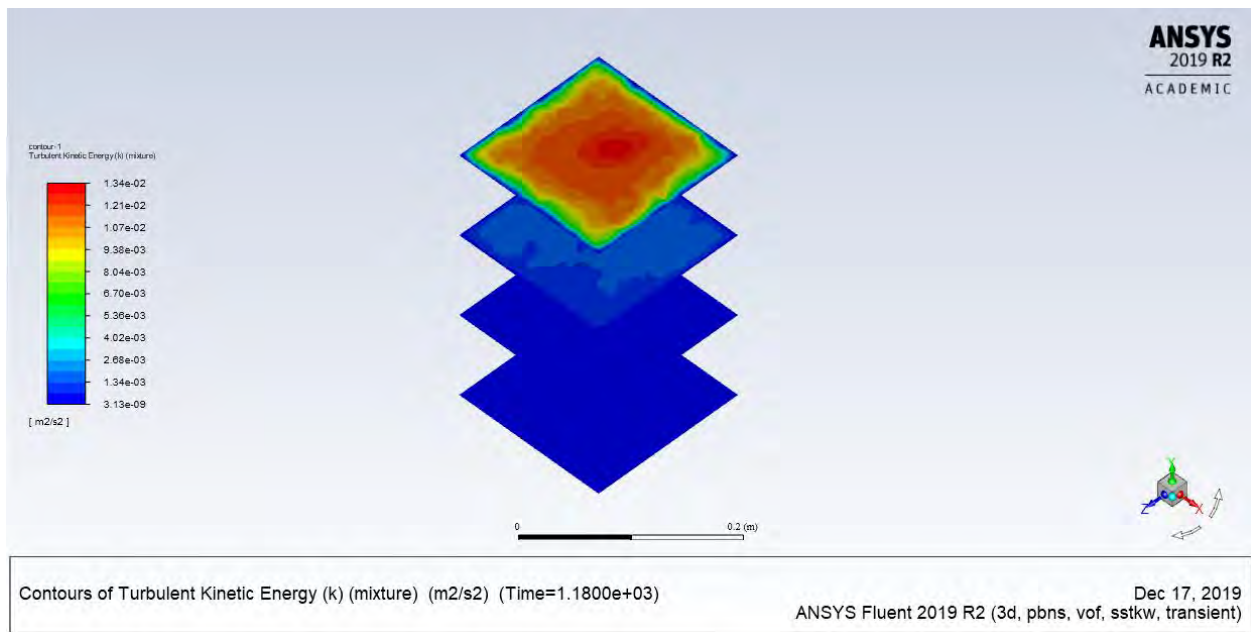
Turbulence kinetic energy (TKE) contour is shown in Figure 3.40 (a), where the TKE is higher at the air domain due to the higher velocity. It is clear that there is a higher spot of TKE at the top of the tank, which is obviously related to the heat and evaporation coming from the water surface to the ambient air. In Figure 3.40 (b), top view sections of TKE at four different locations are shown, where it is higher at the top compared the rest. Side view sections of TKE at four different location are presented in Figure 3.40 (c), where the value is clearly higher at the air domain due to the air circulation. Comparing these four sections, it becomes evident that TKE at the two sections in the middle of the tank is higher than at the sides due to the evaporation at the center of the tank. Moreover, in the water domain the TKE is still very small compared to its value in the air domain [refer to Figure 3.40 (c)]. It is clear that TKE begins to increase gradually after the interface [refer to Figure 3.40 (d)].

(d) Vorticity

Vorticity contour is shown in Figure 3.41 (a), where the vorticity is higher at the air domain. It is clear that vorticity is higher at the sides of the tank, which can be related to the circulation at this region. Vorticity at top view sections at four different locations is shown in Figure 3.41 (b), where it is higher at the top compared the rest. In Figure 3.41 (c), vorticity at side view sections for four different locations is presented, where the value is clearly higher at the air domain due to the air circulation. By comparing these four sections, it can be seen that the two sections in the middle of the tank have smaller vorticity values than at the sides due to the circulation at the sides of the tank. Moreover, the vorticity in the water domain is still very small compared to its value in the air domain [refer to Figure 3.41 (c)]. It is clear that after the interface vorticity begins to gradually increase [refer to Figure 3.41 (d)].



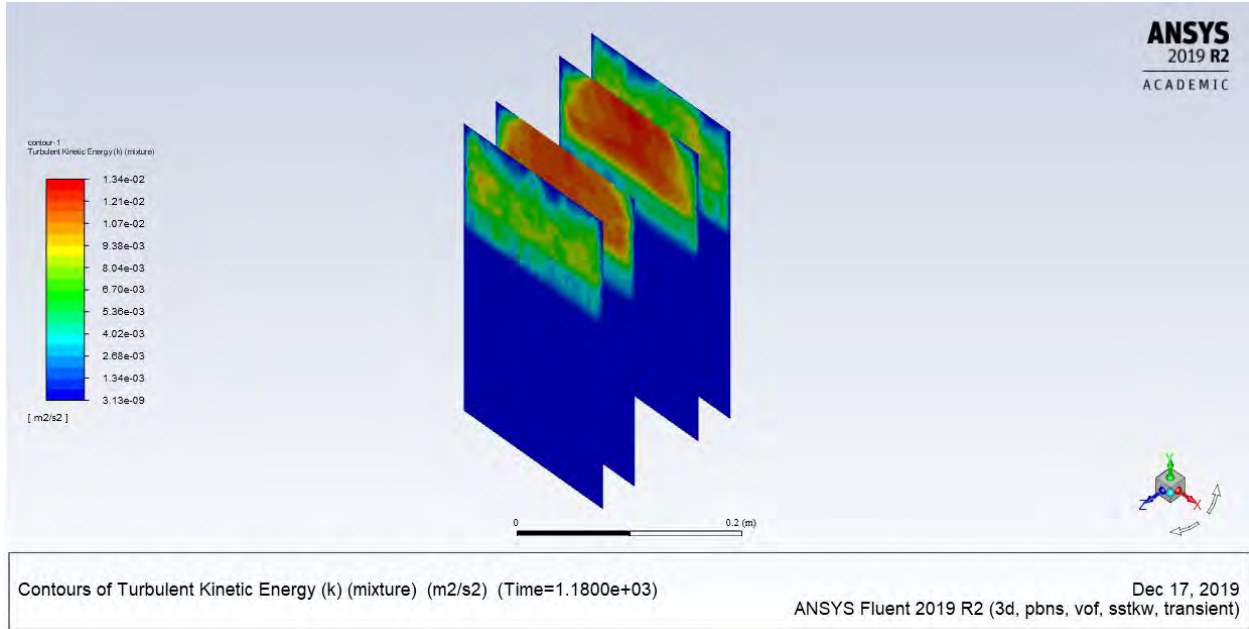
(a)



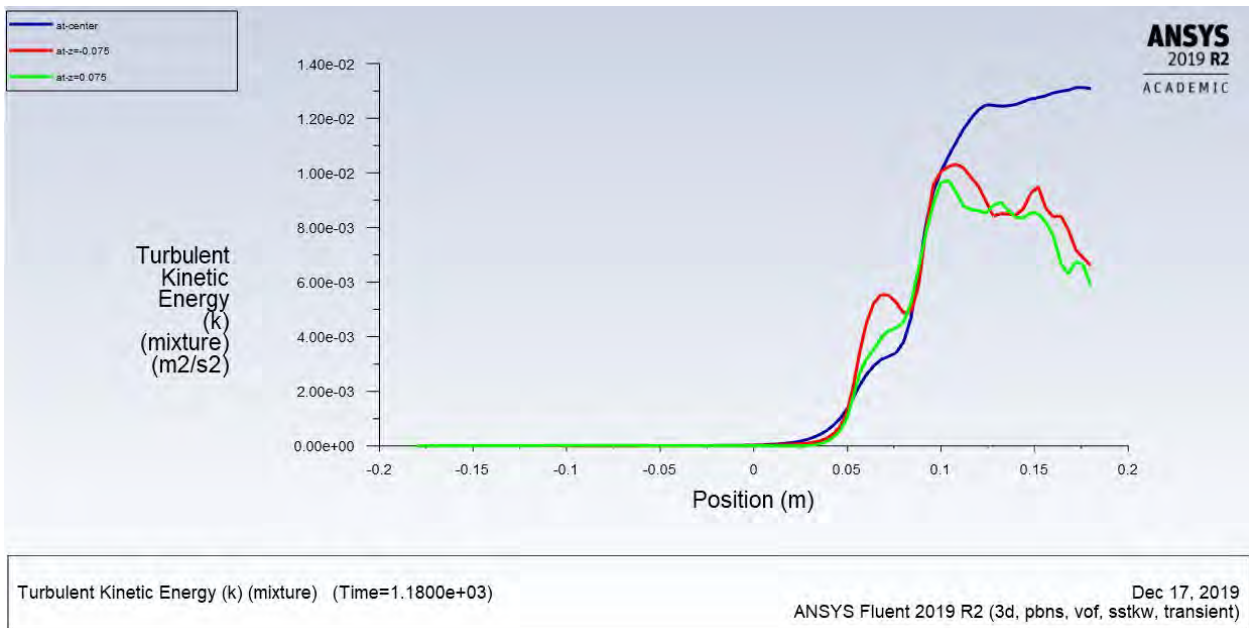
(b)

Figure 3.40: Turbulence kinetic energy at 1180 s (a) Contour of the geometry, (b) Contour of the top view sections, (c) Contour of the side view sections, (d) XY plot.

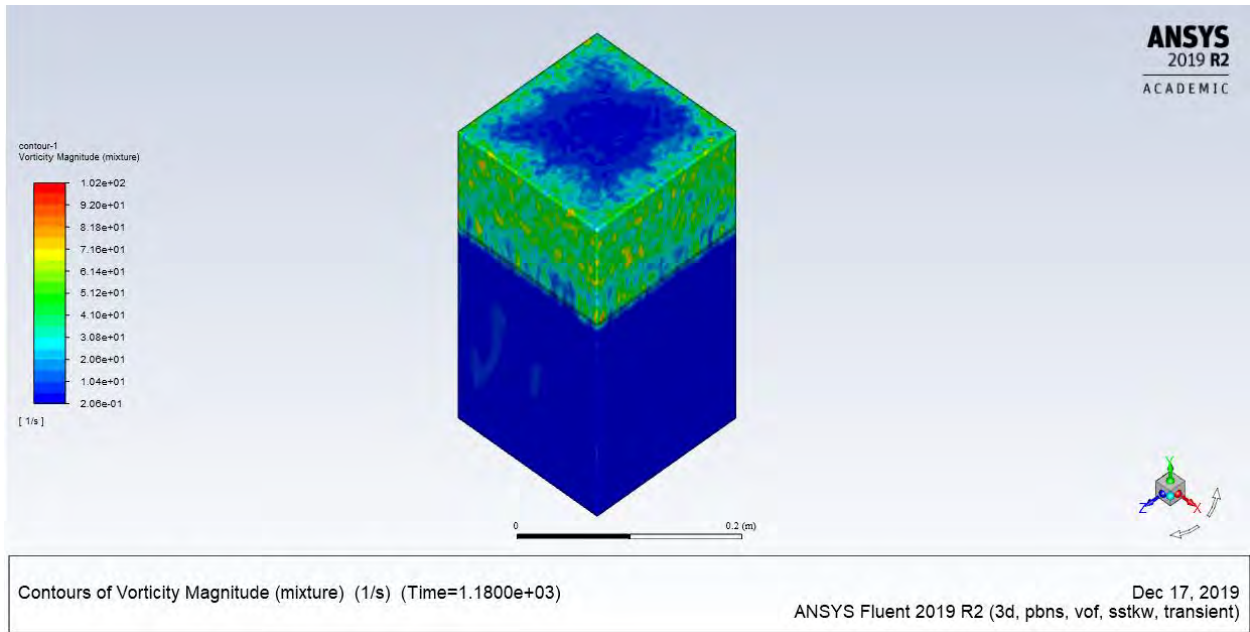
Figure 3.40—continued



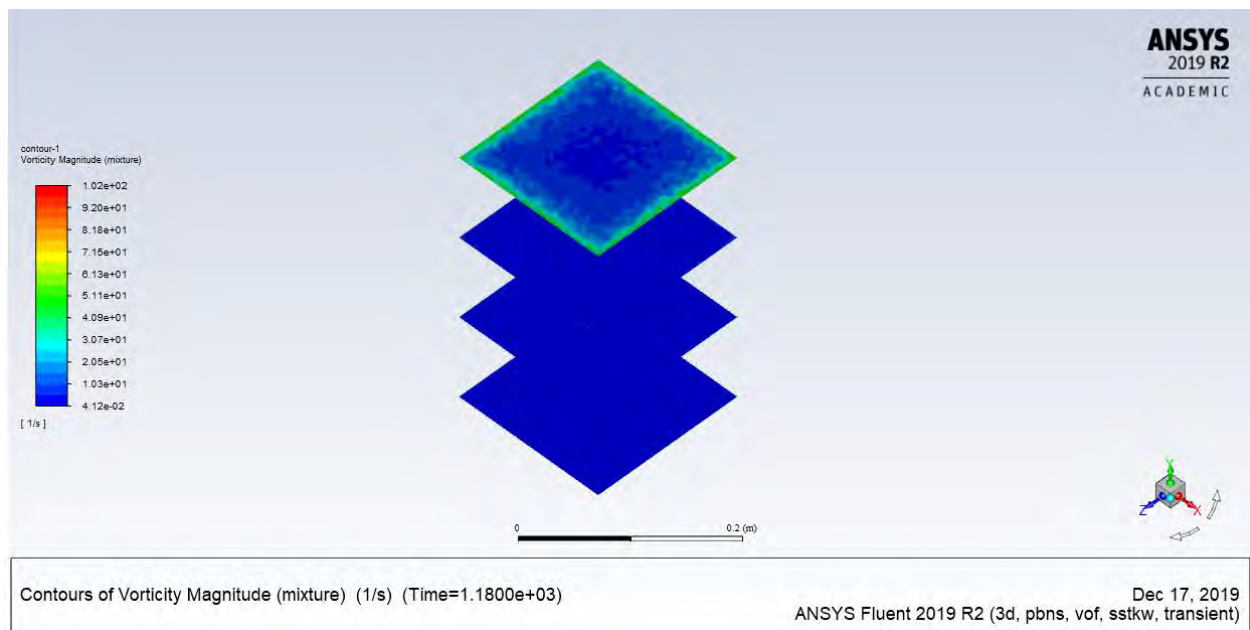
(c)



(d)



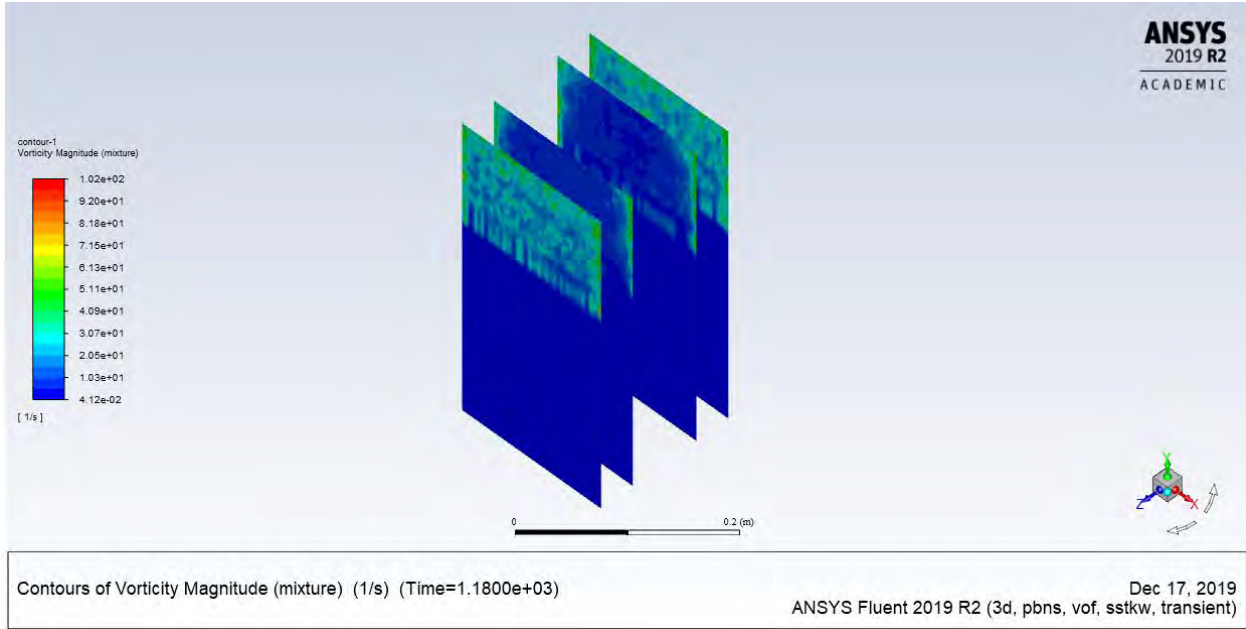
(a)



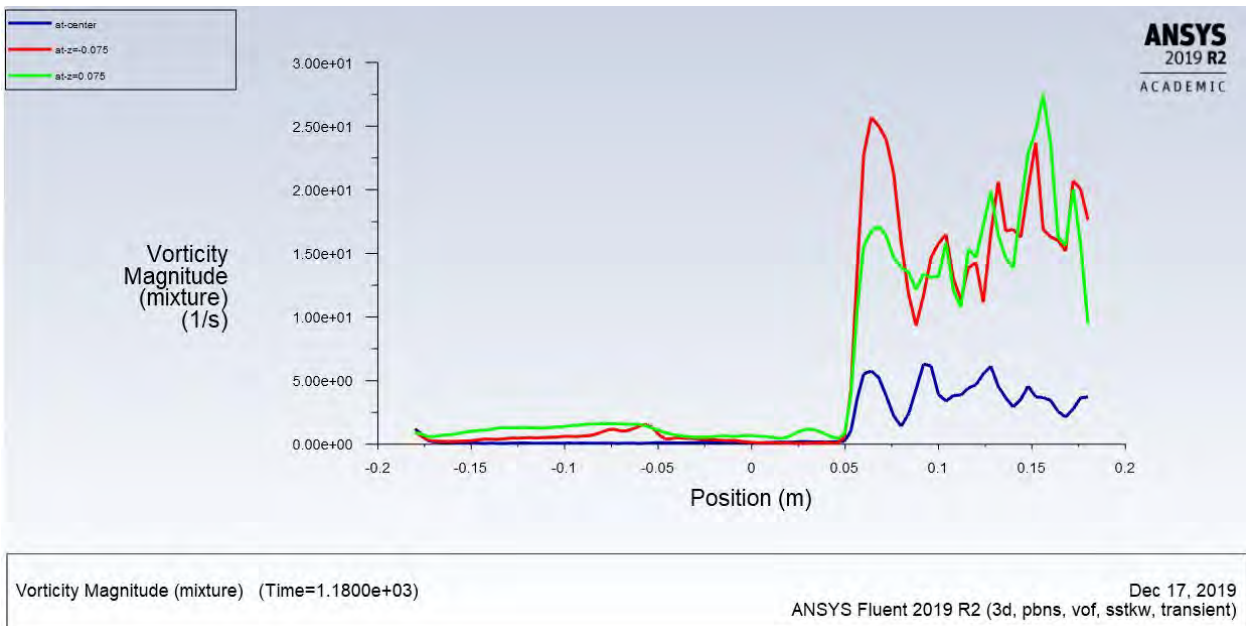
(b)

Figure 3.41: Vorticity at 1180 s (a) Contour of the geometry, (b) Contour of the top view sections, (c) Contour of the side view sections, (d) XY plot.

Figure 3.41—continued



(c)

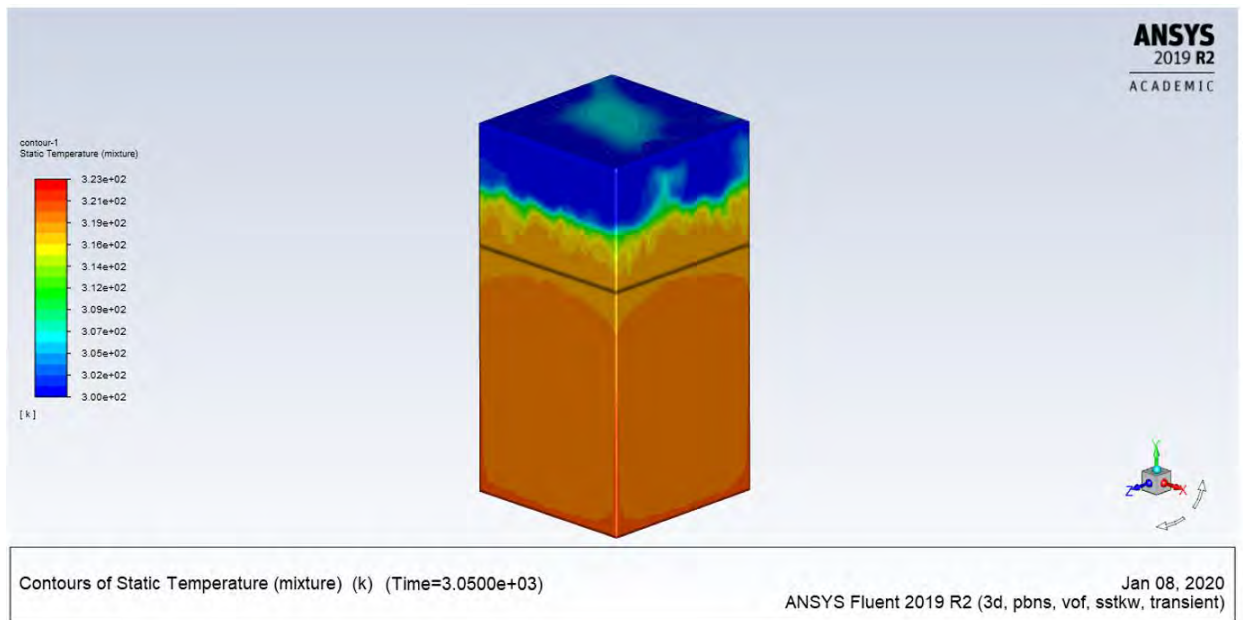


(d)

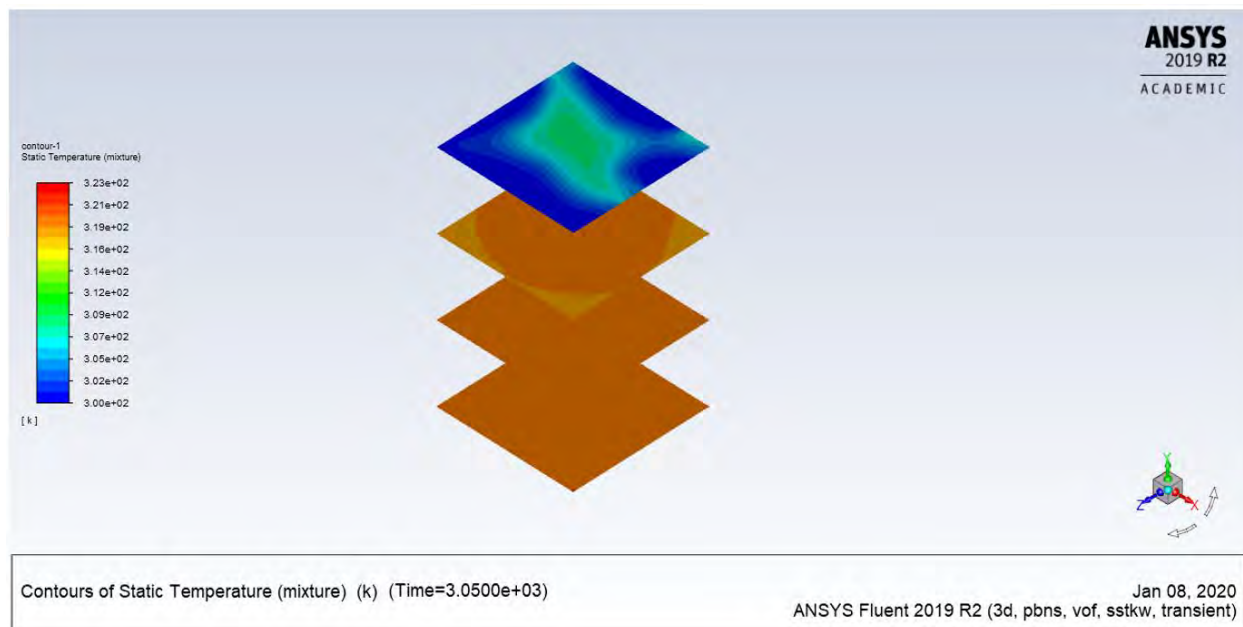
3) At $t = 3050$ Seconds

(a) Temperature

The temperature of the water keeps rising with time, as is evident from Figure 3.42. Figure 3.42 (a) shows the contour temperature of the 3-D geometry, where it is clear that the temperature of the water has reached about 45°C . It is noticeable that the temperature of the air domain has remained at room temperature due to the circulation of air to the ambient air. However, in the air domain the temperature starts to increase from the sides at this time. By looking at the top view sections, it becomes clear that the temperature at the center of the tank is higher than at the sides in air domain, which is related to the circulation of air in this region [refer to Figure 3.42 (b)]. In addition, it can be seen that the temperature starts to rise at the first section from the bottom of the tank. The side view sections are shown in Figure 3.42 (c), wherefrom it is clear that the temperature is equivalent at all locations. The plot in Figure 3.42 (d) shows the temperature before and after the water–air interface at three different locations, wherefrom it is clear that the temperature is higher at the center of the tank in the air domain.



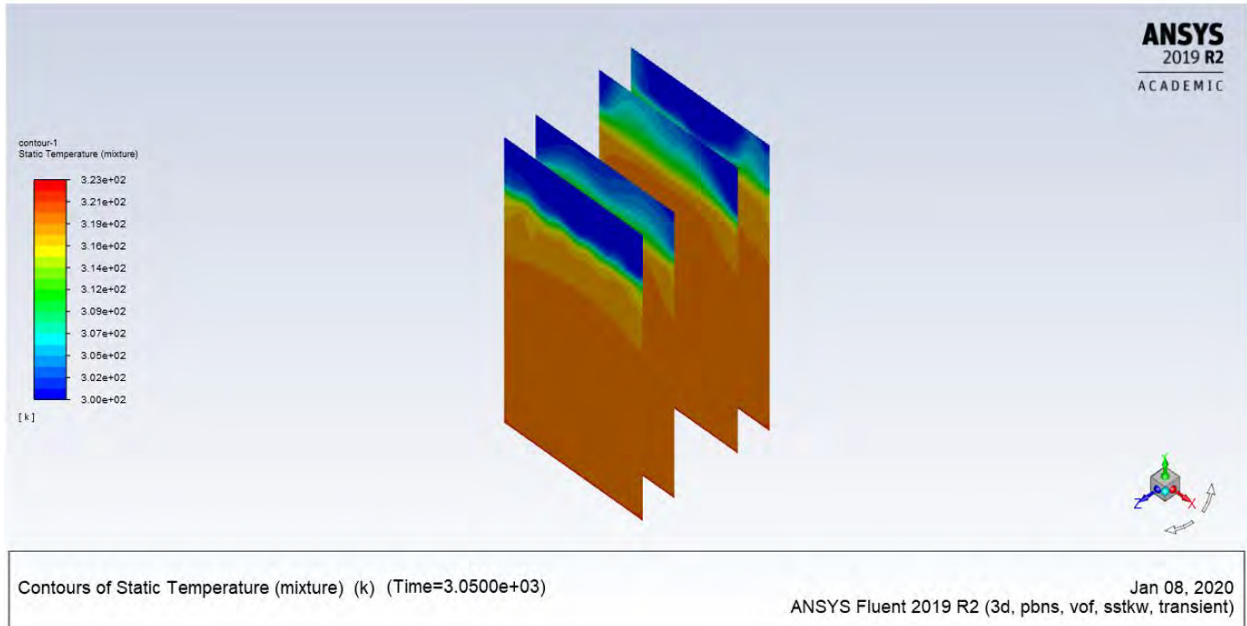
(a)



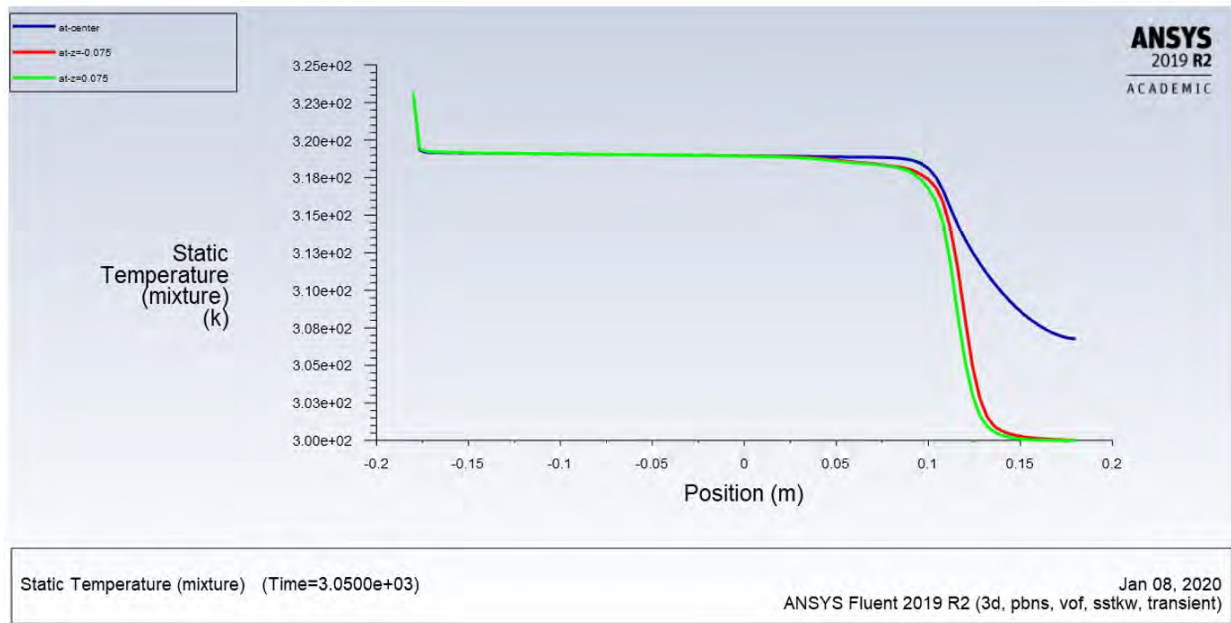
(b)

Figure 3.42: Temperature at 3050 s (a) Contour of the geometry, (b) Contour of the top view sections, (c) Contour of the side view sections, (d) XY plot.

Figure 3.42—continued



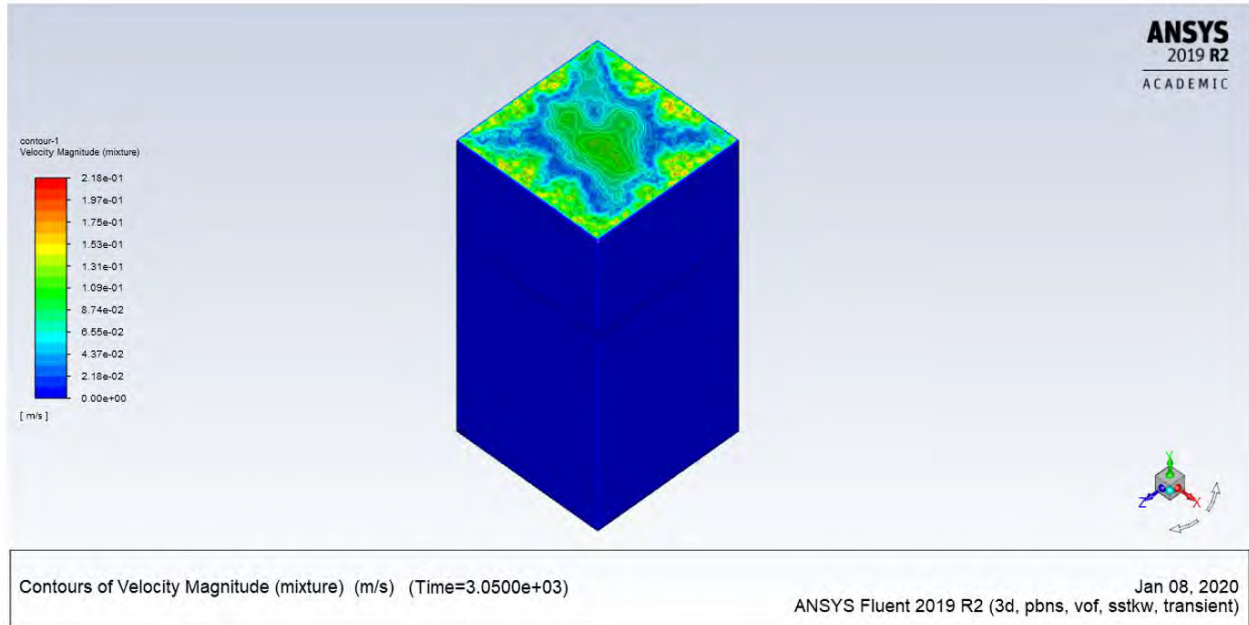
(c)



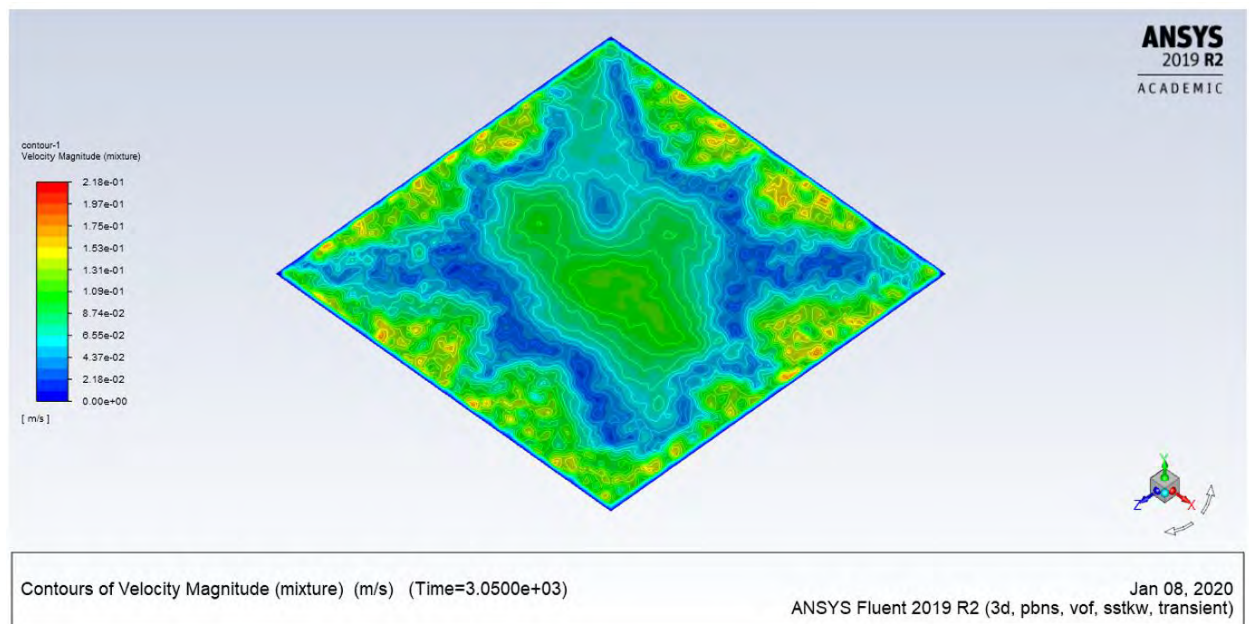
(d)

(b) Velocity

The velocity magnitude for contour and plot is shown in Figure 3.43. It is evident from the top view in Figure 3.43 (a) that the velocity at this time is higher compared to the velocity at $t = 1180$ s, which is due to the rising temperature and the water evaporation at this time. Moreover, it is interesting here to see the Bénard–Rayleigh convection cell that has developed at the surface. These cell patterns are developed as a result of rising temperature and gravity effect at this time as can be clearly seen in Figure 3.43 (b). In Figure 3.43 (c), the top view sections at four different locations are shown, where the higher velocity is found to be at the top. In addition, the cell patterns are clearly visible but with lesser velocity. Moreover, the side view at four different locations is presented in Figure 3.43 (d), where the velocity is higher at the air domain. However, the velocity in the water domain is lesser compared to the air domain, the latter being still noticeable and shown with small scale in Figure 3.43 (e). One reason is a higher velocity developing above the water surface can be related to the evaporation coming from the free water surface along with rising temperature, which increases the circulation in the air domain and hence the velocity. It is clear that this vortex in air domain started from the bottom of the tank, going up to the water surface and then circulating down to the water, where the highest value is near the water surface. This is due to the temperature difference between the bulk water and its surface. It is clear from Figure 3.43 (e) that it is at the bottom of tank where the Bénard–Rayleigh convection started to develop. Figure 3.43 (f) shows the plot of the velocity difference before and after the interface at three different locations where the velocity has increased rapidly above the interface, especially at the center of the tank, due to the air circulation.



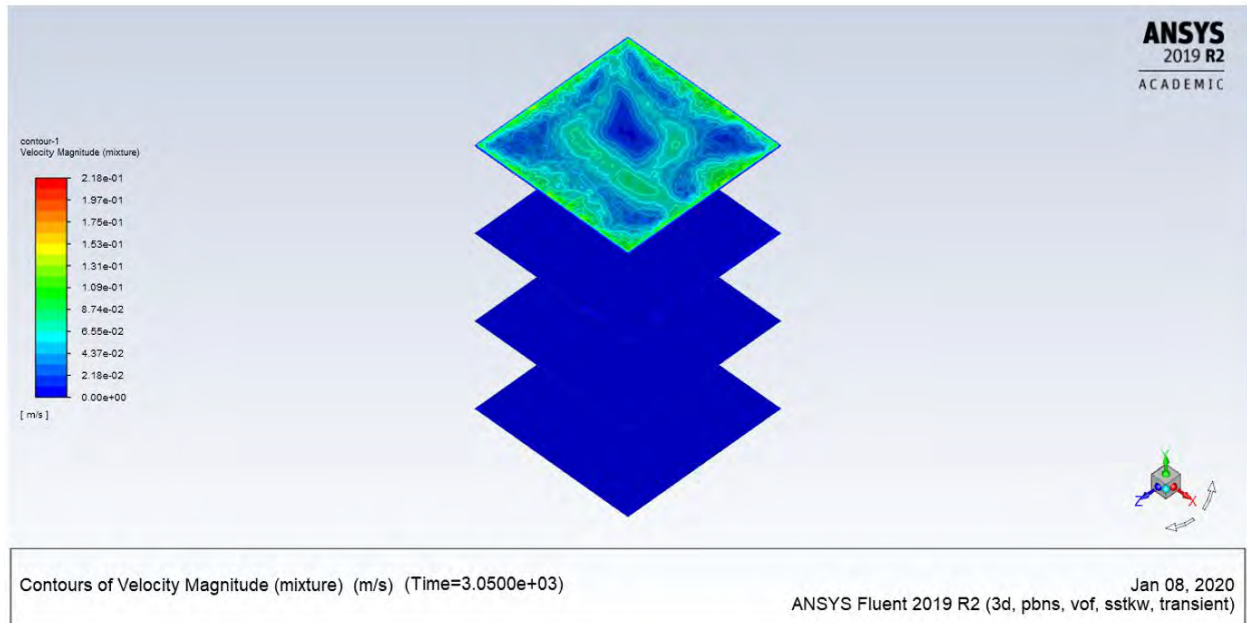
(a)



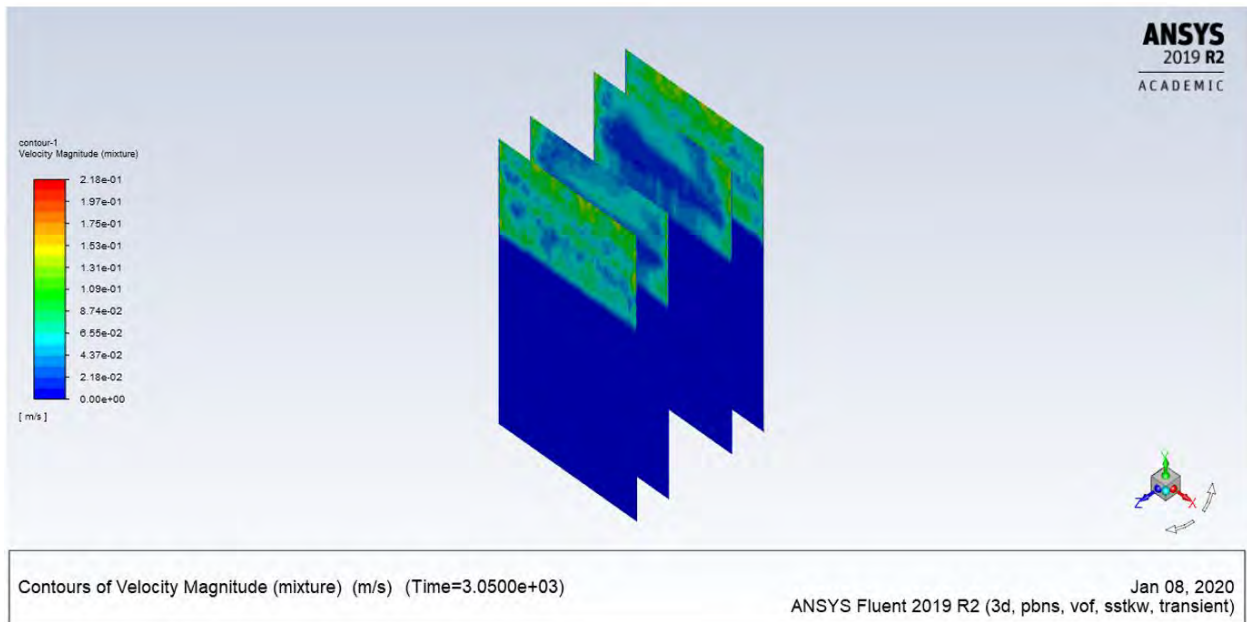
(b)

Figure 3.43: Velocity at 3050 s (a) Contour of the geometry, (b) Top view for the tank, (c) Contour of the top view sections, (d) Contour of the side view sections, (e) Contour in the water domain, (f) XY plot.

Figure 3.43—continued

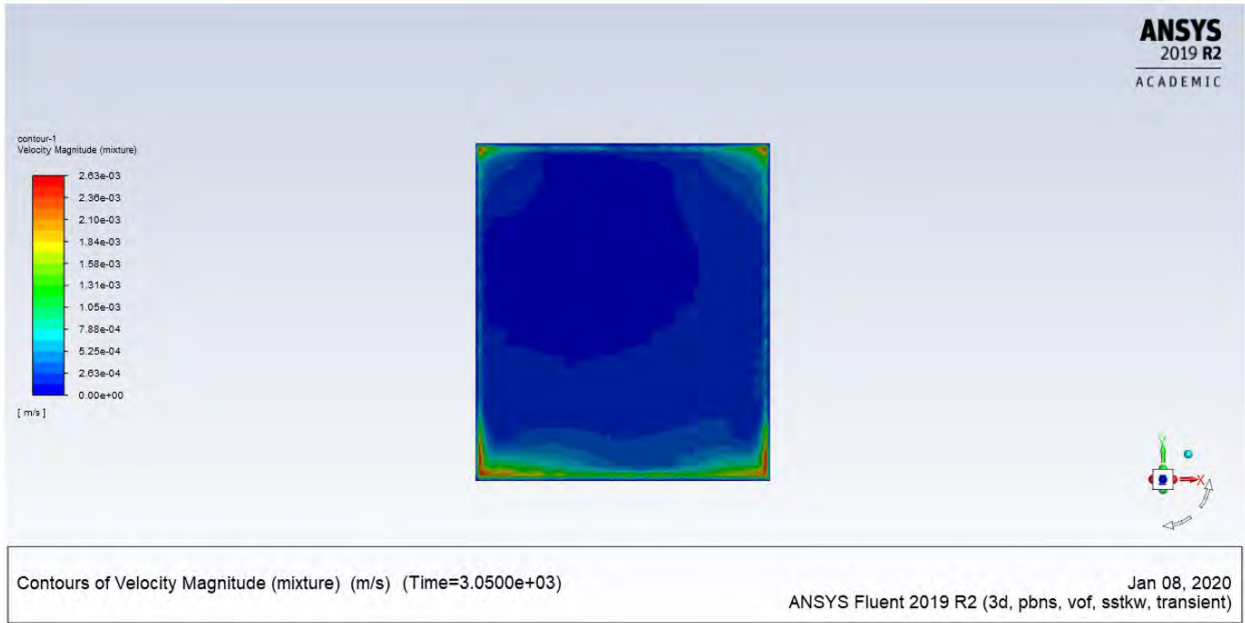


(c)

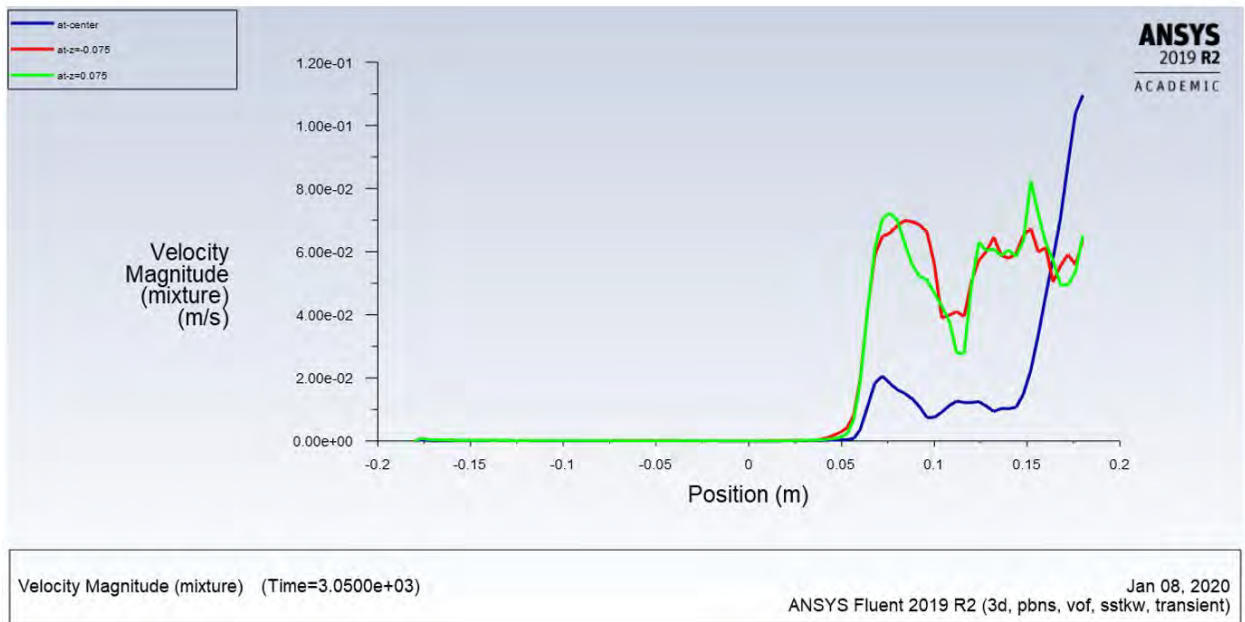


(d)

Figure 3.43—continued



(e)



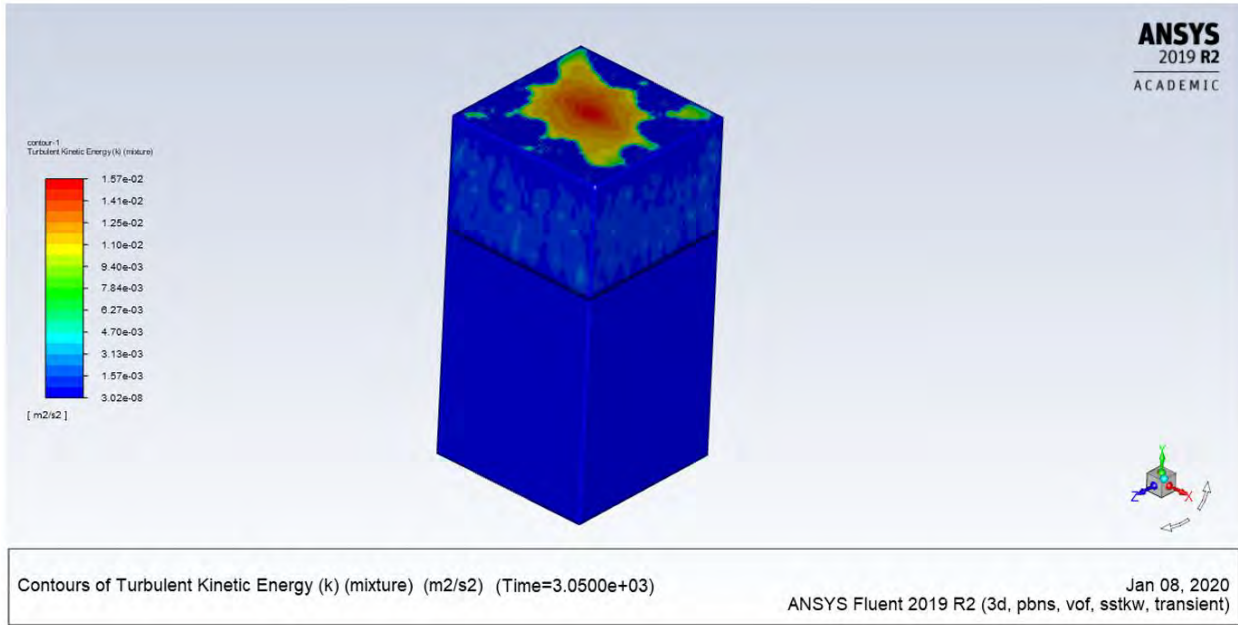
(f)

(c) Turbulence Kinetic Energy

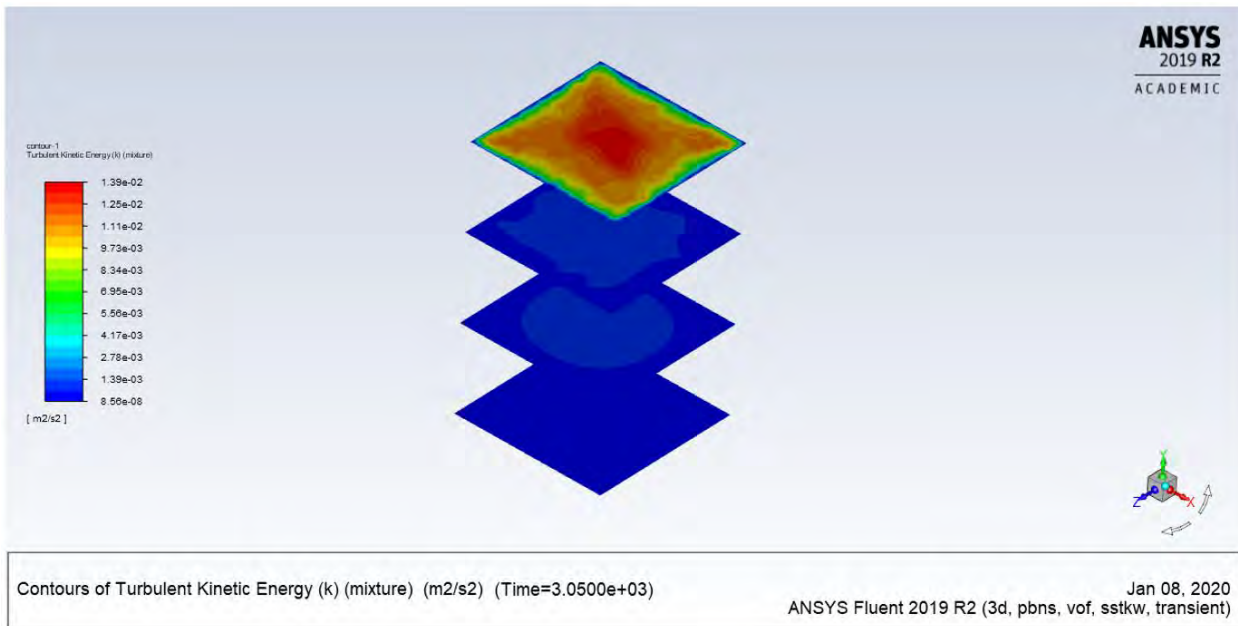
Turbulence kinetic energy (TKE) contour is shown in Figure 3.44 (a), where the TKE is higher at the air domain due to the higher velocity. It is clear that there is a spot of higher TKE at the top of the tank, which is obviously related to the heat and evaporation coming from the water surface to the ambient air. Figure 3.44 (b) shows TKE at top view sections at four different locations, where it is higher at the top compared to the rest. In Figure 3.44 (c), TKE at side view sections for four different locations is presented, where the value is clearly higher at the air domain due to the air circulation. By comparing these four sections, it can be seen that the two sections in the middle of the tank have higher TKE than those at the side due to the evaporation at the center of the tank. Moreover, in the water domain the TKE is still very small compared to the air domain [refer to Figure 3.44 (c)]. It is clear that TKE begins to gradually increase after the interface [refer to Figure 3.44 (d)].

(d) Vorticity

Vorticity contour is shown in Figure 3.45 (a), where the vorticity is higher at the air domain. It is clear that there is higher vorticity at the sides of the tank, which can be related to the circulation at this region. Vorticity at top view sections at four different locations is shown in Figure 3.45 (b), where it is higher at the top compared the rest. Figure 3.45 (c) presents vorticity at side view sections for four different locations, where the value is clearly higher at the air domain due to the air circulation. By comparing these four sections, it can be seen that vorticity at the two sections in the middle of the tank is lesser than at the sides due to the circulation at the sides of the tank. Moreover, the vorticity in the water domain is still very small compared to that in the air domain [refer to Figure 3.45 (c)]. It is clear that vorticity begins to gradually increase after the interface [refer to Figure 3.45 (d)].



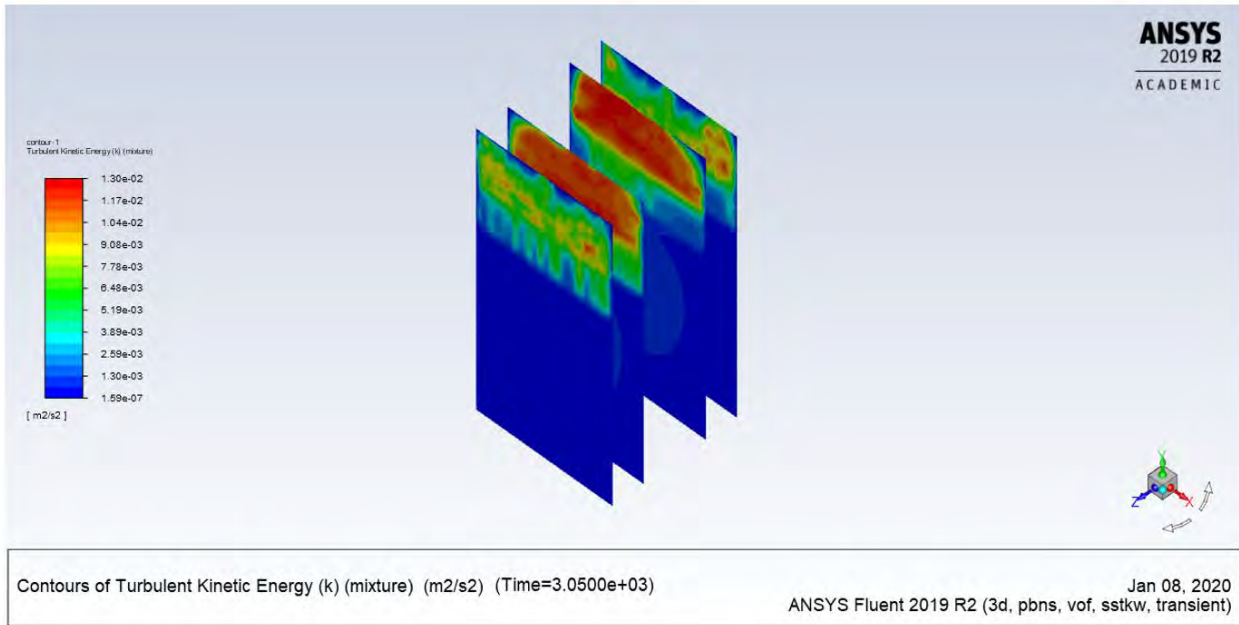
(a)



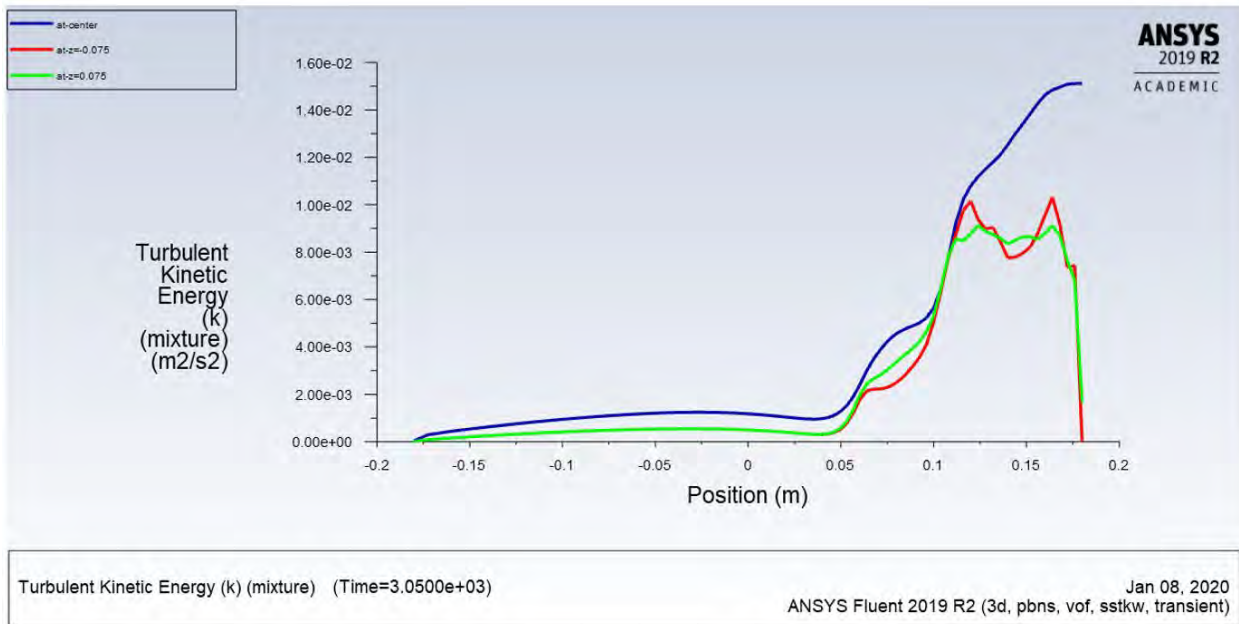
(b)

Figure 3.44: Turbulence kinetic energy at 3050 s (a) Contour of the geometry, (b) Contour of the top view sections, (c) Contour of the side view sections, (d) XY plot.

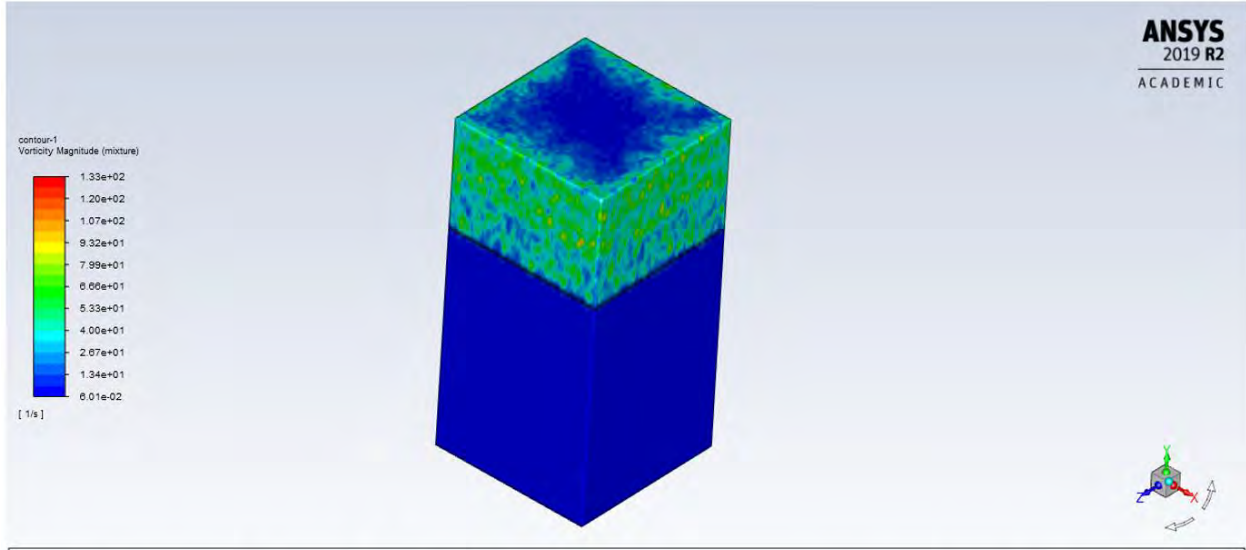
Figure 3.44—continued



(c)



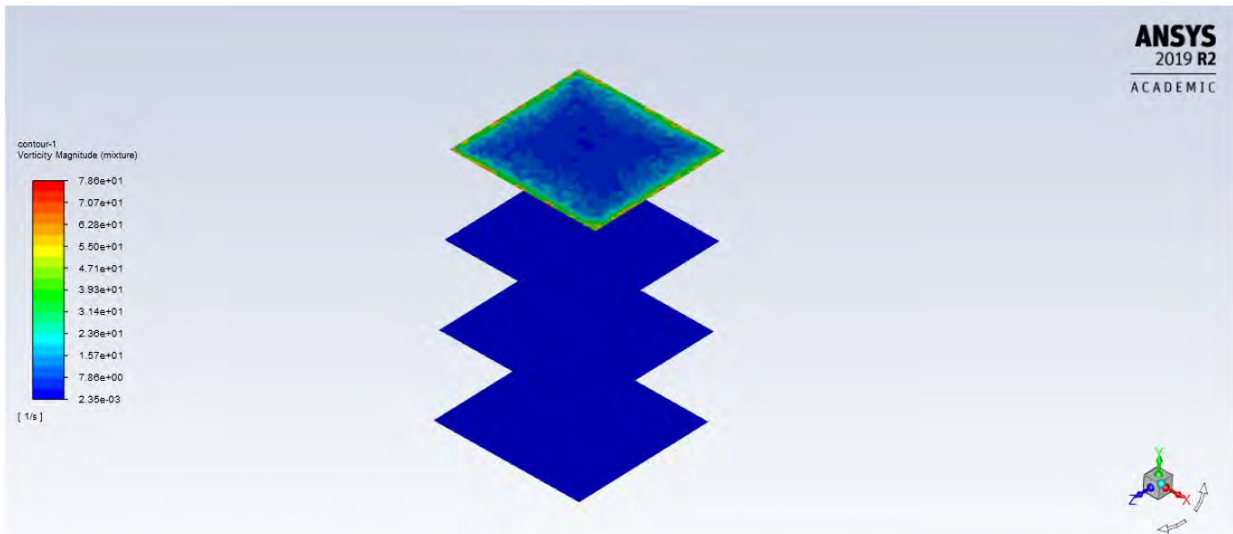
(d)



Contours of Vorticity Magnitude (mixture) (1/s) (Time=3.0500e+03)

Jan 08, 2020
ANSYS Fluent 2019 R2 (3d, pbns, vof, sstkw, transient)

(a)



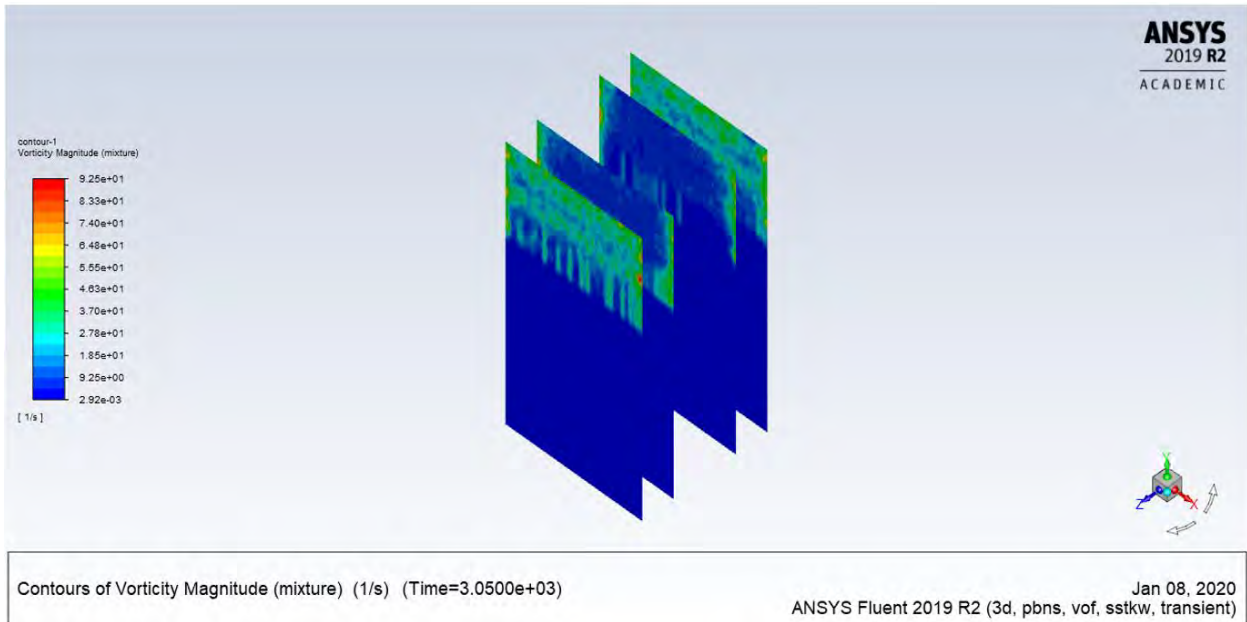
Contours of Vorticity Magnitude (mixture) (1/s) (Time=3.0500e+03)

Jan 08, 2020
ANSYS Fluent 2019 R2 (3d, pbns, vof, sstkw, transient)

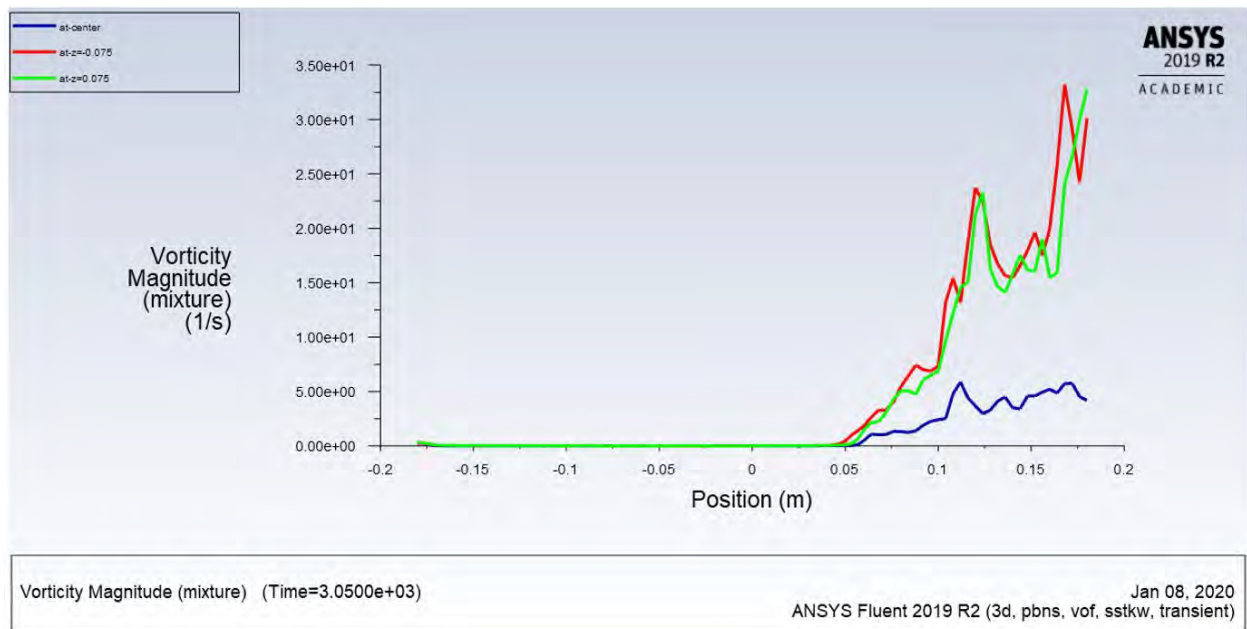
(b)

Figure 3.45: Vorticity at 3050 s (a) Contour of the geometry, (b) Contour of the top view sections, (c) Contour of the side view sections, (d) XY plot.

Figure 3.45—continued



(c)

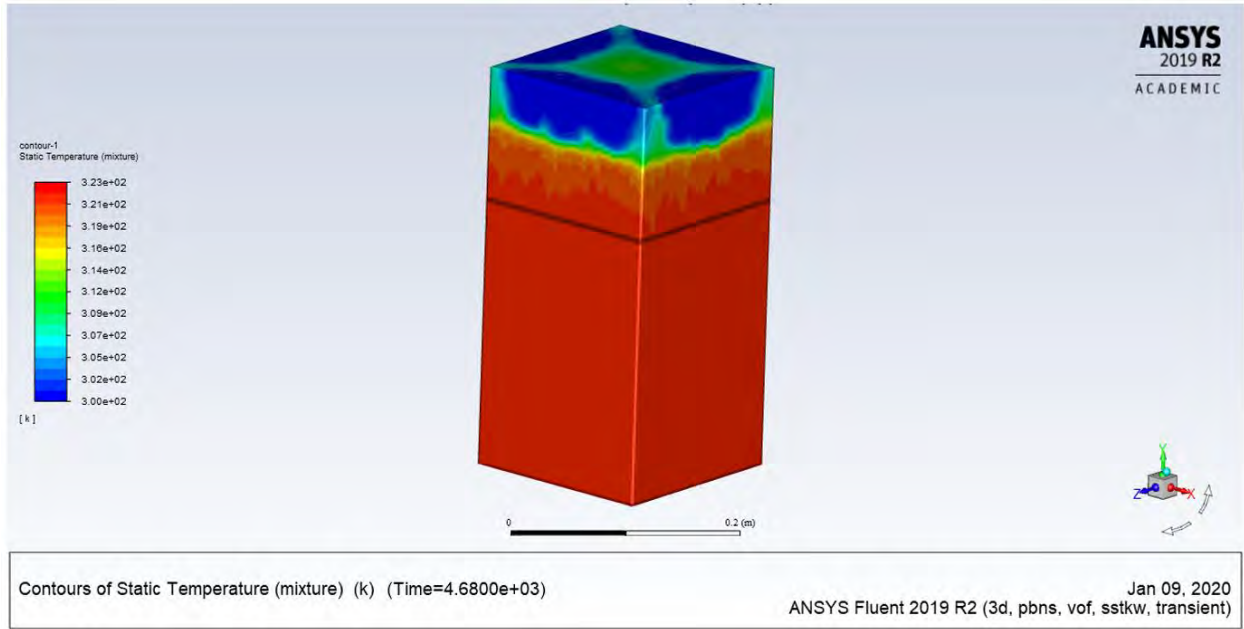


(d)

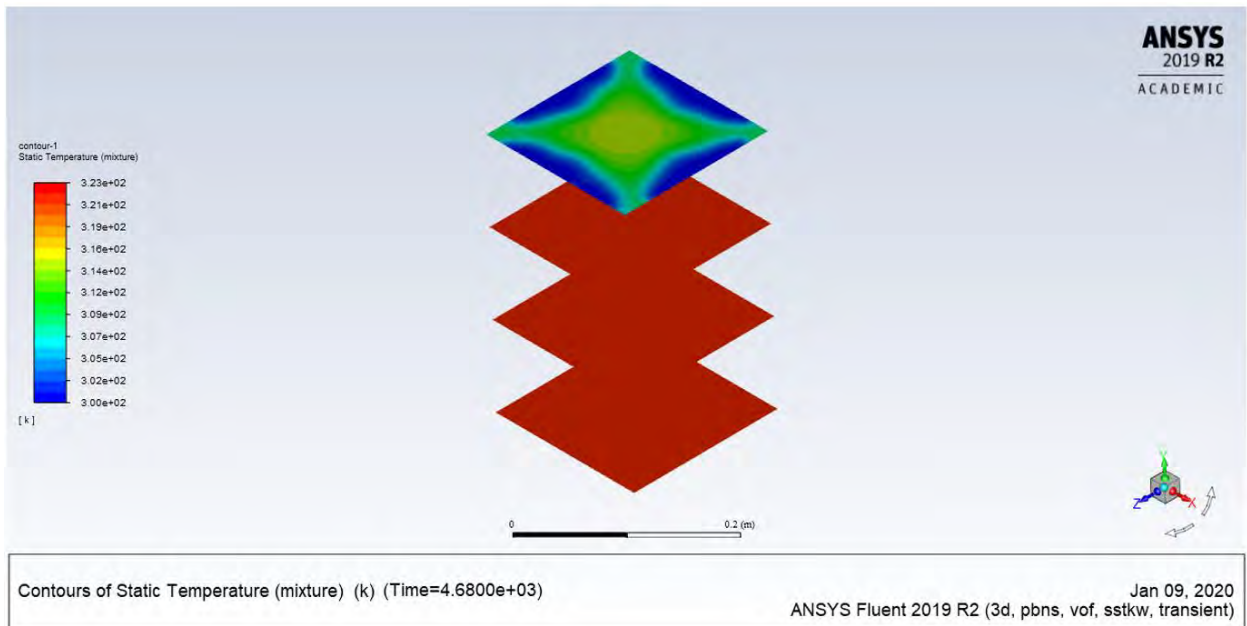
4) At $t = 4680$ Seconds

(a) Temperature

The temperature of the water keeps rising with time, as can be seen in Figure 3.46. Figure 3.46 (a) shows the contour temperature of the 3-D geometry, where it is clear that the temperature of the water has reached 50°C , which is the desirable temperature. It is evident that the temperature of the air domain remains at the room temperature due to circulation into the ambient air. However, in the air domain, the temperature starts to increase from the sides at this time. By looking at the top view sections, it is clear that the temperature at the center of the tank is higher than at the sides in air domain, which is related to the circulation of air in this region [refer to Figure 3.46 (b)]. In addition, it can be seen that the temperature starts to rise at the first section from the bottom of the tank. Figure 3.46 (c) shows the side view sections, wherefrom it is clear that the temperature is equivalent at all locations. The plot in Figure 3.46 (d) shows the temperature before and after the water–air interface at three different locations, where it is clear that the temperature is higher at the center of the tank in the air domain.



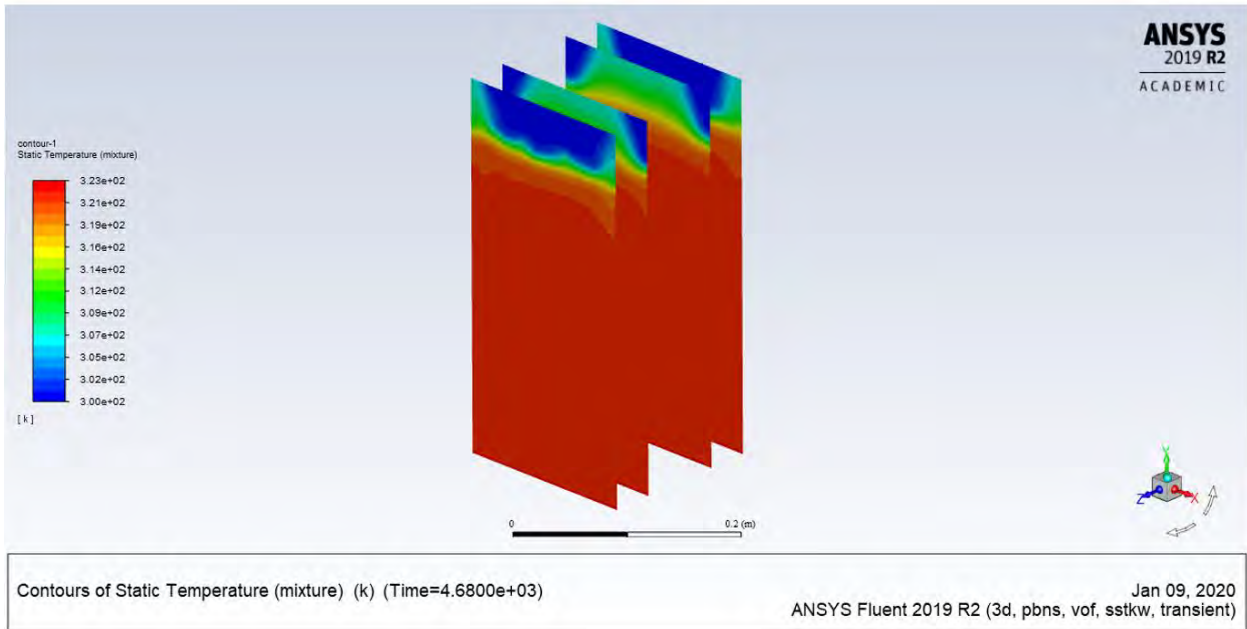
(a)



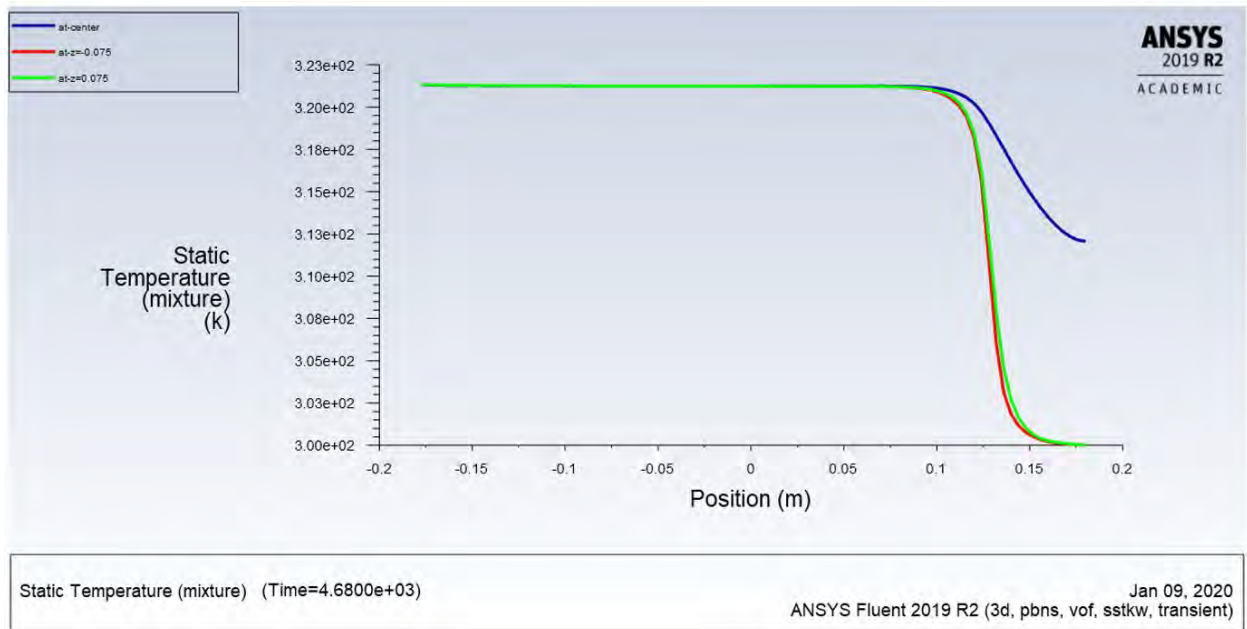
(b)

Figure 3.46: Temperature at 4680 s (a) Contour of the geometry, (b) Contour of the top view sections, (c) Contour of the side view sections, (d) XY plot.

Figure 3.46—continued



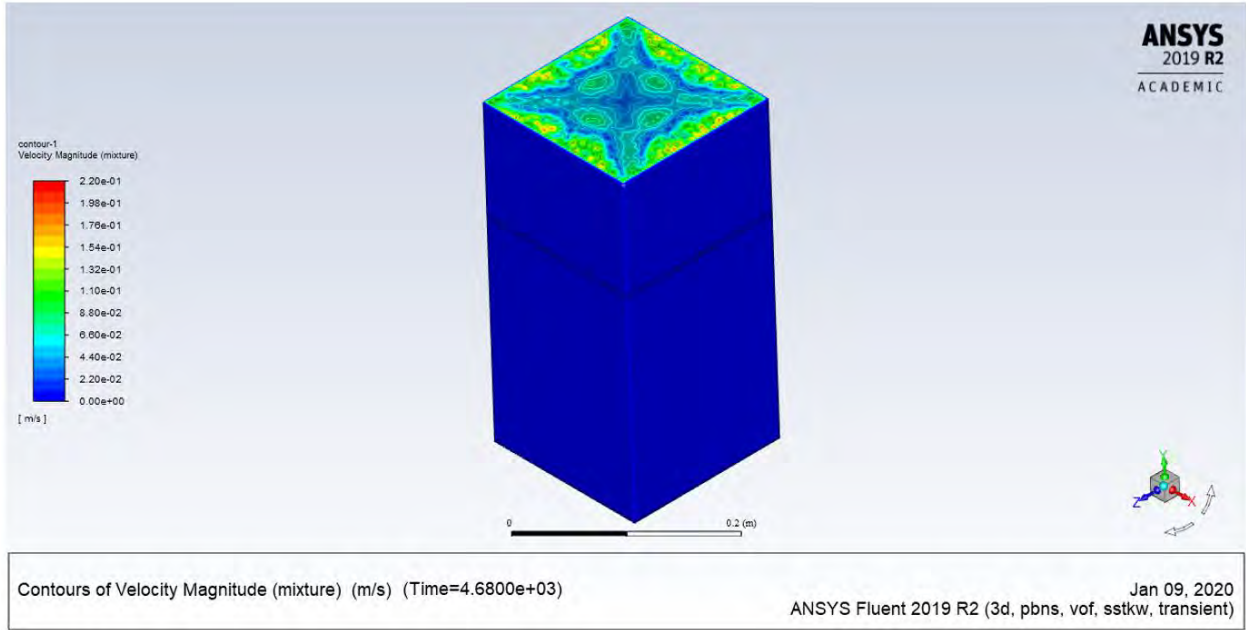
(c)



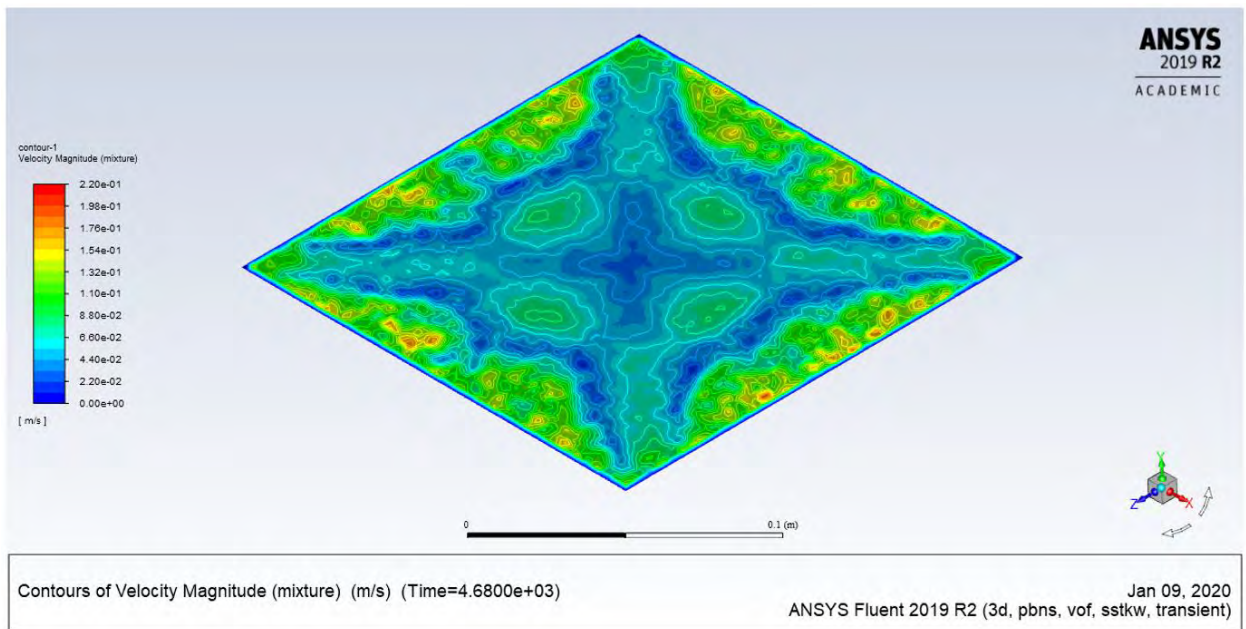
(d)

(b) Velocity

The velocity magnitude for contour and plot is shown in Figure 3.47. It can be seen from the top view in Figure 3.47 (a) that the velocity is higher compared to the velocity at $t = 3050$ s, which is due to the rising temperature and the water evaporation at this time. Moreover, it is interesting here to see the Bénard–Rayleigh convection cell that has developed at the surface. These cell patterns are developed as a result of rising temperature and gravity effect at this time, as can be clearly seen in Figure 3.47 (b). Figure 3.47 (c) shows the top view sections at four different locations, where the highest velocity is found to be at the top. The cell patterns are clearly visible, but with lesser velocity. Moreover, the side views at four different locations are presented in Figure 3.47 (d), where the velocity is higher at the air domain. However, the velocity in the water domain is lesser compared with that in the air domain, the latter being still noticeable and shown with small scale in Figure 3.47 (e). One reason for a higher velocity developing above the water surface can be related to the evaporation coming from the free water surface along with rising temperature, which increases the circulation in the air domain and hence the velocity. It is clear that this vortex in air domain started from the bottom of the tank, going up to the water surface and then circulating down to the water, where the highest value is near the water surface. This is due to the temperature difference between the bulk water and its surface. It is clear from Figure 3.47 (e) that it is at the bottom of the tank where the Bénard–Rayleigh convection started to develop. Figure 3.47 (f) shows the plot of the velocity difference before and after the interface at three different locations where the velocity has increased rapidly above the interface, especially at the center of the tank, due to the air circulation.



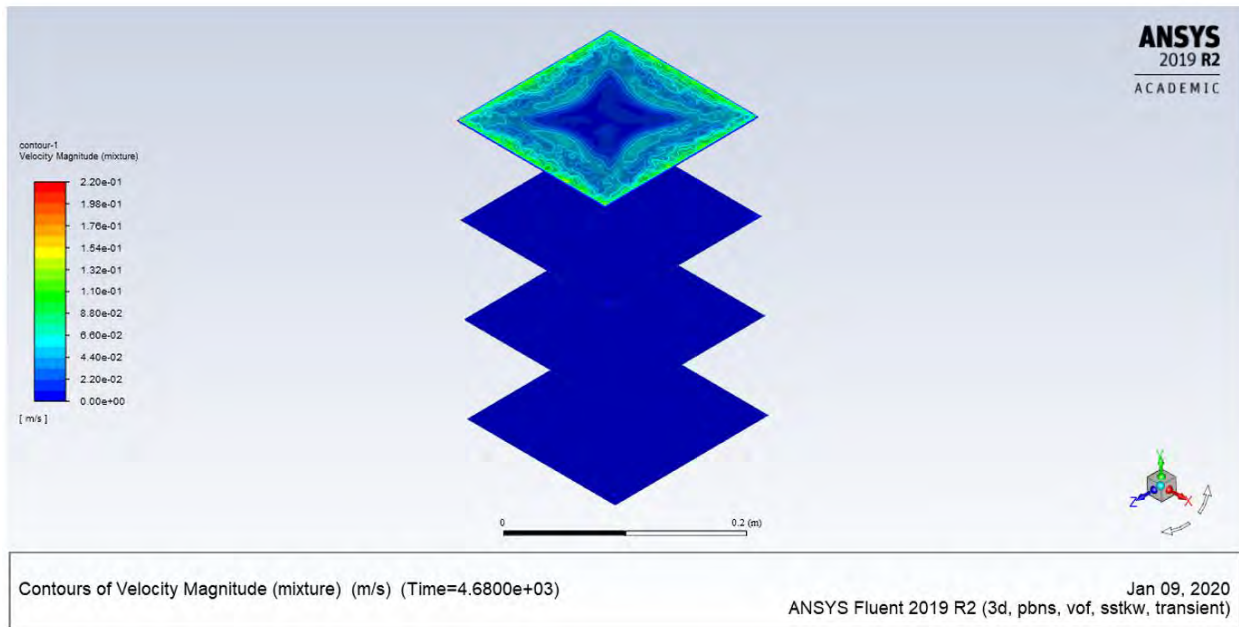
(a)



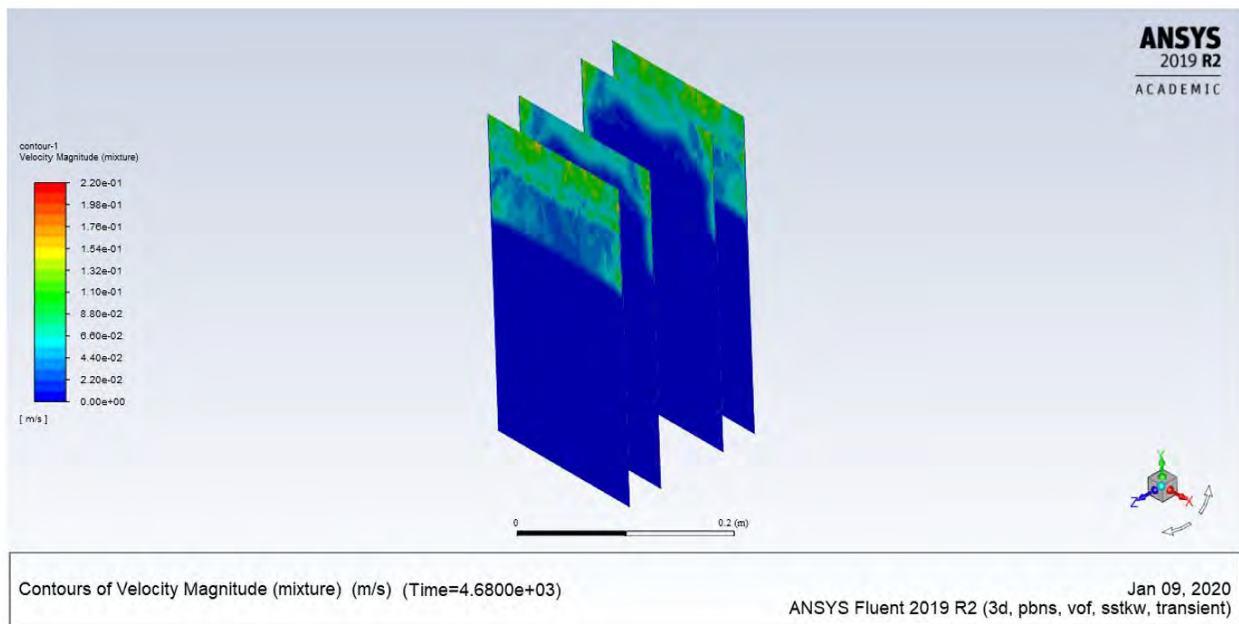
(b)

Figure 3.47: Velocity at 4680 s (a) Contour of the geometry, (b) Top view for the tank, (c) Contour of the top view sections, (d) Contour of the side view sections, (e) Contour in the water domain, (f) XY plot.

Figure 3.47—continued

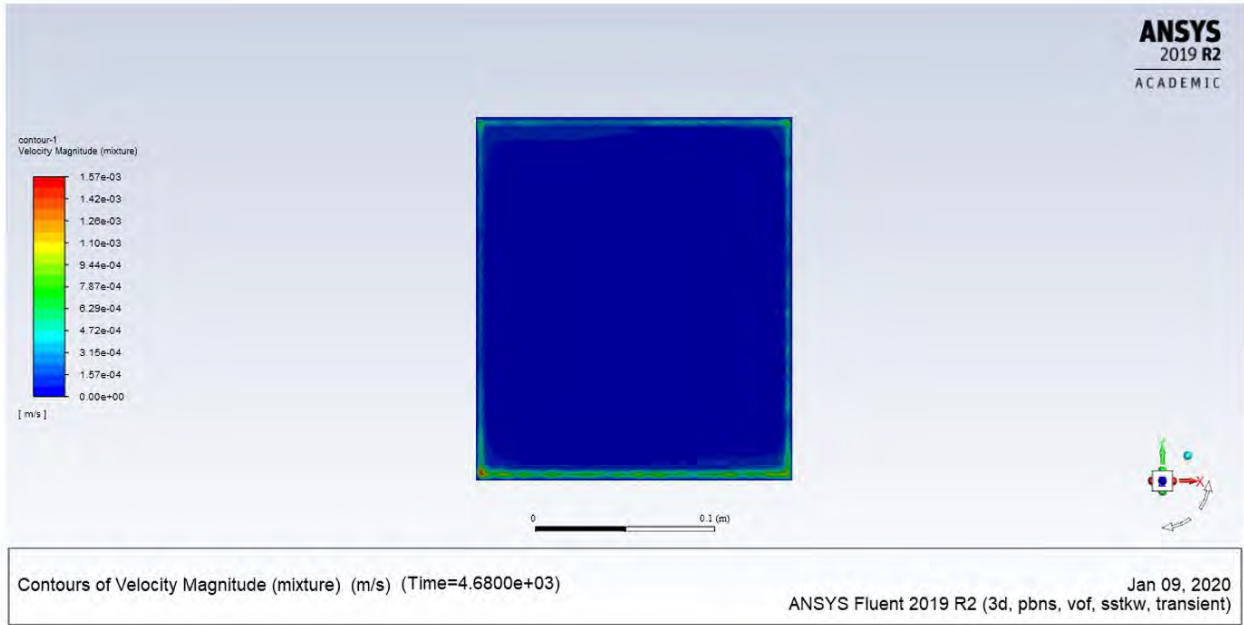


(c)

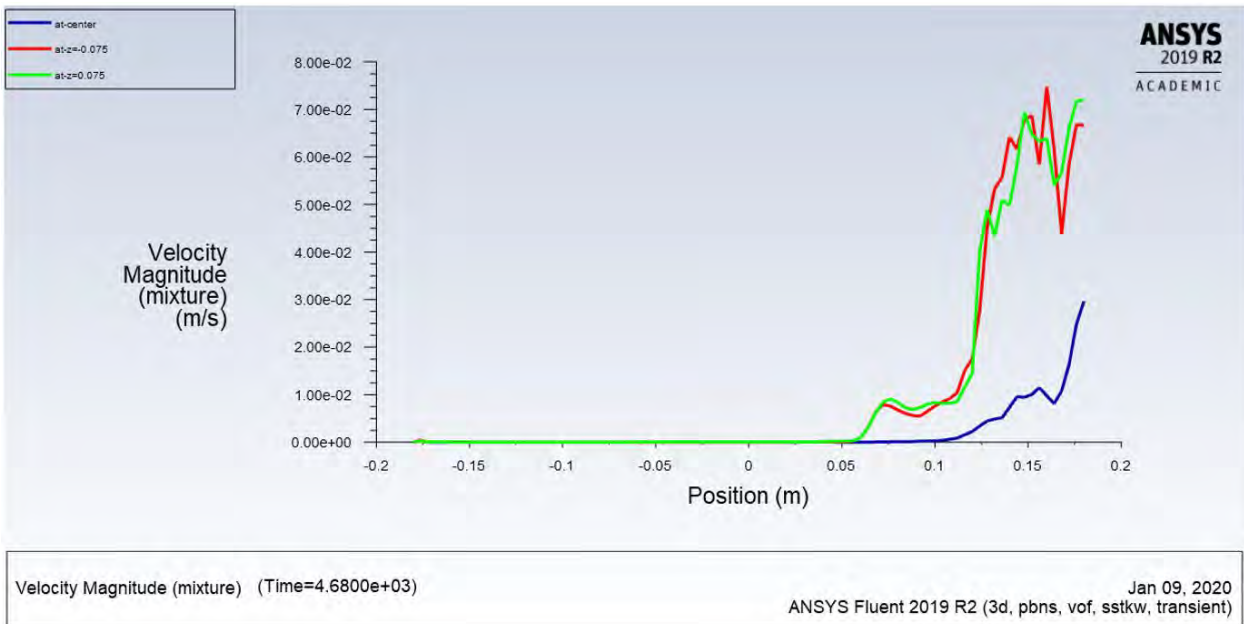


(d)

Figure 3.47—continued



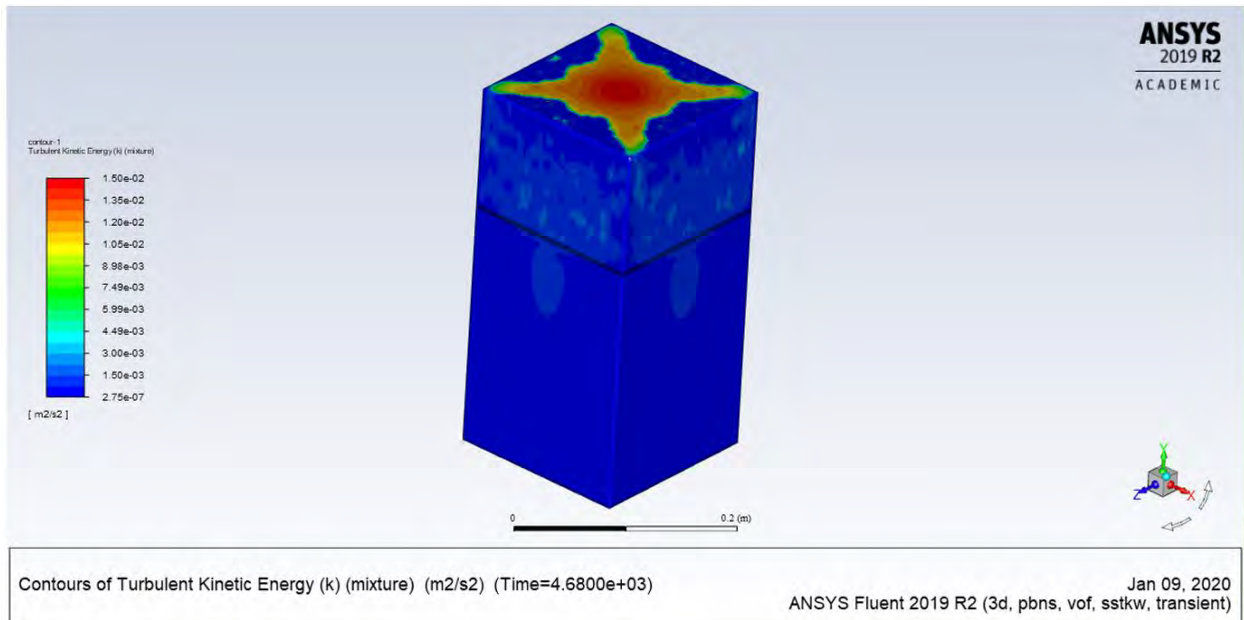
(e)



(f)

(c) Turbulence Kinetic Energy

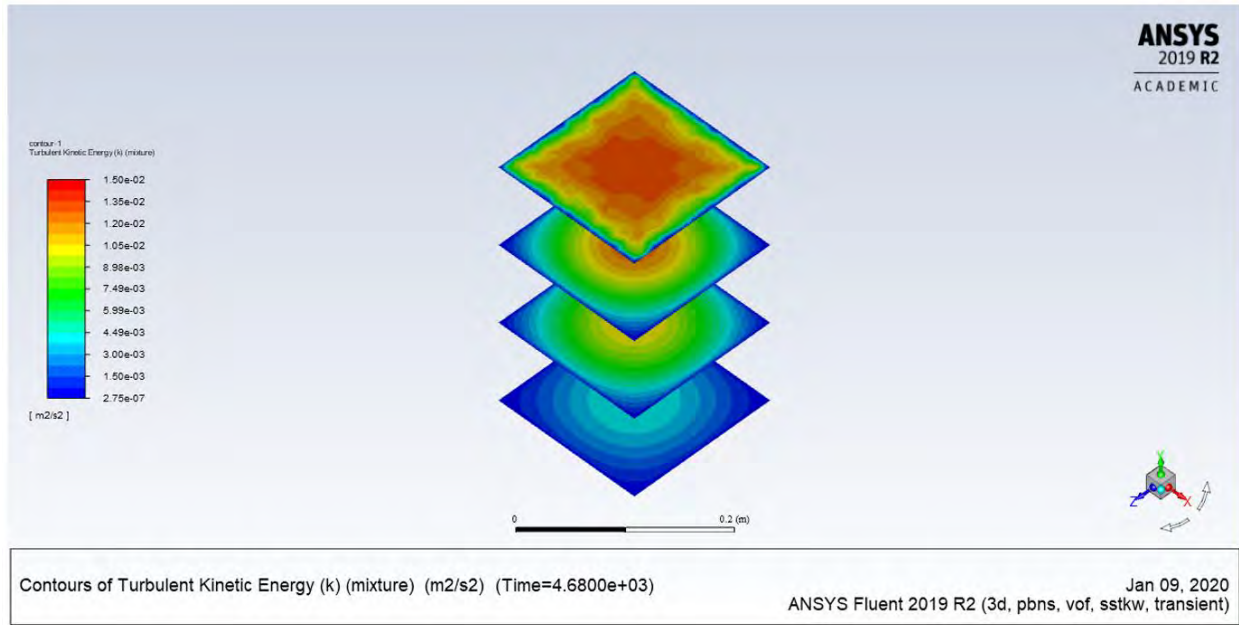
Turbulence kinetic energy (TKE) contour is shown in Figure 3.48 (a), where the TKE is higher at the air domain due to the higher velocity. A larger spot of TKE is evident at the top of the tank, which is obviously related to the heat and evaporation coming from the water surface to the ambient air. TKE at top view sections at four different locations is shown in Figure 3.48 (b), where it is higher at the top compared to the rest. Figure 3.48 (c) presents TKE at side view sections for four different locations, wherein the value is clearly higher at the air domain due to the air circulation. By comparing these four sections, it can be seen that the two sections in the middle of the tank have higher values than those at the sides due to the evaporation at the center of the tank. Moreover, the TKE in the water domain is lesser compared to its value in the air domain [refer to Figure 3.48 (c)]. TKE is higher even in water domain at this time [refer to Figure 3.48 (d)].



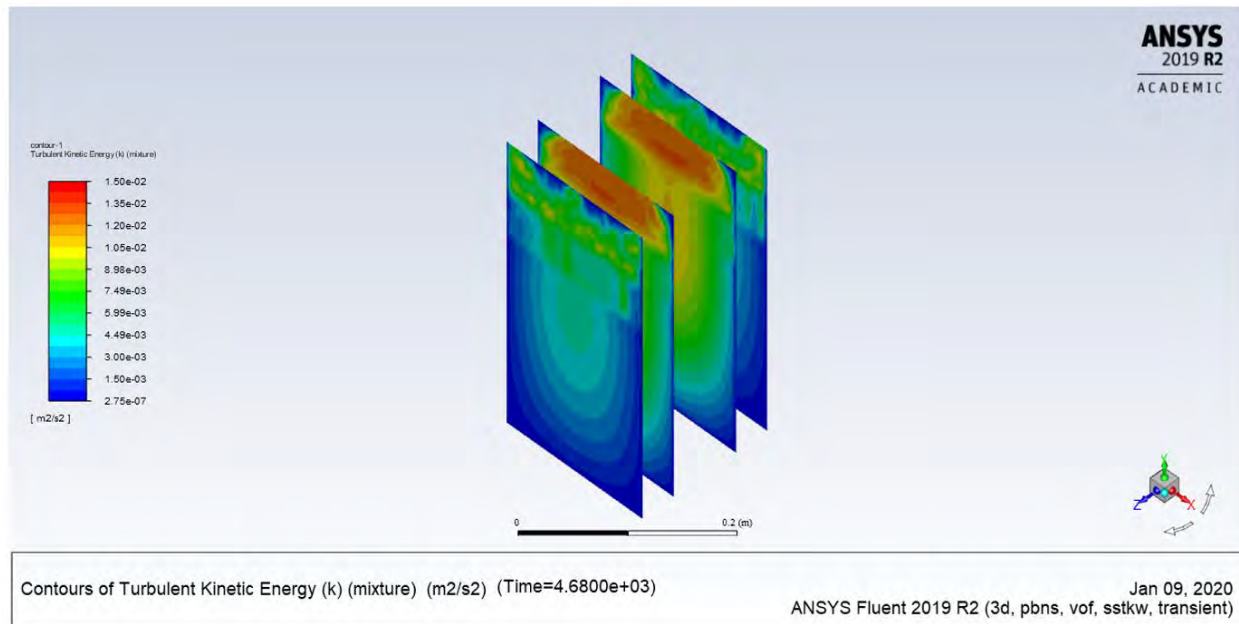
(a)

Figure 3.48: Turbulence kinetic energy at 4680 s (a) Contour of the geometry, (b) Contour of the top view sections, (c) Contour of the side view sections, (d) XY plot.

Figure 3.48—continued

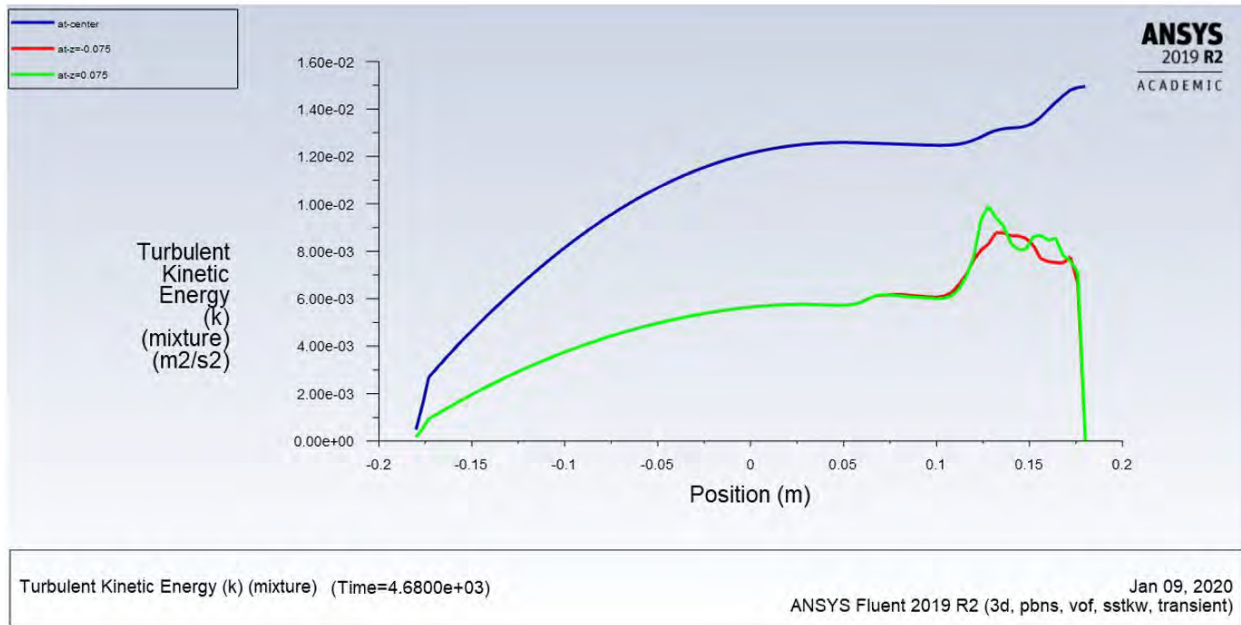


(b)



(c)

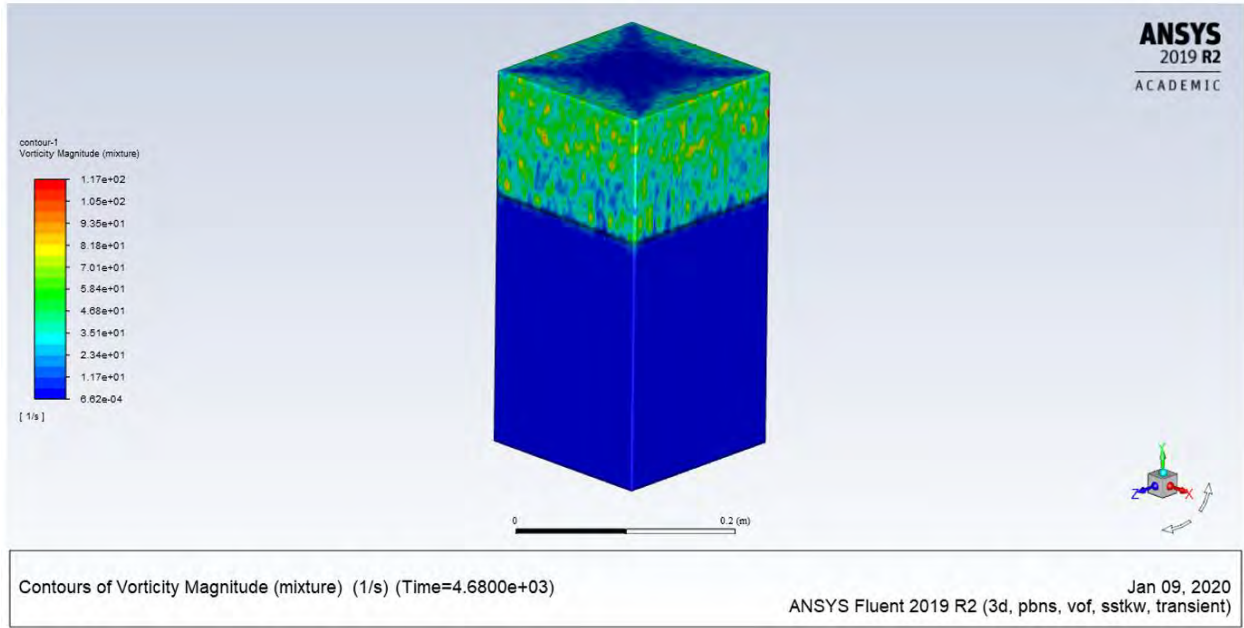
Figure 3.48—continued



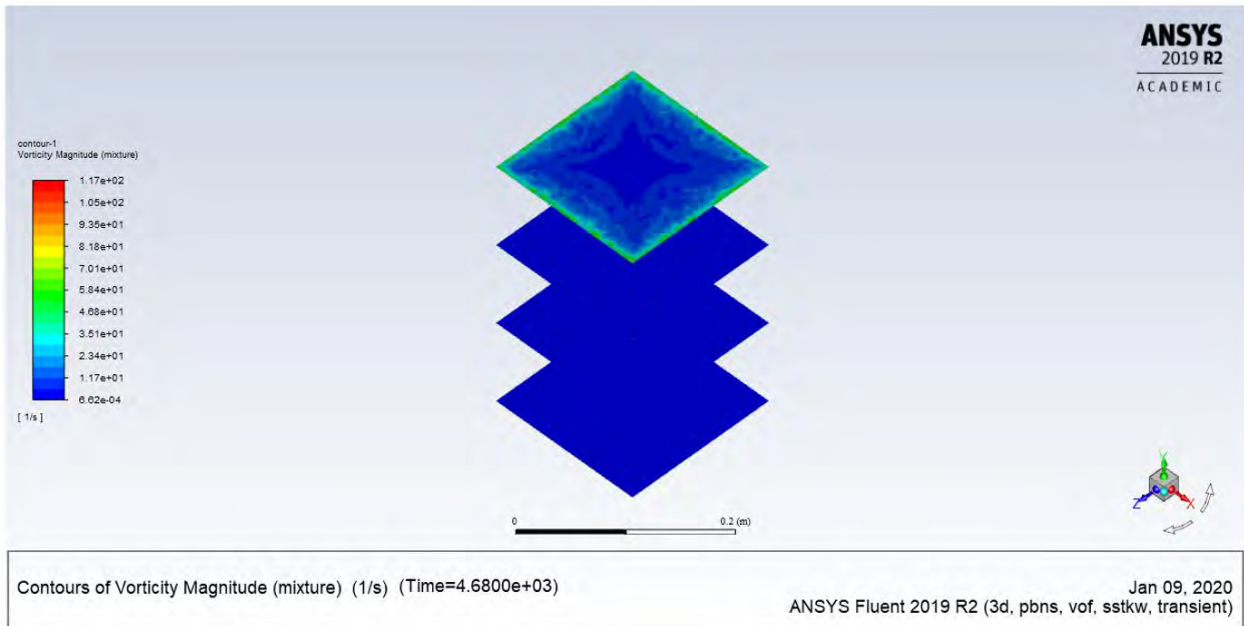
(d)

(d) Vorticity

Vorticity contour is shown in Figure 3.49 (a), where the vorticity is higher at the air domain. It is clear that there is higher vorticity at the sides of the tank, which can be related to the circulation at this region. Vorticity at top view sections at four different locations is shown in Figure 3.49 (b), where it is higher at the top compared to the rest. Vorticity at side view sections for four different locations is presented in Figure 3.49 (c), wherein the value is clearly higher at the air domain due to the air circulation. Comparing these four sections, it is evident that vorticity values at the two sections in the middle of the tank are smaller than at the sides, due to the circulation at the sides of the tank. Moreover, the vorticity in the water domain is still very small compared to its value in the air domain [refer to Figure 3.49 (c)]. It is clear that vorticity begins to gradually increase after the interface [refer to Figure 3.49 (d)].



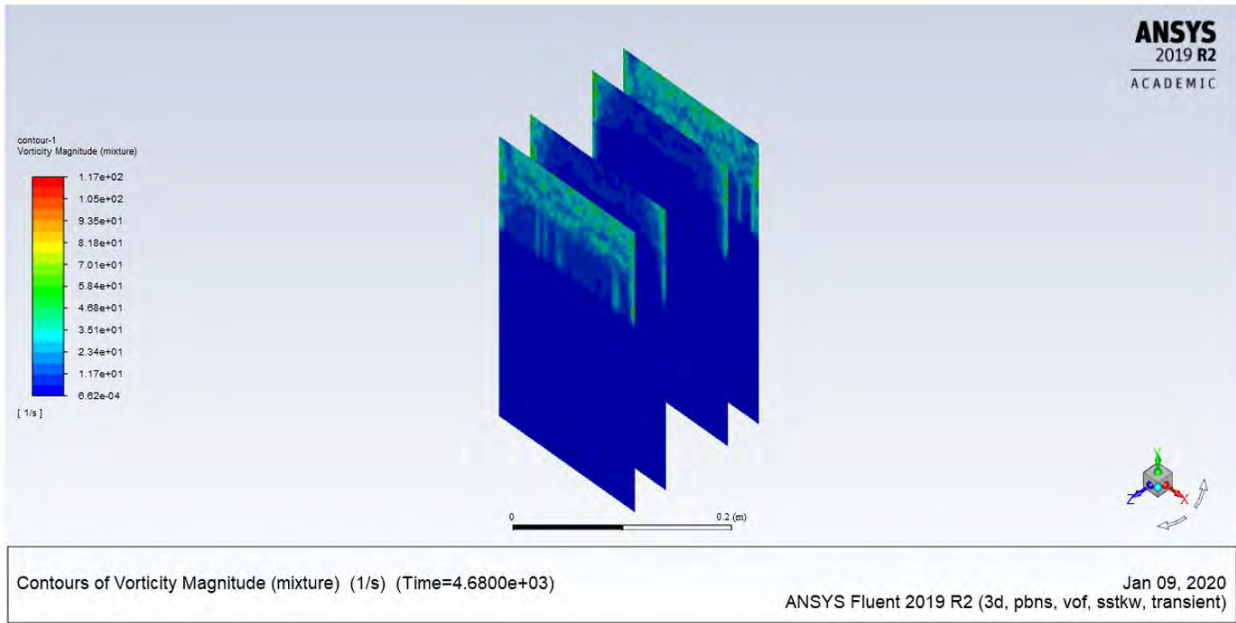
(a)



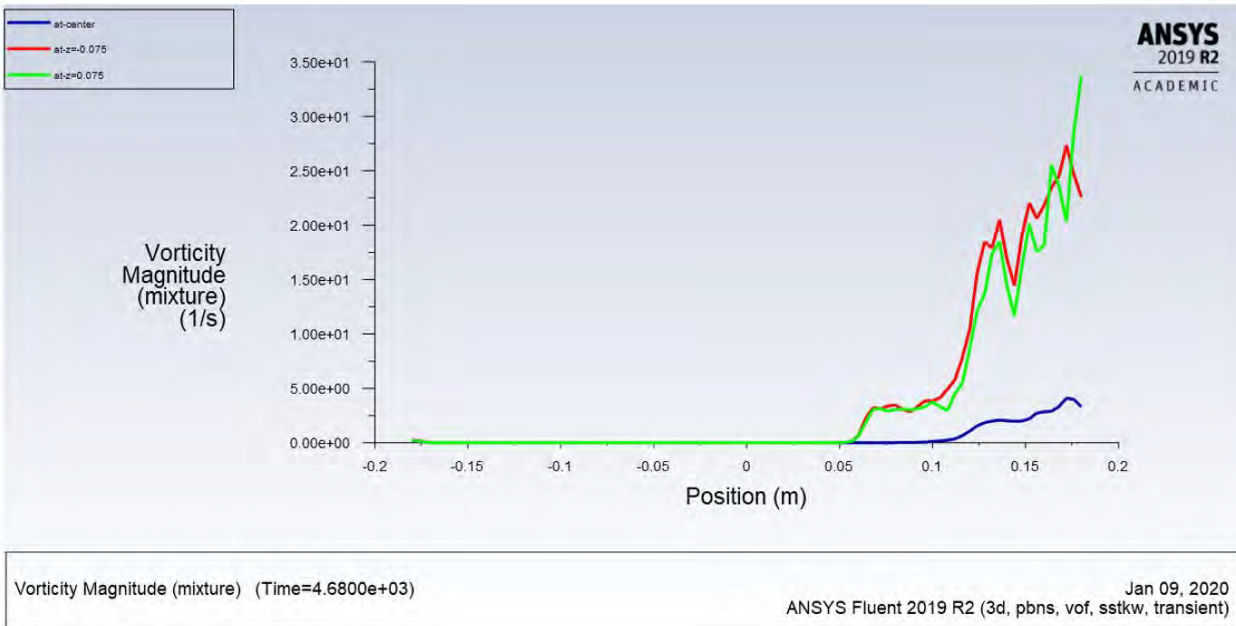
(b)

Figure 3.49: Vorticity at 4680 s (a) Contour of the geometry, (b) Contour of the top view sections, (c) Contour of the side view sections, (d) XY plot.

Figure 3.49—continued



(c)



(d)

3.6 Chapter Conclusion

The developed numerical simulation work (2-D and 3-D) using ANSYS FLUENT 2019 R2 was presented and discussed in detail in this chapter. The evaporation rate and heat and mass transfer at different timesteps of simulation were discussed. Temperature, velocity, vorticity, and turbulence kinetic energy were addressed, which showed an interesting development along with time. In the following chapter, the experimental work is presented and discussed in detail, including the setup and results.

4. EXPERIMENTAL WORK

The objective of this chapter is to present and discuss the setup and results of the experimental work that was developed in our lab (Fluid Dynamics) at WMU. The experimental work and the computations can be divided mainly into four parts. The first part was the study of the evaporation rate along with temperature development. As a result of this first part, a new correlation for free water surface evaporation (Sherwood–Rayleigh relation) was calculated and compared with the previous work. The second part was investigation of the natural convection flow inside the water tank at the sides by utilizing particle image velocimetry in case of free surface evaporation. Following this second part, the flow pattern and the statistical properties of the flow inside the water tank are presented. The third part investigated the flow pattern from the top view of the water tank by using particle image velocimetry. Finally, stereo particle image velocimetry (SPIV) was used to investigate the third component of the flow pattern and its effect on the velocity magnitude. Note that each part of this experimental work had a different setup that was associated with the investigated parameters, as addressed in detail in the following sections.

4.1 Prediction of Sherwood–Rayleigh Correlation

4.1.1 Experimental Setup

This part of the experiment was conducted to predict a Sherwood–Rayleigh correlation to calculate the evaporation rate from the free water surface in case of natural convection. The water tank was fabricated from clear acrylic Plexiglas, with dimensions 0.35 m long, 0.35 m wide, and 0.4 m deep. The thickness of the Plexiglas was 0.03 m and the tank was covered on all sides except the top surface by one half inch of insulation. This insulation reduces wall heat loss from the sides of the tank, thus ensuring that the dominant heat losses are due to the evaporative and convective

losses from the water to the ambient air. The water tank was open from the top (free water surface) to the ambient air. The bottom of the tank was made of aluminum plate with a thickness of 0.02 m in order to have a uniform temperature distribution. The aluminum plate was sealed to Plexiglas from the sides using RTV silicone which is applicable for high temperatures. The electronic instrumentation consisted of a humidity sensor and temperature thermocouple probes (K-type). A humidity sensor was used to record relative humidity, which was placed at a sufficient distance from the water tank so as to not affect the air flow above the water surface. A total of four thermocouple probes were used to detect the water bulk temperature, water surface temperature, ambient temperature, and aluminum plate temperature. The bulk water temperature was represented by the thermocouple probe that was fixed in the middle of the tank depth, assuming that the water was well mixed by natural convection. The aluminum plate temperature was fixed at a desirable temperature for the current study by using a controlling switch that connected to the data acquisition in order to control the temperature. A heater was placed under the aluminum plate, which could heat up the plate and hence the water inside the tank. Moreover, a mass balance was used to measure the evaporation rate from the tank. Another small water tank was placed on the mass balance, which was connected to the test water tank with small tubing. The small tank was covered on top to ensure there was no evaporation that might affect the scale reading. The experimental setup is schematically shown in Figure 4.1. A photograph of the experimental setup before and after insulation is also provided in Figure 4.2. Finally, all of the electronic instrumentation was connected automatically to the data acquisition (SCXI-1000 National Instruments) and LabVIEW equipment to record the data every second, as shown in Appendix B.

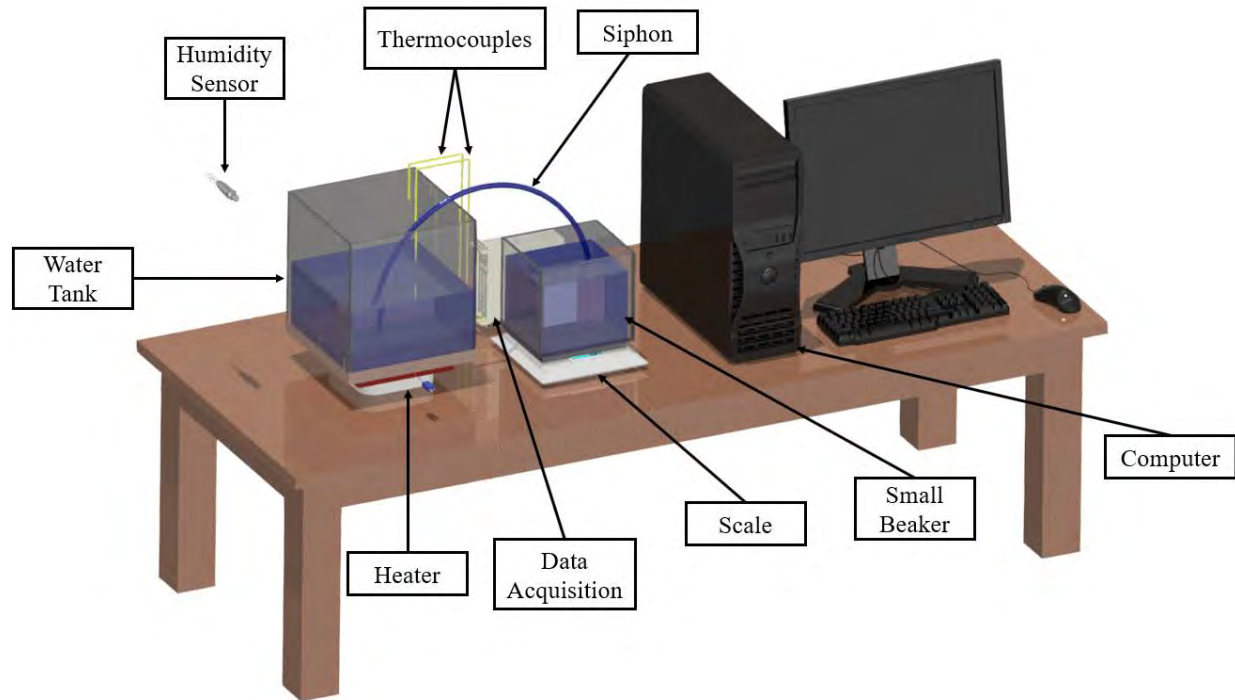
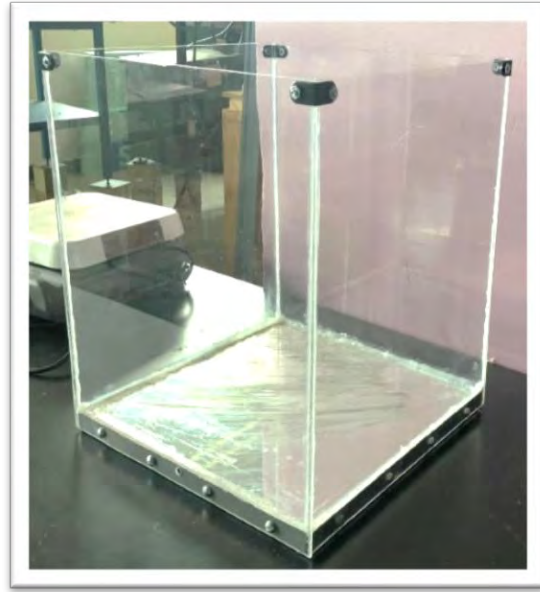


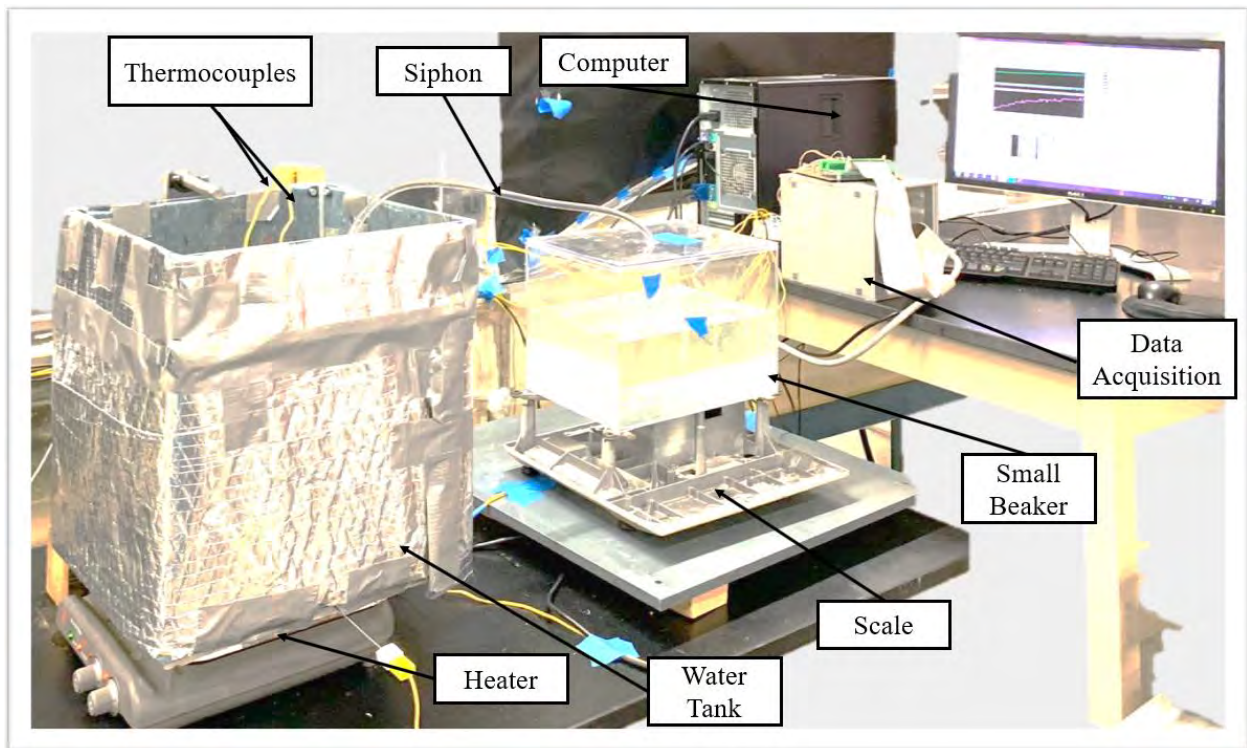
Figure 4.1: Schematic of experimental setup.

4.1.2 Experimental Procedure

The water for the experiment in this part was taken directly from a tap, where its temperature was the same as the room temperature at the beginning of the experiment. The tank along with the small water tank were filled with water, which allowed them to equilibrate. Next, the thermocouple probes and the humidity sensor were placed so as to record the temperature and relative humidity in the course of the experiment. Once the experiment setup was completed the data collection commenced. The experiment ran until the water reached the desirable temperature for the current study, which was 50°C. Note that the bottom of the water tank, which is the aluminum plate, was maintained at a temperature of 50°C. Then, the small tank of water was placed on the electronic balance which was connected with a flexible siphon tube (4 mm in diameter and 100 cm in length) to the tank in order to measure the evaporation mass loss. Therefore, once water from the tank evaporated, water flowed from the small tank to the main tank so as to keep the water in



(a)



(b)

Figure 4.2: (a) Photograph of water tank before insulation, (b) Photograph of experimental setup after insulation.

both tanks at the same level. Hence, the mass measured by the electronic balance decreased, as the measurements were taken. During the course of the experiment the air temperature, bulk water temperature, surface water temperature, relative humidity, and the mass balance were recorded at the rate of one data value every one second. Thus, the recorded data were exported as a sheet file for analysis and processing in MATLAB. The range of Rayleigh number in the current work was from 1.4×10^9 to 1.1×10^{11} , which was calculated using Eq. (1.18) as shown in Figure 4.3. The physical properties of the working fluid (water) are taken at the mean temperature, $T_m = (T_h + T_c)/2$ (36.25°C), as listed in Table 4.1.

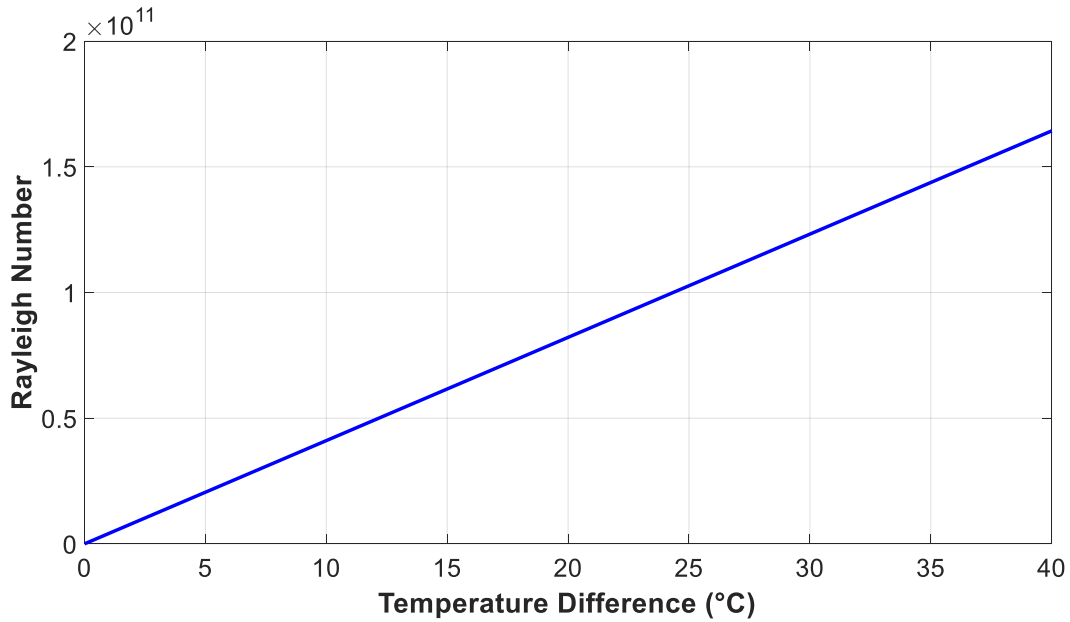


Figure 4.3: The range of Rayleigh number in the current work versus temperature difference (°C).

Table 4.1: Physical properties of the working fluid (water) at the mean temperature (36.25°C).

Gravity	9.81
Thermal Expansion Coefficient	3.23×10^{-3}
Density	9.93×10^2
kinematic viscosity	6.88×10^{-7}
Thermal Diffusivity	1.55×10^{-7}
Specific Heat	4.06×10^3
Conductivity	0.627
Dynamic Viscosity	6.83×10^{-4}
Prandtl Number	4.428

4.1.3 Results and Discussion

The results obtained from the first part of the experimental work are presented and discussed here. The experimental investigation for this part was built to carry out a prediction of a Sherwood–Rayleigh correlation to calculate the evaporation rate from the free water surface in case of natural convection. Two different depths of water were investigated in the current work: 0.17 m and 0.24 m. Note that these two different depths of water were chosen based on the range of the Rayleigh number for the current work.

1) At $D = 0.17$

As mentioned before, the experiment was conducted at two different depths of water. For $D = 0.17$ m, Figure 4.4 shows the time traces of the bulk water temperature, ambient temperature, and the water surface temperature. As expected, the ambient temperature was maintained constant during the experiment. The bulk water temperature trace increased with time, and the total time

taken to reach the desired temperature was 8068 seconds. The surface water temperature followed the same trend as for the bulk water temperature, being about 0.8°C below. The relative humidity was recorded simultaneously, as shown in Figure 4.5. The relative humidity varied very little during the experiment, the maximum variation being typically 0.5%. Moreover, the recorded evaporation mass and the evaporation rate versus time are as shown in Figure 4.6. The evaporation mass was plotted as a result of mass change from the balance. Hence, the differences between the mass change Δm and the time change Δt were calculated and divided by each other, $\Delta m/\Delta t$, in order to calculate the evaporation rate. The mass flux from the tank was then calculated by dividing the evaporation rate by the surface area of the water air interface, as plotted in Figure 4.7.

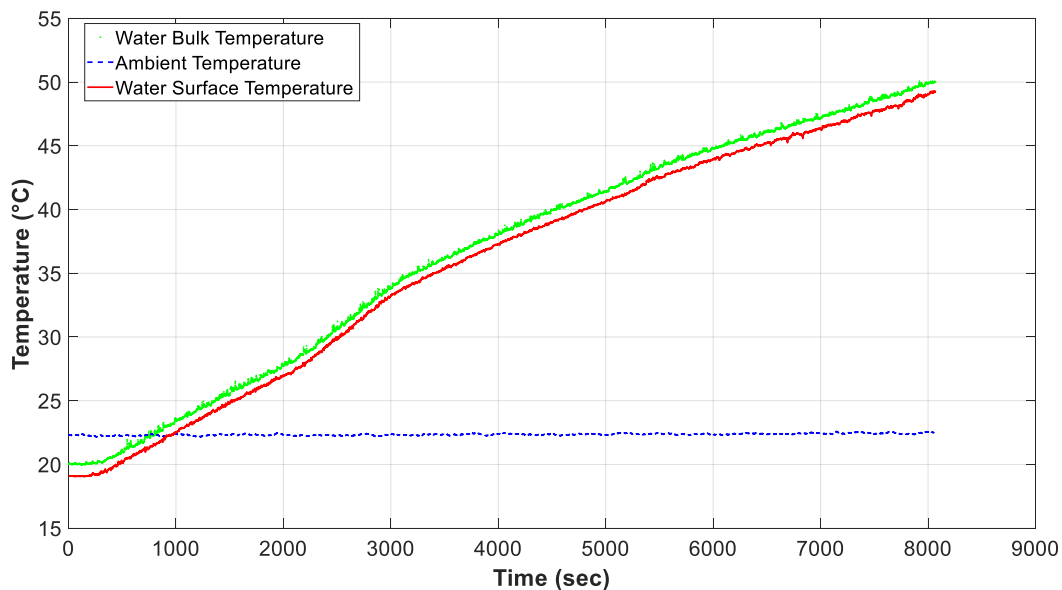


Figure 4.4: The time traces of the water bulk temperature, ambient temperature, and the water surface temperature for $D = 0.17$ m.

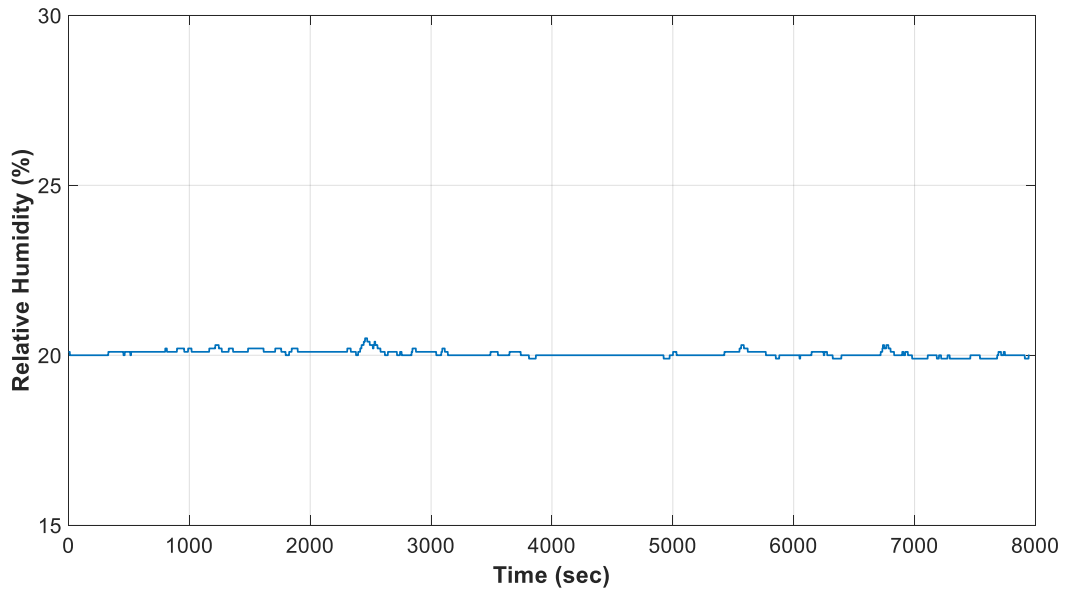


Figure 4.5: The time traces of the relative humidity for $D = 0.17$ m.

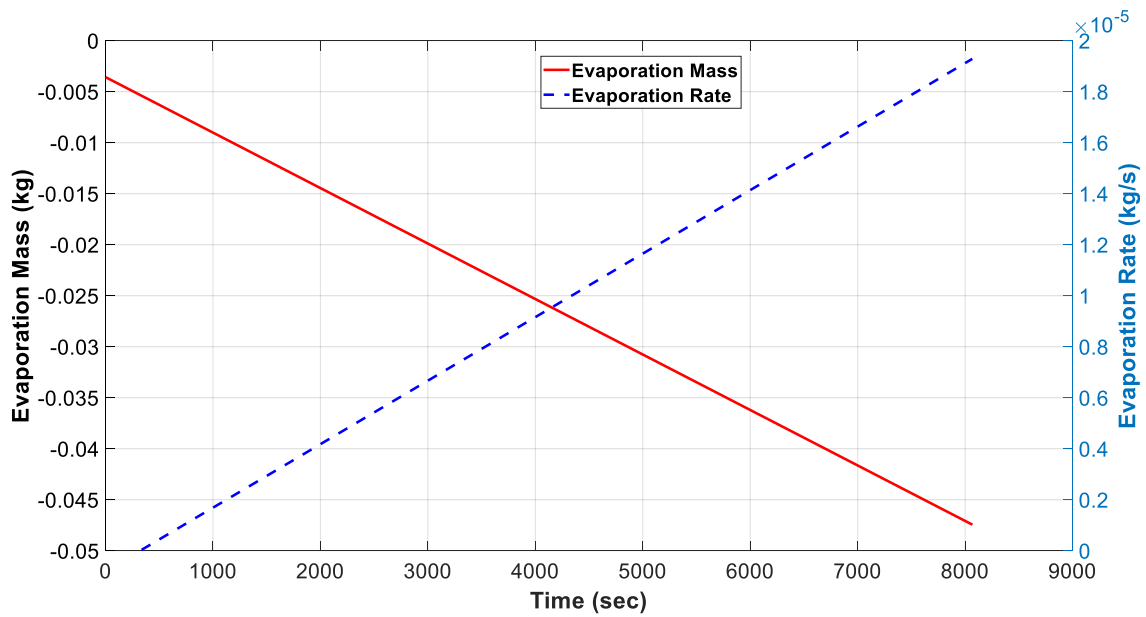


Figure 4.6: Evaporation mass and evaporation rate versus time for $D = 0.17$ m.

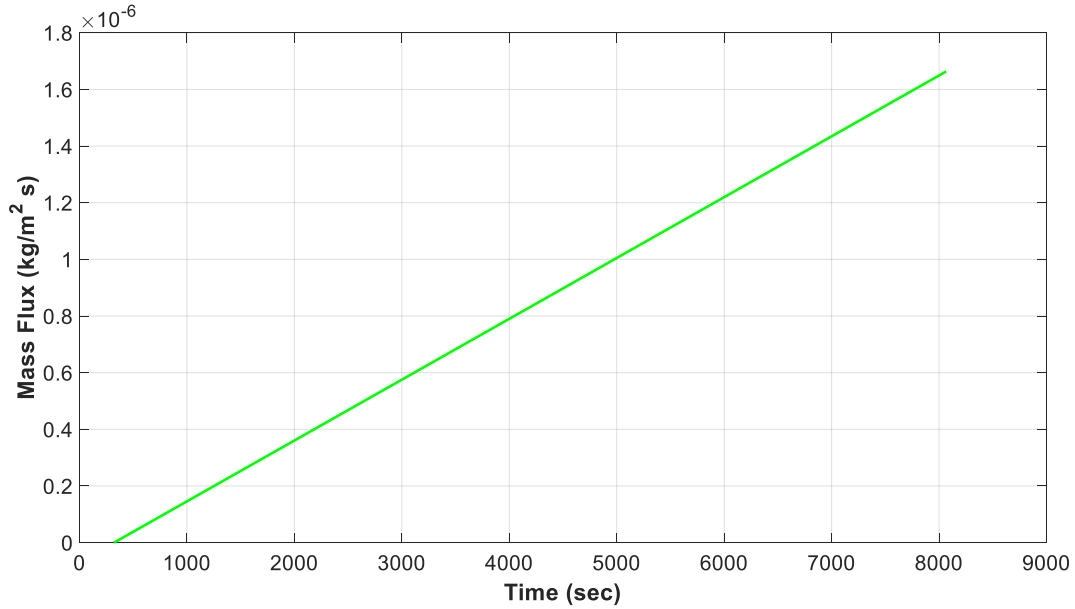


Figure 4.7: The mass flux versus time for $D = 0.17$ m.

Next, the mass transfer coefficient was calculated as defined in Eq. (1.7), whereas the mass flux has been calculated in the plot 4.7, and the difference of water vapor density was calculated by using Eq. (1.8). The mass transfer coefficient versus time is shown in Figure 4.8. In addition, the vapor pressure deficit (VPD) is given by

$$VPD = p_w - (RH) \times p_a \quad (4.1)$$

where (RH) is the measured relative humidity. The saturated pressure for either measured surface temperature or measured ambient temperature can be given by following empirical correlation [43]

$$p = \frac{e^{77.3450 + 0.0057 T - \frac{7235}{T}}}{T^{8.2}} \quad (4.2)$$

where T can be both the measured water surface temperature and the measured ambient temperature. Hence, the vapor pressure deficit is calculated and plotted along with temperature difference (surface and ambient), as in Figure 4.9.

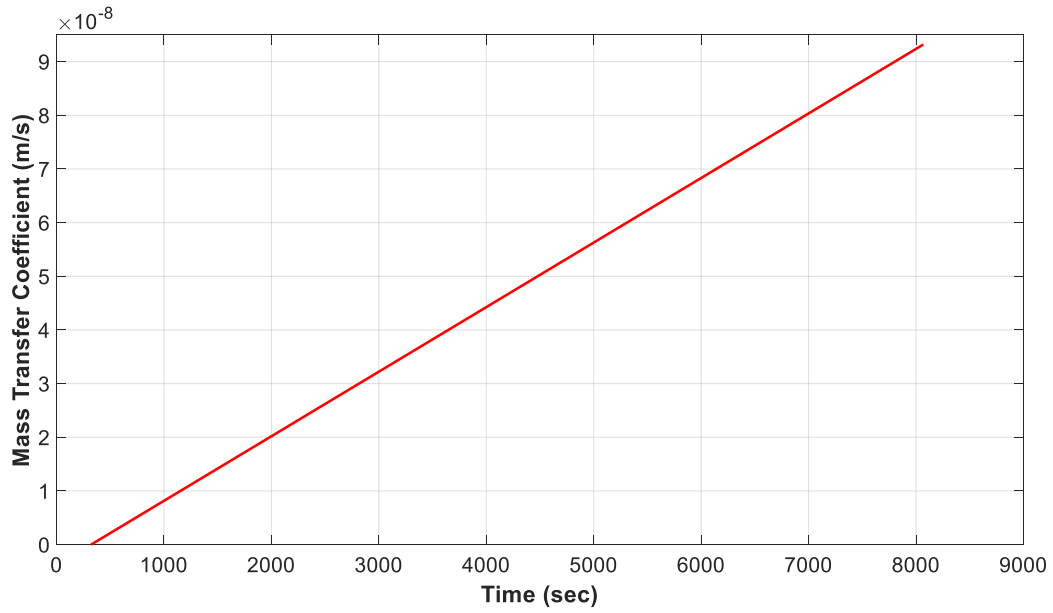


Figure 4.8: The mass transfer coefficient versus time for $D = 0.17$ m.

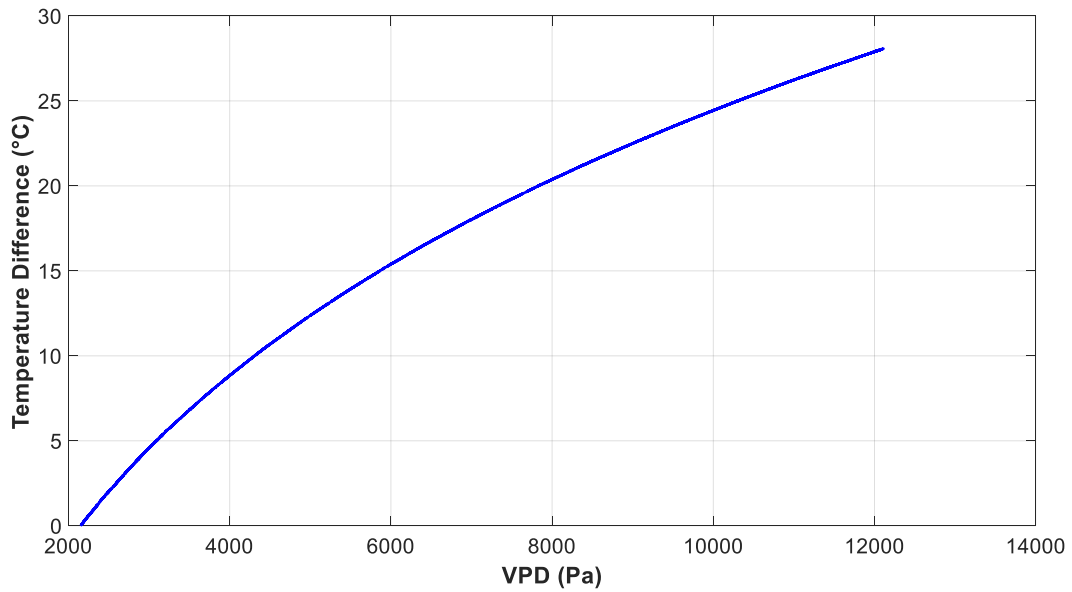


Figure 4.9: The vapor pressure deficit (VPD) versus temperature difference for $D = 0.17$ m.

2) At $D = 0.24$ m

The experiment was then repeated at a water depth of $D = 0.24$ m. The time traces of the bulk water temperature, ambient temperature, and the water surface temperature are shown in Figure 4.10. The ambient temperature remained constant during the experiment, as expected. The bulk water temperature kept increasing to reach the desired temperature, with a total time of 13192 seconds. The relative humidity was recorded as shown in Figure 4.11, where it increased about 2% in the course of this experiment. The recorded evaporation mass and the evaporation rate versus time are shown in Figure 4.12. The evaporation mass was plotted as a result of mass change from the balance. Hence, the differences between the mass change Δm and the time change Δt were calculated and divided by each other, $\Delta m/\Delta t$, in order to calculate the evaporation rate. The mass flux from the tank was then calculated by dividing the evaporation rate by the surface area of the water air interface, as plotted in Figure 4.13.

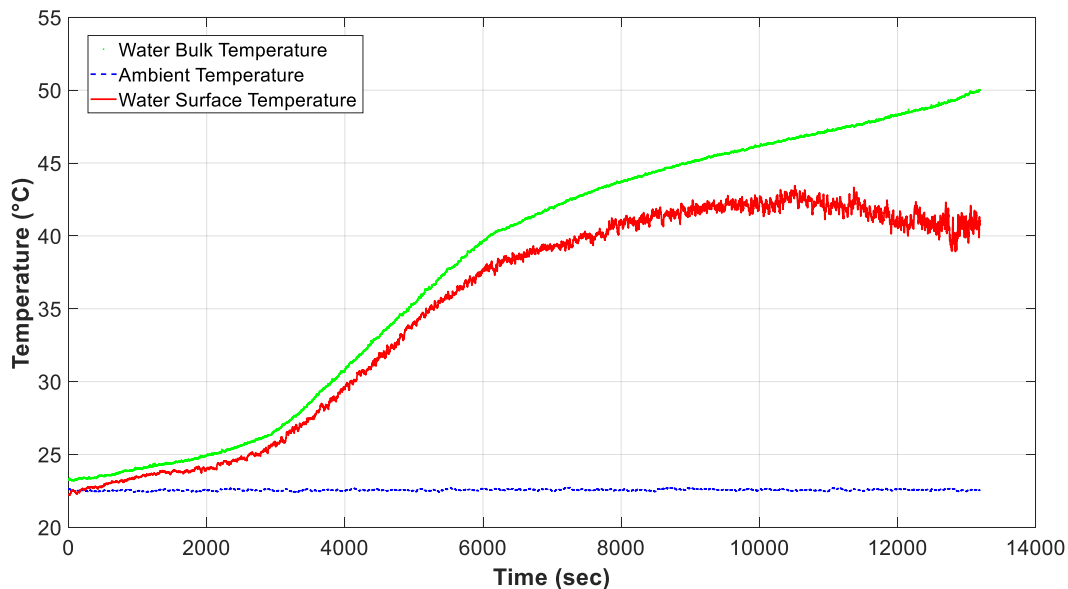


Figure 4.10: The time traces of the water bulk temperature, ambient temperature, and the water surface temperature for $D = 0.24$ m.

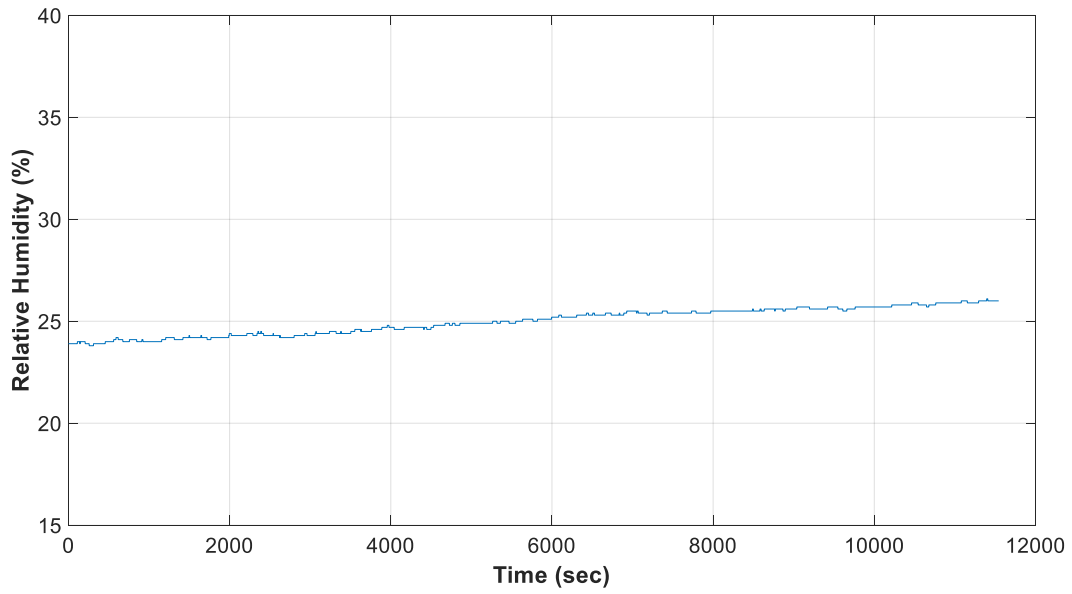


Figure 4.11: The time traces of the relative humidity for $D = 0.24$ m.

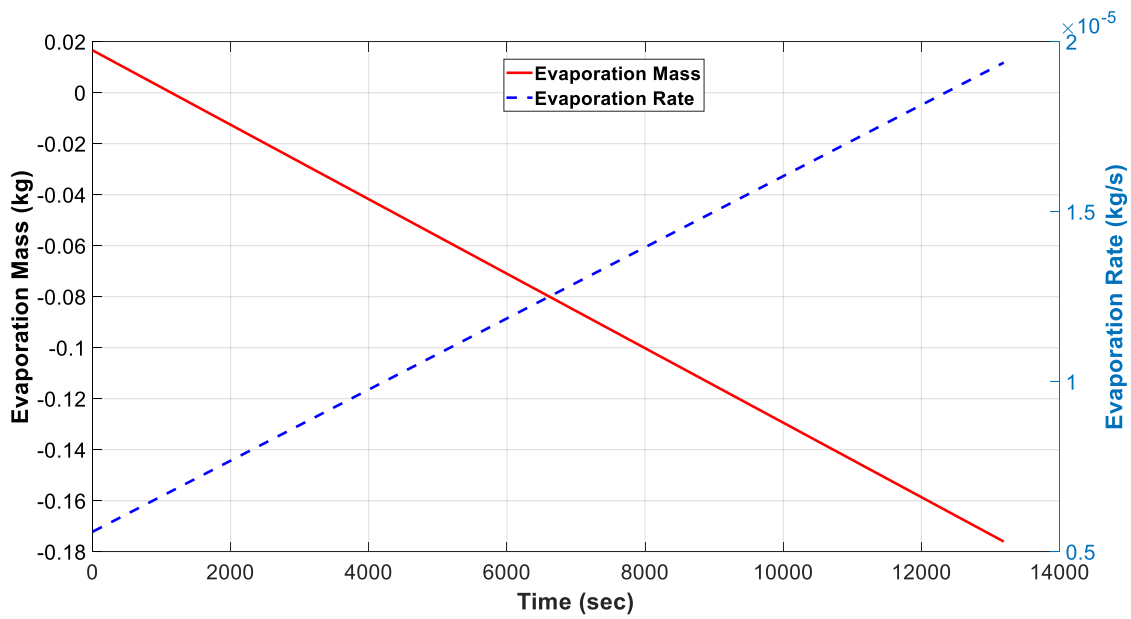


Figure 4.12: Evaporation mass and evaporation rate versus time for $D = 0.24$ m.

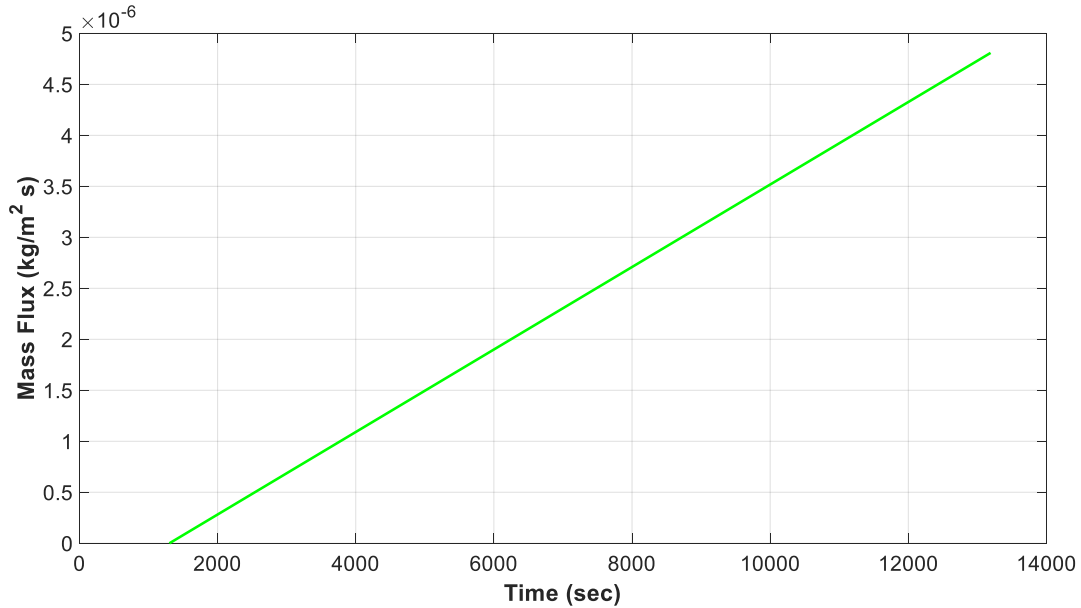


Figure 4.13: The mass flux versus time for $D = 0.24$ m.

Then, the mass transfer coefficient was calculated using (Eq. 1.7), where the mass flux has been calculated in the plot 4.14, and the difference of water vapor density was calculated by using (Eq. 1.8). Figure 4.14 presents the mass transfer coefficient versus time. Moreover, the vapor pressure deficit (VPD) was calculated using Eq. (4.1) and Eq. (4.2), as in Figure 4.15.

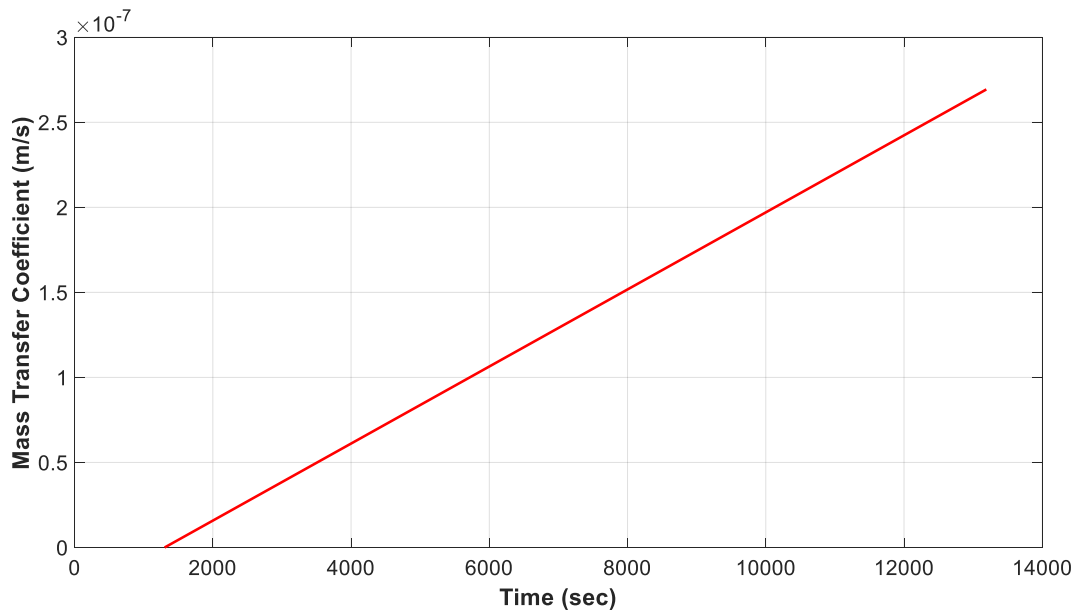


Figure 4.14: The mass transfer coefficient versus time for $D = 0.24$ m.

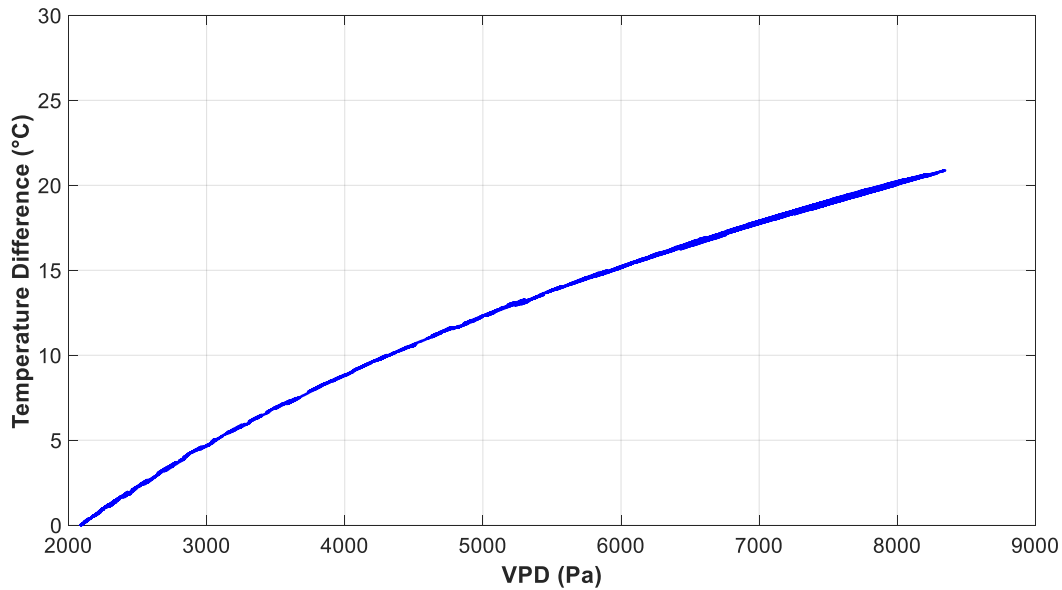


Figure 4.15: The vapor pressure deficit (VPD) versus temperature difference for $D = 0.24$ m.

3) Comparison of $D = 0.17$ m and $D = 0.24$ m

Two different depths of water were investigated in the current work, as discussed previously. Now, the comparison of water evaporation rate and temperature rise inside the water with time is presented. Figure 4.16 shows the rise in the bulk water temperature at these two different depths. It is clear that the desirable temperature (50°C) was reached faster at $D = 0.17$ m for the current work, than at $D = 0.24$ m. However, the temperatures at both depths followed the same trend of rising with time. The evaporation rate at the two different depths is plotted in Figure 4.17. It is clear that the effect of depth on the evaporation rate is limited. However, the evaporation rate at higher depth ($D = 0.24$ m) is higher at the same temperature (50°C). As is known, the evaporation rate is mainly related to the water–air interface area (water surface area), which is the same in the current work ($0.35\text{m} \times 0.35\text{m}$). However, the difference in evaporation rate at $D = 0.24$ m and $D = 0.17$ m in the current work can be related to two main factors, which are the water depth and the distance from the water surface to the top of the tank. In other words, at $D = 0.24$ m, the water surface is close to the top of the water tank, which allows the air circulation to remove the water vapor faster to the ambient

air. On other hand, at $D = 0.17$ m, the air circulation takes more time to remove water vapor to the ambient air, due to the higher distance from water surface to the top of the tank. The variation of water depth can have a greater effect at a larger scale, resulting in higher difference in evaporation rate.

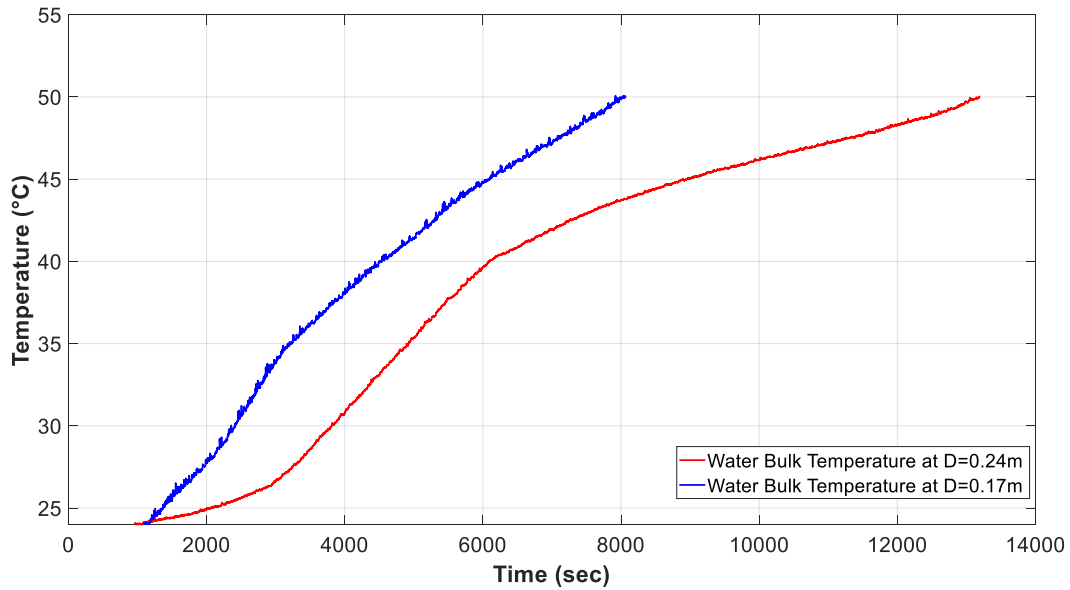


Figure 4.16: The temperature comparison between $D = 0.24$ m and $D = 0.17$ m versus time.

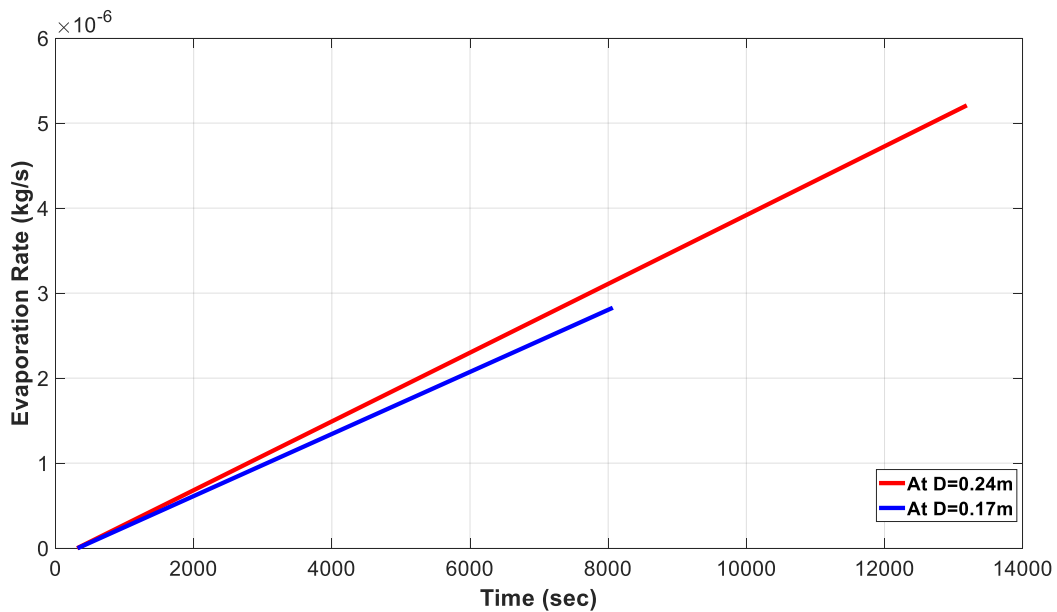


Figure 4.17: The evaporation rate comparison between $D = 0.24$ m and $D = 0.17$ m versus time.

Considering all of the measured parameters discussed previously, the Sherwood number and Rayleigh number were calculated and predicted. The Sherwood number was calculated using Eq. (1.6) along with the measured data. Also, by applying Eq. (1.9) to the measure data, the Rayleigh number was predicted as well. Exporting all the data to Minitab 19 software, a nonlinear regression analysis was conducted to evaluate the empirical correlation between Sherwood number and Rayleigh number in order to predict the evaporation for free water surface in case of natural convection, resulting in the following

$$Sh = 0.589 \times Ra^{0.225} \quad (4.3)$$

The predicted correlation for Sherwood–Rayleigh number is plotted along with the previous correlations, in Figure 4.18. It is clear that the discrepancies between these correlations start to increase along with increasing Rayleigh number. One goal of the current work is to focus and cover the gap of variation in this large Rayleigh number, where the range for this work is defined to be 1.4×10^9 to 1.1×10^{11} . As can be seen in Figure 4.18, the current correlation mostly agrees with the work that has been done by [30]. However, the work done by [30] did not cover the range of Rayleigh number for the current work. Hence, the current correlation can provide more accurate prediction for free water surface evaporation in case of natural convection at a large Rayleigh number.

4.2 Particle Image Velocimetry (PIV) for Water from the Side

4.2.1 Experimental Setup

In this part, the experiment was conducted in order to investigate the flow pattern inside the water from the sides of the tank undergoing evaporation. As mentioned earlier, most of the previous work has studied the flow pattern in case of a closed system where the top and bottom

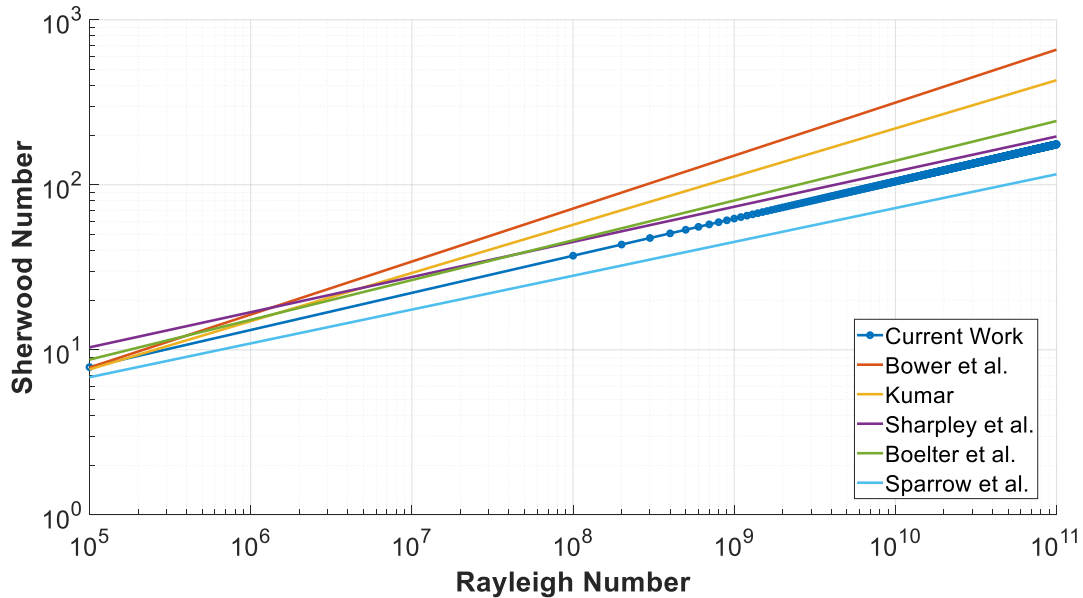


Figure 4.18: The comparison of correlation in the current work with the previous work.

parts are maintained at fixed temperature. However, in the current work the top part is a free surface and undergoing evaporation to ambient air. The same water tank was used along with all the experimental setup as discussed in section 4.1.1, including temperature thermocouple probes and heater. No small beaker was needed for this experiment. A laser and camera were added to the setup in order to apply the PIV technique. The laser is a big sky double pulsed Nd: YAG (Neodymium-Doped Yttrium Aluminum Garnet) laser with a wavelength of 532 nm and 200 mJ/Pulse with a maximum repetition rate of 15 Hz per laser head. The laser was also equipped with a cylindrical lens to convert the laser beam into a laser sheet, where the sheet thickness was about 2 mm. Moreover, A CCD camera (Imager Pro X 2m) was used, which had a resolution of 1600 x 1200 pixels with a bit depth of 14 bit, and the pixel size was 7.4 μ m. The camera had a double exposure feature with an interframe time down to 100 ns and the frame rate was 30 fps at full resolution. The camera was equipped with an adapter to connect it with a NIKON AF NIKKOR zoom lens (50 mm 1:1.8 D) in order to capture the light that scattered from the laser lightened particles.

Hollow glass spheres (HGS-10) with a mean particle diameter of $10\ \mu\text{m}$ and density of $1.1\ \text{g}/\text{cm}^3$ produced by DANTIC DYNIMICS were seeded in the water as tracer particles. Hollow glass spheres are popular as water seeding particles and are known to be the best particles for water flow [44] [45]. The laser and camera were controlled by software from LaVision (DaVis 8.4). The experimental setup is shown schematically in Figure 4.19. A photograph of experimental setup is also shown in Figure 4.20.

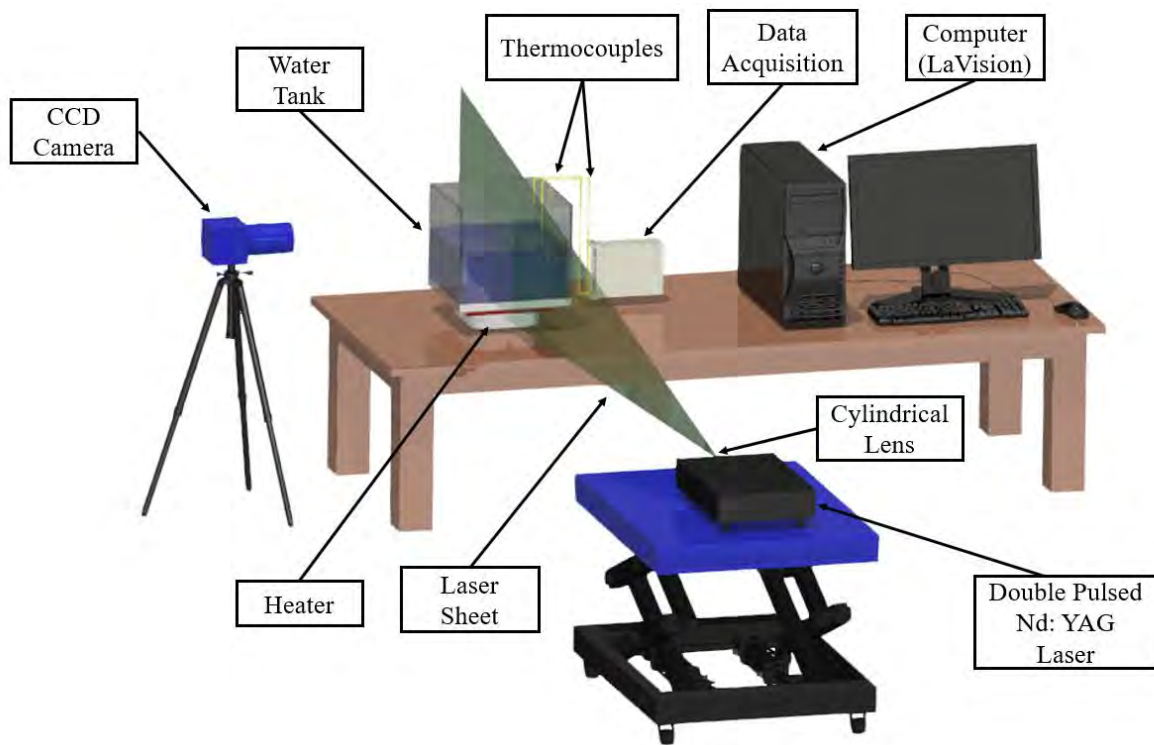


Figure 4.19: Schematic of experimental setup.

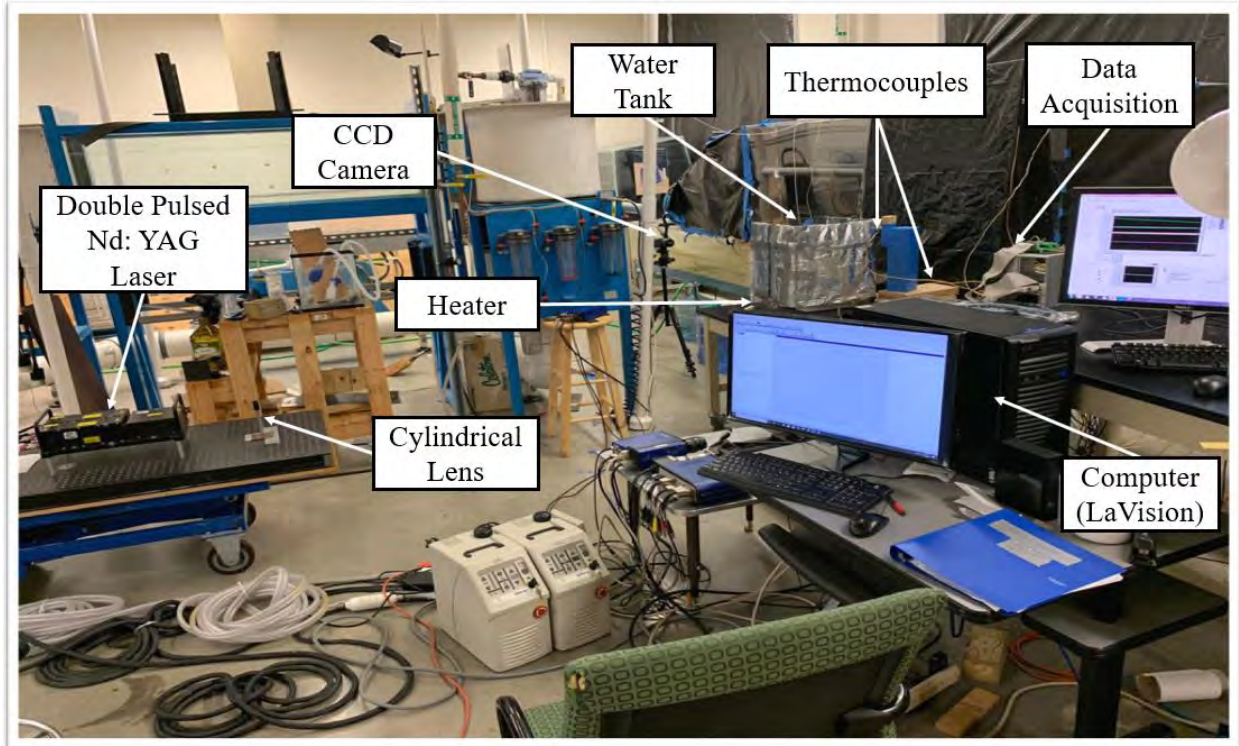


Figure 4.20: Photograph of experimental setup.

4.2.2 Experimental Procedure

Distilled (purified) water was used in this experiment, seeking an accurate flow pattern for the seeding particles. The water temperature was the same as the room temperature, at the beginning of the experiment. Next, the thermocouple probes were placed to record the temperature in the course of the experiment. Once the experiment setup was completed, the data collection and recording commenced. The experiment ran until the water reached the desirable temperature for the current study, which was 50°C. The CCD camera was mounted on one side of the water tank about 1.6 m away in order to have a good view. Also, the camera was set to be perpendicular to the laser sheet. Using the calibration plate (Type 11) along with the calibration algorithm in Davis (8.4), the CCD camera was calibrated perpendicularly to the laser sheet. However, the insulation was removed from the tank side closest to the CCD camera to ensure visibility for the camera and there was a

small slot on the side facing the laser sheet. Moreover, the background of the tank side facing the CCD camera was covered with black paper in order to reduce the illumination. A control unit (synchronizer) was used to provide external triggers for the CCD camera and the pulsed laser sources. In addition, the synchronizer was used to control the delay, Δt (separation time), between the two pulsed laser beams. The firing of pulsed laser beams along with CCD camera exposure was controlled by Davis 8.4 from LaVision. Therefore, the separation time Δt was calculated automatically by Davis 8.4 based on the particle shift.

After setting up the experiment and taking the images, the images' analysis consisted of three steps: pre-processing, image correlation (vector calculation), and post-processing. All three steps were done using DaVis 8.4 developed by LaVision [46]. However, the PIV images can be improved, such as the visibility of seeding particles, image background, and laser reflections, by applying an appropriate pre-processing algorithm. Hence, the PIV images can be ready with a better quality for the correlation. In the current work, the initial interrogation window size was (24 x 24) and the final interrogation window size was (12 x 12). The overlapping was 50% for both initial and final interrogation. Finally, a smooth (Gaussian) 3 x 3 filter was used for the post-processing step. Note that all the processing and statistical calculations (for velocity, vorticity, and turbulent kinetic energy) were done using Davis 8.4 from LaVision. The resulting data were exported and plotted in MATLAB for averaging of 500 images. Two frames of the row of images at t_i and $t_{i+\Delta t}$ before processing are shown in Figure 4.21.

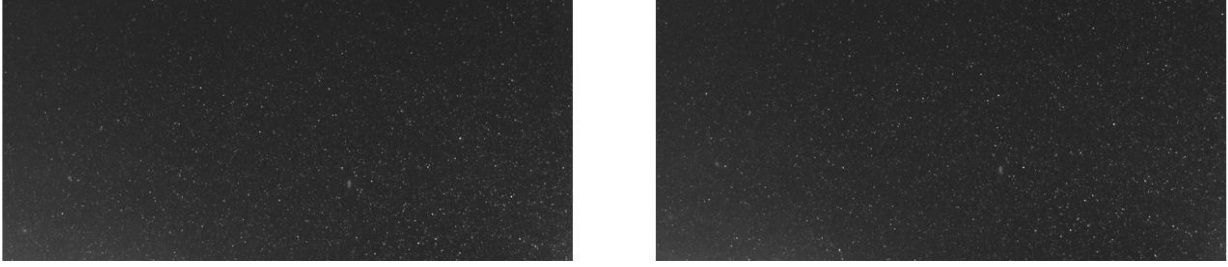


Figure 4.21: Two frames of the row of images at t_i and $t(i+\Delta t)$ before processing.

4.2.3 Results and Discussion

The results obtained from the second part of the experimental work are presented and discussed here. The experimental investigation for this part was built to investigate the flow pattern inside the water from the side of the tank undergoing evaporation. Two different depths of water along with rise in temperature were investigated in the current work, at 0.17 m and 0.24 m.

1) At $D = 0.17$ m

1.1) At $T_b = 28^\circ\text{C}$

(a) Velocity

Figure 4.22 shows the velocity at $T_b = 28^\circ\text{C}$. It is clear from Figure 4.22 (a) that the density difference and thermally induced buoyancy forces initiate natural convection of the water. Hence, the water rises near the left wall to the top of the tank. Once the hot water reaches the water–air interface, it becomes denser and its velocity increases. Therefore, the water flows downward near the right wall with a higher velocity. It was noticed that at this temperature one rotating vortex started to develop. Interestingly, this rotating vortex is near the water–air interface, which can be related to the mass and heat transfer from free water surface to the surroundings. On the other hand, it has been well established in the literature that this vortex develops at the middle of the fluid in case the bottom (hot wall) and top (cold wall) temperatures are fixed, which is not the case

in the current work. Figure 4.22 (b) shows the vertical velocity at different X locations. The velocity is higher near the left and right walls, where the velocity rises upward and downward. At the middle of the tank, the velocity drops due to the rotating vortex and then rises up at the water–air interface. This is clear in Figure 4.22 (c) at different Y locations.

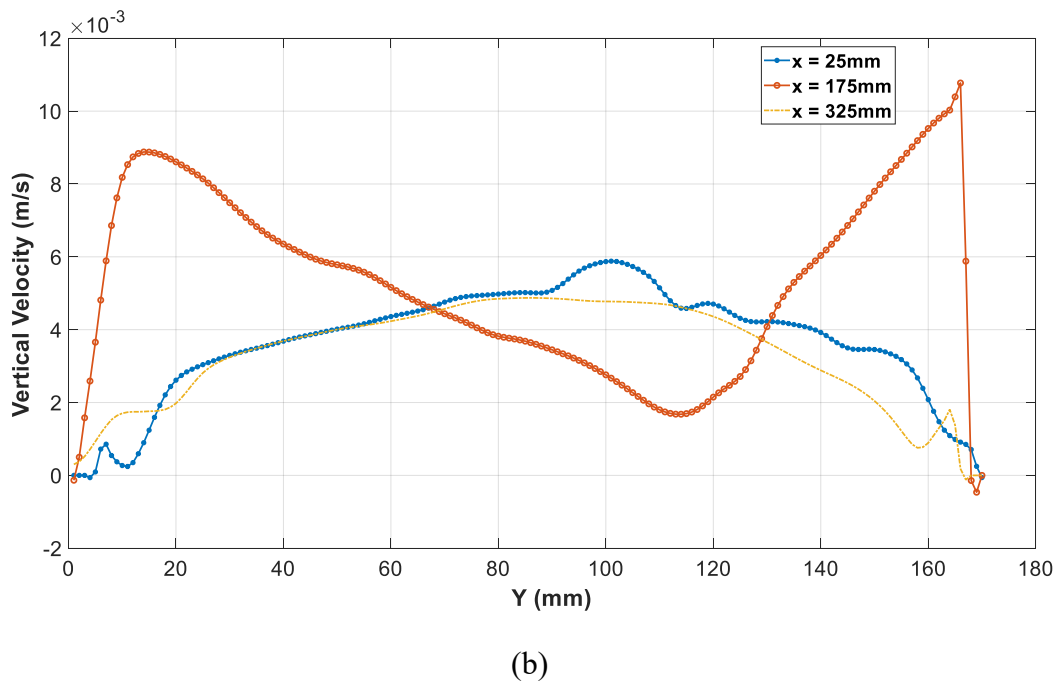
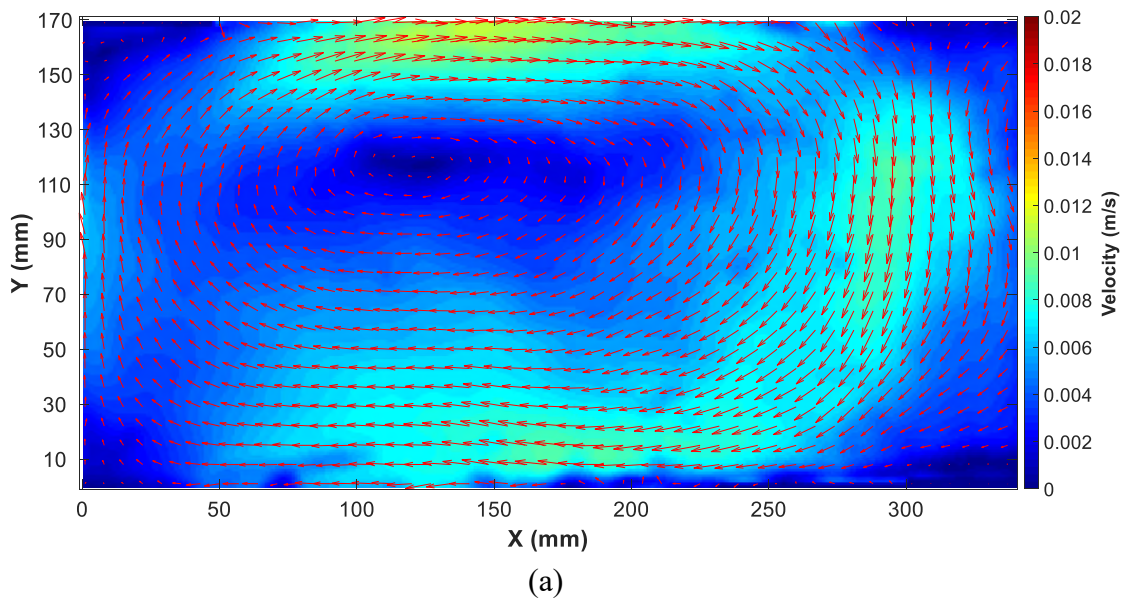
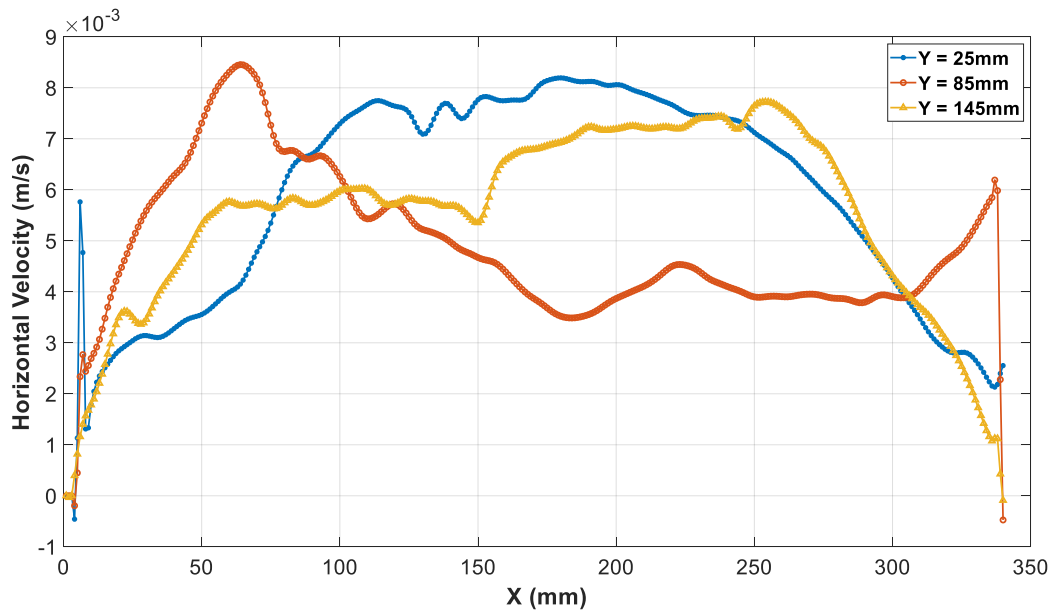


Figure 4.22: (a) Velocity magnitude, (b) XY plot for vertical velocity, (c) XY plot for horizontal velocity at $D = 0.17$ m and $T_b = 28^\circ\text{C}$.

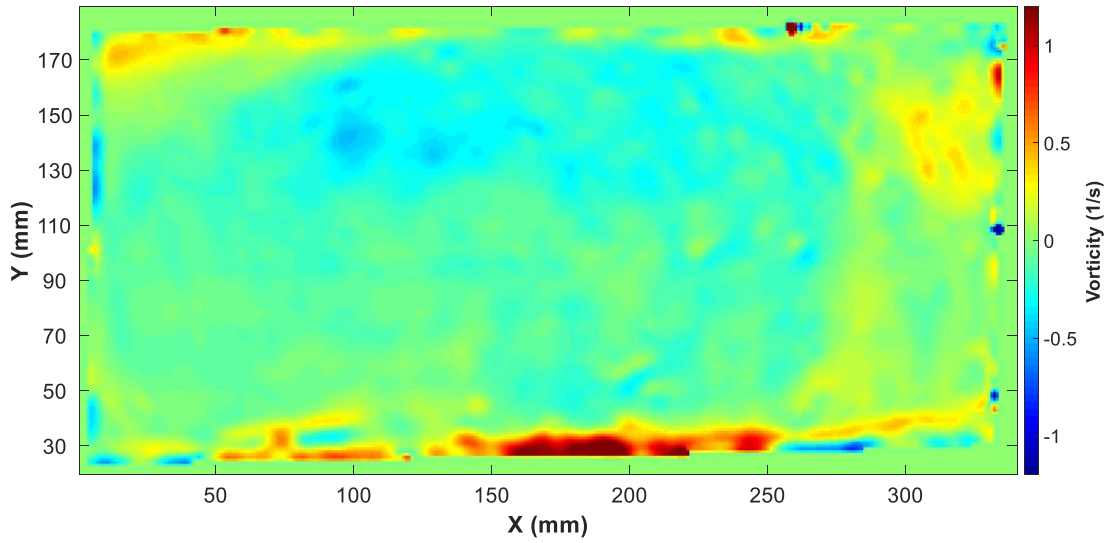
Figure 4.22—continued



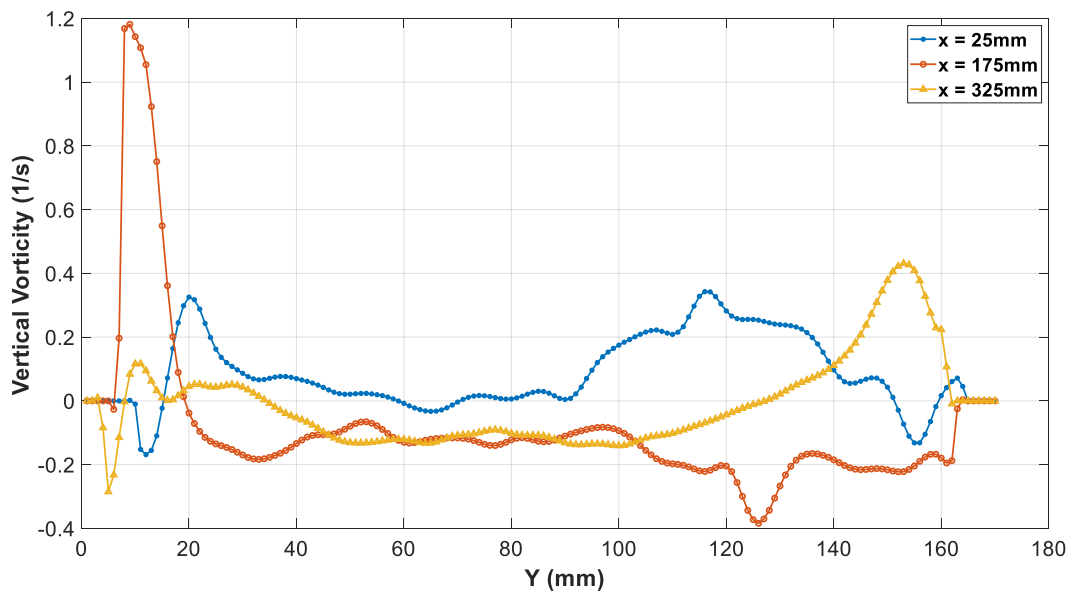
(c)

(b) Vorticity

Vorticity at $T_b = 28^\circ\text{C}$ is shown in Figure 4.23. Figure 4.23 (a) shows vorticity magnitude, where the higher vorticity can be seen at the walls, bottom, and the water–air interface. However, higher vorticity can be seen at the bottom of the tank, where the water starts to heat up and particles begin to rotate. Moreover, the positive vorticity represents the counterclockwise rotational motion of the flow, while the negative vorticity represents the clockwise rotational motion of the flow. Therefore, it is clear that the rotational vortex mentioned in Figure 4.23 (a) has a negative vorticity value. The XY plot for vertical vorticity is presented in Figure 4.23 (b), where the higher values for vorticity appear at the bottom of the tank and the water–air interface. The same trend of behavior is seen in Figure 4.23 (c) for the horizontal vorticity.



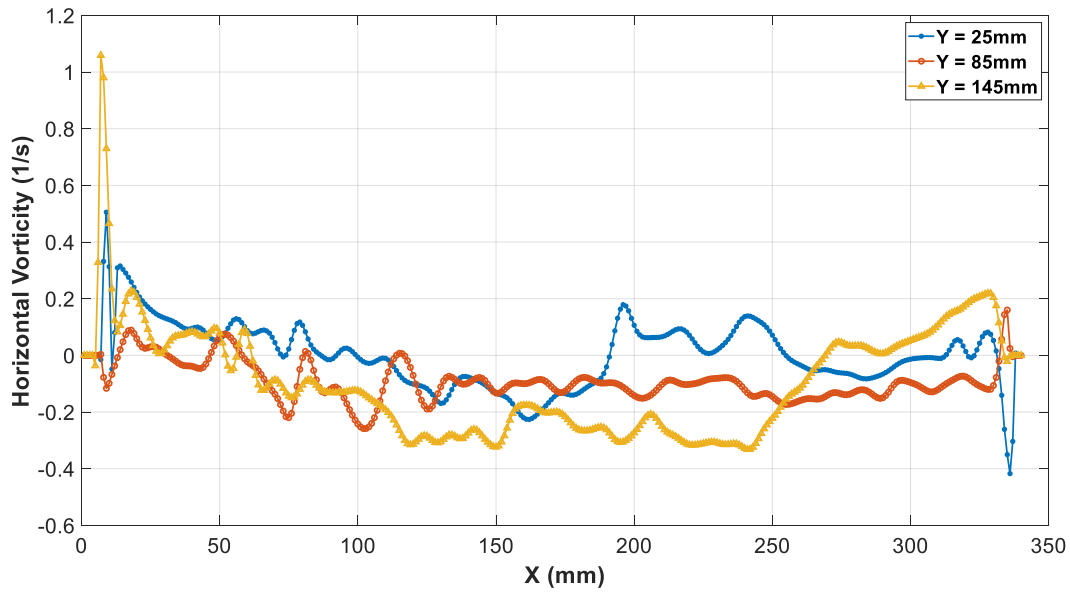
(a)



(b)

Figure 4.23: (a) Vorticity magnitude, (b) XY plot for vertical vorticity, (c) XY plot for horizontal vorticity at $D = 0.17$ m and $T_b = 28^\circ\text{C}$.

Figure 4.23—continued



(c)

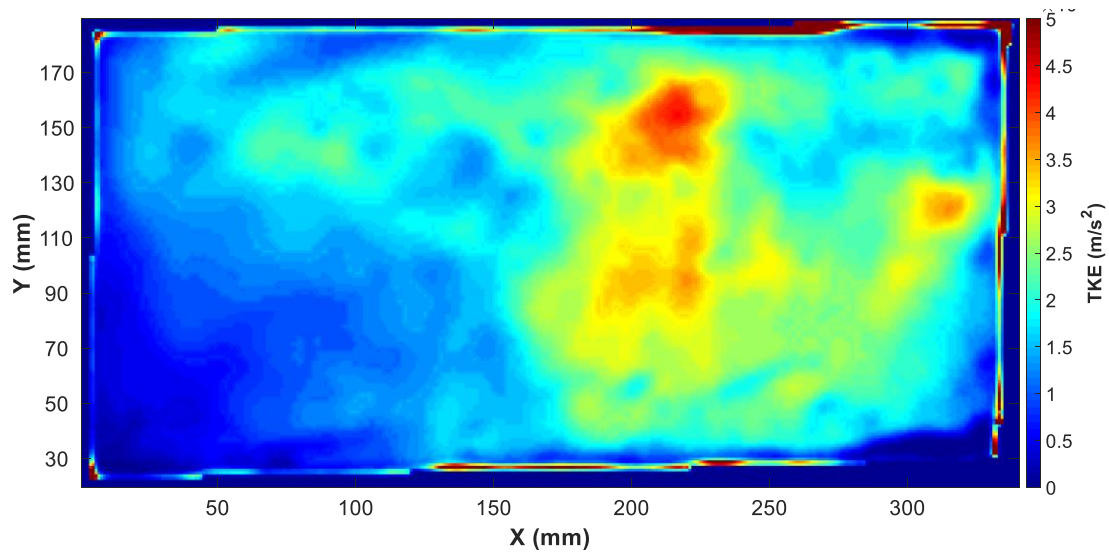
(c) Turbulent Kinetic Energy

The turbulent kinetic energy is shown in Figure 4.24, in order to understand the energy transfers between the mean flow and turbulence. Figure 4.24 (a) shows that a higher TKE appears at the water–air interface and the bottom of the tank. Moreover, some higher TKE appears in the middle of the tank due to the effect of the water–air interface. However, Figures 4.24 (b) and (c) present the vertical and horizontal TKE, respectively.

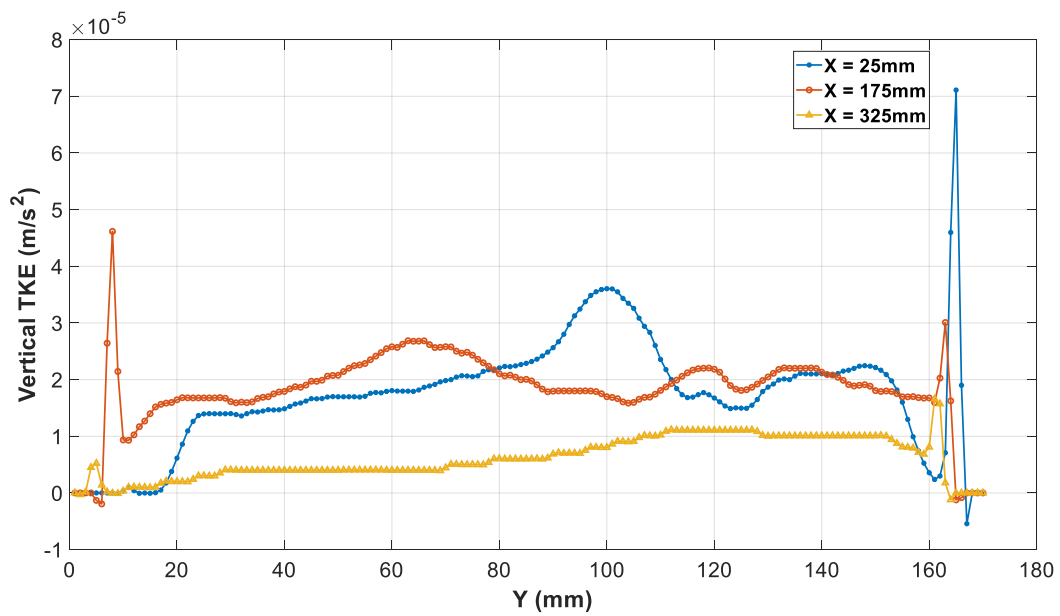
1.2) At $T_b = 38^\circ\text{C}$

(a) Velocity

Figure 4.25 shows the velocity at $T_b = 38^\circ\text{C}$. It is clear that at this time the velocity increases due to the higher temperature of the water, which results in higher difference with the ambient temperature compared to that in Figure 4.22 (a). This can be seen clearly in Figure 4.25 (a), where the velocity at the water–air interface increases and the rotational vortex has moved to the center



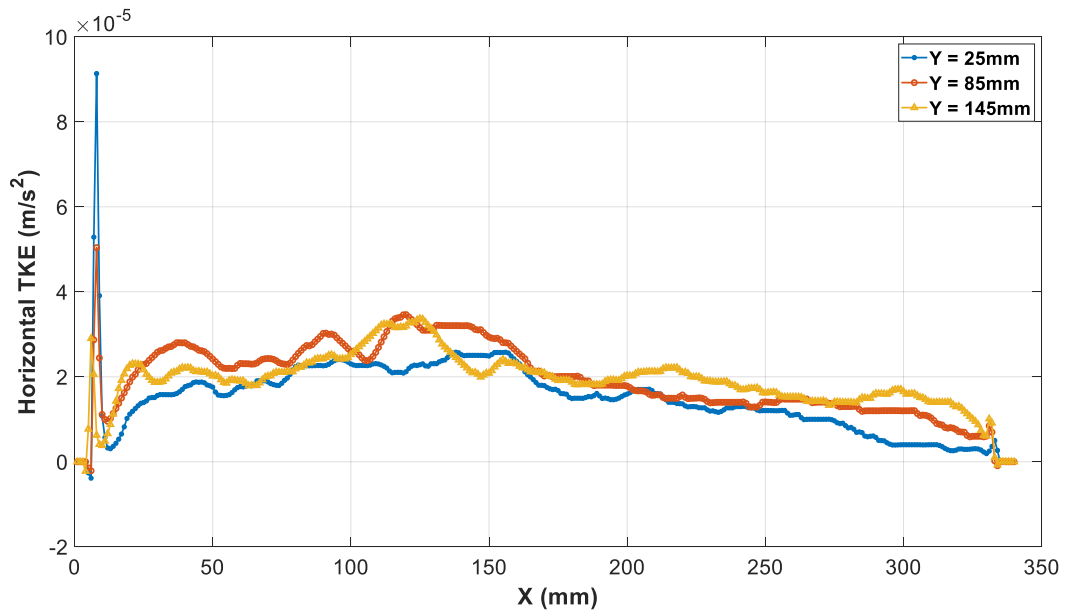
(a)



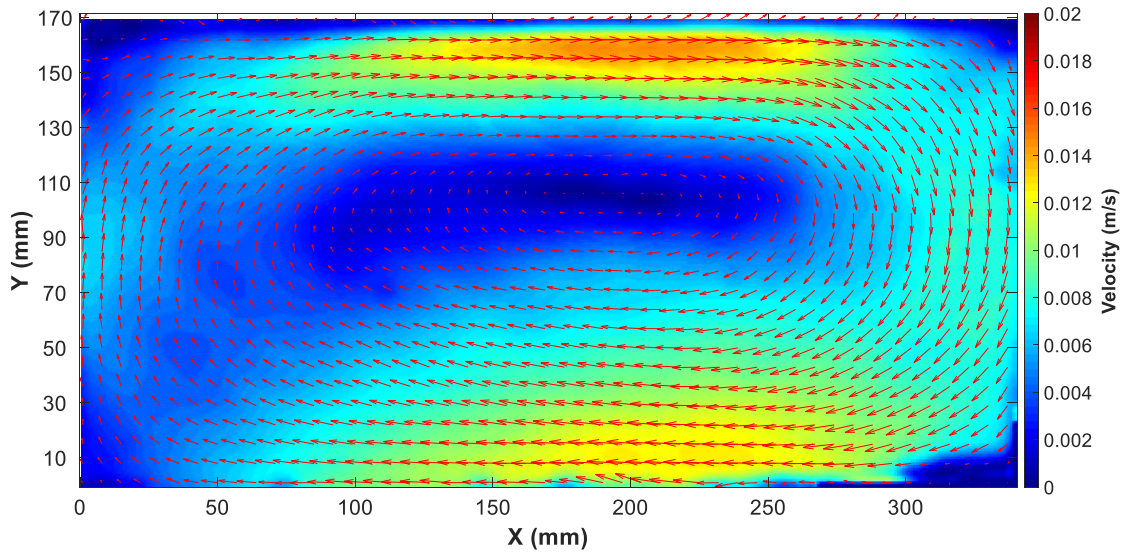
(b)

Figure 4.24: (a) Turbulent kinetic energy magnitude, (b) XY plot for vertical turbulent kinetic energy, (c) XY plot for horizontal turbulent kinetic energy at $D = 0.17$ m and $T_b = 28^\circ\text{C}$.

Figure 4.24—continued



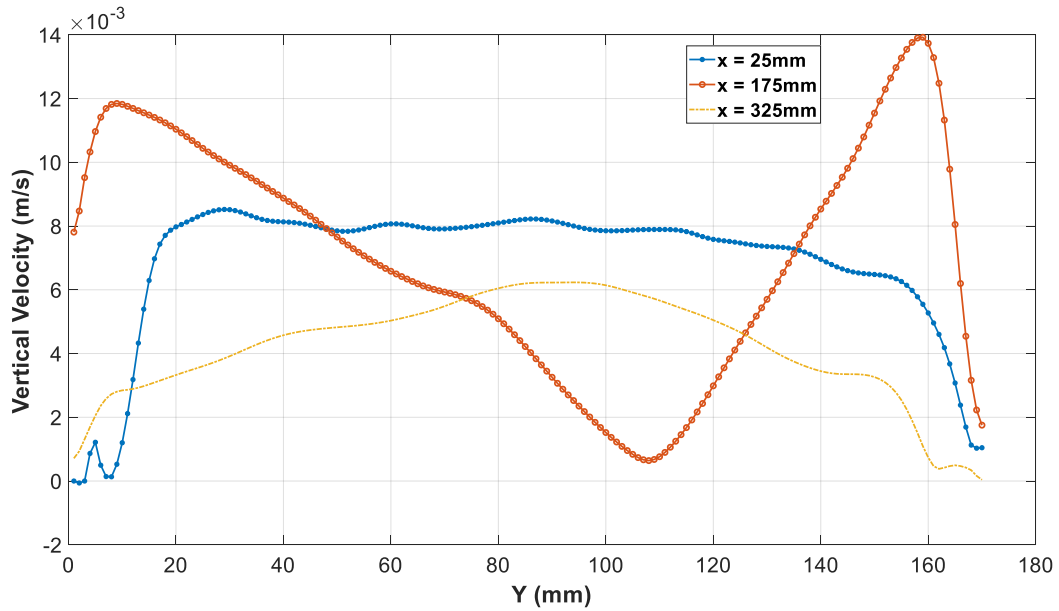
(c)



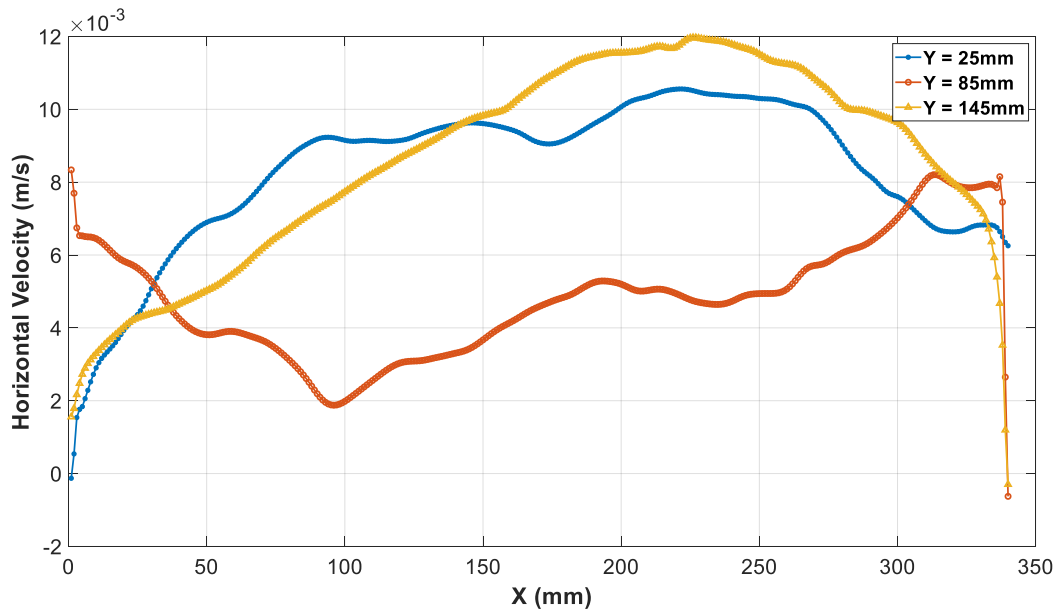
(a)

Figure 4.25: (a) Velocity magnitude, (b) XY plot for vertical velocity, (c) XY plot for horizontal velocity at $D = 0.17$ m and $T_b = 38^\circ\text{C}$.

Figure 4.25—continued



(b)



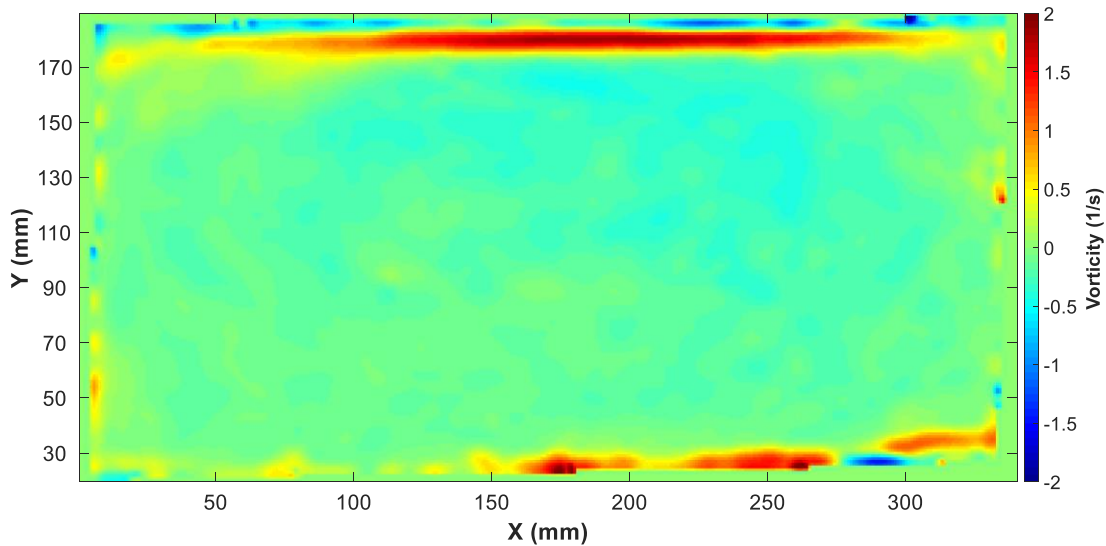
(c)

of the tank but is still close to the interface rather than the bottom of the tank. Moreover, another vortex starts to develop at this time [refer to Figure 4.25 (a)]. Figure 4.25 (b) shows the vertical velocity at different Y locations. At the middle of the tank ($X = 175\text{ mm}$), the velocity almost equals

zero at the rotating vortex and then rises at the water–air interface to reach the maximum value. This is clear in Figure 4.25 (c) at different Y locations.

(b) Vorticity

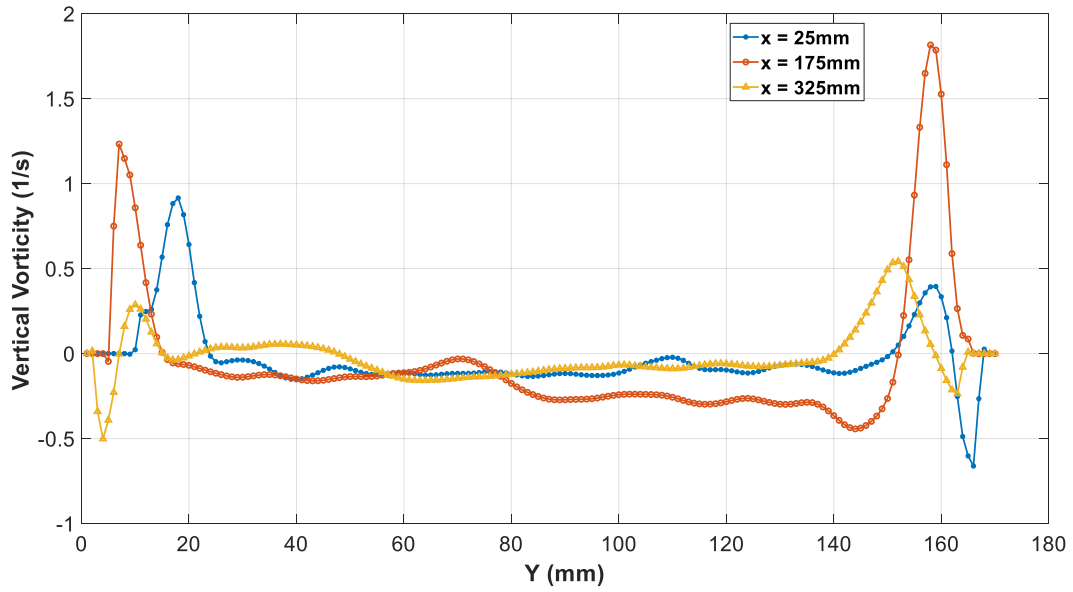
Figure 4.26 shows vorticity at $T_b = 38^\circ\text{C}$. Figure 4.26 (a) shows the vorticity magnitude, where the areas near the walls, bottom, and top of the tank show higher vorticity. It can be seen that negative vorticity appears at the water–air interface at this time, which is due to the mass and heat transfer through evaporation from the free water surface. Moreover, some negative vorticity can be seen in the middle, which has the rotational vortex displayed in Figure 4.25 (a). The XY plot for vertical vorticity is presented in Figure 4.26 (b), where the vorticity has a higher value at this temperature compared to $T_b = 28^\circ\text{C}$. The same trend of behavior is seen in Figure 4.26 (c) for the horizontal vorticity at different Y locations.



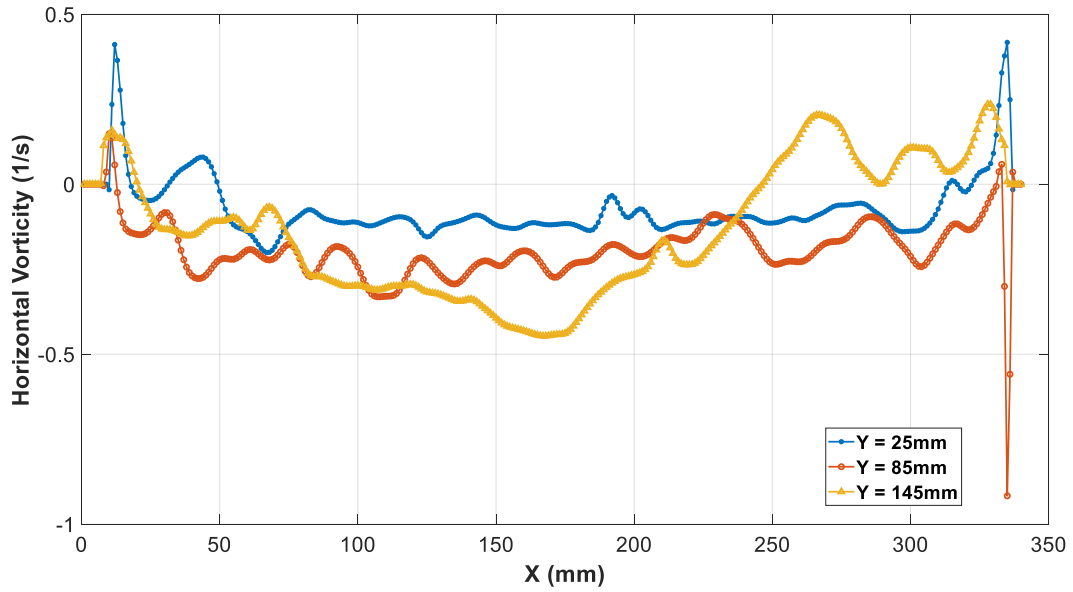
(a)

Figure 4.26: (a) Vorticity magnitude, (b) XY plot for vertical vorticity, (c) XY plot for horizontal vorticity at $D = 0.17$ m and $T_b = 38^\circ\text{C}$.

Figure 4.26—continued



(b)



(c)

(c) Turbulent Kinetic Energy

Figure 4.27 shows the turbulent kinetic energy. Figure 4.27 (a) shows that a higher TKE appears at the water–air interface and at the bottom of the tank. Some higher TKE appears in the middle of the tank due to the effect of the water–air interface. Moreover, a higher TKE appears near the right wall of the tank due to a higher velocity of flow at this region after reaching the water–air interface. Figures 4.27 (b) and (c) present the vertical and horizontal TKE, respectively.

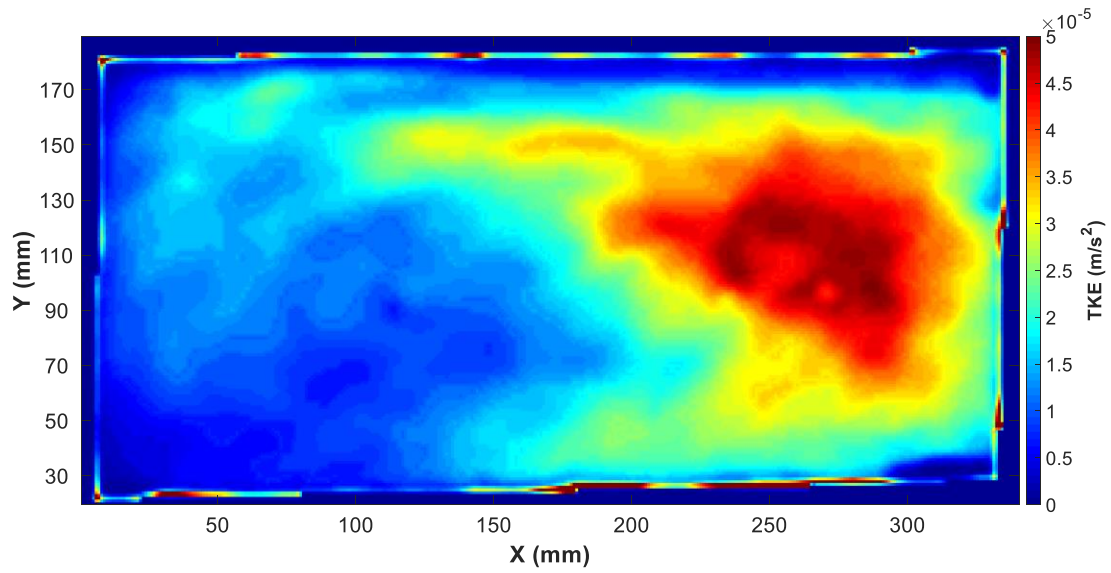
1.3) At $T_b = 46^\circ\text{C}$

(a) Velocity

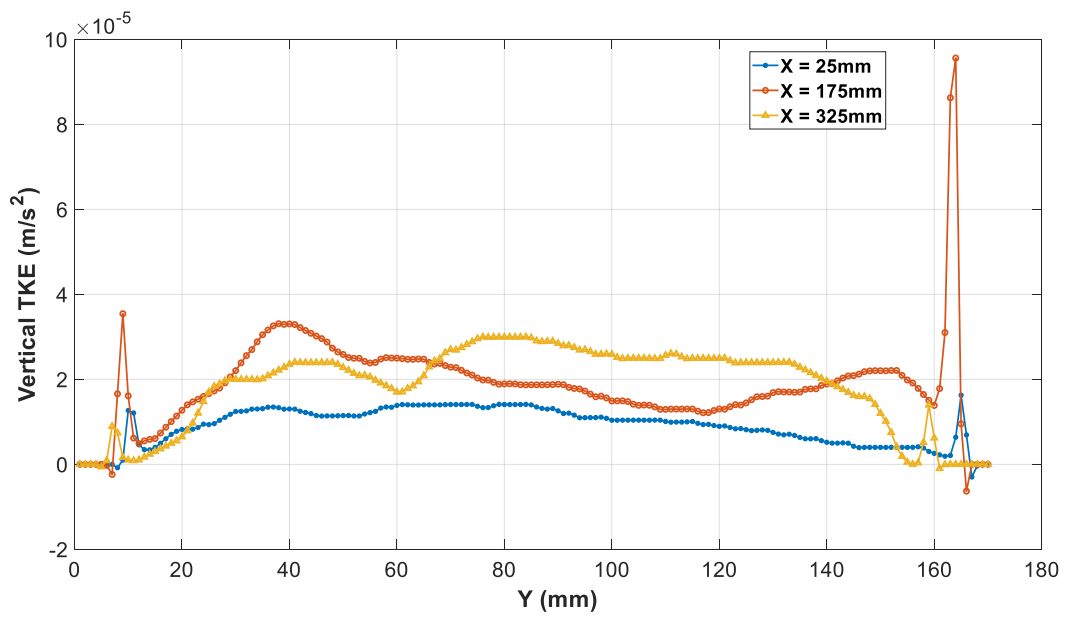
Figure 4.28 shows the velocity at $T_b = 46^\circ\text{C}$. It can be seen that the velocity increases because the water temperature rises, as can be seen clearly in Figure 4.28 (a). However, the two vorticities start to develop clearly at this time [refer to Figure 4.28 (a)]. Figure 4.28 (b) shows the vertical velocity at different Y locations. Here, at the middle of the tank ($X = 175\text{ mm}$), the velocity equals exactly zero at the rotating vortex, which then rises at the water–air interface to reach the maximum value. This is clear in Figure 4.28 (c) at different Y locations.

(b) Vorticity

Figure 4.29 shows vorticity at $T_b = 46^\circ\text{C}$. Figure 4.29 (a) shows the vorticity magnitude, where the regions near the walls, bottom, and top of the tank show higher vorticity. Moreover, some negative vorticity can be seen in the middle of the tank. The XY plot for vertical vorticity is presented in Figure 4.29 (b), where the vorticity has a higher value at this temperature compared to $T_b = 38^\circ\text{C}$. The same trend of behavior is seen in Figure 4.29 (c) for the horizontal vorticity at different Y locations.



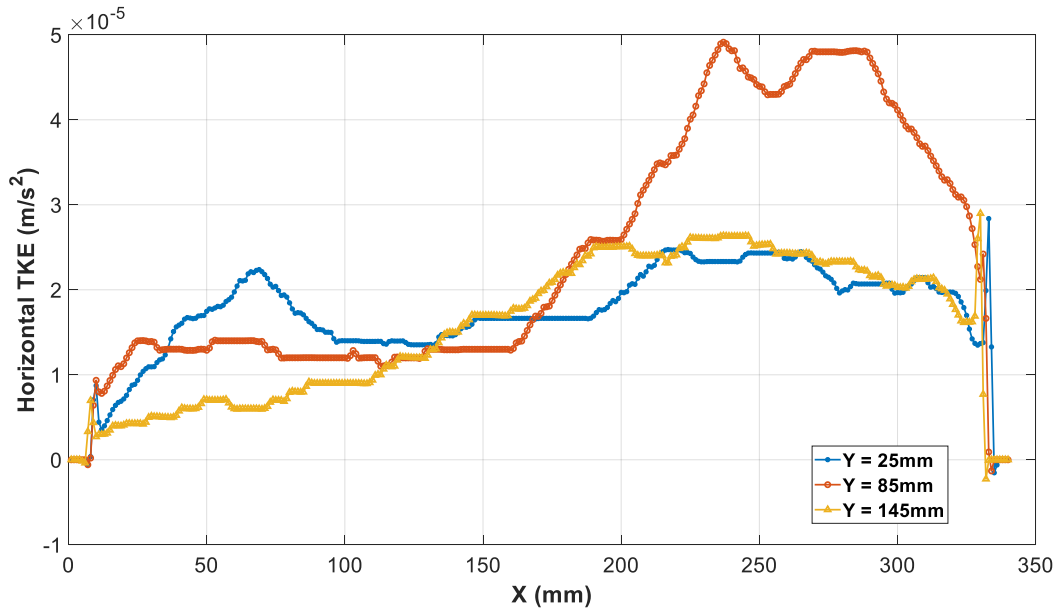
(a)



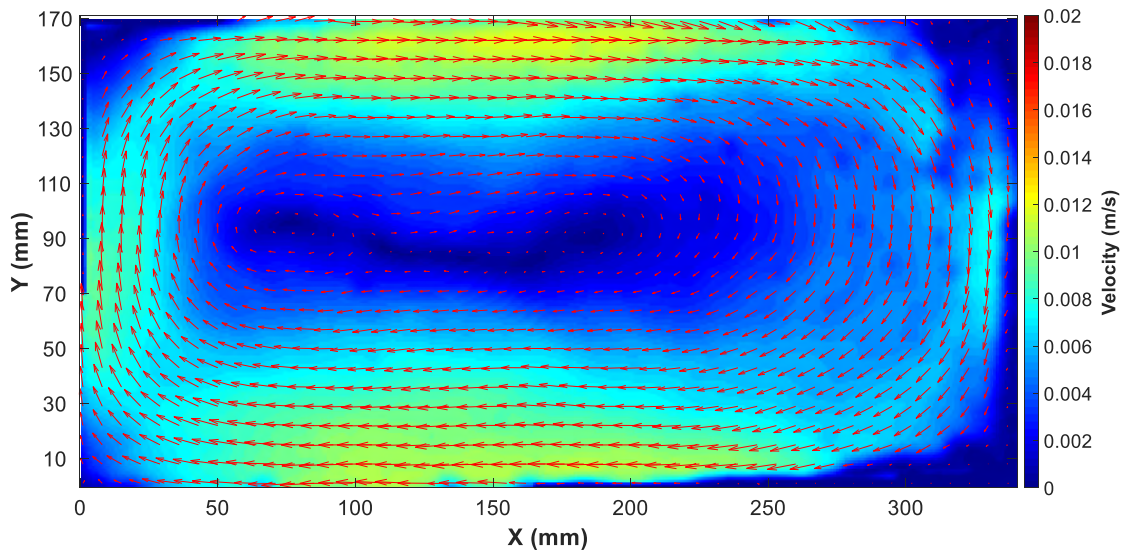
(b)

Figure 4.27: (a) Turbulent kinetic energy magnitude, (b) XY plot for vertical turbulent kinetic energy, (c) XY plot for horizontal turbulent kinetic energy at $D = 0.17$ m and $T_b = 38^\circ\text{C}$.

Figure 4.27—continued



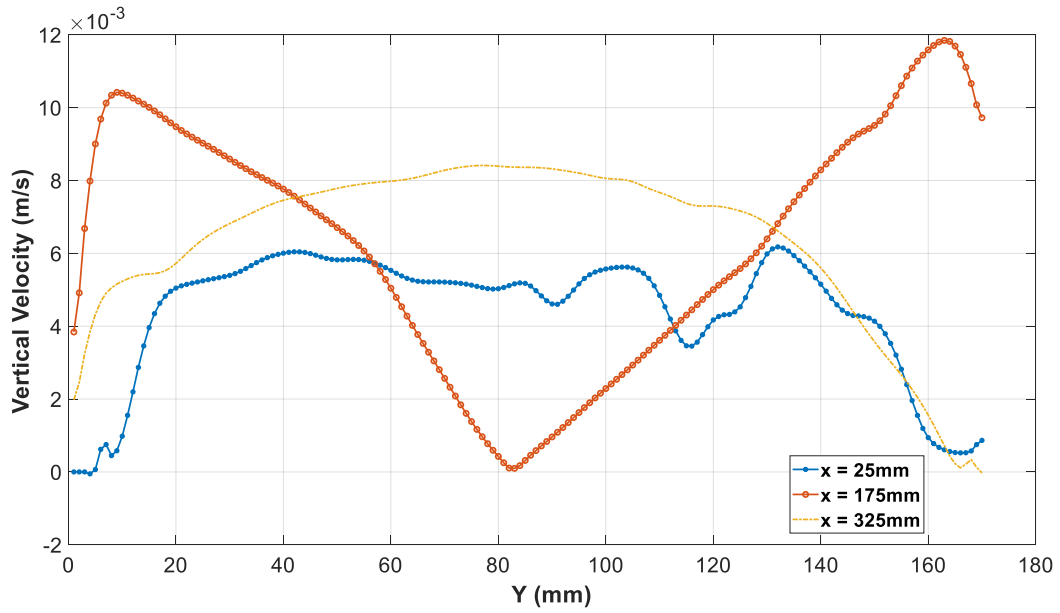
(c)



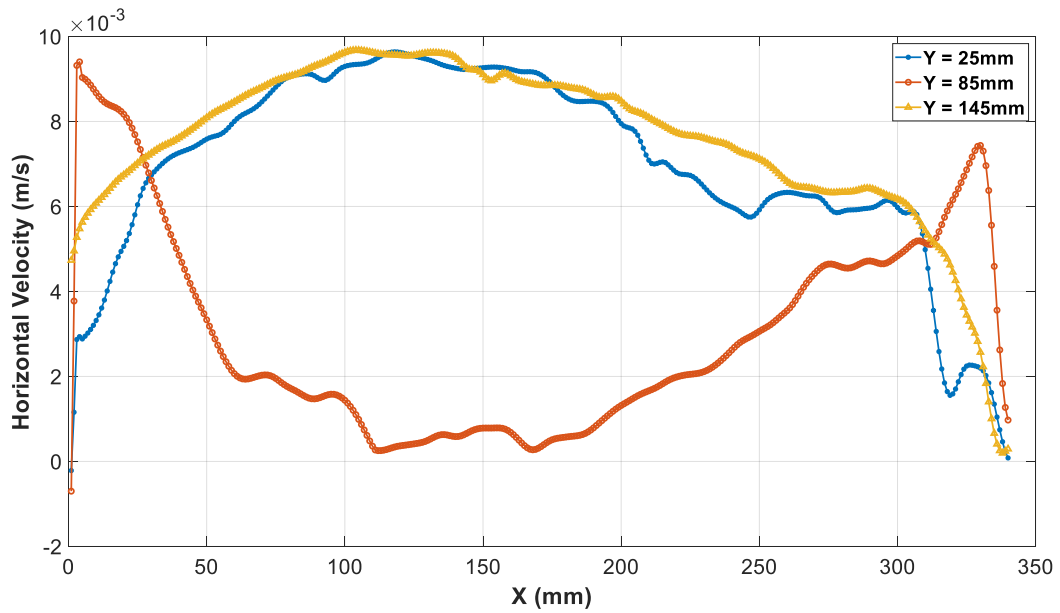
(a)

Figure 4.28: (a) Velocity magnitude, (b) XY plot for vertical velocity, (c) XY plot for horizontal velocity at $D = 0.17$ m and $T_b = 46^\circ\text{C}$.

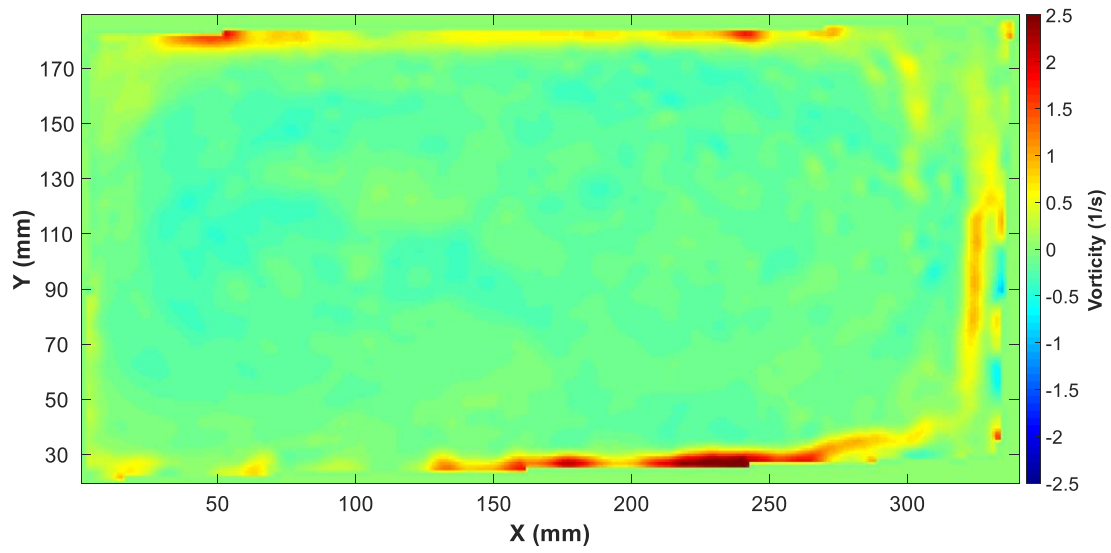
Figure 4.28—continued



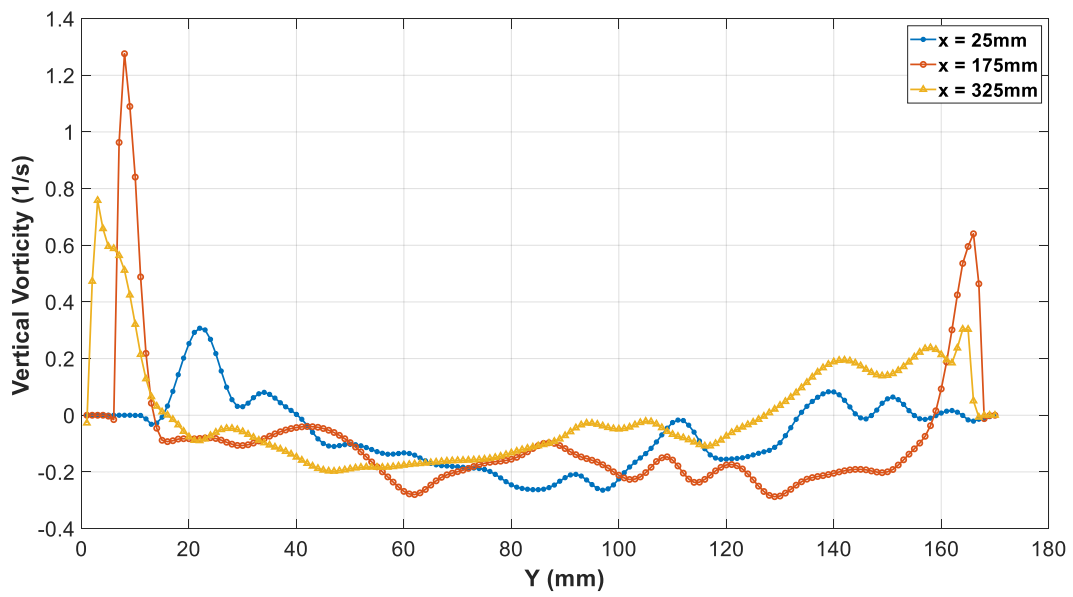
(b)



(c)



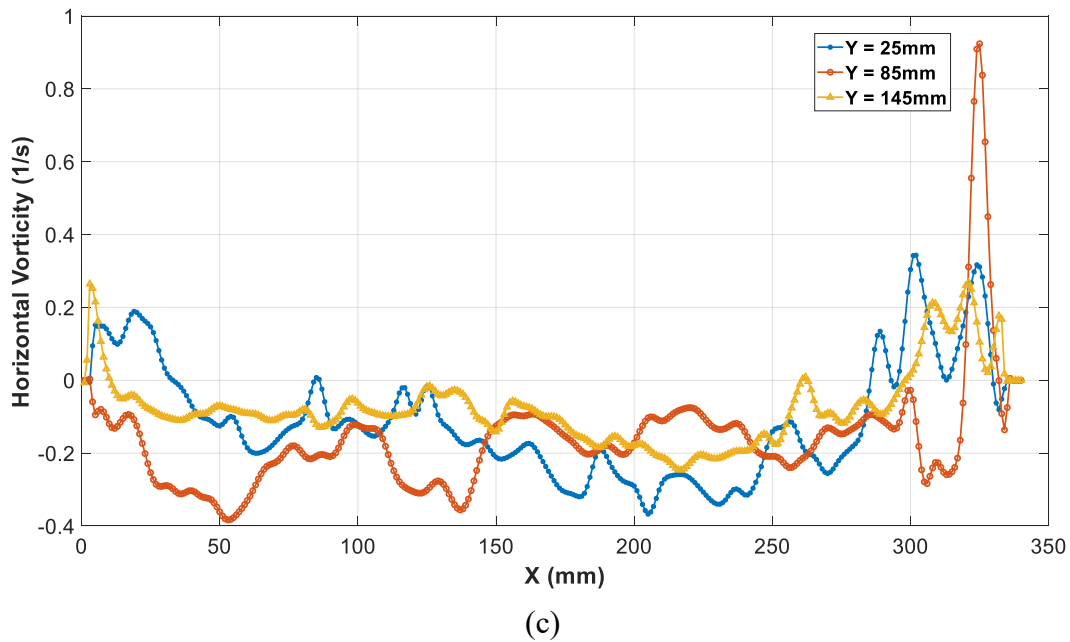
(a)



(b)

Figure 4.29: (a) Vorticity magnitude, (b) XY plot for vertical vorticity, (c) XY plot for horizontal vorticity at $D = 0.17$ m and $T_b = 46^\circ\text{C}$.

Figure 4.29—continued



(c) Turbulent Kinetic Energy

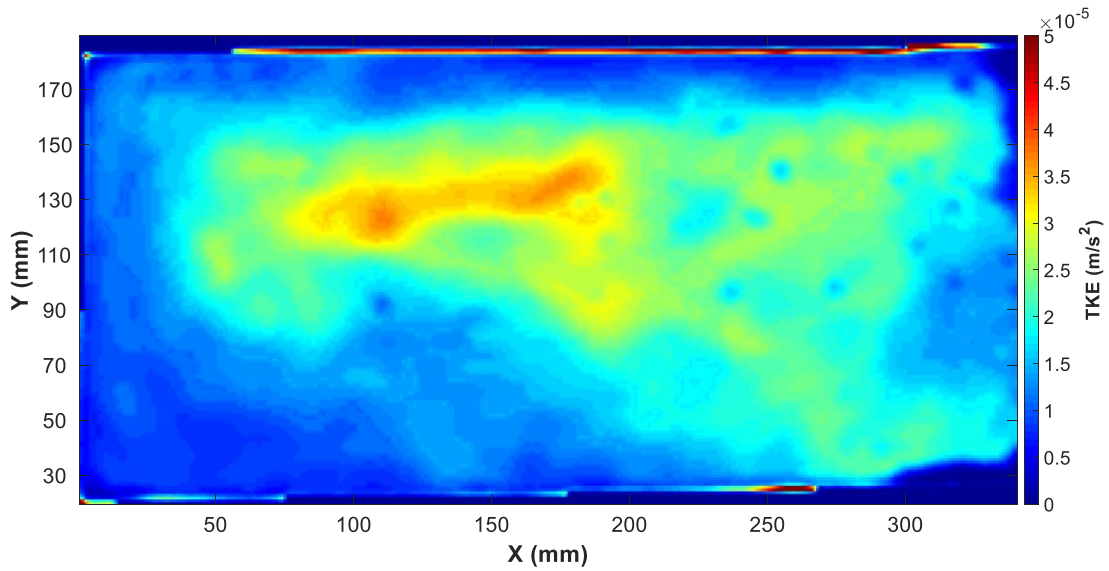
Figure 4.30 shows the turbulent kinetic energy. Figure 4.30 (a) shows that a higher TKE appears at the water–air interface at this time. Moreover, a higher TKE appears in the middle of tank due to effect of the water–air interface. Figures 4.30 (b) and (c) present the vertical and horizontal TKE, respectively.

1.4) At $T_b = 50^\circ\text{C}$

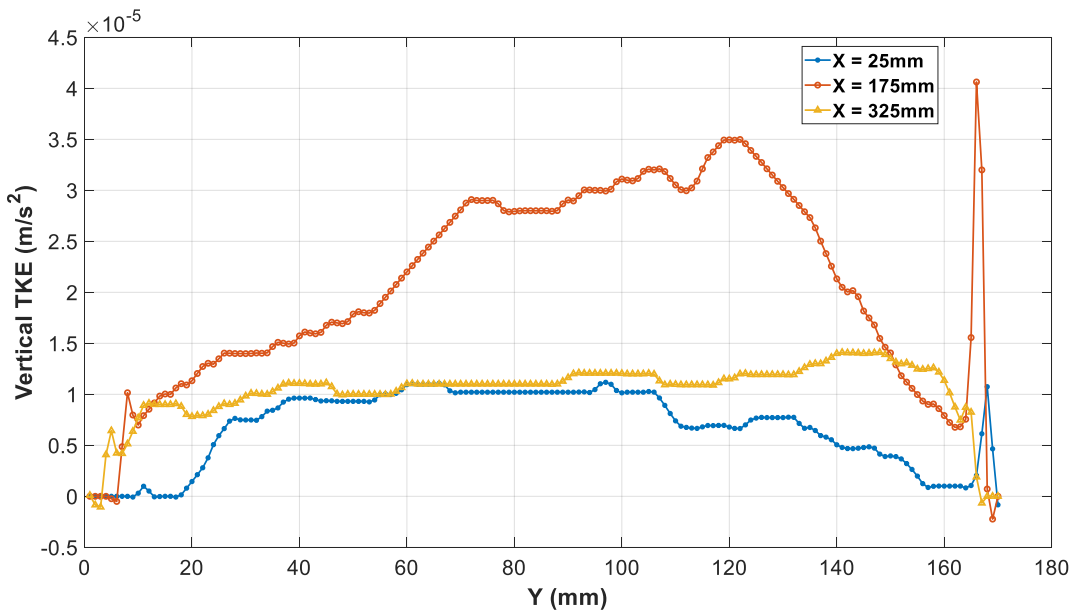
(a) Velocity

Figure 4.31 shows the velocity at $T_b = 50^\circ\text{C}$, which is the desirable temperature for the current work. It is clear that the velocity increases over most of the tank because of the rise in the water temperature, as can be seen in Figure 4.31 (a). However, the two vorticities appear clearly at this time [refer to Figure 4.30 (a)]. Figure 4.31 (b) shows the vertical velocity at different Y locations. Here, at the middle of the tank ($X = 175 \text{ mm}$), the velocity decreases at the rotating vortex, which

then rises up at the water–air interface to reach the maximum value. This is clear in Figure 4.31 (c) at different Y locations.



(a)



(b)

Figure 4.30: (a) Turbulent kinetic energy magnitude, (b) XY plot for vertical turbulent kinetic energy, (c) XY plot for horizontal turbulent kinetic energy at $D = 0.17$ m and $T_b = 46^\circ\text{C}$.

Figure 4.30—continued

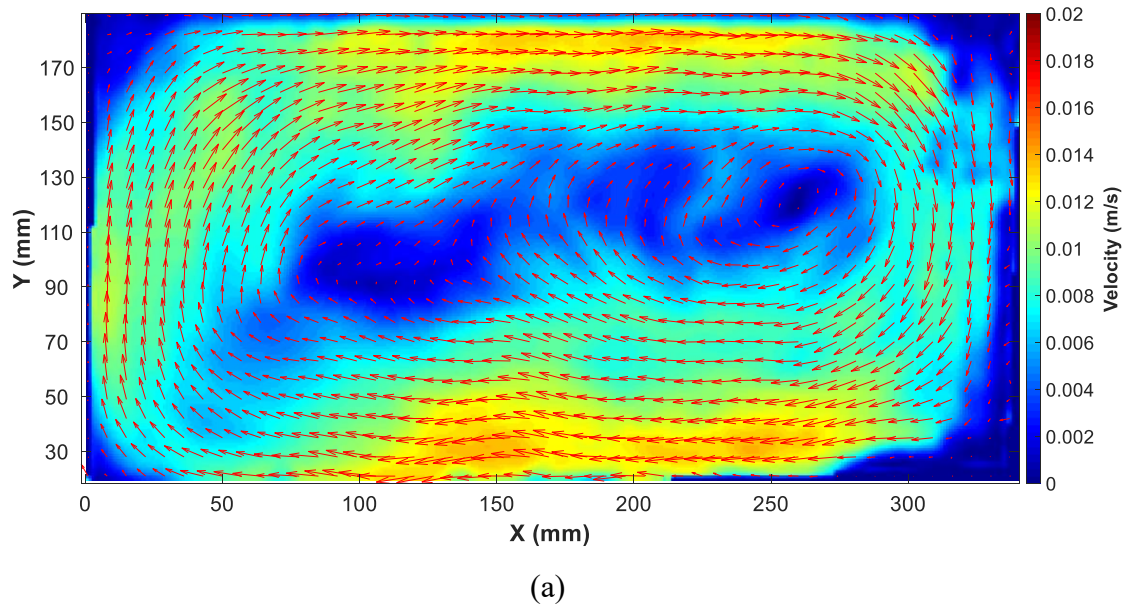
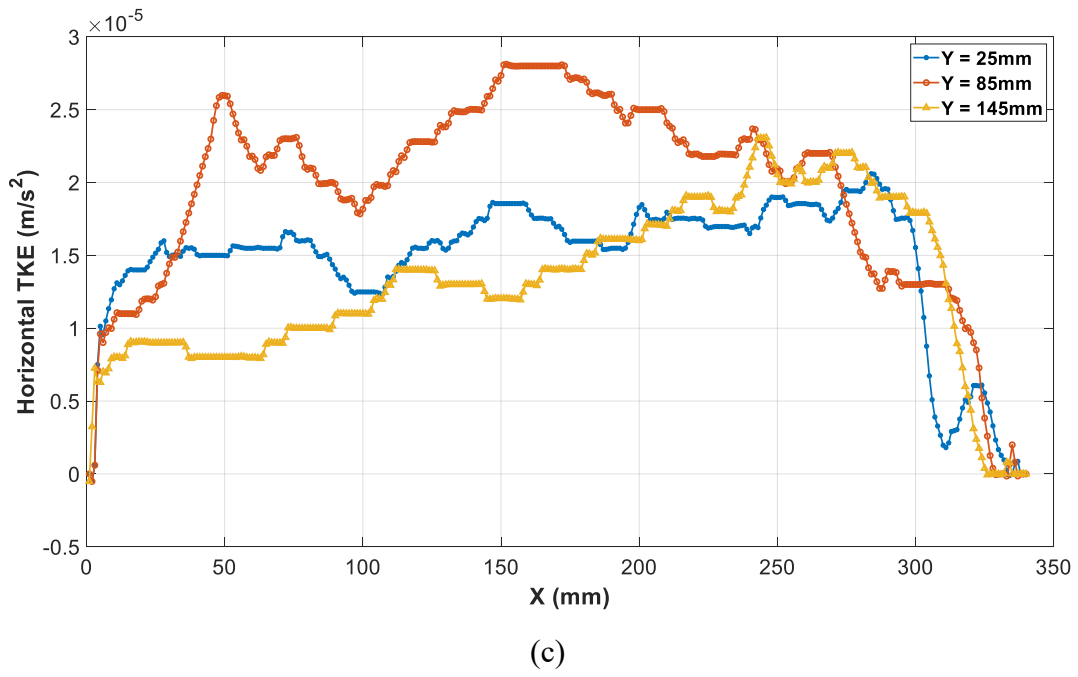
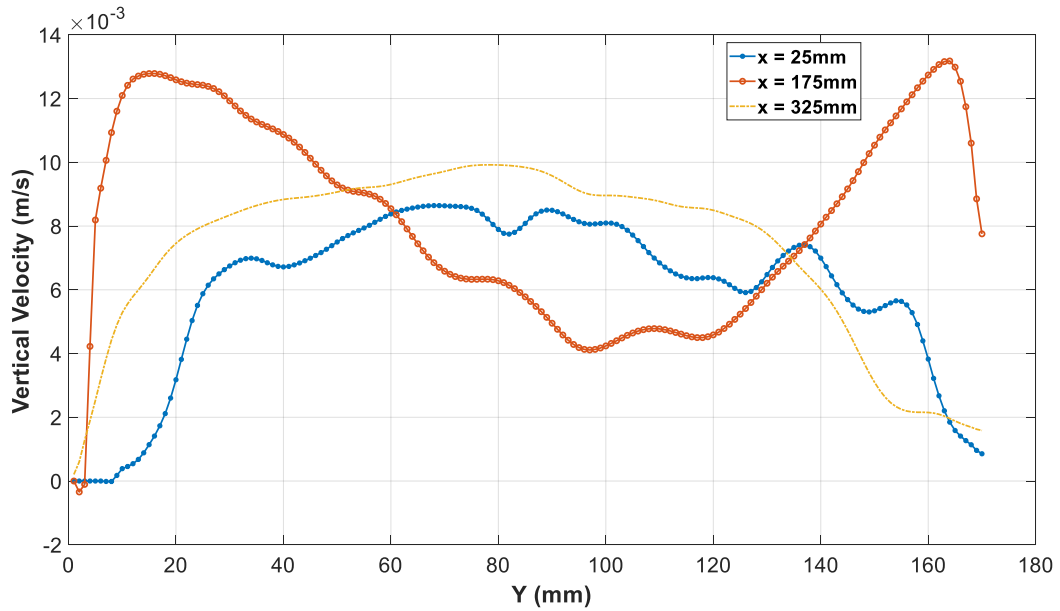
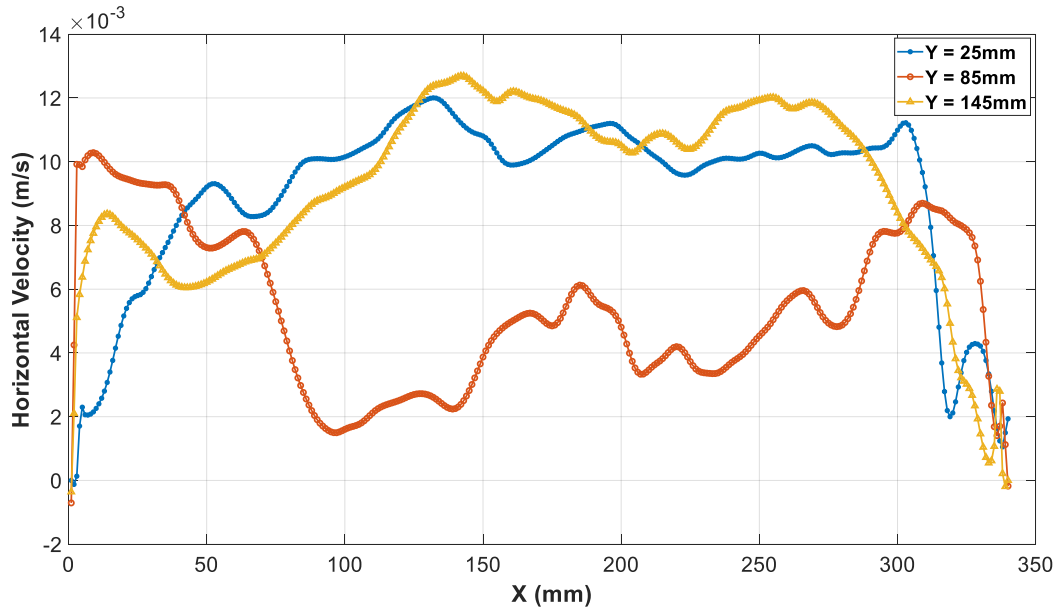


Figure 4.31: (a) Velocity magnitude, (b) XY plot for vertical velocity, (c) XY plot for horizontal velocity at $D = 0.17$ m and $T_b = 50^\circ\text{C}$.

Figure 4.31—continued



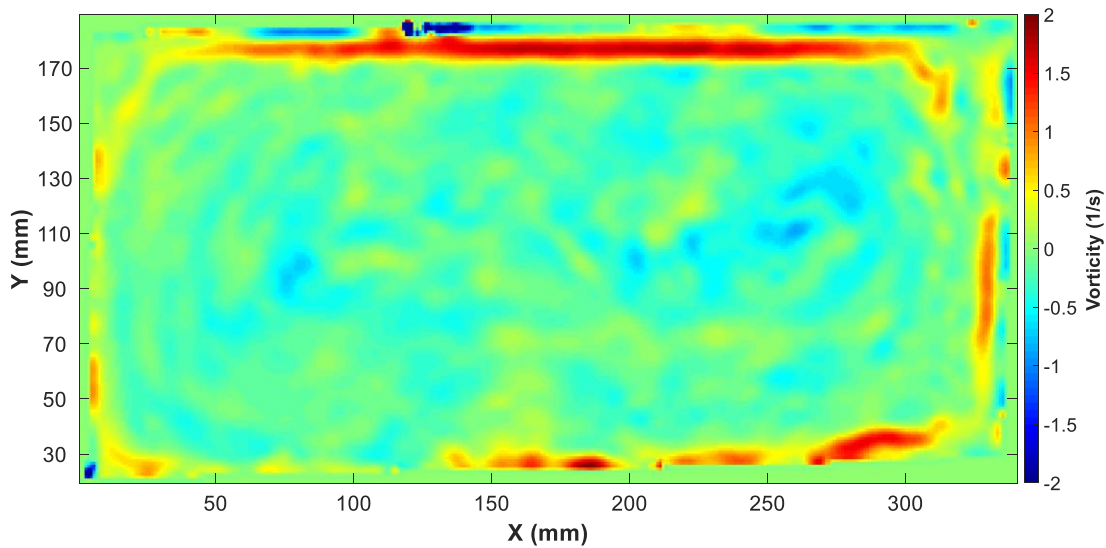
(b)



(c)

(b) Vorticity

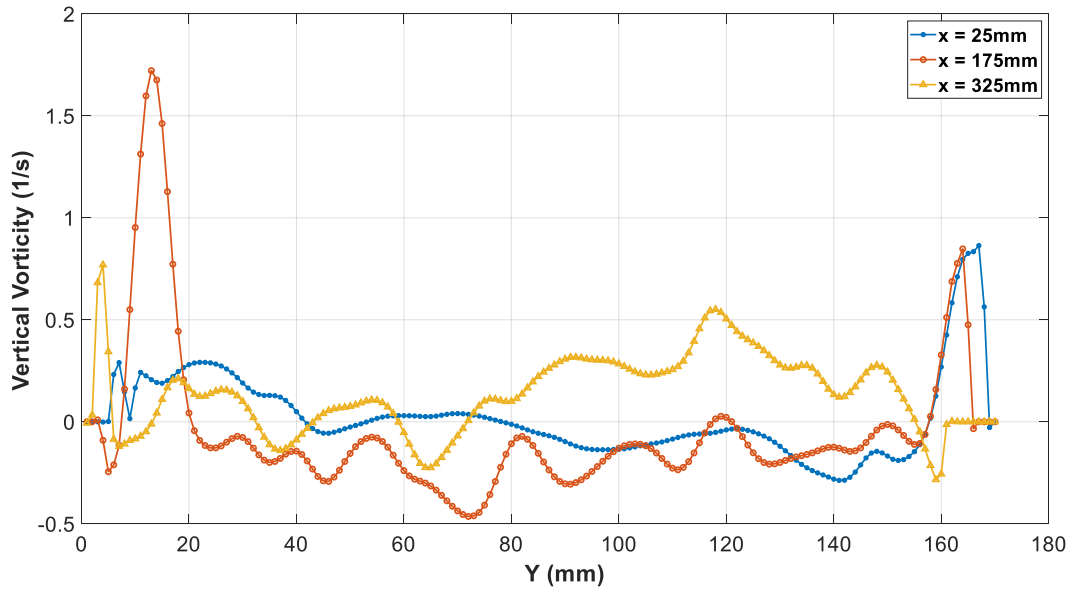
Figure 4.32 shows vorticity at $T_b = 50^\circ\text{C}$. Figure 4.32 (a) shows the vorticity magnitude, where the areas near the walls, bottom, and top of the tank show higher vorticity. Moreover, it is clear that the highest vorticity appears at the water–air interface at this time due to the increase in evaporation [refer to Figure 4.32 (a)]. Some negative vorticity can be seen at the water–air interface because of the effect of the cold air at the free water surface. However, the small velocity mentioned in Figure 4.32 in the middle of the tank shows negative vorticity, as evident. The XY plot for vertical vorticity is presented in Figure 4.32 (b). The same trend of fluctuation in the middle of the tank is seen in Figure 4.32 (c) for the horizontal vorticity at different Y locations.



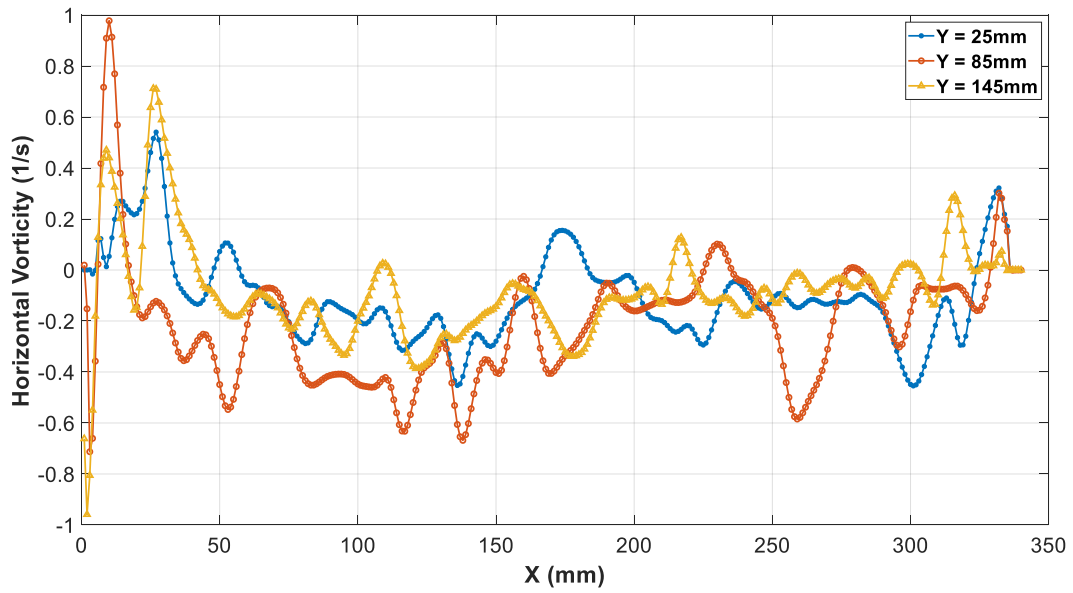
(a)

Figure 4.32: (a) Vorticity magnitude, (b) XY plot for vertical vorticity, (c) XY plot for horizontal vorticity at $D = 0.17$ m and $T_b = 50^\circ\text{C}$.

Figure 4.32—continued



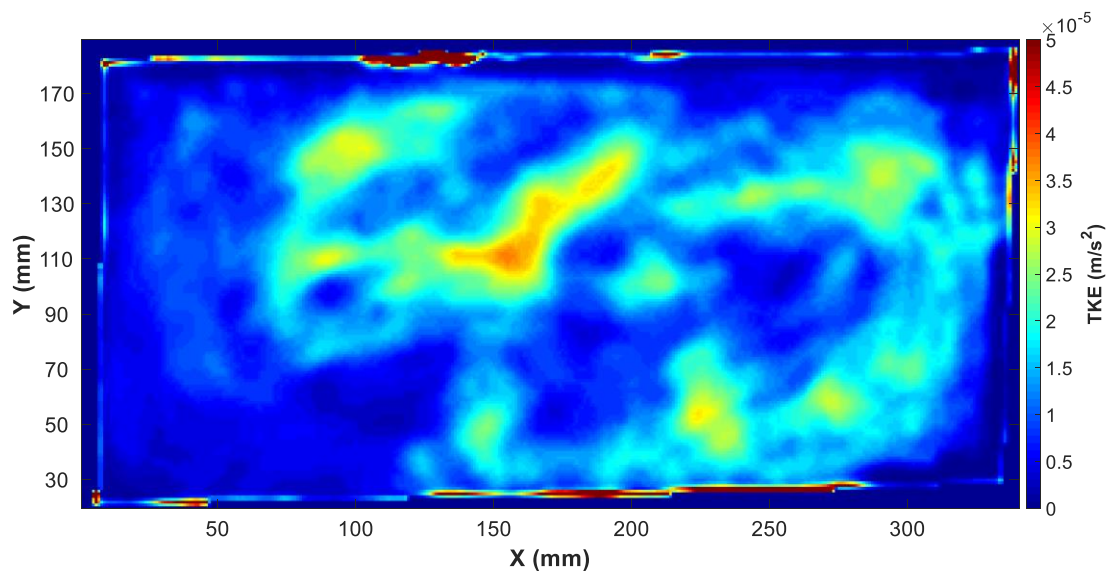
(b)



(c)

(c) Turbulent Kinetic Energy

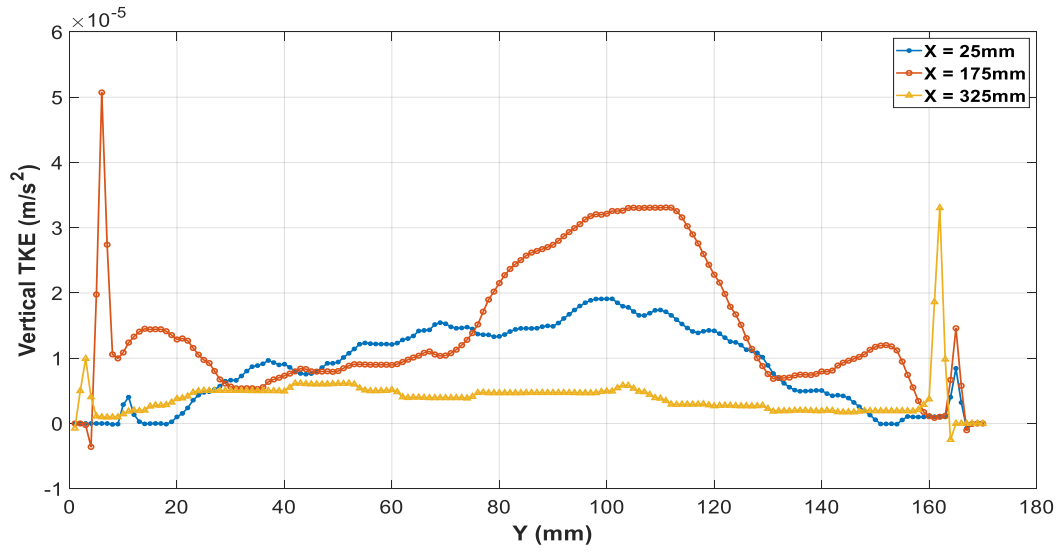
Figure 4.33 presents the turbulent kinetic energy. Figure 4.33 (a) shows a higher TKE appearing at the bottom and at the water–air interface. However, a higher TKE also appears in the middle of the tank due to the effect of rising temperature at this time and the evaporation. Figures 4.33 (b) and (c) present the vertical and horizontal TKE respectively. The fluctuation of TKE in the middle of the tank is clear [refer to Figure 4.33 (c)].



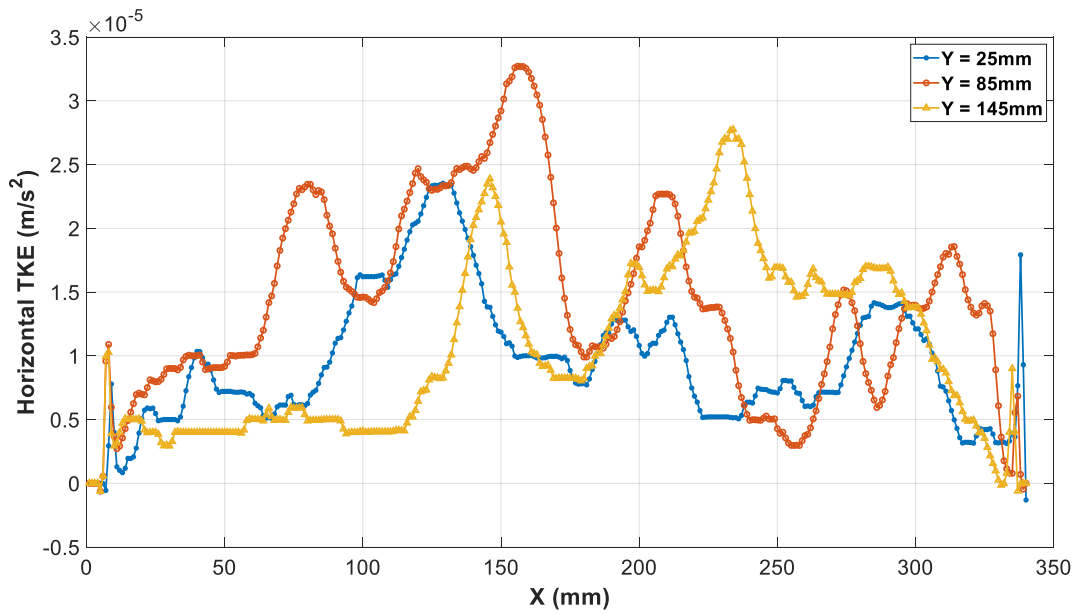
(a)

Figure 4.33: (a) Turbulent kinetic energy magnitude, (b) XY plot for vertical turbulent kinetic energy, (c) XY plot for horizontal turbulent kinetic energy at $D = 0.17$ m and $T_b = 50^\circ\text{C}$.

Figure 4.33—continued



(b)



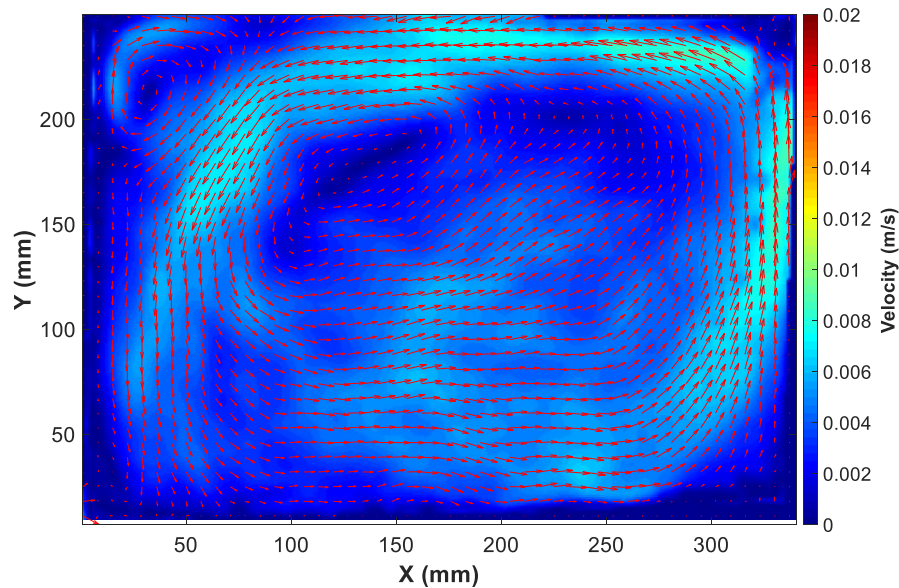
(c)

2) At $D = 0.24$ m

2.1) At $T_b = 28^\circ\text{C}$

(a) Velocity

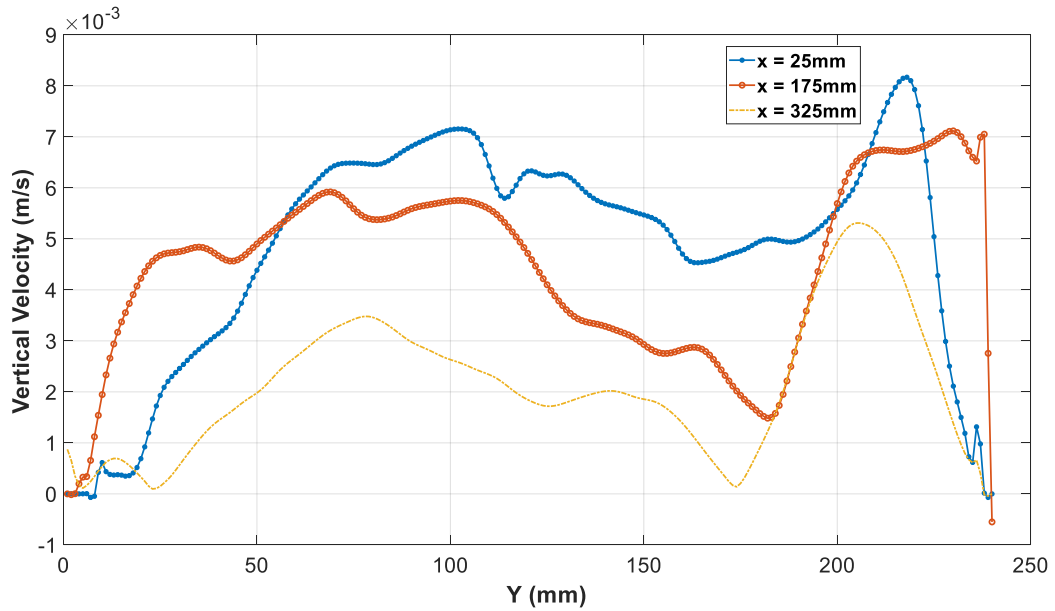
The velocity at $D = 0.24$ m and $T_b = 28^\circ\text{C}$ is shown in Figure 4.34. It is clear that in Figure 4.34 (a) the velocity starts to increase, especially at the walls, bottom, and the water–air interface. It is noticeable that some rotation vortex develops near the water–air interface, due to temperature difference at the free water surface. Interestingly, a rotation vortex can be clearly seen at the left side wall at the water–air interface corner, along with a smaller one at the other side. Figure 4.34 (b) shows the vertical velocity at different X locations. The velocity is higher near the left and right walls, whereas at the middle of the tank the velocity has dropped due to the rotating vortex and then rises up at the water–air interface. This is clear in Figure 4.34 (c) at different Y locations.



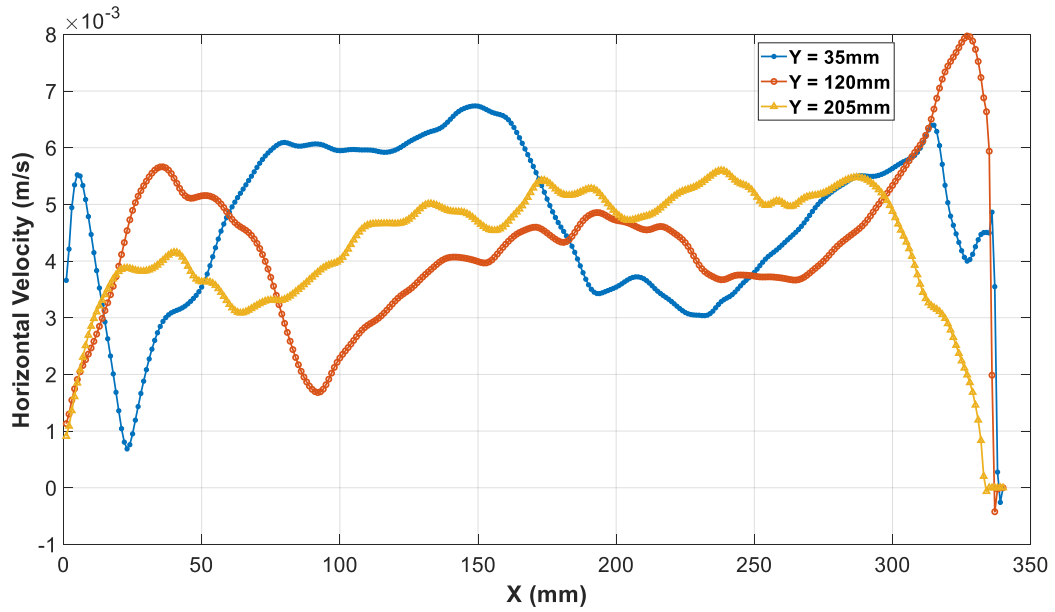
(a)

Figure 4.34: (a) Velocity magnitude, (b) XY plot for vertical velocity, (c) XY plot for horizontal velocity at $D = 0.24$ m and $T_b = 28^\circ\text{C}$.

Figure 4.34—continued



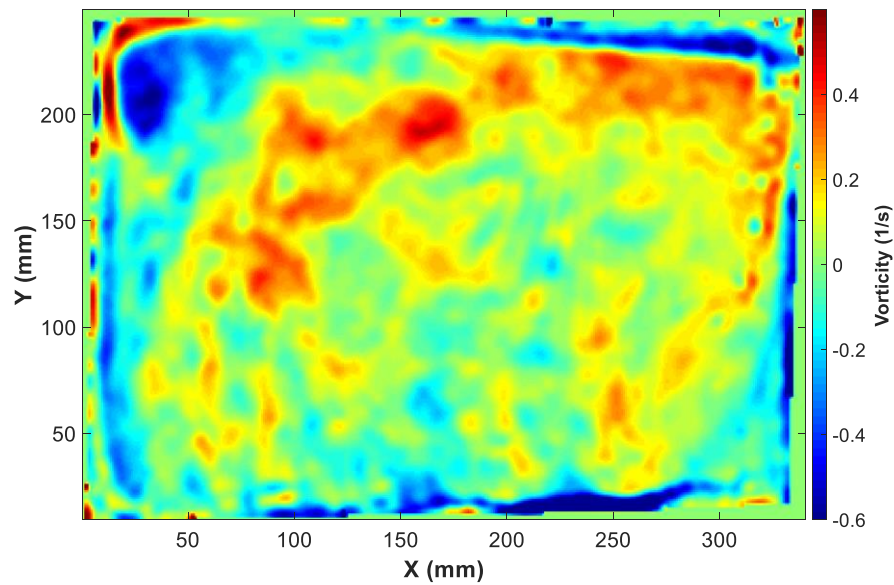
(b)



(c)

(b) Vorticity

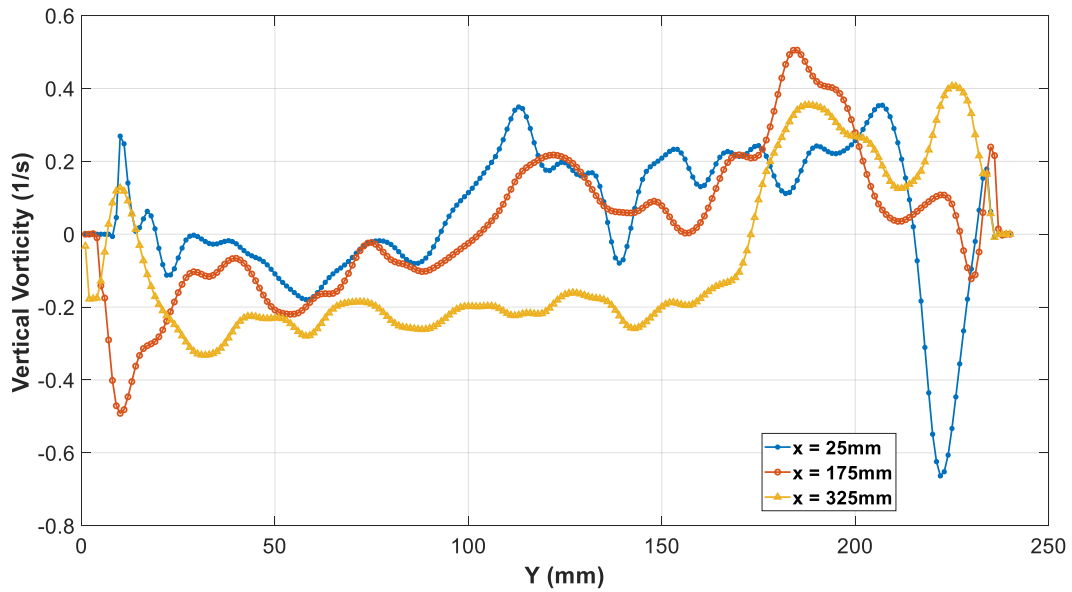
Figure 4.35 shows vorticity at $T_b = 28^\circ\text{C}$. Figure 4.35 (a) shows the vorticity magnitude, where negative vorticity appears near the walls, bottom, and top of the tank. Moreover, it is clear that the highest vorticity appears near the water–air interface at this time due to the mass and heat transfer at the free water surface [refer to Figure 4.35 (a)]. Some negative vorticity can be seen at the left wall top corner due to the rotation vortex at this region. The XY plot for vertical vorticity is presented in Figure 4.35 (b). The same trend of fluctuation in the middle of the tank is seen in Figure 4.35 (c) for the horizontal vorticity at different Y locations.



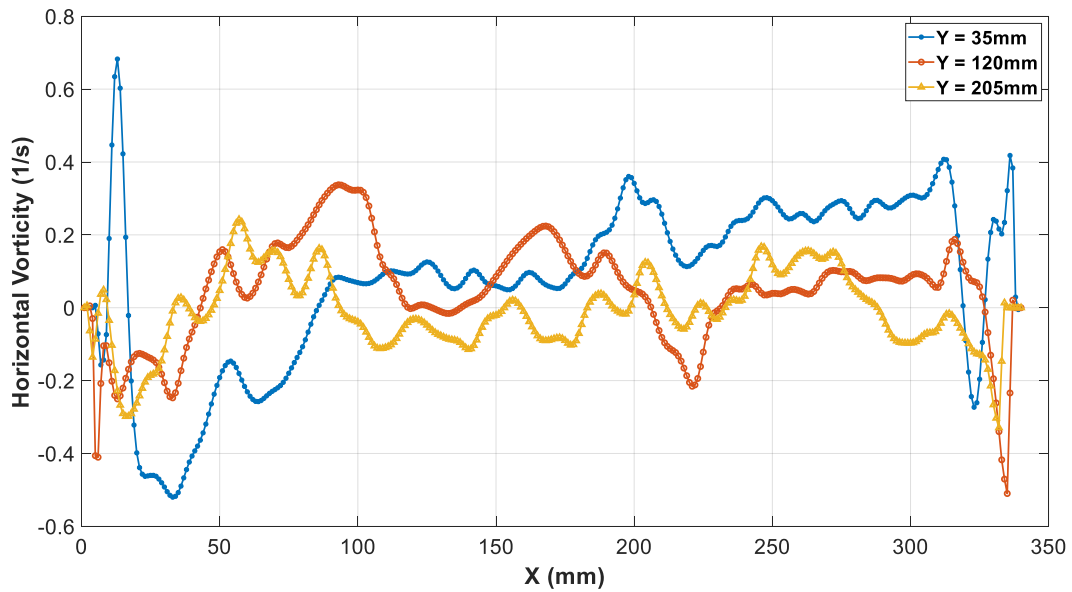
(a)

Figure 4.35: (a) Vorticity magnitude, (b) XY plot for vertical vorticity, (c) XY plot for horizontal vorticity at $D = 0.24\text{ m}$ and $T_b = 28^\circ\text{C}$.

Figure 4.35—continued



(b)

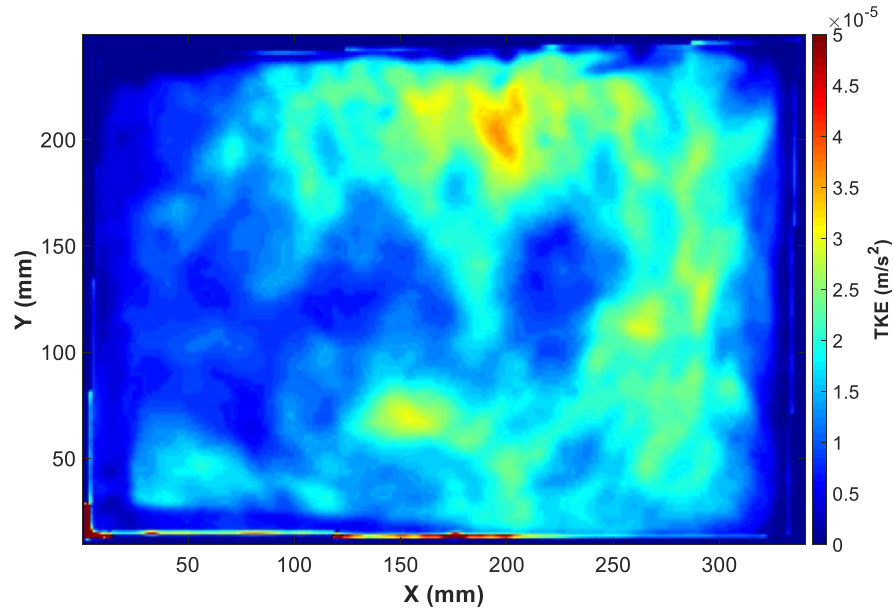


(c)

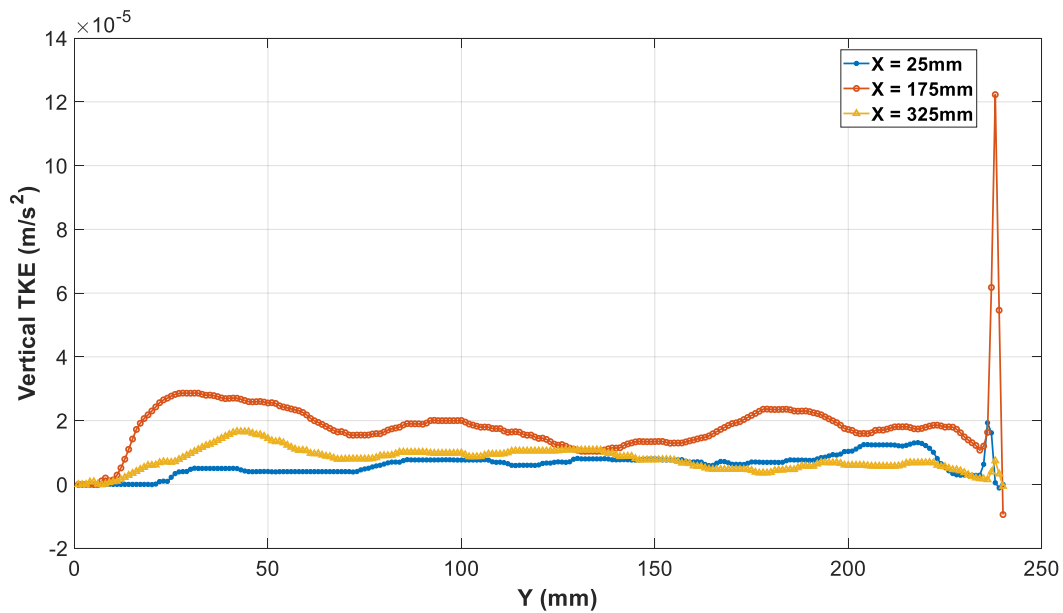
(c) Turbulent Kinetic Energy

The turbulent kinetic energy is shown in Figure 4.36. Figure 4.36 (a) shows that a higher TKE appears near the water–air interface due to temperature difference at the free water surface.

However, Figures 4.36 (b) and (c) present the vertical and horizontal TKE, respectively. The fluctuation of TKE in the middle of the tank is clear [refer to Figure 4.36 (c)].



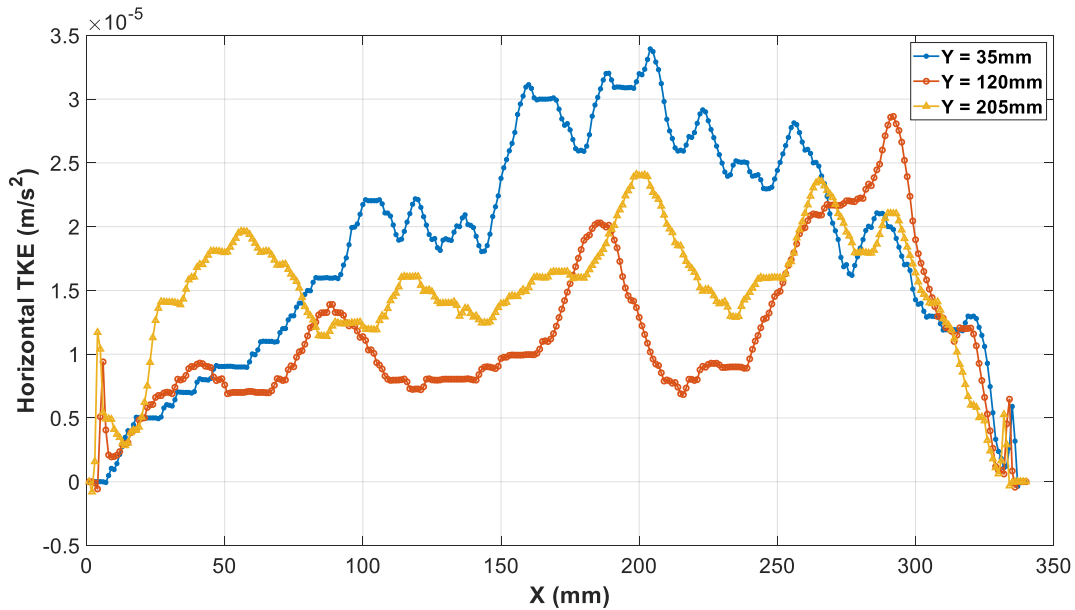
(a)



(b)

Figure 4.36: (a) Turbulent kinetic energy magnitude, (b) XY plot for vertical turbulent kinetic energy, (c) XY plot for horizontal turbulent kinetic energy at $D = 0.24$ m and $T_b = 28^\circ\text{C}$.

Figure 4.36—continued

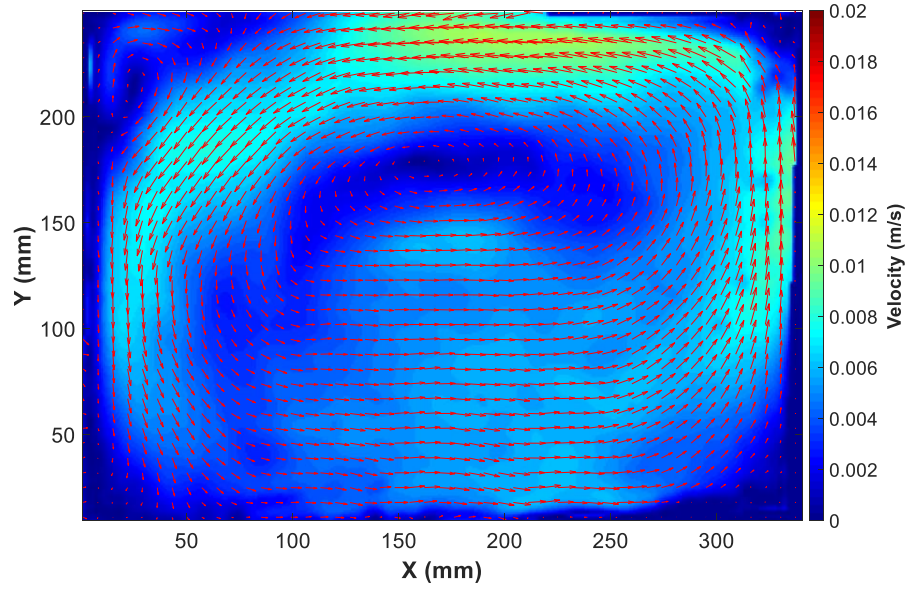


(c)

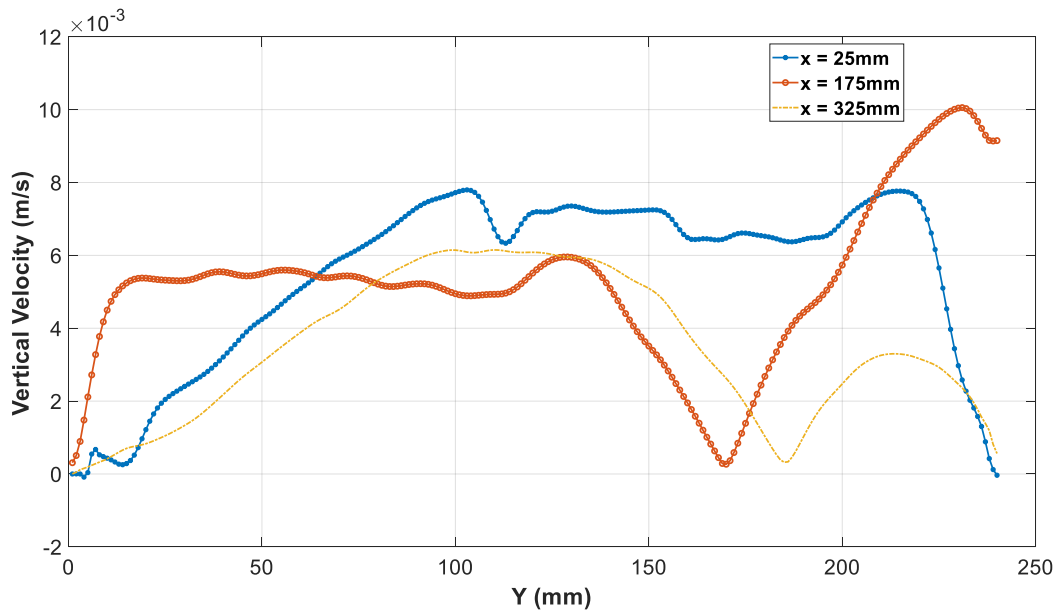
2.2) At $T_b = 38^\circ\text{C}$

(a) Velocity

Figure 4.37 shows the velocity at $T_b = 38^\circ\text{C}$. It can be seen that the velocity increases at the water–air interface due to the rise in the water temperature, which is clear in Figure 4.37 (a). However, the rotation vortex has moved to the center of the tank at this time. A higher velocity is noticed clearly at the walls compared to Figure 4.34 (a). Figure 4.37 (b) shows the vertical velocity at different Y locations. Here, at the middle of the tank ($X = 175\text{ mm}$), the velocity almost equals zero at the rotating vortex, which then rises up at the water–air interface to reach the maximum value. This is clear in Figure 4.37 (c) at different Y locations.



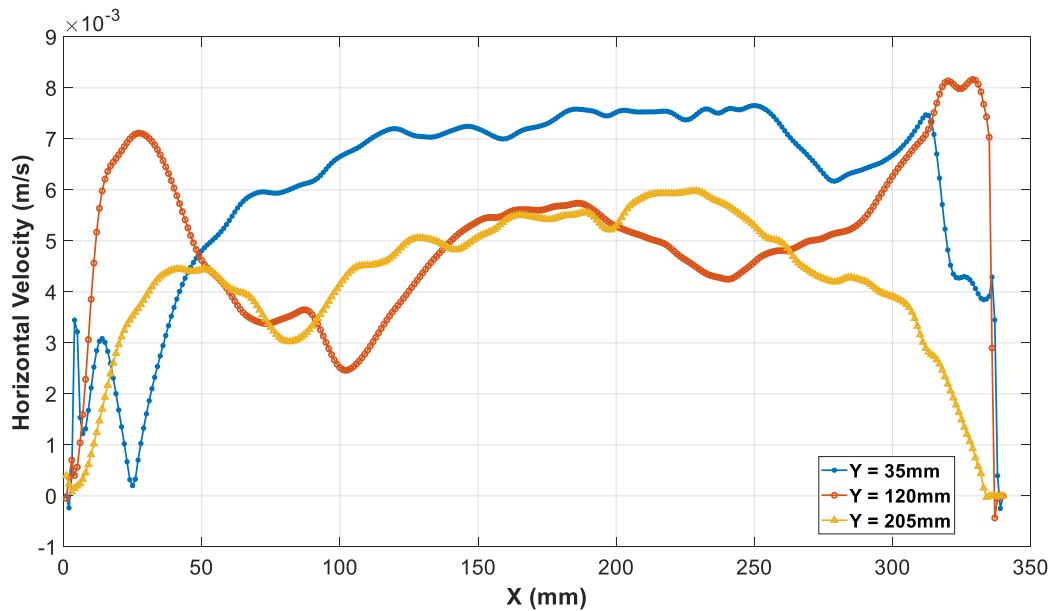
(a)



(b)

Figure 4.37: (a) Velocity magnitude, (b) XY plot for vertical velocity, (c) XY plot for horizontal velocity at $D = 0.24$ m and $T_b = 38^\circ\text{C}$.

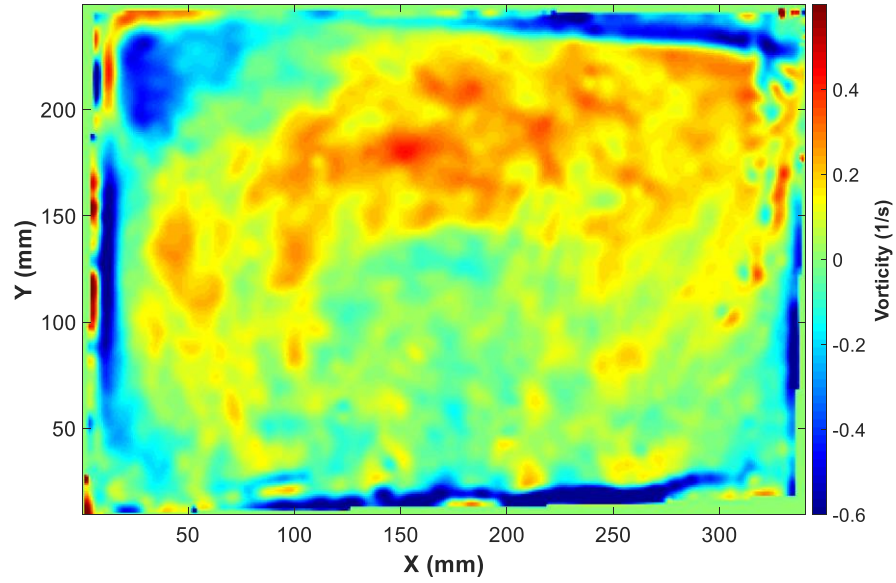
Figure 4.37—continued



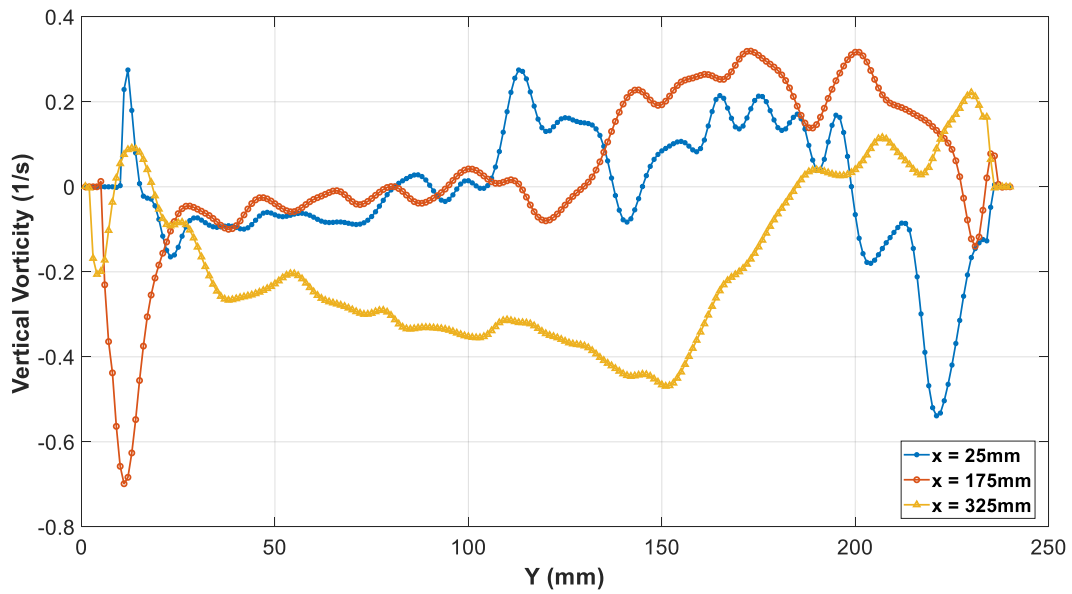
(c)

(b) Vorticity

Figure 4.38 presents vorticity at $T_b = 38^\circ\text{C}$. Figure 4.38 (a) shows the vorticity magnitude, where a negative vorticity appears near the walls, bottom, and top of the tank. Moreover, a higher vorticity can be seen in the middle of the tank near the water–air interface due to the evaporation. In Figure 4.38 (b), the XY plot for vertical vorticity is presented, where the vorticity has some fluctuation at the middle of the tank. The same trend of behavior is seen in Figure 4.38 (c) for the horizontal vorticity at different Y locations.



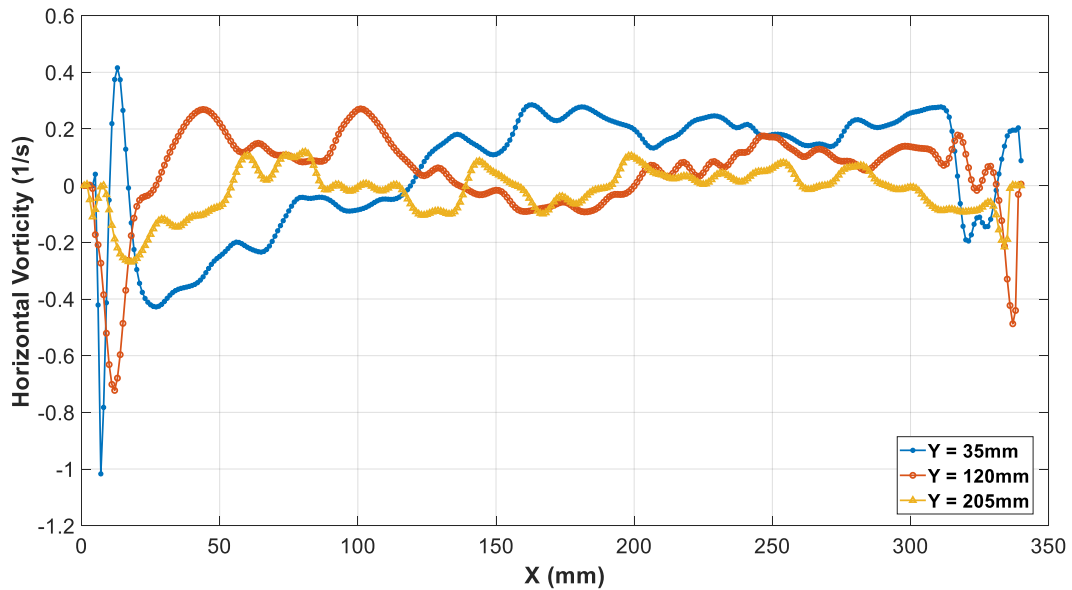
(a)



(b)

Figure 4.38: (a) Vorticity magnitude, (b) XY plot for vertical vorticity, (c) XY plot for horizontal vorticity at $D = 0.24$ m and $T_b = 38^\circ\text{C}$.

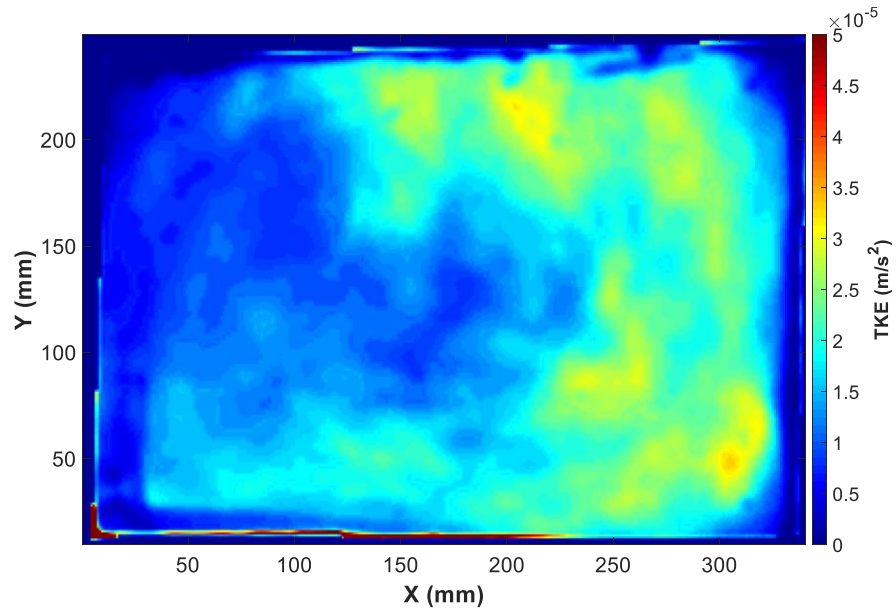
Figure 4.38—continued



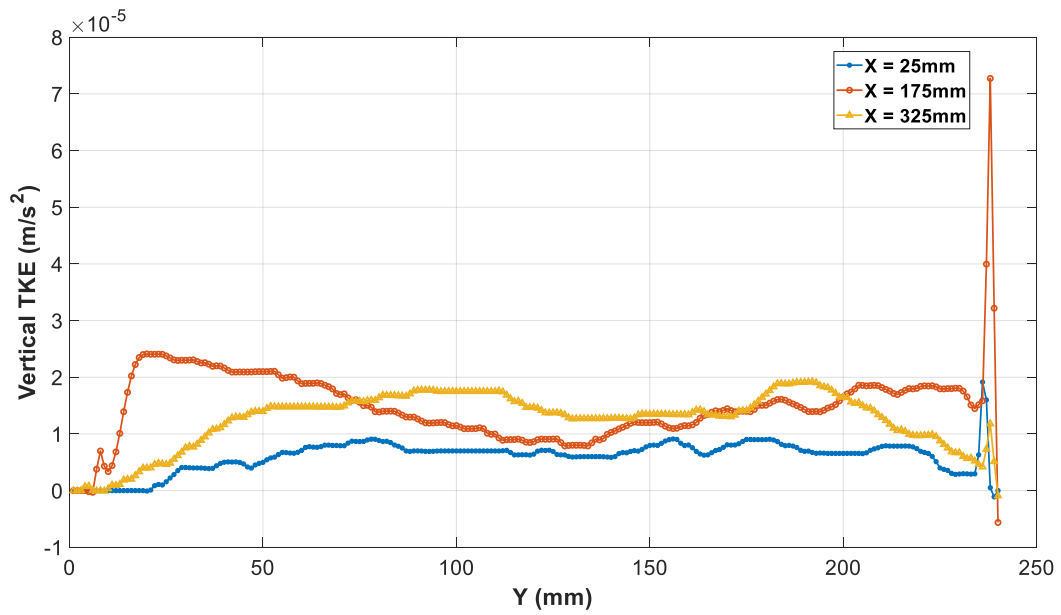
(c)

(c) Turbulent Kinetic Energy

Figure 4.39 presents the turbulent kinetic energy. Figure 4.39 (a) shows that a higher TKE appears at the bottom and near the water–air interface. However, a higher TKE appears in the middle of the tank due to the effect of rising temperature and evaporation at this time. Figures 4.39 (b) and (c) present the vertical and horizontal TKE, respectively. The fluctuation of TKE in the middle of the tank is clear [refer to Figure 4.39 (c)].



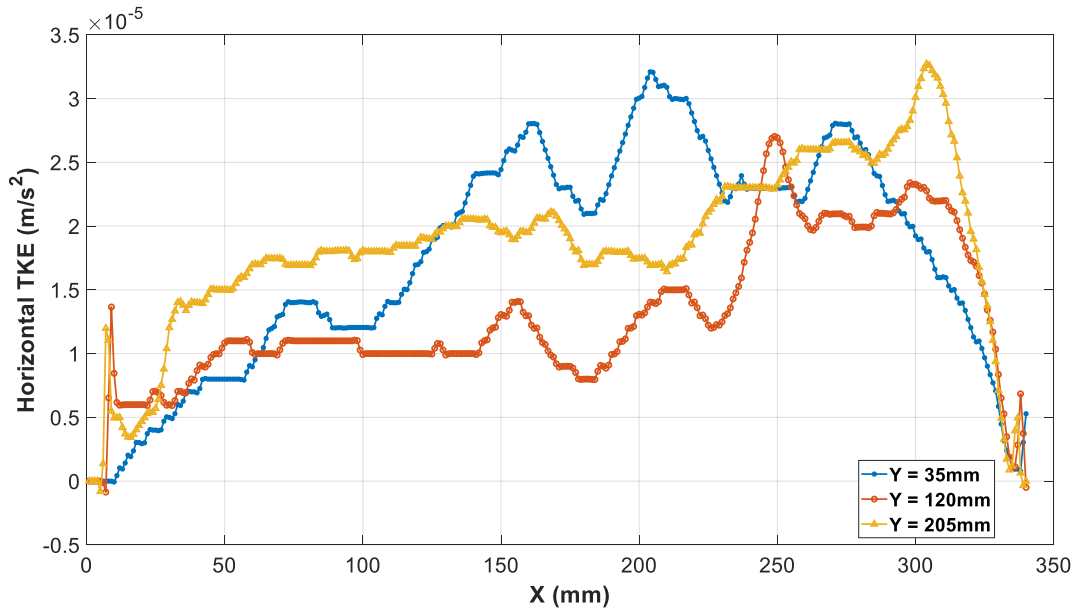
(a)



(b)

Figure 4.39: (a) Turbulent kinetic energy magnitude, (b) XY plot for vertical turbulent kinetic energy, (c) XY plot for horizontal turbulent kinetic energy at $D = 0.24$ m and $T_b = 38^\circ\text{C}$.

Figure 4.39—continued

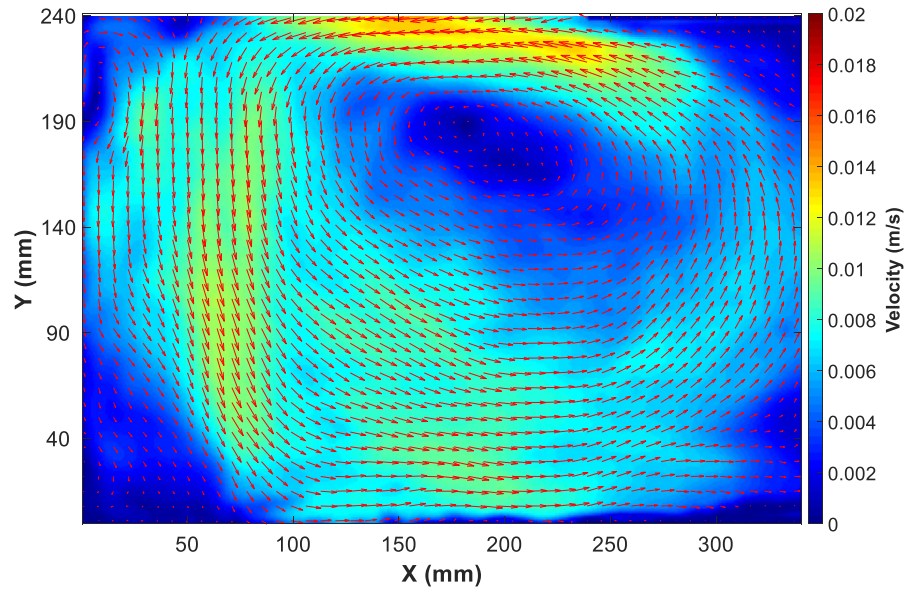


(c)

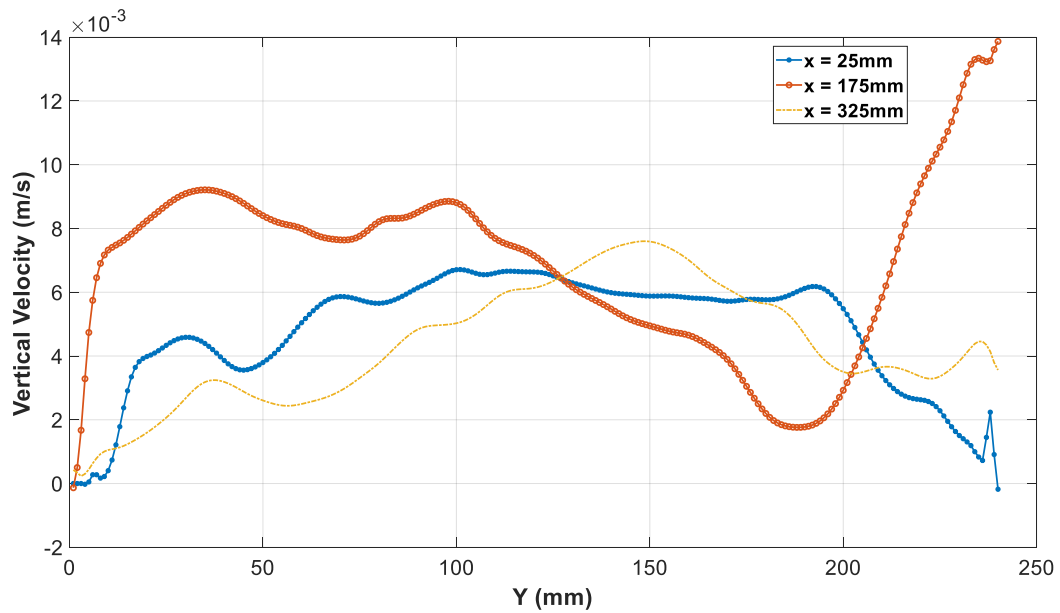
2.3) At $T_b = 46^\circ\text{C}$

(a) Velocity

Figure 4.40 shows the velocity at $T_b = 46^\circ\text{C}$. It is clear that at this time the velocity rises up due to the higher temperature of the water, which results in higher temperature difference with the ambient air compared to Figure 4.37 (a). This can be seen clearly in Figure 4.40 (a), where the velocity at the water–air interface increases, and the rotational vortex has moved to the center of the tank. Figure 4.40 (b) shows the vertical velocity at different Y locations. The horizontal velocity at different X locations is shown in Figure 4.40 (c).



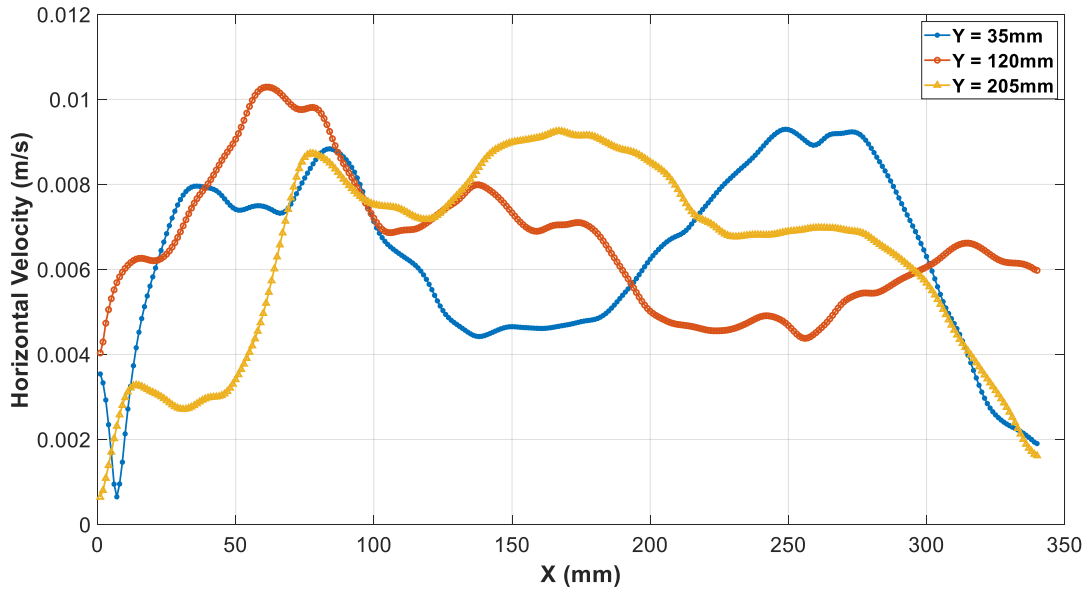
(a)



(b)

Figure 4.40: (a) Velocity magnitude, (b) XY plot for vertical velocity, (c) XY plot for horizontal velocity at $D = 0.24$ m and $T_b = 46^\circ\text{C}$.

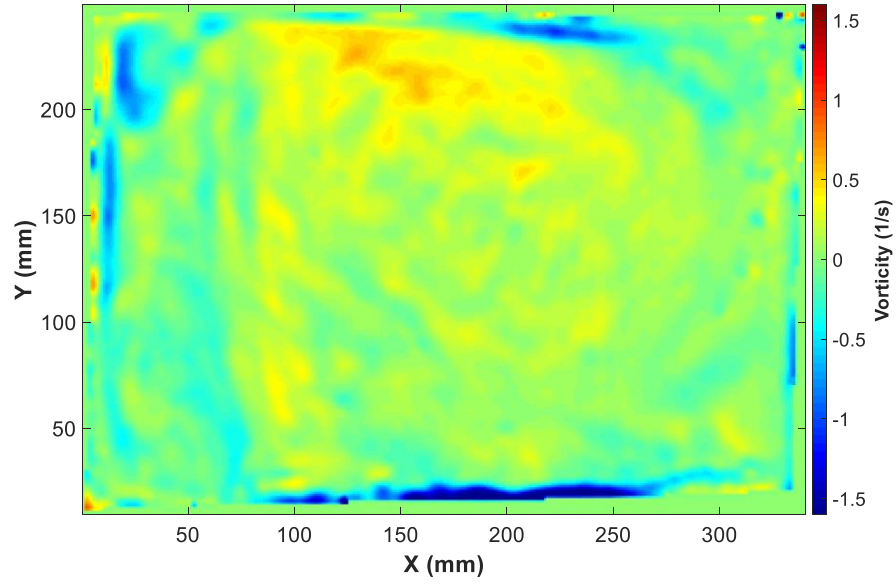
Figure 4.40—continued



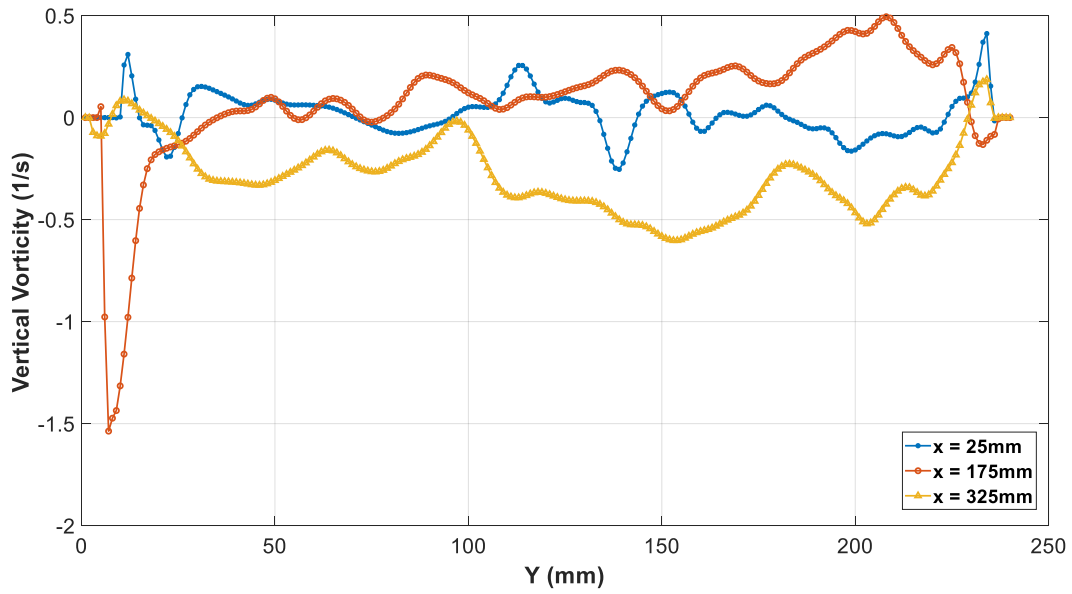
(c)

(b) Vorticity

Figure 4.41 presents vorticity at $T_b = 46^\circ\text{C}$. Figure 4.41 (a) shows the vorticity magnitude, where higher vorticity is evident near the top of the tank. It can be seen that negative vorticity appears at the water–air interface at this time, which is due to the mass and heat transfer through evaporation from the free water surface. Moreover, some negative vorticity can be seen at the bottom of the tank due to the rising temperature. The XY plot for vertical vorticity is presented in Figure 4.41 (b), where the vorticity has a higher value at this temperature compared to $T_b = 38^\circ\text{C}$. The same trend of behavior is seen in Figure 4.41 (c) for the horizontal vorticity at different Y locations.



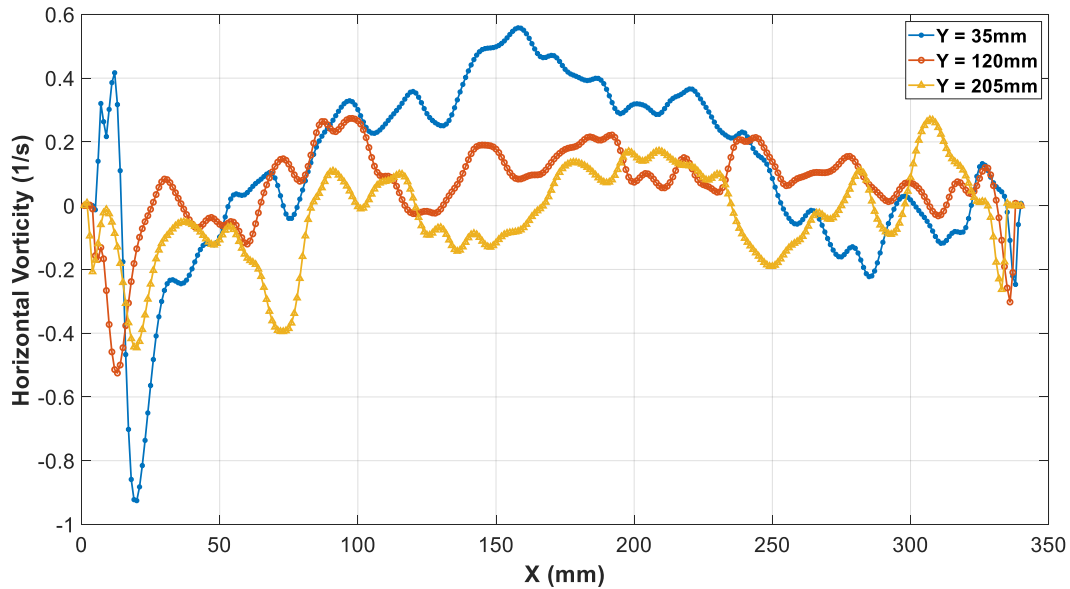
(a)



(b)

Figure 4.41: (a) Vorticity magnitude, (b) XY plot for vertical vorticity, (c) XY plot for horizontal vorticity at $D = 0.24$ m and $T_b = 46^\circ\text{C}$.

Figure 4.41—continued



(c)

(c) Turbulent Kinetic Energy

The turbulent kinetic energy is presented in Figure 4.42. Figure 4.42 (a) shows that a higher TKE appears at the left wall near the water–air interface, due the circulation at this region. However, Figures 4.42 (b) and (c) present the vertical and horizontal TKE, respectively. The fluctuation of TKE in the middle of the tank is clear [refer to Figure 4.42 (c)].

2.4) At $T_b = 50^\circ\text{C}$

(a) Velocity

Figure 4.43 shows the velocity at $T_b = 50^\circ\text{C}$, which is the desirable temperature for the current work. It is clear that the velocity increases at the water–air interface because the water temperature rises at this time, as can be seen in Figure 4.43 (a). However, the two vorticities mostly appear clearly at this time [refer to Figure 4.43 (a)]. Figure 4.43 (b) shows the vertical velocity at different Y locations. Here, at the middle of the tank ($X = 175$ mm), the velocity decreases to zero

at the rotating vortex, which then rises up at the water–air interface to reach the maximum value. This is clear in Figure 4.43 (c) at different Y locations.

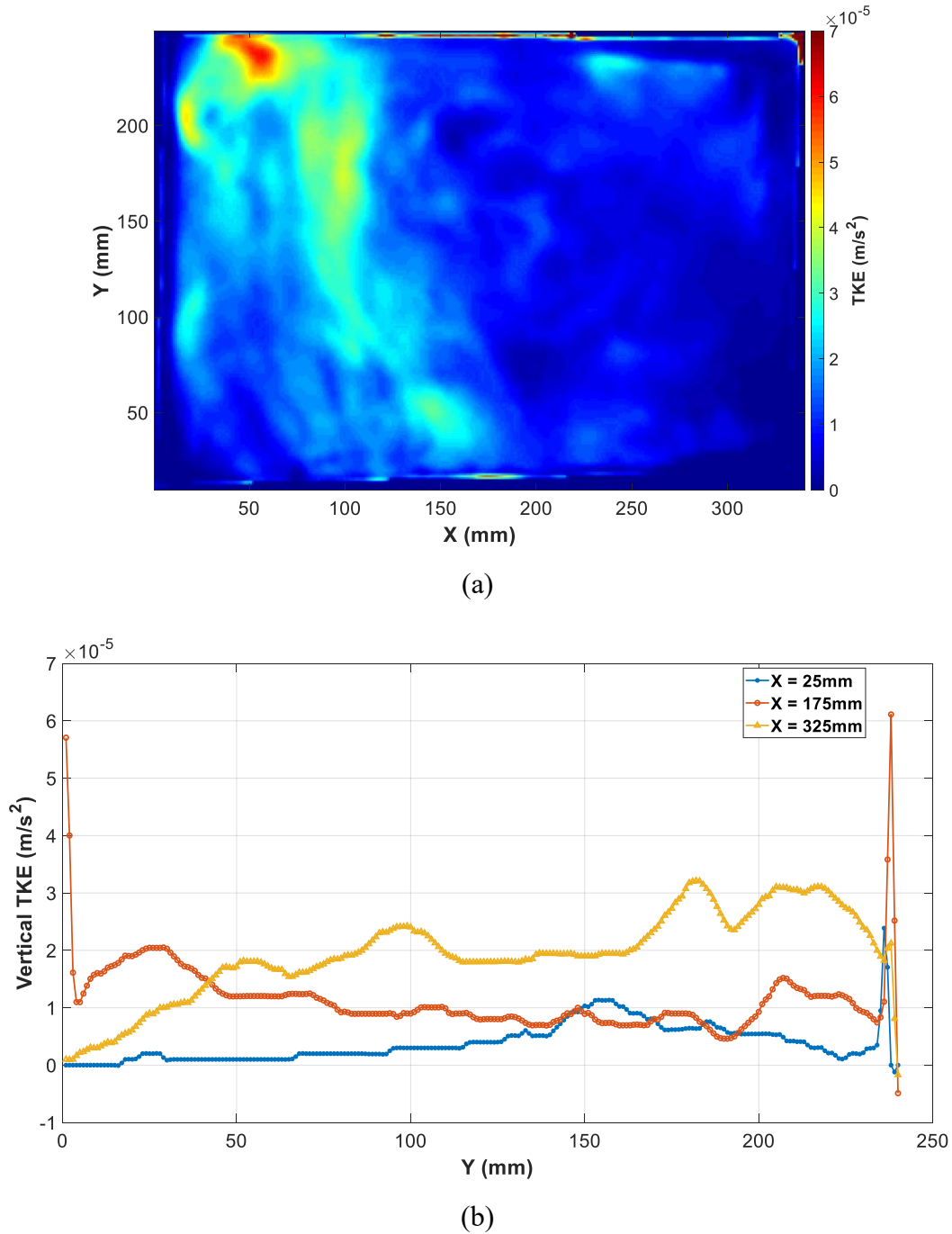


Figure 4.42: (a) Turbulent kinetic energy magnitude, (b) XY plot for vertical turbulent kinetic energy, (c) XY plot for horizontal turbulent kinetic energy at $D = 0.24$ m and $T_b = 46^\circ\text{C}$.

Figure 4.42—continued

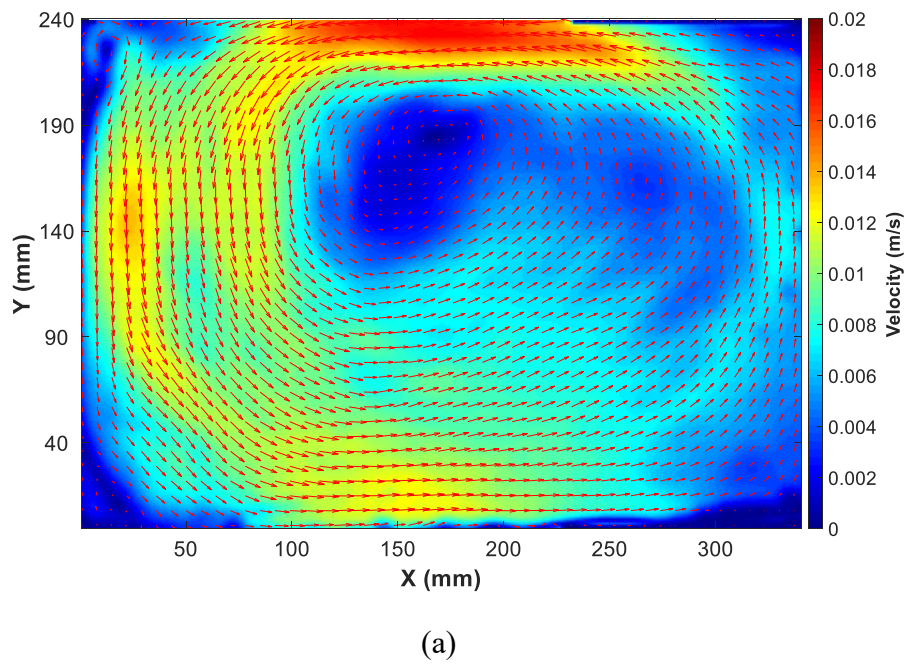
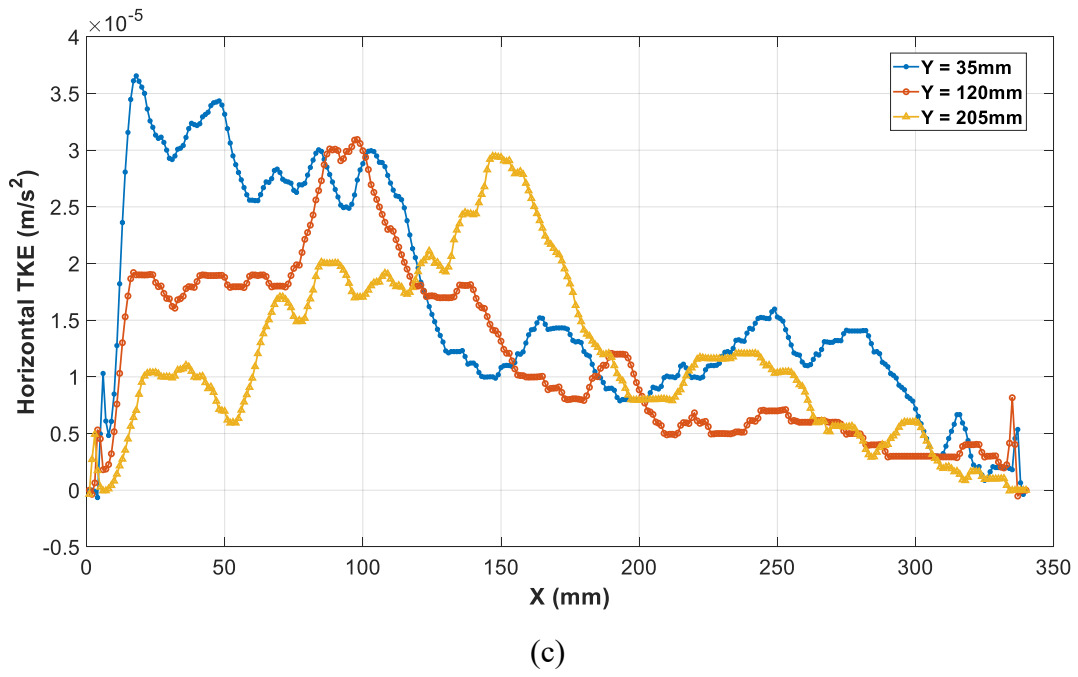
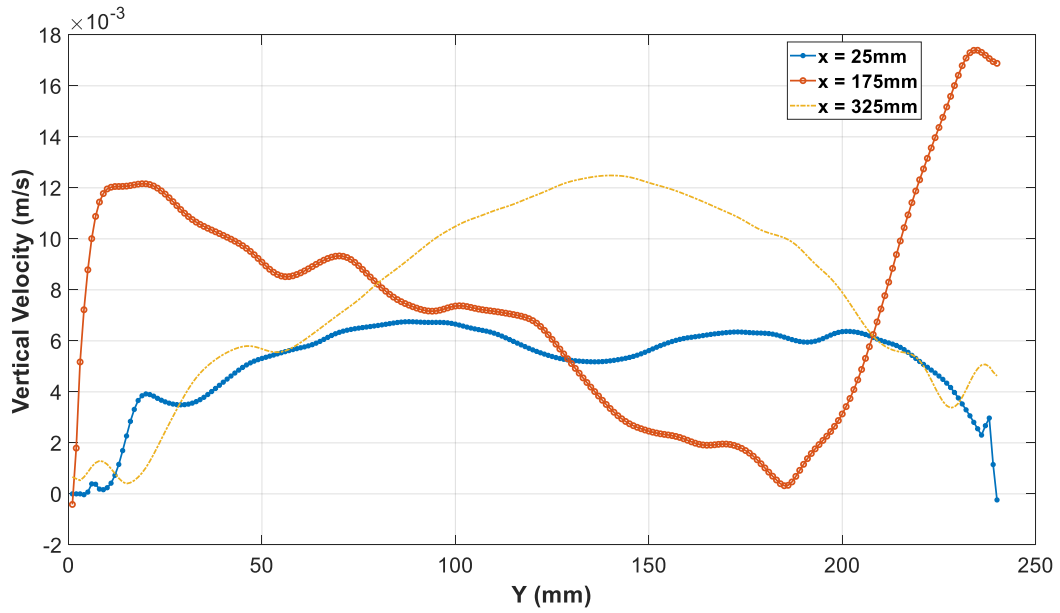
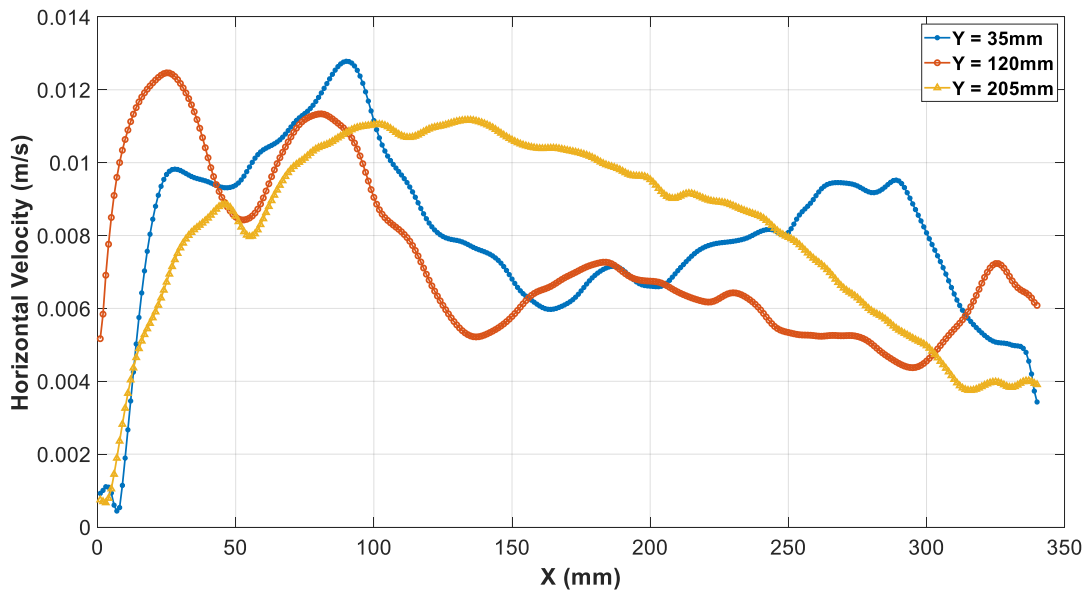


Figure 4.43: (a) Velocity magnitude, (b) XY plot for vertical velocity, (c) XY plot for horizontal velocity at $D = 0.24$ m and $T_b = 50^\circ\text{C}$.

Figure 4.43—continued



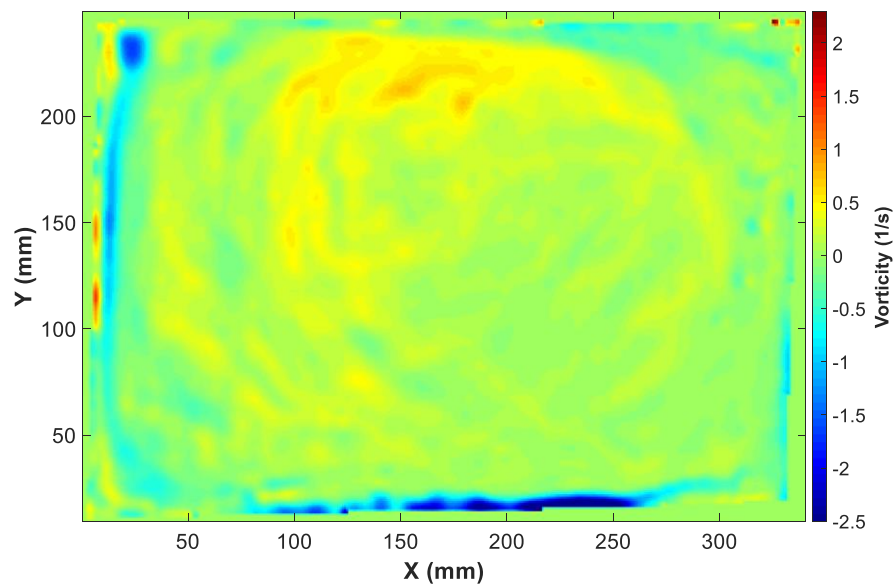
(b)



(c)

(b) Vorticity

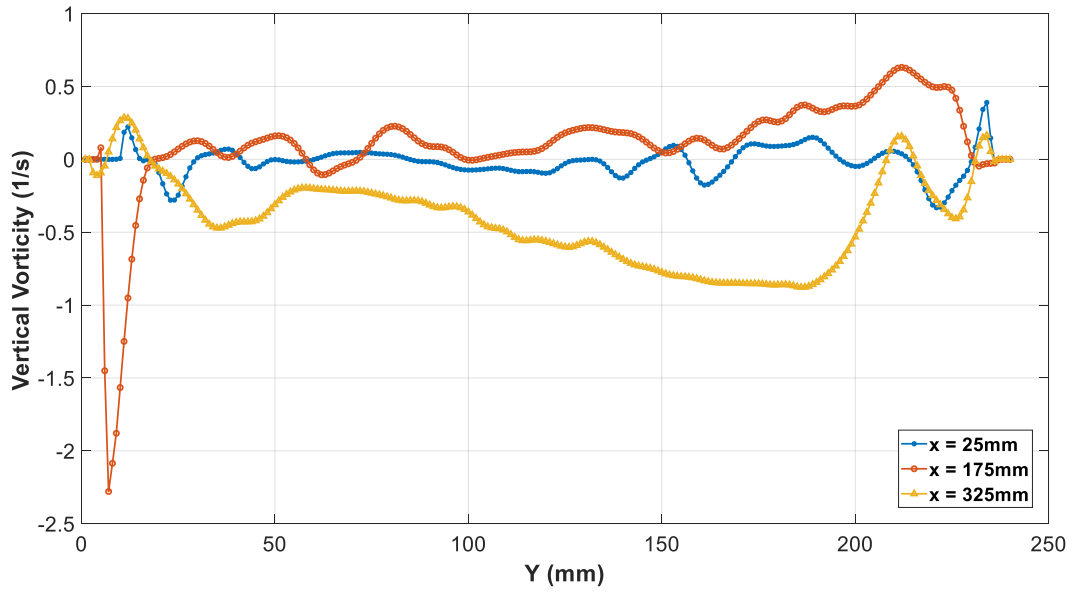
Figure 4.44 shows vorticity at $T_b = 50^\circ\text{C}$. Figure 4.44 (a) shows that the vorticity has the highest value at this time due to the rising temperature. Moreover, it is clear that the highest vorticity appears near the water–air interface at this time, due to the increasing evaporation [refer to Figure 4.44 (a)]. Some negative vorticity can be seen at the water–air interface because of the effect of the cold air at the free water surface. Some negative vorticity can also be seen at the bottom and the walls of the tank. The XY plot for vertical vorticity is presented in Figure 4.44 (b). The same trend of fluctuation in the middle of the tank is seen in Figure 4.44 (c) for the horizontal vorticity at different Y locations.



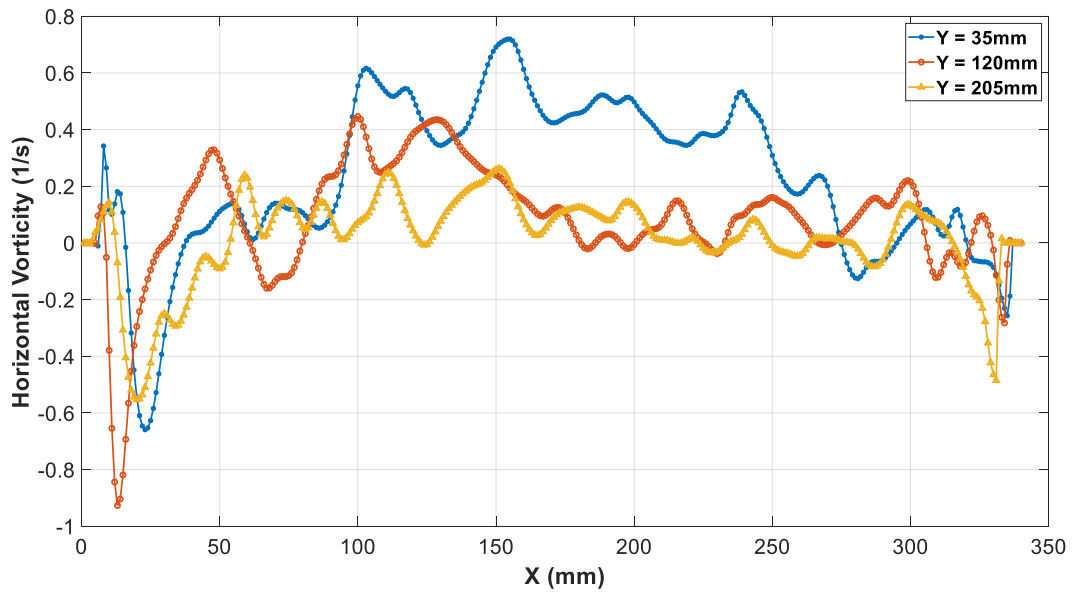
(a)

Figure 4.44: (a) Vorticity magnitude, (b) XY plot for vertical vorticity, (c) XY plot for horizontal vorticity at $D = 0.24$ m and $T_b = 50^\circ\text{C}$.

Figure 4.44—continued



(b)



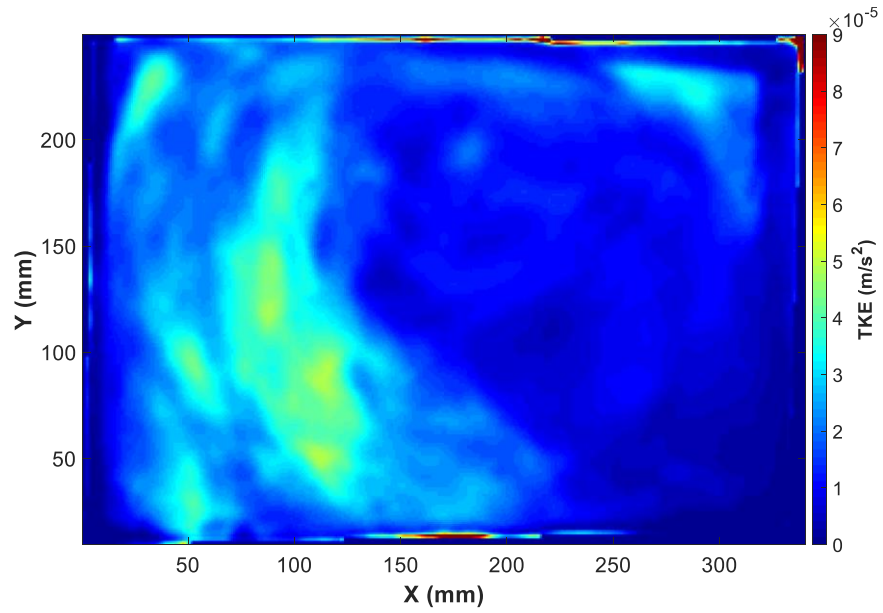
(c)

(c) Turbulent Kinetic Energy

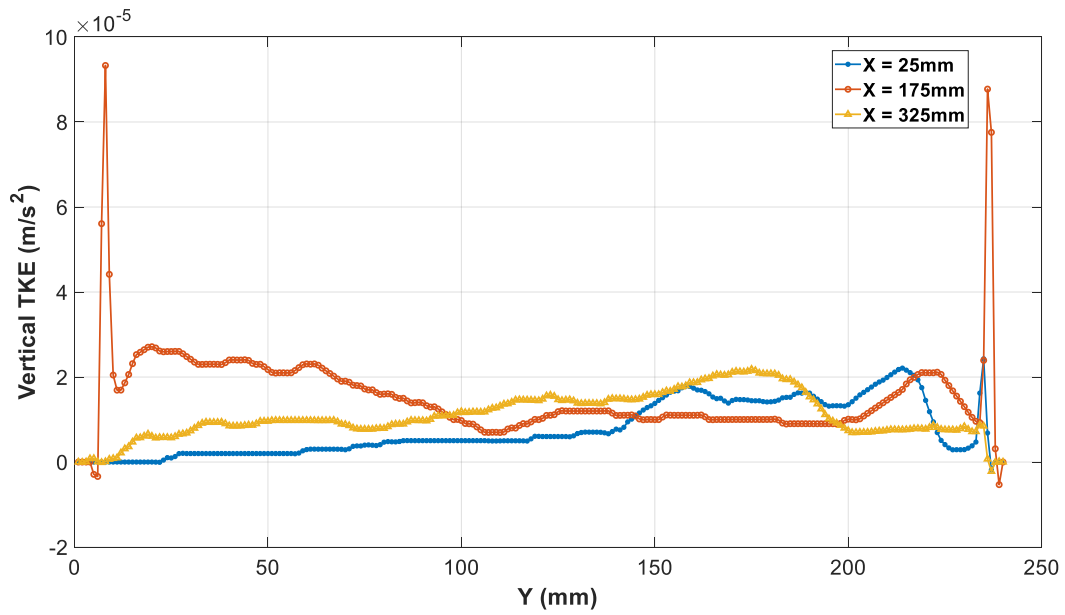
The turbulent kinetic energy is presented in Figure 4.45. Figure 4.45 (a) shows that a higher TKE appears near the left wall, where the water flows downward faster after reaching the water–air interface. However, Figures 4.45 (b) and (c) present the vertical and horizontal TKE, respectively. The fluctuation of TKE in the middle of the tank is clear [refer to Figure 4.45 (c)].

3) Comparison of $D = 0.17$ m and $D = 0.24$ m

Now, the comparison of horizontal velocity at the two different depths is presented. The most important parameter is the development of horizontal velocity near the water–air interface, due to its direct effect on the evaporation rate at the free water surface. Figure 4.46 shows the comparison of the horizontal velocity near the water–air interface for the two depths at $T_b = 50^\circ\text{C}$. It is clear that the velocity at $D = 0.24$ m has a higher value near the interface, which supports our previous finding as reflected in Figure 4.17 and clarifies that the evaporation rate is higher at that time, compared to $D = 0.17$ m. The higher velocity at the interface indicates the higher mass and heat transfer in the form of evaporation from free water surface to the ambient air. However, the horizontal velocity for different temperatures near the water–air interface at $D = 0.17$ m and $D = 0.24$ m is shown in Figure 4.47 and Figure 4.48, respectively. Both depths show that the velocity increases at the water–air interface along with rising temperature. Finally, the streamlines that indicate the direction in which fluid travels at any point in time for different temperatures at $D = 0.17$ m and $D = 0.24$ m are shown in Figure 4.49 and Figure 4.50, respectively.



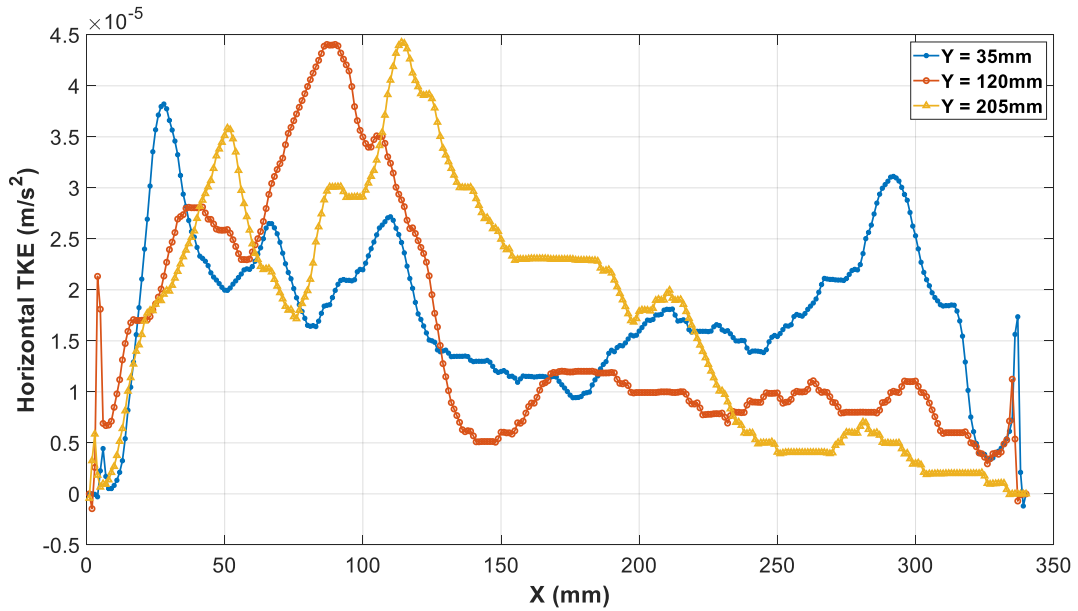
(a)



(b)

Figure 4.45: (a) Turbulent kinetic energy magnitude, (b) XY plot for vertical turbulent kinetic energy, (c) XY plot for horizontal turbulent kinetic energy at $D = 0.24$ m and $T_b = 50^\circ\text{C}$.

Figure 4.45—continued



(c)

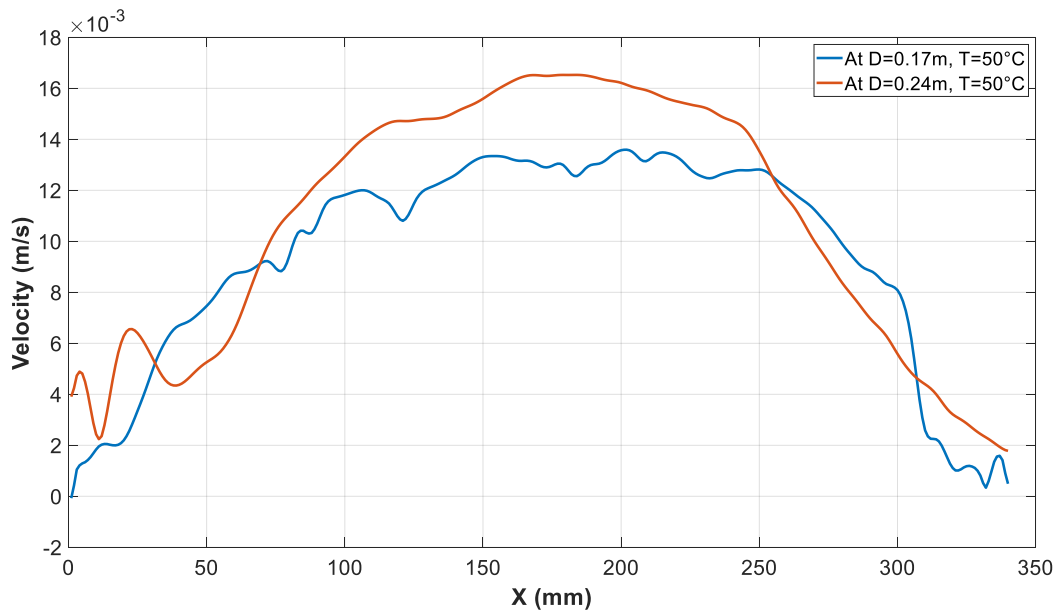


Figure 4.46: Comparison of horizontal velocity near the water–air interface for $T_b = 50^\circ\text{C}$ at $D = 0.17\text{ m}$ and $D = 0.24\text{ m}$.

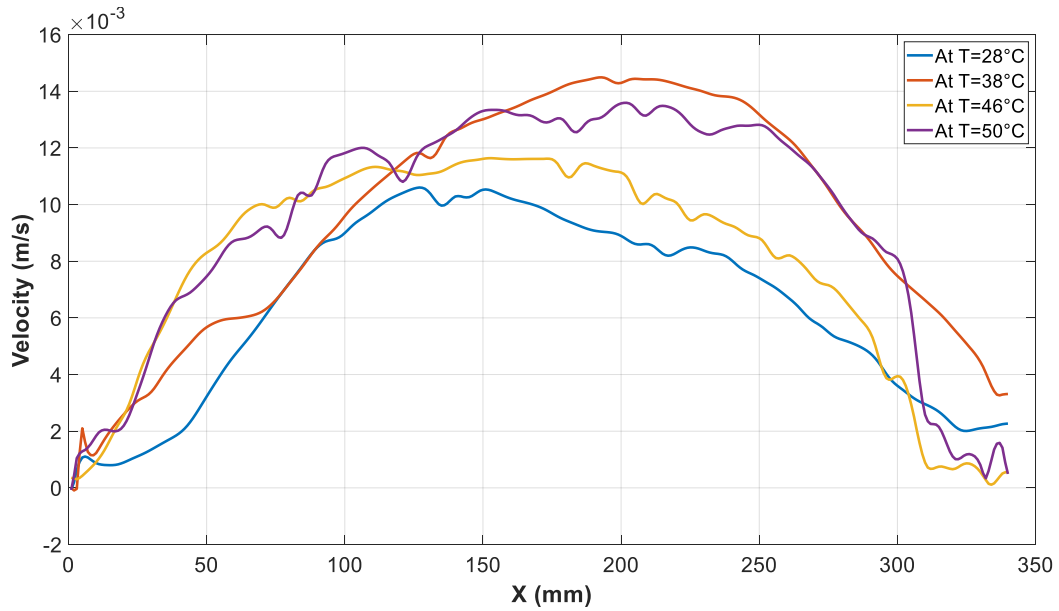


Figure 4.47: Comparison of horizontal velocity near the water–air interface for different temperature at $D = 0.17$ m.

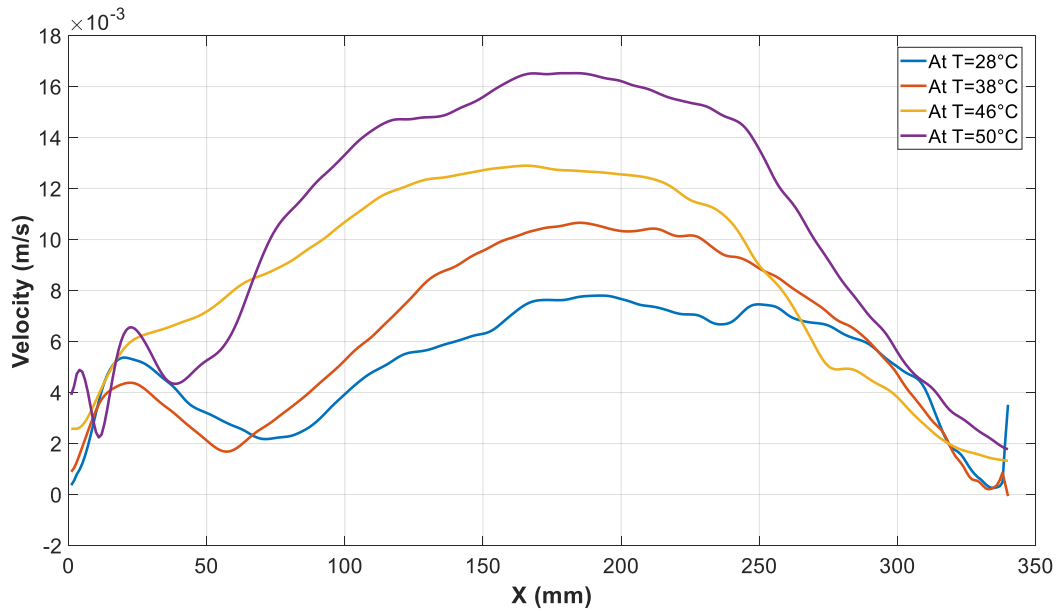


Figure 4.48: Comparison of horizontal velocity near the water–air interface for different temperature at $D = 0.24$ m.

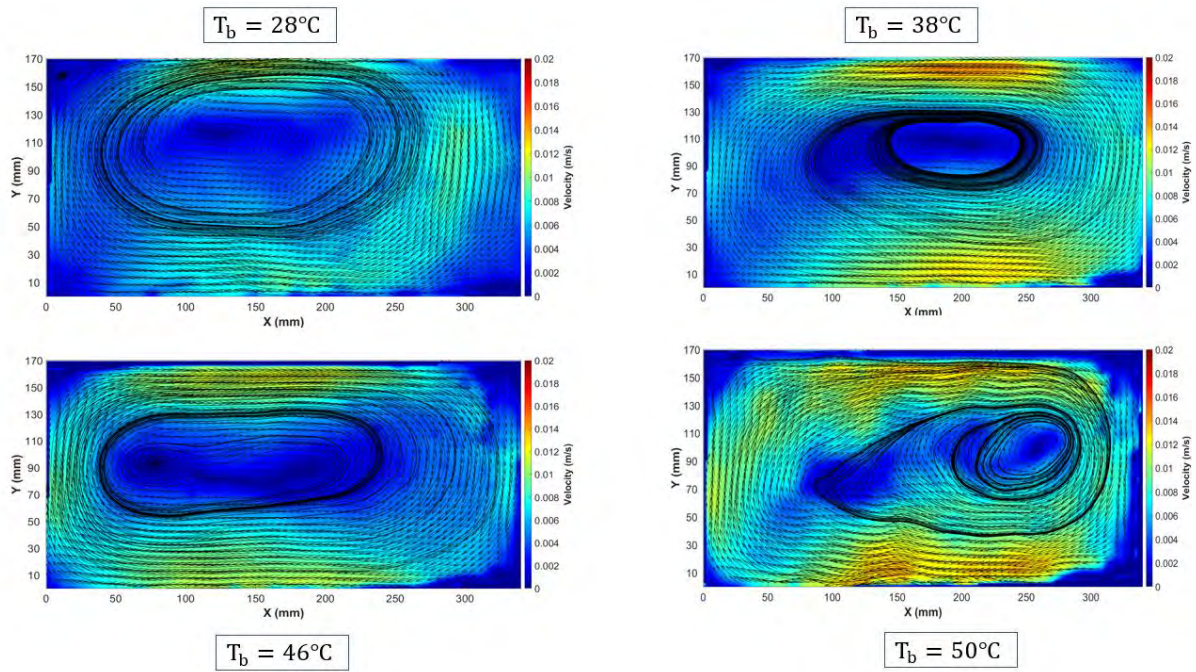


Figure 4.49: Streamlines for different temperatures at $D = 0.17$ m.

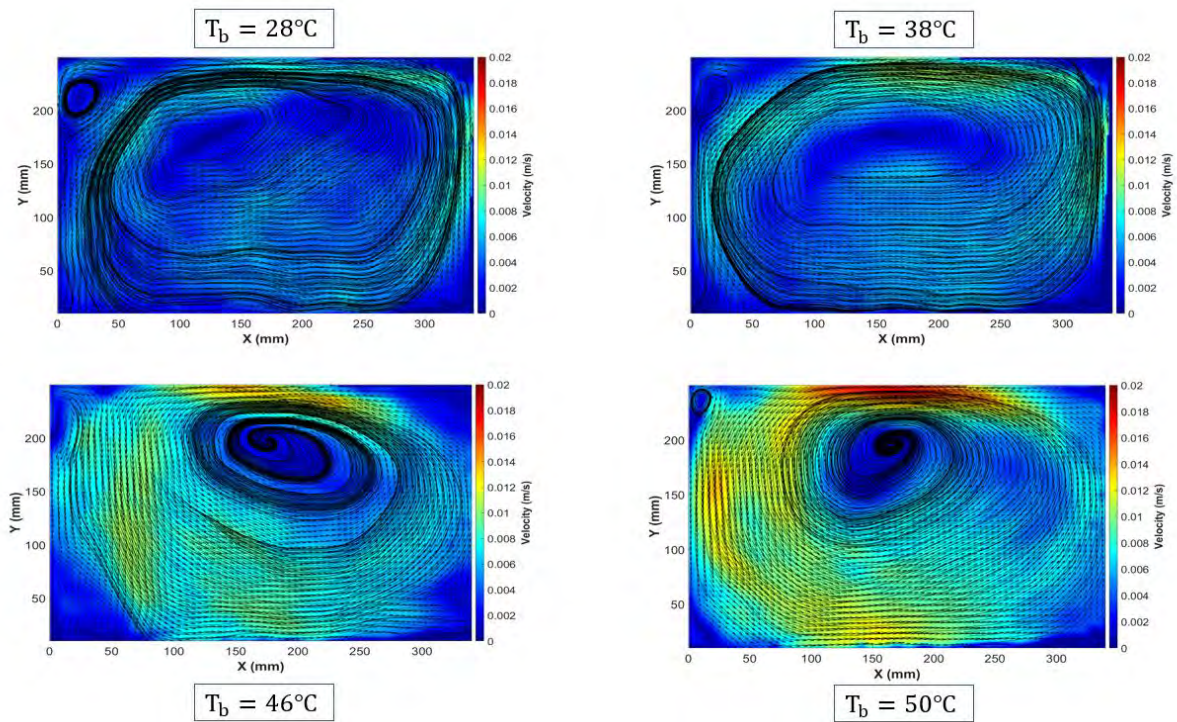


Figure 4.50: Streamlines for different temperatures at $D = 0.24$ m.

4.3 Particle Image Velocimetry (PIV) for Water from the Top

4.3.1 Experimental Setup

In this part, the experiment was conducted to investigate the flow pattern inside the water undergoing evaporation from the top of the tank. As mentioned earlier, most of the previous work studied the flow pattern in case of a closed system, where the top and bottom parts are maintained at fixed temperature. However, in the current work the top part is a free surface undergoing evaporation to ambient air. For the current experiment setup, the same water tank was used along with all the experimental setup discussed previously in section 4.2.1, including thermocouple probes and heater, where the CCD camera was mounted from the top. The schematic and photograph of the experimental setup are shown in Figure 4.51 and Figure 4.52, respectively.

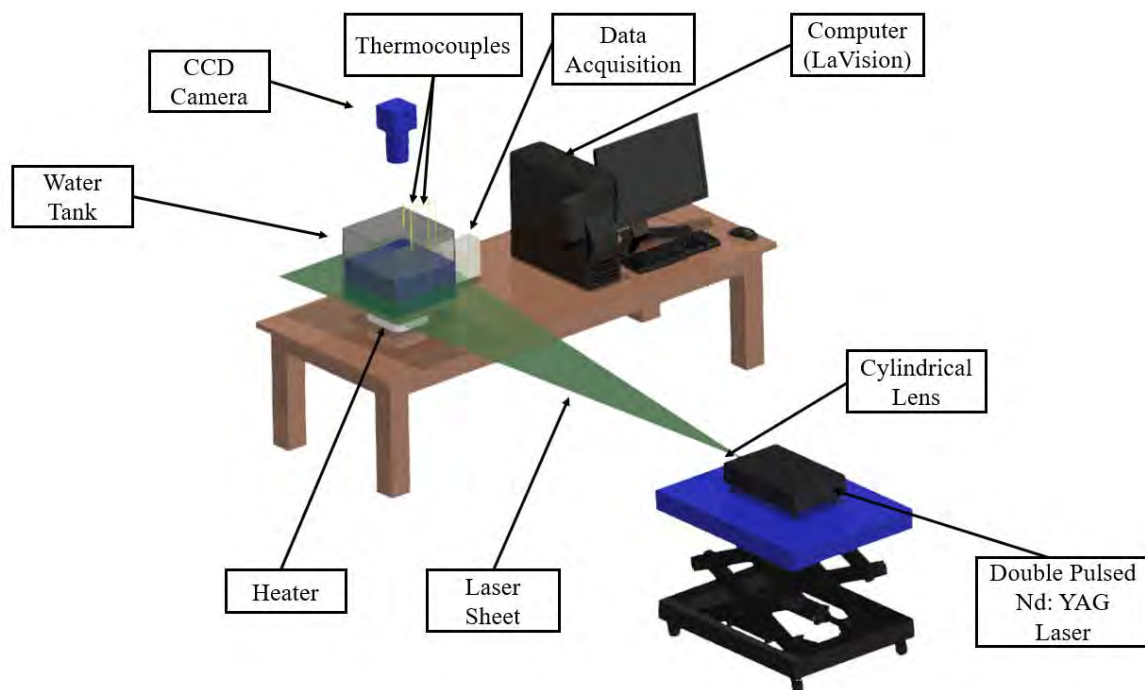


Figure 4.51: Schematic of experimental setup.

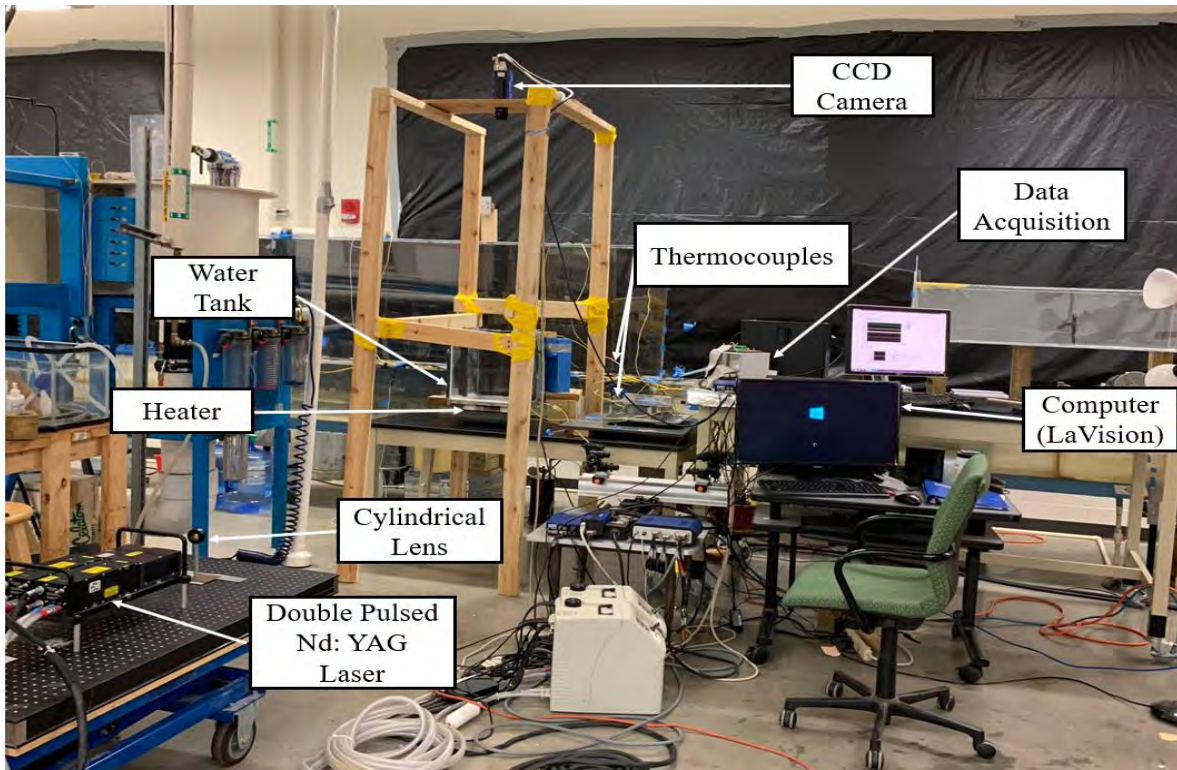


Figure 4.52: Photograph of experimental setup.

4.3.2 Experimental Procedure

The same procedure as discussed in section 4.2.2 was used in this experiment, along with using distilled (purified) water. The change here was of the CCD camera, which was mounted above the water tank at a distance of about 1.5 m in order to have a good view. Also, the camera was set to be perpendicular to the laser sheet, which was horizontal in this experiment. The same calibration plate (Type 11) along with the calibration algorithm in Davis (8.4) was used. However, by taking some images at the beginning, a lot of illumination was found which affected the results. This illumination was coming from the bottom of the tank, which is the aluminum plate. Hence, 838AR Total Ground Carbon Conductive Coating was used to cover the aluminum plate with black in order to reduce the illumination, where the coating allows the temperature to rise at the same time. The resulting data were exported and plotted in MATLAB for averaging of 50 images. Note that

the reason for reducing the number of averaging images was to show the flow pattern. Although the velocity is small, the flow pattern changes fast, so the number of averaging images was reduced to follow the flow pattern. Two frames of the row of images before processing at t_i and $t_{i+\Delta t}$ are shown in Figure 4.53.



Figure 4.53: Two frames of the row of images before processing at t_i and $t_{i+\Delta t}$.

4.3.3 Results and Discussion

The results obtained from the third part of the experimental work are presented and discussed here. The experimental setup for this part was built to investigate the flow pattern from the top view of the water tank undergoing evaporation at $D = 0.24$ m. Two investigations were conducted, one being the flow pattern for variation in temperature at a fixed elevation of $D = 0.12$ m and the other the flow pattern for different elevations at a fixed temperature $T_b = 40^\circ\text{C}$.

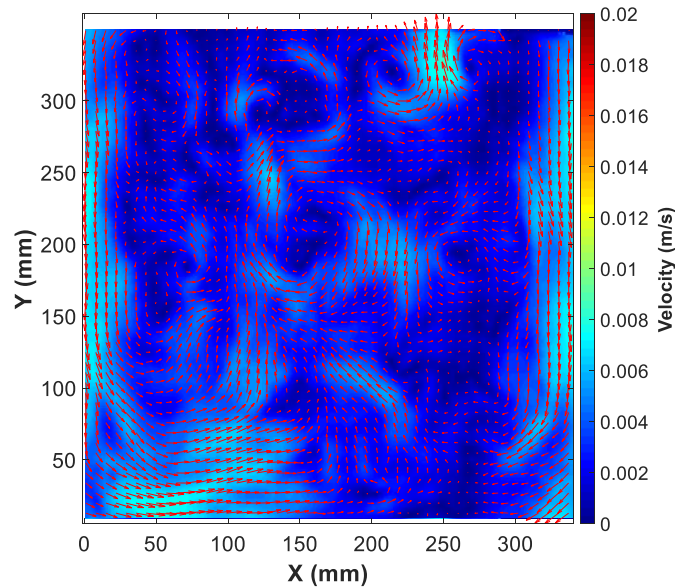
1) At different Temperature along with fixed elevation $D = 0.12$ m

1.1) At $T_b = 28^\circ\text{C}$

(a) Velocity

Figure 4.54 shows the velocity flow pattern from the top view at $T_b = 28^\circ\text{C}$. As evident in Figure 4.54 (a), the flow pattern starts to develop as a small vortex. This vortex is known as Bénard

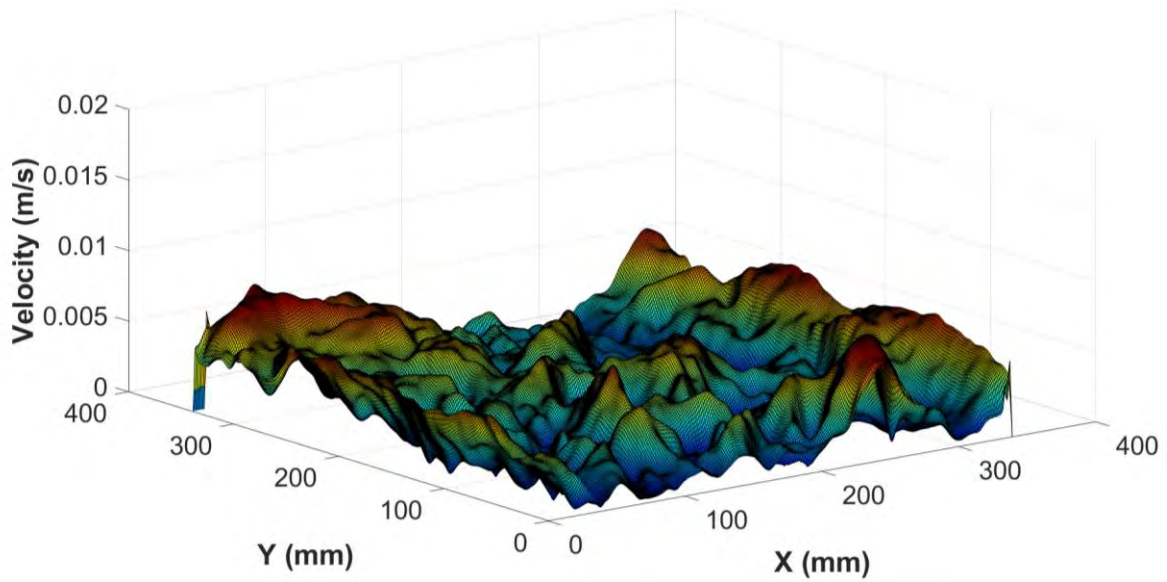
cells, where these cells appear due to the buoyancy and gravity along with density change. The Bénard cells are well known and studied in the literature in the case of fixed temperature from the top and bottom plates, which is not the case in the current work. In the current study, these cells are investigated for a free water surface undergoing evaporation. However, it is clear from Figure 4.54 (a) that a higher velocity appears at the wall of the tank. This can be seen in Figure 4.54 (b), where the velocity magnitude at the surface is plotted. The peaks in Figure 4.54 (b) represent the cells in the middle of the tank. Figure 4.54 (c) shows the velocity at different X locations, where the fluctuations are clearly visible.



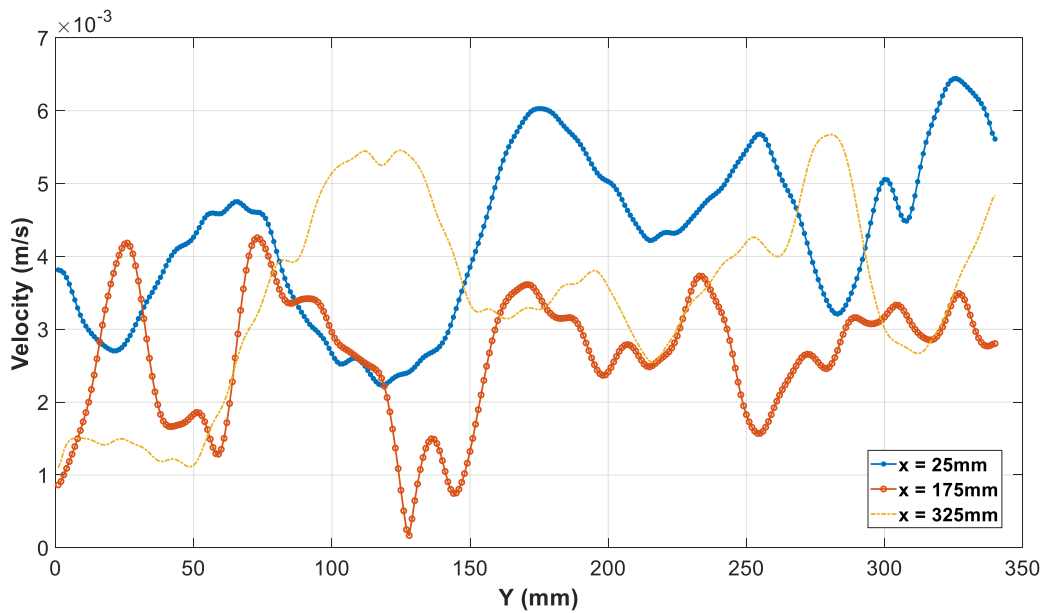
(a)

Figure 4.54: (a) Velocity magnitude, (b) Surface velocity magnitude, (c) XY plot for velocity at $T_b = 28^\circ\text{C}$.

Figure 4.54—continued



(b)

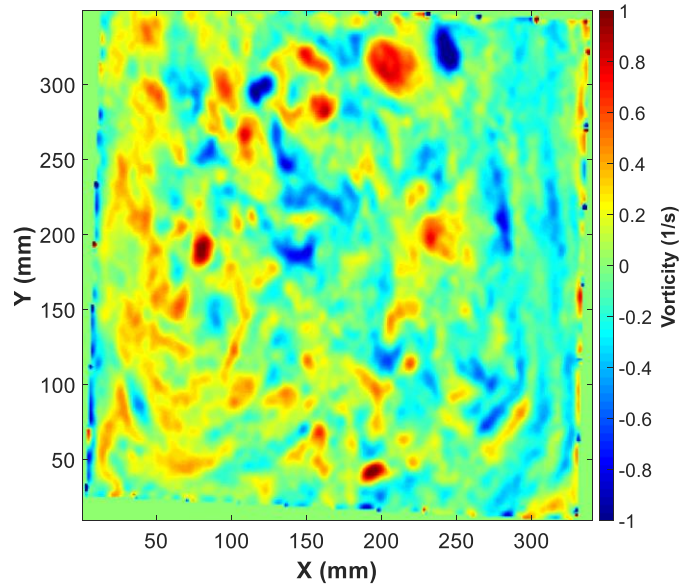


(c)

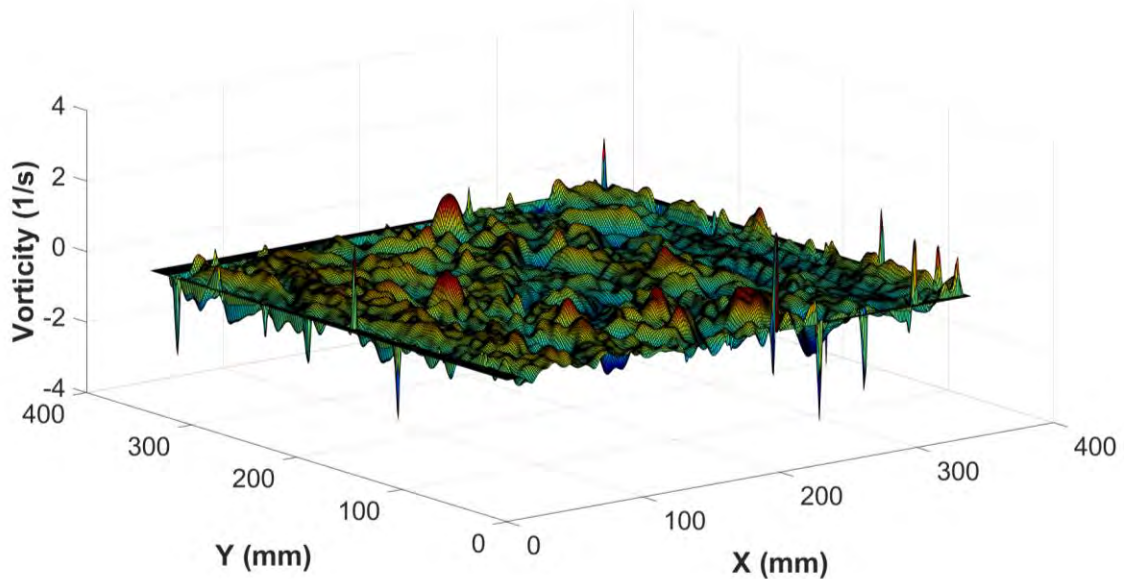
(b) Vorticity

The vorticity is shown in Figure 4.55. Figure 4.55 (a) shows the vorticity magnitude, where it is clear that some negative and positive values appear due to the different directions of the cells'

rotation. This can be seen in Figure 4.55 (b), where the negative and positive vorticities are shown as peaks, which clearly represent the rotation of Bénard cells. Figure 4.55 (c) shows the fluctuations of the vorticity at different points on the X axis.



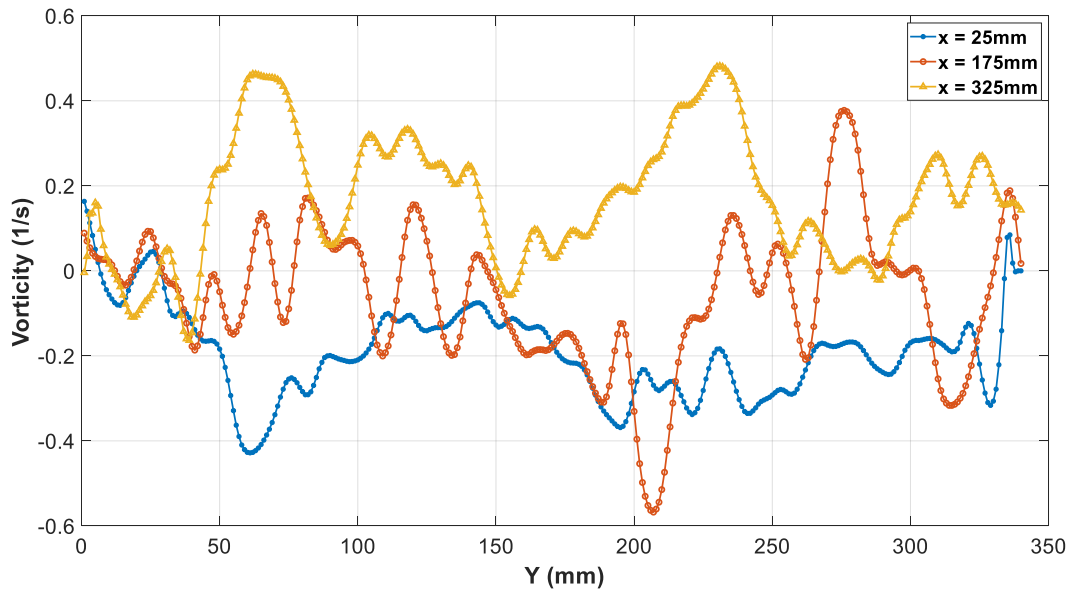
(a)



(b)

Figure 4.55: (a) Vorticity magnitude, (b) Surface vorticity magnitude, (c) XY plot for vorticity at $T_b = 28^\circ\text{C}$.

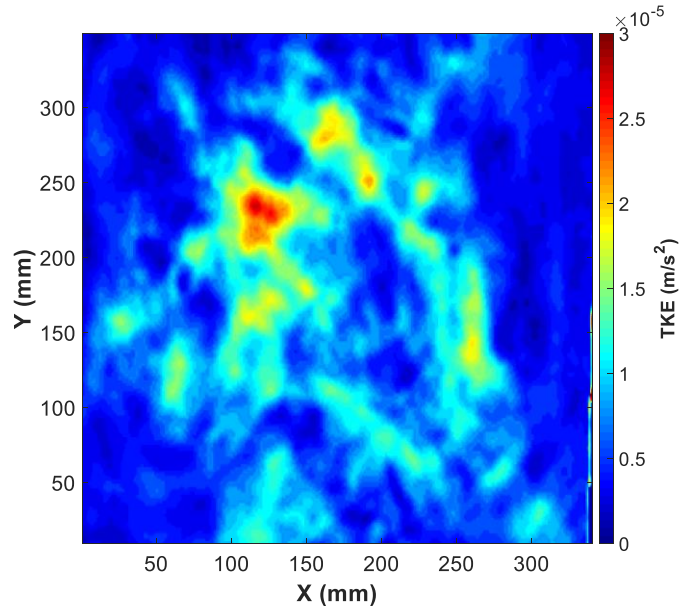
Figure 4.55—continued



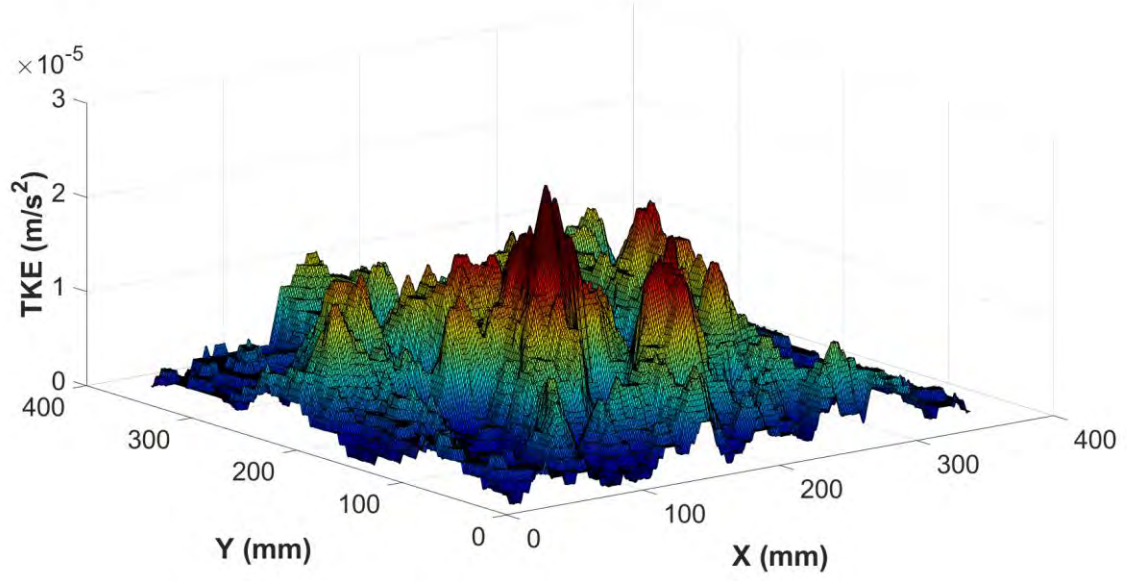
(c)

(c) Turbulent Kinetic Energy

The turbulent kinetic energy at $T_b = 28^\circ\text{C}$ is presented in Figure 4.56. Figure 4.56 (a) shows the turbulent kinetic energy, where a higher value appears at the middle due to surface evaporation at this region. This is even clearer in Figure 4.56 (b), where the turbulent kinetic energy is very small near the walls and higher in the middle of the water tank. The turbulent kinetic energy is plotted at different points on the X axis in Figure 4.56 (c), where it shows a higher value at the center ($X = 175$ mm).



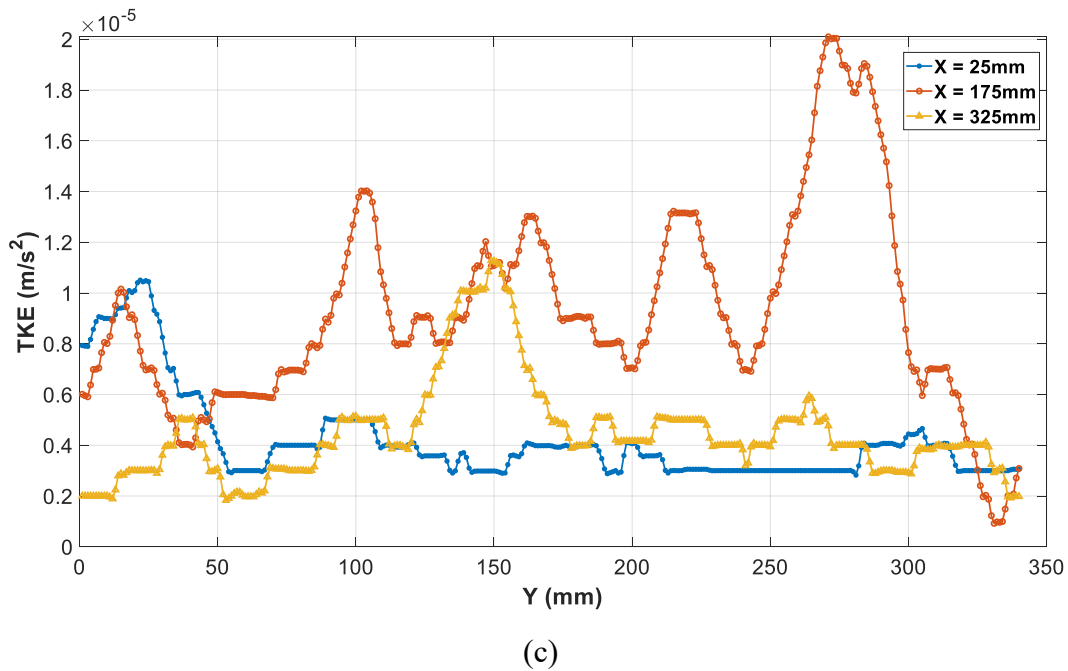
(a)



(b)

Figure 4.56: (a) TKE magnitude, (b) Surface TKE magnitude, (c) XY plot for TKE at $T_b = 28^\circ\text{C}$.

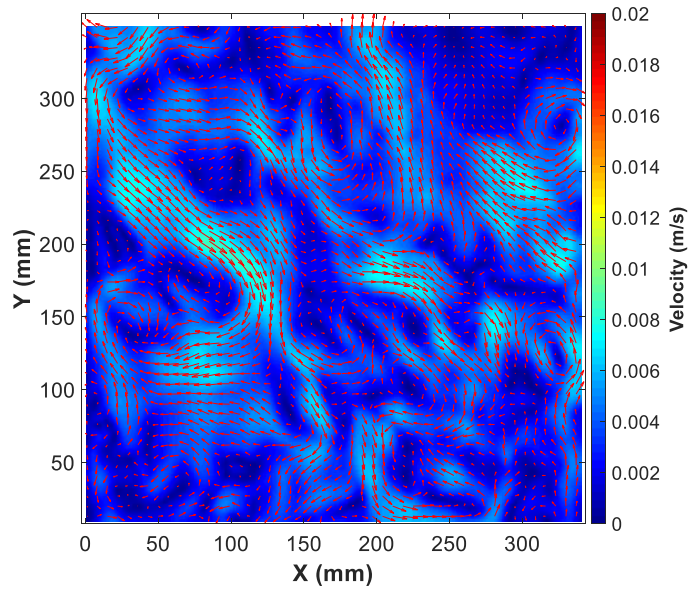
Figure 4.56—continued



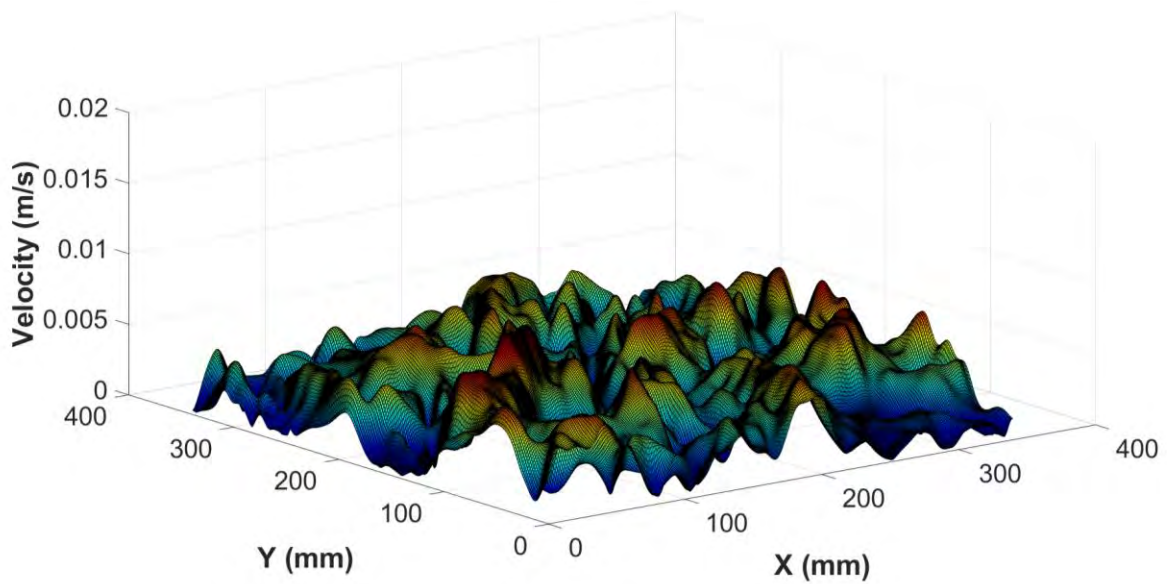
1.2) At $T_b = 38^\circ\text{C}$

(a) Velocity

Figure 4.57 shows the velocity flow pattern from the top view at $T_b = 38^\circ\text{C}$. As can be seen in Figure 4.57 (a), more vortices start to appear compared to $T_b = 28^\circ\text{C}$. Moreover, the velocity at this time shows a higher value along with more rotating cells, which is mainly due to the increasing temperature. This can be seen in Figure 4.57 (b), where the velocity magnitude at the surface is plotted, with the peaks in Figure 4.57 (b) representing the cells in the middle of the tank. Figure 4.57 (c) shows the velocity at different X locations, where the fluctuations are clearly shown.



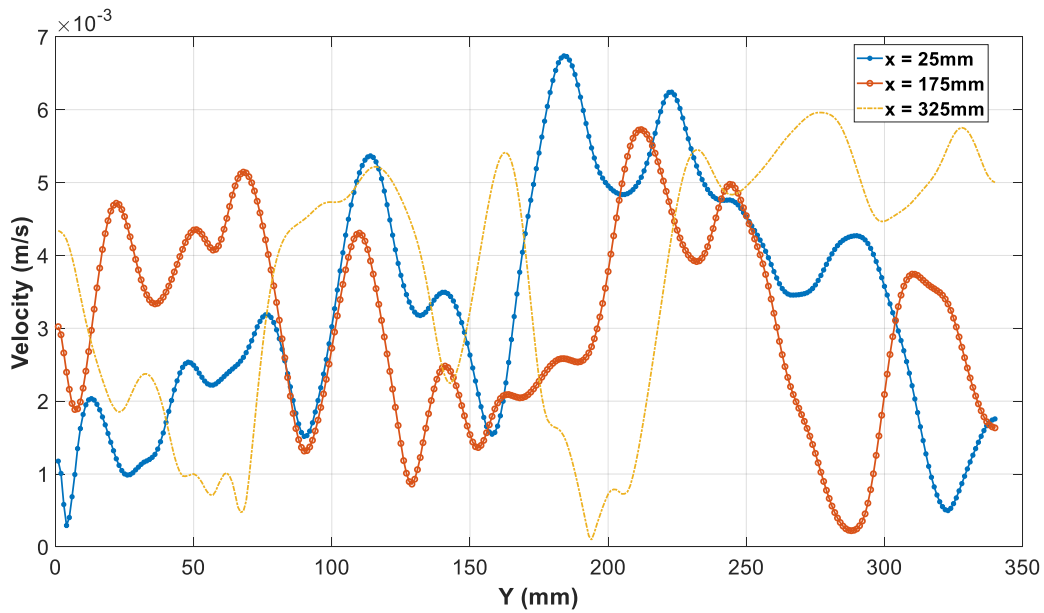
(a)



(b)

Figure 4.57: (a) Velocity magnitude, (b) Surface velocity magnitude, (c) XY plot for velocity at $T_b = 38^\circ\text{C}$.

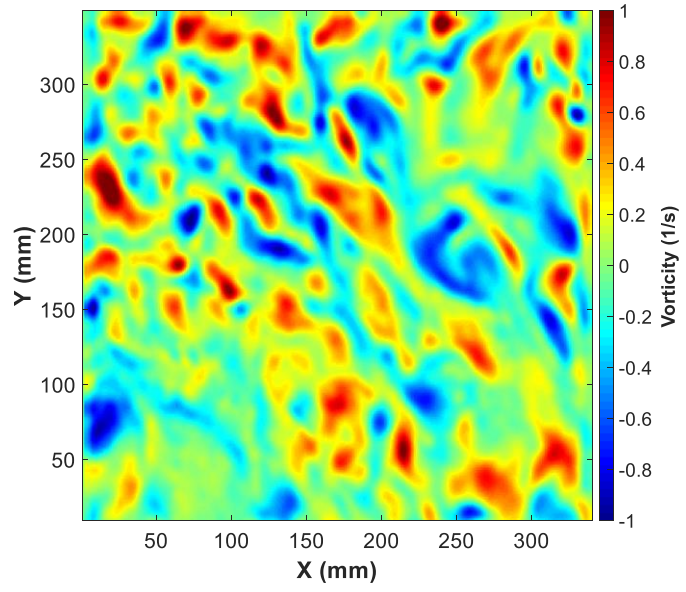
Figure 4.57—continued



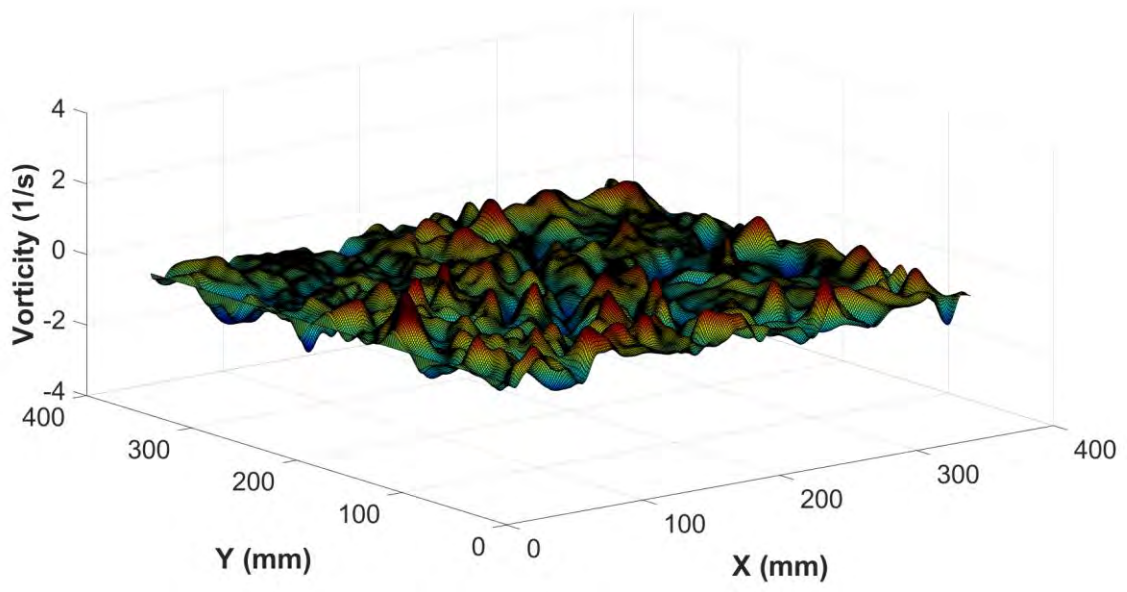
(c)

(b) Vorticity

The vorticity is presented in Figure 4.58. Figure 4.58 (a) shows the vorticity magnitude, where it is clear that some negative and positive values appear due to the different directions of rotation of the cells, being higher at this time compared to $T_b = 28^\circ\text{C}$. This is evident from Figure 4.58 (b), where the negative and positive vorticities are shown as peaks which clearly represent the rotation of Bénard cells. Figure 4.58 (c) shows the fluctuations of vorticity at different points on the X axis.



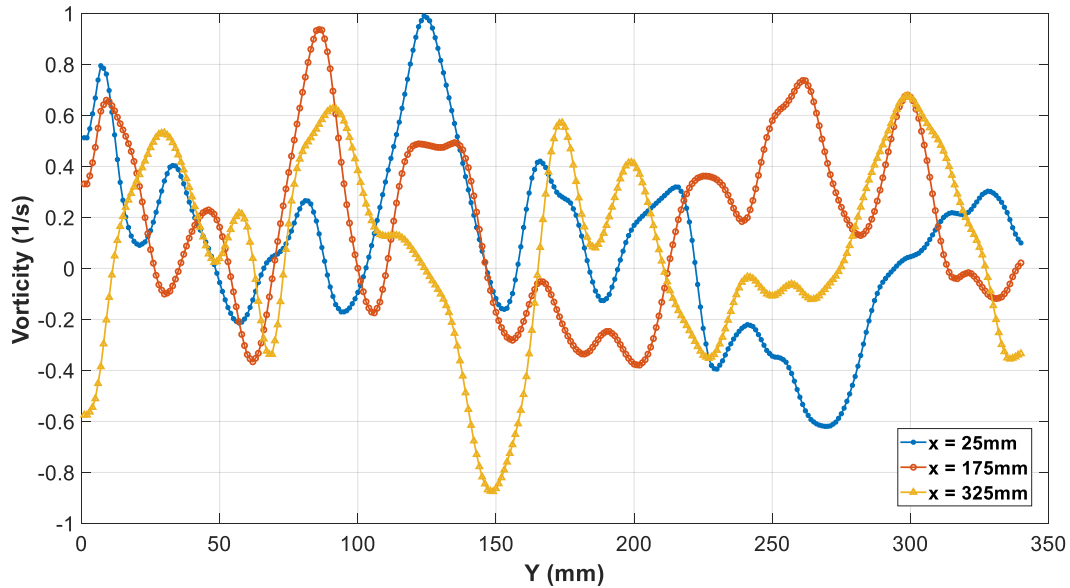
(a)



(b)

Figure 4.58: (a) Vorticity magnitude, (b) Surface vorticity magnitude, (c) XY plot for vorticity at $T_b = 38^\circ\text{C}$.

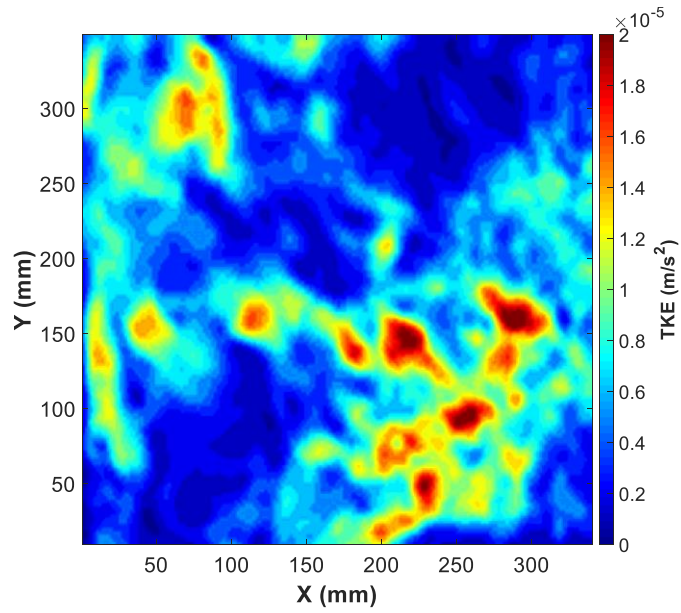
Figure 4.58—continued



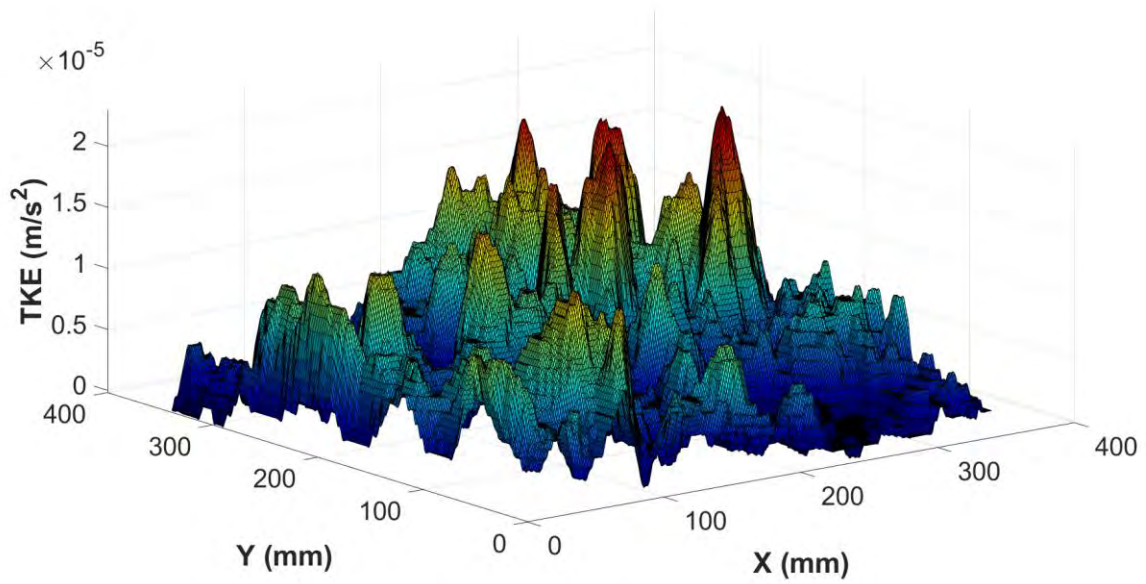
(c)

(c) Turbulent Kinetic Energy

The turbulent kinetic energy at $T_b = 38^\circ\text{C}$ is presented in Figure 4.59. Figure 4.59 (a) shows the turbulent kinetic energy, where a higher value appears at the right side of the tank. This can be related to the effect of surface evaporation at this region. This becomes clearer in Figure 4.59 (b), where the turbulent kinetic energy is very small near the walls and higher in the middle of the water tank. The turbulent kinetic energy is plotted at different points on the X axis in Figure 4.59 (c), where it shows a higher value at the center ($X = 175 \text{ mm}$), which is the middle of the tank.



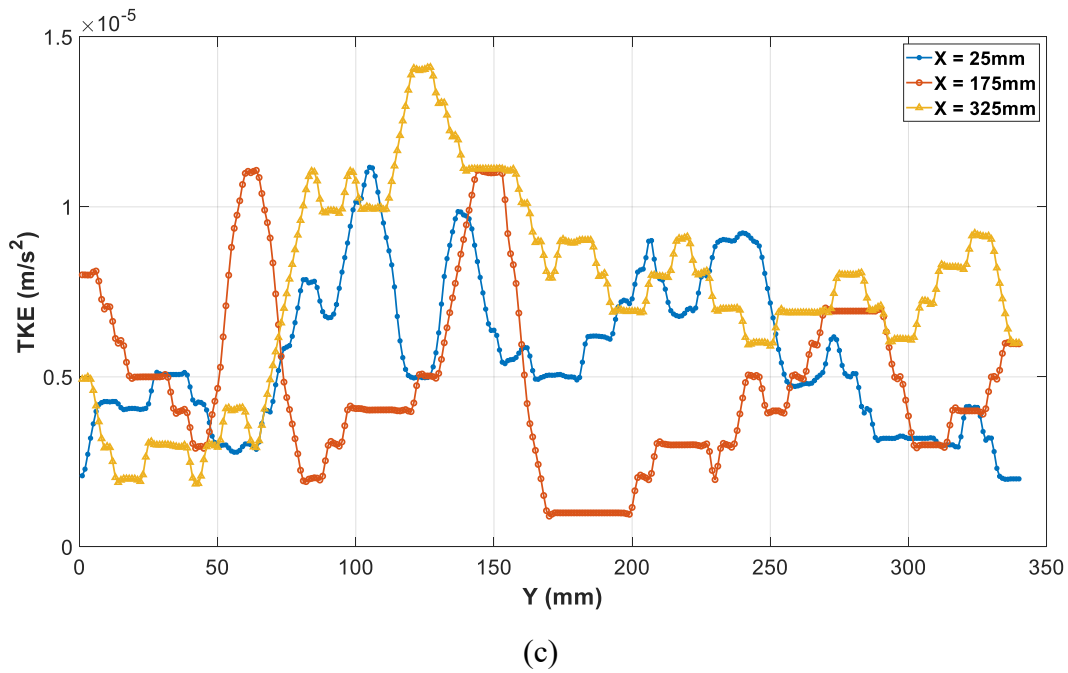
(a)



(b)

Figure 4.59: (a) TKE magnitude, (b) Surface TKE magnitude, (c) XY plot for TKE at $T_b = 38^\circ\text{C}$.

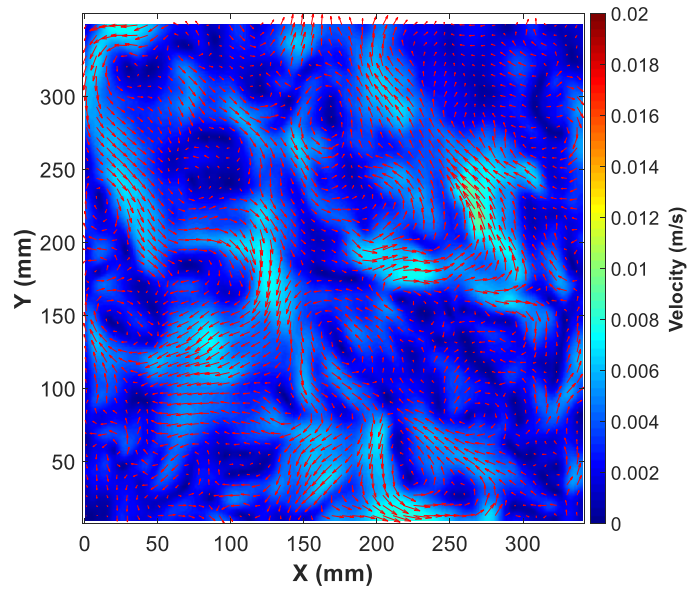
Figure 4.59—continued



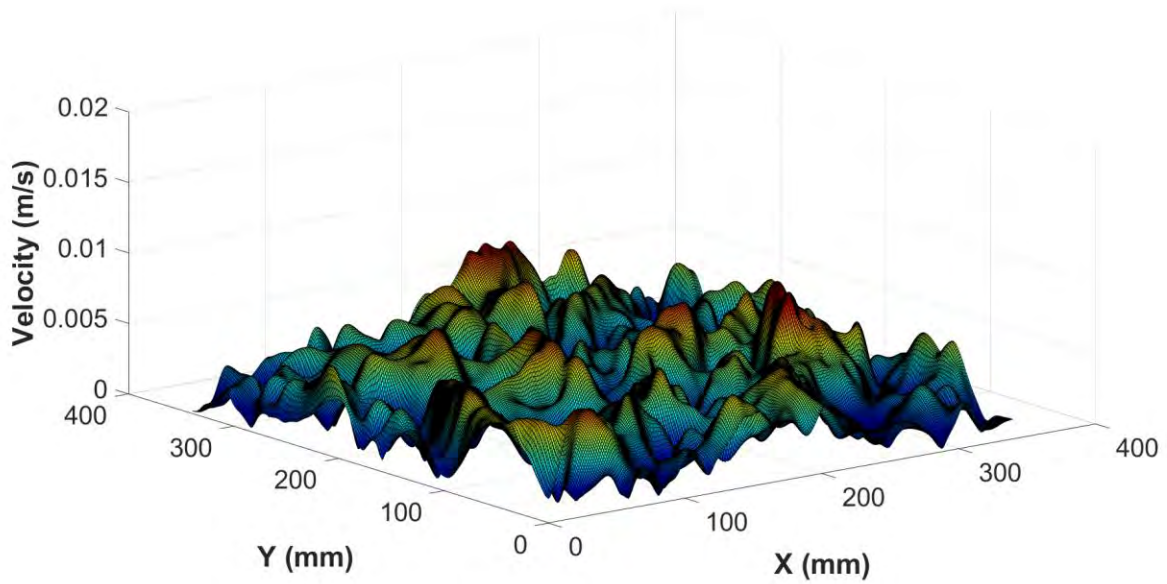
1.3) At $T_b = 48^\circ\text{C}$

(a) Velocity

Figure 4.60 shows the velocity flow pattern from the top view at $T_b = 48^\circ\text{C}$. As can be seen in Figure 4.60 (a), more and higher vortices start to appear compared to $T_b = 38^\circ\text{C}$, which is related to the rise in temperature and the effect of evaporation. This is visible in Figure 4.60 (b), where the velocity magnitude at the surface has been plotted, with the peaks representing the cells in the middle of the tank. Figure 4.60 (c) shows the velocity at different X locations, where the fluctuations are clearly shown.



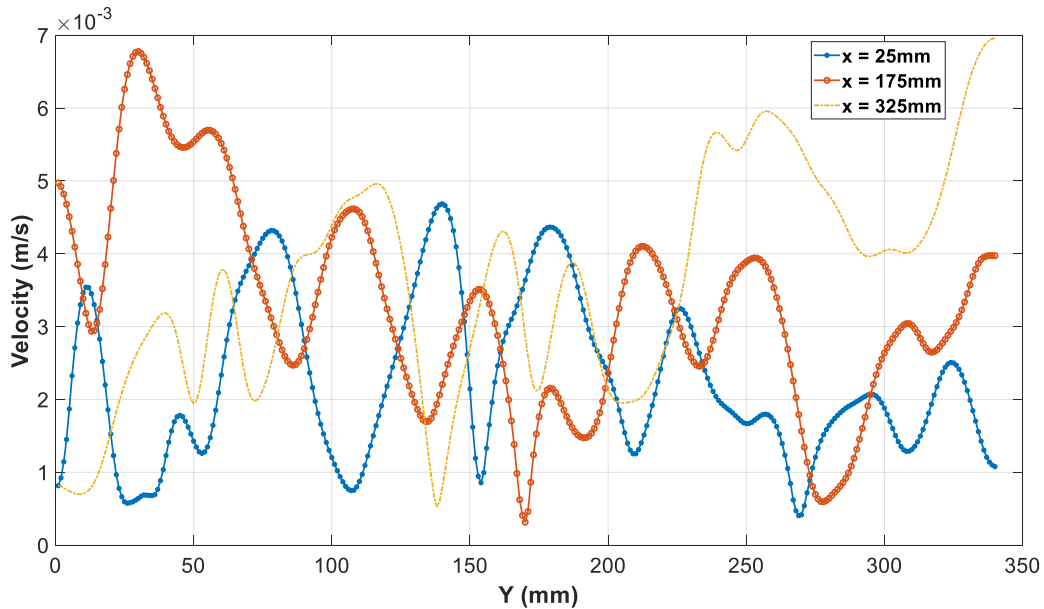
(a)



(b)

Figure 4.60: (a) Velocity magnitude, (b) Surface velocity magnitude, (c) XY plot for velocity at $T_b = 48^\circ\text{C}$.

Figure 4.60—continued



(c)

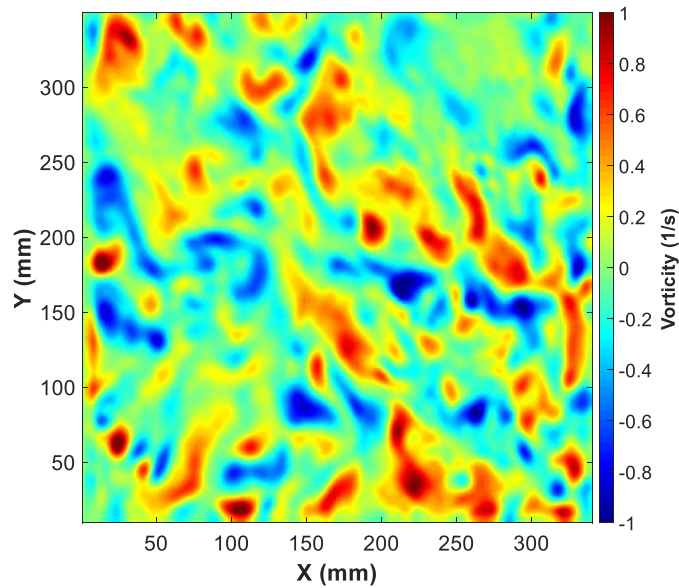
(b) Vorticity

The vorticity is shown in Figure 4.61. At this time more and higher vortices appear due to the increase in temperature and evaporation, as can be seen in Figure 4.61 (a). However, some negative and positive values appear due to different directions of rotation of the cells. This can be seen in Figure 4.61 (b), where the negative and positive vorticities are shown as peaks, which clearly represent the rotation of Bénard cells. Figure 4.61 (c) shows the fluctuations of vorticity at different points on the X axis.

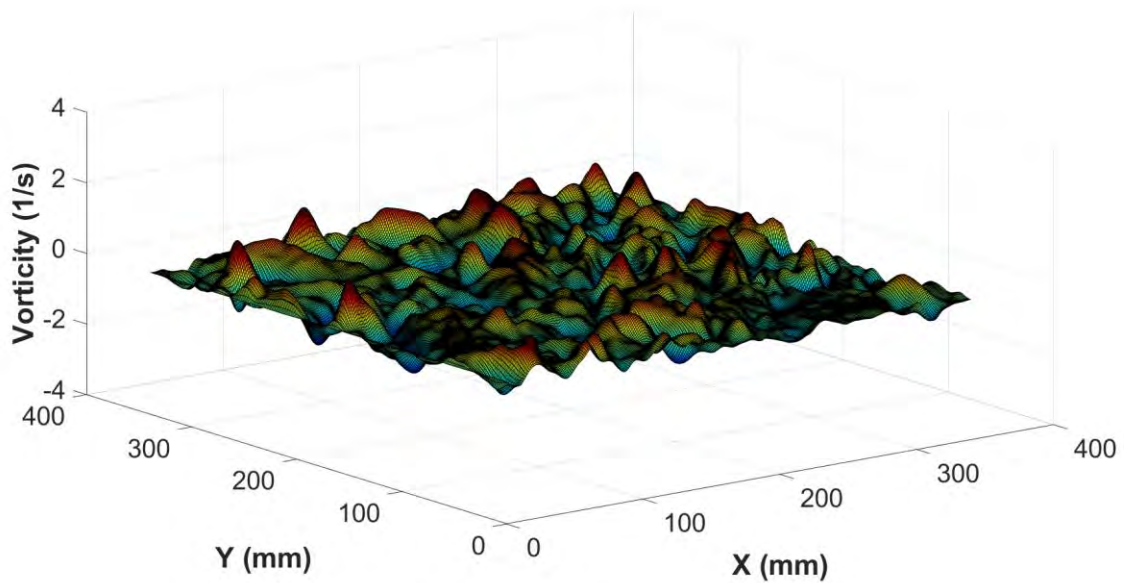
(c) Turbulent Kinetic Energy

The turbulent kinetic energy at $T_b = 48^\circ\text{C}$ is shown in Figure 4.62. Figure 4.62 (a) shows the turbulent kinetic energy, where a higher value appears at the right side of the tank, which can be related to the effect of surface evaporation at this region. This becomes clearer in Figure 4.62

(b), where the turbulent kinetic energy is very small near the walls and higher at this region of the water tank. The turbulent kinetic energy is plotted at different points on X axis in Figure 4.62 (c).



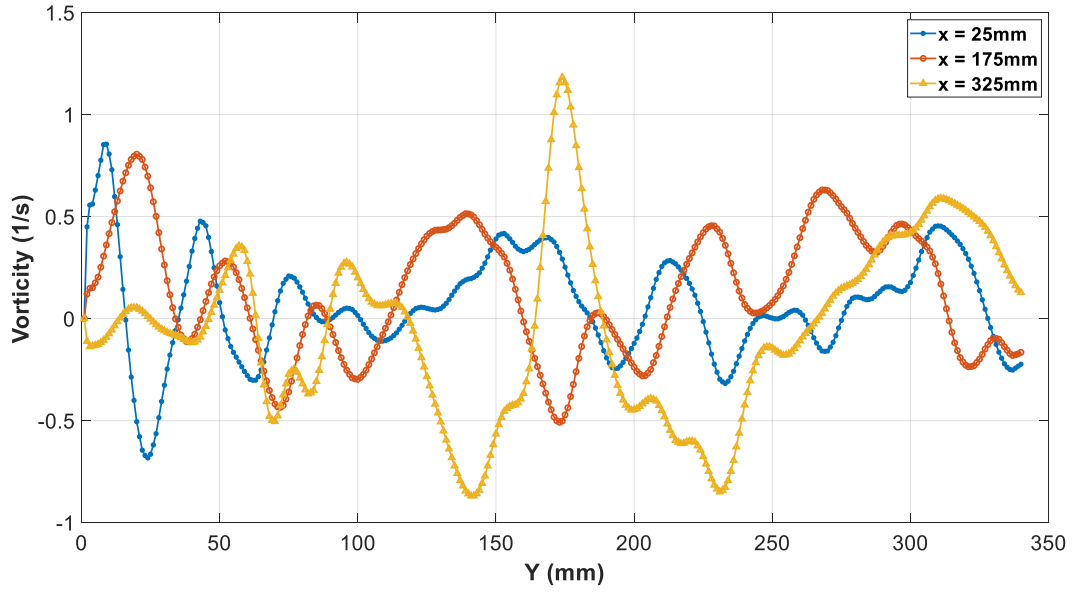
(a)



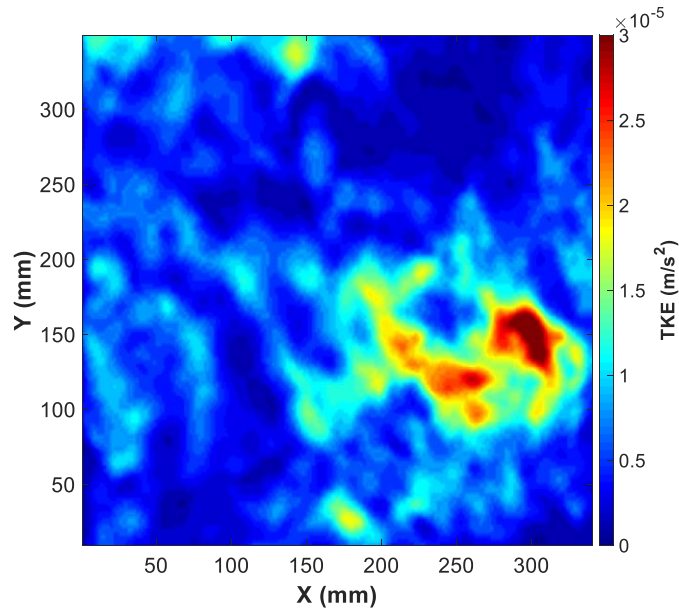
(b)

Figure 4.61: (a) Vorticity magnitude, (b) Surface vorticity magnitude, (c) XY plot for vorticity at $T_b = 48^\circ\text{C}$.

Figure 4.61—continued



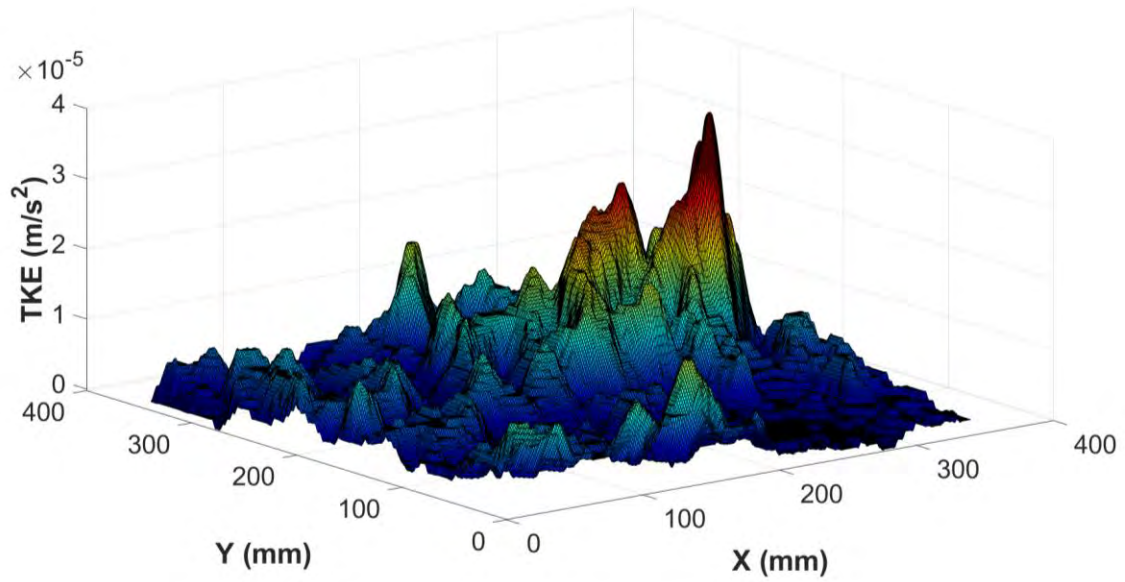
(c)



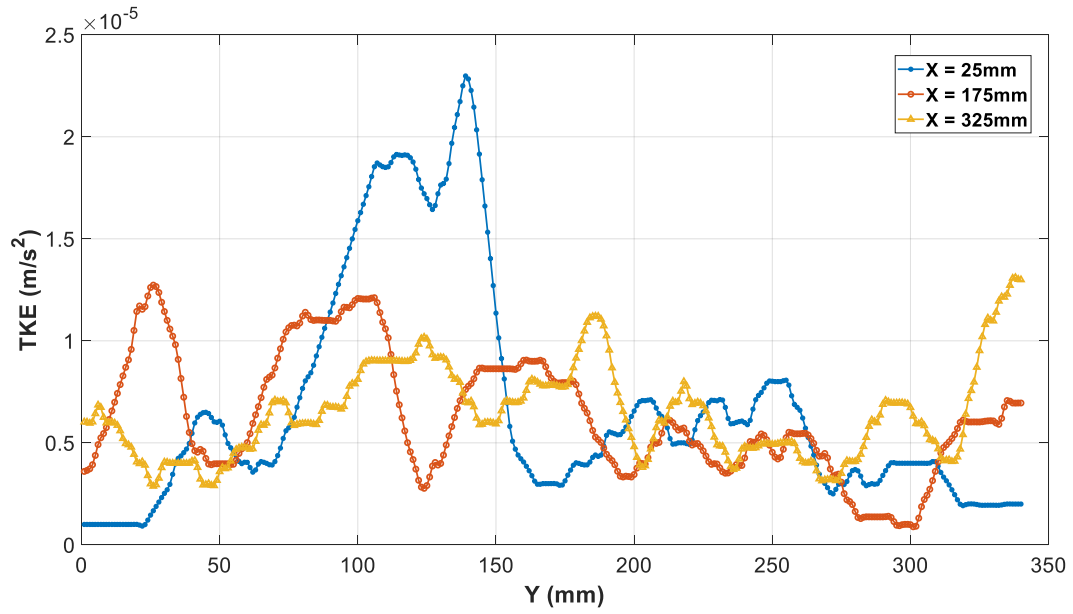
(a)

Figure 4.62: (a) TKE magnitude, (b) Surface TKE magnitude, (c) XY plot for TKE at $T_b = 48^\circ\text{C}$.

Figure 4.62—continued



(b)

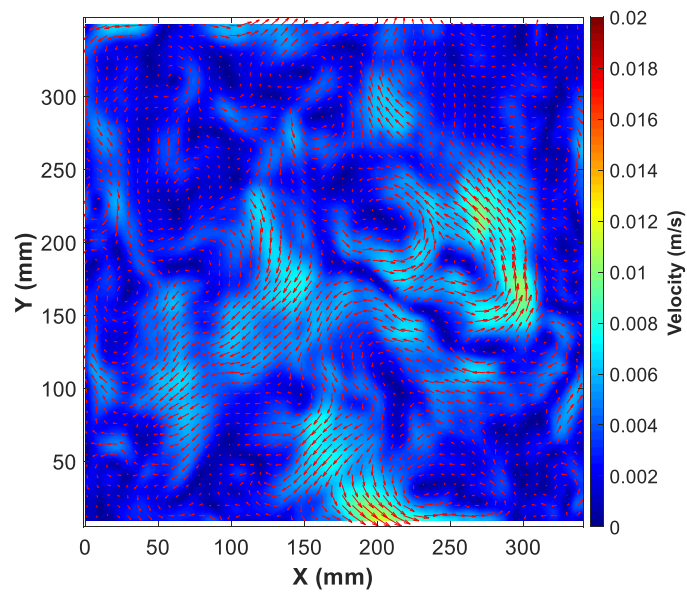


(c)

1.4) At $T_b = 50^\circ\text{C}$

(a) Velocity

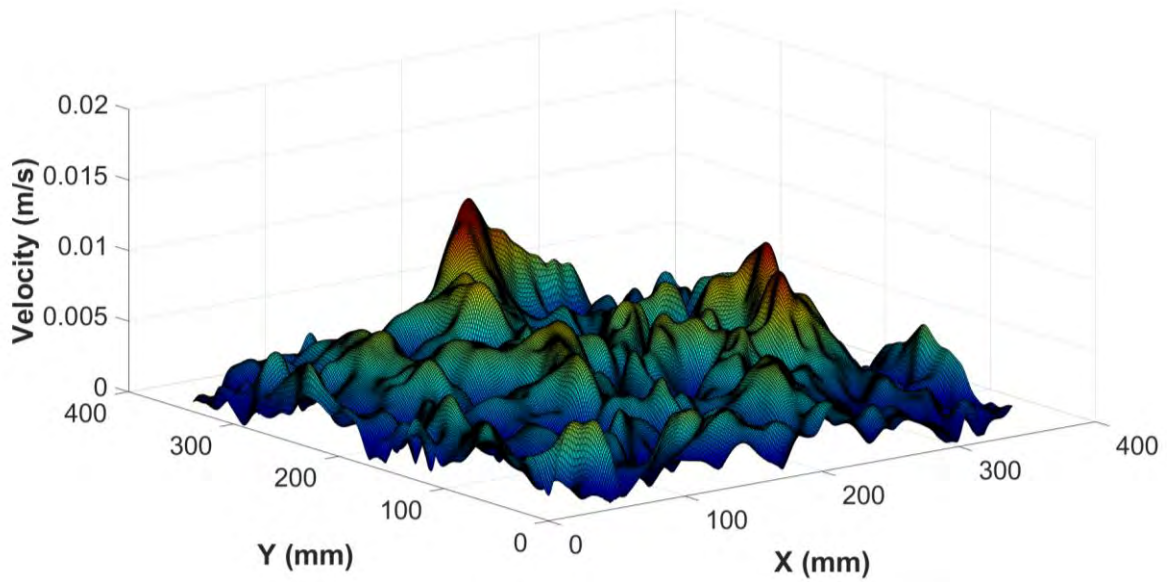
Figure 4.63 shows the velocity flow pattern from the top view at $T_b = 50^\circ\text{C}$, which is the desirable temperature for the current study. As can be seen in Figure 4.63 (a), some more and higher vortexes appear compared to $T_b = 48^\circ\text{C}$, which is related to the rising temperature and the effect of evaporation. This is visible in Figure 4.63 (b), wherein the surface velocity magnitude is plotted, with the peaks representing the cells in the middle of the tank. Figure 4.63 (c) shows the velocity at different X locations, where the fluctuations are clearly shown.



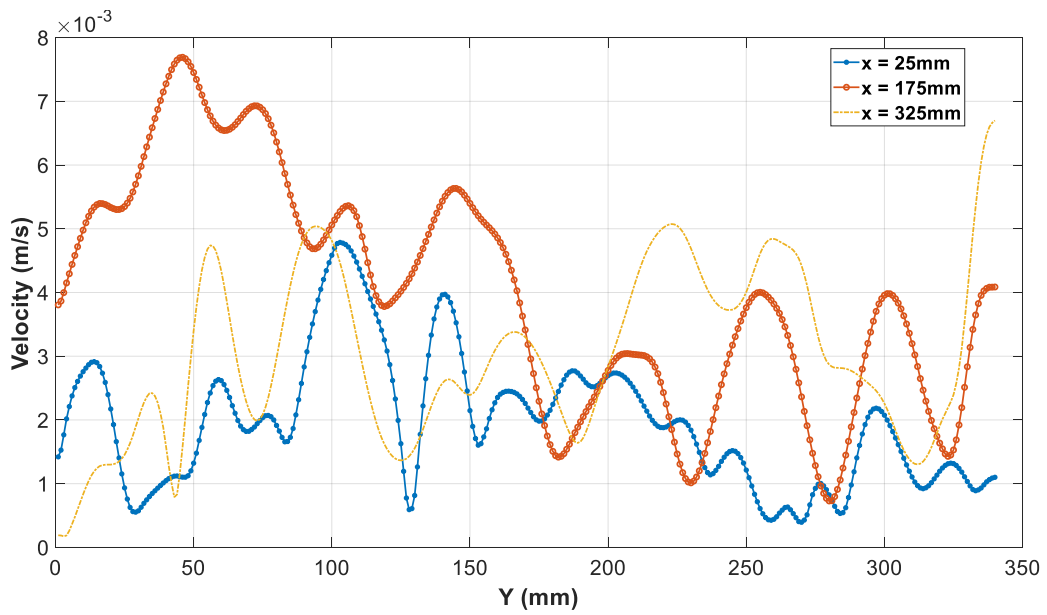
(a)

Figure 4.63: (a) Velocity magnitude, (b) Surface velocity magnitude, (c) XY plot for velocity at $T_b = 50^\circ\text{C}$.

Figure 4.63—continued



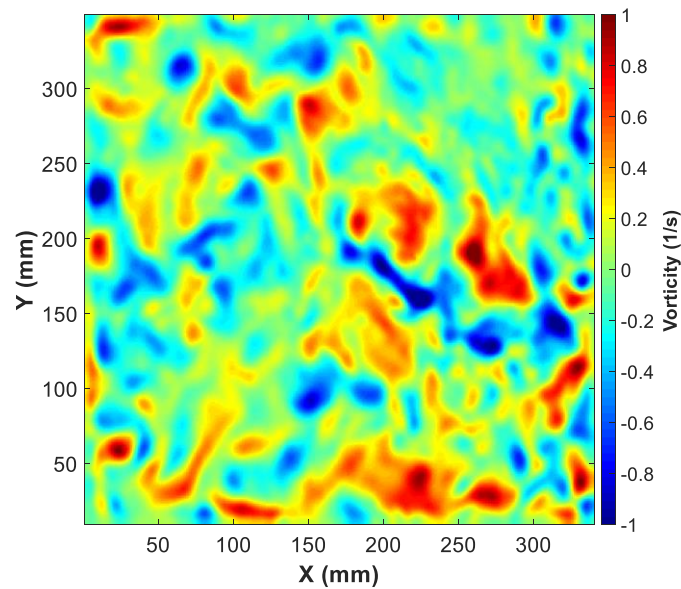
(b)



(c)

(b) Vorticity

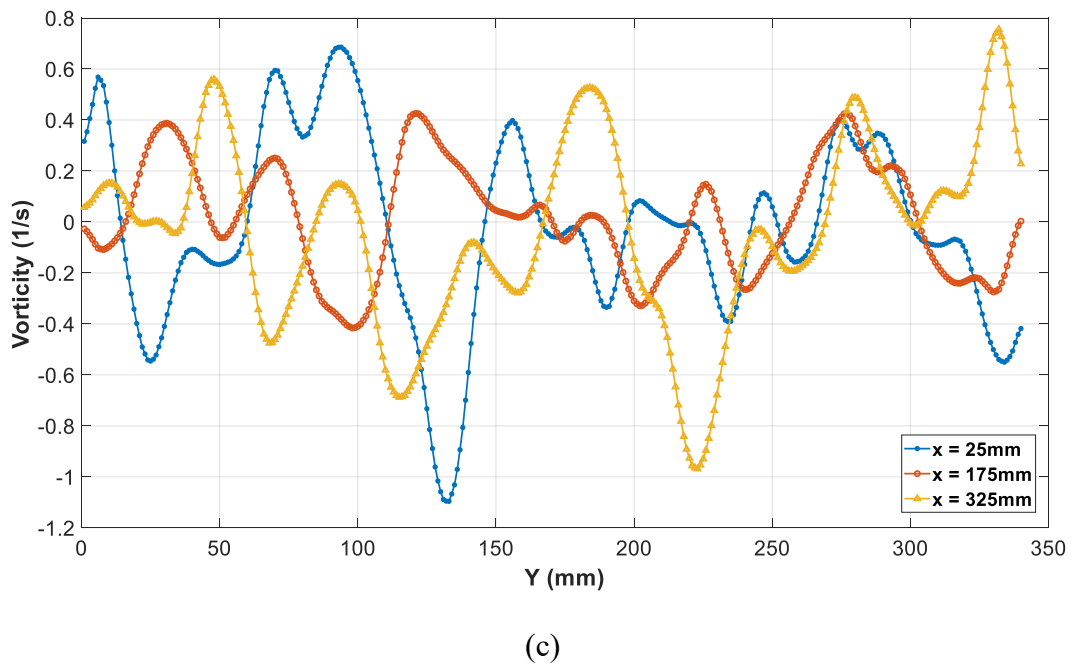
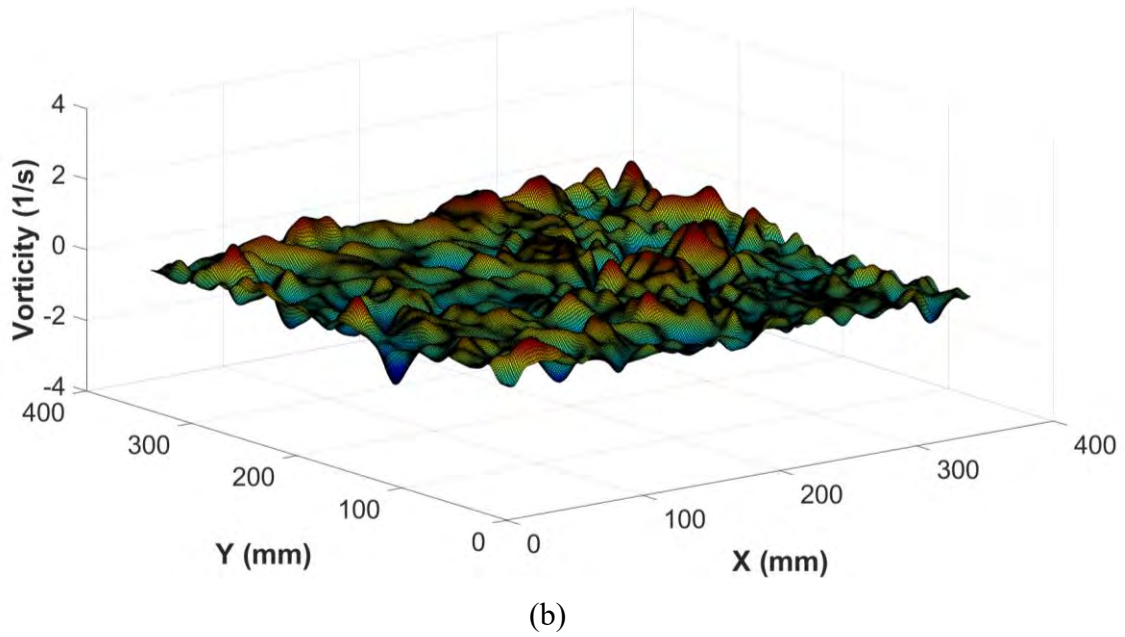
Figure 4.64 presents the vorticity. At this time higher vortices appear due to the increase in temperature and evaporation, as can be seen in Figure 4.64 (a). However, some negative and positive values appear due to the different directions of rotation of the cells. This is evident in Figure 4.64 (b), where the negative and positive vorticities are shown as peaks which clearly represent the rotation of Bénard cells. Figure 4.64 (c) shows the fluctuations of vorticity at different points on the X axis.



(a)

Figure 4.64: (a) Vorticity magnitude, (b) Surface vorticity magnitude, (c) XY plot for vorticity at $T_b = 50^\circ\text{C}$.

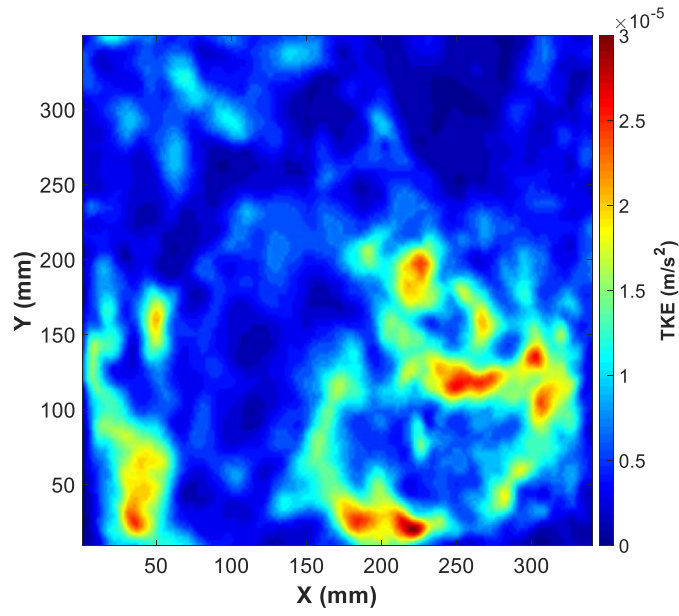
Figure 4.64—continued



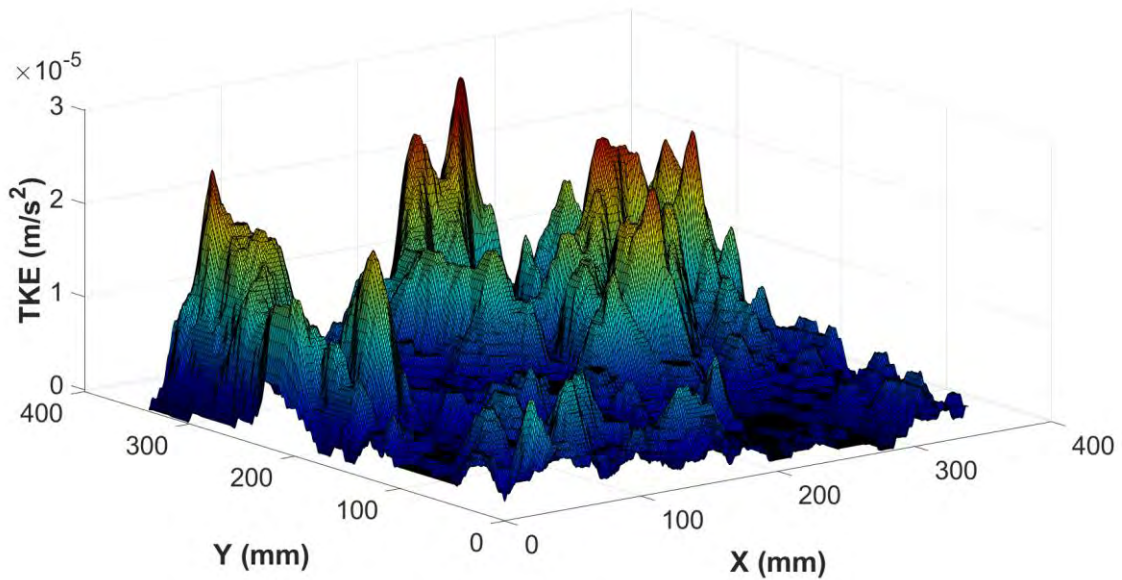
(c) Turbulent Kinetic Energy

Figure 4.65 presents the turbulent kinetic energy at $T_b = 50^\circ\text{C}$. Figure 4.65 (a) shows the turbulent kinetic energy, where a higher value appears close to the middle of the tank, which can

be related to the effect of surface evaporation at this region. This becomes clearer in Figure 4.65 (b), where the turbulent kinetic energy is very small near the walls and higher at this region of the water tank. The turbulent kinetic energy is plotted at different points on X axis in Figure 4.65 (c).



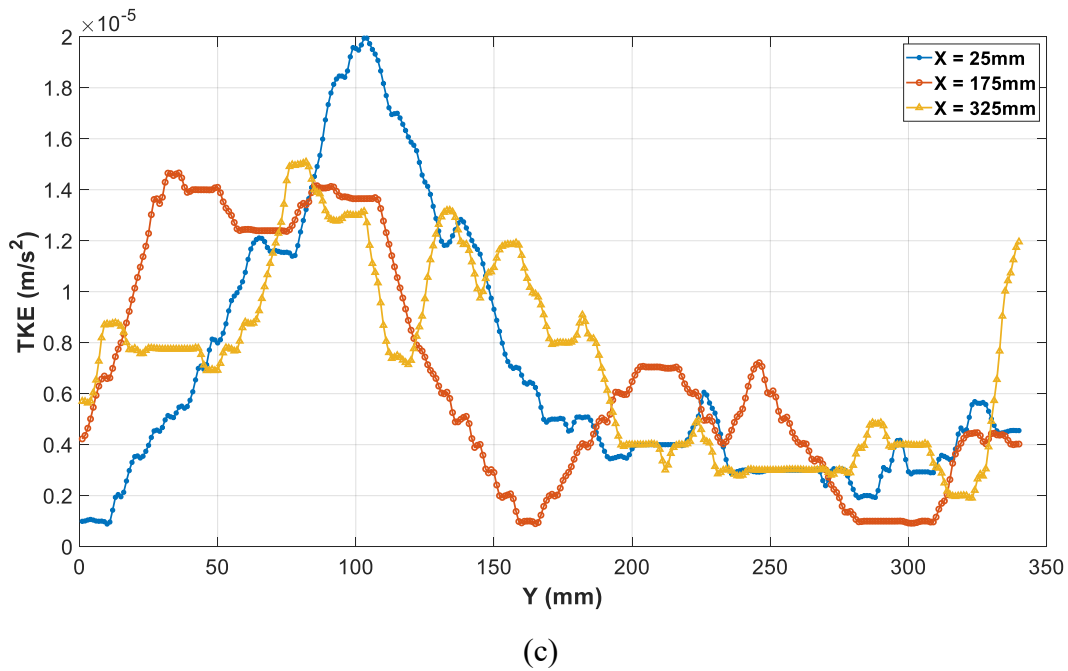
(a)



(b)

Figure 4.65: (a) TKE magnitude, (b) Surface TKE magnitude, (c) XY plot for TKE at $T_b = 50^\circ\text{C}$.

Figure 4.65—continued

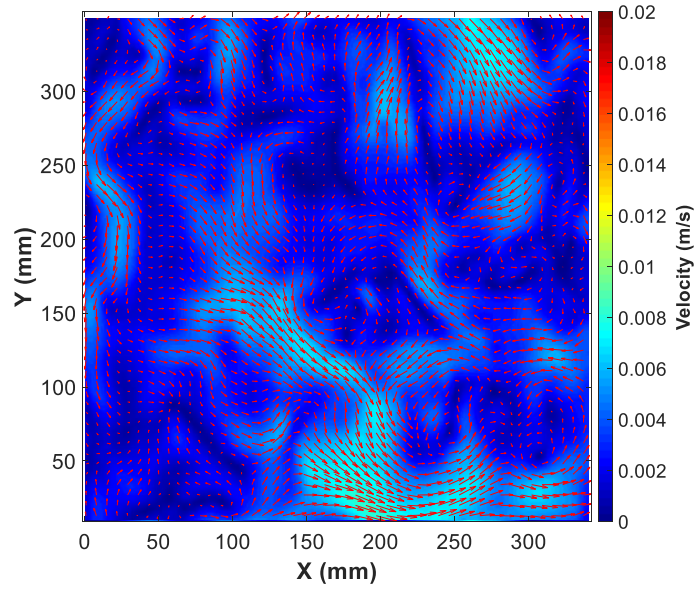


2) At different elevations along with fixed temperature $T_b = 40^\circ\text{C}$

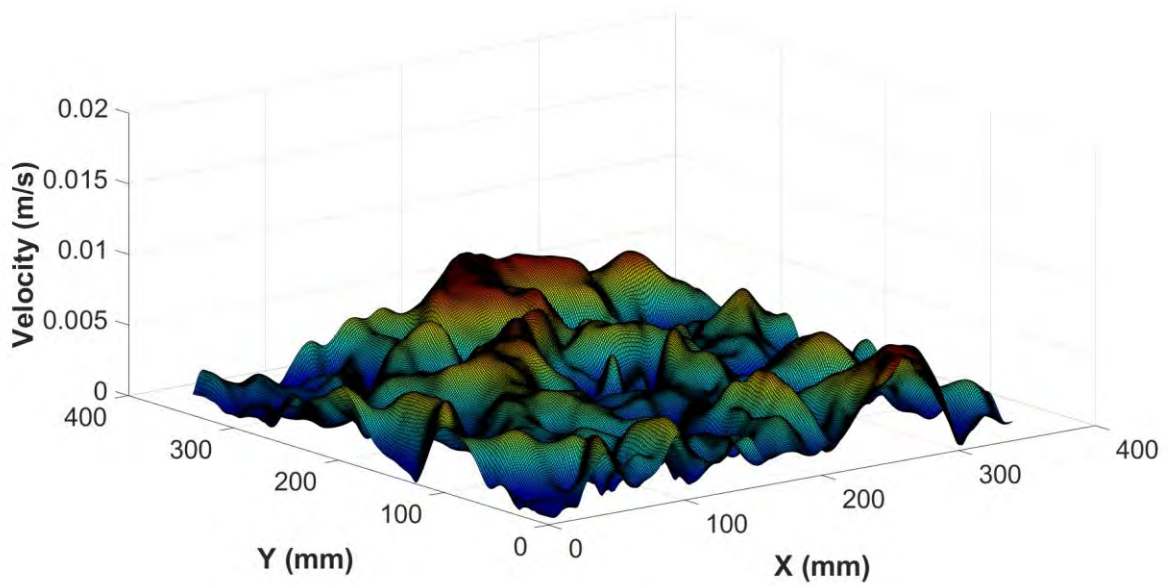
2.1) At $D = 0.07\text{ m}$

(a) Velocity

Figure 4.66 shows the velocity flow pattern from the top view at $D = 0.07\text{ m}$. As can be seen in Figure 4.66 (a), the flow pattern starts to rise from the bottom of the water tank due to the temperature coming from the aluminum plate. Some small vortices can be seen at this elevation, with a higher velocity close to the walls of the water tank [refer to Figure 4.66 (a)]. This becomes visible in Figure 4.66 (b), wherein the surface velocity magnitude is plotted. The peaks in Figure 4.66 (b) represent the cells in the middle of the tank. Figure 4.66 (c) shows the velocity at different X locations, where the fluctuations are clearly shown.



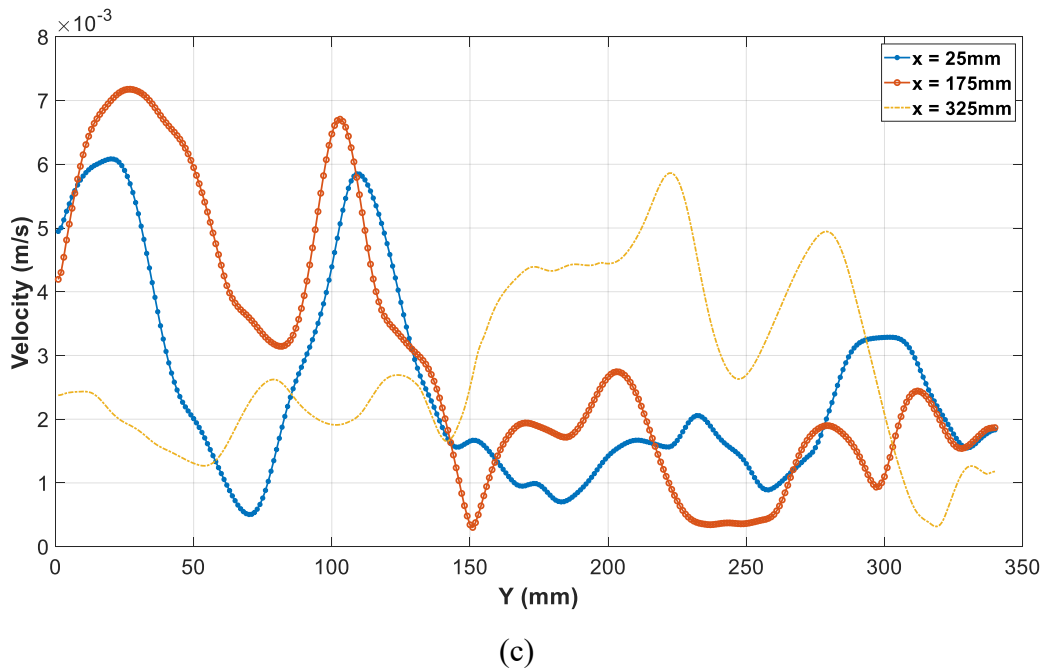
(a)



(b)

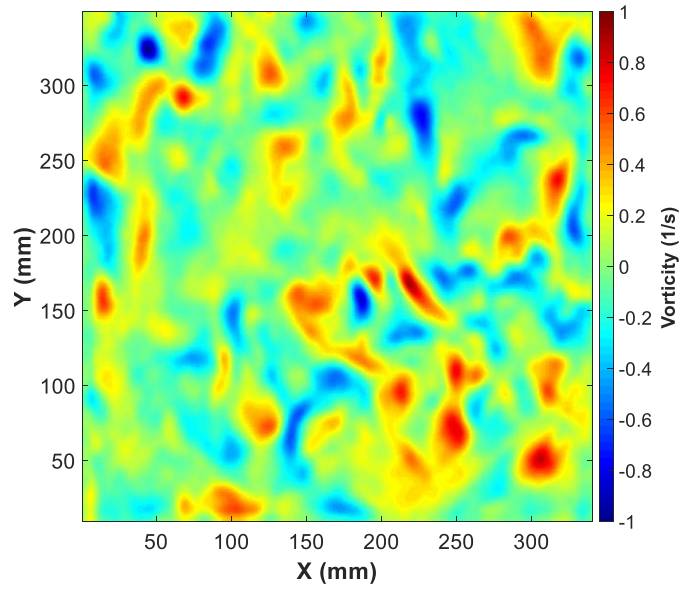
Figure 4.66: (a) Velocity magnitude, (b) Surface velocity magnitude, (c) XY plot for velocity at $D = 0.07$ m.

Figure 4.66—continued

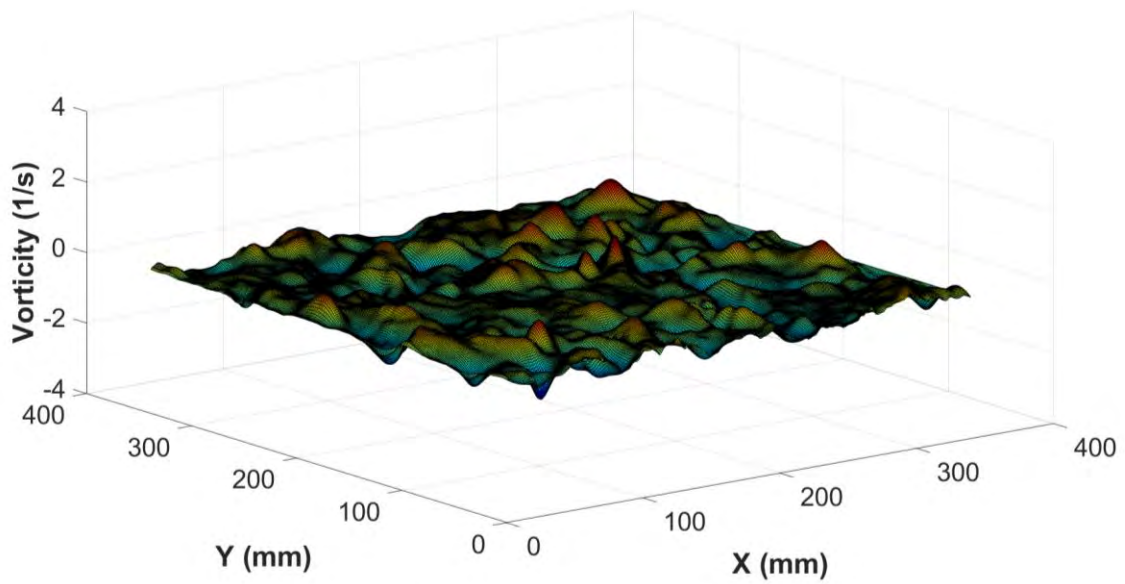


(b) Vorticity

Figure 4.67 shows the vorticity. Higher vortices appear at this elevation due to the increasing temperature, where this elevation $D = 0.07$ m is close to the heated aluminum plate, as can be seen in Figure 4.67 (a). However, some negative and positive values appear due to the different directions of rotation of the cells. This can be seen in Figure 4.67 (b), where the negative and positive vorticities are shown as peaks which clearly represent the rotation of Bénard cells. Figure 4.67 (c) shows the fluctuations of vorticity at different points on the X axis.



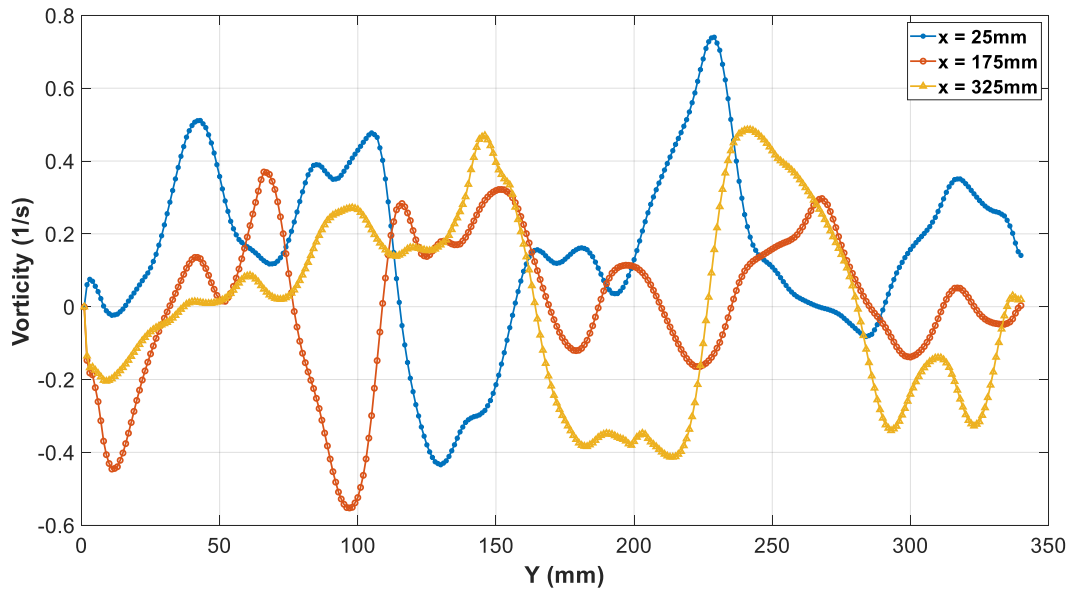
(a)



(b)

Figure 4.67: (a) Vorticity magnitude, (b) Surface vorticity magnitude, (c) XY plot for vorticity at $D = 0.07$ m.

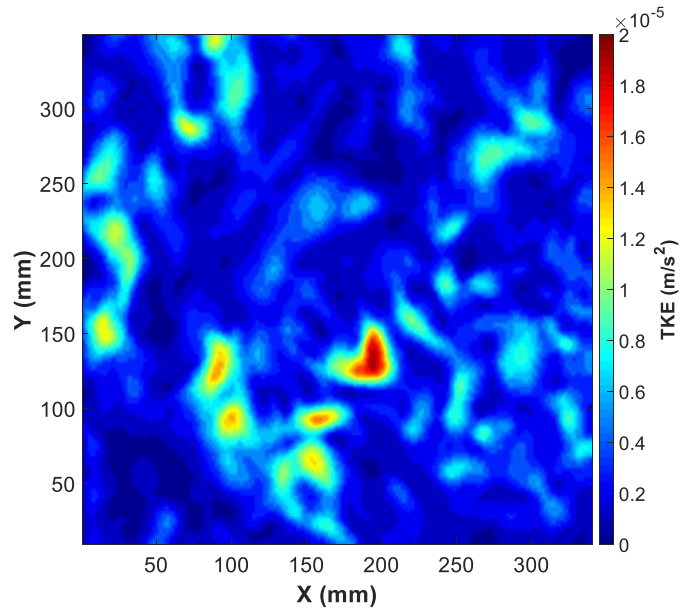
Figure 4.67—continued



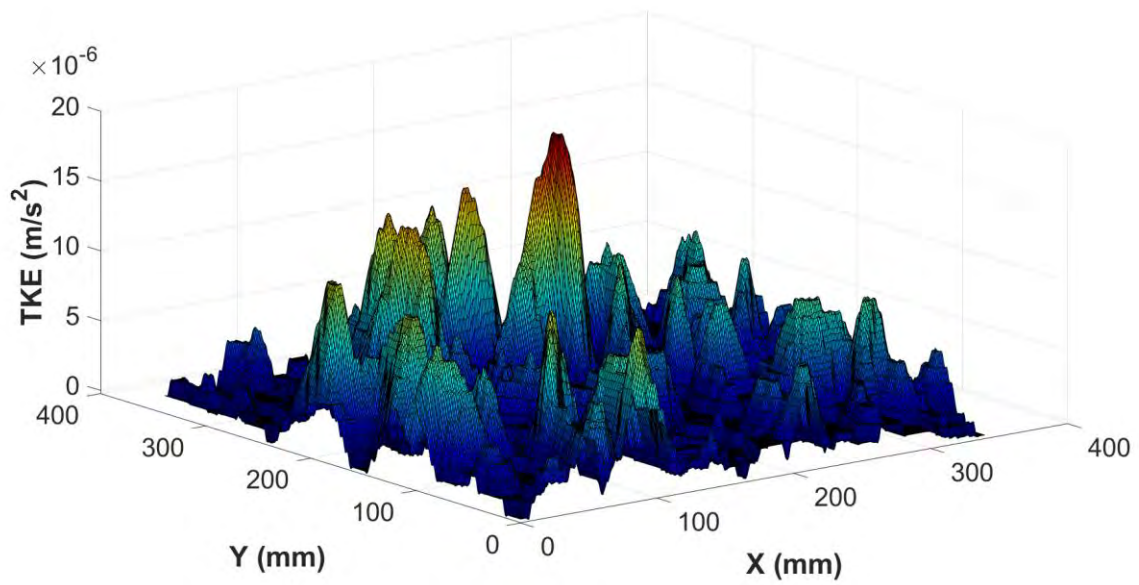
(c)

(c) Turbulent Kinetic Energy

Figure 4.68 presents the turbulent kinetic energy at $D = 0.07$ m. Figure 4.68 (a) shows the turbulent kinetic energy, where a higher value appears close to the middle of the tank. This becomes clearer in Figure 4.68 (b), where the turbulent kinetic energy is very small near the walls and higher at this region of the water tank. The turbulent kinetic energy is plotted at different points on the X axis in Figure 4.68 (c).



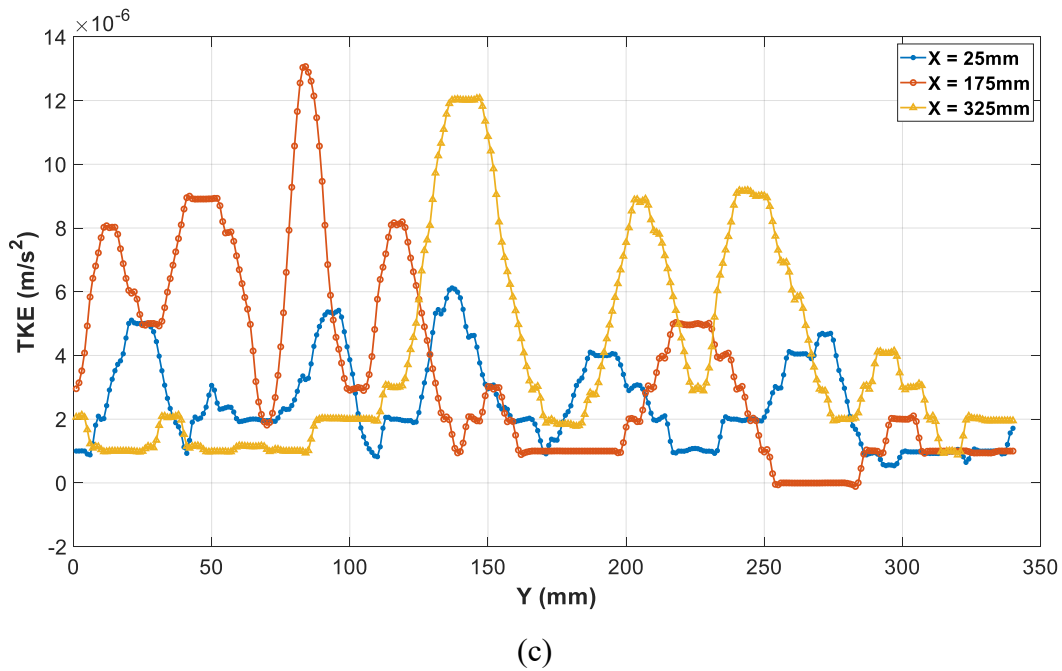
(a)



(b)

Figure 4.68: (a) TKE magnitude, (b) Surface TKE magnitude, (c) XY plot for TKE at $D = 0.07 \text{ m}$.

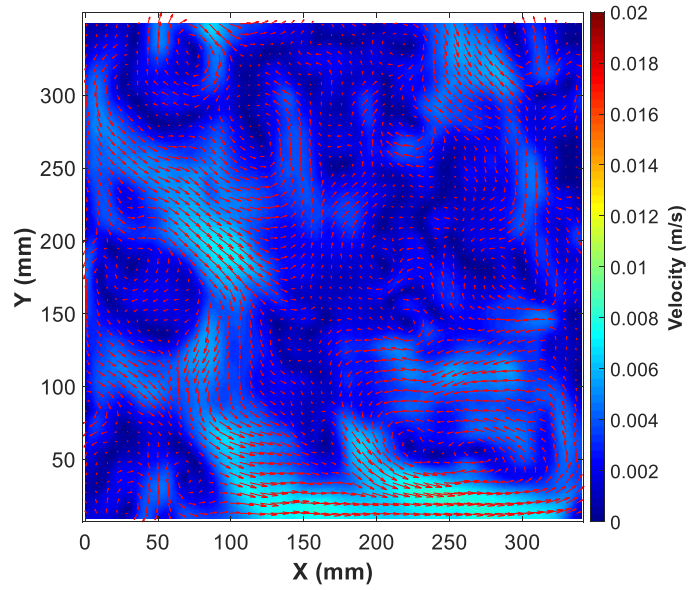
Figure 4.68—continued



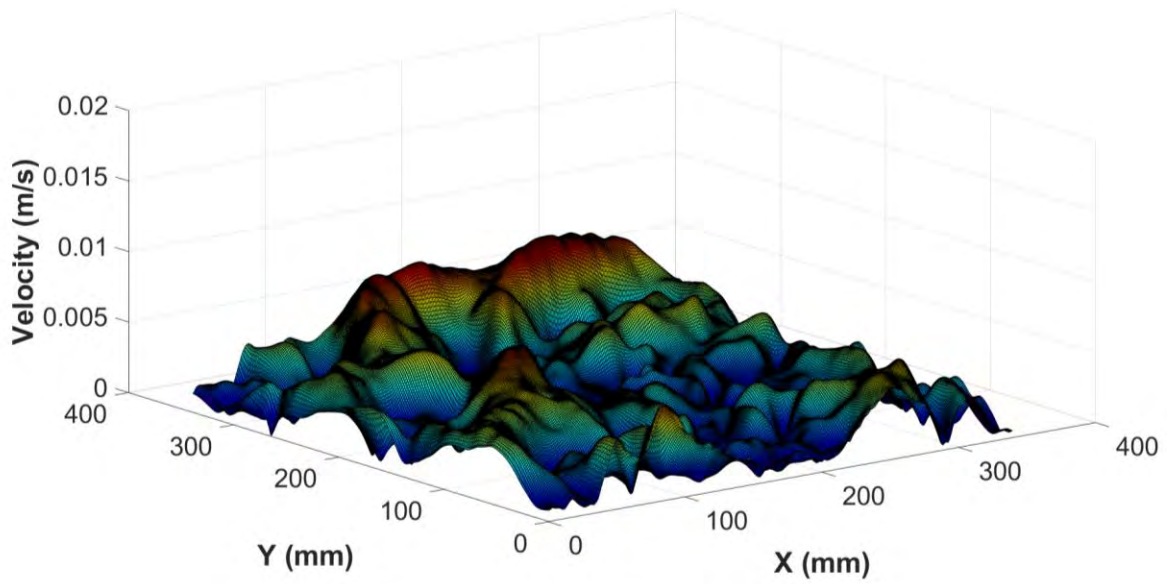
2.2) At $D = 0.14$ m

(a) Velocity

Figure 4.69 shows the velocity flow pattern from the top view at $D = 0.14$ m. As can be seen in Figure 4.69 (a), more vortices start to develop at this higher elevation. Some higher vortices can be seen at this elevation compared to $D = 0.07$ m, with a higher velocity close to the walls of the water tank [refer to Figure 4.69 (a)]. This becomes visible in Figure 4.69 (b), wherein the surface velocity magnitude is plotted, with the peaks representing the cells in the middle of the tank. Figure 4.69 (c) shows the velocity at different X locations, where the fluctuations are clearly shown.



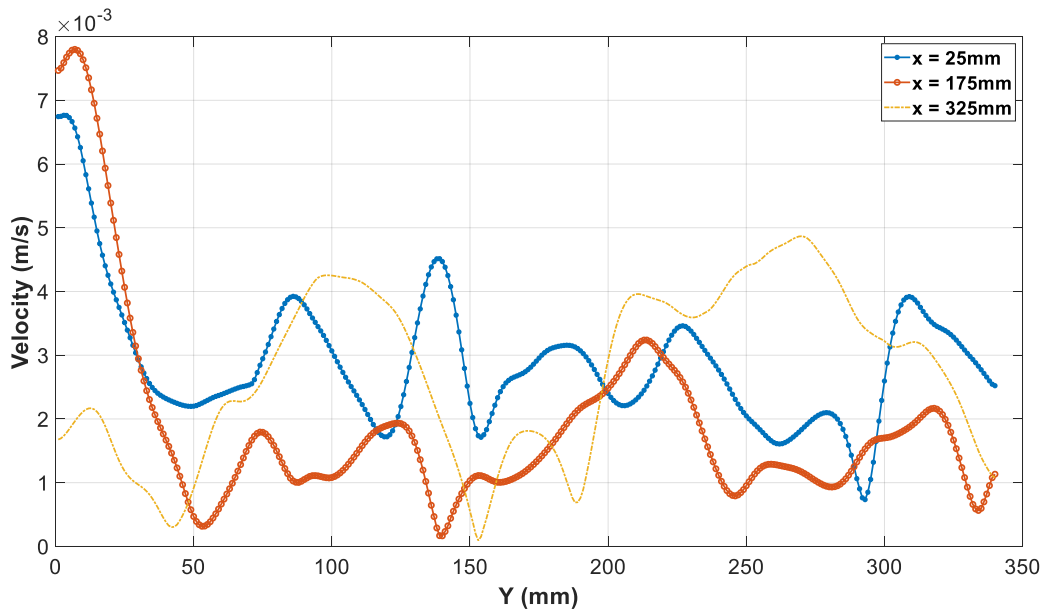
(a)



(b)

Figure 4.69: (a) Velocity magnitude, (b) Surface velocity magnitude, (c) XY plot for velocity at $D = 0.14$ m.

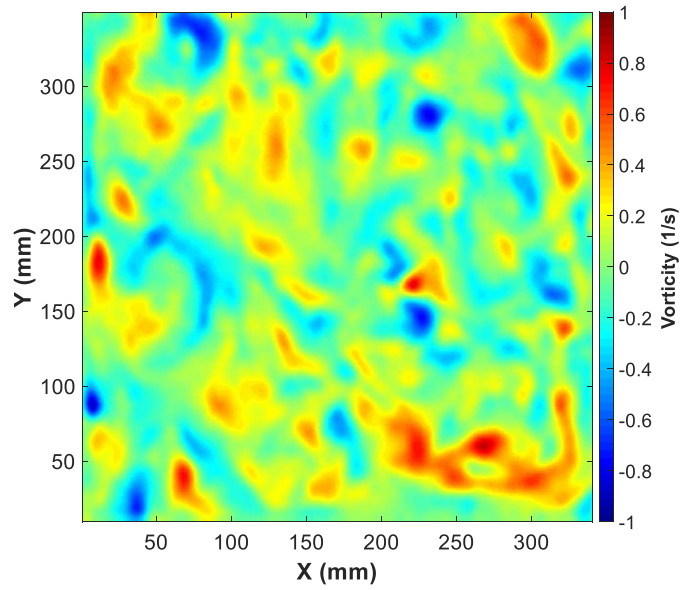
Figure 4.69—continued



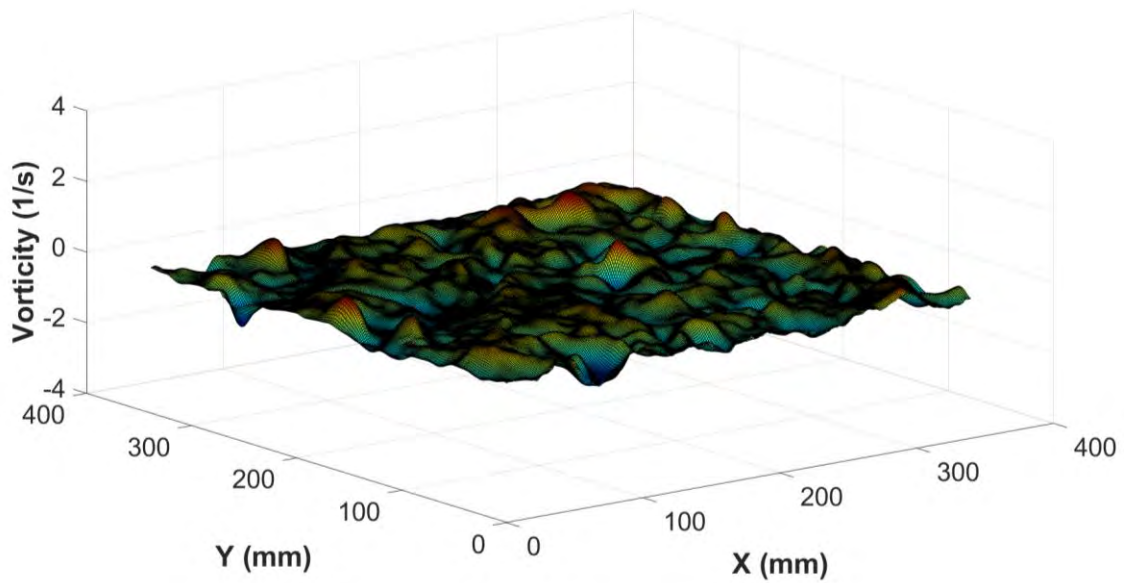
(c)

(b) Vorticity

Figure 4.70 shows the vorticity. Higher vortices appear at this elevation due to the increasing temperature difference, as can be seen in Figure 4.70 (a). However, some negative and positive values appear due to the different directions of rotation of the cells. This can be seen in Figure 4.70 (b), where the negative and positive vorticities are shown as peaks which clearly represent the rotation of Bénard cells. Figure 4.70 (c) shows the fluctuations of vorticity at different points on the X axis.



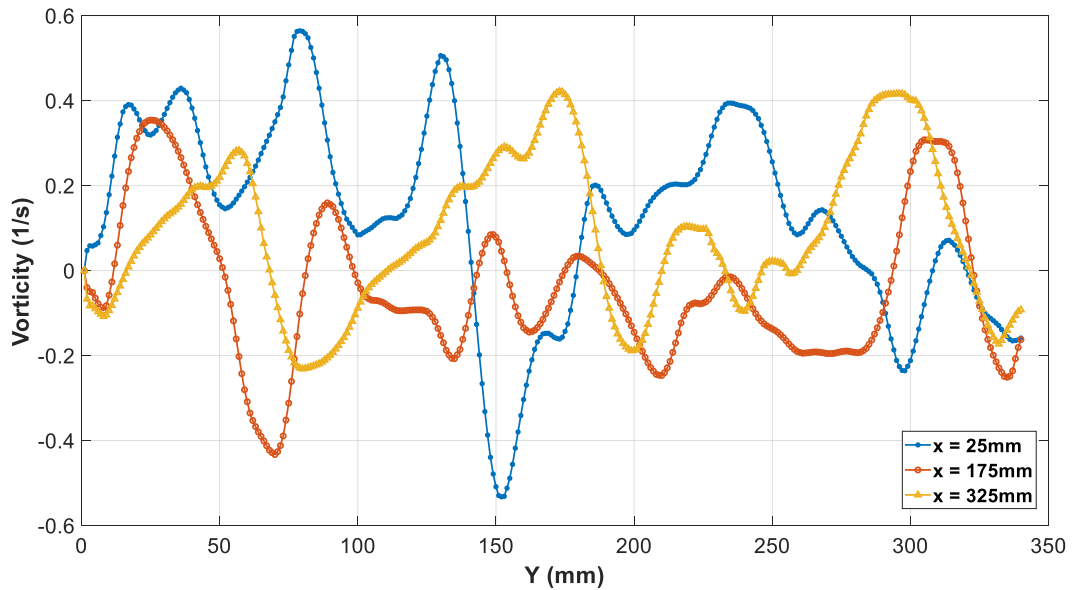
(a)



(b)

Figure 4.70: (a) Vorticity magnitude, (b) Surface vorticity magnitude, (c) XY plot for vorticity at $D = 0.14$ m.

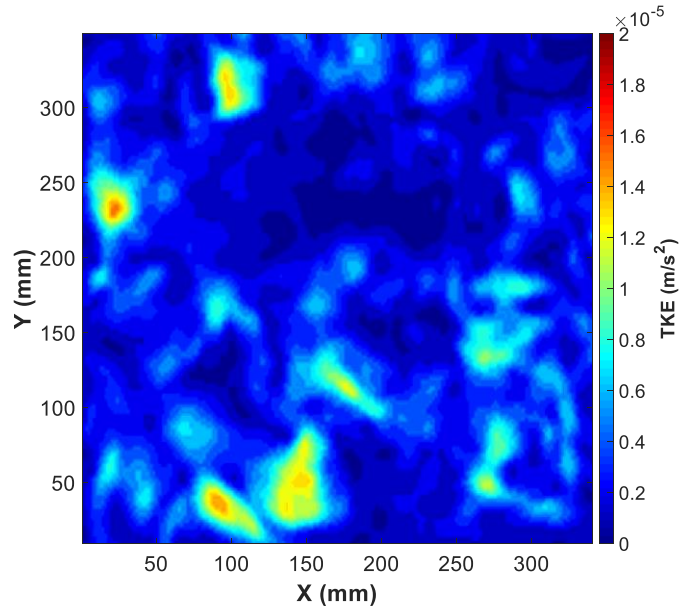
Figure 4.70—continued



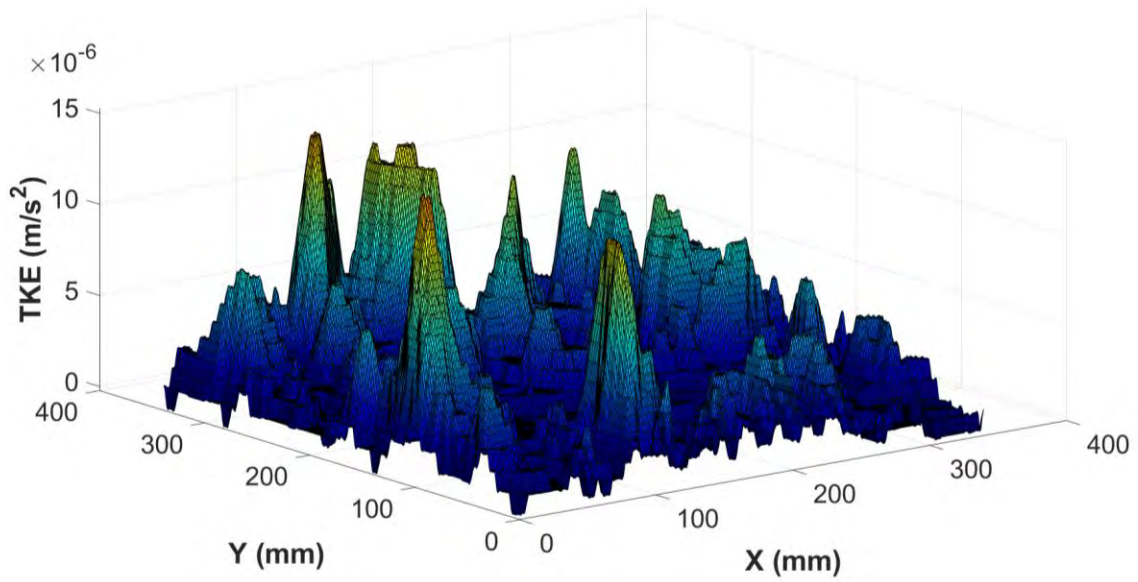
(c)

(c) Turbulent Kinetic Energy

Figure 4.71 presents the turbulent kinetic energy at $D = 0.14$ m. Figure 4.71 (a) shows the turbulent kinetic energy, where a higher value appears close to the walls of the tank. This becomes clearer in Figure 4.71 (b), where the turbulent kinetic energy is higher near the walls of the water tank. The turbulent kinetic energy is plotted at different points on the X axis in Figure 4.71 (c).



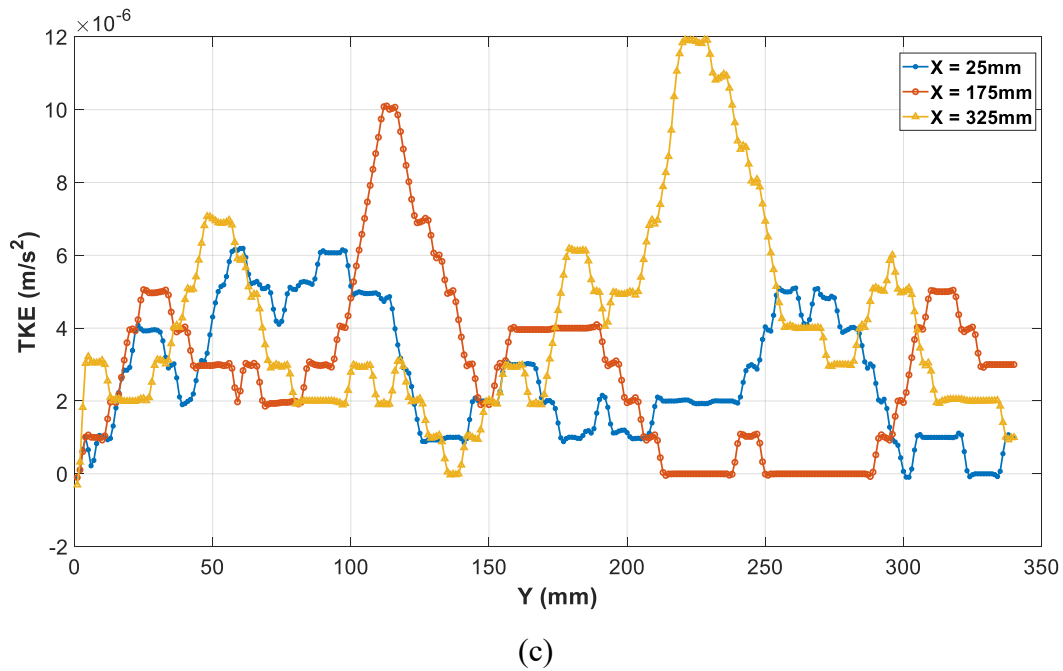
(a)



(b)

Figure 4.71: (a) TKE magnitude, (b) Surface TKE magnitude, (c) XY plot for TKE at $D = 0.14$ m.

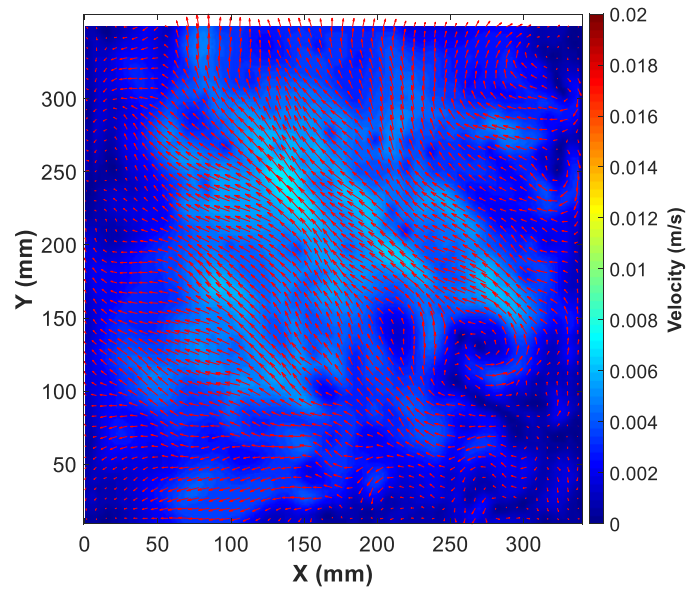
Figure 4.71—continued



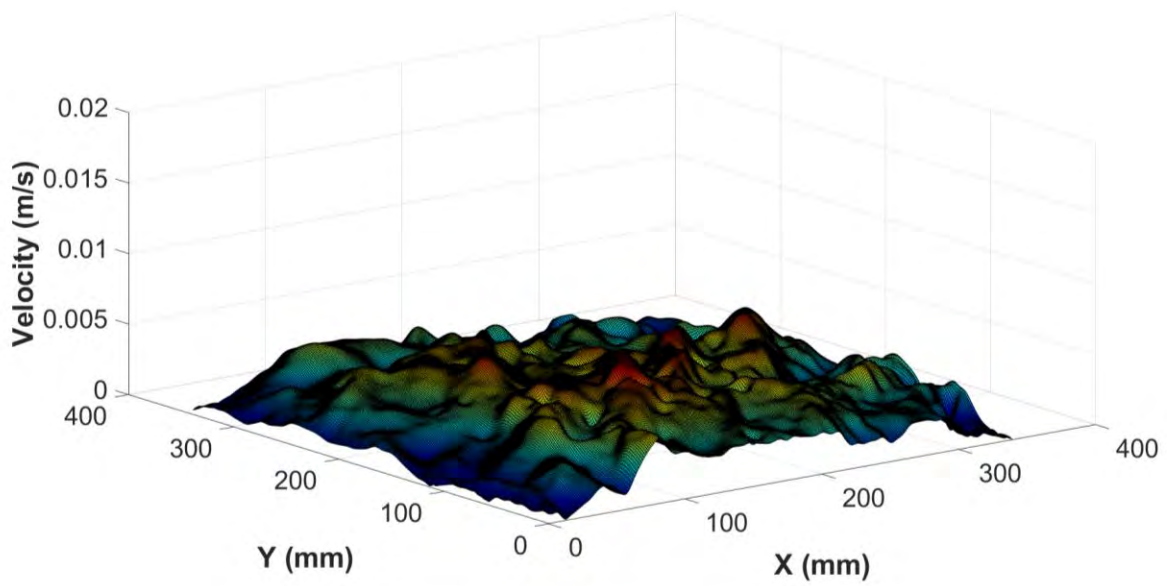
2.3) At $D = 0.21 \text{ m}$

(a) Velocity

Figure 4.72 shows the velocity flow pattern from the top view at $D = 0.21 \text{ m}$. As can be seen in Figure 4.72 (a), the flow pattern becomes more turbulent and loses vortex rotation, which is mainly due to the elevation from the bottom of the water tank. However, some vortices still can be seen spatially near the walls of the water tank. Interestingly, higher velocity can be seen at the middle of the tank due to the evaporation and moving molecules at that elevation which is close to the free surface. This is visible in Figure 4.72 (b), wherein the surface velocity magnitude is plotted, and the higher velocity can be clearly seen at the middle of the water tank. Figure 4.72 (c) shows the velocity at different X locations, where the fluctuations are clearly shown along with a higher velocity at the middle of the water tank ($X = 175 \text{ mm}$).



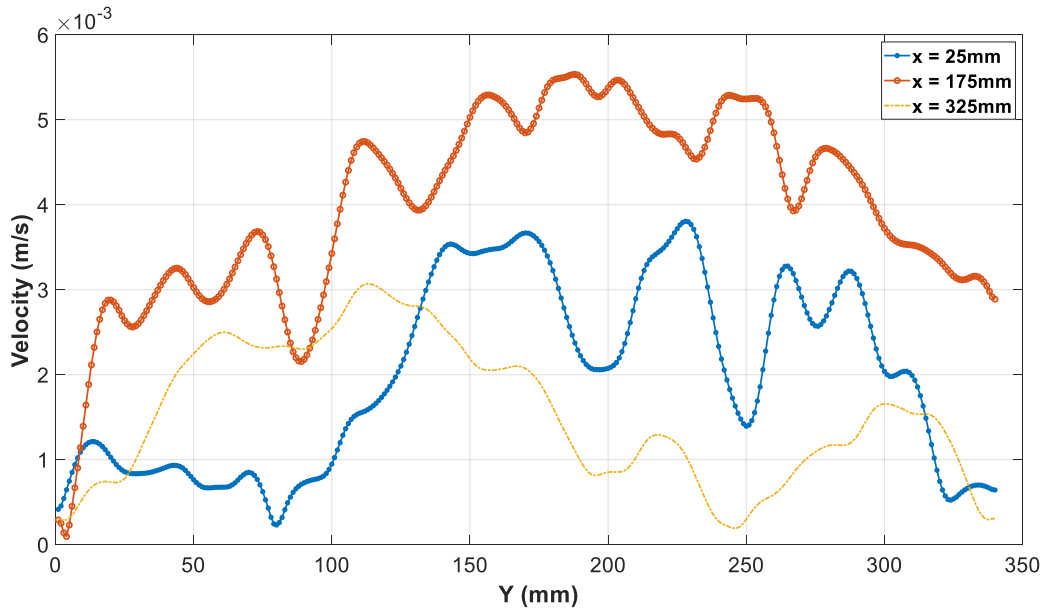
(a)



(b)

Figure 4.72: (a) Velocity magnitude, (b) Surface velocity magnitude, (c) XY plot for velocity at $D = 0.21$ m.

Figure 4.72—continued



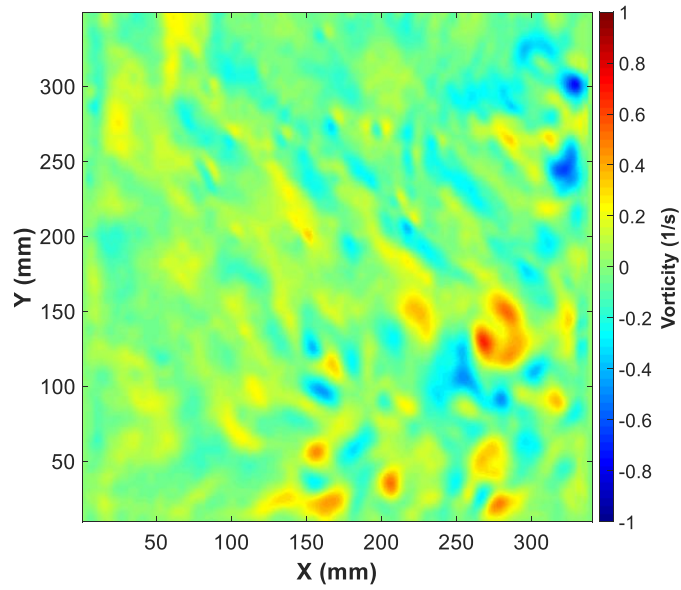
(c)

(b) Vorticity

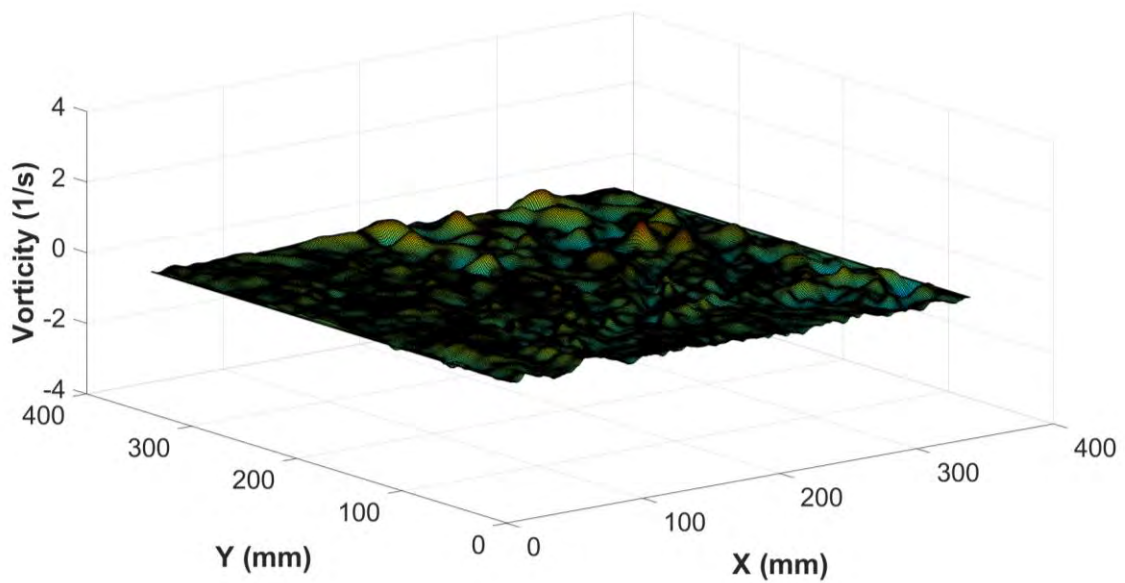
Figure 4.73 shows the vorticity. Some negative and positive values appear due to the different directions of rotation of the cells. This can be seen in Figure 4.73 (b), where the negative and positive vorticities are shown as peaks which clearly represent the rotation of Bénard cells. Figure 4.73 (c) shows the fluctuations of vorticity at different points on the X axis.

(c) Turbulent Kinetic Energy

Figure 4.74 presents the turbulent kinetic energy at $D = 0.21$ m. Figure 4.74 (a) shows the turbulent kinetic energy, where a higher value appears close to the walls of the tank. This becomes clearer in Figure 4.74 (b), where the turbulent kinetic energy is higher near the walls of the water tank. The turbulent kinetic energy is plotted at different points on the X axis in Figure 4.74 (c).



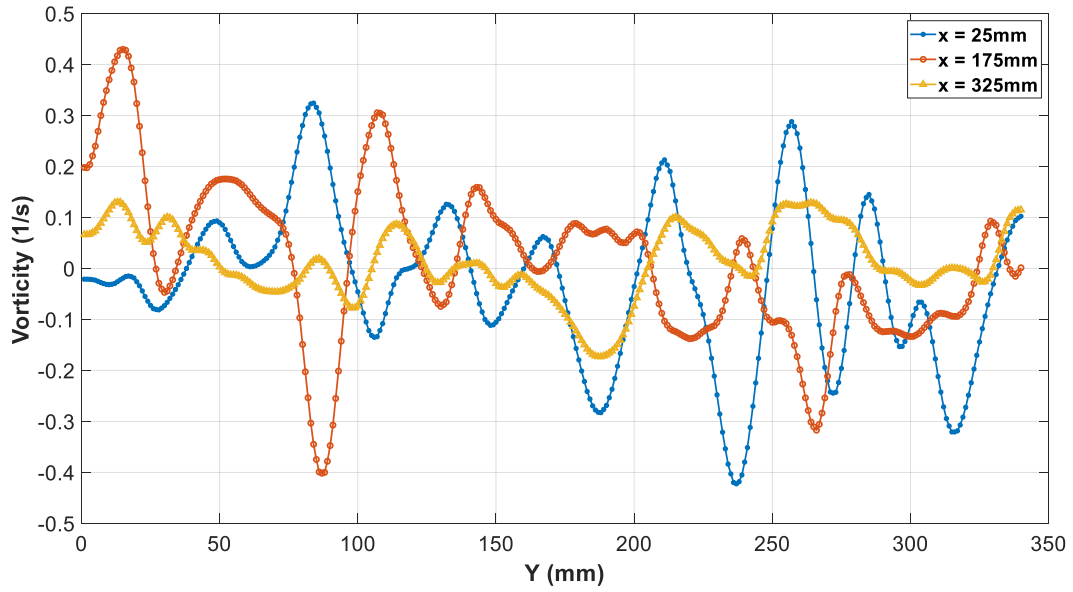
(a)



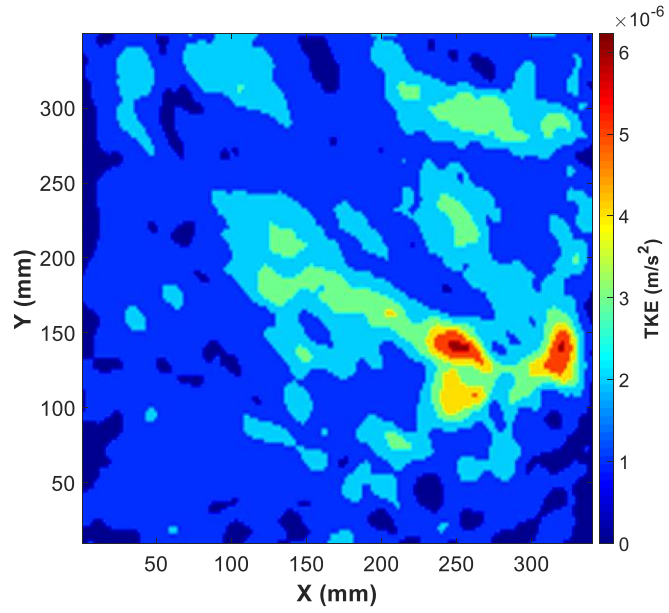
(b)

Figure 4.73: (a) Vorticity magnitude, (b) Surface vorticity magnitude, (c) XY plot for vorticity at $D = 0.21$ m.

Figure 4.73—continued



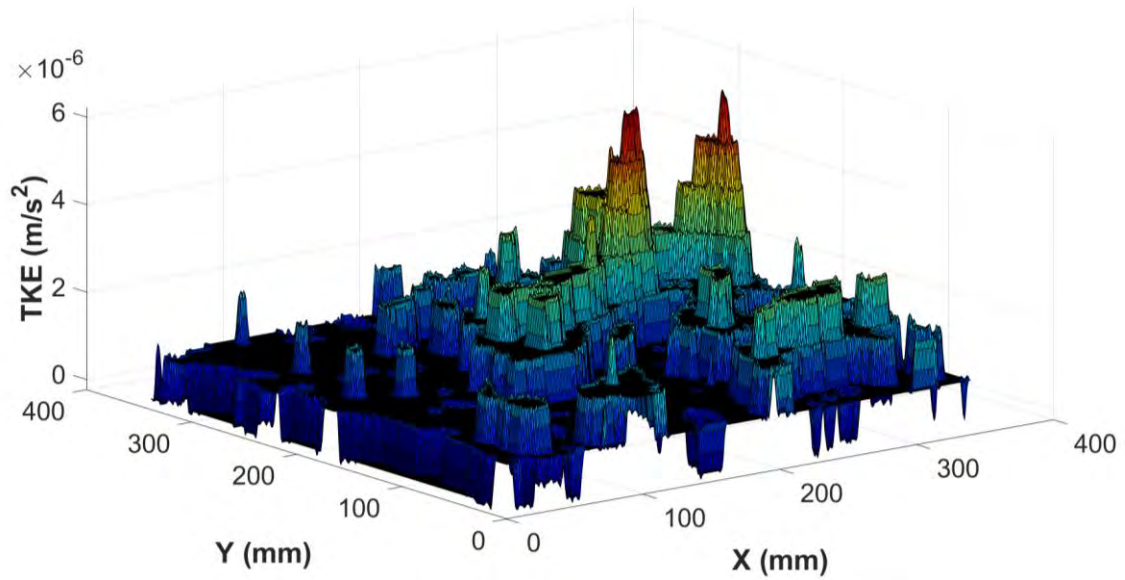
(c)



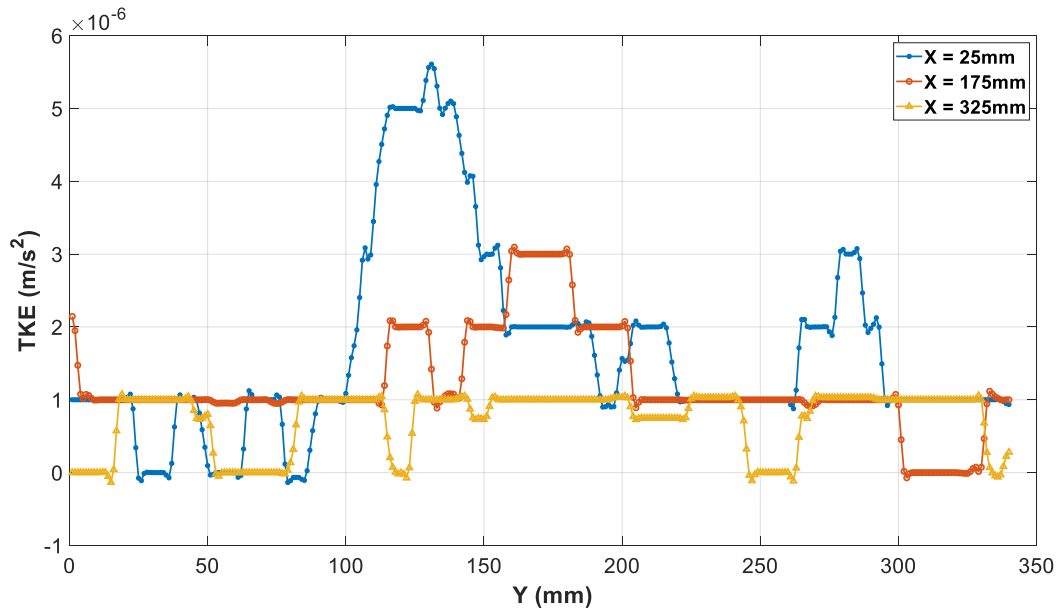
(a)

Figure 4.74: (a) TKE magnitude, (b) Surface TKE magnitude, (c) XY plot for TKE at D = 0.21 m.

Figure 4.74—continued



(b)



(c)

4.4 Stereo Particle Image Velocimetry (SPIV)

4.4.1 Experimental Setup

In this part, the experiment was conducted using SPIV to investigate the flow pattern inside the water from the side of the tank undergoing evaporation. None of the studies conducted so far in the literature have used SPIV to investigate the flow pattern in case of a free water surface. The main advantage of using SPIV in the current work is being able to compute the third component of velocity V_z , which is important to understand the flow pattern in Z direction inside the tank. The same water tank was used for the current experiment, along with all the experimental setup discussed previously in section 4.2.1, including temperature thermocouple probes and heater. However, in this experiment two CCD cameras were used in order to calculate V_z . The schematic and photograph of the experimental setup are shown in Figure 4.75 and Figure 4.76, respectively.

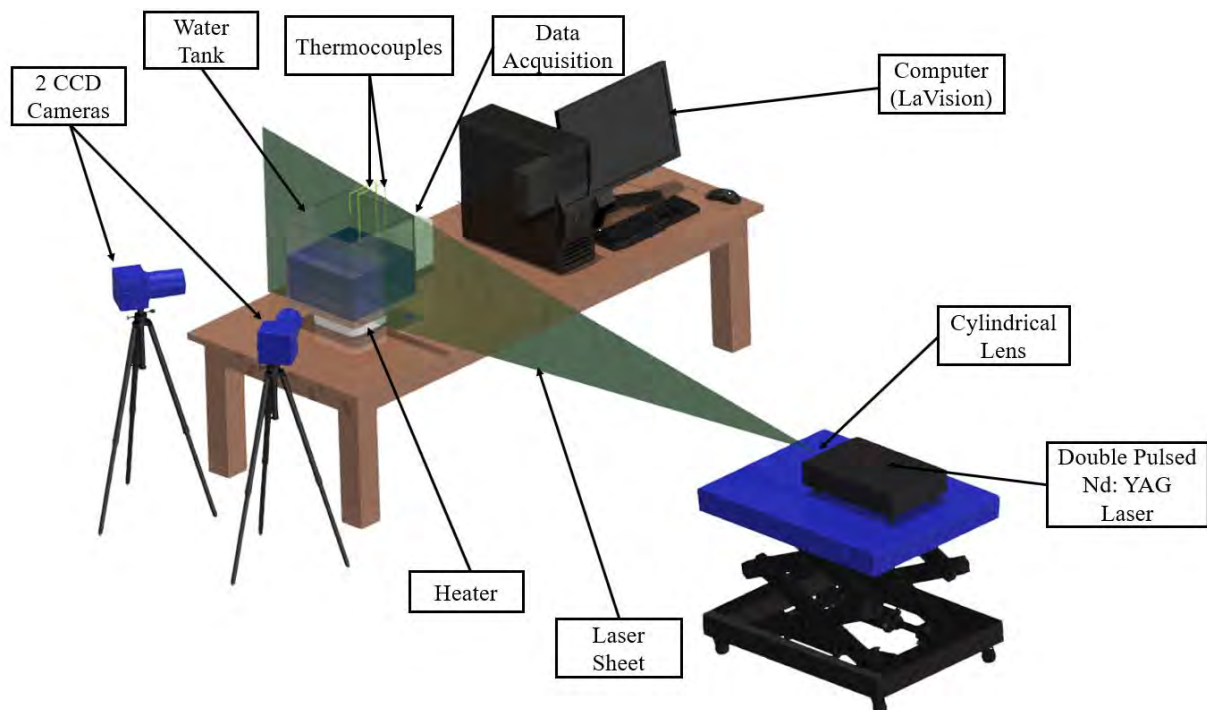


Figure 4.75: Schematic of the experimental setup.

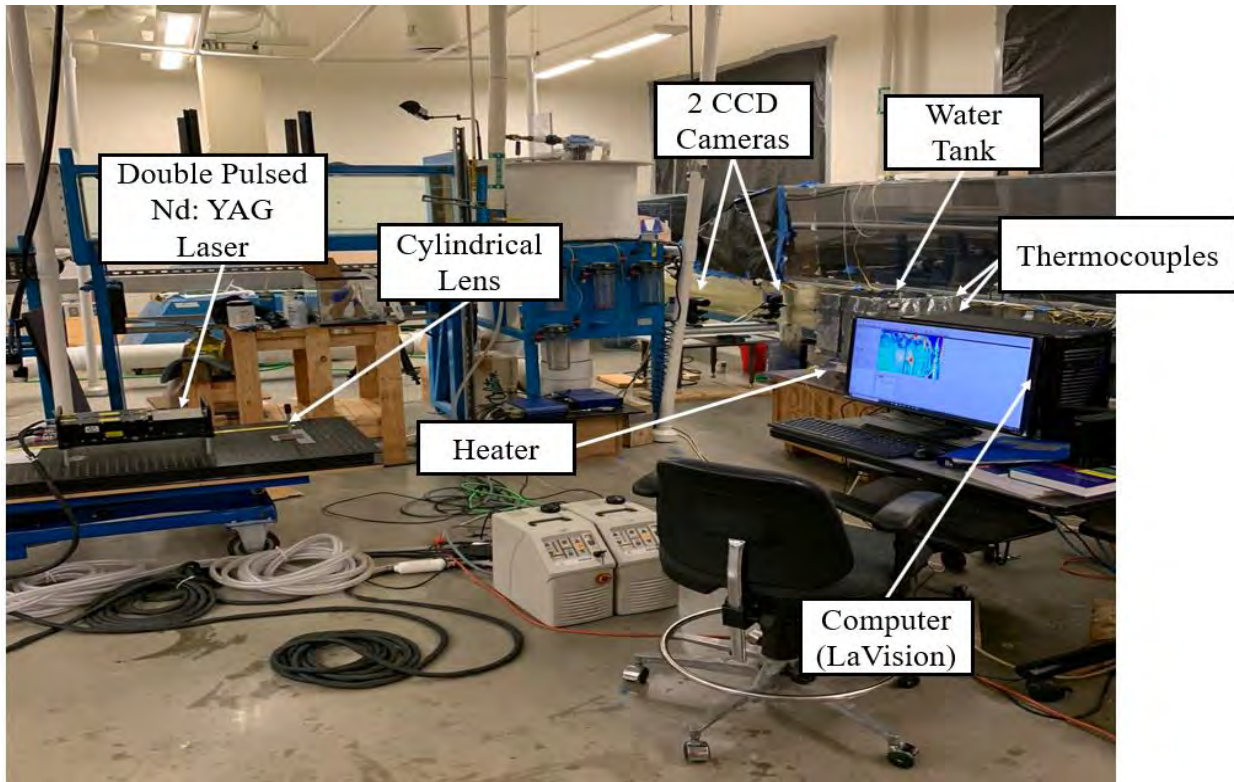


Figure 4.76: Photograph of the experimental setup.

4.4.2 Experimental Procedure

The same procedure as discussed in section 4.2.2 was used in this experiment, along with the use of distilled (purified) water. The change here was of using two CCD cameras instead of one. These two cameras were mounted on one side of the water tank at a distance of about 1.3 m in order to have a good view. Moreover, the two cameras were mounted at an angle of 45° in order to calculate the third component of the velocity V_z . Note that the calibration for SPIV is quite different from the calibration for the planar PIV. To elaborate, for SPIV all three velocity components (V_x, V_y, V_z) in a light sheet are measured. It is based on the principle of stereoscopic imaging, where two cameras capture the image of the illuminated tracer particles from different angles. An initial calibration procedure involves viewing a calibration plate (Type 11) which is placed typically at the position of the light sheet in order to compute the mapping functions between measurement

volume and camera images. Often, some misalignment remains between the reference plane defined by the calibration plate and the true measurement plane, which results in some errors in the final velocity field. Hence, subsequent SPIV self-calibration using actual recording images has become the standard procedure to correct even large misalignments. Consequently, in the current work, after taking the images, SPIV self-calibration was used based on the real images in order to reduce the error of the final velocity field, as described schematically in Figure 4.77. Calibration algorithm along with processing of the images was carried out in Davis (8.4). Thereafter, the results data for averaging of 500 images were exported and plotted in MATLAB. Two frames of the row images for each camera before processing at t_i and $t_{i+\Delta t}$ are shown in Figure 4.78.

4.4.3 Results and Discussion

The main reason for conducting the SPIV experiment was to calculate the third component of velocity V_z and investigate its effect on the results, along with comparison between all three components (V_x, V_y, V_z) at three different temperatures. As is known, in case of three components and two components the velocity magnitude can be defined using Eq. (1.25) and Eq. (1.26), respectively. Hence, the comparison by using two components (V_x and V_y) and including the third component V_z is carried out in order to discover the effect of V_z on the velocity magnitude. Three different temperatures are represented.

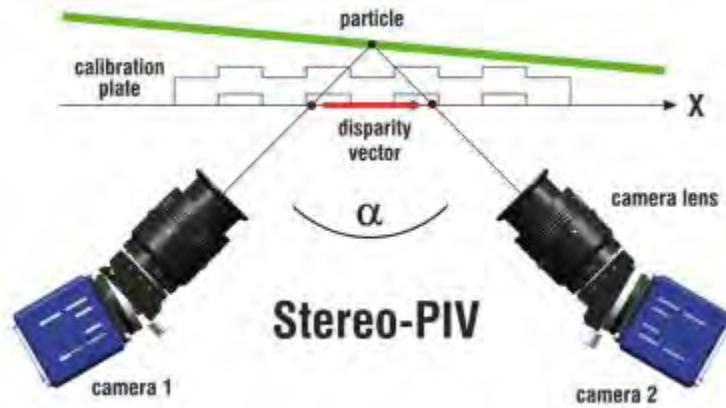


Figure 4.77: Schematic of the SPIV self-calibration [47].

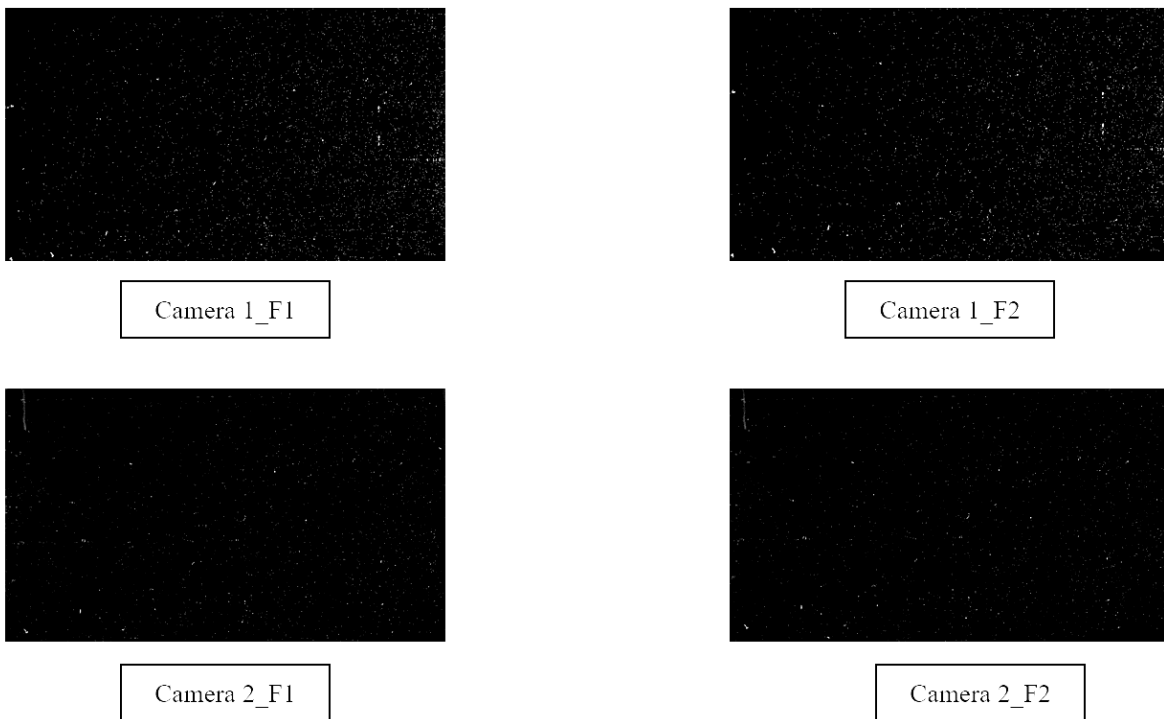


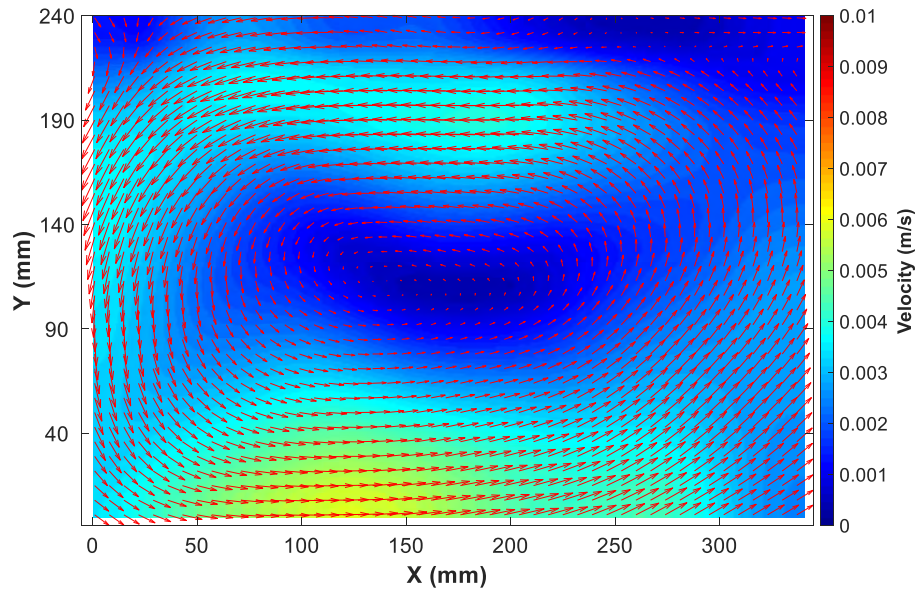
Figure 4.78: Two frames of the row images for each camera before processing at t_i and $t(i+\Delta t)$.

1) Velocity at $T_b = 28^\circ\text{C}$

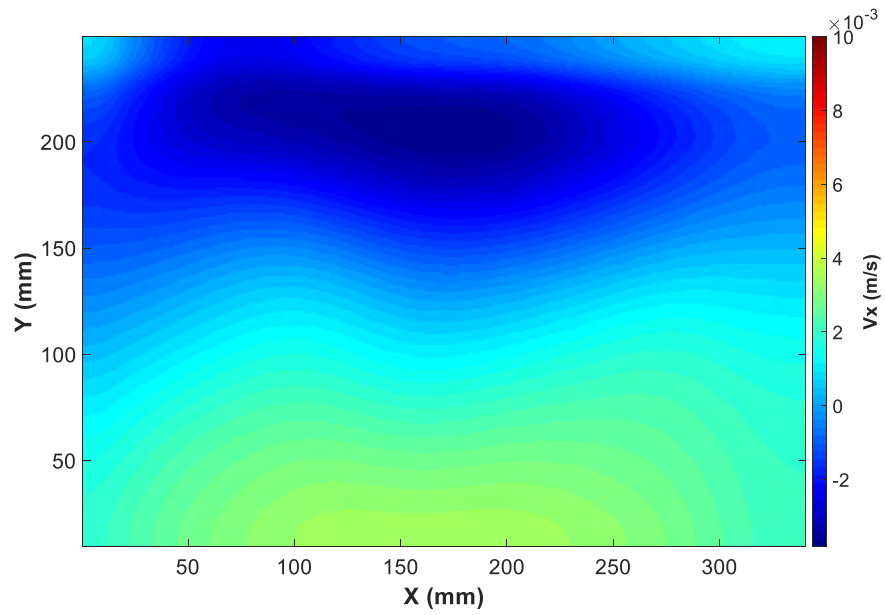
As mentioned previously, the main reason for conducting the SPIV experiment was to investigate the third component of velocity and see its effect on the flow and velocity magnitude.

Figure 4.79 shows the velocity magnitude for all three components. Figure 4.79 (a) shows the

velocity to be higher near the bottom of the tank and near the water surface, with a vortex at the middle of the water tank. Hence, the effect of all three components (V_x , V_y , V_z) is included in Figure 4.79 (a). However, Figure 4.79 (b) shows the velocity V_x , which interestingly is shown to be higher in X-direction near the bottom of the water tank. This makes sense, where the flow starts to move anticlockwise in X-direction until the right wall of the water tank and then starts to move upward to the free surface [see the vectors' direction in Figure 4.79 (a)]. However, some more high velocities with negative values can be seen near the water surface, which means the flow starts to move in the opposite direction. On the other hand, the velocity V_y is shown in Figure 4.79 (c), where the higher values appear on the walls of the water tank, being either negative or positive, which represents the direction of flow. This makes sense as well, where the flow near the walls of the water tank is in Y-direction [see vectors' direction in Figure 4.79 (a)]. Looking at the velocity V_z in Figure 4.79 (d), a high velocity is seen almost everywhere, such as near the bottom of the water tank, walls and water surface, either negative or positive. Hence, by looking at all three velocity components (V_x , V_y , V_z), the effect of all three can be noticed. V_x and V_z mostly dominate near the bottom and top of the water tank, whereas V_y mostly dominates near the walls of the water tank. This becomes clearer in Figure 4.80 (a) and Figure 4.80 (b), where all three velocity components (V_x , V_y , V_z) along with V are plotted vertically and horizontally. It is clear from Figure 4.80 (a) that the velocity V_y has a negligible effect on the velocity magnitude V , whereas in Figure 4.80 (b) it has the most effect on the velocity magnitude V . Finally, in order to show the benefit of SPIV which includes the third velocity component along with investigating the effect of V_z , Figure 4.81 is plotted. Figure 4.81 (a) and Figure 4.81 (b) show the velocity magnitude including and excluding V_z in vertical and horizontal direction, respectively. As a result, the effect of the velocity V_z on the velocity magnitude is clear, especially in the vertical direction. Hence, the flow in the current work is clearly three-dimensional.



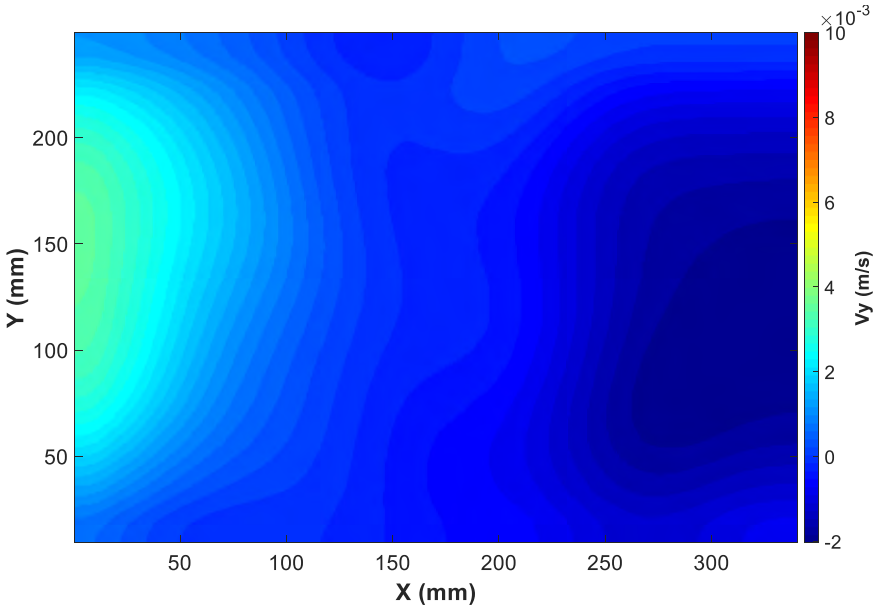
(a)



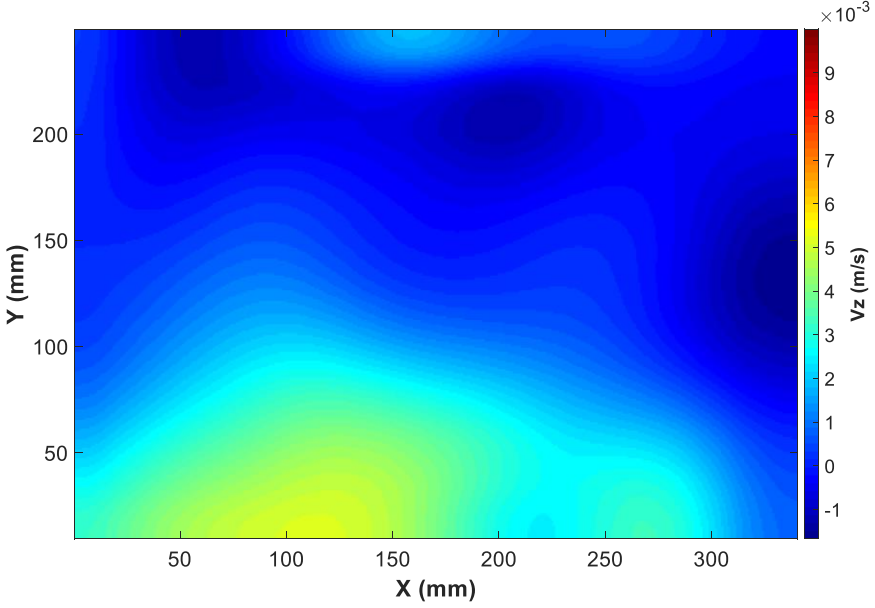
(b)

Figure 4.79: (a) Velocity magnitude for all three components, (b) Velocity V_x , (c) Velocity V_y , (d) Velocity V_z at $T_b = 28^\circ\text{C}$.

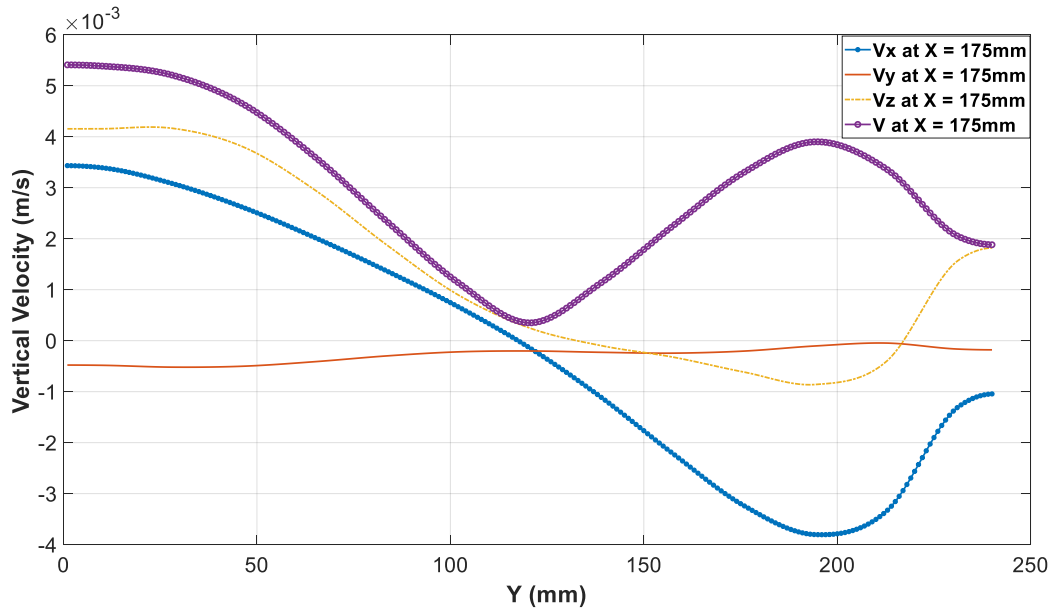
Figure 4.79—continued



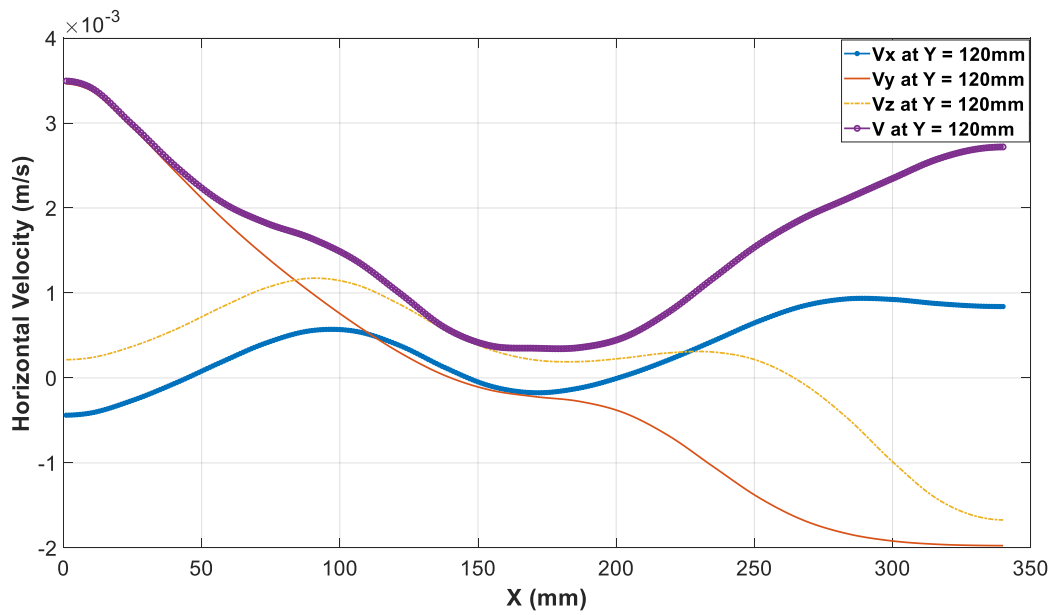
(c)



(d)

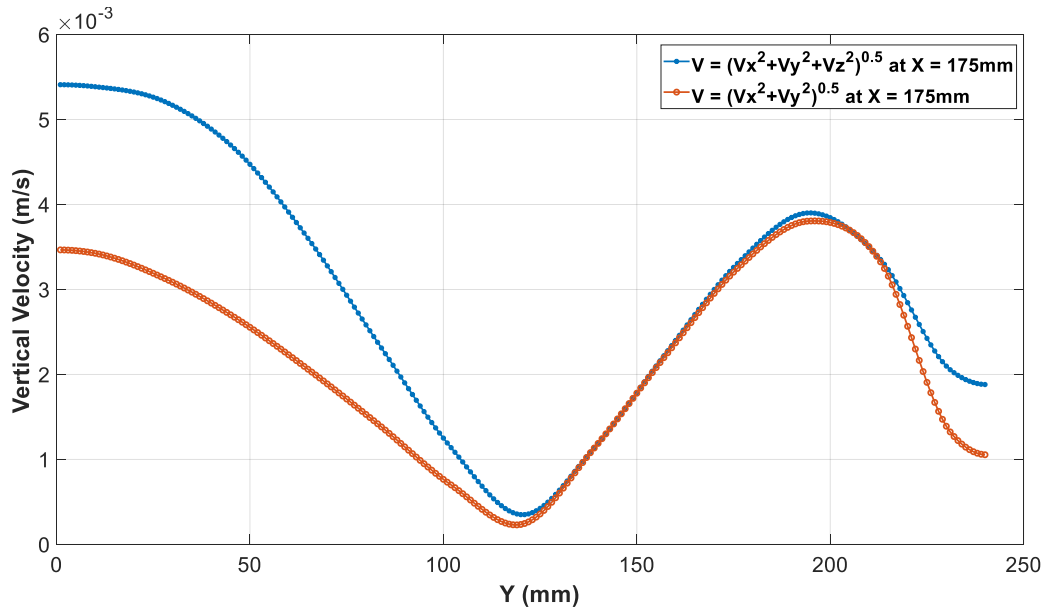


(a)

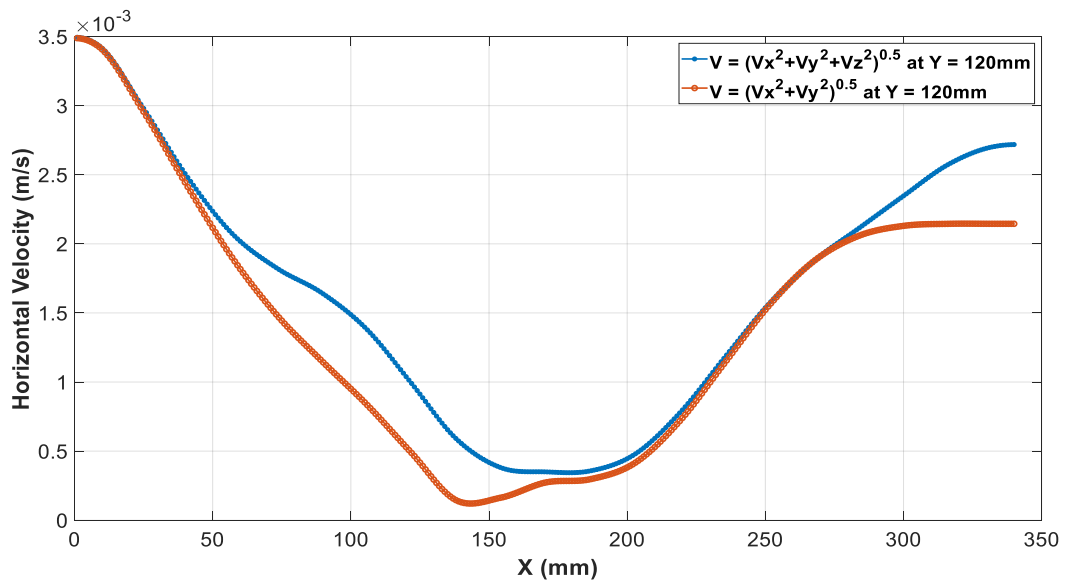


(b)

Figure 4.80: (a) XY plot for vertical velocity magnitude for all three components, (b) XY plot for horizontal velocity magnitude for all three components at $T_b = 28^\circ\text{C}$.



(a)



(b)

Figure 4.81: (a) Comparison of vertical velocity magnitude for three components and two components, (b) Comparison of horizontal velocity magnitude for three components and two components at $T_b = 28^\circ\text{C}$.

Finally, a MATLAB code was written to plot the vectors' direction and magnitude as shown in Figure 4.82, where XY green plane represents the laser sheet. It can be seen some vectors are directed upward and some downward which represent V_z direction. The vectors direction for V_x and V_y are shown as well along with magnitude.

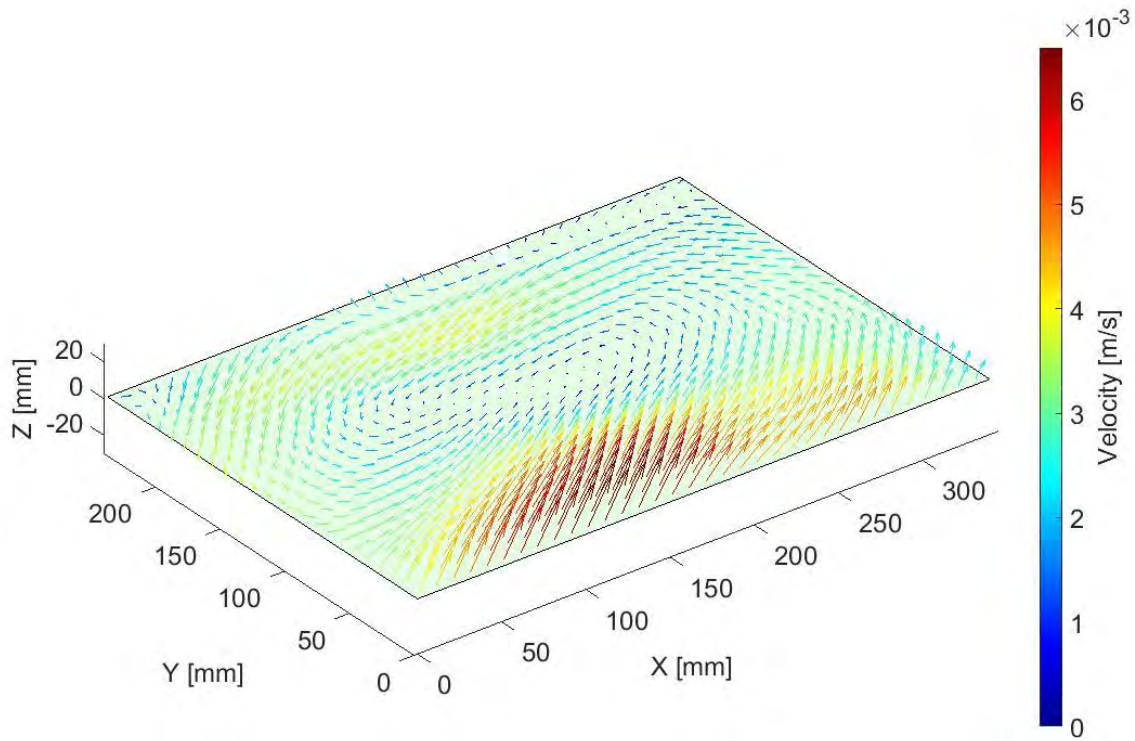
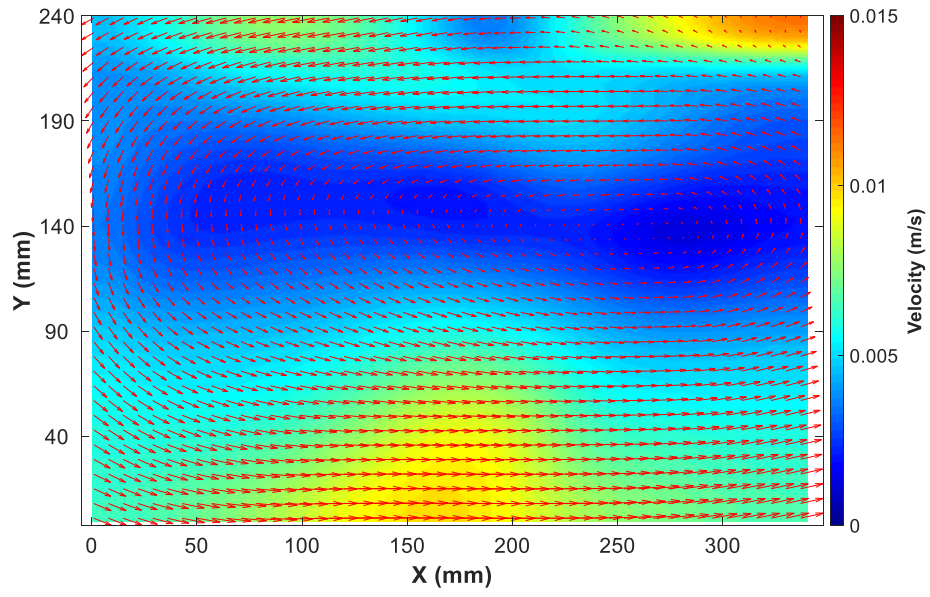


Figure 4.82: 3-D plot for velocity magnitude and direction.

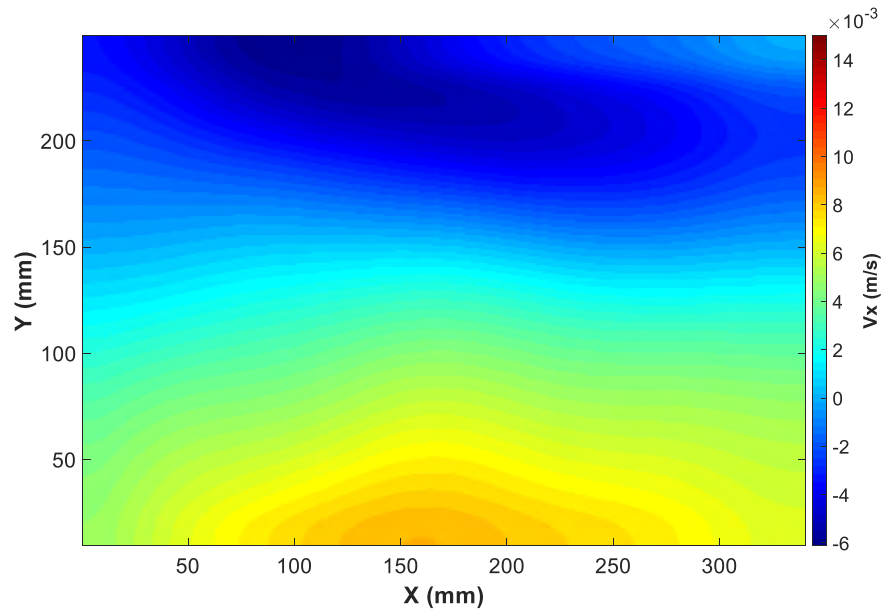
2) Velocity at $T_b = 38^\circ\text{C}$

The investigation is now conducted and discussed for a higher temperature: $T_b = 38^\circ\text{C}$. Figure 4.82 shows the velocity magnitude for all three components. At this time, it can be seen clearly in Figure 4.82 (a) that the velocity is higher near the bottom of the tank and near the water surface, with two vortices at the middle of the water tank due to the rise in temperature and surface evaporation, respectively. Therefore, the effect of all three components (V_x, V_y, V_z) is included in Figure 4.82 (a). However, Figure 4.82 (b) shows the velocity V_x , which interestingly is shown to

be higher in X-direction near the bottom and the surface of the water tank. This higher velocity is positive near the bottom and negative near the surface, which indicates the direction [see vectors' direction in Figure 4.82 (a)]. On the other hand, the velocity V_y is shown in Figure 4.82 (c), where the higher values appear near the walls of the water tank, being either negative or positive, which represents the direction of flow. It is clear that it is higher at this time compared to $T_b = 28^\circ\text{C}$. In addition, looking at the velocity V_z in Figure 4.82 (d), a high velocity is seen almost everywhere, such as near the bottom of the water tank, walls, and water surface, either negative or positive. Hence, just as we have mentioned previously, looking at all three velocity components (V_x , V_y , V_z), the effect of all three can be noticed. V_x and V_z mostly dominate near the bottom and top of the water tank, whereas V_y mostly dominates near the walls of the water tank. This becomes clearer in Figure 4.83 (a) and Figure 4.83 (b), where all three velocity components (V_x , V_y , V_z) along with V are plotted vertically and horizontally. It can be seen that in Figure 4.83 (a) the velocity V_y has a negligible effect on the velocity magnitude V , whereas in Figure 4.83 (b) it has the most effect on the velocity magnitude V . Figure 4.84 (a) and Figure 4.84 (b) show the velocity magnitude including and excluding V_z in vertical and horizontal direction. Consequently, the effect of the velocity V_z on the velocity magnitude in vertical and horizontal direction is clear. Note that the effect is higher in the horizontal direction at this time, compared to $T_b = 28^\circ\text{C}$. Finally, as can be seen in Figure 4.86 where the XY green plane represents the laser sheet. It can be seen some vectors are directed upward and some downward which represent V_z direction. The vectors' direction for V_x and V_y are shown as well, along with magnitude.



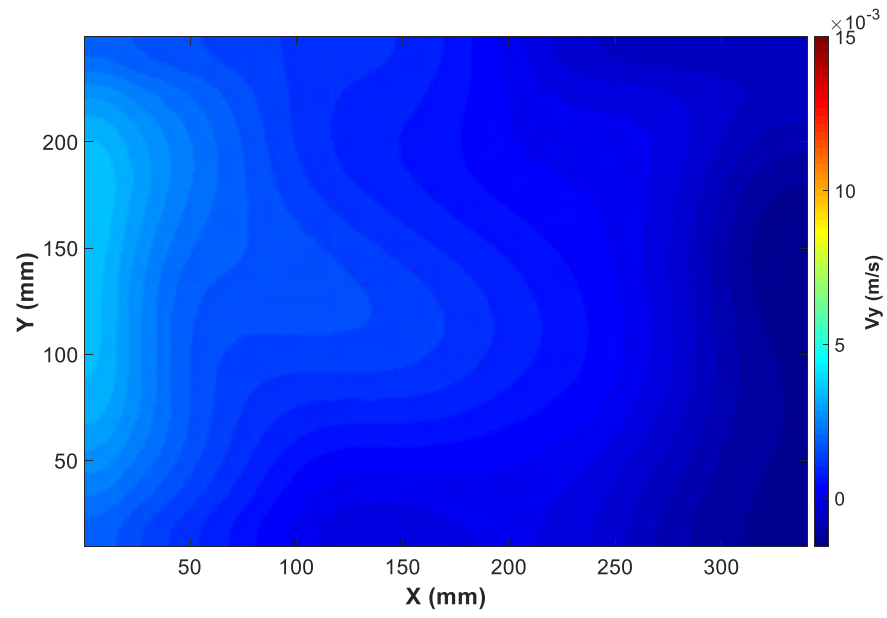
(a)



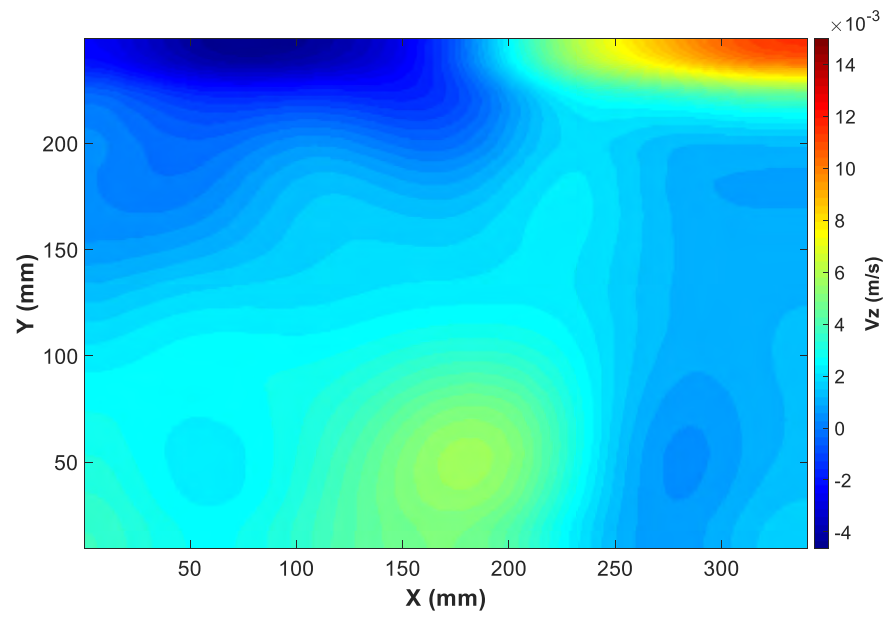
(b)

Figure 4.83: (a) Velocity magnitude for all three components, (b) Velocity V_x , (c) Velocity V_y , (d) Velocity V_z at $T_b = 38^\circ\text{C}$.

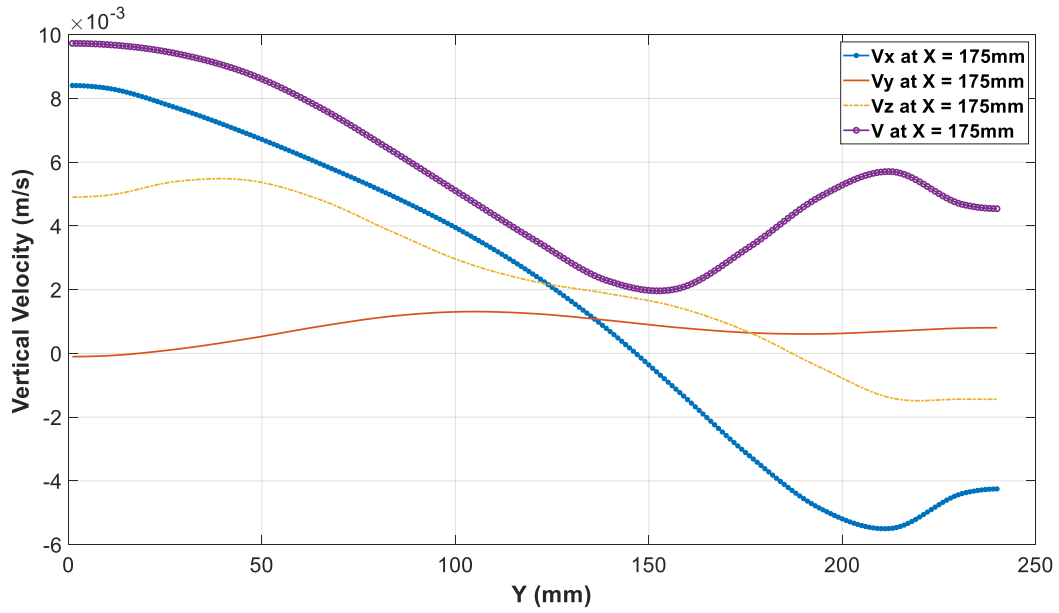
Figure 4.83—continued



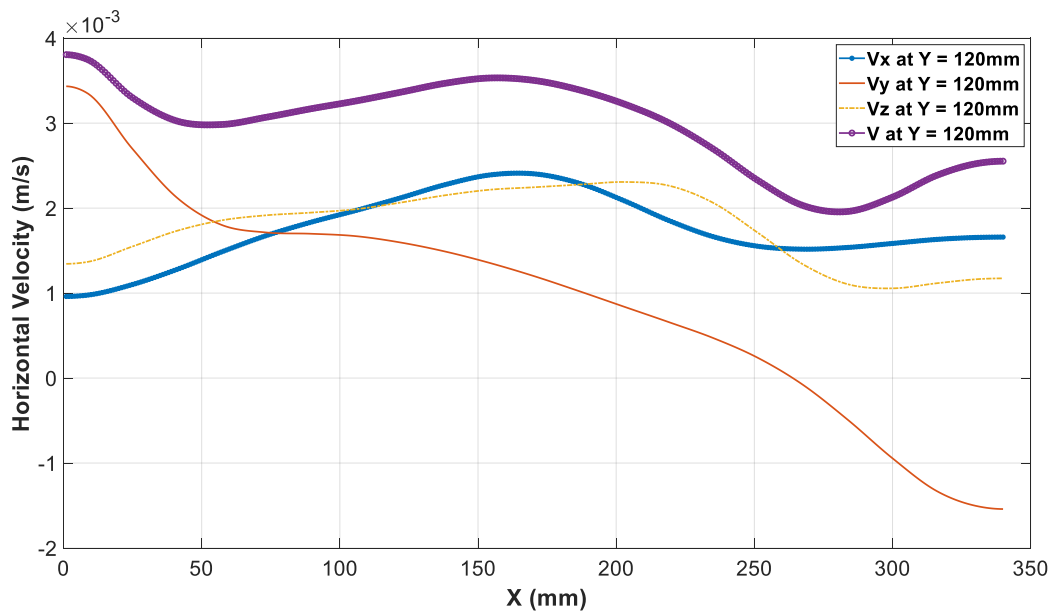
(c)



(d)

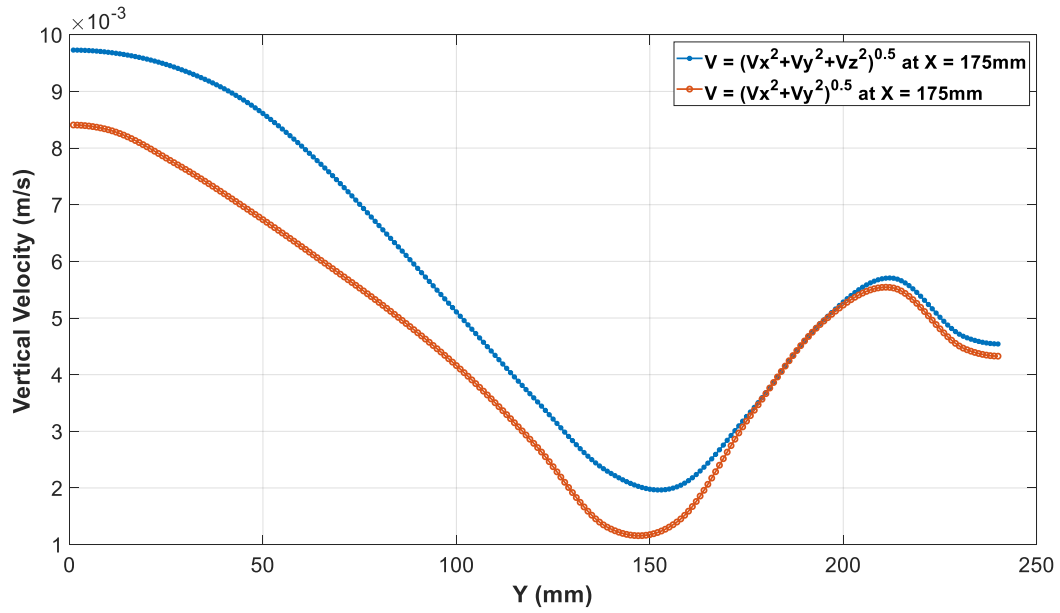


(a)

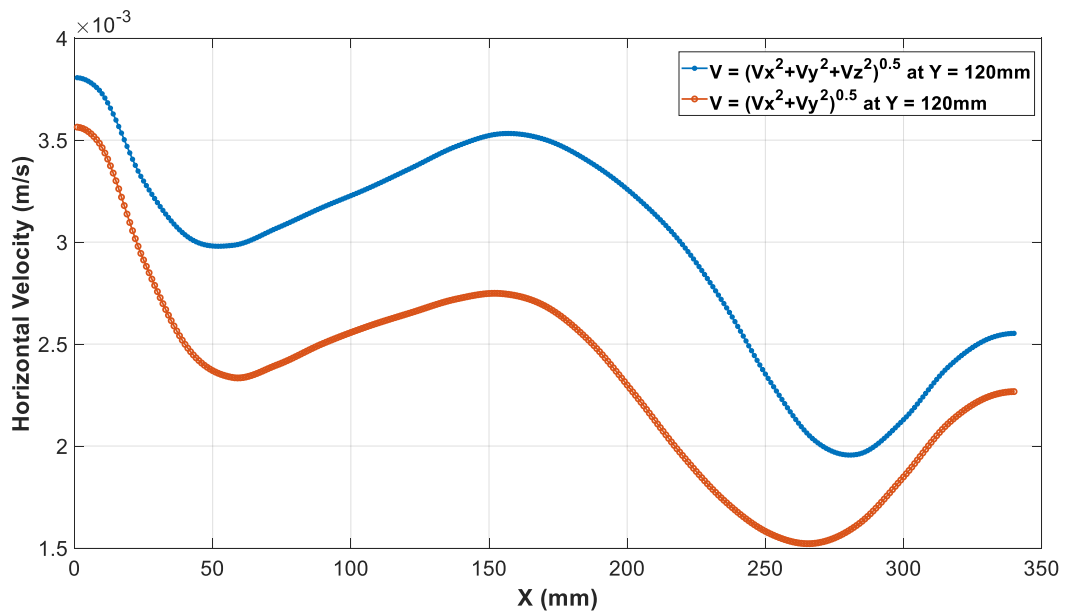


(b)

Figure 4.84: (a) XY plot for vertical velocity magnitude for all three components, (b) XY plot for horizontal velocity magnitude for all three components, at $T_b = 38^\circ\text{C}$.



(a)



(b)

Figure 4.85: (a) Comparison of vertical velocity magnitude for three components and two components, (b) Comparison of horizontal velocity magnitude for three components and two components, at $T_b = 50^\circ\text{C}$.

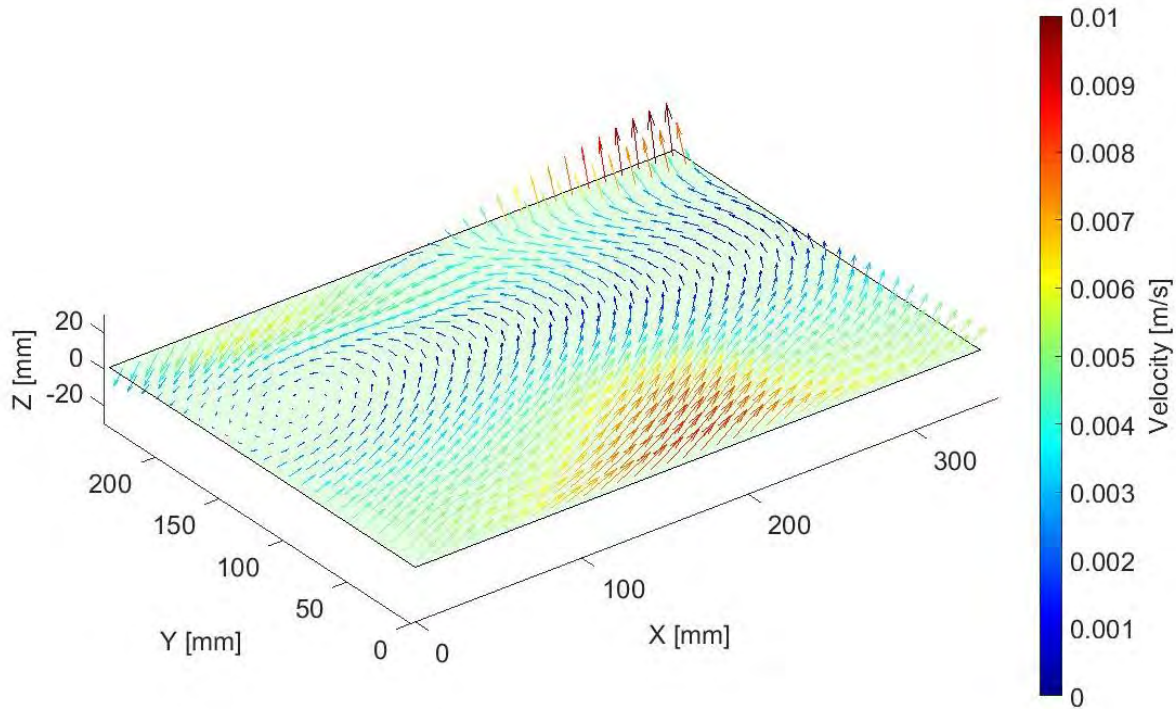
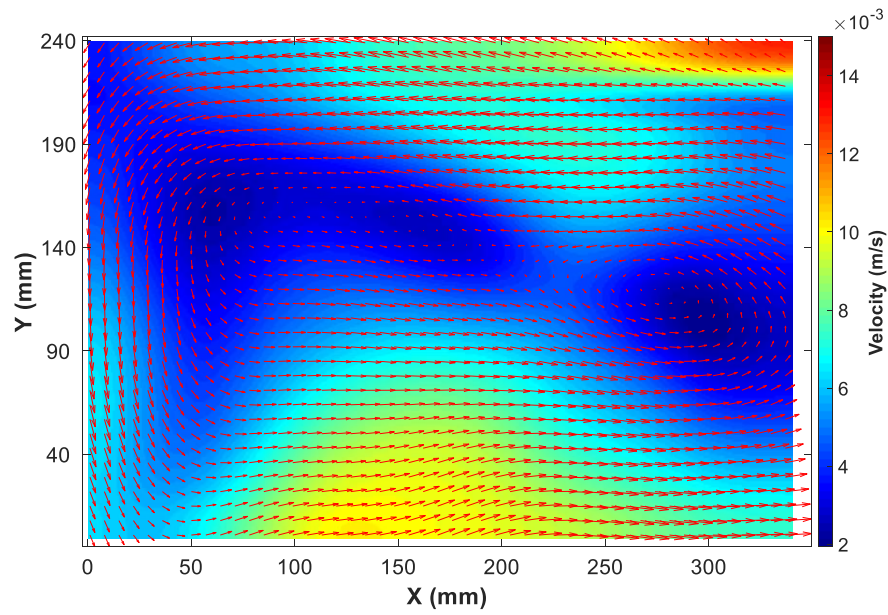


Figure 4.86: 3-D plot for velocity magnitude and direction.

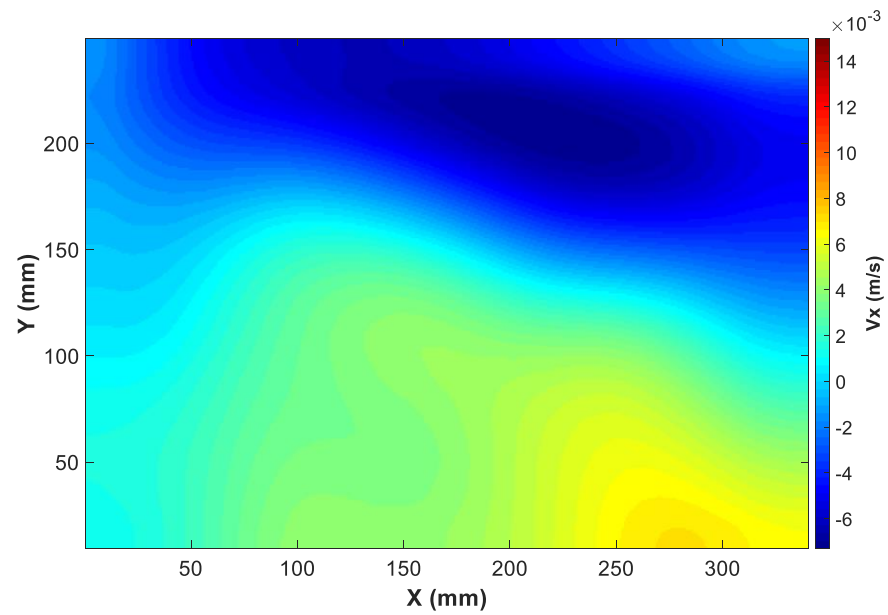
3) Velocity at $T_b = 50^\circ\text{C}$

The investigation is now conducted and discussed at the desirable temperature for the current work, $T_b = 50^\circ\text{C}$. Figure 4.87 shows the velocity magnitude for all three components. At this time, it can be seen clearly in Figure 4.87 (a) that the velocity is higher near the bottom of the tank and near the water surface, with two bigger vortices at the middle of the water tank due to the rise in temperature and surface evaporation, respectively. Hence, the effect of all three components (V_x, V_y, V_z) is included in Figure 4.87 (a). However, Figure 4.87 (b) shows the velocity V_x which is higher in X-direction near the bottom and the surface of the water tank. Interestingly, this higher velocity is positive near the bottom and negative near the surface, which indicates the direction [see vectors' direction in Figure 4.87 (a)]. The positive velocity reaches the middle of the water tank compared to $T_b = 38^\circ\text{C}$, which is mainly due to the rise in temperature. On the other hand, the velocity V_y is shown in Figure 4.87 (c), where the higher values appear at the walls of the water tank,

being either negative or positive, which represents the direction of flow. It is clear that it is higher at this time compared to $T_b = 38^\circ\text{C}$, along with some velocity in the middle of the water tank. In addition, by looking at the velocity V_z in Figure 4.87 (d), a high velocity is shown almost everywhere, such as near the bottom of the water tank, walls, and water surface, being either negative or positive. Hence, as mentioned previously, looking at all three velocity components (V_x , V_y , V_z), the effect of all three can be noticed. V_x and V_z mostly dominate near the bottom and top of the water tank, whereas V_y mostly dominates near the walls of the water tank. This becomes clearer in Figure 4.88 (a) and Figure 4.88 (b), where all three velocity components (V_x , V_y , V_z) along with V are plotted vertically and horizontally, respectively. It can be seen that in Figure 4.88 (a) the velocity V_y has some small effect at higher temperature compared to $T_b = 28^\circ\text{C}$ and $T_b = 38^\circ\text{C}$, whereas in Figure 4.86 (b) it still has the most effect on the velocity magnitude V . Figure 4.89 (a) and Figure 4.89 (b) show the velocity magnitude with and without V_z in vertical and horizontal direction, respectively. As a result, the effect of the velocity V_z on velocity magnitude at this time either in vertical or horizontal direction is clear. To conclude, the velocity V_z has a significant effect on the velocity magnitude either in vertical or horizontal direction, especially at higher temperature. Finally, as can be seen in Figure 4.90 where XY green plane represents the laser sheet. It can be seen some vectors are directed upward and some downward which represent V_z direction. The vectors' direction for V_x and V_y are shown as well along with magnitude.



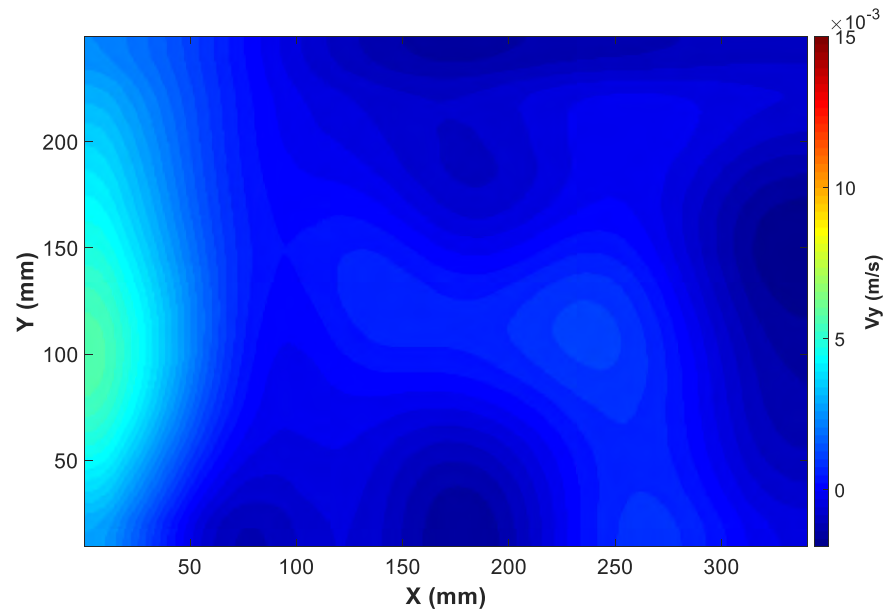
(a)



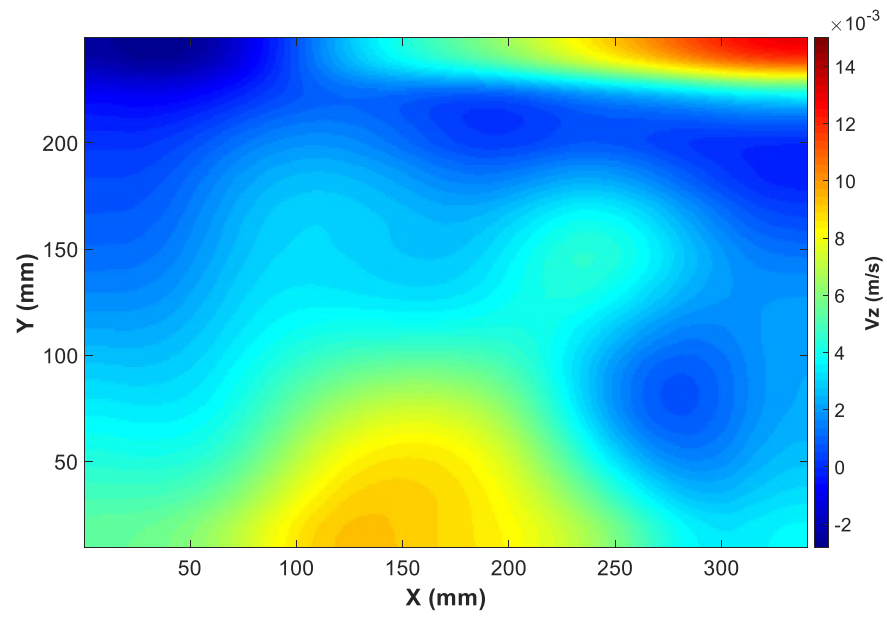
(b)

Figure 4.87: (a) Velocity magnitude for all three components, (b) Velocity V_x , (c) Velocity V_y , (d) Velocity V_z at $T_b = 50^\circ\text{C}$.

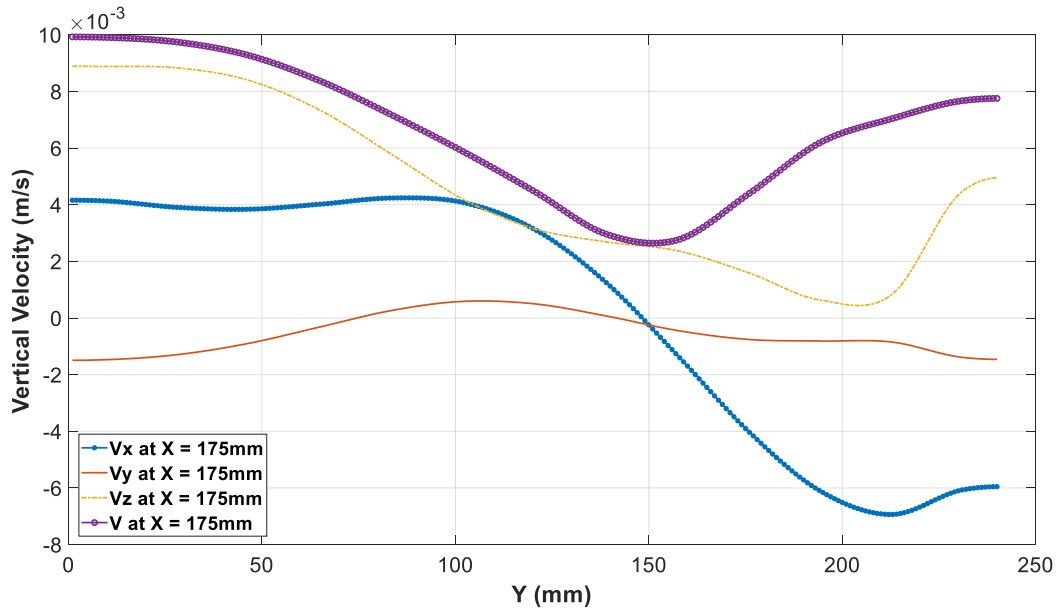
Figure 4.87—continued



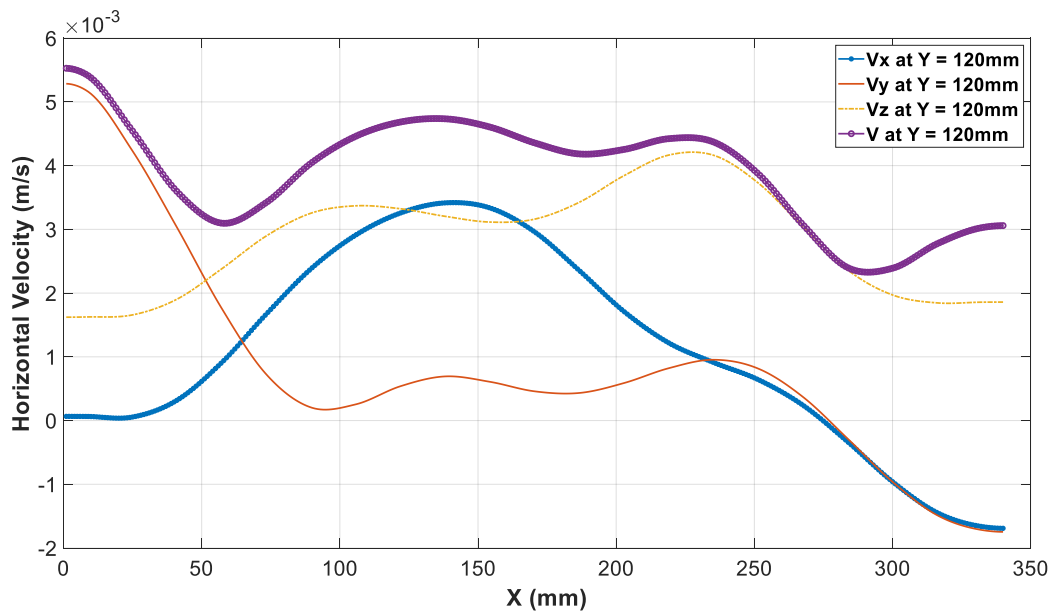
(c)



(d)

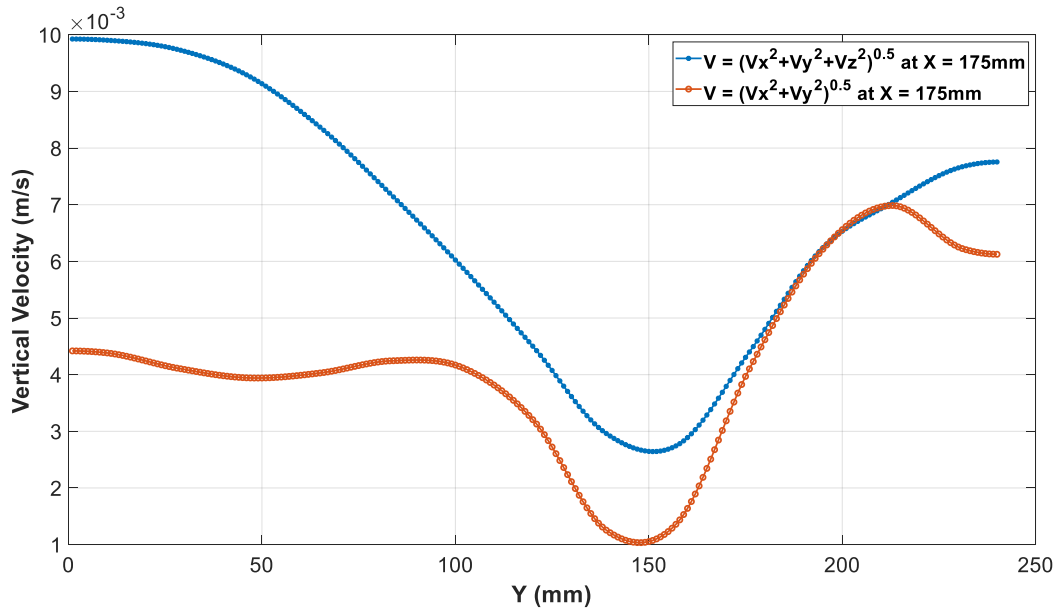


(a)

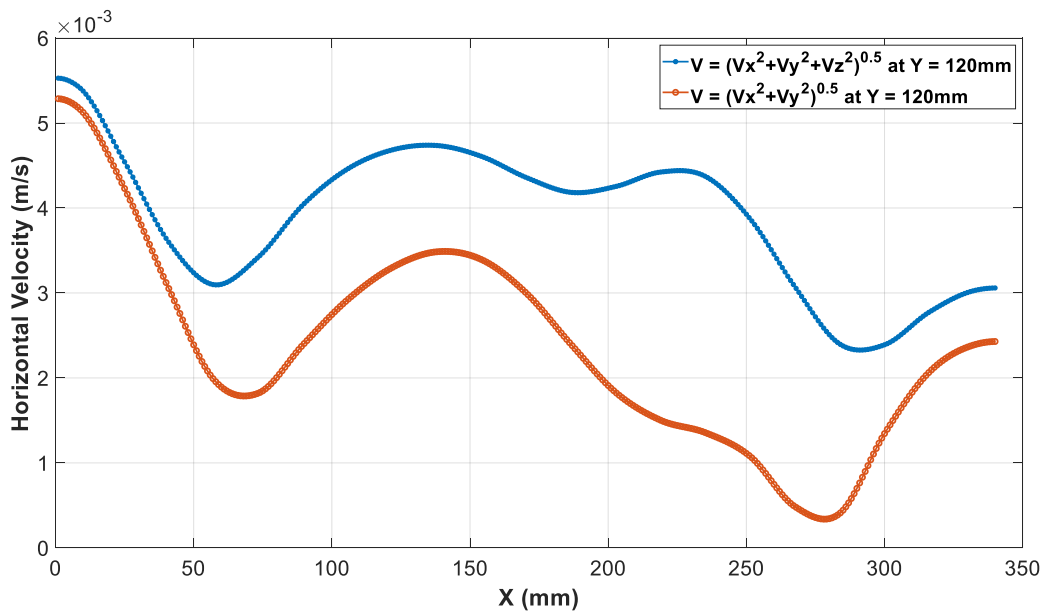


(b)

Figure 4.88: (a) XY plot for vertical velocity magnitude for all three components, (b) XY plot for horizontal velocity magnitude for all three components at $T_b = 50^\circ\text{C}$.



(a)



(b)

Figure 4.89: (a) Comparison of vertical velocity magnitude for three components and two components, (b) Comparison of horizontal velocity magnitude for three components and two components at $T_b = 50^\circ\text{C}$.

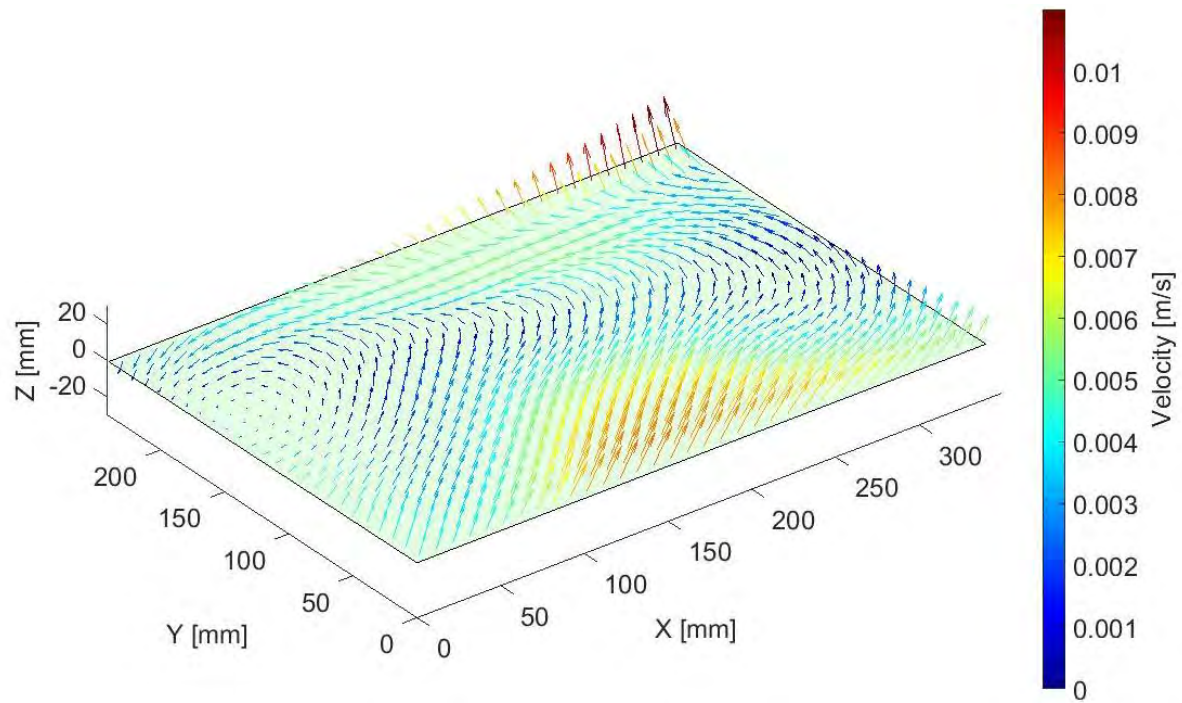


Figure 4.90: 3-D plot for velocity magnitude and direction.

4.5 Uncertainty Analysis

The uncertainties in the results presented here are mainly due to the instrumental uncertainties and the uncertainties introduced in the calculations due to the processing method employed. The measuring devices and their accuracy, along with the ranges of measurements, are listed in Table 4.2.

Table 4.2: The range and accuracy of the measuring devices.

Devices	Range	Accuracy
K-type Thermocouples	0–920°C	0.4°C
Relative Humidity	15%–90%	±3% RH, ±1°C
Digital balance	0–30Kg	±0.1g
Wallace & Tiernan barometer	0–50 Psi	0.066%

4.6 Chapter Conclusion

In this chapter, the experimental work conducted was presented and discussed in detail. The objective of this chapter was to present and discuss the setup and results of the experimental work that was developed in our lab (Fluid Dynamics) at WMU. The experimental work can be divided mainly into four parts. The first part was the study of the evaporation rate along with temperature development. As a result of this first part, a new correlation for free water surface evaporation (Sherwood–Rayleigh relation) was calculated and compared with the previous work. The second part was investigation of the natural convection flow inside the water tank from the side by utilizing particle image velocimetry, in case of free surface evaporation. As a result of this second part, the flow pattern and the statistical properties of the flow inside the water tank were presented. The third part investigated the flow pattern from the top view of the water tank by using particle image velocimetry. Finally, stereo particle image velocimetry (SPIV) was used in order to investigate the third component of the flow pattern and its effect on the velocity magnitude. A comparison between the numerical simulation and the experimental work is presented and discussed in the following chapter.

5. COMPARISON OF NUMERICAL SIMULATION AND EXPERIMENTAL WORK

The objective of this chapter is to compare the results of the numerical simulation and the experimental work carried out in the current work. As already discussed in Chapter 3, the numerical simulation was done at a water depth of 0.24 m along with time and temperature development. Therefore, the experimental results at the same depth ($D = 0.24$ m) are compared to the numerical simulation. The two main factors that affect the flow pattern for free water surface evaporation in the case of natural convection are temperature and velocity. Hence, these two factors are compared and discussed.

5.1 Temperature Comparison

The comparison of temperature development in the water tank for numerical simulation and experimental work versus time is shown in Figure 5.1. Note that the default temperature in ANSYS fluent is 300 K (26.85°C), where the numerical simulation was started at this temperature. In contrast, the temperature for the experimental work was based on the room temperature at the measurement time. As can be seen in Figure 5.1, the comparison of the numerical simulation to the experimental work starts at 300 K (26.85°C). The results agree, except for small discrepancies which can be related to the temperature control at 50°C for the bottom part. However, while the two plots show the same trend of rise in temperature along with time, the experimental work reaches the desirable temperature faster than the numerical simulation by a few seconds.

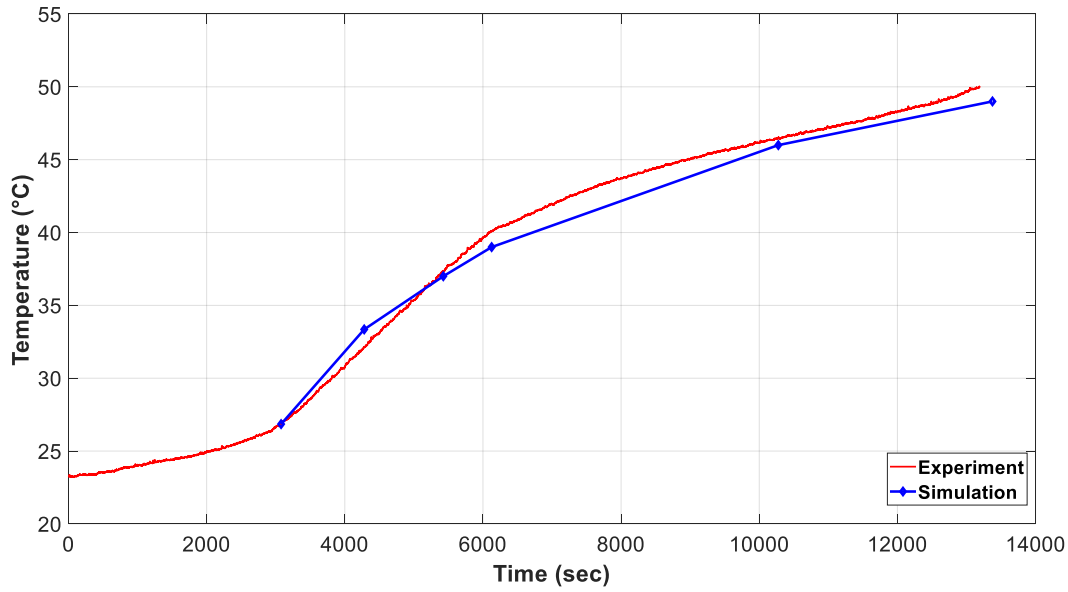


Figure 5.1: The comparison of temperature development in the water tank for numerical simulation and experimental work versus time.

5.2 Velocity Comparison

The comparison of the horizontal velocity near the water–air surface for numerical simulation and experimental work is shown in Figure 5.2. The numerical simulation velocity was exported as a data file to MATLAB. The average velocity at the recorded temperature as discussed in Chapter 3 and Chapter 4 for the numerical simulation and the experimental work, respectively, was then calculated. This average velocity is plotted and compared in Figure 5.2. However, it is clear that the numerical simulation result shows a higher velocity compared to the experimental work, which is reasonable due to some experimental error such as the density of seeding particles. Both plots show a similar trend, where the velocity is higher once it reaches the surface and then starts to flow downward which results in small velocity near the corner. This is clear from Figure 5.3, where the comparison of velocities from both numerical simulation and experimental work is shown.

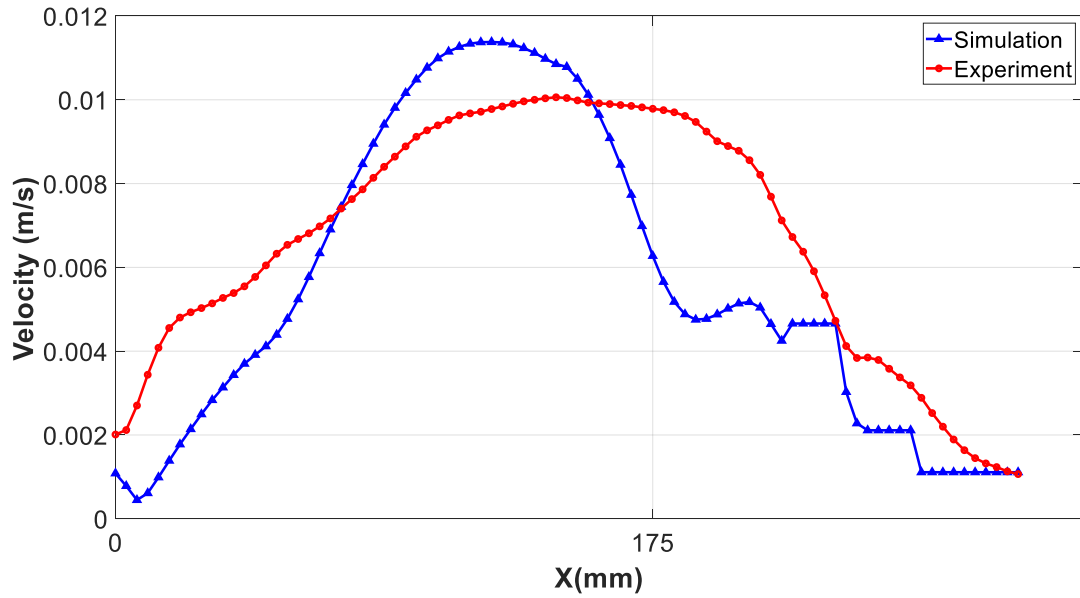


Figure 5.2: The comparison of the horizontal velocity near the water–air surface for numerical simulation and experimental work.

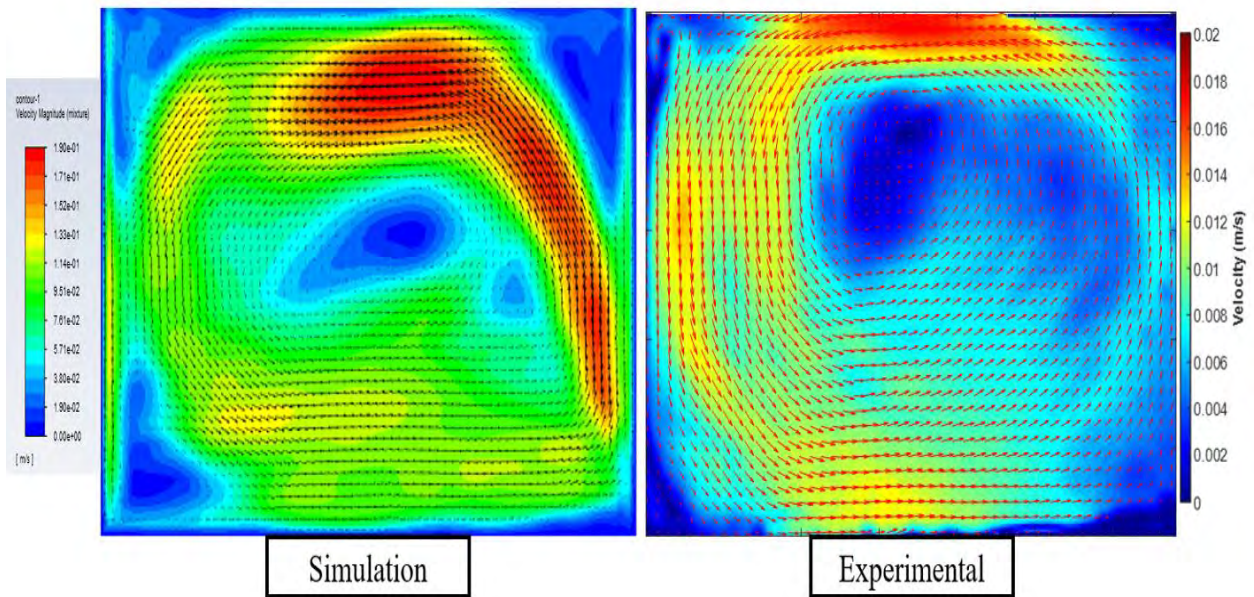


Figure 5.3: The comparison of velocities from both numerical simulation and experimental work.

5.3 Chapter Conclusion

A comparison between the numerical simulation and experimental work was presented and discussed in this chapter. The numerical simulation was done first at a water depth of 0.24 m along with time and temperature development. Therefore, the experimental results at the same depth ($D = 0.24$ m) were compared to the numerical simulation. The two main factors that affect the flow pattern for free water surface evaporation in case of natural convection are temperature and velocity, which were compared and discussed here.

6. CONCLUSION

The current work focused on conducting a comprehensive study experimentally and numerically of free water surface evaporation in case of natural convection, along with its flow pattern from side and top. First, an experiment was conducted to predict Sherwood–Rayleigh correlation for free water surface evaporation in the case of natural convection in the range of $1.4 \times 10^9 < Ra < 1.1 \times 10^{11}$, which is based on measuring the room air temperature, the bulk water temperature, the surface temperature, the room relative humidity, and the mass loss due to evaporation. Further, another experiment was performed utilizing particle image velocimetry (PIV) in order to investigate the flow pattern in case of a free surface undergoing evaporation. This investigation for flow pattern was conducted from the side and top of the water tank. In addition, a two-dimensional (2-D) and three-dimensional (3-D) numerical simulation was carried out to study the flow pattern along with rising temperature. As a part of the numerical simulation, a user-defined function (UDF) code was developed and compiled to investigate the surface evaporation. A comparison followed between the numerical simulation and experimental work, and a discussion. Finally, an experiment was implemented using stereo particle image velocimetry (SPIV) for calculating the third velocity component, wherein the effect of the third component was addressed and discussed, which showed its effect on the flow pattern velocity magnitude.

REFERENCES

- [1] J. P. Holman, *Heat Transfer*, New York: McGraw-Hill, 2010.
- [2] J. C. Berg, A. Acrivos, M. Boudart, "Evaporative convection," *Advances in Chemical Engineering*, vol. 6, pp. 61–124, 1966.
- [3] E. Sartori, "A critical review on equations employed for the calculation of the evaporation rate from free water surfaces," *Solar Energy*, vol. 68, pp. 78–89, 2000.
- [4] E. E. Adams, D. J. Cosler, K. R. Helfrich, "Evaporation from heated water bodies: predicting combined forced plus free convection.," *Water Resources Research*, vol. 26, pp. 25–435, 1990.
- [5] W. Brutsaert, *Evaporation into the Atmosphere*[insert colon here?] *Theory, History, and Applications*, Dordrecht, Holland: Theory, History, and Applications, 1982.
- [6] H. L. Penman, "Natural evaporation from open water, bare soil and grass," *Proc. Roy. Soc.*, vol. A-193, pp. 120–145, 1948.
- [7] M. Taga, T. Matsumoto, T. Ochi, "Studies on membrane viscosity stabilized solar pond," *Solar Energy*, vol. 45, pp. 315–324, 1990.
- [8] D. M. Deaves, I. G. Lines, "The nature and frequency of low wind speed conditions," *Journal of Wind Engineering*, vol. 73, p. 1–29, 1998.
- [9] J. D. Lenters, T. K. Kratz, C. J. Bowser, "Effects of climate variability on lake evaporation: results from a long-term energy budget study of Sparkling Lake, northern Wisconsin (USA)," *Journal of Hydrology*, vol. 308, pp. 168–195, 2005.
- [10] L. Rayleigh, "On convection currents in a horizontal layer of fluid, when the higher temperature is on the under side," *Phil. Mag.*, vol. 32, pp. 529–546, 1916.
- [11] H. Bénard, "Les tourbillons cellulaires dans une nappe liquide," *Rev. Gén. Sci. Pure Appl.*, vol. 11, pp. 1261–1271, 1309–1328, 1900.
- [12] R. J. Goldstein, E. M. Sparrow, D. C. Jones, "Natural convection mass transfer adjacent to horizontal plates," *Int. J. Heat Mass Transfer*, vol. 16, pp. 1025–1035, 1973.
- [13] J. R. Lloyd, W. R. Moran, "Natural convection adjacent to horizontal surface of various planforms," *J. Heat Transfer*, vol. 96, pp. 443–447, 1974.
- [14] E. M. Sparrow, G. K. Kratz, M. J. Schuerger, "Evaporation of water from a horizontal surface by natural convection," *J. Heat Transfer*, vol. 105, pp. 469–475, 1983.

- [15] M. Raffel, C. E. Willert, J. Kompenhans, *Particle Image Velocimetry: A Practical Guide*. Springer Verlag: ISBN 3-540-63683-8, 1998.
- [16] D. B. Barker, M. E. Fourney, "Measuring fluid velocities with speckle patterns," *Optics Letters*, vol. 1, pp. 135–137, 1977.
- [17] T. D. Dudderar, P. G. Simpkins, "Laser speckle photography in a fluid medium," *Nature*, vol. 270, pp. 45–47, 1977.
- [18] R. J. Adrian, "Scattering particle characteristics and their effect on pulsed laser measurements of fluid flow: speckle velocimetry vs. particle image velocimetry," *Applied Optics*, vol. 23, pp. 1690–1691, 1984.
- [19] C. J. D. Pickering, N. A. Halliwell, "Laser speckle photography and particle image velocimetry: photographic film noise," *Applied Optics*, vol. 23, pp. 2961–2969, 1984.
- [20] R. J. Adrian, C. S. Yao, "Pulsed laser technique application to liquid and gaseous flows and the scattering power of seed materials," *Applied Optics*, vol. 24, pp. 44–52, 1985.
- [21] R. J. Adrian, "An image shifting technique to resolve directional ambiguity in double-pulsed velocimetry," *Applied Optics*, vol. 25, pp. 3855–3858, 1986.
- [22] R. D. Keane, R. J. Adrian, "Theory of cross-correlation analysis of PIV images," *Applied Scientific Research*, vol. 49, pp. 191–215, 1992.
- [23] M. Raffel, C. E. Willert, J. Kompenhans, *Particle Image Velocimetry: A Practical Guide*. Heidelberg: Springer, 1998.
- [24] A. Melling, "Tracer particles and seeding for particle image velocimetry," *Meas. Sci. Technol.*, vol. 8, pp. 1406–1416, 1997.
- [25] W. Lauterborn, A. Vogel, "Modern optical techniques in fluid mechanics," *Annu. Rev. Fluid Mech.*, vol. 16, pp. 223–244, 1984.
- [26] A. K. Prasad, "Particle image velocimetry," *Current Science*, vol. 79, pp. 51–60, 2000.
- [27] P. Buchhave, "Particle image velocimetry—status and trends," *Experimental Thermal and Fluid Science*, vol. 5, pp. 586–604, 1992.
- [28] A. Cenedese, A. Paglialunga, "Digital direct analysis of a multiexposed photograph in PIV," *Exp. Fluids*, vol. 8, pp. 273–280, 1990.
- [29] M. Raffel, C. E. Willert, S. T. Wereley, J. Kompenhans, *Particle Image Velocimetry-A Practical Guide*. Springer-Verlag, 2007.

- [30] B. F. Sharpley, L. M. K. Boelter, "Evaporation of water into quiet air from a one foot diameter surface," *Ind. Eng. Chem.*, vol. 30, pp. 1125–1131, 1938.
- [31] L. M. K. Boelter, H. S. Gordon, B. F. Sharpley, "Free evaporation into air of water from a free horizontal quiet surface," *Ind. Eng. Chem.*, vol. 38, pp. 596–600, 1946.
- [32] S. M. Bower, J. R. Saylor, "A study of the Sherwood–Rayleigh relation for water undergoing natural convection-driven evaporation," *International Journal of Heat and Mass Transfer*, vol. 105, pp. 3055–3063, 2009.
- [33] N. Kumara, J. H. Arakerib, "Natural convection driven evaporation from a water surface," *Science Direct*, vol. 15, pp. 108–115, 2015.
- [34] W. Chen, S. Chen, X. Yuan, H. Zhang, B. Liu, K. Yu, "PIV measurement for Rayleigh convection and its effect on mass transfer," *Chinese Journal of Chemical Engineering*, vol. 22, no. 10, pp. 1078–1086, 2014.
- [35] C. Buffone, K. Sefiane, "Controlling evaporative thermocapillary convection using external heating: an experimental investigation," *Experimental Thermal and Fluid Science*, vol. 32, no. 6, pp. 1287–1300, 2008.
- [36] F. Corvaro, M. Paroncini, "Experimental analysis of natural convection in square cavities heated from below with 2D-PIV and holographic interferometry techniques," *Experimental Thermal and Fluid Science*, vol. 31, no. 7, pp. 721–739, 2007.
- [37] H. K. Versteeg, W. Malalasekera, *Computational Fluid Dynamics*. England: Pearson Edu. Ltd, 2007.
- [38] C. E. Brennen, *Fundamentals of Multiphase Flows*. [this appears to be a book, not a journal article] Cambridge University Press, p. 0521 848040, 2005.
- [39] G. B. Wallis, *One-dimensional Two-phase Flow*. New York: McGraw-Hill Book Company, 1969.
- [40] T. B. Jackson, R. Anderson, "A fluid mechanical description of fluidized beds," *I & EC Fundam*, vol. 6, pp. 527–534, 1967.
- [41] R. M. Bowen, *Theory of Mixtures*. New York: A. C. Eringen, 1976.
- [42] ANSYS, "UDF," ANSYS, Inc., 2009.
- [43] Y. Marechal, "The molecular structure of liquid water delivered by absorption spectroscopy in the whole IR region completed with thermodynamics data," *Journal of Molecular Structure*, vol. 1004, pp. 146–155, 2011.

- [44] F. Scarano, "Tomographic PIV: principles and practice," *Meas. Sci. Technol. Top.*, vol. 24, p. 28, 2013.
- [45] A. Melling, "Tracer particles and seeding for particle image velocimetry," *Meas. Sci. Technol.*, vol. 8, pp. 1406–1416, 1997.
- [46] LaVision, Flow Master, Germany: Gottingen, 2016.
- [47] R. J. Adrian, "Twenty years of particle image velocimetry," *Experiments in Fluids*, vol. 39, pp. 159–169, 2005.
- [48] LaVision, FlowMaster, LaVision, 2013.
- [49] O. Törnblom, Introduction course in particle image velocimetry, El. doc., 2004.

APPENDICES

Appendix A (UDF Code)

```

/*****
UDF to apply mass transfer rate from liquid to gas (vapor) phase at the interface
*****/
#include "udf.h"
#include "materials.h"
#include "sg.h"
#include "sg_mphase.h"
#include "flow.h"
#include "mem.h"
#include "metric.h"

#define MW_W 18.0          /*Water molecular weight*/
#define MW_A 29.0          /*air molecular weight*/
#define R 8.314           /*Universal gas constant*/
#define pi 3.14159        /* PI number*/
#define Rho_air 1.22      /*Air density [kg/m3]*/
#define Pwa 7384.94       /*(Pw-Pa) [Pa]*/
#define Va 0              /* Air Velocity [m/s]*/

DEFINE_MASS_TRANSFER(liq_gas_source, c, thread, from_index, from_species_index, to_index,
to_species_index)
{
/***** Declare variables *****/
real b, m_lg, T_cell, P_cell, P_sat;
/*real NV_VEC(G);*/
real X_W, Y_W, Y_A;
real cur_ts;
face_t f;
real D[ND_ND], DX, DY;
int i, pdomain_index, kk;
real ad;
Thread *liq = THREAD_SUB_THREAD(thread, from_index);
Thread *gas = THREAD_SUB_THREAD(thread, to_index);

/***** Define variables *****/
T_cell = C_T(c,thread); /*cell mixture temperature*/
P_cell = C_P(c,thread); /*cell mixture pressure*/
cur_ts = CURRENT_TIMESTEP; /* real time step size (in seconds)*/

m_lg = 0.0;
if (C_VOF(c,liq)!=0 && C_VOF(c,liq)!=1)
{
/* compute saturation pressure for water vapor using polynomial fit */
P_sat = 0.638780966e-8*pow(T_cell-273.15,6)+0.203886313e-5*pow(T_cell-273.15,5) +
0.30224699e-3*pow(T_cell-273.15,4) + \
0.265027242e-1*pow(T_cell-273.15,3) +1.43053301*pow(T_cell-273.15,2)+
44.3986062*(T_cell-273.15) + 611.176750;

/* calculate molar fraction X_W from mass fraction Y_W */
Y_W = C_VOF(c,gas)*C_R(c,gas)/ (C_VOF(c,liq)*C_R(c,liq) + C_VOF(c,gas)*C_R(c,gas)
+ (1-C_VOF(c,liq)-C_VOF(c,gas))*Rho_air);
Y_A = (1-C_VOF(c,liq)-C_VOF(c,gas))*Rho_air)/ (C_VOF(c,liq)*C_R(c,liq) +
C_VOF(c,gas)*C_R(c,gas) + (1-C_VOF(c,liq)-C_VOF(c,gas))*Rho_air);
}
}

```

```

X_W = (Y_W/MW_W)/((Y_W/MW_W) + (Y_A/MW_A));

/**** Compute the interfacial area density ****/

DX=0.0;
DY=0.0;
  for (kk=0; kk<4; kk++)
  {
    F_AREA(D,C_FACE(c,thread,kk), C_FACE_THREAD(c,thread,kk));
    if (ABS(D[0])>DX)
      DX = ABS(D[0]);
    if (ABS(D[1])>DY)
      DY = ABS(D[1]);
  }
/* Message("mesh dimensions are [%g,%g]!\n",DX,DY);*/
ad = DX/(DY*DX); /* calculate interfacial area density*/
/*Message("AD = %f\n",ad);*/
/**** Computed the area density ad = length of interface / area of cell ****/
/* Compute m_lg*/
if (P_sat - (P_cell*X_W) > 0.0)
{
  b = 1.22 - 0.19*Va + 0.038*Va*Va;
  m_lg = cur_ts * ad * (1e-6)*(20.56+27.21*Va+6.92*Va*Va)*pow(0.001*Pwa,b);
}

}

return (m_lg); /* return value of mass transfer rate */

}

```

Appendix B (LabVIEW Window)

